



National Library
of Canada

Acquisitions and
Bibliographic Services Branch

395 Wellington Street
Ottawa, Ontario
K1A 0N4

Bibliothèque nationale
du Canada

Direction des acquisitions et
des services bibliographiques

395, rue Wellington
Ottawa (Ontario)
K1A 0N4

Your file *Votre référence*

Our file *Notre référence*

NOTICE

The quality of this microform is heavily dependent upon the quality of the original thesis submitted for microfilming. Every effort has been made to ensure the highest quality of reproduction possible.

If pages are missing, contact the university which granted the degree.

Some pages may have indistinct print especially if the original pages were typed with a poor typewriter ribbon or if the university sent us an inferior photocopy.

Reproduction in full or in part of this microform is governed by the Canadian Copyright Act, R.S.C. 1970, c. C-30, and subsequent amendments.

AVIS

La qualité de cette microforme dépend grandement de la qualité de la thèse soumise au microfilmage. Nous avons tout fait pour assurer une qualité supérieure de reproduction.

S'il manque des pages, veuillez communiquer avec l'université qui a conféré le grade.

La qualité d'impression de certaines pages peut laisser à désirer, surtout si les pages originales ont été dactylographiées à l'aide d'un ruban usé ou si l'université nous a fait parvenir une photocopie de qualité inférieure.

La reproduction, même partielle, de cette microforme est soumise à la Loi canadienne sur le droit d'auteur, SRC 1970, c. C-30, et ses amendements subséquents.

Canada

University of Alberta

Concentration Fluctuations
and their
Probability Distributions
in Laboratory Plumes



by

Brian William Zelt

A thesis
submitted to the Faculty of Graduate Studies and Research
in partial fulfilment of the requirements for the degree of
Doctor of Philosophy

Department of Mechanical Engineering

Edmonton, Alberta
Fall 1992



National Library
of Canada

Acquisitions and
Bibliographic Services Branch

395 Wellington Street
Ottawa, Ontario
K1A 0N4

Bibliothèque nationale
du Canada

Direction des acquisitions et
des services bibliographiques

395, rue Wellington
Ottawa (Ontario)
K1A 0N4

Your file *Votre référence*

Our file *Notre référence*

The author has granted an irrevocable non-exclusive licence allowing the National Library of Canada to reproduce, loan, distribute or sell copies of his/her thesis by any means and in any form or format, making this thesis available to interested persons.

L'auteur a accordé une licence irrévocable et non exclusive permettant à la Bibliothèque nationale du Canada de reproduire, prêter, distribuer ou vendre des copies de sa thèse de quelque manière et sous quelque forme que ce soit pour mettre des exemplaires de cette thèse à la disposition des personnes intéressées.

The author retains ownership of the copyright in his/her thesis. Neither the thesis nor substantial extracts from it may be printed or otherwise reproduced without his/her permission.

L'auteur conserve la propriété du droit d'auteur qui protège sa thèse. Ni la thèse ni des extraits substantiels de celle-ci ne doivent être imprimés ou autrement reproduits sans son autorisation.

ISBN 0-315-77421-5

Canada

University of Alberta
Release Form

Name of Author:

Brian William Zelt

Title of Thesis:

**Concentration Fluctuations
and their
Probability Distributions
in Laboratory Plumes**

Degree:

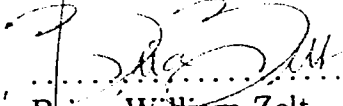
Doctor of Philosophy


Year this degree granted:

Fall 1992

Permission is hereby granted to the University of Alberta Library to reproduce single copies of this thesis and to lend or sell such copies for private, scholarly, or scientific research purposes only.

The author reserves all other publication and other rights in association with the copyright in the thesis, and except as hereinbefore provided neither the thesis nor any substantial portion thereof may be printed or otherwise reproduced in any material form whatever without the author's prior written permission.


.....
Brian William Zelt
17409-95 Street, Apt.14,
Edmonton, Alberta,
Canada
T5Z 2B2

Date : 

The University of Alberta
Faculty of Graduate Studies and Research

The undersigned certify that they have read, and recommend to the Faculty of
Graduate Studies and Research for acceptance, a thesis entitled

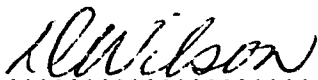
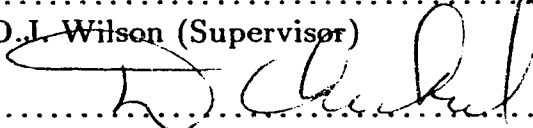
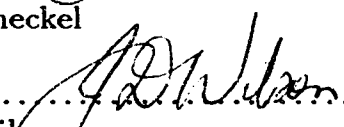
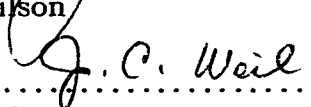
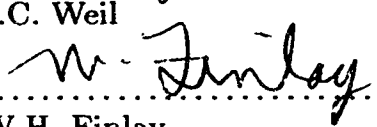
**Concentration Fluctuations
and their
Probability Distributions
in Laboratory Plumes**

submitted by

Brian William Zelt

in partial fulfilment of the requirements for the degree of

Doctor of Philosophy.


.....
D.L. Wilson (Supervisor)

.....
M.D. Checkel

.....
J.W. Wilson

.....
J.C. Weil

.....
W.H. Finlay

Date : June 1, 1952

This work is dedicated to my wife.

Abstract

This study investigates the dispersion of a neutrally buoyant saline tracer in a water channel boundary layer to determine what probability distribution is best for use in dispersion modelling. Using four different source configurations, the clipped-Normal, Gamma and log-Normal probability distributions were found to represent the evolution of the plume concentration with down wind distance. The down wind locations where the concentration distributions changed were found to be a function of plume spread size. The distribution of the temporal derivative of the concentration fluctuations was also observed to change with down wind distance. The concentration derivative is well represented by an Exponential frequency distribution, but may be represented by a Gaussian frequency distribution for small plume spread sizes.

To predict the parameters for the probability distributions, a Gaussian cross wind higher order moment model is developed. The higher order total moments of concentration, rather than central moments, are predicted by the model. The first four total moments are observed to have Gaussian cross wind profiles. A spectral model is developed to predict temporal derivative variances of the concentration fluctuations.

The exceedance times theory by Rice (1944-45), which was recently investigated by Kristensen, Weil and Wyngaard (1988), is used to create an exceedance statistics model for an intermittent plume. The exceedance theory is developed using the Exponential and Gaussian distributions for the derivative distribution. Observed exceedance statistics are well represented by the intermittent plume model using the concentration probability distribution and higher order total moment models.

Acknowledgments

First I would like to thank my wife, parents and friends, to whom I am grateful, for their support, advice and friendship.

My thanks are personally extended to Wayne Pittman whose presence was often required to kick start electronic equipment in a way only he could do. I am grateful to him for finishing my data collection tasks which became overwhelming in time consumption. Thank you also to Iain Walker and Cliff Johnston for their help in data collection. Moral support by Iain Walker, Alan Wilson and Andrew Hay throughout this project was invaluable.

An editor's job is often thankless, but I thank mine despite the norm — especially my wife, Dr. Peter Janele and my Uncle Norm Folkers.

I wish to thank the faculty of Mechanical Engineering staff and shop technicians for their assistance throughout the years.

Finally, I wish to thank my supervisor, Dr. David Wilson, for his guidance, insight and patience which helped me bring this study to a close. Graduate committee members, Dr. John Wilson and Dr. David Checkel, helped focus my ambitious quest down to a mere seven year study.

Contents

Abstract	v
Acknowledgements	vi
Nomenclature	xxviii
Chapter 1	
Introduction	1
1.1 Study Outline	3
1.2 Brief Overview of Related Research	3
Chapter 2	
Experimental Apparatus	5
2.1 Overview of Experimental Apparatus	5
2.2 Laser Doppler Anemometer	7
2.3 Concentration Measurement	9
2.4 Concentration Sources	10
Chapter 3	
Water Channel Velocity Field	14
3.1 The Turbulent Boundary Layer	14
3.1.1 Boundary Layer Development	15
3.1.2 Cross-Wind Uniformity of the Boundary Layer	16
3.2 Fluctuation Time Scale Calculations	21

Contents

Abstract

Acknowledgements

Nomenclature

Chapter 1

Introduction

1.1 Study Outline

1.2 Brief Overview of Related Research

Chapter 2

Experimental Apparatus

2.1 Overview of Experimental Apparatus

5.1.7	Weibull Distribution	106
5.1.8	Beta Distribution	107
5.2	Probability Distribution Truncation	108
5.3	PDF Parameter Estimation	111
5.4	Concentration Probability Distributions	112
5.4.1	Plume Centre-line Probability Distributions	115
5.4.2	Overview	134
5.5	Probability Distributions of Concentration Derivatives	134
5.6	Intermittency Prediction	149
5.7	Conclusions	155

Chapter 6

Concentration Fluctuation Statistics	156
6.1 Description of a Similarity Theory	156
6.1.1 Budget Equations for \bar{c} and $\overline{c'^2}$	157
6.1.2 Budget Equation for $\overline{c'^2}$	158
6.1.3 Budget Equation for $\overline{c'^3}$	158
6.1.4 Budget Equation for $\overline{c'^4}$	159
6.1.5 Closure Model	160
6.1.6 Gaussian Solution for Higher Order Moments	160
6.2 Plume Moment Standard Deviations	171
6.2.1 Profile Normalization	175
6.2.2 Plume Standard Deviations of Higher Order Moments	176
6.3 Intermittency Threshold	181
6.4 Similarity Theory Application to Cross-Wind Profiles	181
6.5 Centre-line Evolution of the Concentration Total Moments	187
6.6 Concentration Spectra	187
6.6.1 Relating k_e to Λ_f	192
6.6.2 Von Kármán General Spectrum for Scalar Fluctuations	193

6.6.3	Relating k_o to Λ_c	194
6.6.4	Viscous Convective Range	195
6.6.5	Relating k_o to Λ_c in Batchelor Range	196
6.6.6	Observed Concentration Spectra	196
6.6.7	Concentration Integral Time Scales	201
6.6.8	Lagrangian-Eulerian Time Scale Ratio	201
6.7	Concentration Microscales	204
6.8	Concentration Derivatives	211
6.9	Effect of Probe Response Time on Observed Variance	215
6.10	Conclusions	216

Chapter 7

Inter-Event time PDFs	219
7.1 Theory	220
7.1.1 Threshold Crossing Probabilities	221
7.1.2 Joint PDF Approach	224
7.2 Threshold Crossing Intermittent Signals	226
7.2.1 Normal PDF for the Concentration Derivative	229
7.2.2 Exponential PDF for the Concentration Derivative	230
7.3 Average Number of Exceedances	234
7.4 Average Duration of Excursions Above a Threshold	240
7.5 Down-Wind Predictions of N^+ and T^+	250
7.6 Exceedance Time PDFs	250
7.7 Threshold Crossing Scale	256
7.8 Conclusions	262

Chapter 8

Conclusions	263
8.1 Theoretical/Analytical/Computational	264
8.2 Observed and Predicted Concentration Fluctuation Statistics	266
8.3 Theoretical Developments	267
8.4 Unresolved Issues	268

References	269
Appendix A	
Velocity Analysis Procedures	281
A.1 Position Change Due to Change in Index of Refraction	281
A.2 Spectral Estimation Techniques	285
A.3 Velocity Bias Correction Techniques	285
A.4 Fringe Bias Correction Techniques	289
A.5 Detecting and Eliminating Stray Velocity Processing Errors	290
A.6 Velocity Shear Stress Measurements	293
A.7 Turbulence Time Scale of Vertical Velocity Component	294
Appendix B	
Concentration Analysis Procedures	297
B.1 Digital Filtering	297
B.2 Derivative measurement	300
B.2.1 Newton-Gregory Approximating Function	301
B.2.2 FIR Filter Approximating Function	302
B.3 Moment Analysis	314
B.4 Determining Profile Cross-Wind Spreads	316
B.5 Normalization of Profile Moments	319
B.6 Probability and Threshold Crossing Distributions	321
B.7 Concentration Intermittency Threshold Level	322
Appendix C	
One-Dimensional Energy Spectrum	326
Appendix D	
Conductivity Detector Design	328
D.1 Recent Developments in Conductivity Probes	328
D.1.1 Design of the Micro-Probe	329

D.1.2	Design of the Aspirated Probe	329
D.1.3	Design of a New Stable Probe	331
D.2	Probe Stability	332
D.2.1	Plating Procedure	332
D.3	Calibration	334
D.3.1	Static Calibration	334
D.3.2	Describe Non-Linear Calibration System	335
D.3.3	Temperature Sensitivity Correction	338
D.4	Construction Procedure of the Micro-Probe	341
 Appendix E		
Gamma PDF for Derivative		344
 Appendix F		
Data Set Statistics		346
 Appendix G		
Gamma PDF Singularity		348
 Appendix H		
Higher Order Moment Gaussian Solutions		351
H.1	One Dimensional Solution	352
H.2	Axisymmetric Solution	354
H.3	Order of magnitude Analysis for ϵ_n	357

List of Tables

3.1	Comparison of concentration integral time scales calculated by FFT spectra and by equation (3.7), for concentration data sets from a jet/plume source at $x/h_s = 20$	30
3.2	Typical Characteristic Values from the Atmosphere and from the Water Channel Simulation	69
3.3	Boundary Layer Simulation Parameters in 3300:1 Scale	70
4.1	Typical Probe Time Responses with a 1.0 mm Flushing Length	89
5.1	Maximum Likelihood Estimates of Statistical Parameters	112
5.2	Comparison of Goodness of Fit Results for Various Methods for a Single Selected Probability Distribution	115
B.1	Coefficients for a Fourth Order FIR filter Differentiator	307
B.2	Ratio of the Derivative Approximation for the Hanning and Triangle Window for White Noise spectrum, $\sigma_{\dot{c},true}^2/\sigma_{\dot{c},obs}^2$	309
B.3	Ratio of the Derivative Approximation for the Hanning and Triangle Window for a k^{-1} spectrum, $\sigma_{\dot{c},true}^2/\sigma_{\dot{c},obs}^2$, for 125 Hz cutoff and $\Lambda_c=1$ cm.	310
D.1	Effects of temperature on conductivity measurements	339
F.1	Vertical Jet Source— Micro-Probe Data	346
F.2	Jet/Plume Source	347
F.3	Iso-Kinetic Source	347

F.4 Iso-Kinetic Facing Up Stream Source	347
---	-----

List of Figures

2.1	Schematic of Water Channel Experimental Apparatus	6
2.2	A schematic representation of the Laser Doppler Anemometer system.	8
2.3	Schematic of the sources used in the study	12
2.4	The excess jet velocity of the jet/plume source with down-wind distance.	13
3.1	Schematic of the boundary layer trip used to excite a well developed velocity profile.	17
3.2	Variation of the mean velocity profile with distance down-stream. . .	18
3.3	Variation of the intensity of velocity fluctuations profile with distance down-stream.	19
3.4	Variation of the integral scales of velocity fluctuations profile with distance down-stream.	20
3.5	Cross-wind mean velocity profiles showing homogeneity of water channel flow. The mean concentration profile is overlaid on the figure to show the width of the channel that is covered by the dispersing plume.	22
3.6	Cross wind profiles of turbulent intensity showing deviation of intensity. The mean concentration profile is overlaid on the figure to show the width of the channel that is covered by the dispersing plume.	23
3.7	Cross wind profiles of integral length scale of turbulence showing relative sameness across the water channel and growth with downstream distance.	24
3.8	Effect of time averaging on the sample variance normalized by the non-averaged variance for a Markov spectrum.	26

3.9	Effect of time averaging window size on time scale calculation.	28
3.10	Comparison of velocity fluctuation time scales in the water channel boundary layer, at the source location, using the FFT method and the time-averaged variance method. The FFT method shows less scatter but wrong values near the ground, whereas the variance method contains considerable scatter.	29
3.11	Distribution of value of $0.5(w'/\bar{u})$, which has been proposed to equal the ratio of the Lagrangian time scale to the Eulerian length scale. . .	32
3.12	Log-law fit to velocity profiles showing the effect of displacement height (top) and a comparison of the log-law fit to a power-law fit (bottom). . .	34
3.13	Distribution of shear stress in the boundary layer with a linear fit in the wall region to determine the wall shear stress $\tau_w/\rho = u_*^2$	36
3.14	Horizontal distribution of the turbulent shear stress in the boundary layer at the source height.	37
3.15	Schematic of height measurement and roughness elements.	39
3.16	Profiles of the vertical velocity fluctuations and the horizontal velocity fluctuations as a ratio of the friction velocity.	44
3.17	Profiles of the vertical velocity fluctuations as a ratio of the along wind velocity fluctuations.	45
3.18	Schematic drawing of two plumes illustrating the importance of the integral length scales in the dispersion of a plume in comparison to the source size. A large length scale to size ratio causes the plume to meander much more than a small ratio.	47
3.19	Profiles of along wind integral length scales of turbulence close to the ground.	48
3.20	Variation of the along wind integral length scale with height in the lower third of the boundary layer showing a power-law fit with exponent, $n = 0.64$	49
3.21	Profiles of the vertical time scale of turbulence fluctuations.	51
3.22	Comparison of the along wind time scale to the vertical time scale. . .	52
3.23	Horizontal profile of the ratio of the along wind time scale to the vertical time scale showing a constant ratio of $T_x/T_z = 1.7$	53

3.24	Vertical profile of the ratio of the along wind time scale to the vertical time scale showing a constant ratio of $T_x/T_z = 1.7$	55
3.25	The one-dimensional energy spectrum of the velocity fluctuations at $z/h_s = 0.2$ showing that the water channel simulation may be equally represented by an inertial sub-range model or a Markov model.	56
3.26	The one-dimensional energy spectrum of the velocity fluctuations at $z/h_s = 1.0$ showing that the water channel simulation may be equally represented by an inertial sub-range model or a Markov model.	57
3.27	The one-dimensional energy spectrum of the velocity fluctuations at $z/h_s = 2.0$ showing that the water channel simulation may be equally represented by an inertial sub-range model or a Markov model.	58
3.28	The one-dimensional energy spectrum of the velocity fluctuations at $z/h_s = 3.0$ showing that the water channel simulation may be equally represented by an inertial sub-range model or a Markov model.	59
3.29	The turbulent kinetic energy dissipation-rate profile for the rough wall boundary layer in the water channel, using (3.38).	63
3.30	Variation of the Taylor microscale, λ_u , in the boundary layer at the source location, using (3.46).	64
3.31	Ratio of the integral time scale to the Taylor microscale in the water channel boundary layer. Λ_u is determined by direct measurement and λ_u is determined using (3.46).	65
3.32	Profile of the probability distribution of velocity in the water channel showing that the velocity distribution is Gaussian, irrespective of the distribution of the first derivative and the underlying stochastic process.	67
4.1	Schematic of the probe dropping apparatus.	73
4.2	Example of a probe drop response output showing the near exponential response for a micro-probe.	74
4.3	Schematic of the probe close contact experiment.	75
4.4	Concentration time series signal showing the effects of probe response induced lag. Data is for the jet/plume source using the glass-micro probes.	77

4.5	Illustration of modelling a concentration time series as a step function and as a ramp function.	79
4.6	Simulated time series of a first order response probe step deconvolution illustrating the ability to reconstruct the original time series. Noise was added to the first order response to simulate a real signal.	80
4.7	Step response deconvolution of a measured concentration signal showing an adequate reconstruction of the supposed true concentration signal. Data is for the jet/plume source using the glass-micro probes.	82
4.8	Simulated time series of a first order response probe ramp deconvolution illustrating the ability to reconstruct the original time series. Noise was added to the first order response to simulate a real signal. Note the large amount of ringing due to the comparative time constants of the process and the probe.	83
4.9	Ramp response deconvolution of a measured concentration signal showing a very noisy reconstruction of the supposed true concentration signal. Data is for the jet/plume source using the glass-micro probes.	84
4.10	Spectra of the step response deconvolution and ramp response deconvolution. Data is for the jet/plume source using the glass-micro probes.	86
4.11	A typical concentration time series signal for the jet/plume source using the glass micro-probe with step response deconvolution and digital filtering.	87
4.12	A typical concentration time series signal for the jet/plume source using the glass micro-probe with ramp response deconvolution and digital filtering.	88
4.13	Example of the effect of: a) Energy spectrum, uncorrected for probe response. b) Energy spectrum corrected for probe response showing in the increased noise in high frequency ranges. c) Energy spectrum corrected and digitally filtered energy spectra. Data is for the jet/plume source using the glass micro-probe.	90
5.1	The clipped-Normal probability distribution is created from the Normal distribution by truncation of negative values and renormalization of the positive values so that the area under the curve is unity.	100

5.2	The transformation of the clipped-Normal distribution to the one parameter Exponential distribution when the intermittency varies from near unity to near zero.	103
5.3	Effect of PDF truncation on the theoretical fit of a PDF model to a data set.	110
5.4	Comparison of PDF fit by the maximum likelihood procedure (a) and the moment estimator procedure (b), showing that different conclusions may be drawn about which PDF model better fits the data.	113
5.5	Example of goodness of fit test results on a typical observed probability distribution, far down-wind of the source.	116
5.6	Example of goodness of fit test results on a typical observed probability distribution, near the source.	117
5.7	Evolution of the PDF on the centre-line of the jet/plume source. Data not normalized (top) and normalized by the conditional mean value (bottom).	119
5.8	Evolution of the PDF on the centre-line of the iso-kinetic source. Data not normalized (top) and normalized by the conditional mean value (bottom).	120
5.9	Evolution of the PDF on the centre-line of the vertical ground level source. Data not normalized (top) and normalized by the conditional mean value (bottom).	121
5.10	Evolution of the PDF on the centre-line of the up-stream facing iso-kinetic source. Data not normalized (top) and normalized by the conditional mean value (bottom).	122
5.11	Truncated centre-line PDF (top) and truncated CCDF (bottom) of the jet/plume source at a location of $\sigma_y/\Lambda = 0.05$	123
5.12	Truncated centre-line PDF (top) and truncated CCDF (bottom) of the jet/plume source at a location of $\sigma_y/\Lambda = 0.10$	124
5.13	Truncated centre-line PDF (top) and truncated CCDF (bottom) of the jet/plume source at a location of $\sigma_y/\Lambda = 0.13$	125
5.14	Truncated centre-line PDF (top) and truncated CCDF (bottom) of the jet/plume source at a location of $\sigma_y/\Lambda = 0.20$	126

5.15	Truncated centre-line PDF (top) and truncated CCDF (bottom) of the jet/plume source at a location of $\sigma_y/\Lambda = 0.36$	127
5.16	Truncated centre-line PDF (top) and truncated CCDF (bottom) of the jet/plume source at a location of $\sigma_y/\Lambda = 0.63$	128
5.17	Truncated centre-line PDF (top) and truncated CCDF (bottom) of the jet/plume source at a location of $\sigma_y/\Lambda = 0.95$	129
5.18	PDF fit results for the jet/plume source in the water channel boundary layer.	130
5.19	PDF fit results for the iso-kinetic source in the water channel boundary layer.	131
5.20	PDF fit results for the vertical jet source in the water channel boundary layer.	132
5.21	PDF fit results for the up-stream facing iso-kinetic source in the water channel boundary layer.	133
5.22	PDF of the derivative of concentration fluctuations using a 4 th order windowed FIR derivative.	136
5.23	PDF of the derivative of concentration fluctuations using a 20 th order windowed FIR derivative.	137
5.24	Down-wind evolution of the PDF of the derivative of concentration fluctuations using a 20 th order FIR derivative for the jet/plume source.	139
5.25	Down-wind evolution of the PDF of the derivative of concentration fluctuations using a 20 th order FIR derivative for the jet/plume source.	140
5.26	Down-wind evolution of the PDF of the derivative of concentration fluctuations using a 20 th order FIR derivative for the iso-kinetic source.	141
5.27	Down-wind evolution of the PDF of the derivative of concentration fluctuations using a 20 th order FIR derivative for the iso-kinetic source.	142
5.28	Down-wind evolution of the PDF of the derivative of concentration fluctuations using a 20 th order FIR derivative for the up-wind facing iso-kinetic source.	143
5.29	Down-wind evolution of the PDF of the derivative of concentration fluctuations using a 20 th order FIR derivative for the up-wind facing iso-kinetic source.	144

5.30	Down-wind evolution of the PDF of the derivative of concentration fluctuations using a 20 th order FIR derivative for the vertical jet source.	145
5.31	Cross-wind evolution of the PDF of the derivative of concentration fluctuations using a 20 th order FIR derivative close to the jet/plume source.	146
5.32	Cross-wind evolution of the PDF of the derivative of concentration fluctuations using a 20 th order FIR derivative far down-wind of the jet/plume source.	147
5.33	Profile of the predicted intermittency using the Gamma, log-Normal and clipped-Normal probability distributions and experimental higher order moments, for the jet/plume source at locations $x/h_s = 1.2$ and $x/h_s = 2.4$	150
5.34	A typical profile of the predicted intermittency using the Gamma, log-Normal and clipped-Normal probability distributions and experimental higher order moments, for the jet/plume source at locations $x/h_s = 4.4$ and $x/h_s = 9.4$	151
5.35	A typical profile of the predicted intermittency using the Gamma, log-Normal and clipped-Normal probability distributions and experimental higher order moments, for the jet/plume source at locations $x/h_s = 19.4$ and $x/h_s = 30.0$	152
5.36	The centre-line evolution of the predicted intermittency using the PDF models for the jet/plume source and the iso-kinetic source.	153
5.37	The centre-line evolution of the predicted intermittency using the PDF models for the vertical jet source and the up-stream facing iso-kinetic source.	154
6.1	Gaussian fit to a typical set of the first four higher order moments for the jet/plume source. Each moment is normalized by its fit maximum centre-line value and its fit standard deviation.	163
6.2	Normalized higher order moments with a Gaussian fit for the jet/plume source. Each moment is normalized by its fit maximum centre-line value and its fit standard deviation.	164

6.3	Normalized higher order moments with a Gaussian fit for the jet/plume source. Each moment is normalized by its fit maximum centre-line value and its fit standard deviation.	165
6.4	Normalized higher order moments with a Gaussian fit for the iso-kinetic source. Each moment is normalized by its fit maximum centre-line value and its fit standard deviation.	166
6.5	Normalized higher order moments with a Gaussian fit for the iso-kinetic source. Each moment is normalized by its fit maximum centre-line value and its fit standard deviation.	167
6.6	Normalized higher order moments with a Gaussian fit for the up-wind facing iso-kinetic source. Each moment is normalized by its fit maximum centre-line value and its fit standard deviation.	168
6.7	Normalized higher order moments with a Gaussian fit for the up-wind facing iso-kinetic source. Each moment is normalized by its fit maximum centre-line value and its fit standard deviation.	169
6.8	Normalized higher order moments with a Gaussian fit for the vertical jet source. Each moment is normalized by its fit maximum centre-line value and its fit standard deviation.	170
6.9	Jet/Plume source (top) and Iso-Kinetic source (bottom) plume spread evolution with down-wind distance.	172
6.10	Vertical ejecting ground level source (top) and up-stream facing iso-kinetic source (bottom) plume spread evolution with down-wind distance.	173
6.11	Jet/Plume source (top) and Iso-Kinetic source (bottom) higher order plume standard deviations ratio of $\sigma_{y,n}/\sigma_{y,1}$ evolution with down-wind distance. Solid lines are (6.68).	179
6.12	Vertical jet source (top) and up-stream facing horizontal source (bottom) higher order plume standard deviations ratio of $\sigma_{y,n}/\sigma_{y,1}$ evolution with down-wind distance. Solid lines are (6.68).	180
6.13	The effect of threshold level on the observed intermittency in the far fringes of the plume showing that a threshold level equivalent to $8 \sigma_{noise}$ is required.	182

6.14	The variance of the concentration fluctuations for the data for the jet/plume source in Figure 6.1, (top), and for data near the up-stream facing iso-kinetic source (bottom).	183
6.15	The conditional mean concentration for the jet/plume source data in Figure 6.1. Similarity and probability models used to determine the theory lines.	185
6.16	The intensity of concentration fluctuations for the data for the jet/plume source in Figure 6.1, (top), and the conditional intensity for the same set of data, (bottom).	186
6.17	The centre-line evolution of the higher order total moments for the jet/plume source (top) and the iso-kinetic source (bottom).	188
6.18	The centre-line evolution of the higher order total moments for the vertical jet source (top) and the up-stream facing iso-kinetic source (bottom).	189
6.19	Influence of the concentration molecular diffusivity on the concentration fluctuation spectrum for large wave numbers.	197
6.20	Spectrum of the concentration fluctuations in the water channel. Slope for large k is k^{-1}	200
6.21	The concentration integral time scales across the jet/plume source at the same location as Figure 6.1.	202
6.22	The evolution of the concentration integral time scale ratio, for all the sources, with down-wind distance.	203
6.23	Comparison of the prediction of the ratio of the concentration integral time scale to Eulerian time scale by Sykes (1984).	205
6.24	Microscale of concentration fluctuations on the plume centre-line for all the sources.	208
6.25	Conditional microscale of concentration fluctuations on the plume centre-line for all the sources.	209
6.26	Cross-wind variation of conditional microscale of concentration fluctuations for the jet/plume source, ($\lambda_u \approx 1.15$ cm)	210

6.27	Power spectrum of the derivative of concentration fluctuations showing the exceptional agreement between the data, and the theoretical spectrum. The theory takes into account probe filtering and the filtering effects of the derivative procedure.	213
6.28	Comparison of the derivatives predicted by spectral techniques compared to the derivative determined numerically from the data.	214
6.29	The effect of detector response on the concentration variance for a Markov spectrum and a Batchelor Range k^{-1} spectrum.	217
7.1	Illustration of the threshold crossing problem with the nomenclature used to describe it.	222
7.2	Schematic illustration of $T^+ \propto 1/f_p(c)$ near zero threshold level compared to the conditional mean.	233
7.3	Cross-wind distribution of the number of exceedances per second for the jet/plume source at a threshold level of $c^*/\overline{c_p} = 1.0$. Normal PDF derivative (top) and total model (bottom).	235
7.4	Cross-wind distribution of the number of exceedances per second for the jet/plume source at a threshold level of $c^*/\overline{c_p} = 1.0$. Conditional model (top) and similarity model (bottom).	236
7.5	Cross-wind distribution of the number of exceedances per second for the jet/plume source at a threshold level of $c^*/\overline{c_p} = 0.2$ (left) and $c^*/\overline{c_p} = 0.5$ (right). Prediction using the total moments (top) and by the similarity theory (bottom). Symbols as per Figure 7.3	238
7.6	Cross-wind distribution of the number of exceedances per second for the jet/plume source at a threshold level of $c^*/\overline{c_p} = 2.0$ (left) and $c^*/\overline{c_p} = 5.0$ (right). Prediction using the total moments (top) and by the similarity theory (bottom). Symbols as per Figure 7.3	239
7.7	Down-wind distribution of the number of exceedances per second for a threshold level of $c^*/\overline{c_p} = 1$ and data for all sources. Prediction using the total moments.	241
7.8	Cross-wind distribution of the average duration of exceedances for the jet/plume source at a threshold level of $c^*/\overline{c_p} = 1$. Normal PDF derivative (top) and total model (bottom).	242

7.9	Cross-wind distribution of the average duration of exceedances for the jet/plume source at a threshold level of $c^*/\bar{c}_p = 1$. Conditional model (top) and similarity model (bottom).	243
7.10	Cross-wind distribution of the average duration of exceedances for the jet/plume source at a threshold level of $c^*/\bar{c}_p = 0.2$ (left) and $c^*/\bar{c}_p = 0.5$ (right). Prediction using the total moments (top) and by the similarity theory (bottom). Symbols as per Figure 7.3	245
7.11	Cross-wind distribution of the average duration of exceedances for the jet/plume source at a threshold level of $c^*/\bar{c}_p = 2.0$ (left) and $c^*/\bar{c}_p = 5.0$ (right). Prediction using the total moments (top) and by the similarity theory (bottom). Symbols as per Figure 7.3	246
7.12	Down-wind distribution of the average duration of exceedances for a threshold level of $c^*/\bar{c}_p = 0$ and data for all sources. Prediction using total moments.	247
7.13	Down-wind distribution of the average duration of exceedances for a threshold level of $c^*/\bar{c}_p = 1$ and data for all sources. T^+ determined using total moments.	248
7.14	Down-wind distribution of the average duration of exceedances for a threshold level of $c^*/\bar{c}_p = 5$ and data for all sources. T^+ determined using total moments.	249
7.15	Down-wind distribution of N^+ and T^+ for the jet/plume source at a threshold level of $c^*/\bar{c}_p = 0.1$. N^+ and T^+ determined using total moments.	251
7.16	Down-wind distribution of N^+ and T^+ for the jet/plume source at a threshold level of $c^*/\bar{c}_p = 0.2$. N^+ and T^+ determined using total moments.	252
7.17	Down-wind distribution of N^+ and T^+ for the jet/plume source at a threshold level of $c^*/\bar{c}_p = 1$. N^+ and T^+ determined using total moments.	253
7.18	Down-wind distribution of N^+ and T^+ for the jet/plume source at a threshold level of $c^*/\bar{c}_p = 2$. N^+ and T^+ determined using total moments.	254

7.19	Down-wind distribution of N^+ and T^+ for the jet/plume source at a threshold level of $c^*/\overline{c_p} = 5$. $nplus$ and T^+ determined using total moments.	255
7.20	The distribution of the exceedance times, T^+ , above a threshold for the jet/plume source with a threshold of $c^*/\overline{c_p} = 0$ (top) and $c^*/\overline{c_p} = 0.2$ (bottom).	257
7.21	The distribution of the exceedance times, T^+ , above a threshold for the jet/plume source with a threshold of $c^*/\overline{c_p} = 1$ (top) and $c^*/\overline{c_p} = 2$ (bottom).	258
7.22	The distribution of the exceedance times, T^+ , above a threshold for the jet/plume source with a threshold of $c^*/\overline{c_p} = 5$ (top) and $c^*/\overline{c_p} = 10$ (bottom).	259
7.23	The cross-wind variation of the crossing scale ratio for the jet/plume source (top) and cross-wind profiles at the same plume size locations for all sources (bottom).	261
A.1	Correcting the apparent LDA crossing point for refraction angles into the water channel.	283
A.2	Schematic illustrating the velocity bias in laser Doppler measurements.	287
A.3	Schematic showing how fringe bias error occur.	291
A.4	Example of stray points recorded by the LDA counter processor. Data collected at $x=1000$ mm from the source at the source height.	292
A.5	Estimation of the variation of the time scales of velocity fluctuations when rotating the laser optics through 90 degrees using an ellipse.	296
B.1	Positive skew error caused by the first order, backward difference approximation of the first derivative for the concentration data set. Data is jet/plume source at $x/h_s = 4.4$, $y/\sigma_y = 0$ at the source height.	303
B.2	Negligible skew error for second order, central difference approximation of the first derivative for the concentration data set. Data is jet/plume source at $x/h_s = 4.4$, $y/\sigma_y = 0$ at the source height.	304
B.3	4 th order Hanning window derivative approximation time series, showing the accurate derivative behaviour, but inaccurate magnitudes.	311

B.4	20 th order Hanning window derivative approximation time series, showing the ringing due to Gibb's phenomenon.	312
B.5	Amplitude response of the ideal FIR differentiator using a Hanning window for increasing order of the derivative approximation.	313
B.6	Threshold times determined by linearly interpolation between data sample end points.	323
B.7	Schematic representation of how the background noise level is used to form a tracer concentration threshold level.	325
D.1	Schematic of three conductivity probes; the two-wire probe developed by Bara (1985), the single electrode micro probe and the single electrode aspirated probe.	330
D.2	Micro-probe electroplating circuit design.	333
D.3	Effective resistance of a probe in a conducting solution.	336
D.4	Effect of temperature on the measured conductivity relative to a reference temperature using equation (D.16) (top). Relative fractional error of temperature compensation using a reduced number of coefficients with respect to the complete Hewitt equation (D.16). (bottom)	340

Nomenclature

A	a constant in the $-5/3$ inertial subrange model, $A = 1.7$.	E_1	the one sided, one dimensional energy spectrum, $[x^2 \text{ s}]$
c	concentration, $[\text{g/l}]$	$\mathcal{F}(x)$	is a function of x
\dot{c}	temporal derivative of concentration, $[\text{g/l/s}]$	$f()$	probability density distribution function, PDF
\bar{c}, C	mean concentration, $[\text{g/l}]$	$F()$	cumulative probability density function, CDF
c^*	concentration threshold level, $[\text{g/l}]$	$F'()$	complementary cumulative probability density function, CCDF
$\overline{c^n}$	time average of the n^{th} zero based moment of concentration, $[(\text{g/l})^n]$	f_s	sample rate, $[\text{Hz}]$
$\overline{c_p^n}$	time average of the n^{th} zero based moment of conditional concentration, $[(\text{g/l})^n]$	f_o	$f_s/2$, cutoff frequency, $[\text{Hz}]$
\mathcal{D}	molecular diffusivity, $[\text{cm}^2/\text{s}]$	h_r	height of the roughness elements, $[\text{mm}]$
d	the log-law displacement thickness, $[\text{mm}]$	h_s	source height $[\text{mm}]$
Δt	sample rate, $[\text{s}]$	H	approximate boundary layer height $[\text{mm}]$
E	the one sided, three dimensional spectral energy density, $[x^2 \text{ s}]$	i^2, i_p^2	concentration fluctuation intensities for the total concentration moments and for the conditional concentration moments

i_u^2, i_v^2, i_w^2	turbulence intensity for the along-wind velocity fluctuations, cross-wind fluctuations and vertical fluctuations.
k_s	equivalent sand grain roughness, [cm]
k_1	the one dimensional wave number, [1/cm]
K	eddy transport coefficient
L	a large length scale, [cm]
ℓ_d	diffusive length scale based on the one dimensional
n	power-law exponent
N^+	number of exceedances of c^* per unit time diffusion equation
\mathcal{P}	production energy, [cm ³ /s ²]
Re_k	roughness Reynold's number
Re	Reynold's number
SF	scale factor for lengths between the water channel boundary layer and the atmospheric boundary layer.
t	time, [s]
T	integral time scale, [s]
T	sample time, [s]

T^+	time duration of an event above c^* , [s]
T^-	time duration of an event below c^* , [s]
T_R	return time, interval time between positive crossings of c^* , [s]
T_e	exposure time to a concentration, [s]
u, v, w	velocity in the along-wind, cross-stream and vertical, [cm/s]
u', v', w'	fluctuation velocity components in the along-wind, cross-stream and vertical, [cm/s]
U, V, W	mean velocity in the along-wind, cross-stream and vertical directions, [cm/s]
U_H	along-wind velocity at the boundary layer height, [cm/s]
u_*	friction velocity, [cm/s]
u_s	characteristic fluctuating component, [cm/s]
U_s	characteristic mean velocity component, [cm/s]
x, y, z	distance in the along-wind, cross-wind and vertical directions, [mm]

z_o roughness height defined
log-law velocity profile,
[mm]

Greek

β ratio of Lagrangian to
Eulerian length scales

$\delta_x(a)$ dirac delta function of
variable x at location a .

δ_y plume half width,
 $= 2\sqrt{\ln(2)}\sigma_y$, [mm]

η Kolmogorov micro-scale,
[cm]

ϵ dissipation energy, [cm³/s²]

γ intermittency, the fraction
of time the concentration
signal is above zero

$\Gamma()$ the gamma function

γ_1 first shape factor, or
skewness

γ_2 second shape factor, or
kurtosis

κ von Kármán constant

λ Taylor micro scale, [cm]

Λ integral length scale, [cm]

Λ_p effective concentration
probe length scale, [cm]

μ'_n zero based, (total), n^{th}
moment of a PDF model

μ_n central n^{th} moment of a
PDF model

ν kinematic viscosity,
[cm²/s]

ω_i weighting function

π 3.14159..

ρ fluid density, [cm³/s]

σ_x^2 variance of the turbulent
quantity x . [mm]

σ_y^2 variance of the plume
profile about the plume
centroid, [mm]

σ_u^2 variance of the along-wind
velocity fluctuations,
[(cm/s)²]

τ_d dissipation time, [s]

τ_w shear stress at the wall

τ_p probe time response

Subscripts

atmos pertaining to the
atmosphere

a averaged or smoothed
component, flat window
average of data samples

E Eulerian

eff effective or measured
component

L	Lagrangian
model	pertaining to the water channel model
o	center-line or maximum value
p	a conditional value, signal when a concentration signal is present
s	characteristic value
u, v, w	Eulerian velocity components, along-wind, cross-wind and vertical
x, y, z	Eulerian reference components, along-wind, cross-wind and vertical

Chapter 1

Introduction

In the past few years interest in turbulent dispersion modelling has grown. Part of the reason for this is increased industrial development and especially the increase in development of the refining of oil and natural gas resources. In Alberta, approximately one sixth of the producing gas wells contain large amounts of toxic hydrogen sulphide; some as high as 90% by volume. Due to these high concentrations of toxic gases, government agencies and refining industries have a special interest in turbulent plume dispersion for public and worker safety reasons. A recent accidental release, the 1982 Lodgepole release, near Drayton Valley, Alberta, has brought safety concerns to the public. These concerns are currently sparking interest in the ability to perform more careful analyses of how well the down-wind concentrations from accidental or planned releases can be determined. A more accurate knowledge of the possible fluctuations of the concentration levels is now required. Most importantly, knowledge of what the peak concentrations could be down-wind of a release source, and the probability of them occurring is necessary.

Because of the random nature of turbulence and concentration fluctuations, the mean concentration profile predictions are insufficient to fully describe the risk of exposure down-wind of toxic gas releases. Therefore, the higher order moments of concentration, which describe the concentration fluctuations, need to be estimated to better understand exposure risks. The higher order moments can be used to determine the parameters of a probability distribution model. The probability density distribution of concentration fluctuations is a more practical model as a mathematical description. Whereas the mean concentration profile has been extensively and quite successfully modelled mathematically, the higher order moments are less so, and the probability density distributions are even less so. However, given its importance in model development, a probability density distribution description of a dispersing plume is imperative.

The frequency of periods above or below a concentration threshold value, provides information that may be used to determine the risk of exposure of a down-wind receptor. The time between threshold crossings statistics and time to return to a concentration value are two statistics that may be determined once a well defined probability model is developed. Because the underlying mathematics for the exceedance time statistics have not been solved, the expected form of the exceedance distributions is not known. However, physical modelling bypasses the solving of the equations and allows quantitative models to be developed based on the observed statistics and the underlying physics.

The development of a practical model for use in risk analysis calculations therefore requires knowledge of the probability distribution of the concentration fluctuations. The statistics required by such a model must be predicted by analysis of the concentration fluctuations, which may be achieved by modelling the higher order moments. The probability distribution model may then be applied to determine exceedance and return time probabilities. Each step is an important development in the formation of a hazard assessment model.

This thesis uses experimental data collected in a laboratory water channel boundary layer to determine what probability distribution is best for use in dispersion modelling. To predict the necessary parameters for the probability distribution, a higher order moment model is developed, (in the cross-wind direction only), and a spectral model is developed to predict temporal derivative variances of the concentration fluctuations. These models are used to expand the applications of the exceedance times theory, (Rice 1944-45, recently investigated by Kristensen, Weil and Wyngaard, 1988), to create an exceedance statistics model for an intermittent plume. These three developments are important steps towards understanding concentration fluctuations.

This study investigates the dispersion of a neutrally buoyant saline tracer in a water channel boundary layer. A high momentum jet source is the primary test case, for which models of the cross-wind variation of concentration fluctuations, and probability distributions will be modelled. Because source configurations can play an important role in the development of the concentration fluctuation statistics, a vertical ground level jet, an iso-kinetic injection and an up-wind facing "iso-kinetic" source configuration are also used to compare and contrast the results. The strength of this study lies in the fact that these comparisons can be made using a stationary boundary layer and a consistent-quality data set.

1.1 Study Outline

The research in this study is presented in eight chapters.

Chapter 2: The experimental apparatus is described and a description of the collected data set is provided. The different source configurations are described.

Chapter 3: The water channel velocity boundary layer is investigated using measurements from a laser doppler anemometer.

Chapter 4: The analysis methods used to analyze the conductivity detector output are described. A method for correcting for instrument time response is developed.

Chapter 5: The evolution of the probability distributions down-wind of four saline tracer sources is investigated. Simple engineering probability models are fit to the distributions. The evolution of the concentration time derivative probability distribution is also investigated.

Chapter 6: A similarity model is developed for the budget of the higher order moments of concentration. A generalization of the Von Kármán spectrum is developed for use with k^{-n} data, and specifically the k^{-1} convective-dissipation range. The spectrum is used to determine the variance of the concentration time derivative.

Chapter 7: The recent analysis by Kristensen, Weil and Wyngaard (1988), is expanded to predict the exceedance statistics of an intermittent plume. The exceedance frequency and the time duration of events above a threshold are determined using the water channel boundary layer data.

Chapter 8: The results and findings are concluded. Topics for further study are suggested.

1.2 Brief Overview of Related Research

Barry (1977) has often been quoted as having said that it was unlikely that a single probability distribution could be used to represent (for all sources, all locations and all flows) the dispersion process. The possibility of using a single best fit probability distribution when different sources are considered has not been investigated using a consistent set of data. Furthermore, probability distribution profile observations in

the literature are typically sparsely represented; a result of insufficient data sample times of atmospheric data sets which suffer from non-stationary conditions. These analyses are inadequate if peak concentrations are to be represented accurately.

To apply an observed probability distribution to other applications, the parameters of the distribution must be predictable. For intermittent plumes, a two parameter probability distribution requires the first three concentration moments. Models exist for the first two moments, (Sawford, 1986; Sykes, 1986; Wilson, Robins, and Fackrell, 1985), which predict the concentration second total moment or the variance. Alternatively, only the first two moments are required if the intermittency is also known. However, models for intermittency are not found in the literature. Lagrangian stochastic particle tracking modelling may be used to predict the mean and variance. (Durbin, 1980; Sawford, 1982), but these models apply to homogeneous turbulence, (so far, and not boundary layer turbulence) and are computationally too intensive for rapid engineering calculations.

Exceedance theory is based on the time intervals of the Eulerian stochastic concentration fluctuation process. Rice (1944-45) pioneered the theories for the mean exceedance statistics which are in use today. The Fokker-Planck-Kolmogorov equation, which governs the exceedance statistics, remains unsolved, (Roberts, 1988). The theory by Rice (1944-45) has been applied to atmospheric turbulence by Panofsky and Dutton (1984). Kristensen, Weil and Wyngaard (1988) have applied this theory to a non-intermittent plume. Their application assumed a Gamma concentration distribution and a Normal concentration derivative distribution.

Further discussions of the literature related to this study are presented in the chapters to follow.

Chapter 2

Experimental Apparatus

2.1 Overview of Experimental Apparatus

The range of experimental apparatus used in the present study, and the technical expertise required to design, operate and repair the equipment was diverse. The major components of the study apparatus are illustrated in Figure 2.1. The water channel, or flume, was a recirculating system with a total volume of approximately 4300 litres. The flow rate was controlled by regulating the flow rate through the pumps in the return lines. The depth was controlled by varying the height of a weir gate at the down-stream end of the channel. The settling tank at the head of the channel contained filter screens and flow straighteners which ensured that no pump generated turbulence was introduced into the test section. The water channel floor was covered with *Lego* base plate to form a uniform roughness. In the inlet of the test section was a boundary layer trip constructed of *Lego* building blocks. This is discussed in section 3.1.1.

The tracer was a neutrally-buoyant salt-water-ethanol solution, (Bara, 1985). The source salt concentration was 50 g/l with a flow rate of 2.0 ml/s. The tracer was released into the water channel using a 23 litre tank which was pressurized to approximately 25 psig. The flow rate of the tracer was monitored using a rotameter and controlled with a micro-needle valve. Flexible tubing connected the tracer supply to one of the four sources studied.

Velocity statistics were measured with a Laser Doppler Anemometer, (LDA). An LSI-11/23 mini-computer collected the data from the LDA tracker processor and analyzed the data into a form that was acceptable to plot. Assembly language and Fortran programs were intermixed in a CPU time sharing program format to create an interactive, automated data acquisition system.

Concentration detectors developed by Bara (1985) were not suitable for the measurements planned for the present study, so new detectors were developed. These efforts are described in Chapter 4 and Appendix D.

2.2 Laser Doppler Anemometer

Velocity data sets were collected using a single component Laser Doppler Anemometer system, hereafter LDA. The system developed for the present study is shown in Figure 2.2.

The system originally included a manual traversing system, and manual analogue data reading from a tracker signal processor. The system was redesigned, so that the traversing was computer controlled in the vertical direction, (y), and the cross-stream direction, (z), and manual in the stream-wise direction, (x). A computer controlled data acquisition system collected analogue data from the tracker processor and analyzed the data. Since data sample rates from the LDA were inherently random, with random waiting periods between data points, the data acquisition system was designed to analyze the incoming data during the waiting periods. Upon completion of the specified time average, the analyzed time series was available for plotting. Later when a counter processor was acquired for LDA use, a greater sample rate was achieved and the asynchronous analysis was no longer possible with the computer being used. The system was then redesigned for direct storage of the data to disk, hard or floppy, for later analysis by dedicated data analysis programs. This off-line analysis allowed data to be re-analyzed in different ways (e.g. spectral or time series analysis) and proved to be more useful.

The LDA was operated in back scatter mode, so that the optics both deflected the laser beams and collected the scattered light. The laser was a 16 mW Helium-Neon. Bragg cell frequency shifting was implemented to increase the signal data rate, to prevent fringe bias errors (discussed in Appendix A) and to ensure a positive velocity reading. A beam expander was also used to enhance the signal quality and to reduce the measurement volume.

The water channel was initially seeded using $0.5\mu\text{m}$ silicon particles. An alternative seeding, titanium particles, was later found to produce a higher particle density at less cost.

The limitation of the single component LDA system was its inability to determine the cross-wind velocity statistics. The present study is an investigation of the cross-wind profiles of the plume statistics which are influenced by the cross-wind intensity, v'/\bar{v} and the cross-wind integral length scale, Λ_v . However, based on the regular

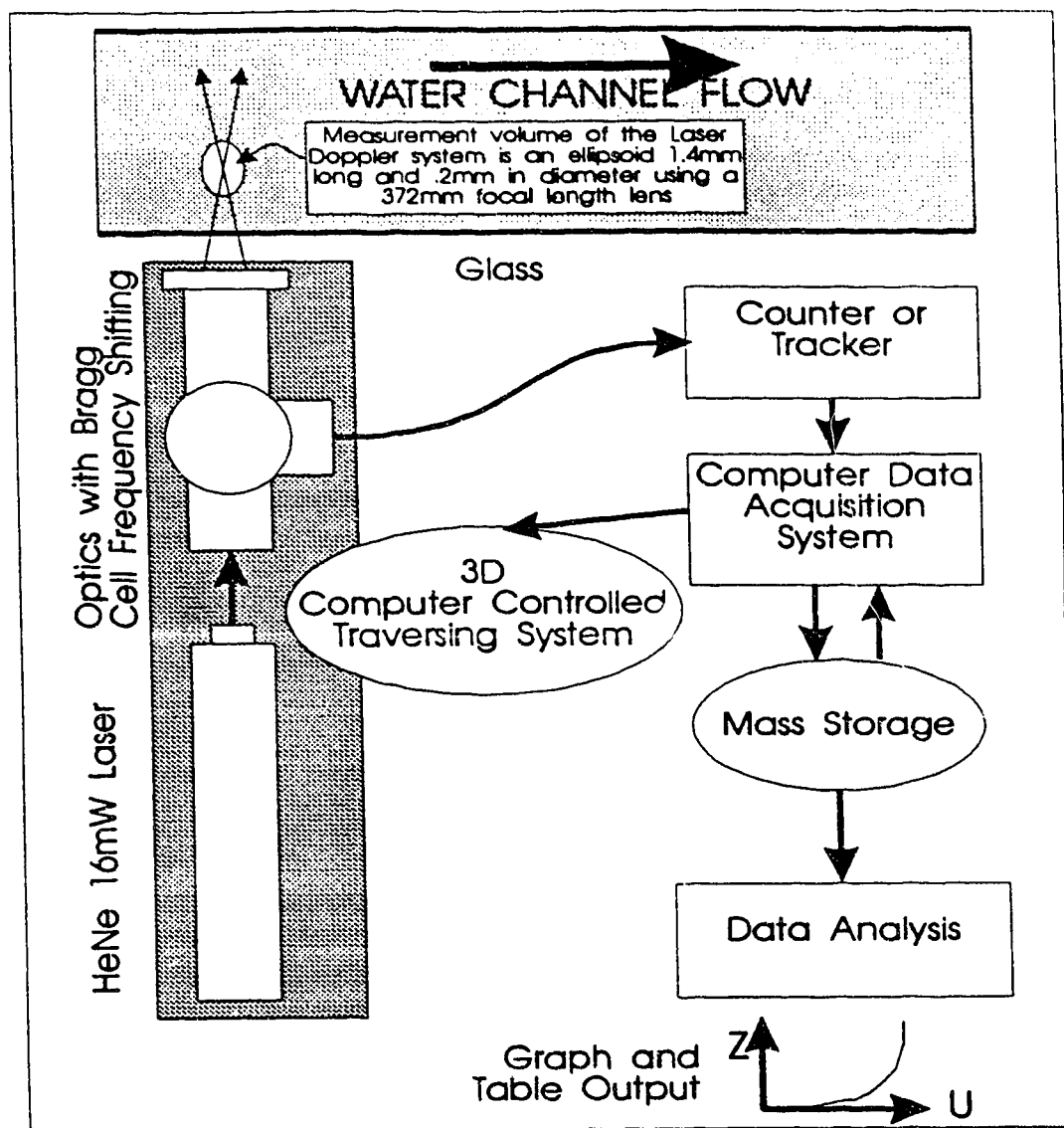


Figure 2.2: A schematic representation of the Laser Doppler Anemometer system.

nature of the observed down-wind component statistics and vertical component statistics, the unknown cross-wind component could be assumed to be proportional. Therefore, the concentration statistics were scaled with along-wind velocity statistics, which were a substitute for the unknown cross-wind velocity statistics.

With the acquisition of a *counter type* LDA signal processor, many of the velocity measurements were repeated to provide more accurate turbulence statistics. The author began the process of re-collecting the data, which was taken over by others under the supervision of the author. The data collection followed the experimental techniques and used the data acquisition computer programs developed by the author. The LDA data acquisition system was automated, and required, almost, only the positioning of the LDA and starting the data collection computer program. The counter signal processor data was made available for use by the author for the present study.

2.3 Concentration Measurement

The concentration data sets were collected using an array of eight conductivity detectors (or probes), arranged in a rake with probes 2 cm apart. Conductivity data sets were measured at a sample rate of 250 Hz for 500 sec. The 500 sec time-averaging interval spans approximately 2000 integral time scales.

Two different fast response conductivity detectors were developed and used in this study. The first detector (hereafter micro-probe) was constructed of 3 mm glass tubing which was heated and drawn to a fine point. The tip of the hollow tube was filled with *Woods* metal, (a low melting point alloy composed of 50% Bi, 25% Pb, 12.5% Sn, 12.5% Cd by weight). The exposed part of the probe tip was electroplated with gold and platinum to improve probe stability. The probe incorporates one electrode, in contrast to previously-published two-electrode (Bara 1985) or four-electrode designs (Head 1983), in an attempt to overcome some of the problems in previous designs. Although the sensing volume of the micro-probe was much smaller than previous designs, this probe exhibited problems with the stability of the calibration over an extended period. The second detector (hereafter new-probe) was designed to overcome these problem. The details of this robust conductivity probe are currently being published elsewhere. The concentration detectors are described in detail in Chapter 4 and in Appendix D.

Data for the present study were collected using both probes. The author collected all the data using the micro-probe. Others, under supervision of the author, collected the remaining data using the new-probe and the data acquisition systems and computer programs developed by the author.

2.4 Concentration Sources

Concentration data were collected down-wind (or down-stream) of four different sources, which are illustrated in Figure 2.3. The principal source used in this study was the jet/plume source. The analysis and theory development was tested using the data collected for this source and then later tested using the other three source types. The source numbers shown in Figure 2.3 refer to the experimental source names.

Jet/Plume Source: A 1.0 mm internal-diameter (I.D.) tube injecting horizontally down-wind, on the water channel centre-line, at a height of 50 mm, (approximately $1/3$ the boundary layer height). A flow rate of 2.0 ml/s created a turbulent jet. The excess jet velocity is shown in Figure 2.4. The turbulent jet decayed to 10% of the mean free stream velocity within $x/h_s < 4.4$ or $x/\Lambda_u < 4.4$ where h_s is the source height, Λ_u is the integral length scale of the velocity fluctuations, and x is the distance down-wind. By $x/h_s = 9.4$ or $x/\Lambda_u = 9.4$ the excess velocity was negligible. The dispersing material then behaved like a passive plume for the rest of the travel distance examined.

Down-Wind Iso-Kinetic Source: The same source flow rate was used as with the jet/plume source, but a diameter of 3.45 mm I.D. The tracer material left the source with the same speed as the local approach velocity. Because the velocity leaving the source was low, the plume was laminar and had a *spaghetti* like appearance. Flow visualization revealed that the laminar tracer material maintained its near source character far down-wind, ($x/h_s > 20$).

Vertical Jet Source: A 1.0 mm I.D. tube injected vertically into the boundary layer. The source was mounted at ground level, at a height equal to the top of the roughness elements on the floor of the water channel. The source flow rate equalled the jet/plume source and was a turbulent jet. Flow visualization showed that the vertical jet produced more meandering of the plume than the jet/plume source.

Up-Wind Facing Iso-Kinetic Source: Identical to the down-wind facing iso-kinetic source, except that it was turned to inject the tracer directly wp-wind against the flow. The tracer material travelled only a very short distance wp-wind before being carried back down-wind. The source tended to shed regular vortices (of tracer) which produced irregular results close to the source. The data collected from this source was included to show the robustness of the models developed.

The schematic representations of the sources in Figure 2.3 will be used as icons in the figures in the chapters to follow, to indicate the source configuration.

The data sets were collected by the author for the jet/plume source and for the vertical jet source. Data, for later studies in the water channel with the same boundary layer, but using the iso-kinetic source and wp-wind facing iso-kinetic source, were collected by others under the supervision of the author. The jet/plume source experiments were repeated using the new-probe and data were collected at more down-wind locations than the original data set. These data sets were also made available for use in the present study. The experimental techniques and the data acquisition system were developed by the author and given to those collecting the data.

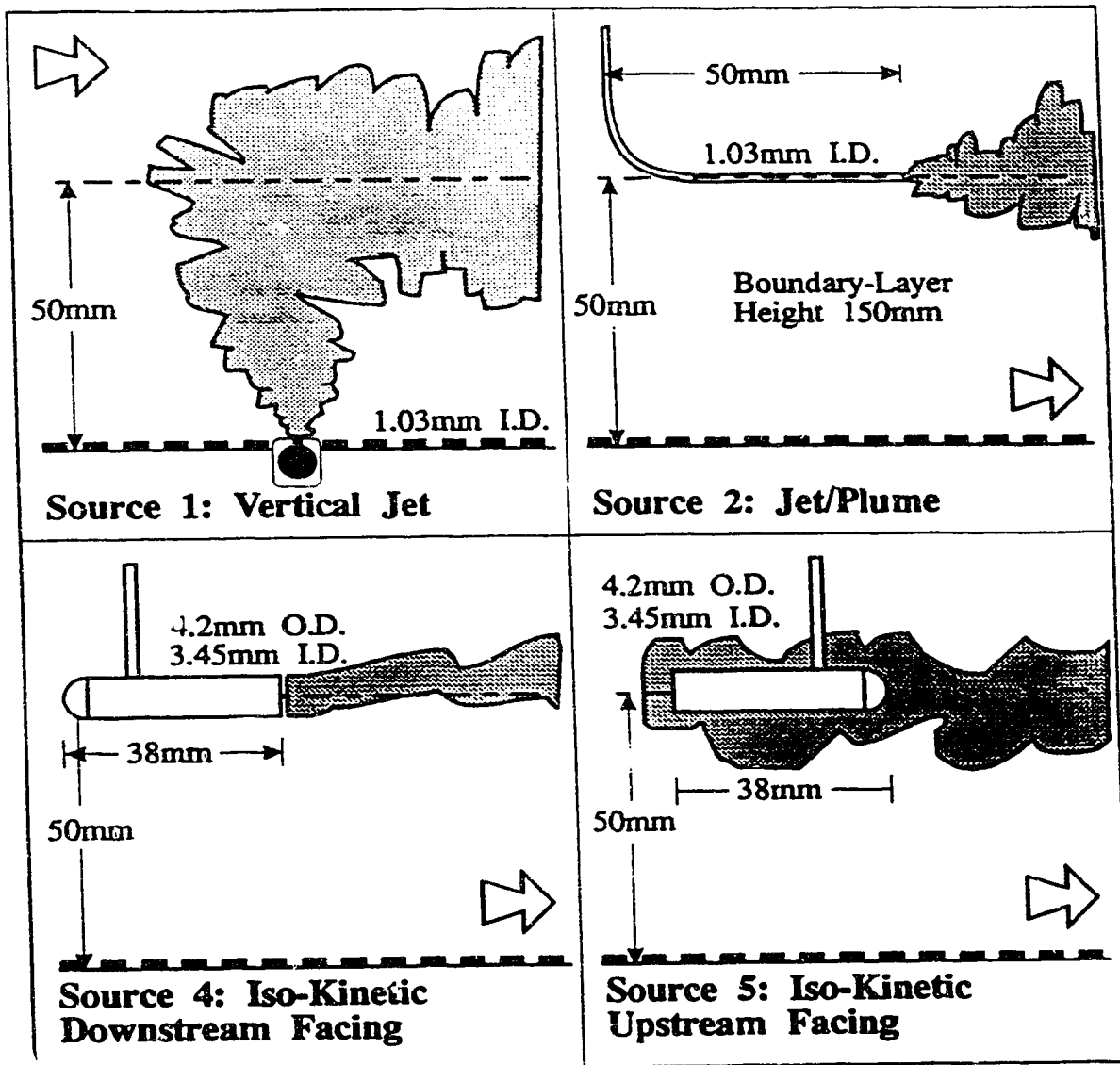


Figure 2.3: Schematic of the sources used in the study

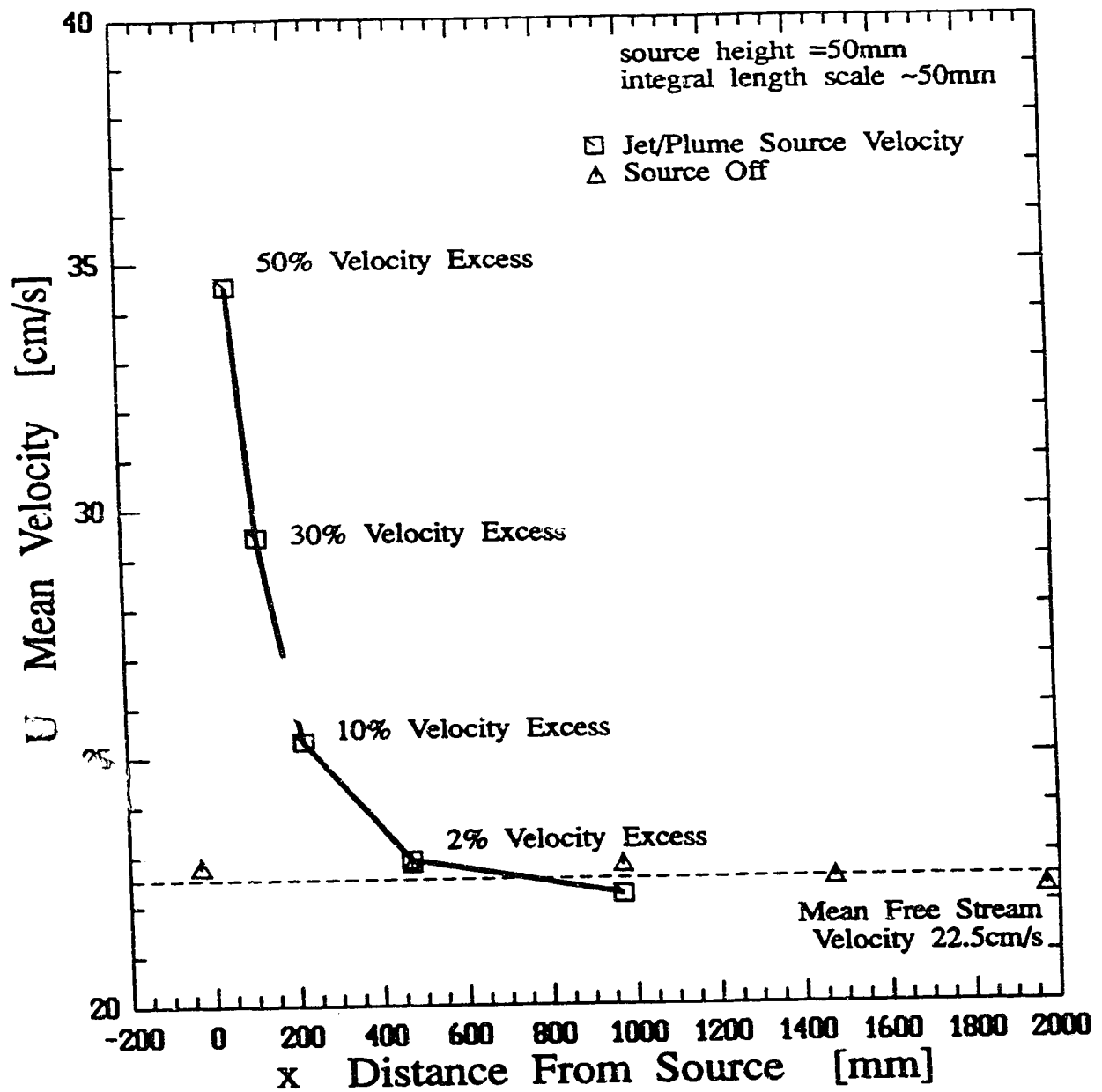


Figure 2.4: The excess jet velocity of the jet/plume source with down-wind distance.

Chapter 3

Water Channel Velocity Field

In this chapter the water channel velocity field is described and a comparison is made with the atmospheric boundary layer velocity field. Although atmospheric simulation is not the principle focus of this research, early work in this thesis research area favoured a realistic atmospheric boundary layer simulation. Since this boundary layer was adequate for the current studies, (as it is a nearly horizontally homogeneous shear flow), it was maintained and used to project the study results to full scale atmospheric applications.

The nominal environment selected for this dispersion study is an atmospheric boundary layer which is representative of the conditions typical for full scale dispersion incidents in neutral stratification. The water channel boundary layer was investigated to ensure that the characteristics of the model were be comparable to the full scale atmosphere.

In this chapter the mean velocity profile, the intensity of velocity fluctuations, and the turbulent time scales are presented.

3.1 The Turbulent Boundary Layer

In the atmosphere, almost any conceivable mean velocity profile may be measured, owing to the complex influences of topography, stratification, non-stationarity, and mesoscale inhomogeneity. The neutrally stable condition is an atmospheric condition which occurs rarely and may be considered a specialized condition since it is free from the thermodynamic and statistical complexities which may be found in unstable or stable stratification. Only on very windy and cloudy days might the conditions be considered neutral, in the sense of a stationary flow being in equilibrium with

its forcing. Because it is extremely difficult to simulate stratified atmospheric flow, the neutral stratified condition was the selected environment in which to perform this study. Neutral stratification could be simulated reasonably easily. It is typically characterized by strong winds and a mean velocity profile that is often described by a logarithmic-law or a power-law expression in height above the ground. These two expressions are described later in this chapter.

With an experimentally adjusted boundary trip and ground surface roughness, a series of vertical and horizontal profiles were taken to investigate the velocity statistics. Three vertical centre-line velocity profiles were measured at locations of 2000 mm, 3000 mm, and 4000 mm measured from the start of the water channel. These locations span the test section used for the dispersion experiments. (The concentration sources were located at 2030 mm). At the same locations, horizontal profiles at a height of 50 mm, were measured to check for lateral uniformity of the boundary layer. This height was selected to match the tracer source height.

3.1.1 Boundary Layer Development

Channel flows with a rough ground surface create log-law velocity profiles, Nezu (1986) and Steffler, Rajaratnam, and Peterson (1983). If allowed to develop naturally, the flow entering the water channel would eventually form a *fully developed* boundary layer with a log-law mean velocity profile that would extend to the free water surface. The channel length of five metres, used in this study, is insufficient for the boundary layer to naturally develop fully. To reduce the channel length required to create the fully developed boundary layer, a boundary layer trip was used to excite the flow by adding turbulence and drag in those regions where the boundary layer develops these characteristics when grown naturally. A water depth of 300 mm was used. For the surface roughness selected in the water channel, this depth was too large for the boundary layer to reach the free surface. Therefore, given the flow depth, a boundary layer was created which was *well developed*, (as opposed to a fully developed boundary layer), where the mean velocity changed little with change in down-stream position. It was also desirable that the well developed boundary layer have profiles of velocity fluctuation intensities and integral length scales of turbulence which would change little with down-stream location.

After forty trials, a boundary layer trip producing the desired well developed boundary layer characteristics was created, Figure 3.1. The trip incorporated tall pillars moderately spaced to generate large scale turbulence, and a castellated trip-wall which produced a significant increase in turbulence near the ground surface.

The mean velocity profile in the test section region, was not fully developed, and evolved with distance down-stream. The largest variations in the profile are in the region above the tracer plume and above boundary layer height, see Figure 3.2. The increase in the mean velocity at the boundary layer height is about 5% over the first metre of the test section where most of the dispersion experiments were performed and another 5% over the next metre of travel. The depth of the boundary layer, H , may be estimated from Figure 3.2 to be 150 mm.

The profile of the along-wind velocity fluctuation intensity varied little with down-stream distance, see Figure 3.3. The integral length scales of the velocity fluctuations, (see section 3.2 for the method of determining the integral length scales), however, vary significantly with down-stream location, from the start of the test section to the end of the water channel, see Figure 3.4. The length scale increase varies by 20% over the test section region, $x=0$ mm to $x=1000$ mm. The increase in the fluctuation scale may cause the observed concentration plume widths to grow at a different rate than would be predicted in homogeneous turbulence. However, this variation in the scale will be assumed small, and will not be accounted for in the the dispersion estimates.

3.1.2 Cross-Wind Uniformity of the Boundary Layer

The horizontal mean velocity profiles shown in Figure 3.5 show less than 10% deviation from the mean across the width of the channel to within about 25 mm from the glass side wall. Closer than 25 mm to the side wall, the side wall boundary layer has a significant effect. This reduces the effective test section width to approximately 600 mm, corresponding to about six plume half-widths at the furthest down-stream location where tests were conducted.

In this investigation the higher moments of the concentration fluctuations, $\overline{c^2}$, $\overline{c^3}$ and $\overline{c^4}$, are important and have increased effective plume widths associated with each moment. At the furthest down-wind location studied, the plume width was still significantly less than the available 600 mm channel width. There was sufficient room for the plume to disperse uninhibited, yet not entirely unaffected. The side walls limit the large scales of turbulence which determine the amount of meandering that is observed. This is a problem in most test facilities except when very large wind tunnels are used, and even then, the large scale fluctuations of the atmosphere cannot be simulated.

The turbulence intensity measured along a profile across the channel, which is shown in Figure 3.6, varies less than 15% from its cross-wind average. Closer than 80 mm to the side wall, the intensity increases to a value of about $i_u^2 = 0.15$.

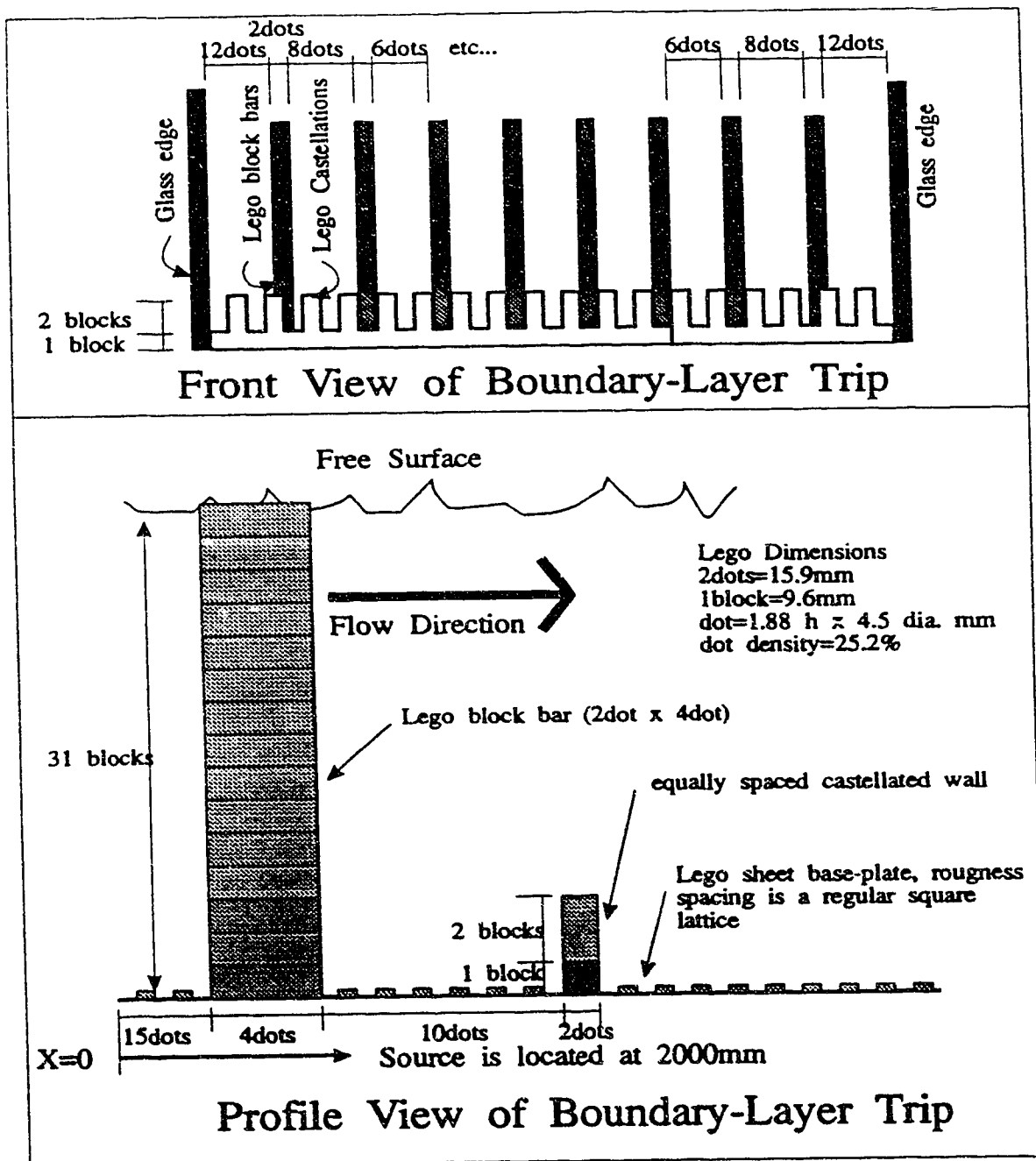


Figure 3.1: Schematic of the boundary layer trip used to excite a well developed velocity profile.

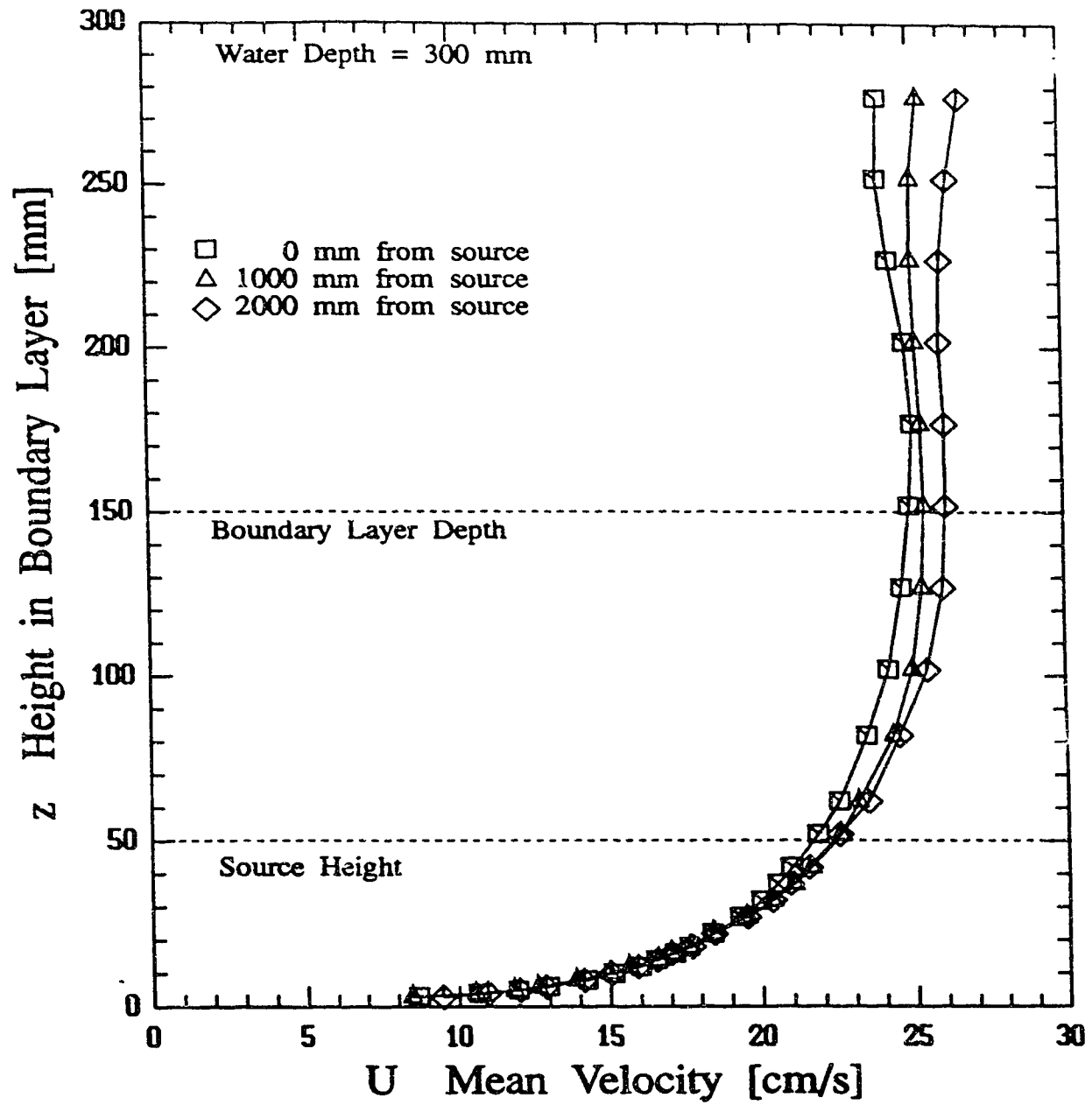


Figure 3.2: Variation of the mean velocity profile with distance down-stream.

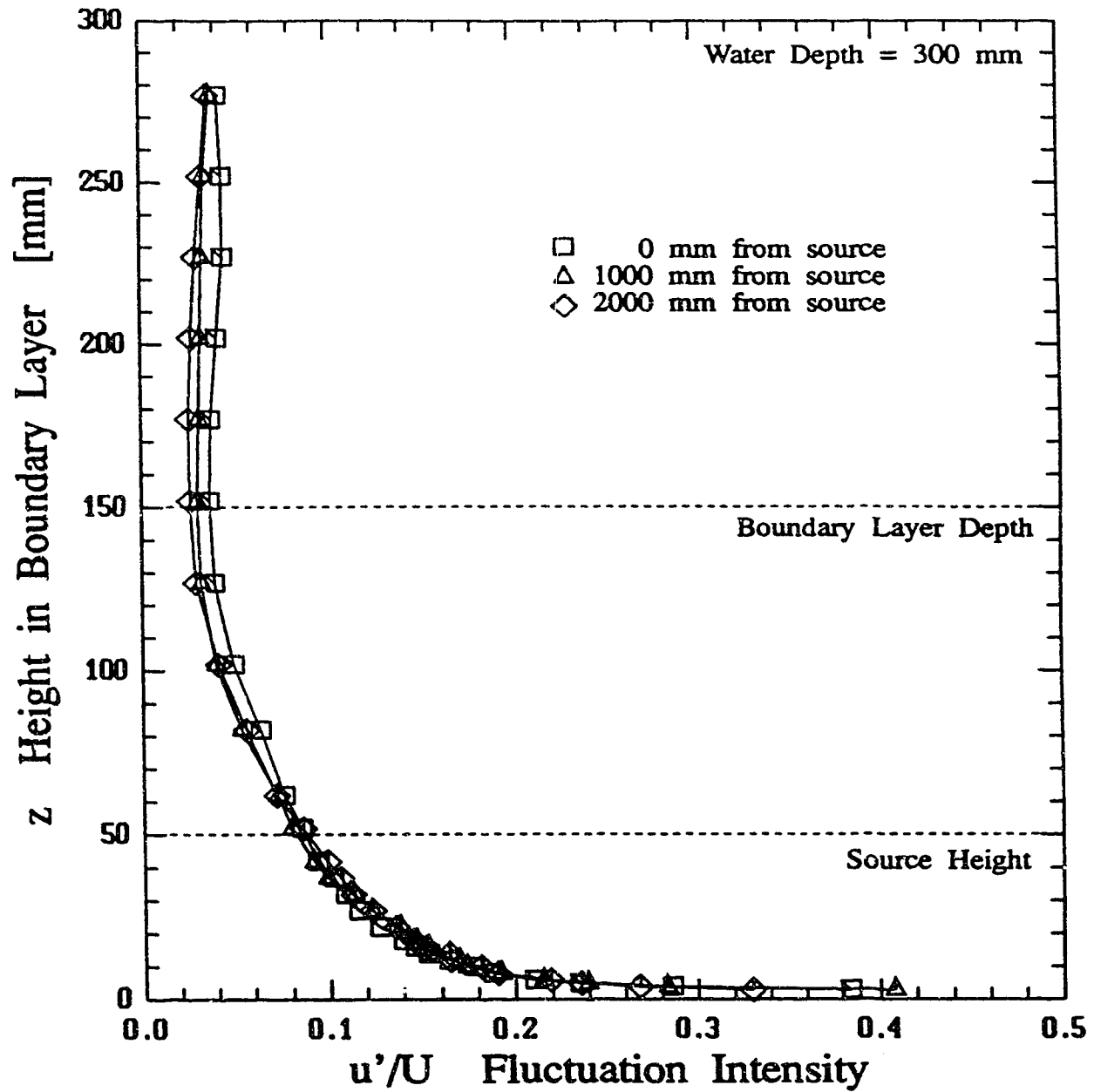


Figure 3.3: Variation of the intensity of velocity fluctuations profile with distance down-stream.

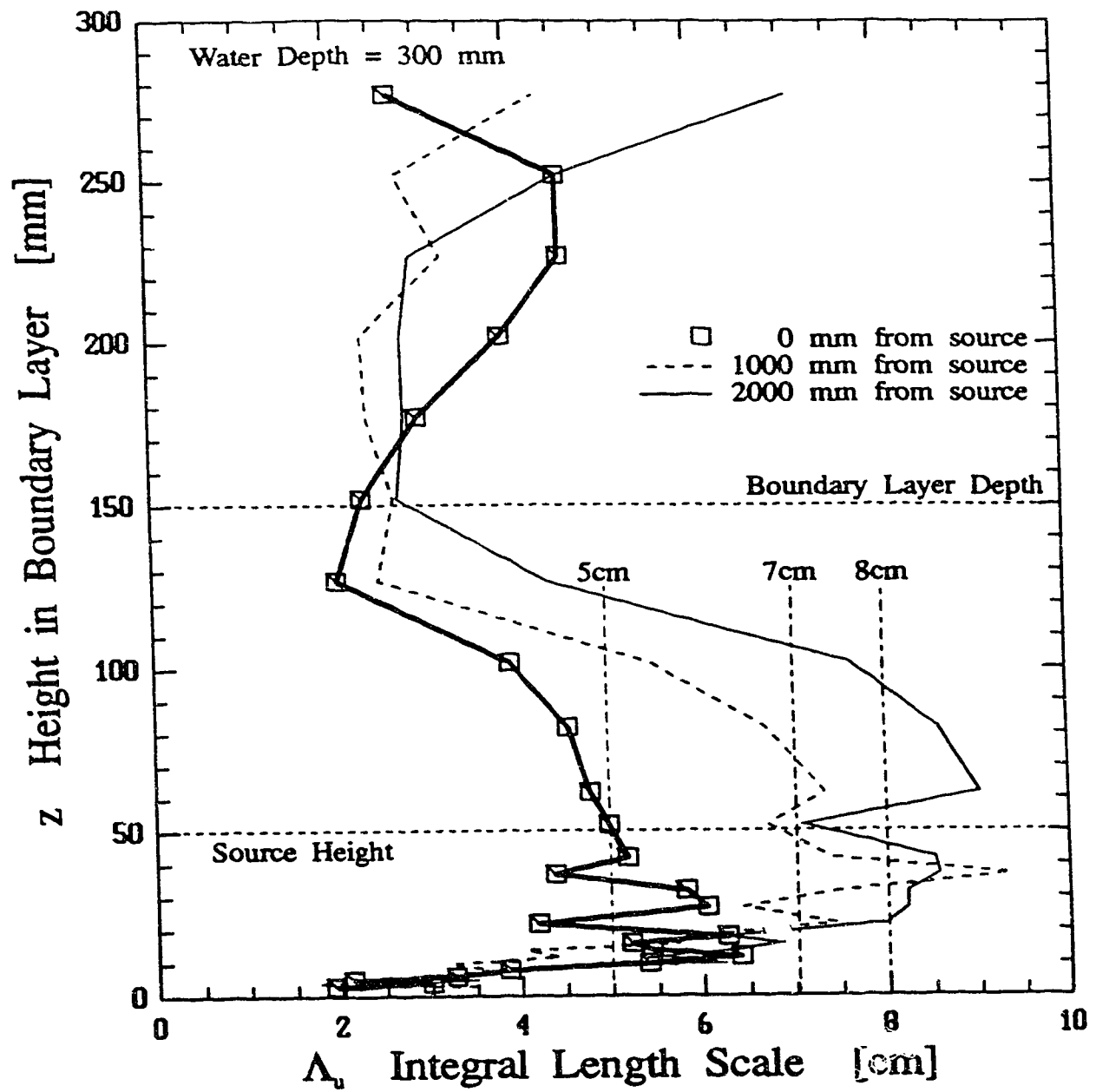


Figure 3.4: Variation of the integral scales of velocity fluctuations profile with distance down-stream.

The integral length scales of turbulence in the cross-stream direction, Figure 3.7, are further confirmation that the water channel produces a turbulent flow that is acceptably homogeneous in the y -direction.

3.2 Fluctuation Time Scale Calculations

Researchers modelling the atmosphere in wind tunnels and water channels rarely present this important flow statistic as requested by Hanna, Briggs, and Hosker (1982). Typically, the time scales of turbulence may be derived from the energy spectrum which would be calculated using a fast Fourier transform, FFT, see Appendix C.

An alternative method for determining turbulence time scales may be found by considering G.I. Taylor's Lagrangian statistical theory of diffusion in homogeneous turbulence. It is presented in brief by Tennekes and Lumley (1972), Hinze (1975), and in Pasquill and Smith (1983). The method compares the variance of a data set smoothed over a determined time interval to the variance of the non-smoothed data set to get the time scales of turbulence. Bara and Netterville (1985) have successfully used this procedure for measurements in the atmosphere using LIDAR. This method, discussed in section 3.2.1, is also successfully applied to the concentration data in this study.

3.2.1 Alternative to the FFT Spectral Analysis Time Scale

The integral time scale of turbulence may be determined by considering the effects of finite averaging of a data time series. If a time series was averaged using a rectangular window function, of size t_a , see for example Stanely, Dougherty, and Dougherty (1984) p.230, the effect on the time series is to remove all the high frequency information leaving only large scales of motion. The effect on the energy spectrum is to reduce the amplitude by an amount given by,

$$\phi^2(f) = \left(\frac{\sin \pi t_a f}{\pi t_a f} \right)^2 \quad (3.1)$$

Equation (C.3) may be re-written using (3.1) as,

$$\overline{u'^2_{t_a}} = \int_0^\infty F(f) \left(\frac{\sin \pi t_a f}{\pi t_a f} \right)^2 df \quad (3.2)$$

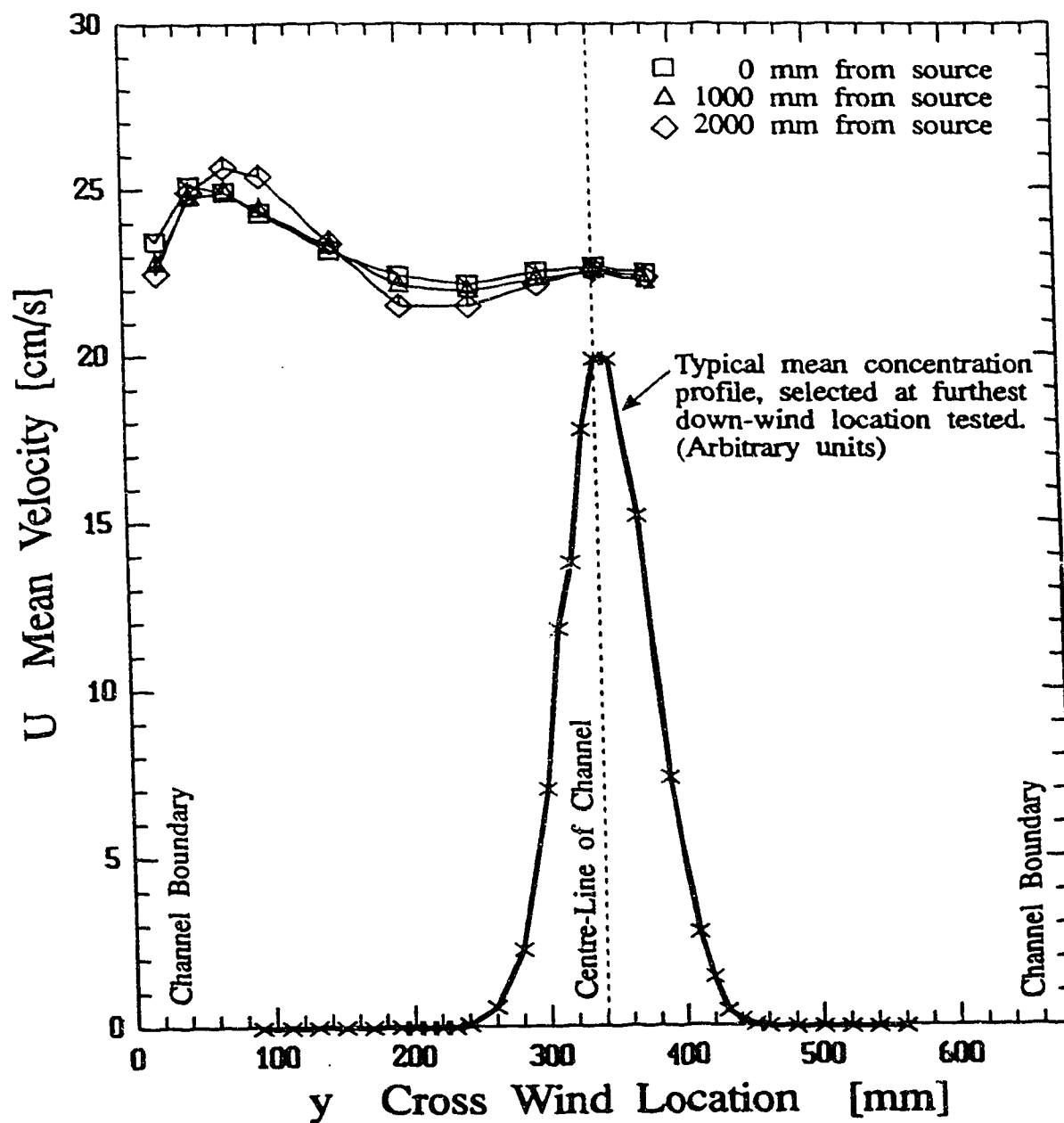


Figure 3.5: Cross-wind mean velocity profiles showing homogeneity of water channel flow. The mean concentration profile is overlaid on the figure to show the width of the channel that is covered by the dispersing plume.

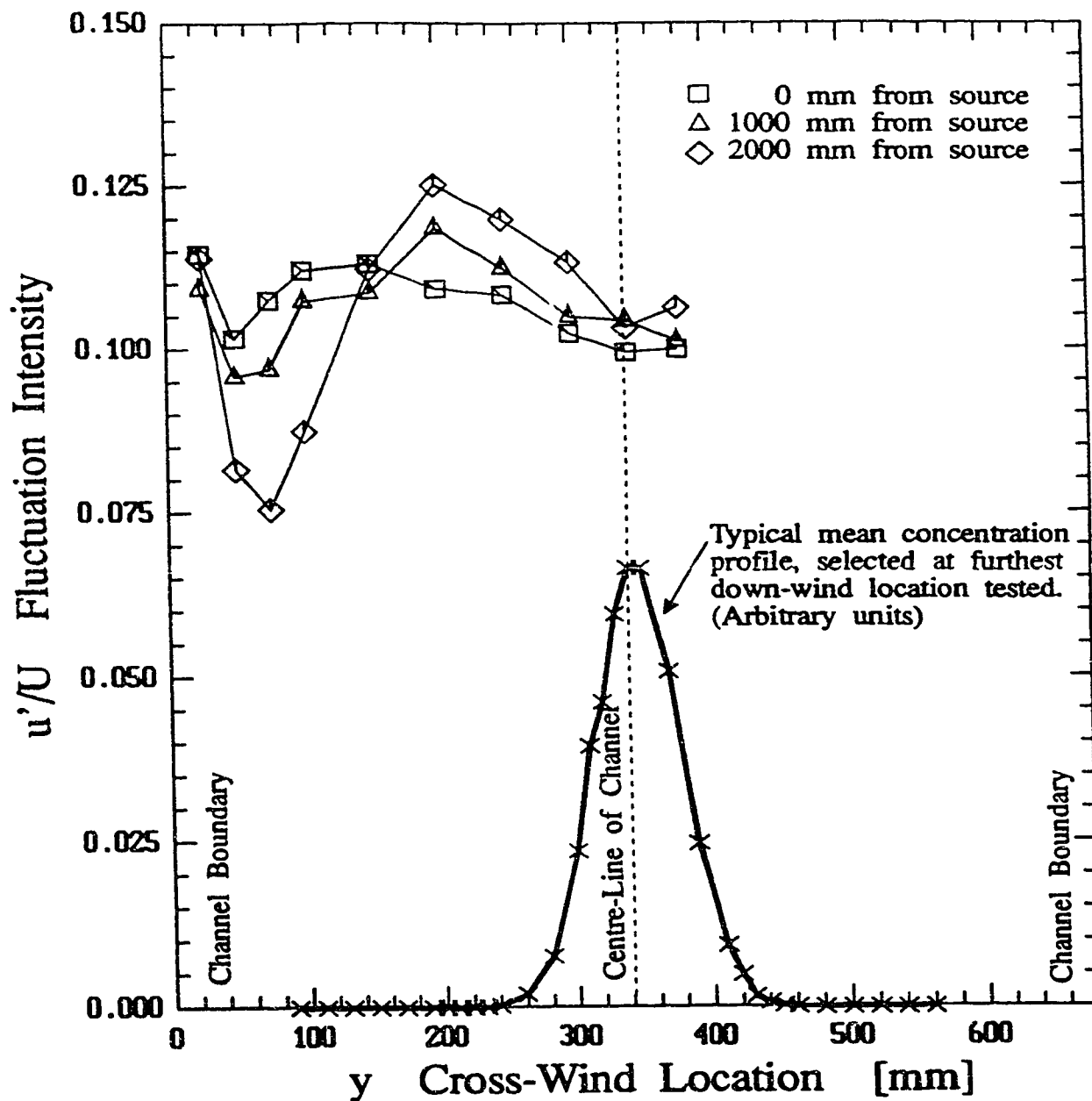


Figure 3.6: Cross wind profiles of turbulent intensity showing deviation of intensity. The mean concentration profile is overlaid on the figure to show the width of the channel that is covered by the dispersing plume.

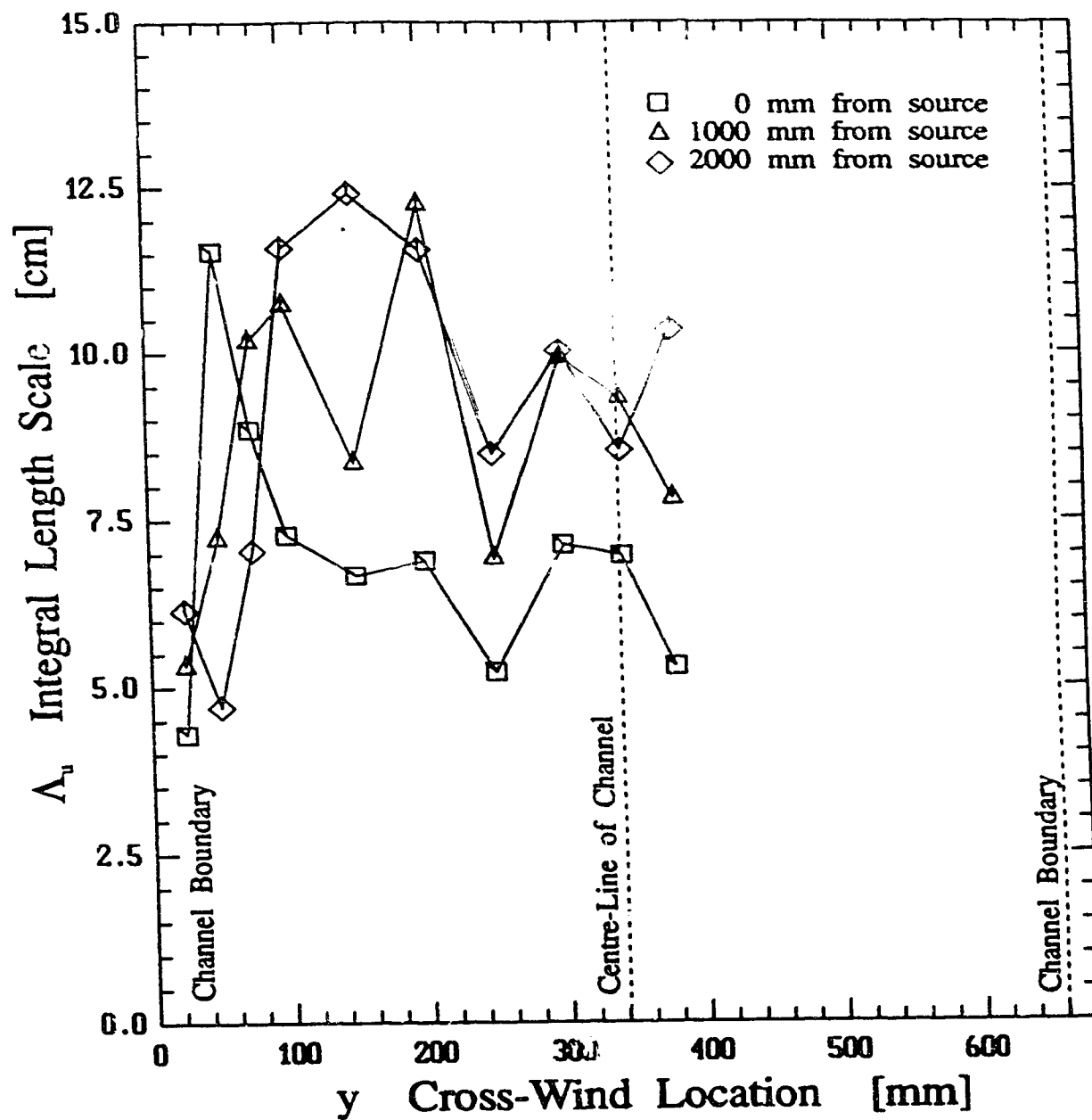


Figure 3.7: Cross wind profiles of integral length scale of turbulence showing relative sameness across the water channel and growth with downstream distance.

or may be written in terms of the normalized energy spectrum as,

$$\overline{u'^2_{t_a}} = \overline{u'^2} \int_0^\infty E(f) \left(\frac{\sin \pi t_a f}{\pi t_a f} \right)^2 df \quad (3.3)$$

Since the behaviour of spectra for velocity fluctuations and concentration fluctuations at low frequencies are the same, namely $E(f_{\text{low}}) \propto k^0$, any representative spectrum may be substituted for $E(f)$ in (3.3). The Markov spectrum is a simple spectral model which smoothly changes from $k^{-6/3}$ for high frequencies to k^0 at low frequencies and is easy to manipulate mathematically. Substituting the Markov energy spectrum equation (C.8) into (3.3), the effect of averaging may be determined,

$$\overline{u'^2_{t_a}} = 4\overline{u'^2} \int_0^\infty \frac{T_E}{1 + (2\pi T_E f)^2} \left(\frac{\sin \pi t_a f}{\pi t_a f} \right)^2 df \quad (3.4)$$

Integration by parts leads to,

$$\overline{u'^2_{t_a}} = 2\overline{u'^2} \frac{T_E}{t_a} \left[1 - \frac{T_E}{t_a} (1 - \exp(-\frac{t_a}{T_E})) \right] \quad (3.5)$$

For values of time $t_a/T_E > 50$, see Figure 3.8, (3.5) reduces to

$$\overline{u'^2_{t_a}} = 2\overline{u'^2} \frac{T_E}{t_a} \quad (3.6)$$

From which the time scale T_E may be determined by,

$$T_E = \frac{t_a \overline{u'^2_{t_a}}}{2\overline{u'^2}} \quad (3.7)$$

Pasquill and Smith (1983) show that because the energy spectrum in atmospheric flows is independent of frequency at low frequencies, the spectrum $E(f)$ may be removed from the integral in (3.3). Therefore, the result in (3.7) is not only a characteristic of the Markov spectrum used in this example.

However, the expression (3.7) is a function of the averaging method used to determine the smoothed variance. For example if a triangle window is used instead of a rectangle window, the time scale is determined by, for large t_a/T_E ,

$$T_E = \frac{t_a \overline{u'^2_{t_a}}}{2.667\overline{u'^2}} \quad (3.8)$$

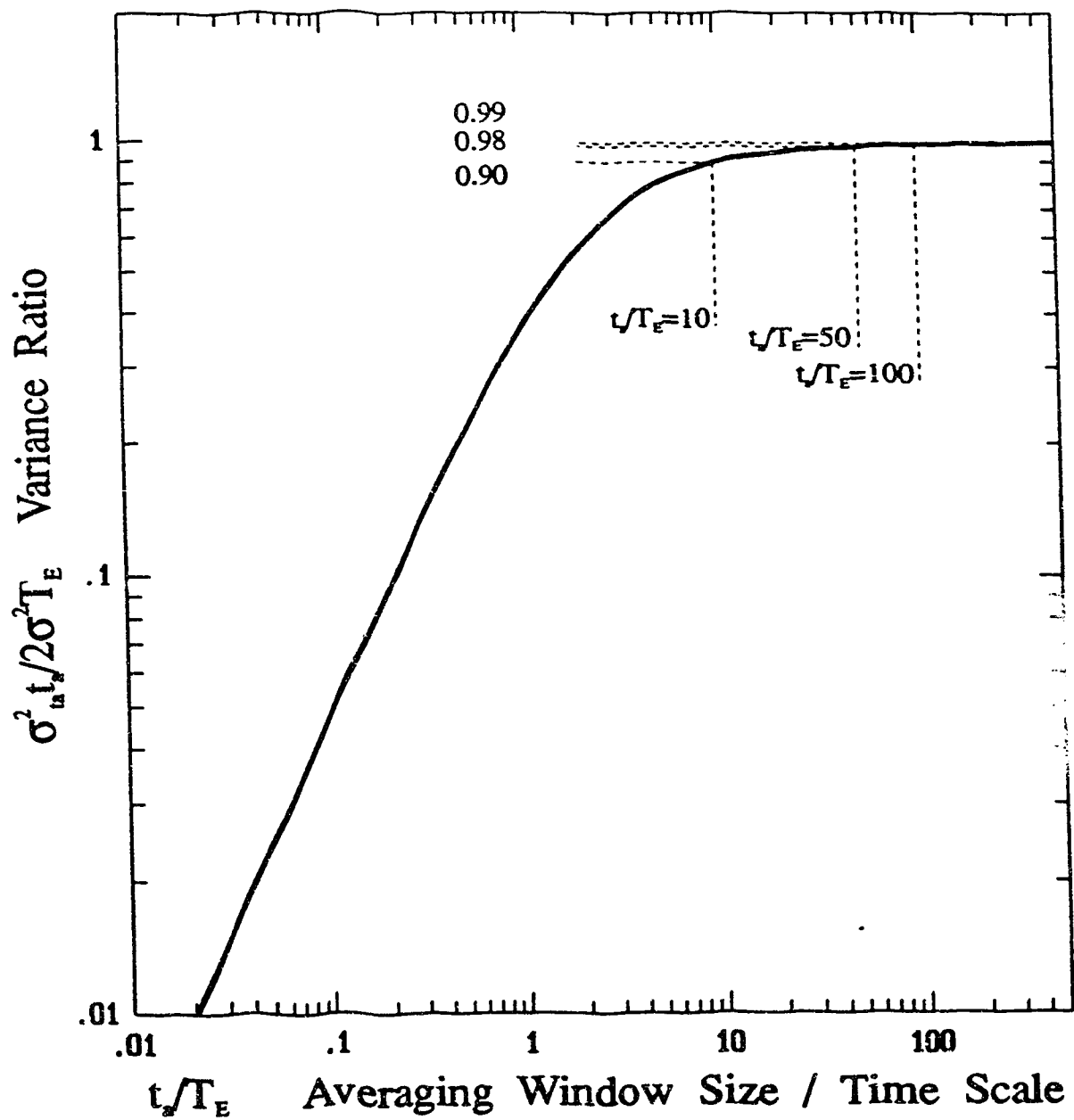


Figure 3.8: Effect of time averaging on the sample variance normalized by the non-averaged variance for a Markov spectrum.

Alternatively, a second order Butterworth low pass digital filter may be used to determine $\overline{u_{t_a}^{'2}}$. The time scale in this case would be given by, for large values of t_a/T_E ,

$$T_E = \frac{\sqrt{2}t_a\overline{u_{t_a}^{'2}}}{\overline{u^{'2}}} \quad (3.9)$$

However, the triangle window procedure does not allow the computational reduction steps possible in the rectangular window method. The Butterworth filter procedure does not converge as quickly as the rectangular window method, implying that extremely large values of t_a/T_E are required.

Practical use of (3.7) is not possible without selecting a value for the averaging time, t_a . Using Figure 3.8 a time-average of about $t_a \geq 50 T_E$ is required to get an accurate estimate of the time scale. Alternatively, t_a may be determined by iterating on T_E by slowly increasing t_a ; T_E will increase and finally converge to a constant value, as shown in Figure 3.9.

This method for calculating the time scale of turbulence has a significant advantage in computer computation time savings over the FFT procedure. The FFT procedure requires in the order of $N \log N$ multiplications, whereas the time averaging technique requires in the order of only $2N$ multiplications. For large data sets this means almost an order of magnitude saving in analysis time.

Comparisons between the scale measurements using the FFT method and the time averaging method agree within about 15% as shown in Table 3.1. The table compares the calculated time scale for a number of concentration time series data sets. Similar results may be obtained for time scale comparisons using velocity data sets. Due to the differences in analysis procedures a small random variation was expected and observed. There is no need to correct the time scale predicted by (3.7) by iterating using (3.5). When $t_a \geq 50 T_E$ the iteration corrects the calculated time scale by less than one percent. Considering the scatter observed in the scale calculations by any method, a correction is not justified. In summary, (3.7) produces accurate results quickly, without the complications of averaging FFT produced energy spectra.

Application of (3.7) to velocity fluctuation time scales provides a different insight into the scale calculation, see Figure 3.10. The FFT calculated scale shows an increasing scale trend towards the ground. The FFT procedure produces results with little apparent data variation. The time-averaged variance method predicts the correct decreasing time scale trend near the ground. The profile shown, (and others taken in the boundary layer) are not smooth curves, and contain much scatter. The reason the FFT method may be in error near the ground, is unlikely to be a result of the the velocity bias errors which are not accounted for in the FFT procedure, but are

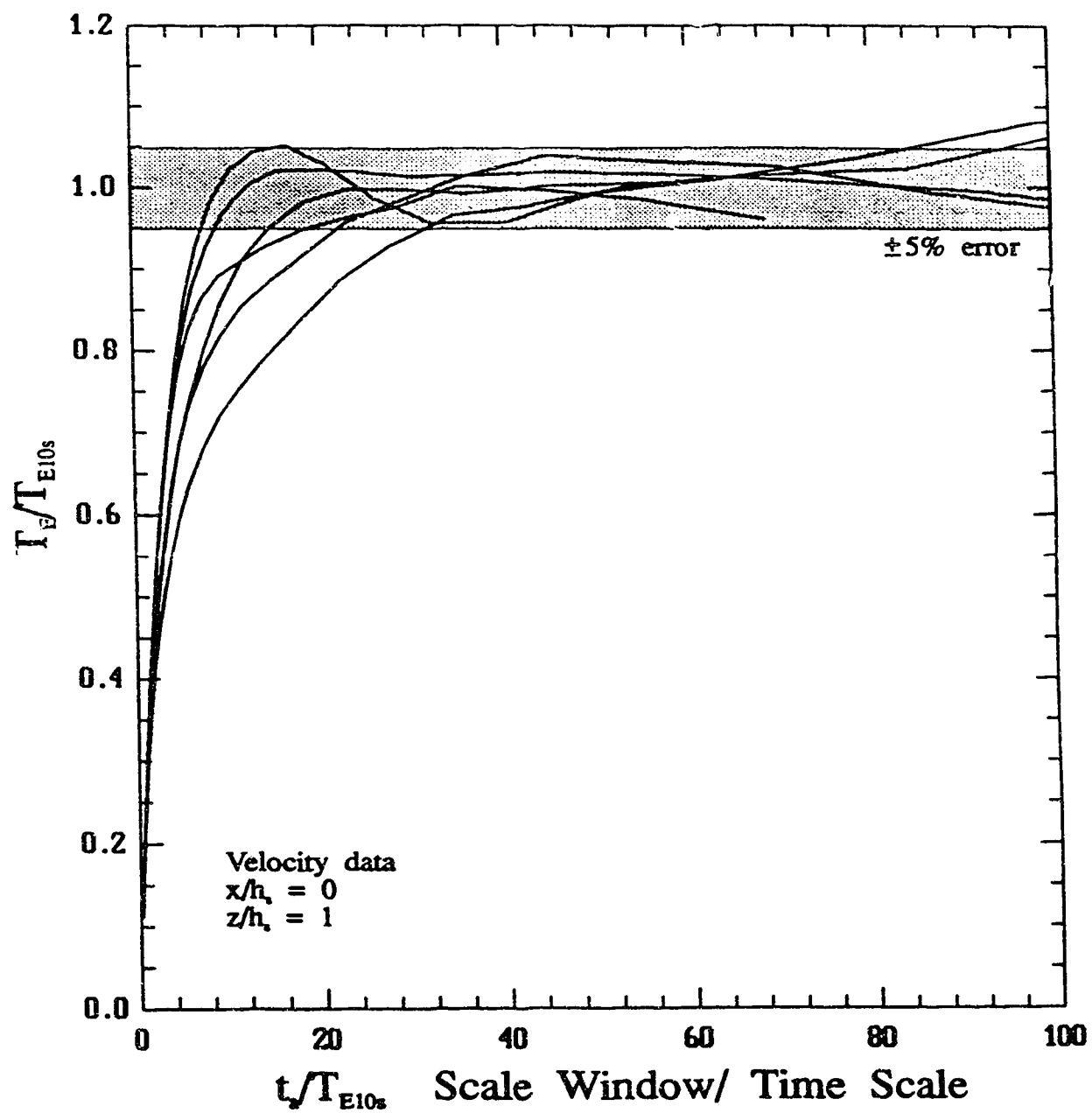


Figure 3.9: Effect of time averaging window size on time scale calculation.

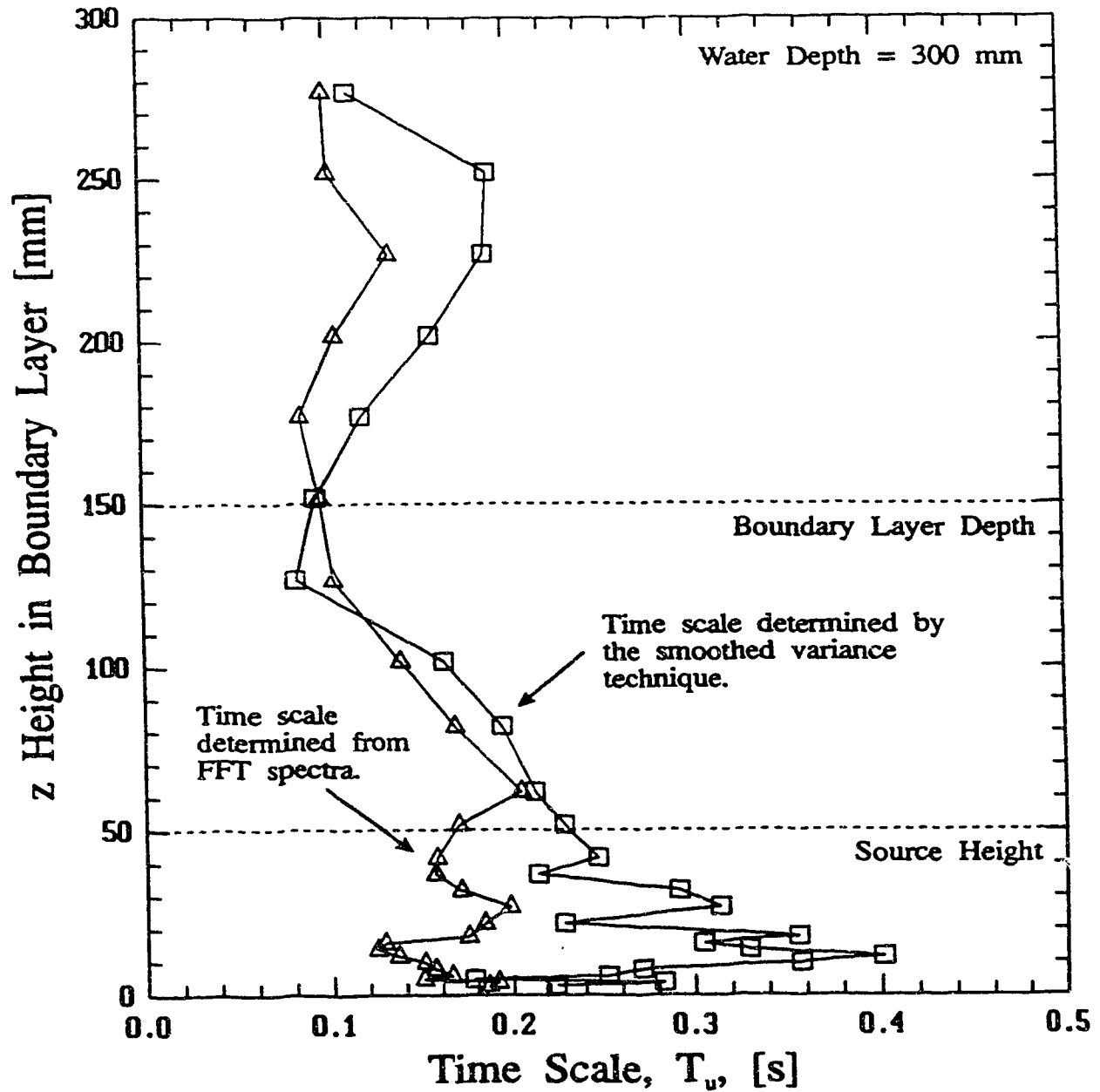


Figure 3.10: Comparison of velocity fluctuation time scales in the water channel boundary layer, at the source location, using the FFT method and the time-averaged variance method. The FFT method shows less scatter but wrong values near the ground, whereas the variance method contains considerable scatter.

Table 3.1: Comparison of concentration integral time scales calculated by FFT spectra and by equation (3.7), for concentration data sets from a jet/plume source at $x/h_s = 20$.

Intermittency	FFT T_u msec	Time Averaged T_u msec	Error %
.49	62.55	38.69	-38.2
.614	43.00	38.36	-10.8
.659	42.10	46.83	11.2
.531	41.16	34.95	-15.1
.324	53.03	84.94	63.3
.141	50.46	54.46	7.9
.040	39.81	40.41	1.5
.008	25.06	27.37	9.2
average absolute error ^a ≈ 15			

^aExcluding the largest and smallest relative errors.

accounted for in the variance method. If the bias correction in the variance smoothed scale method is removed, the results still do not match the FFT time scale results near the ground. The difference between the procedure results could be caused by an averaging window, for the smoothed variance technique, which is too small for the observed increase in fluctuation intensity near the ground.

Overall, the time-averaged variance procedure is a powerful tool to provide fluctuation time scale estimates from turbulence data easily. Given the difficulty of the calculations for both procedures, the results from the smoothed variance technique are in good agreement with the FFT analysis and may provide more accurate measurements in cases such as the LDA velocity biased data.

3.2.2 Lagrangian-Eulerian Time Scale Ratio

The Lagrangian time scale, T_L , can be estimated from the Eulerian time scale, T_E , using an assumed constant ratio, β , Hinze (1975) p.419, (first Uberoi and Corrsin, 1953, Fay and Pasquill, 1959, Baldwin and Mickelsen, 1962),

$$\beta = T_L/T_E \quad (3.10)$$

Hinze notes that $\beta > 1$ in the atmosphere however some researchers have found that β may be less than unity. This will not affect the results here, as only the Eulerian

time scale may be determined. The actual value of β remains undetermined and would be a property of the turbulent flow being studied.

Reid (1979) suggests that,

$$T_L/T_E = \beta = \frac{0.5}{w'/\bar{u}} \quad (3.11)$$

Saffman (1962) proposes that the ratio is a function of the intensity of the along wind fluctuations given by,

$$T_L/T_E = \beta = c \frac{\bar{u}}{u'} \quad (3.12)$$

where he estimated that $\beta = 5.6$ or $c = 0.8$ for atmospheric turbulence. Wells (1982) experimental study determined values of β in the range from 1 to 20. Wang, Stock, and Lamb (1988) determine c in the range 0.53 to 0.75, where c is a function of; the intensity, the wave number at the spectral peak, and Eulerian time scale, in a numerical integral. Although it is not practical for back of the envelope calculations, it does show that variability in β is explainable, or at least expected. Using the water channel data, Figure 3.11 was generated using (3.11). It may be concluded that the water channel results are consistent with the findings of others, given above.

The energy spectrum, $E(f)$, may be determined from a time series by sequentially averaging the results of a Fourier analysis on data blocks of size 2^M . The data blocks may be of virtually any size. The chosen size depends only on the memory capacity of the computer performing the computation, the resolution of the spectra desired and the analysis time allowed on the computer. Although the resolution of the Fourier analysis is affected by the choice of M , the accuracy is not affected. The higher resolution of a larger M_1 distributes the same error over a greater number output data points than a smaller M_2 , (Press, et al. 1988).

Fast Fourier transforms were used to determine the energy spectra. Data blocks of 1024 points were used to generate spectra from data sets of 125,000 data points. This allowed an average of about 60 transforms with overlapping windows and reduced the spectral estimate variance sufficiently to produce usable output. Larger data blocks did not allow sufficient averaging of the transforms and much smaller data blocks did not provide a good estimate of the $E(0)$ value. A large amount of the estimated variance appears in the low frequency outputs, and therefore using the 1024 data block size, an average of the $E(f_0 = 0)$ and the $E(f_1)$ output data points were used as an estimate of $E(0)$.

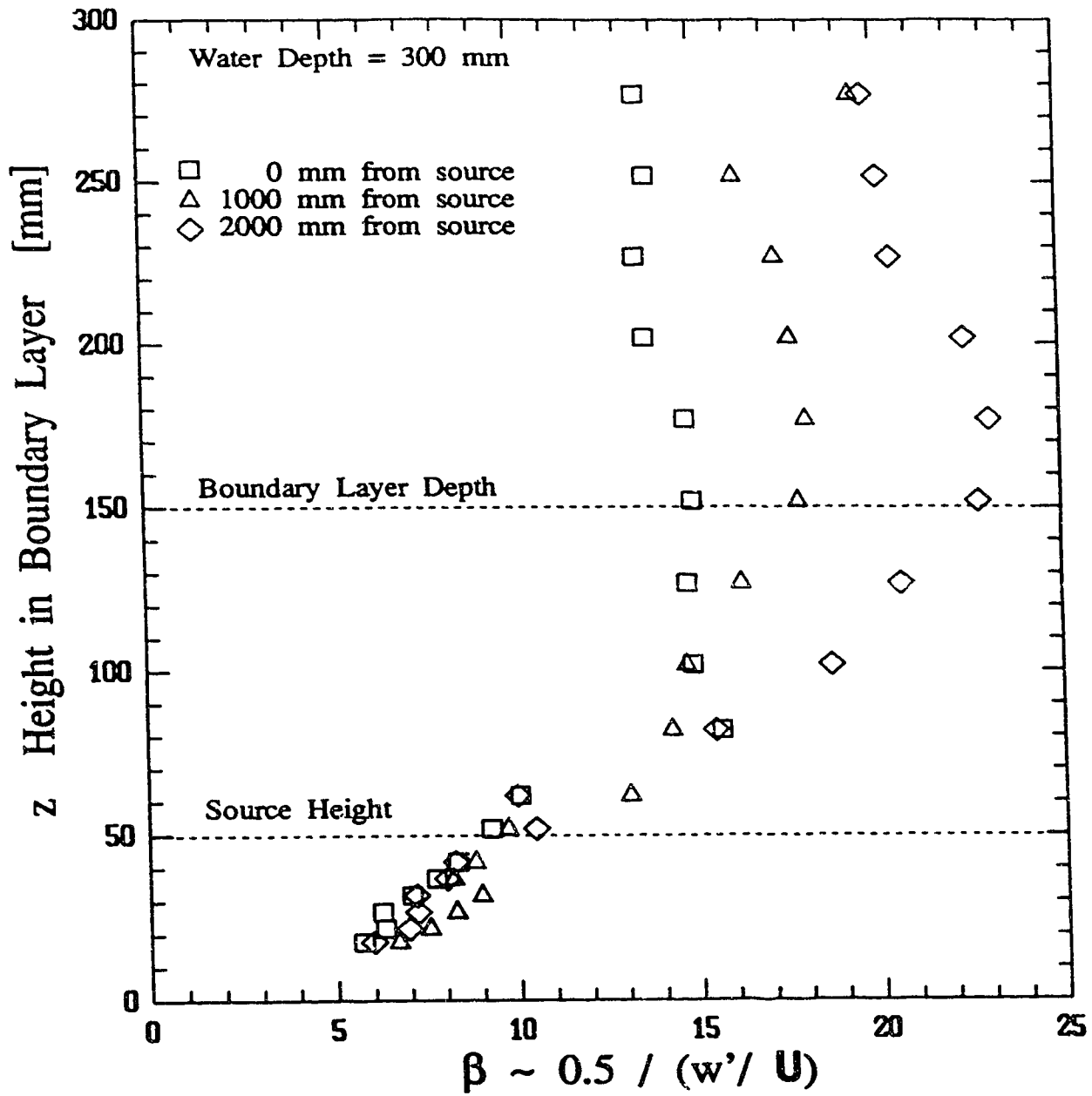


Figure 3.11: Distribution of value of $0.5(w'/\bar{u})$, which has been proposed to equal the ratio of the Lagrangian time scale to the Eulerian length scale.

3.3 Vertical and Cross-Wind Flow Profiles

Having created a well developed boundary layer in the water channel that is essentially homogeneous at any given height for the important statistics of the turbulence of the flow, attention may now be turned to examining the characteristics of the flow more closely.

3.3.1 Logarithmic Velocity Profile

The mean velocity profile during neutrally stable conditions in the atmosphere, may be represented by a simple logarithmic relationship, Tennekes (1973), Simiu (1973), Counihan (1975), Pasquill and Smith (1983), and Panofsky and Dutton (1984). The log-law expression relating the mean velocity to the height in the boundary layer with the friction velocity, u_* , is,

$$\frac{U}{u_*} = \frac{1}{\kappa} \ln \left(\frac{z - d}{z_o} \right) \quad (3.13)$$

where:

- u_* is the wall shear stress friction velocity.
- κ is the Von Kármán constant, $\kappa = 0.4$.
- d is the zero-plane displacement height.
- z_o is the roughness length scale.

The length z is measured from the true ground position, (the bottom of the roughness element valleys). The friction velocity, u_* , is a dimensional relationship to the ground wall shear stress, $u_* = \sqrt{\tau_w/\rho}$. The parameter, d , is the surface displacement height, which is the height at which the mean drag acts on the flow above the ground surface roughness elements.

The log-law relationship was fitted to the mean velocity measurements using least squares, with the assumption that all the errors were non-Gaussian in the mean velocity, U , see Figure 3.12. It was determined that the log-law profile fits well throughout most of the boundary layer. Using data in the lower two thirds of the boundary layer depth, (recall $H=150$ mm), u_* and z_o values were found to have only a small variation with down-stream location.

$$\begin{aligned} u_* &= 1.51 \pm 3\% \text{ cm/s} \\ z_o &= 0.15 \pm 15\% \text{ mm} \end{aligned}$$

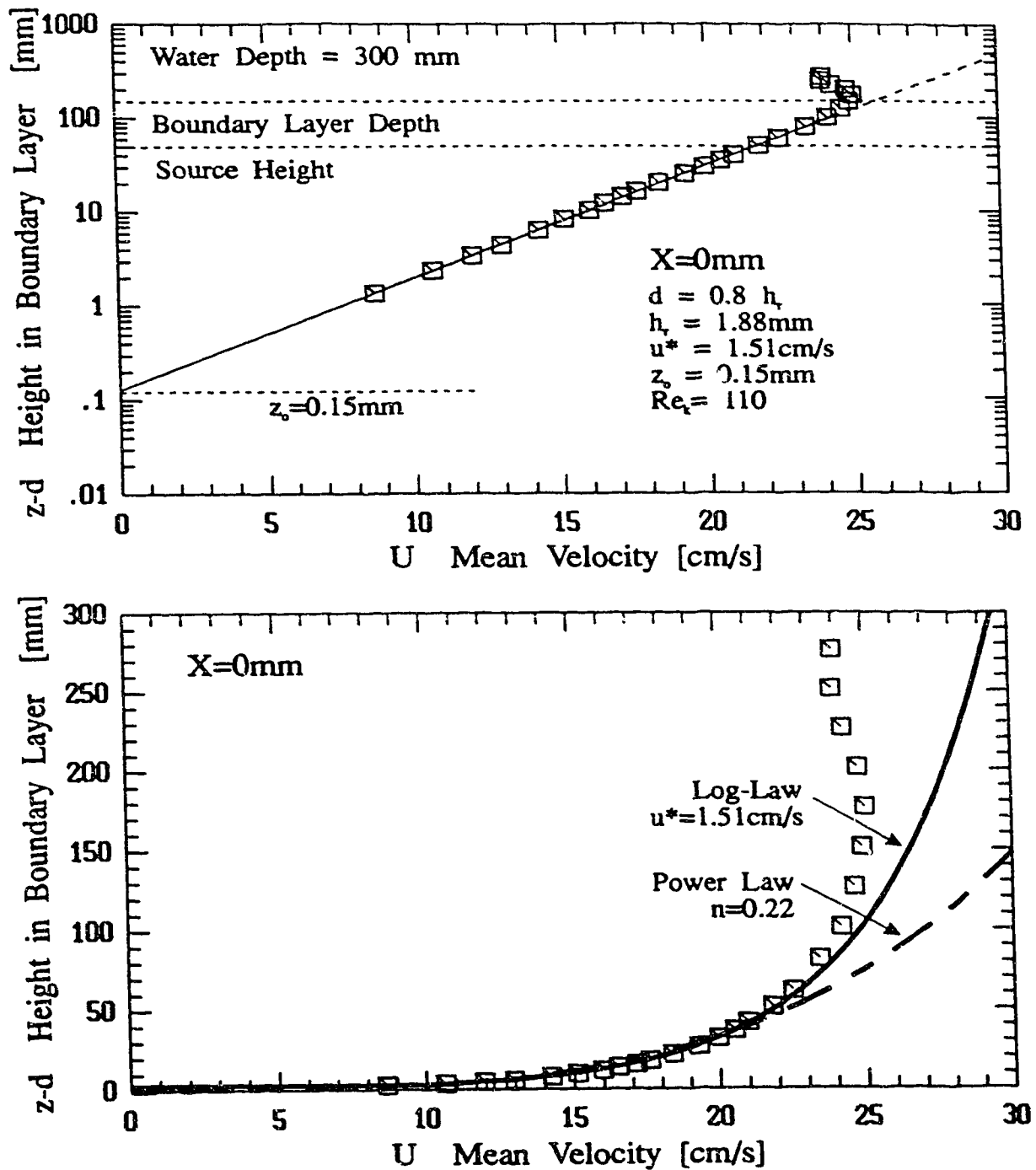


Figure 3.12: Log-law fit to velocity profiles showing the effect of displacement height (top) and a comparison of the log-law fit to a power-law fit (bottom).

The friction velocity, u_* , may also be determined by examining the total shear stress distribution in a *fully developed* boundary layer. (where $\partial U/\partial x \equiv 0$), Nezu and Rodi (1986),

$$\frac{\tau}{\rho} = -\overline{u'w'} + \nu \frac{\partial U}{\partial z} = u_*^2 \left(1 - \frac{z}{H}\right) \quad (3.14)$$

where $u_*^2 = \tau_w/\rho$ and τ_w is the shear stress extrapolated from (3.14) at the wall ($z = 0$). Which predicts that the variation of the shear stress near the wall has a constant slope,

$$\frac{\partial}{\partial z} \left(\frac{\tau}{\rho} \right)_{\text{as } z \rightarrow 0} = \frac{-u_*^2}{H} = \text{constant} \quad (3.15)$$

In Figure 3.13, shear data are shown for all locations. A linear relationship similar to (3.14) was used to extrapolate $\frac{\tau}{\rho}$ near the wall, but (3.14) did not represent the data in the outer part of the boundary layer. The wall shear stress, or u_* , was determined to be $u_* = 1.38 \text{ cm/s}$, using a least squares estimate assuming non-Gaussian errors, over the range $0 < z < 75 \text{ mm}$. This value compares well with the log-law determined u_* . The 8% difference is within the accuracy of extrapolation to the wall from the 20 mm height.

The distribution of the shear stress horizontally across the boundary layer at the source height is presented in Figure 3.14. The distributions have a mean of $0.766 \pm 0.3 \text{ cm}^2/\text{s}$. Although there is scatter in the data, the general form suggests that the shear stress across the profile, in the y -direction, is not constant. This will affect both the measured vertical and horizontal concentration profiles, but not significantly because most of the variation is far off the centre-line of the water channel.

The theoretical applicability of the logarithmic velocity profile is limited to a shallow surface layer where the shear stress may be considered constant. (The log-law velocity profile is often derived on the basis of an approximately constant, or negligibly varying, shear stress, but alternative derivations use only scaling arguments.) However, in most practical situations, there is not a true constant shear stress layer, even in the atmosphere. The surface layer is approximately the lower 10% of the boundary layer (Tennekes and Lumley, 1972, Simiu, 1973). When the friction velocity is used as an estimating parameter, the profile may be used at even greater heights. The friction velocity, u_* , is a surface parameter which is independent of height. The roughness of the surface therefore determines the flow characteristics, if it is fully rough flow, (see section 3.3.3).

The use of the log-law relationship for determining the roughness length is limited

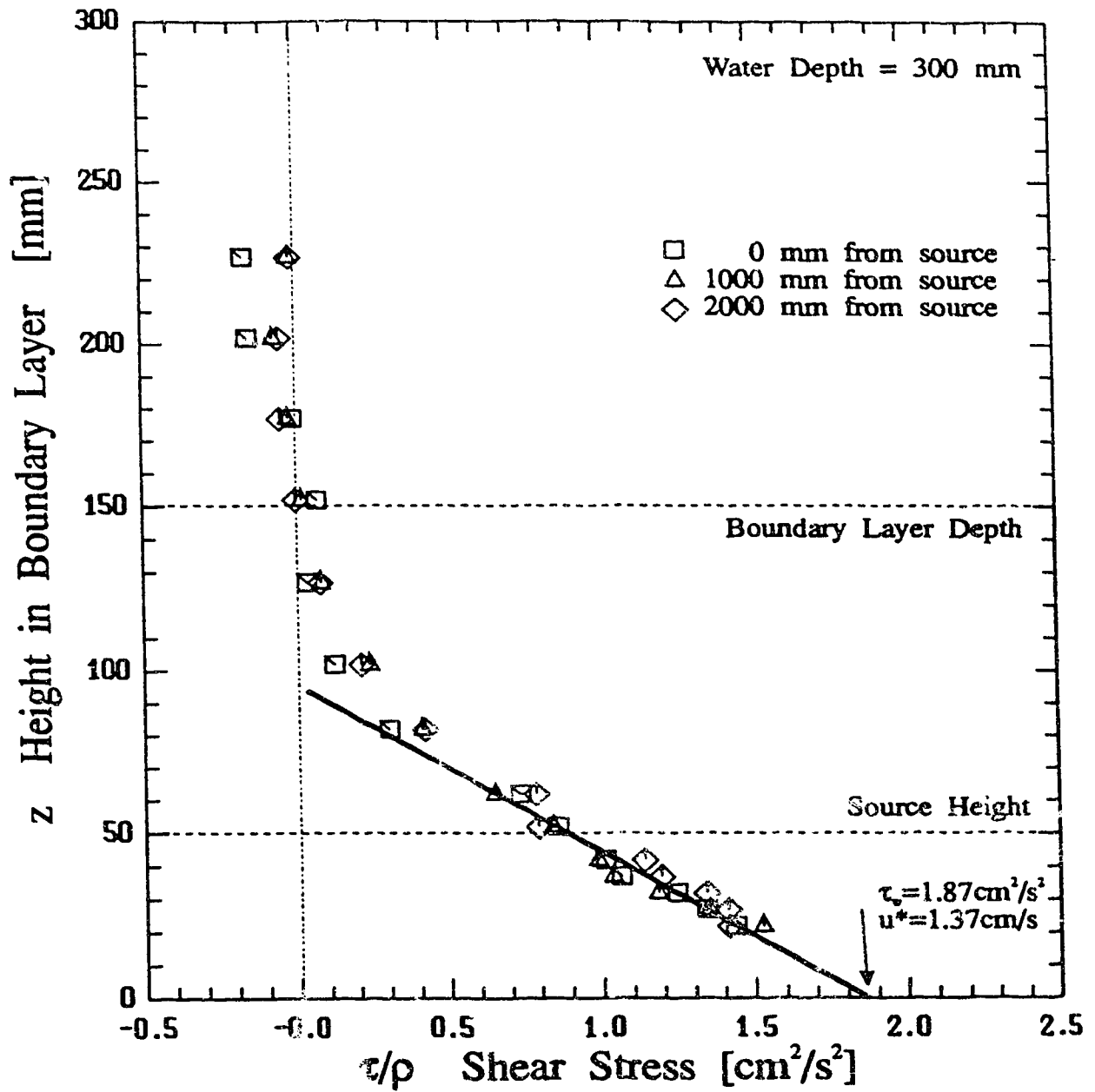


Figure 3.13: Distribution of shear stress in the boundary layer with a linear fit in the wall region to determine the wall shear stress $\tau_w/\rho = u_*^2$.

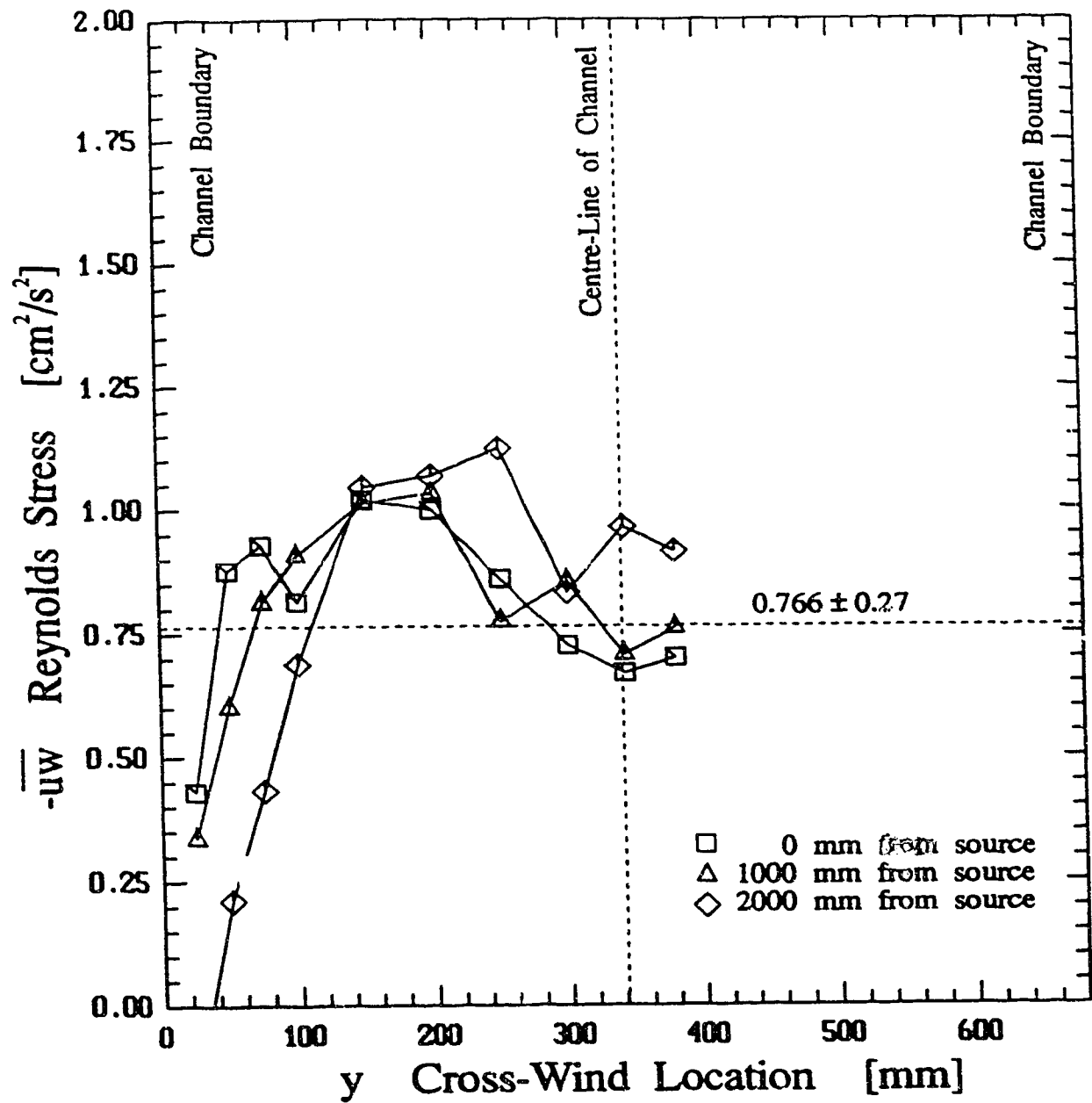


Figure 3.14: Horizontal distribution of the turbulent shear stress in the boundary layer at the source height.

by the criterion of Counihan (1975) or Hinze (1975),

$$\frac{u_* z_o}{\nu} > 2.5 \text{ or } 5 \quad (3.16)$$

If this criterion is met, the effects of the viscous sub-layer are small and may be neglected. This criterion however may be a function of the roughness type and should not be considered a definite guide (Counihan, 1975). In the water channel flow,

$$\frac{u_* z_o}{\nu} \approx \frac{(1.51)(0.15)}{(0.01)} \approx 2.3 \quad (3.17)$$

This value is close to the suggested viscous limit, but the log-law extrapolation for z_o is probably reasonable here.

Displacement Height in the Log-Law Velocity Profile

A simple definition of the displacement height, d , in (3.13), is the average surface height obtained by flattening out all the ground roughnesses to a smooth surface. Experimental investigations by Thom (1971) have related the displacement height to the level of the mean momentum sink. Jackson (1981) shows that the roughness height, z_o , is the length scale which is related to the magnitude of the shear stresses acting on a surface, whereas the displacement height, d , is related to the distribution of the shear forces.

Between z_o and d , the roughness height, z_o , is the more important parameter, and d may often be neglected or simply estimated, Jackson (1981). For a wide range of flow conditions and roughnesses the approximation of $d/h_r = 0.7$ is reasonable, (Jackson, 1981), where h_r is the height of the roughness. As the roughness elements get more densely packed so that their apparent roughness, z_o , decreases, the displacement height will approach the height of the top of the roughness elements, see Figure 3.15. Large, scattered roughness elements tend to lower the displacement height. Although $d = 0.7 h_r$ may provide a reasonable estimate it must be kept in mind that d will be sensitive to the roughness density.

A rigorous analysis for determining d is possible, as suggested by Jackson (1981), by considering the momentum equation in the horizontal direction and the continuity equation. An expression for d may be generated by integrating the variation in horizontal stresses including the Reynolds stress over the surface area. Alternatively, a less rigorous procedure, which was used in this analysis, determines d graphically as the value required to fit the data in the wall region of the flow to the log-law relationship, Panofsky and Dutton (1984). The wall region in which the log-law

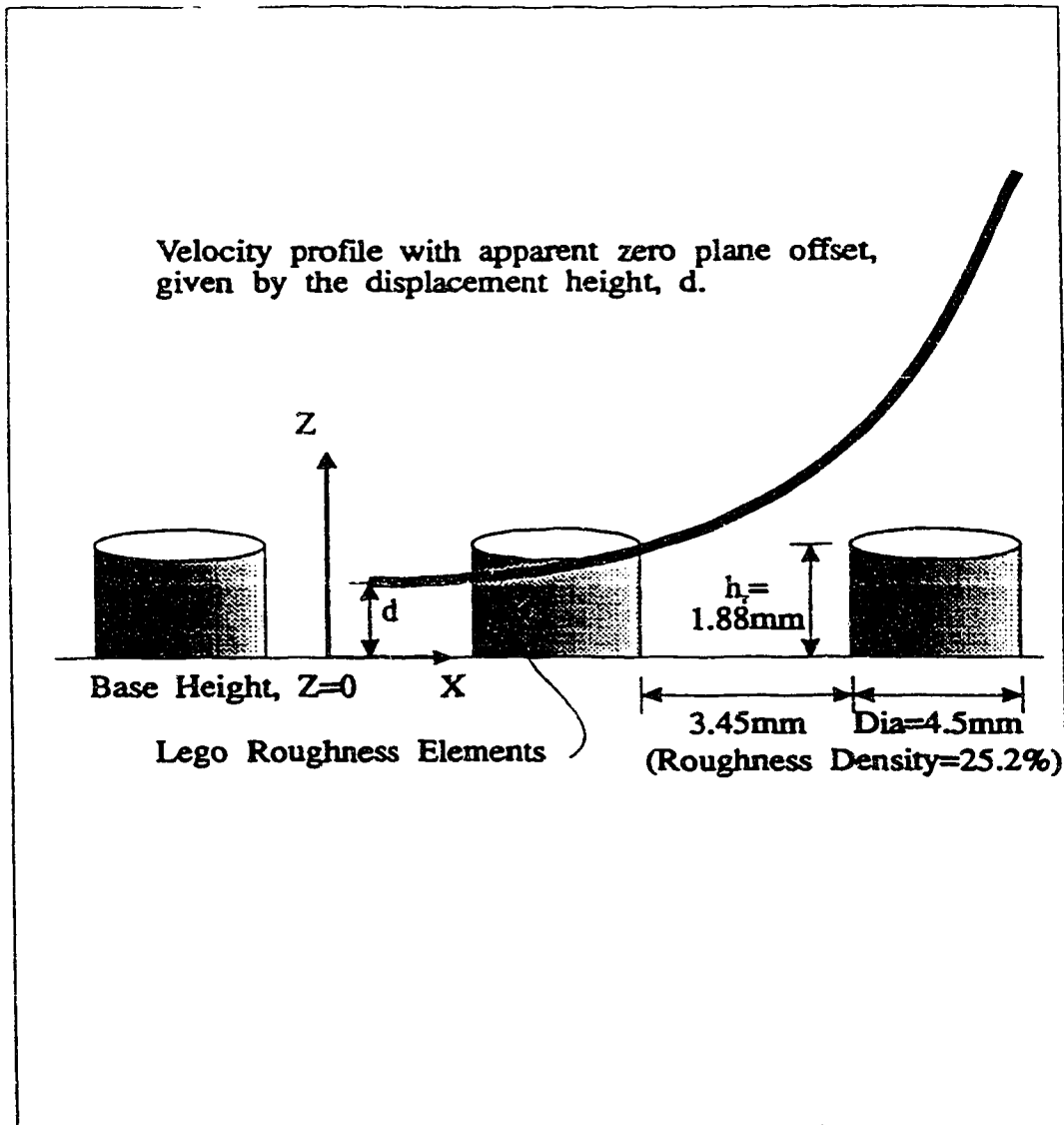


Figure 3.15: Schematic of height measurement and roughness elements.

relationship applies rigorously is approximately 10% of the boundary layer thickness. However, the relationship works well over much of the boundary layer. This study arbitrarily uses 2/3 of the boundary layer depth for the fit region. The displacement height of $d = .8 h_r$ was found to represent the data adequately. The initial position of the laser beam is done by eye and is estimated to be within $\pm 0.5\text{mm}$ of z and y . This accuracy is within the resolution possible for determining d graphically.

The Von Kármán Constant

In the literature, the value of the Von Kármán constant, κ , is generally taken to be 0.4. It has recently been allowed to float between 0.33. (Tennekes, 1973, Tennekes and Lumley, 1972) and 0.41 (Nezu and Rodi, 1986, Steffler, Rajaratnam, and Peterson, 1983). It is important to know which value to use because this affects the calculated friction velocity, u_* , by as much as 20%, Tennekes (1973). Experiments suggest that the value of κ depends on the roughness of the terrain. Tennekes suggests that $\kappa = 0.35$ is the best choice when surface Rossby numbers¹ correspond to smooth terrain and $\kappa = 0.40$ is suitable for rough terrain flows. Hinze (1975) reports that values greater than 0.40 exist. Pasquill and Smith (1983) also report that values above 0.40 are advocated. Hogstrum (1985) did a very careful study of κ in the atmosphere and concluded that $\kappa = 0.4 \pm 0.01$, (likewise Dyer and Bradley, 1982). The Kansas experiments gave $\kappa = 0.35$, but almost certainly due to bad shear stress measurements.

The above discussion suggests that the accuracy with which one can determine the friction velocity from a velocity profile is strongly limited by the uncertainty in the Von Kármán constant.

A value of $\kappa = 0.40$ (rough terrain) is applicable for use in this study for the roughness in the boundary layer in the water channel. Pasquill and Smith (1983), and Tennekes (1973) also imply that 0.40 may be better suited for rough surfaces. Nezu (1986) points out that deviations from the standard log-law should not be accounted for by adjusting κ but rather by adding a wake function to the end of (3.13). This added complexity was not considered necessary for this study.

¹The Rossby number is a statistic describing the importance of the coriolis force in comparison to the inertial force.

3.3.2 Power-Law Mean Velocity Profile

The velocity profiles were fit to the power-law expression, (3.18), in the boundary layer region using the least squares method. The power-law is given as:

$$\frac{U}{U_1} = \left(\frac{z}{z_1} \right)^n \quad (3.18)$$

Which may also be expressed as,

$$U = K_n z^n \quad (3.19)$$

For the boundary layer in this study, the exponent and coefficients for each of the profiles varied less than $\sim 3\%$ of the values below.

$$\begin{aligned} K_n &= 9.5 \frac{\text{cm/s}}{\text{mm}^n} \\ n &= 0.22 \end{aligned}$$

The power-law profile does not represent the data well for the boundary layer in this study, probably because the boundary layer is well developed, but not fully developed.

3.3.3 Roughness Reynolds Number

An index of when the flow acts independently of the viscosity is the roughness Reynolds number, Re_k . When sufficiently high, the flow is dependent upon the wall roughness and not the fluid viscosity. This means that the flow is Reynolds number independent for turbulence intensity and for integral length scale to boundary layer thickness ratio. As long as the flow is fully rough, a model to full-scale Reynolds number mismatch can usually be safely ignored.

The roughness Reynolds number may be determined through the expression for flow over a densely packed sand grain roughness, Hinze (1975) p.617,

$$\frac{U}{u_*} = \frac{1}{\kappa} \ln \left(\frac{z}{k_s} \right) + 8.5 \quad (3.20)$$

If we equate this expression with the log-law relationship in (3.13), it is found that,

$$\frac{k_s}{z_o} = \exp(8.5\kappa) = 30 \quad (3.21)$$

From the experiments of Nikuradse, Hinze (1975) p.635 suggests that Re_k be at least 55 for fully rough flow.

$$Re_k = \frac{u_* k_s}{\nu} > 55; \quad \nu = 0.01 \text{ cm}^2/\text{s} \quad (3.22)$$

Hinze also advises that this value is for flow over uniform sand roughness and that the value could change appreciably for different roughness types. Tennekes and Lumley, (1972) p.165 suggests that Re_k be greater than 30. Plate (1971) suggests the critical value be $Re_k > 70$, and Counihan (1975) suggests $Re_k > 40$. In the boundary layer used in this study.

$$Re_k \approx \frac{1.51 * (0.015 * 30)}{0.01} \approx 68$$

It may be concluded that the flow in the water channel simulation may be considered "fully rough" since the roughness Reynolds number exceeds the critical values suggested in the literature.

3.3.4 Profiles of Turbulence Velocities

The profiles in the vertical direction of the horizontal turbulent intensity, Figure 3.3, show the typical trends found in boundary layer flows. There are no full scale data available for direct comparison but the data collected does compare favourably to profiles of intensity in a log-law boundary layer.

Nezu and Rodi (1986), and Hanna, Briggs, and Hosker, (1982), use the following universal functions for u'/u_* and w'/u_* in the equilibrium region ($50 < zu_*/\nu < Hu_*/\nu$) where the turbulent energy production is approximately in balance with the viscous dissipation.

$$\frac{u'}{u_*} = a_u \exp(-b_u z) \quad (3.23)$$

$$\frac{w'}{u_*} = a_w \exp(-b_w z) \quad (3.24)$$

where a_u , a_w , b_u and b_w are empirical constants. Hanna Briggs, and Hosker, suggest that $a_u = 2.0$, $a_w = 1.3$, and b_u and b_w are related to the coriolis parameter and u_* .

In the water channel, a least squares fit in the boundary layer produces, (see Figure 3.16)

$$\frac{u'}{u_*} = 1.95 \exp(-0.0083 z) \quad (3.25)$$

$$\frac{w'}{u_*} = 1.17 \exp(-0.0070 z) \quad (3.26)$$

The water channel observed value of a_u is within 2.5% of Hanna, Briggs, and Hosker, prediction and a_w is within 10%.

The fluctuation levels in the near surface region of $15 < z/z_o < 60$, averaged over the three measurement locations, is found to be,

$$\frac{u'}{u_*} = 1.85 \pm 0.1$$

This is in agreement with published values,

Panofsky and Dutton, (1984)	$u'/u_* = 2.39$
Hanna, Briggs and Hosker, (1982)	$u'/u_* = 2.0$
Counihan, (1975)	$u'/u_* = 1.8 - 1.9$
Nezu and Rodi, (1985)	$u'/u_* = 2.2 - 2.6$
Grass, (1971)	$u'/u_* = 2.0$
Nakagawa, Nezu, Ueda, (1975)	$u'/u_* = 1.8$

The anisotropy ratio, the variance of the velocity fluctuations in the vertical direction to the along wind velocity fluctuations, is plotted in Figure 3.17. Three regions are present; a surface layer, $0 < z < 75$ mm with $w'/u' \simeq 0.57 \pm 0.06$, a transition region $75 < z < 125$ mm, and an outer flow region, $z > 125$ mm with $w'/u' \simeq 0.85 \pm 0.07$. The value in the outer flow region resembles grid turbulence, and may be a result of slowly decaying turbulence generated at the boundary layer trip. The flow in that region is therefore, more isotropic than in the shear dominated region close to the rough surface. In the surface layer, the water channel $w'/u' = 0.60$. This represents good agreement with,

Panofsky and Dutton, (1984)	$w'/u' = 0.52$
Hanna, Briggs and Hosker, (1982)	$w'/u' = 0.65$
Counihan, (1975)	$w'/u' = 0.50$

3.3.5 Integral Length Scales of Turbulence

The length scales of velocity fluctuations are important in the dispersion of the plume in the water channel. The scales of turbulence in the environment govern the effective plume spread. To understand why, refer to the schematic plumes in Figure 3.18 which consider a plume dispersing in the wind. If the turbulence scales are large compared to the plume diameter, then the plume will be pushed around similar to the meandering behaviour of the tail of a kite. The measured lateral

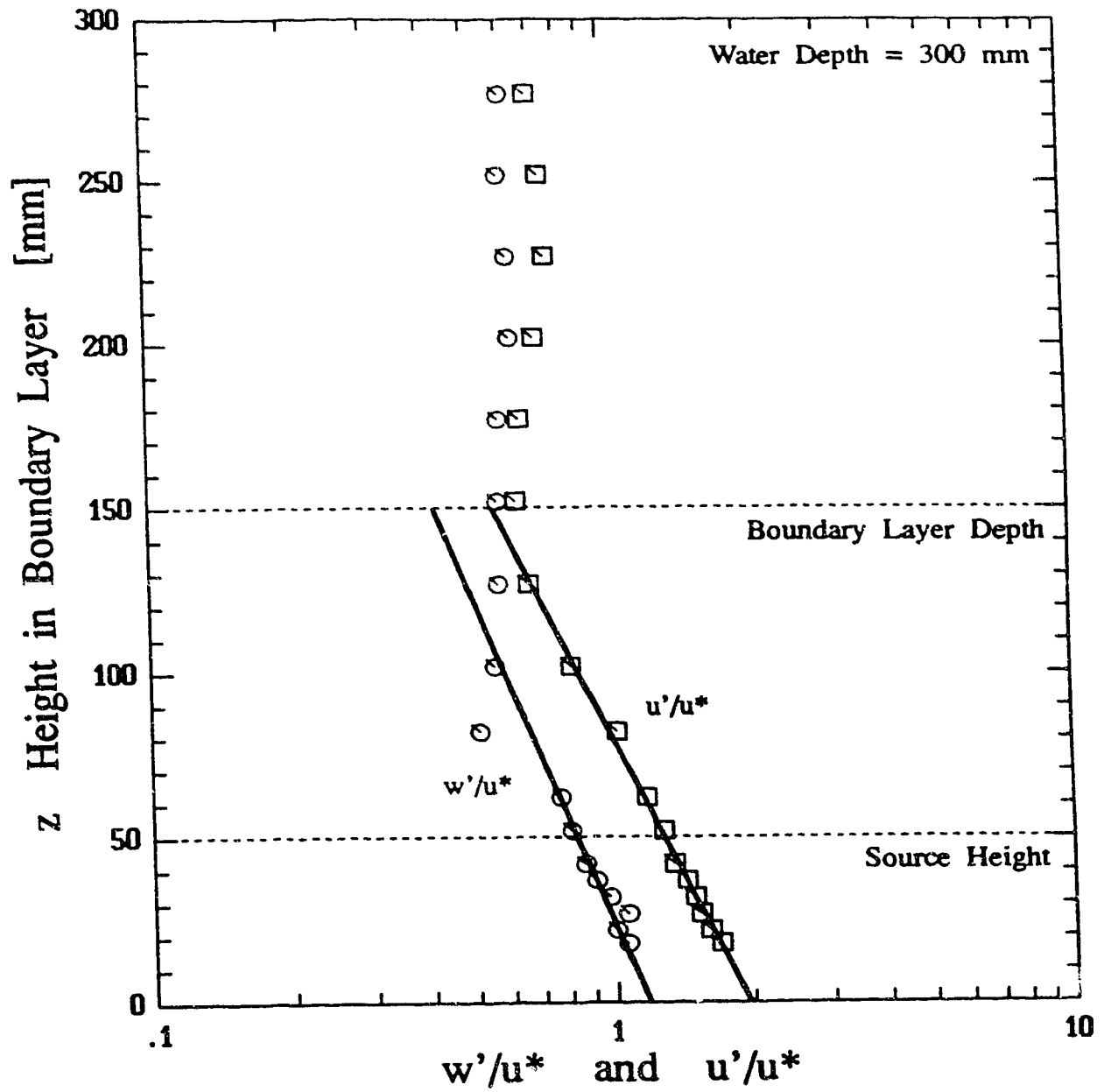


Figure 3.16: Profiles of the vertical velocity fluctuations and the horizontal velocity fluctuations as a ratio of the friction velocity.

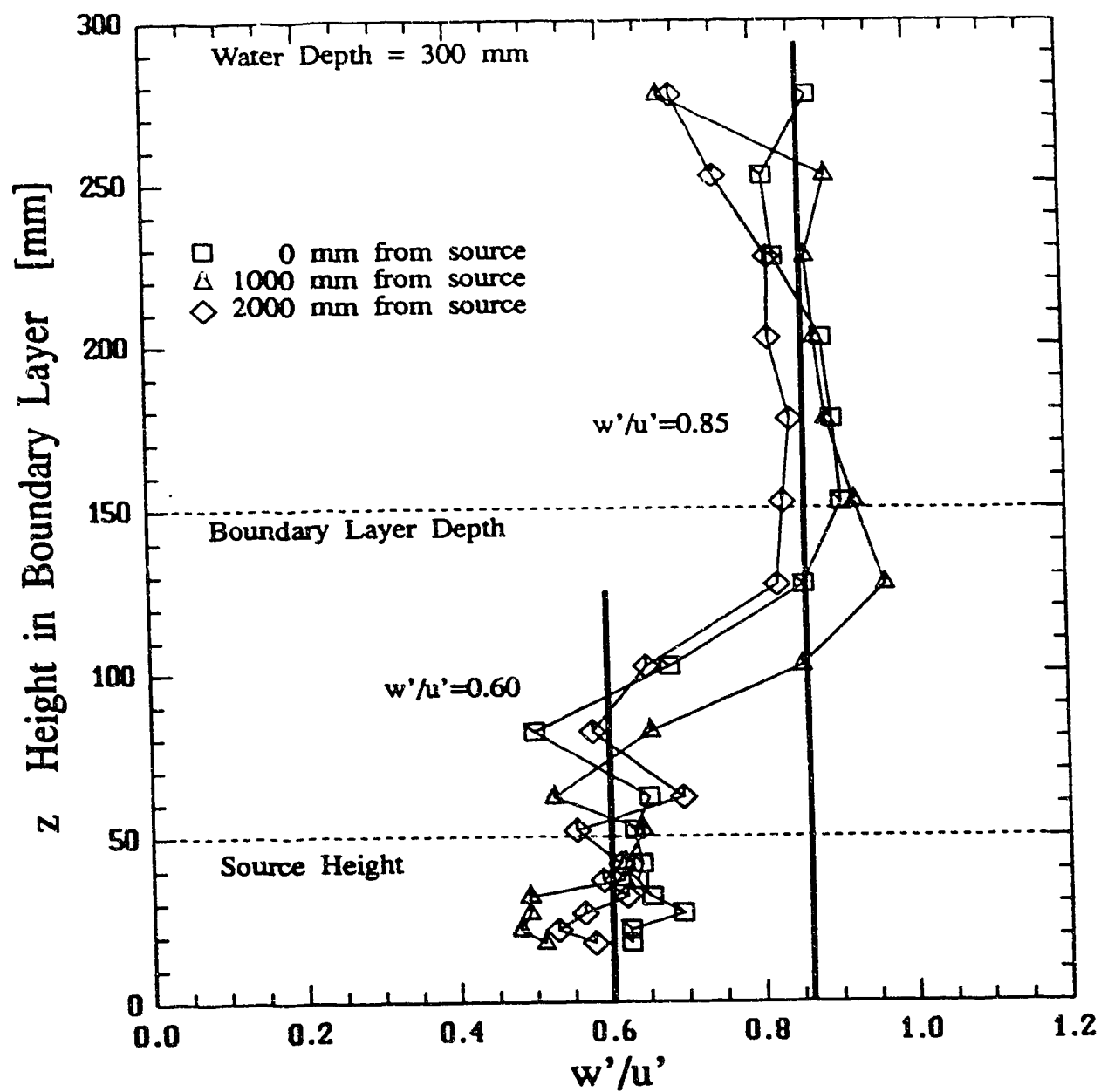


Figure 3.17: Profiles of the vertical velocity fluctuations as a ratio of the along wind velocity fluctuations.

dispersion of this plume is the result of time averaging. A non-zero concentration signal will be observed only a fraction of the observation time period. When the scales of turbulence are small compared to the plume diameter, the process may be modelled as effectively diffusive. The dispersion observed in the plume, is then a result of time averaged values of a concentration signal which is non-zero most of the time, except for far from the plume axis, Gifford (1982).

Researchers recording measurements in the atmosphere have difficulty determining turbulent length scales. Part of the reason for this is the long time averaging period required to make consistent measurements. The atmosphere exhibits variations, (e.g. in temperature), on times scales out to millions of years, such that no averaging time is satisfactory. Typically, a time period of several thousand time scales is required for a statistically repeatable average. Kaimal, Clifford, and Lataitis (1989) show that a sample time equal to 10,000 integral time scales is required to correctly determine variances due to improper convergence of the high spectral frequencies when the data sample is truncated. In the atmosphere, 2000 time scales would correspond to a period of about 16 hours for an atmospheric length scale of 150 m, $((150\text{m}/5\text{m/s}) \times (2000 \text{ averages}/60^2) \approx 16\text{hrs})$. It is extremely unlikely, (impossible due to diurnal cycle), that one would observe stationary conditions for a period this long in the atmosphere.

Turbulent Length Scale Profiles

The integral length scales of along wind turbulence are shown in Figure 3.4. The trends in the scale profiles in the simulation data are also those observed in the full scale data, Counihan (1975). The scales in both flows peak at about one third of the boundary layer height. The region close to the ground is expanded in Figure 3.19.

Counihan (1975) and Pasquill and Smith (1983) suggest a power-law relationship, with exponent $n \approx 1$, for the increase in the turbulent integral scale with height in the lower third of the boundary layer. Data sets reviewed by Counihan suggest that the exponent is sensitive to terrain roughness, especially for scales near the ground. The experimental boundary layer is in good agreement with the power-law relationship as shown in Figure 3.20, using $n = 0.64$.

Counihan suggests that the integral length scale of velocity fluctuations, Λ_u , decreases with an increase in surface roughness and increases with height up to about $1/3$ to $1/2$ the boundary layer height. Beyond this height, Λ_u decreases for further increases in height and becomes independent of surface roughness. These trends are observed in the profiles for the scales in the water channel.

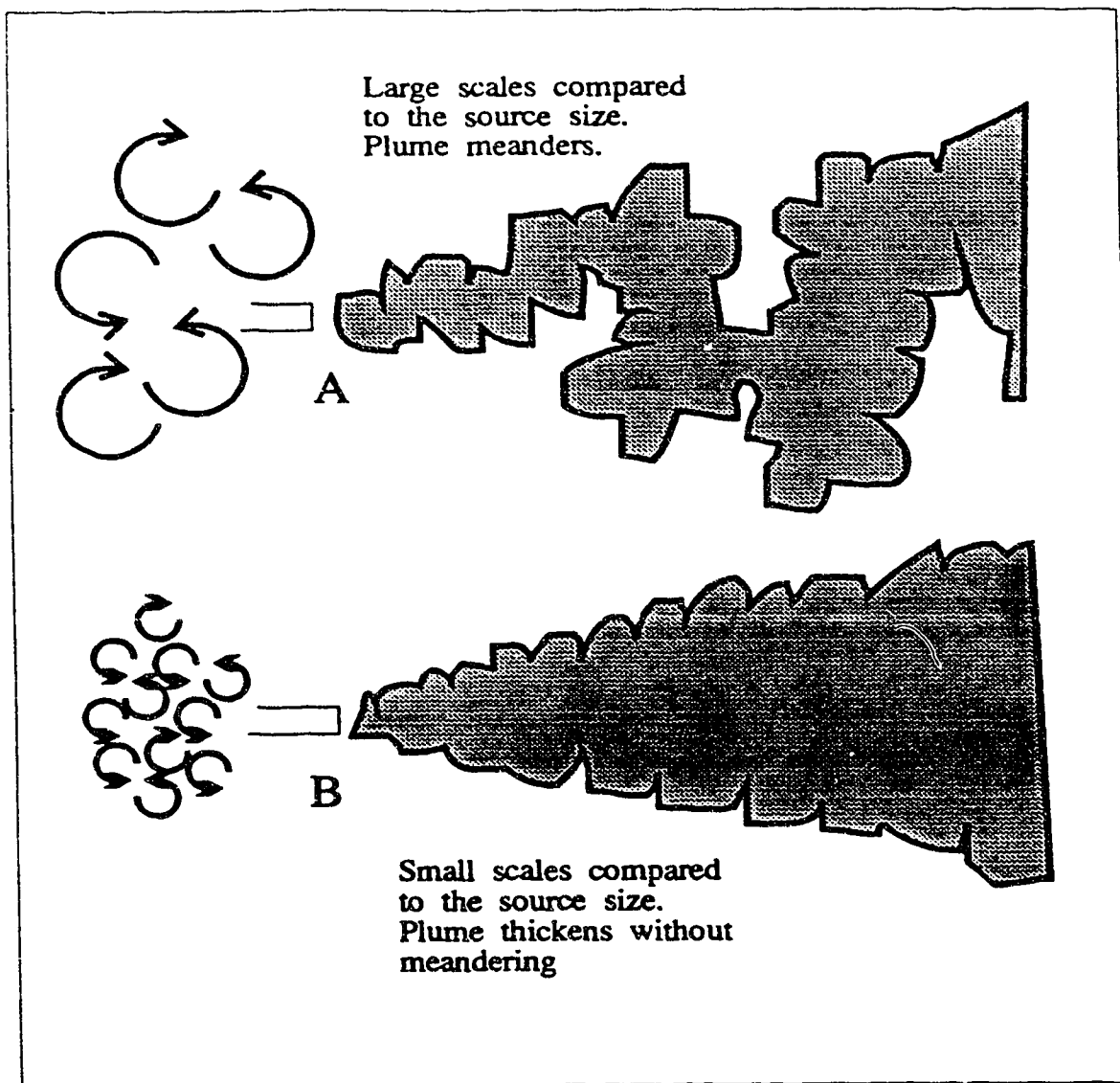


Figure 3.18: Schematic drawing of two plumes illustrating the importance of the integral length scales in the dispersion of a plume in comparison to the source size. A large length scale to size ratio causes the plume to meander much more than a small ratio.

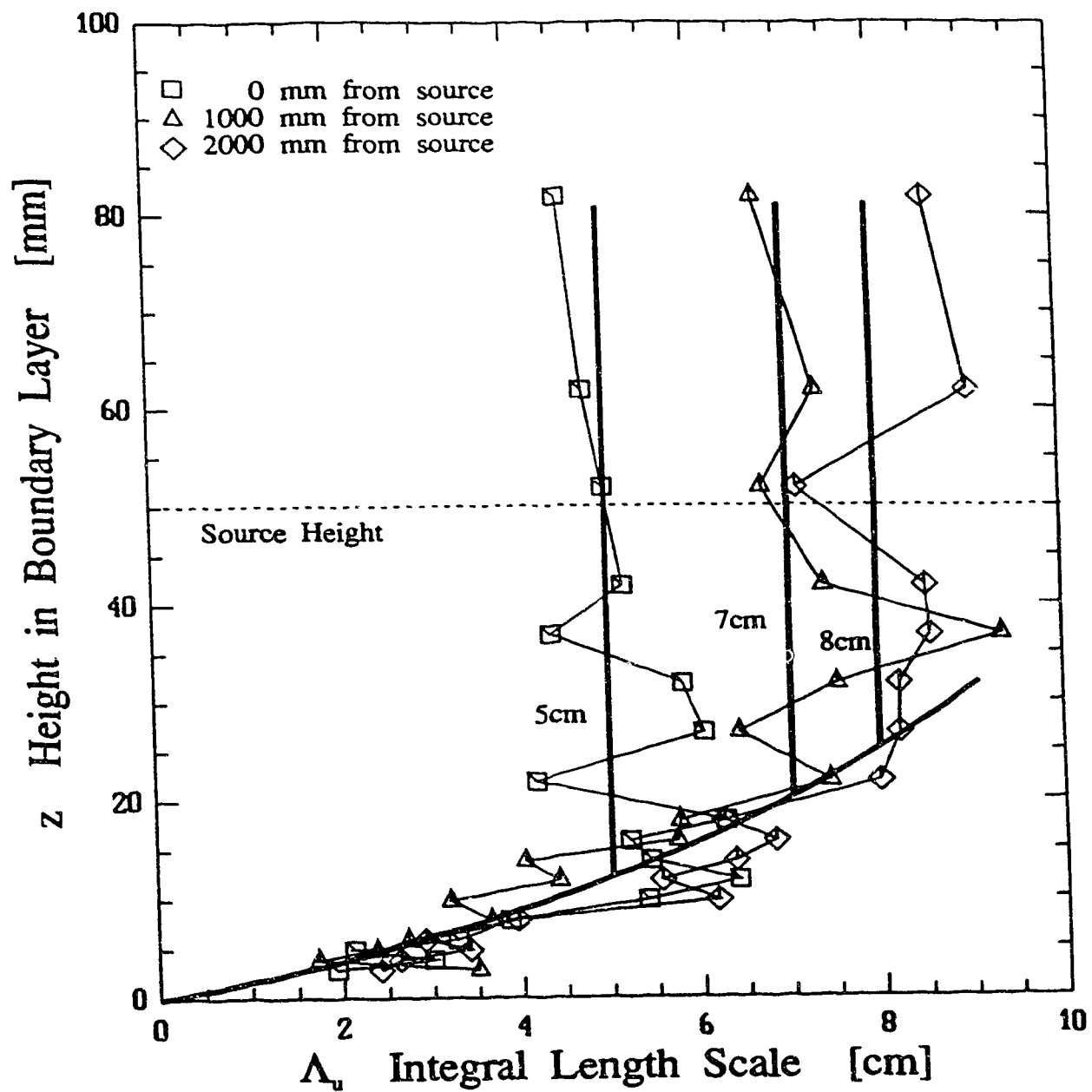


Figure 3.19: Profiles of along wind integral length scales of turbulence close to the ground.

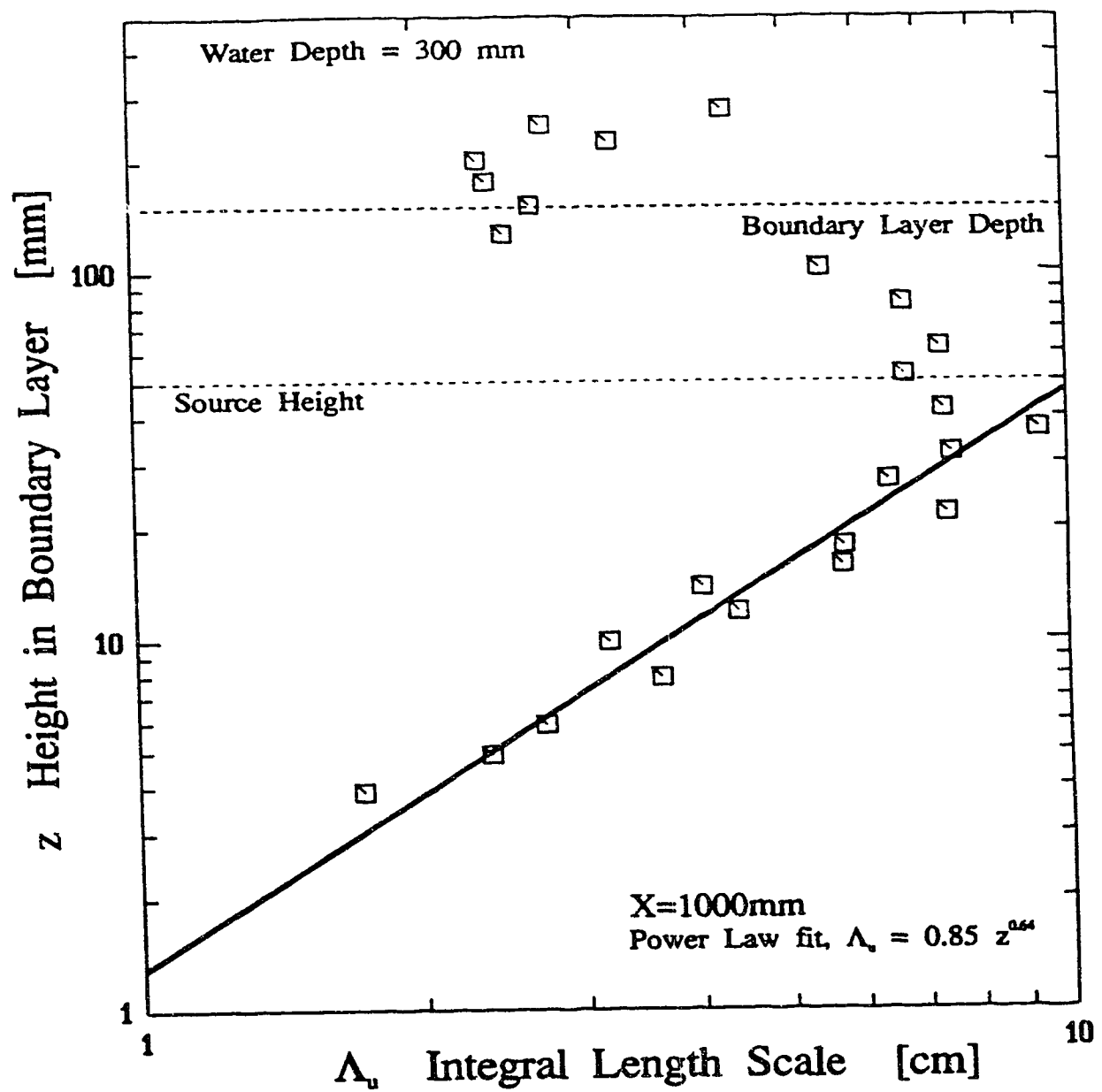


Figure 3.20: Variation of the along wind integral length scale with height in the lower third of the boundary layer showing a power-law fit with exponent, $n = 0.64$.

Vertical Length Scale Profiles

The vertical length scale, L_z , is reported by Counihan from Pasquill (1961) to vary as $L_z \approx 0.5z$ up to about 1/4 of the boundary layer height, at which point L_z remains constant with further increases in height.

Scaling the vertical time scale of the eddy size to a length scale, by $\Lambda_w = W T_w$, does not make sense since the vertical mean velocity is, $W \simeq 0$. Using the horizontal mean velocity, U , does not create a length which means anything physically. Unless the vertical scale, Λ_w , is measured directly using spatial correlation, it may be better to consider the time scales in the vertical direction.

The LDA measurements in the water channel do not measure the vertical time scales near the ground wall due to the interference of the ground wall with the laser beams. The distribution of the vertical time scales near the wall is therefore not known. Above approximately 1/4 of the boundary layer height the scales tend to decrease and then become constant over the rest of boundary layer height. In Figure 3.21, the vertical profiles for the three data collection locations are shown.

These trends are in reasonable agreement with Counihan's observations, although this flow statistic is not generally measured or reported elsewhere.

The time scale in the along wind direction is compared to the time scale in the vertical direction in Figure 3.22. The along wind time scale is always larger than the vertical time scale. Counihan's review suggest that the ratio of the *length* scales forms a constant, (at least qualitatively),

$$\frac{L_x}{L_z} = 1.3 \quad (3.27)$$

It is unclear from Counihan's review how L_z was formed, but it is probably that the along wind mean velocity was used. Therefore, the ratio of *time* scales should be the same,

$$\frac{L_x}{L_z} = \frac{T_x/U}{T_z/U} = \frac{T_x}{T_z} = 1.3 \quad (3.28)$$

The ratio of time scales is plotted in Figure 3.23. The data show that the time scale ratio, T_x/T_z , in the water channel is approximately a constant, 1.7 ± 0.6 , with considerable scatter. Counihan reports that L_z is independent of surface roughness, but that L_x is not. However, he reports that there is evidence that the ratio of the scales is independent of surface roughness. Clearly, there is some ambiguity in what is expected, and the ratio of scales for the water channel data presented here is greater than expected, but still forms a constant ratio of length scales.

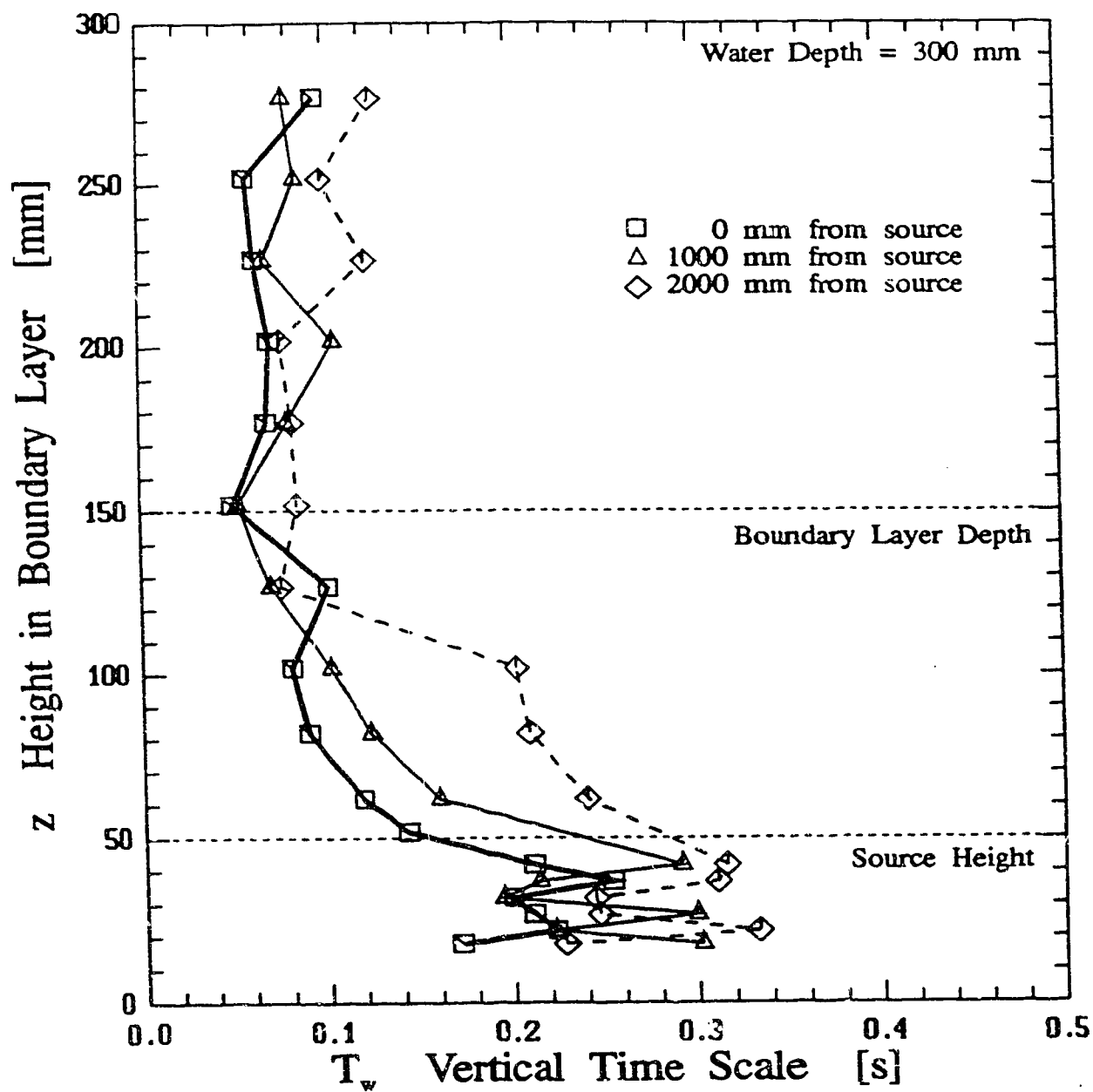


Figure 3.21: Profiles of the vertical time scale of turbulence fluctuations.

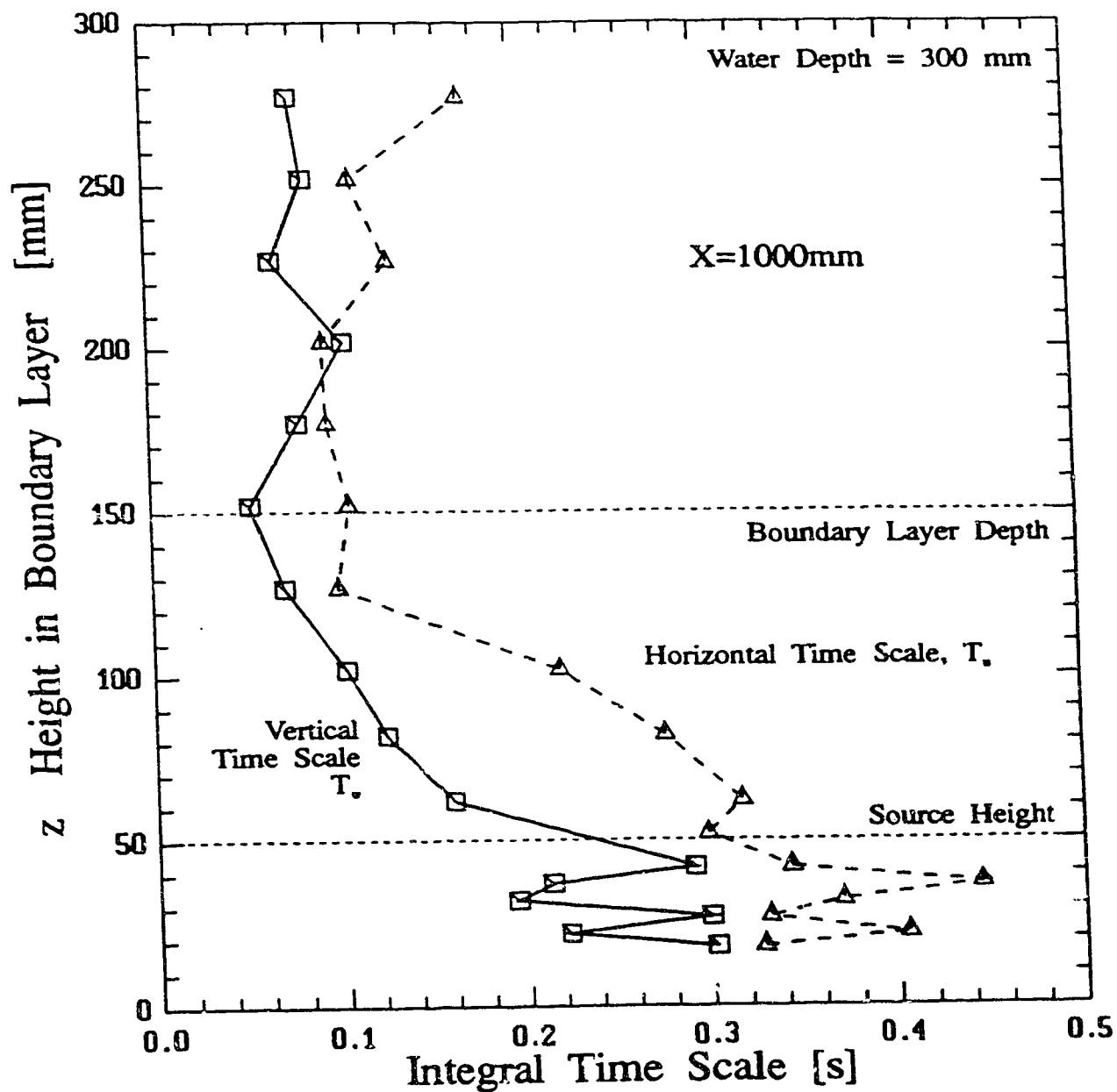


Figure 3.22: Comparison of the along wind time scale to the vertical time scale.

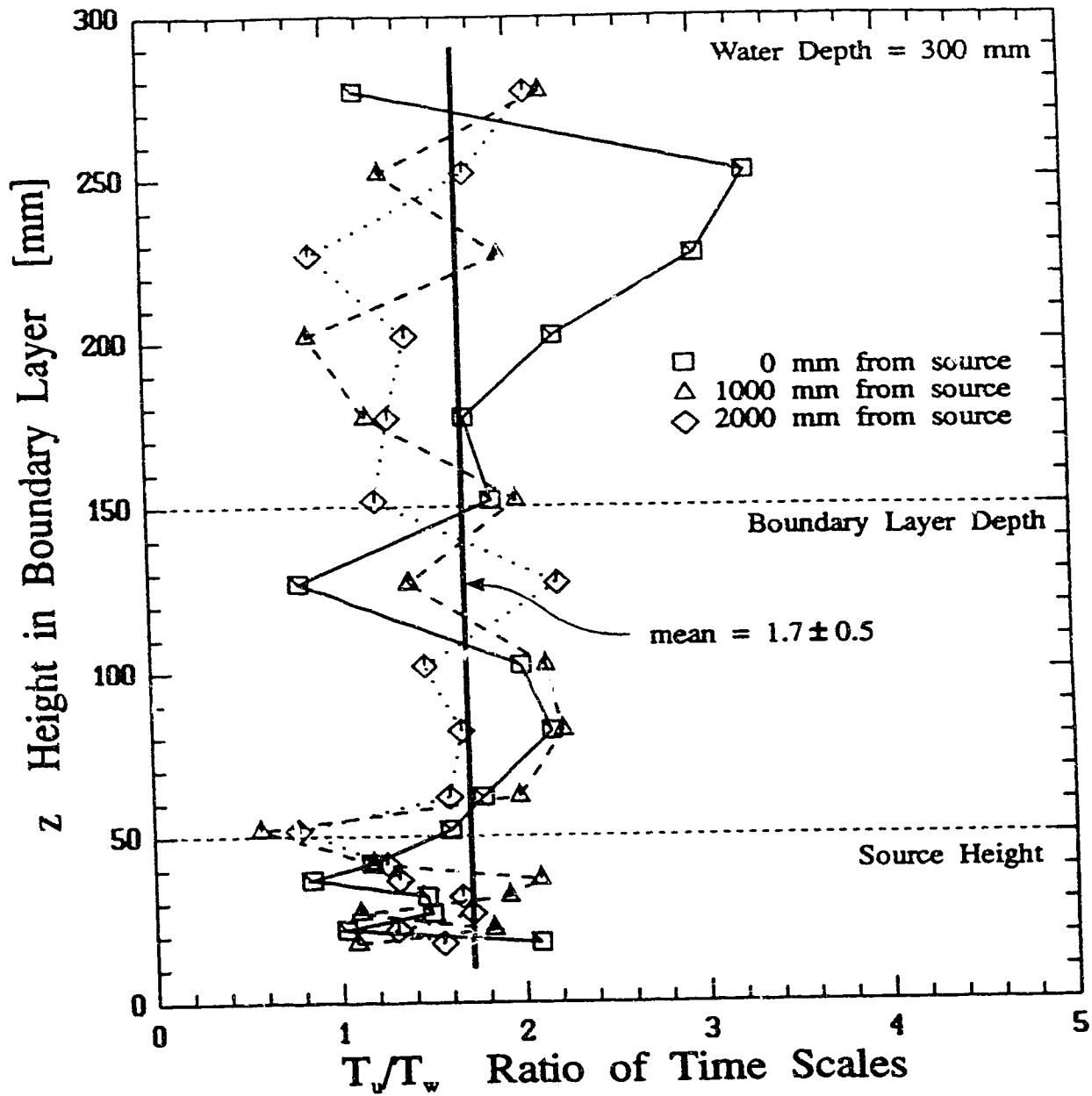


Figure 3.23: Horizontal profile of the ratio of the along wind time scale to the vertical time scale showing a constant ratio of $T_x/T_z = 1.7$.

The distribution of scale ratio horizontally across the channel is shown in Figure 3.24. The time scale ratio is approximately constant, but is a little greater than that reported in the vertical profile. The fact that the horizontal profile produces a greater value is not surprising, because of the scatter in the profiles. The fact that there is a difference may suggest that the procedures of data collection for this variable may have to be more precise.

3.3.6 Dissipation Rate and Energy Spectrum

The power spectrum of the velocity fluctuations is shown in Figure 3.25, Figure 3.26, Figure 3.27 and Figure 3.28 at the source location at heights of $z/h_s = 0.2, 1.0, 2.0$ and 3.0 respectively. The spectra are equally well represented by either a $-5/3$ inertial sub-range model or a $-6/3$ Markov model. The $-5/3$ model representation allows the simulation to be compared directly with the atmospheric turbulence where, with the large Reynolds numbers present, an inertial sub-range is often found. The Markov model representation is often used in Lagrangian stochastic simulations because the Lagrangian velocity spectrum has a $-6/3$ high frequency behaviour, (on theoretical grounds), and is often more easily manipulated in complex formulations.

If an inertial sub-range is assumed to exist in the large to small scale turbulence energy cascade in the water channel simulation, a $-5/3$ spectrum may be used to estimate the turbulent kinetic energy dissipation rate, ϵ , the rate of energy transfer through the cascade. The $-5/3$ one dimensional energy spectrum is modelled by, (Hinze (1975) p.255),

$$E_1(k_1, t) = \frac{18}{55} A \epsilon^{2/3} k_1^{-5/3} \quad (3.29)$$

where ϵ is the energy dissipation and k_1 is the one dimensional wave number. Hinze gives $A = 1.7$ for most conditions, although there is considerable variation in A according to other experimenters, Hinze (p.255). The value of A has been determined using large Reynolds number (isotropic) flows in ocean channels.

Alternatively, a generalization of the Von Kármán one dimensional energy spectrum is given by, (see (6.67)),

$$E_1(k_1, t) = \frac{2/\pi u'^2 \Lambda_f}{\left(1 + \left(\frac{\Gamma(n-1/2)}{\sqrt{\pi}\Gamma(n)}\right)^2 \Lambda_f^2 k_1^2\right)^n} ; n > 1/2 \quad (3.30)$$

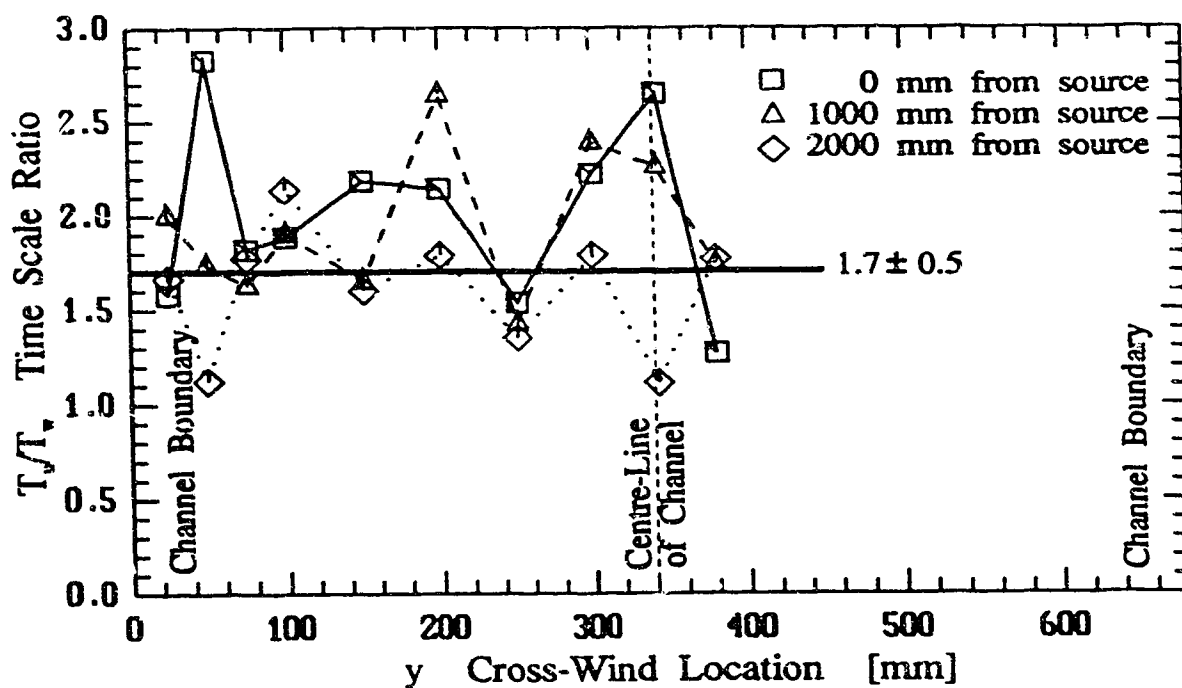
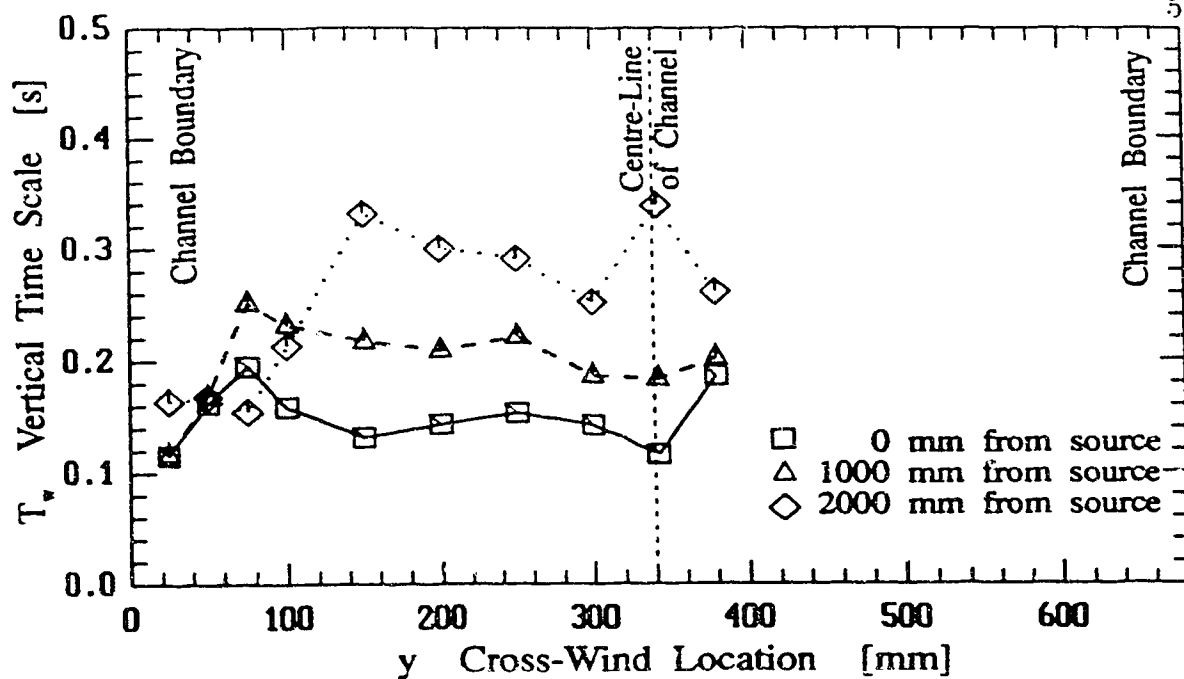


Figure 3.24: Vertical profile of the ratio of the along wind time scale to the vertical time scale showing a constant ratio of $T_x/T_z = 1.7$.

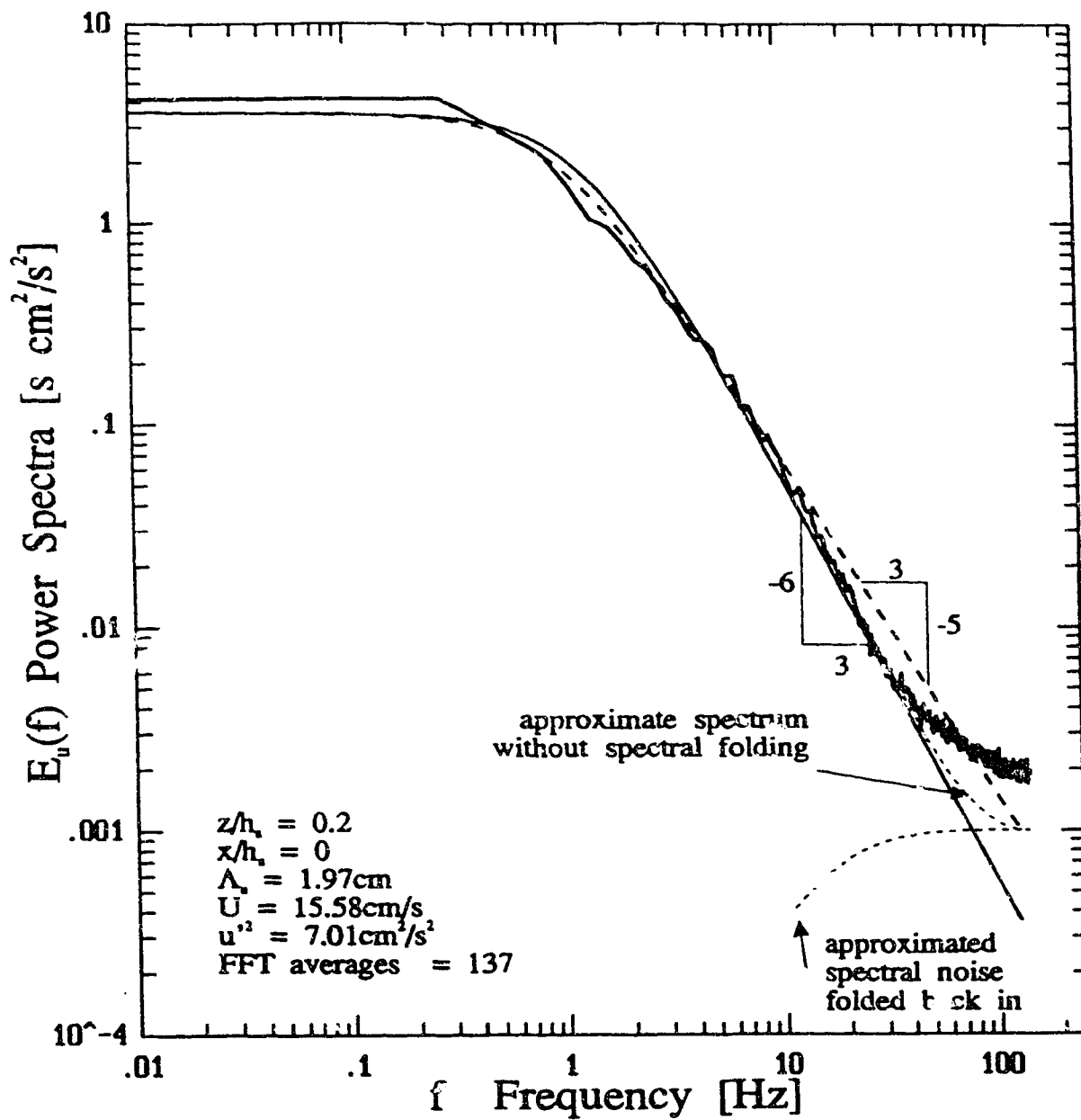


Figure 3.25: The one-dimensional energy spectrum of the velocity fluctuations at $z/h_s = 0.2$ showing that the water channel simulation may be equally represented by an inertial sub-range model or a Markov model.

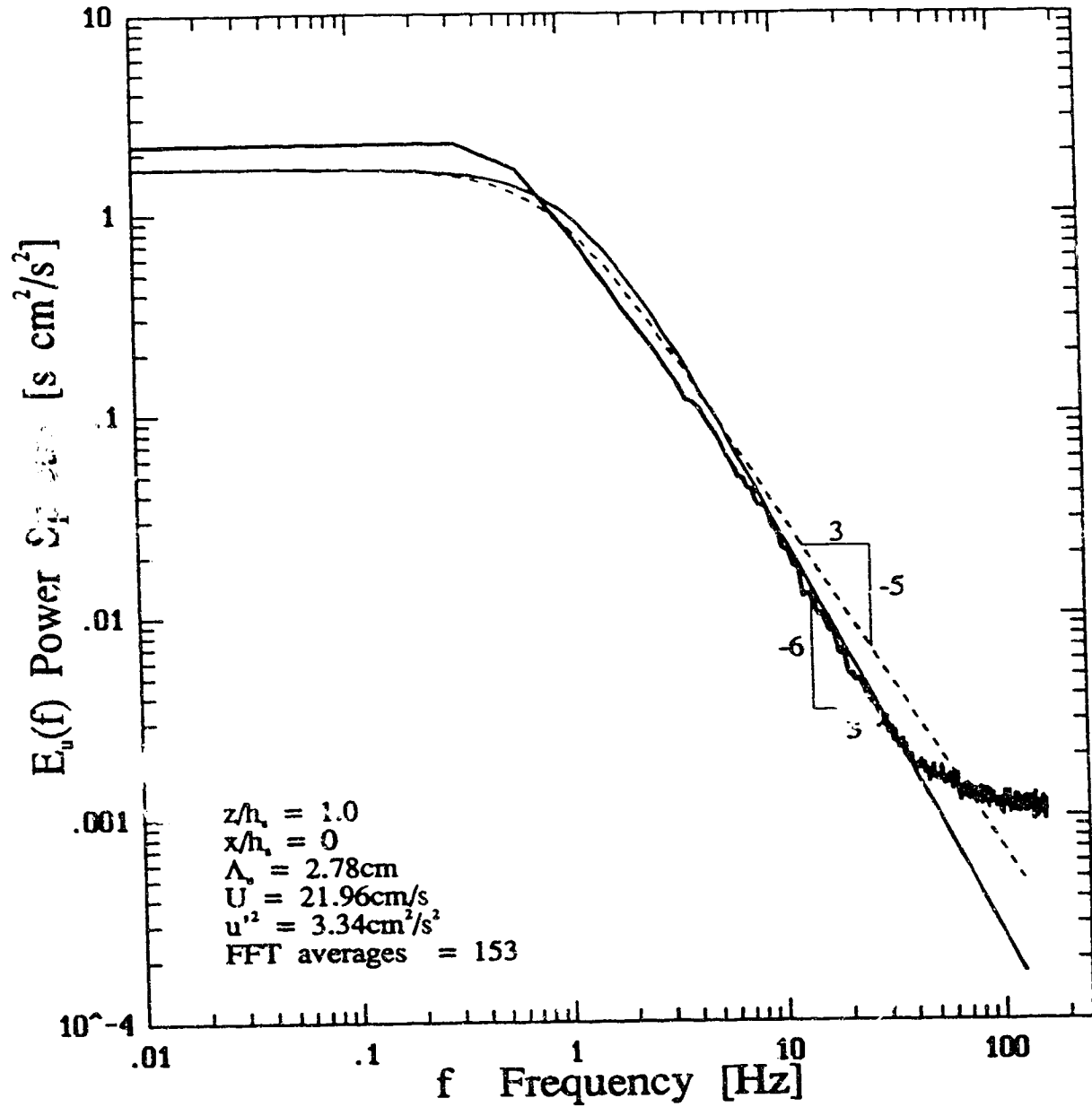


Figure 3.26: The one-dimensional energy spectrum of the velocity fluctuations at $z/h_s = 1.0$ showing that the water channel simulation may be equally represented by an inertial sub-range model or a Markov model.

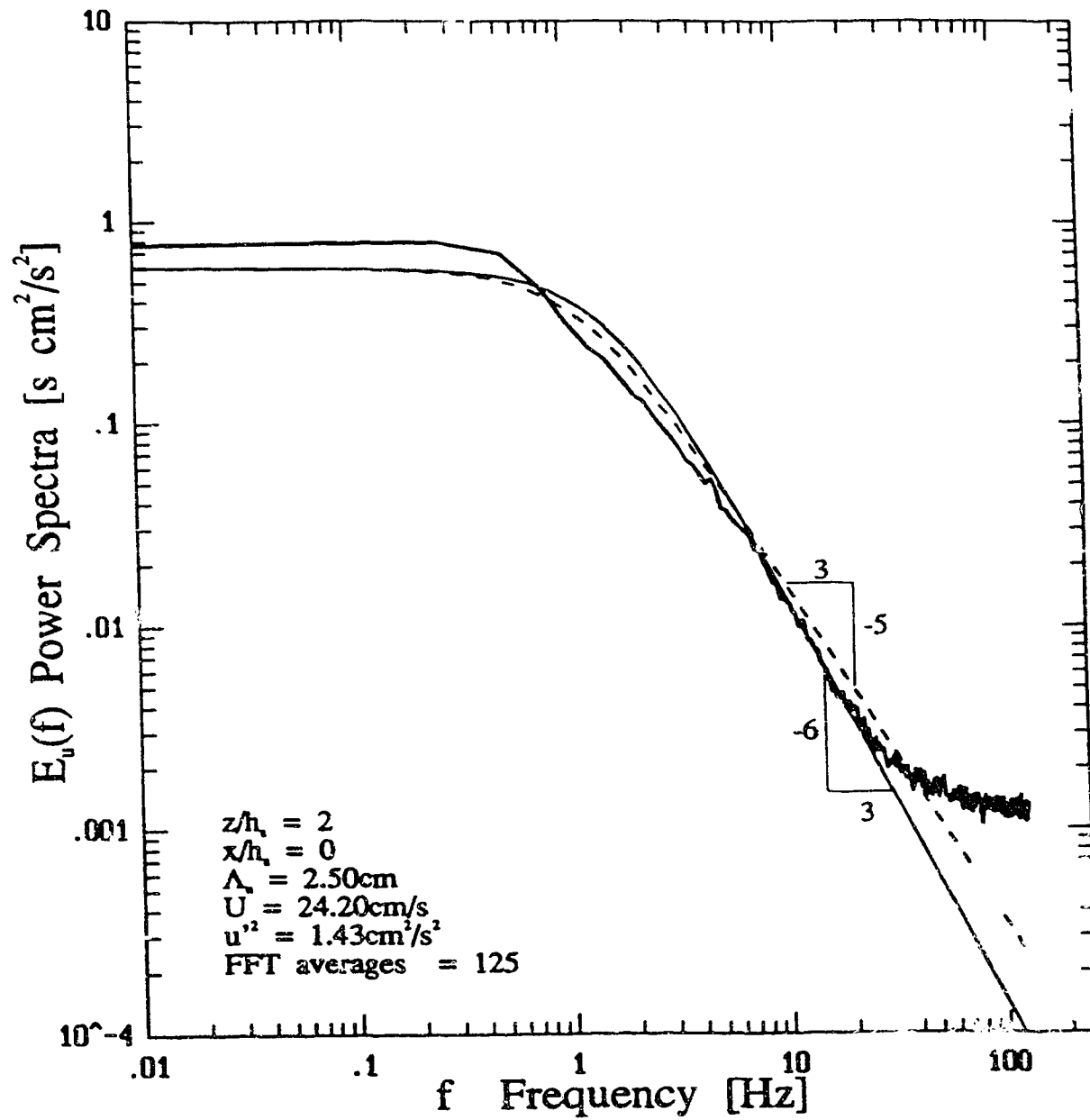


Figure 3.27: The one-dimensional energy spectrum of the velocity fluctuations at $z/h_s = 2.0$ showing that the water channel simulation may be equally represented by an inertial sub-range model or a Markov model.

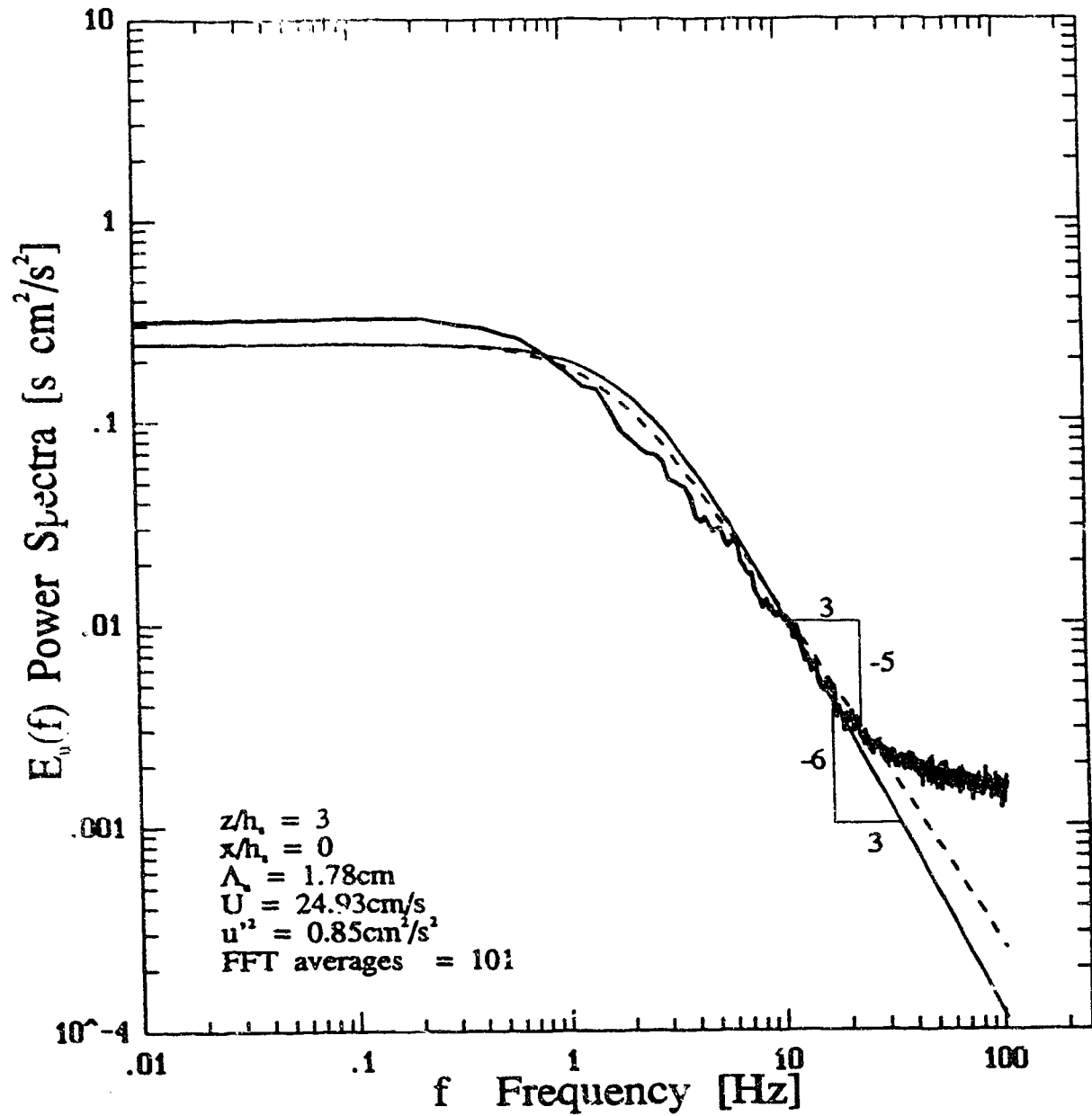


Figure 3.28: The one-dimensional energy spectrum of the velocity fluctuations at $z/h_s = 3.0$ showing that the water channel simulation may be equally represented by an inertial sub-range model or a Markov model.

where for a $-5/3$ slope at the higher wave numbers the exponent, $n = 5/6$. The constant in the denominator involving the gamma functions may be reduced to,

$$\alpha = \frac{\Gamma(n - \frac{1}{2})}{\sqrt{\pi} \Gamma(n)} = \frac{2.67893}{\sqrt{\pi} 1.128787} = 1.34 \quad (3.31)$$

Then, for a sufficiently large k_1 , the "1" in the denominator of (3.30) may be neglected, producing,

$$E_1(k_1, t)|_{k_1 \text{ large}} = \frac{2}{\pi} \frac{u'^2 \Lambda_f}{\alpha^{5/3} \Lambda_f^{5/3} k_1^{5/3}} = \frac{2}{\pi} \alpha^{-5/3} u'^2 \Lambda_f^{-2/3} k_1^{-5/3} \quad (3.32)$$

Equating this expression to (3.29), yields,

$$\frac{18}{55} A \epsilon^{2/3} = \frac{2}{\pi} \alpha^{-5/3} u'^2 \Lambda_f^{-2/3} \quad (3.33)$$

On rearranging

$$\epsilon^{2/3} = \frac{110}{18\pi} A^{-1} \alpha^{-5/3} u'^2 \Lambda_f^{-2/3} \quad (3.34)$$

By substituting and reducing, with $A = 1.7$ and $\alpha = 1.34$,

$$\epsilon = 0.59 \frac{u'^3}{\Lambda_f} \quad (3.35)$$

The energy dissipation-rate calculated in this way does not take into account the anisotropic nature of the boundary layer flow. An anisotropic estimate of the dissipation-rate may be obtained by substituting u_s for u' in (3.35),

$$\epsilon = 0.59 \frac{u_s'^3}{\Lambda_f} \quad (3.36)$$

where,

$$u_s^2 = \frac{1}{3} (u'^2 + v'^2 + w'^2) \quad (3.37)$$

From Panofsky and Dutton (1984) p.160, $v'^2/u'^2 = 0.64$ and $w'^2/u'^2 = 0.25$. Therefore, an estimate for ϵ which takes into account the anisotropy of the flow is,

$$\epsilon = 0.295 \frac{u'^3}{\Lambda_f} \quad (3.38)$$

The variation of the dissipation-rate in the boundary layer, calculated using experimental values of $\overline{u'^2}$, A_f and (3.38), is shown in Figure 3.29 (open symbols). For comparison, ϵ can be calculated using (3.29) and an anisotropic estimate for $A \rightarrow A_1$. Nieuwstadt and van Dop (1982) cite results from the Minnesota experiments, that give $A_1 = (2\pi)^{2/3} \frac{55}{18} a_1 = 1.56$, where $a_1 = 0.15$. Then solving (3.29), with A_1 and $k_1 = 2\pi/\overline{u}$, ϵ may be estimated directly from the FFT determined spectrum using,

$$\epsilon = \left(\frac{2\pi E(k_1)}{a_1} \right)^{3/2} \left(\frac{f}{\overline{u}} \right)^{5/2} \quad (3.39)$$

Data shown in Figure 3.29 (solid symbols) were determined using (3.39) by averaging ϵ over the range $3 < f < 10$ Hz. This range corresponds to the nearly constant slope region of the $E_1(k_1)$ spectrum. ($E_1(k_1)$ spectrum data was $x = 0$ mm from the source. See Figure 3.25 to Figure 3.28 for selected examples.) These data show reasonable agreement, except above the boundary layer height, where energy densities are low and the spectral estimate of ϵ is more difficult to determine.

A simple model for the dissipation is to assume local equilibrium of the energy production-rate, \mathcal{P} , and the energy dissipation-rate, ϵ , throughout the boundary layer. Then,

$$\epsilon \approx \mathcal{P} = -\overline{u'w'} \frac{\partial U}{\partial z} \quad (3.40)$$

Using the log-law velocity profile, (3.13), (neglecting the zero plane displacement height d),

$$\frac{\partial U}{\partial z} = \frac{u_*}{\kappa z} \quad (3.41)$$

The shear stress expression (3.14) for a fully developed boundary layer may be substituted for $-\overline{u'w'}$, then,

$$\epsilon = \frac{u_*^3}{\kappa z} \left(1 - \frac{z}{H} \right) \quad (3.42)$$

where $H = 150$ mm and $u_* = 1.51$ cm/s. The dissipation-energy calculated using (3.42) is shown as the solid line in Figure 3.29. This estimate assumes only that production equals dissipation and a fully-developed log-law shear layer. The disagreement in the figure indicates that the production of turbulence energy exceeds the energy dissipation-rate, as estimated from the data and directly from the spectra. Townsend [1976] finds a similar twofold increase, in the energy production over the energy dissipation, for a smooth wall boundary layer, however, there is a balance within 20% for rough wall pipe flow away from the near wall effects. The imbalance causes the boundary layer to grow with down stream distance, which is observed in the mean velocity profiles. In the outer part of the boundary layer, the flow is

primarily a decaying wake from the row of vortex generator bars at the inlet of the water channel. This causes ϵ to decrease with x in that region.

The Taylor microscale, λ_f , is defined by,

$$\frac{1}{2} \overline{\left(\frac{\partial u}{\partial x} \right)^2} \equiv \frac{u'^2}{\lambda_u^2} \quad (3.43)$$

For large Reynolds number flows, the small-scale turbulence is approximately isotropic. Therefore the relation, (Hinze, 1975, p.225),

$$\epsilon = 15\nu \frac{u'^2}{\lambda_u^2} \quad (3.44)$$

may be used to estimate λ_u . Rearranging this equation for λ_u and substituting (3.38), then,

$$\lambda_u^2 = \frac{15\nu u'^2}{0.295 u'^3 / \Lambda_u} = 50.8 \frac{\nu \Lambda_u}{u'} \quad (3.45)$$

Therefore, the Taylor microscale may be estimated from the velocity variance and the Eulerian integral scale as,

$$\lambda_u \approx 7 \sqrt{\frac{\nu \Lambda_u}{u'}} \quad (3.46)$$

The variation of the Taylor microscale in the boundary layer at the source location is shown in Figure 3.30. These data were generated using observed u' and Λ_u data, and (3.46). The dissipation time scale of the velocity fluctuations may therefore be determined as,

$$\tau_\epsilon = \lambda_u / \bar{u} \quad (3.47)$$

A typical value of τ_ϵ in the water channel at the source height is, $\tau_\epsilon = 0.05$ s, (using $\lambda_u = 1.15$ cm, $\bar{u} = 22.5$ cm/s, $u' = 2.25$ cm/s, $\Lambda_u = 5$ cm, $\nu = 0.01$ cm²/s).

An interesting ratio to consider is the integral length scale, Λ_u , divided by the Taylor microscale, λ_u , shown in Figure 3.31. What makes this figure interesting is that the spread between the integral scale and the Taylor microscale is only a factor of five. This is due to the low Reynolds number flow found in the water channel.

3.3.7 Probability Distributions for Velocity

“The two most outstanding features of atmospheric turbulence which have been revealed are that its spectrum has a characteristic shape and that its probability structure is not Gaussian.”

—Dutton (1970).

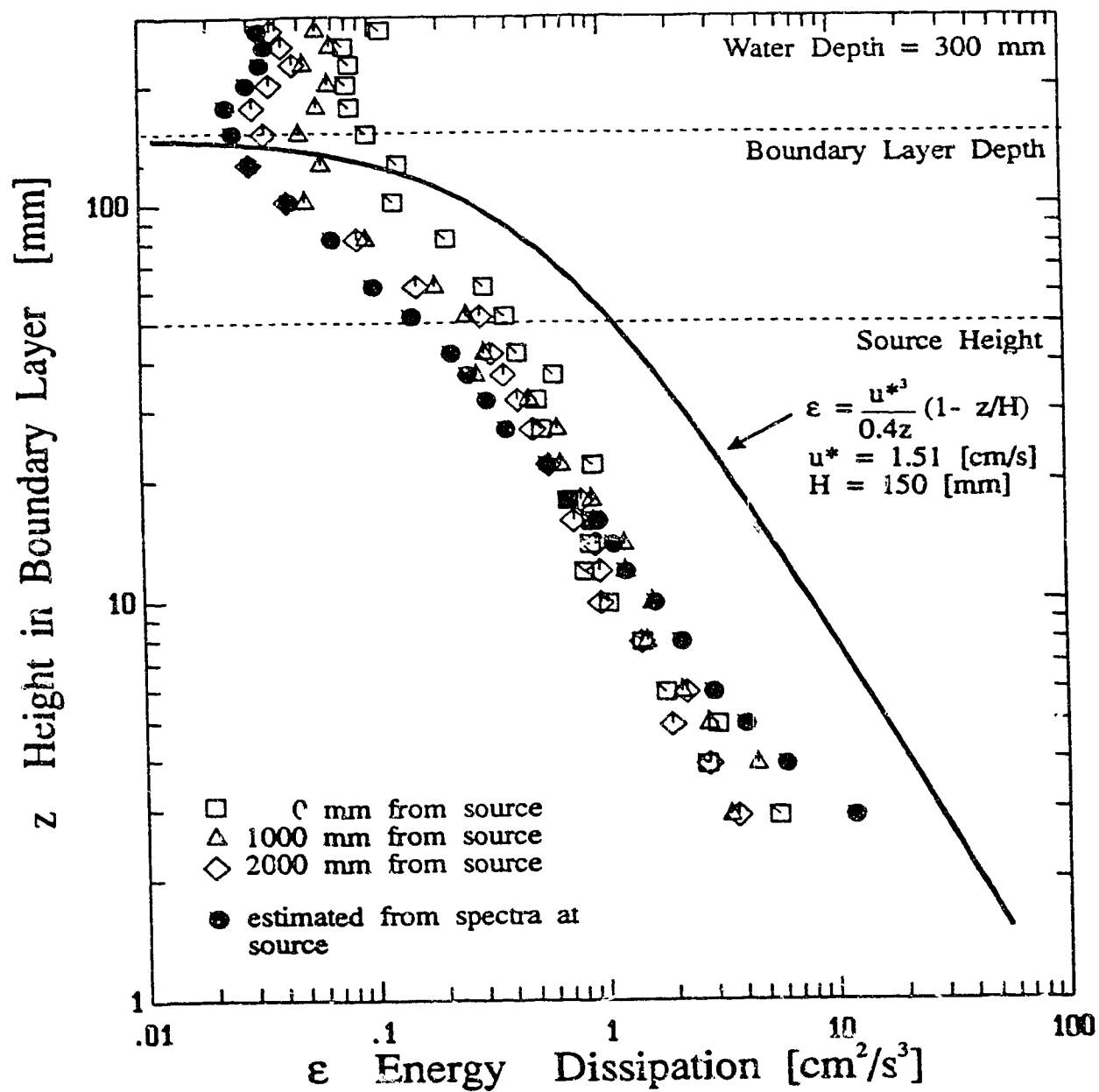


Figure 3.29: The turbulent kinetic energy dissipation rate profile for the rough wall boundary layer in the water channel, using (3.38).

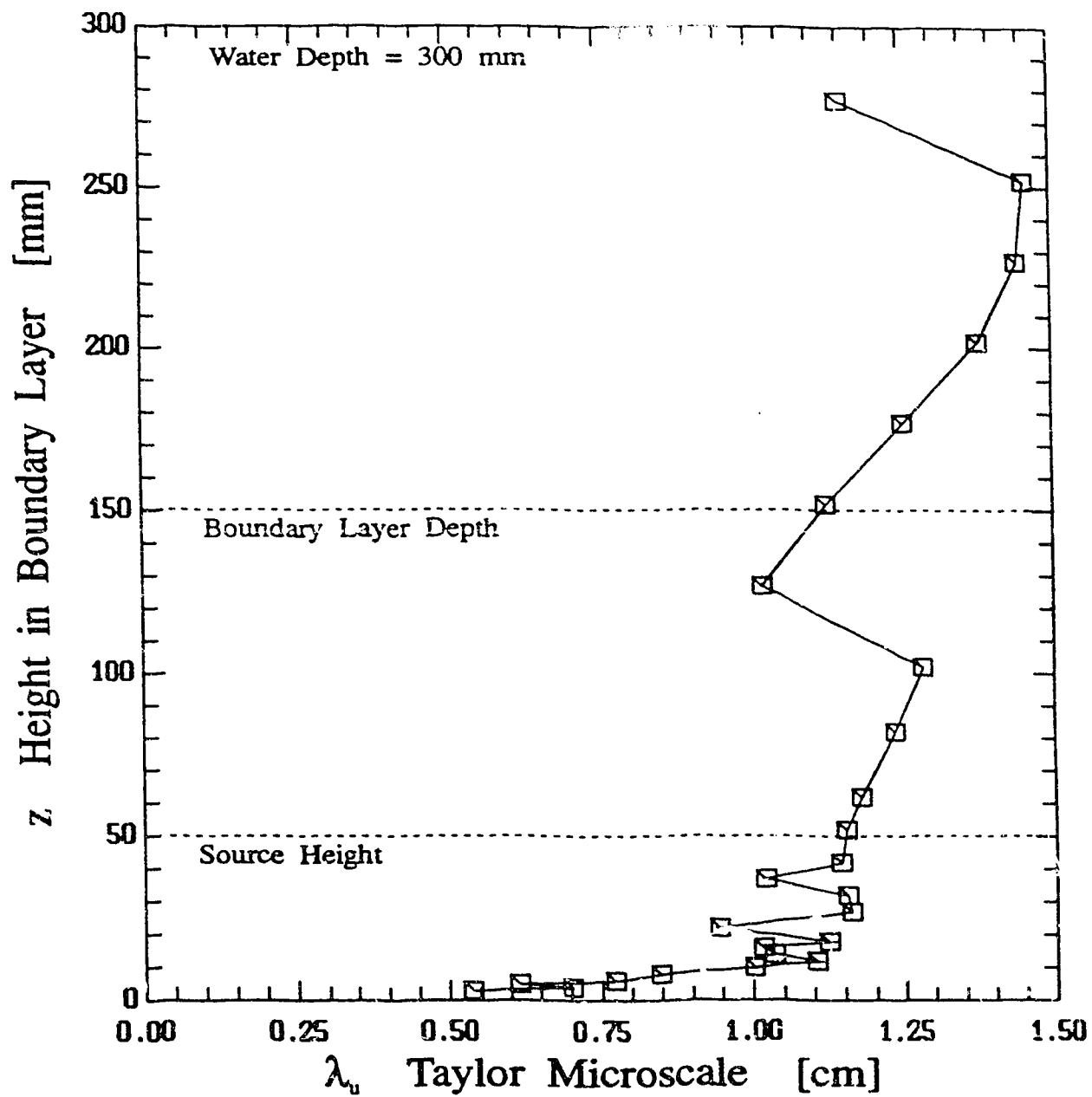


Figure 3.30: Variation of the Taylor microscale, λ_u , in the boundary layer at the source location, using (3.46).

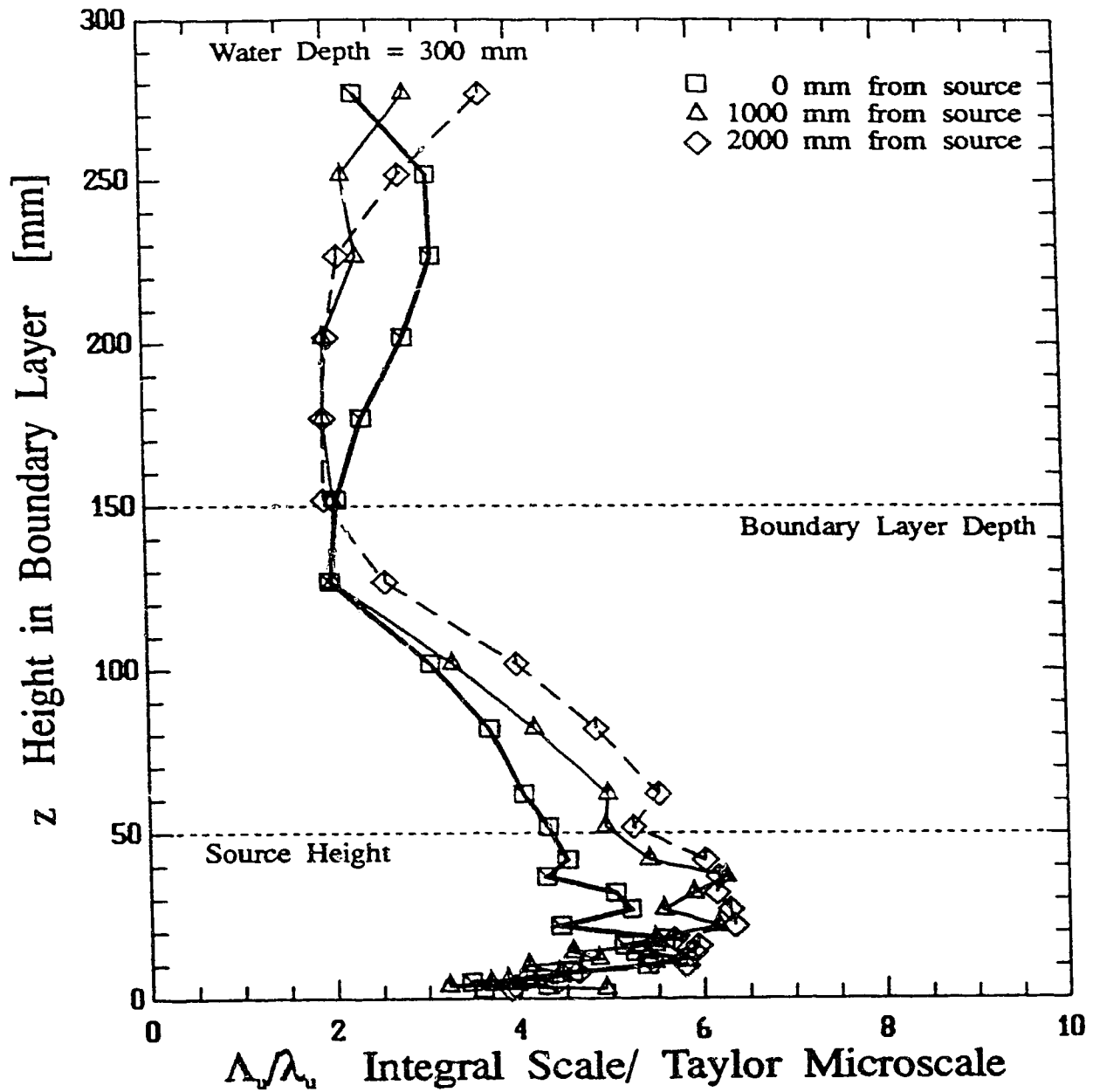


Figure 3.31: Ratio of the integral time scale to the Taylor microscale in the water channel boundary layer. Λ_u is determined by direct measurement and λ_u is determined using (3.46).

What Dutton said 20 years ago remains true today. The data on the atmosphere show that atmospheric turbulence is apparently a stochastic process which is not in general Gaussian in structure (but may be described as approximately Gaussian under some conditions) — but a process for which the assumption of independence between the velocity function and its first derivatives is a reasonable one, to the extent tested by Dutton. This conclusion is in agreement with the observed exceedance statistics. Therefore the velocity function must follow a first order Markov process, van Dop, Nieuwstadt and Hunt, (1985).

Counihan (1975) reports observations which support that the velocity probability distribution is Gaussian, at least within $\pm 3u'$. Beyond $\pm 3u'$ there is some evidence that the normal distribution is not applicable. Profiles of probability distributions of velocity in the water channel, see Figure 3.32, show that the turbulence is well represented by a Gaussian assumption, which supports the conclusion that the distribution of velocity may be Gaussian even if the underlying process is not stochastically Gaussian. The distribution of the first derivative of the velocity in the water channel could not be determined because of the random nature of the LDA velocity data.

3.4 Scale Factors for Atmospheric Simulation

Direct comparison of statistics in the model to statistics in the atmosphere is made possible with the use of a scaling parameter for the model. The scaling factor that is used for the fully rough boundary layer is the ratio of the boundary layer thickness of the model to that of the full scale. The ratio of Reynolds numbers do not form the scaling parameter since it may be shown that for fully rough flow the intensity of fluctuations or scale to boundary layer thickness ratios are independent of the Reynolds number. Using the boundary layer thickness, the scale factor, SF , is given by,

$$SF = \frac{H_a}{H_m}$$

where H_a is the boundary layer thickness of the atmosphere and H_m is the boundary layer thickness of the water channel model. Using a nominal atmospheric boundary layer thickness of 500 m, Counihan (1975), and the water channel boundary layer thickness of 0.15 m, the scale factor is,

$$SF \approx 3300$$

Time values and concentration values may be related through the use of the scale factor and expressions using characteristic lengths in both flows. Clearly, the water

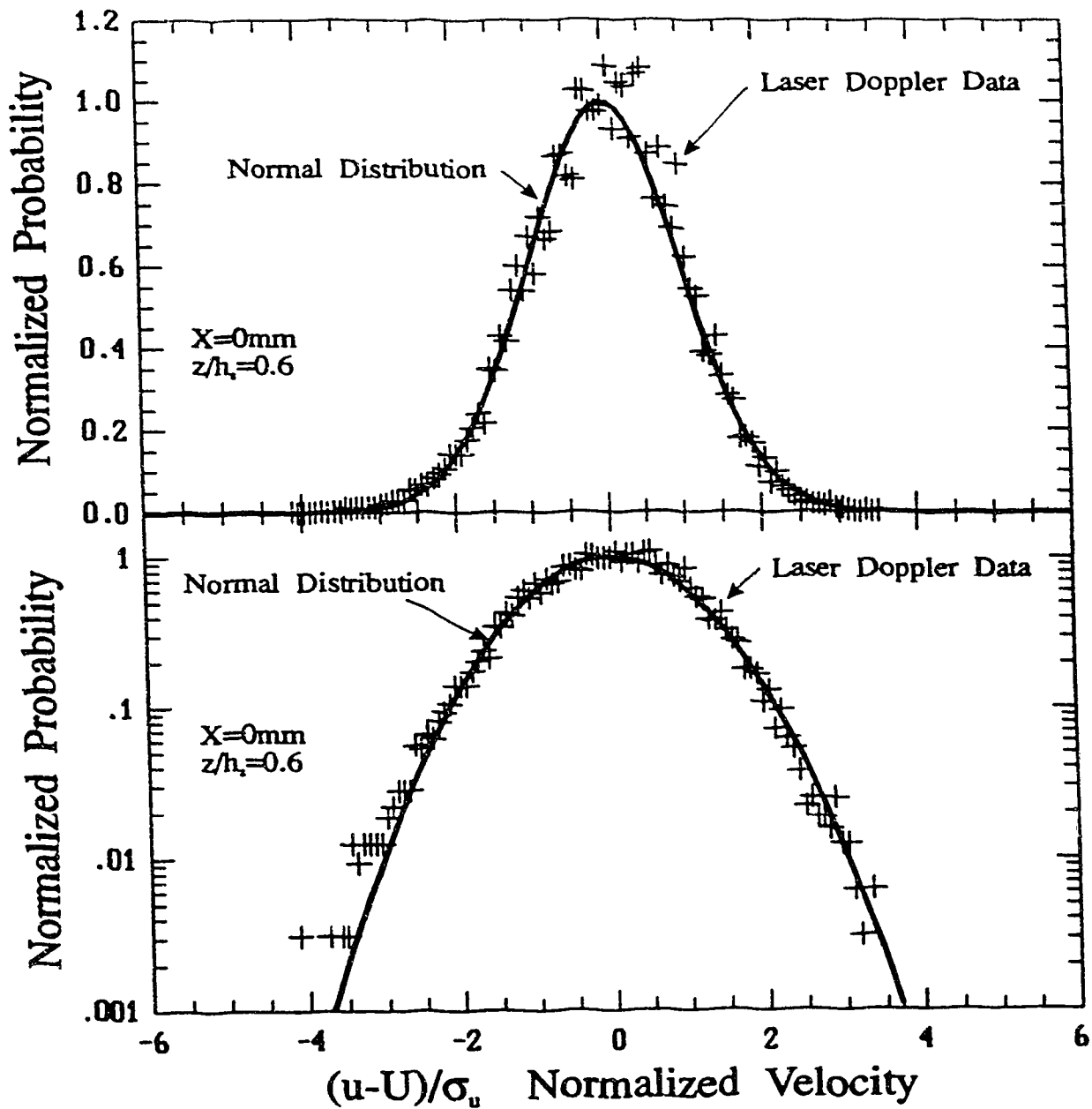


Figure 3.32: Profile of the probability distribution of velocity in the water channel showing that the velocity distribution is Gaussian, irrespective of the distribution of the first derivative and the underlying stochastic process.

channel model cannot match the flow parameters exactly. It is expected, however, that based upon the log-law mean velocity profile with fully rough flow, the range of scales available in the water channel and the scaling parameters, agree with full scale measurements.

3.4.1 Range of Scales Comparison

There are two ranges of atmospheric scales of motion that the simulation is not physically able to model: the very large scale motions, which result in wind variations over periods of hours and even flow reversals, and the very small scales, which finalize the dissipation of turbulent dissipation energy.

The ratio of the large scale eddies to the dissipation eddy sizes is found by equating relationships for the energy dissipation. Based on the cascade of energy in the inertial sub-range, Hinze (1975, p.225).

$$\epsilon \approx 0.8 \left(\frac{u_s^3}{\ell_e} \right) \quad (3.48)$$

where u_s is a characteristic turbulence velocity, ℓ_e is the energy containing length scale, and, ϵ , is the energy dissipated by viscosity. ϵ is also given by,

$$\epsilon = \frac{\nu^3}{\eta^4} \quad (3.49)$$

Equating the dissipation rates for typical large scales and the Kolmogorov scales results in,

$$\frac{\nu^3}{\eta^4} \approx 0.8 \frac{u_s^3}{\ell_e} \quad (3.50)$$

Multiplying by ℓ_e^4 ,

$$\frac{\ell_e^4}{\eta^4} \approx 0.8 \frac{u_s^3 \ell_e^3}{\nu^3} \quad (3.51)$$

Then,

$$\frac{\ell_e}{\eta} \approx (0.8)^{1/4} \left(\frac{u_s}{U_s} \right)^{3/4} \left(\frac{\ell_e U_s}{\nu} \right)^{3/4} \quad (3.52)$$

And substituting for the scaling parameters, $u_s \rightarrow \sqrt{u'^2}$, $U_s \rightarrow U_H$, $\ell_e \rightarrow \Lambda_u$. Hinze shows that $\ell_e = 0.75\Lambda_u$ for a spectrum with an inertial sub-range. In section 6.6.1 of

Table 3.2: Typical Characteristic Values from the Atmosphere and from the Water Channel Simulation

Parameter	Water Channel ^a	Neutral Atmosphere	Wind Tunnel
Λ_u	5 cm	150 m	1 m
U_H	22.5 cm/s	7 m/s	2 m/s
$\sqrt{u'^2}$	2.25 cm/s	0.7 m/s	0.2 m/s
ν	0.01 cm ² /s	1.5×10^{-5} m ² /s	1.5×10^{-5} m ² /s
D	1.2×10^{-5} cm ² /s ^a	1.4×10^{-1} cm ² /s ^b	1.4×10^{-1} cm ² /s ^b

^asalt in water

^bwater vapour in air

the present study, it is shown that that $\ell_c = \Lambda_u$ for a Markov spectrum. Ignoring the 0.95 fraction, the ratio of large scales to small scales is approximately given by,

$$\frac{\Lambda_u}{\eta} \approx \left(\frac{\sqrt{u'^2}}{U_H} \right)^{3/4} \left(\frac{\Lambda_u U_H}{\nu} \right)^{3/4} \quad (3.53)$$

Typical values from the water channel simulation and for the atmosphere in neutrally stable conditions, (Counihan, 1975), are given in Table 3.2. By substitution,

$$\frac{(\Lambda_u/\eta)_{\text{atmosphere}}}{(\Lambda_u/\eta)_{\text{water channel}}} = \frac{136000}{220} \approx 620 \quad (3.54)$$

This means that the water channel can simulate a range of scales from the largest of approximately 5 cm, to the smallest of about 0.25 mm. This compares to the much larger range of 150 m to about 1 mm found in the atmosphere. There are two reasons why the loss of scales in the high frequency range is not disturbing. First, the smallest scale in the atmosphere which is of interest would be on the order of 2 to 10 m. In the event of a toxic gas release and using a typical wind speed of 7 m/s, this scale would subject a person to approximately one second of a gaseous contaminant. Any scales smaller than this could be considered harmless in terms of a possible toxic potential. The fine scales would act on the plume to decrease its intermittency by diffusion and widen the plume. Therefore, the simulation produces a conservative estimate of the concentration in comparison to a release in the atmosphere.

In the water channel the 0.25 mm resolution is equivalent to a 1 m scale in the atmosphere. This implies that the model scale range encompasses the range of scales of interest in the full scale atmosphere. Secondly, the measurement response time of

Table 3.3: Boundary Layer Simulation Parameters in 3300:1 Scale

Parameter	Model	Scaled Up	Neutral Atmosphere ^a
Boundary Layer Thickness, H	150 mm	500 m	500 ± 50 m
Roughness Scale z_0	0.15 mm	0.5 m	1 to 4 m
Power Law n	0.21	0.21	0.2 ± 0.03
Turbulence Intensity $\frac{\sqrt{u'^2}}{U}$ at 30 m	0.18	0.18	0.20 ± 0.03
Integral Length Scale Λ_u at 30 m	40 mm	130 m	130 ± 50 m
Integral Length Scale Λ_u at 50 m	55 mm	180 m	200 ± 50 m

^aFrom Counihan (1975).

the concentration detector has an equivalent length scale in the order of 1 to 2 mm. Any scales in the model smaller than this would not be detected by the measuring equipment. For comparison, a full scale sensor device such as LIDAR, has a typical spatial resolution of 12x60 m. Therefore, the measurements made in the water channel have better spatial resolution for measuring peak concentrations than those collected in the full scale.

3.4.2 Boundary Layer Overview

A summary of the parameters representing the simulation boundary layer and the typical atmospheric neutrally stable boundary layer is given in Table 3.3. Several of the measurements that would be made at typical meteorological tower heights in the atmosphere are scaled to the water channel for comparison. It is clear that the model presented for the study of the concentration fluctuations adequately describes a full scale situation. According to the scaled up z_0 values, the flow over the *Lego* roughness describes a very rough full scale terrain. This roughness range is suitable for the description of flow over an urban area or a forested area. If the full scale terrain was a level wheat field, (with a corresponding small z_0 value), the observed plume spreads would be smaller than those observed in water channel environment.

Chapter 4

Conductivity Detector Response

This study investigates peak concentrations and time intervals between the concentration peaks, however, the conductivity detector developed by Bara (1985) did not have a sufficient time response to resolve the peak concentrations. Two fast response detectors were developed and used in the present study. The first detector, (hereafter micro-probe), was constructed of glass tubing and had a very small detection surface. Its time response was fast but its ability to hold a conductivity calibration was poor. This detector required frequent calibrations. The second detector, (hereafter new-probe), will be described in publications elsewhere. The new-probe had an equally fast time response and did not require frequent calibrations. The development of the conductivity detectors, and methods used for calibrating and correcting for temperature sensitivity, are described in Appendix D.

The time response of the conductivity detectors was still not fast enough to resolve the highest frequency concentration fluctuations. This caused problems when determining the intermittency of the signal. The detectors were, however, still a significant improvement over Bara (1985) in that they were able to better resolve the peak concentrations.

In this chapter the correction for the time response attenuation of the conductivity detectors is presented.

4.1 Dynamic Testing of the Probe Response Time

Following the method suggested by Bara (1985), the micro-probes were dropped through a fresh water/salt water interface to test the probe response time. The apparatus shown in Figure 4.1, was designed by the author and used to move a probe

at a known rate through a saline to fresh water interface. A 5 g/l saline solution was slowly gravity driven through screens inside a stainless steel collar with a bevelled top edge. The flowing saline solution spilled over the top collar edge and flowed to the bottom of the reservoir because the saline solution was more dense than the surrounding fresh water. The interface of saline to fresh water was sharp because of the low molecular diffusivity of the saline solution and because it was continually being refreshed by the upward flow. Using a variable speed motor connected to a highly pitched threaded rod, a conductivity detector mounted to the threaded rod was driven through the saline interface. The output of a slot switch mounted on the variable speed motor generated a signal that was used to determine the speed of the detector crossing the interface. The response of the detector and the slot switch output were recorded by a computer data acquisition system.

Analysis of the probe response to the step change in concentration, proved that the micro-probe had an associated probe response time which was first order exponential. A first order process has a characteristic time constant, τ_p , which, in this case, is dependent on the drop speed. The product of the drop speed and time constant yields a characteristic response length scale, called a flushing length, Λ_p . The flushing length was previously found by Bara (1985), and represents the amount of tracer solution that must pass the probe tip before the probe is able to respond (or partially respond).

Using the probe construction process and the plating procedure described in Appendix D, a consistent flushing length of about 1.0 mm was found to be characteristic of the micro-probe, see Figure 4.2. The new-probe had the same response length. This length was found to be independent of the probe inner diameter of the micro-probe. The first order exponential response of the probe is easy to manipulate mathematically and may be used to correct the signal attenuation due to the response time. These corrections are discussed in the next sections.

The probe response length was also investigated in terms of a physical length by observing the signal attenuation when the probe is brought within close contact to a static non-conducting barrier, see Figure 4.3. The probe was found to be sensitive to the direction of approach of a barrier however the distance at which the probe became sensitive to the barrier was comparable to the flushing length determined by the probe drop apparatus.

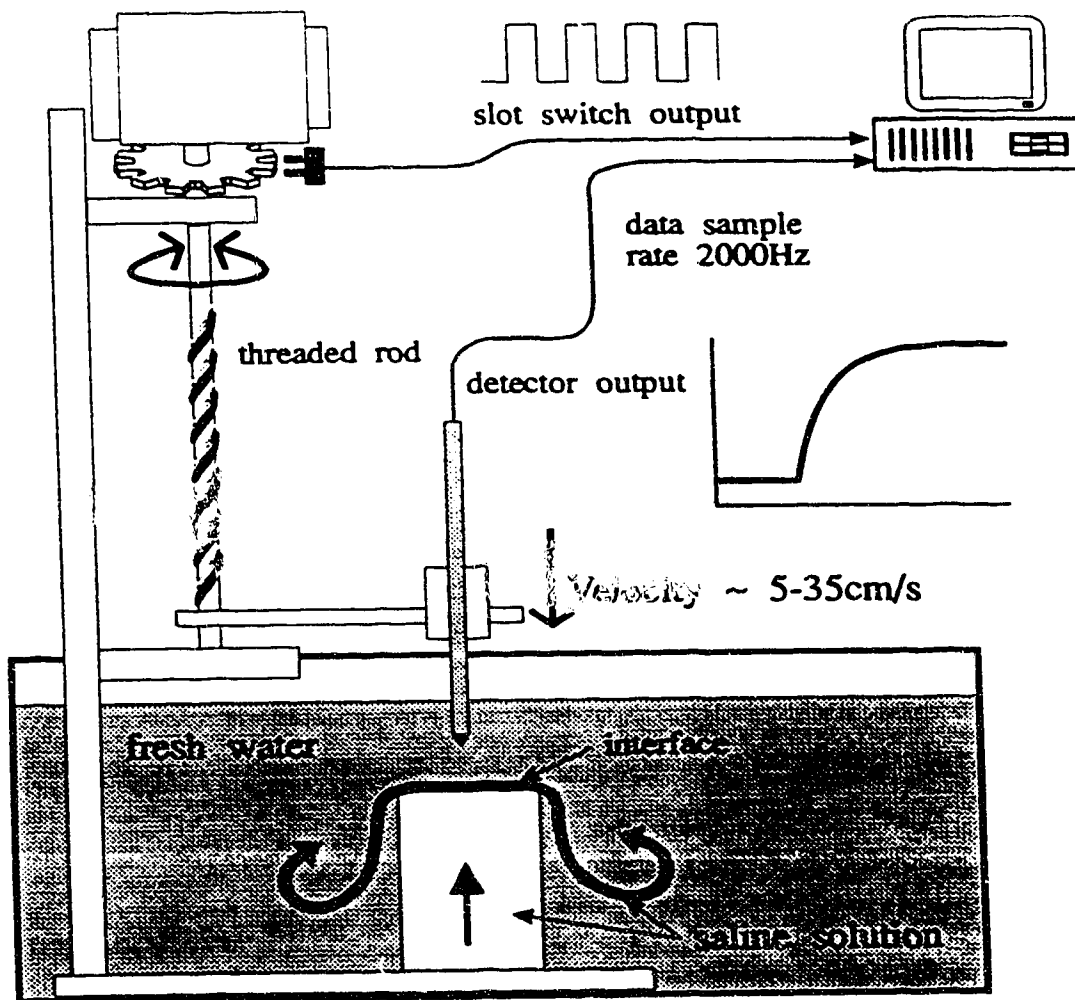


Figure 4.1: Schematic of the probe dropping apparatus.

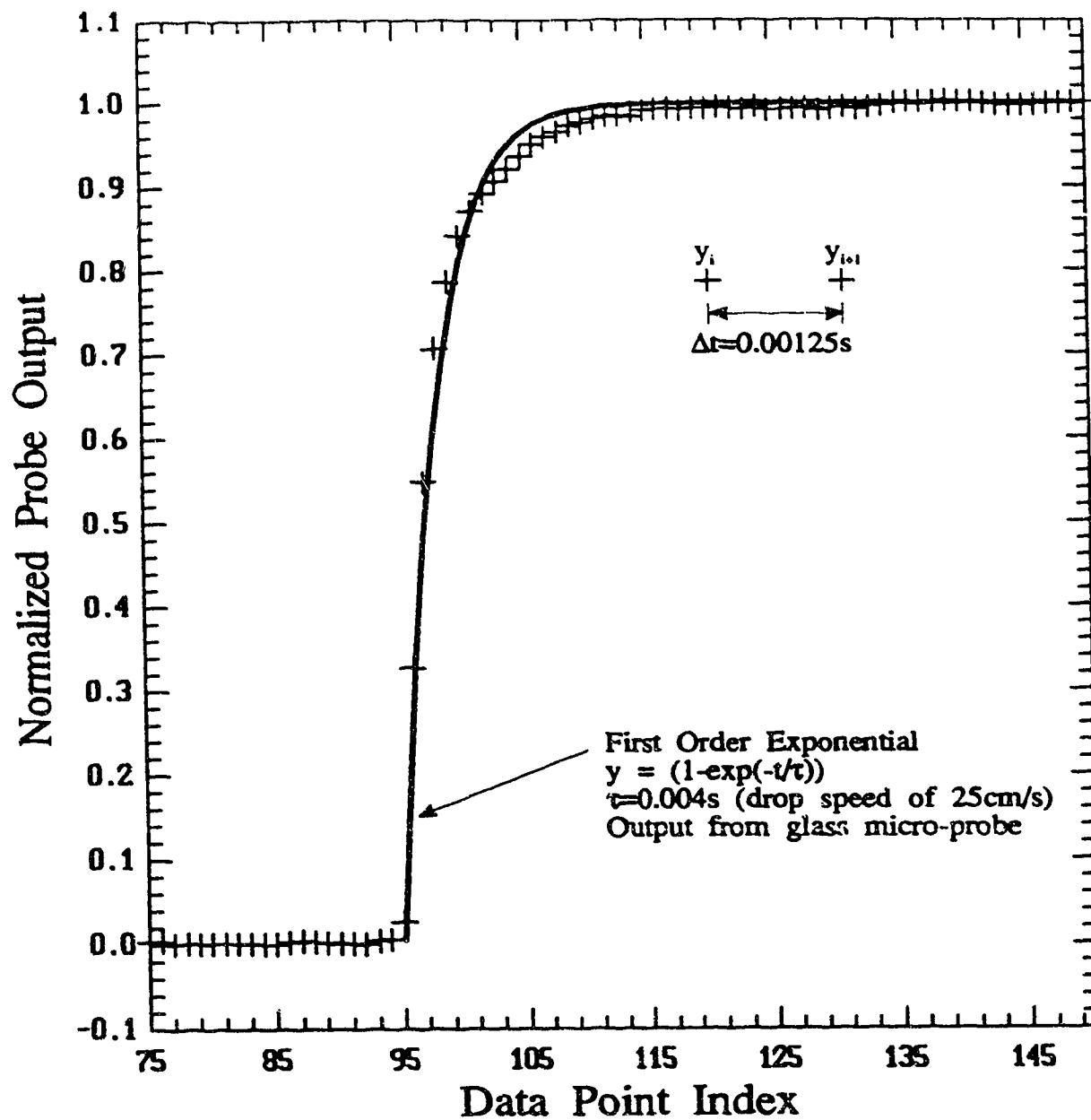


Figure 4.2: Example of a probe drop response output showing the near exponential response for a micro-probe.

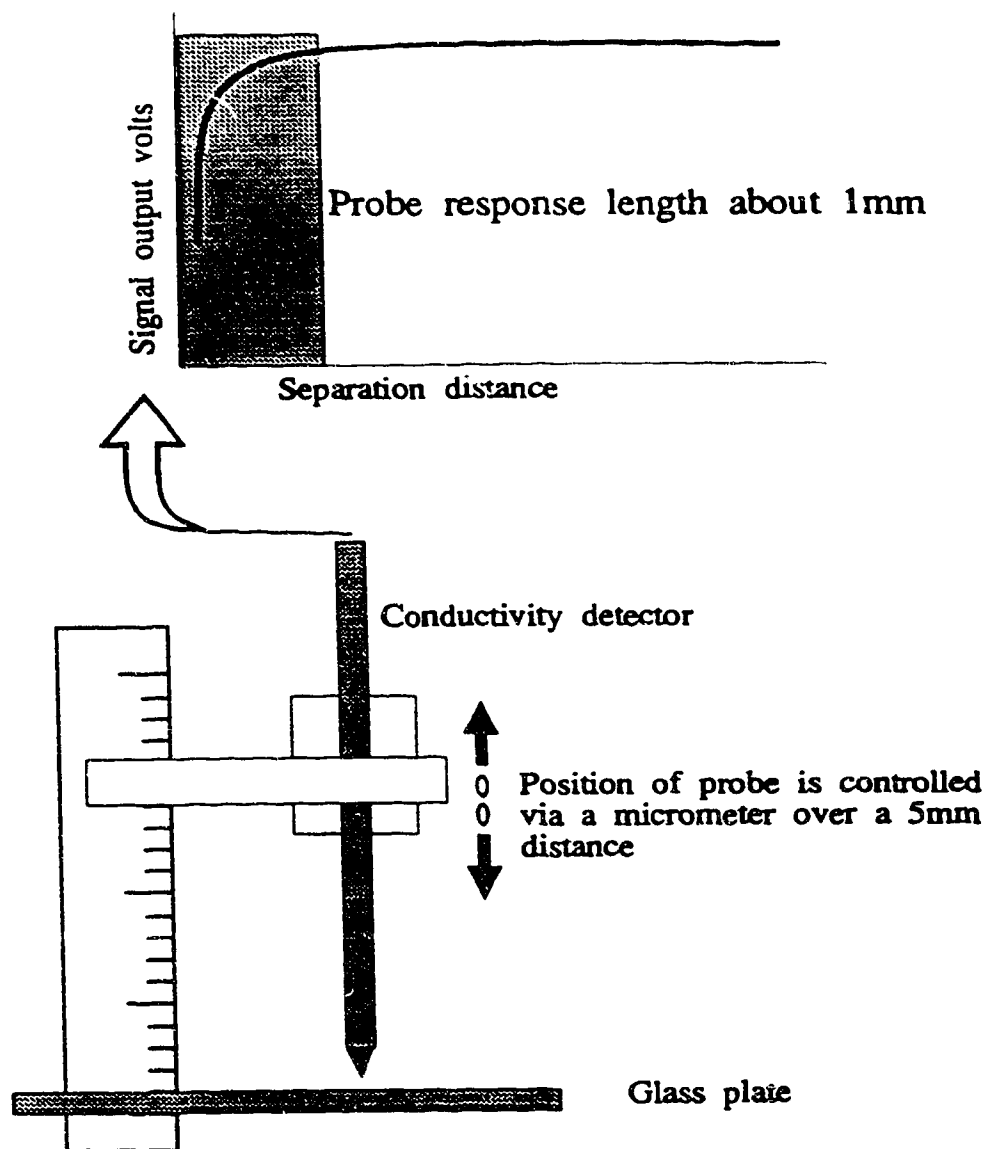


Figure 4.3: Schematic of the probe close contact experiment.

4.2 Correction of the Time Series Signal For Probe Time Response

There are two ways that the response time of the detector may be corrected. The first may be performed after the detector signal has been analyzed. This correction to the variance and concentration fluctuation time scale is discussed in section 6.9. The second may be performed by correcting the time series signal itself, and discussed in the following.

If the time response of an instrument is known and is first order, then a simple correction may be used to regain the non-attenuated time series signal. The interest in peak concentrations and time duration of concentration signals in turbulent concentration fluctuation analysis makes this correction an important one. In addition, conditional averaging errors depend strongly on an accurate determination of when the concentration signal is present. The correction to the time series signal will remove the long decay periods illustrated in Figure 4.4. Due to probe response, measured concentrations rarely reach zero, except when the time between concentration eddies is large. This causes an error in the calculated intermittency. This response time attenuation is noticed when the concentration falls to zero. The peak concentrations are also affected by the probe response. This is not visible when examining the time series data.

The detector response is close to a first order system with time constant, τ , and a system gain $K=1.00$, (Zelt, Wilson and Bara, 1985). The unity gain is an important part of the description because it stipulates the final signal value from the probe is identical to the actual concentration signal value. For a first order system, driven by a step change in input, the final signal value will be within 5% of the non-attenuated signal after only three time constants.

The first order process description of the inputs and outputs may be represented by the following non-linear system.

$$\frac{dy(t)}{dt} = \mathcal{F}(y(t), x(t)) \quad (4.1)$$

Where $x(t)$ is the concentration signal and $y(t)$ is the concentration signal measured by a probe. A forward difference equation may be used to approximate the derivative.

$$\frac{dy}{dt} \approx \frac{y_{n+1} - y_n}{T} \quad (4.2)$$

Where T is the time step between the discrete events, and n is the current time step in the time series signal.

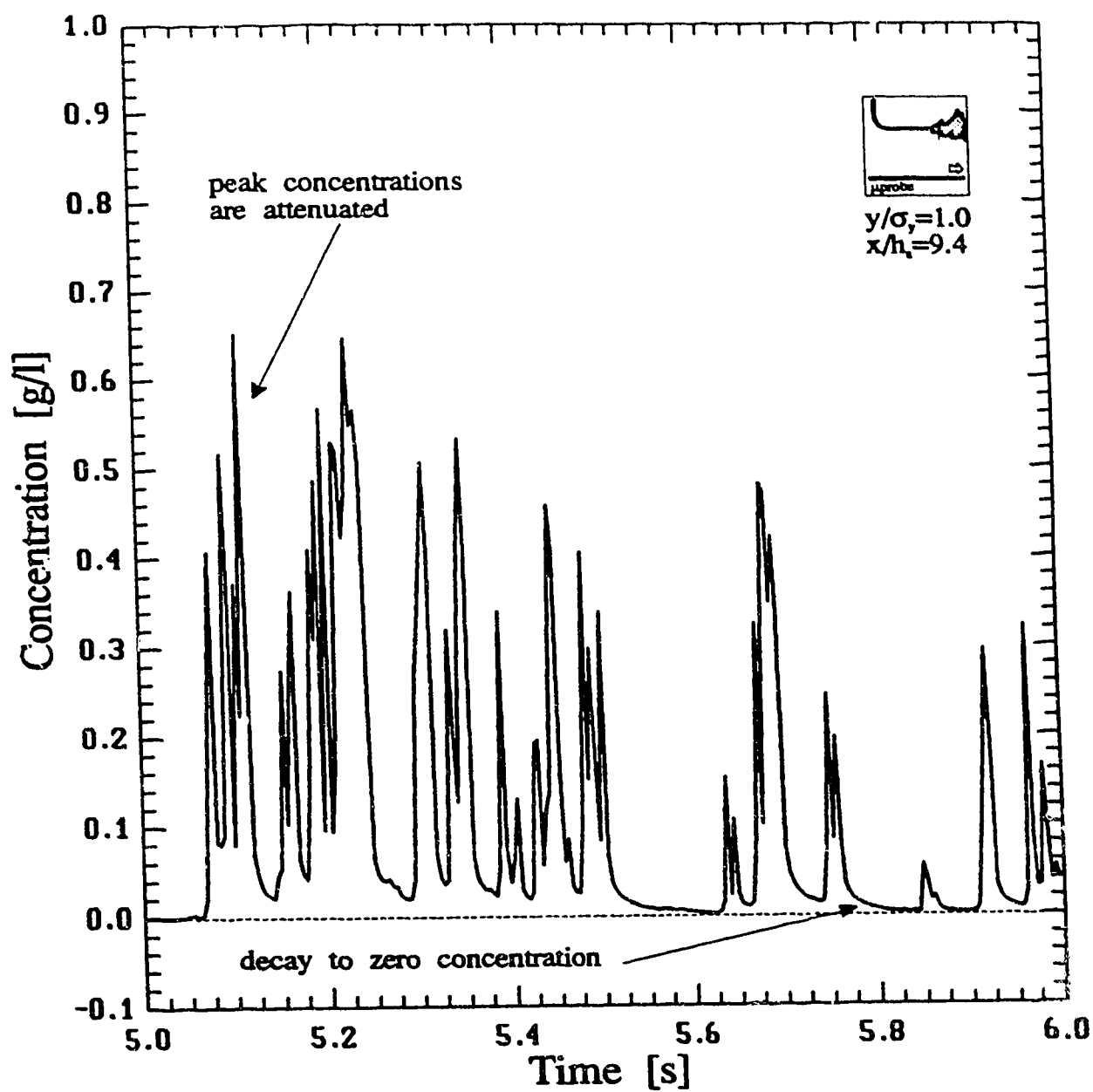


Figure 4.4: Concentration time series signal showing the effects of probe response induced lag. Data is for the jet/plume source using the glass-micro probes.

Digital representation of a time series signal is generally a step function. In Figure 4.5, the step approximation to a time series signal is represented. The step function is used because it is mathematically easy to represent and transform.

Assuming that $\mathcal{F}(y(t), x(t))$ is a linear first order equation, a step is described by the following equation.

$$\tau \frac{dy(t)}{dt} + y(t) = x(t), \quad x(t) = K(\text{a constant}) \mid t \geq 0 \quad (4.3)$$

This equation may be solved using Laplace transforms, yielding the following result:

$$\frac{K - y(t)}{K - y(0)} = \exp\left(\frac{-t}{\tau}\right) \quad (4.4)$$

Where if the gain, K , is unity, then the input concentration signal may be determined by solving for K . Also, for a data set we may discretize the solution for a time step Δt ,

$$K = x_n = \left(\frac{y_n - y_{n-1} \exp\left(\frac{-\Delta t}{\tau}\right)}{1 - \exp\left(\frac{-\Delta t}{\tau}\right)} \right) \quad (4.5)$$

where:

- y_n is the measured concentration at time step n in the process.
- y_{n-1} is the measured concentration at time step $n - 1$ in the process.
- x_n is the process original concentration.
- τ is the time constant of the detector.
- Δt is the time between samples in the measurement process.

The correction is independent of the starting value and only depends on the current output value and the next observed value. Since the entire time series data signal is available for analysis, the forward next observed data point is readily available. This correction is applied to an exact first order response simulation and is shown in Figure 4.6. The simulated signal, in Figure 4.6, was a square wave which was attenuated using a first order response process. Gaussian distributed noise with 1% rms magnitude of the square wave height, was added to simulate a real system. The second frame shows that the first order step response deconvolution equation in (4.5) regenerates the original square wave with accuracy despite the added noise.

Application of the step response deconvolution to an observed concentration signal is shown in Figure 4.7 for a micro-probe with a flushing length of $\Lambda_p = 1$ mm. The

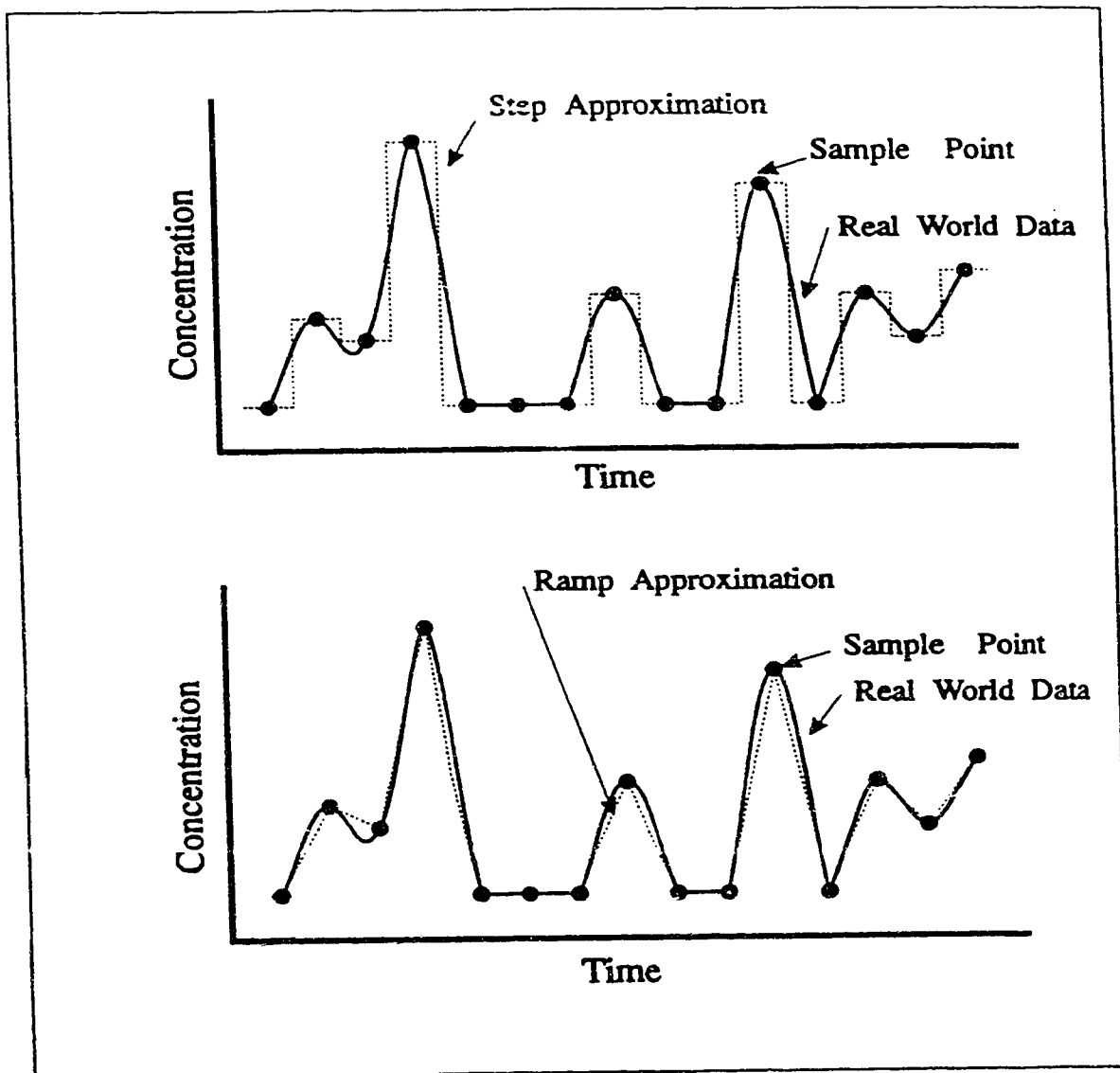


Figure 4.5: Illustration of modelling a concentration time series as a step function and as a ramp function.

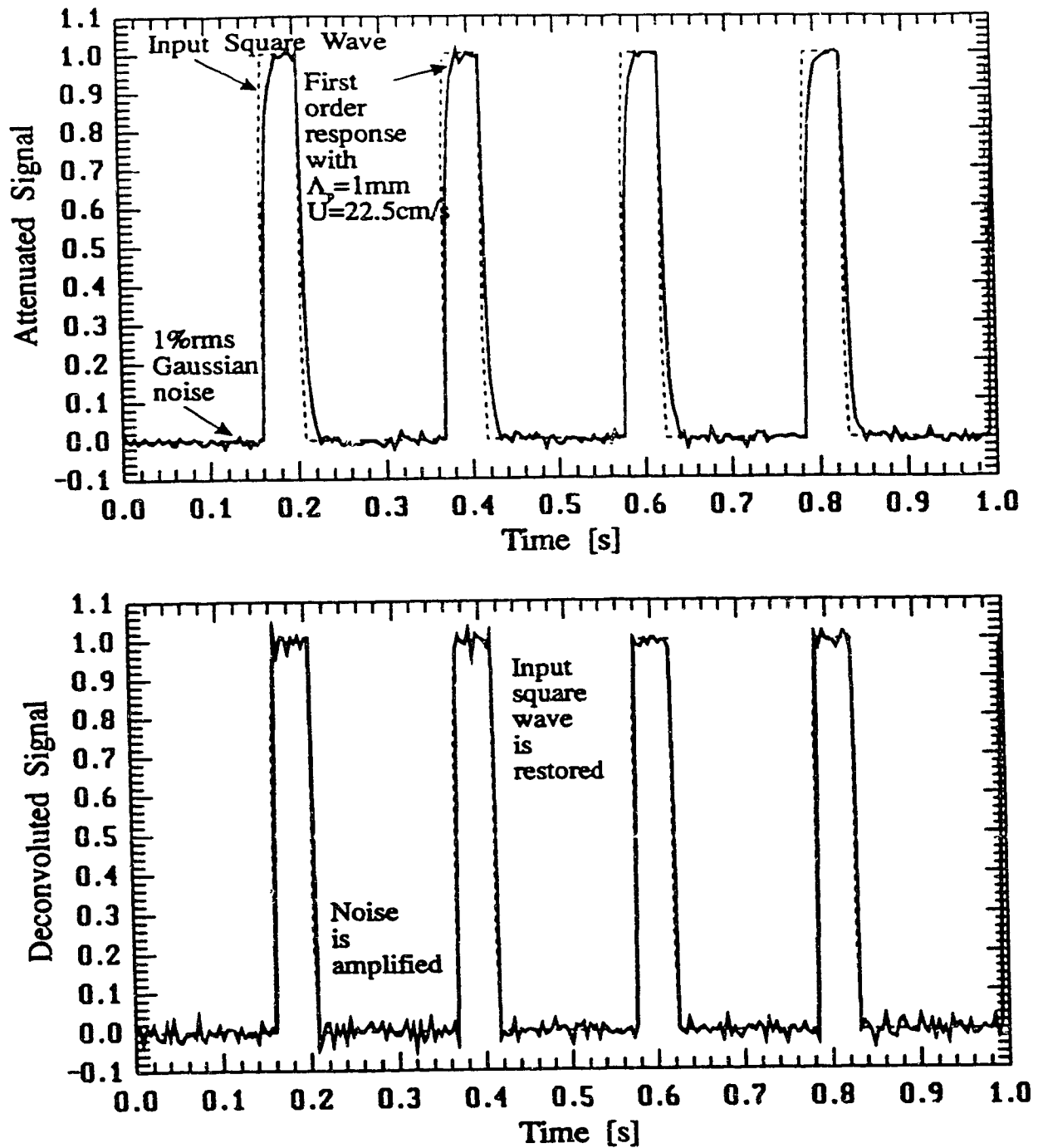


Figure 4.6: Simulated time series of a first order response probe step deconvolution illustrating the ability to reconstruct the original time series. Noise was added to the first order response to simulate a real signal.

input signal is reconstructed adequately from the attenuated data that the probe records. The deconvoluted signal, though noisy, reduces the peak concentration truncation error considerably and the over-estimation of the intermittency.

A more realistic model for the response of the concentration process in (4.1) is a linear (ramp) response, such that:

$$\tau \frac{dy(t)}{dt} + y(t) = K_1 t + x(0), \quad K_1 (\text{a constant}) \mid t \geq 0 \quad (4.6)$$

The ramp response is illustrated in Figure 4.5. Real processes have inertia and therefore cannot respond as a step function. The ramp function therefore would be a simple estimate for the change in concentration from one time step to the next.

The ramp response equation may be solved using Laplace transforms,

$$y(t) = \left(e^{-t/\tau} + \frac{t}{\tau} - 1 \right) \tau K_1 + (1 - e^{-t/\tau}) x(0) + e^{-t/\tau} y(0) \quad (4.7)$$

Discretizing this equation over a time step Δt ,

$$\begin{aligned} \tau K_1 &= \tau \left(\frac{x(t) - x(0)}{t} \right) = \frac{x(\Delta t) - x(0)}{\frac{\Delta t}{\tau}} \\ y(t) &= y(\Delta t) = y_n \\ y(0) &= y_{n-1} \\ x(t) &= x(\Delta t) = x_n \\ x(0) &= x_{n-1} \end{aligned}$$

The ramp response equation equivalent to (4.5) is,

$$x_n = x_{n-1} + \frac{\Delta t}{\tau} \frac{y_n - y_{n-1} + (y_{n-1} - x_{n-1})(1 - e^{-\Delta t/\tau})}{\Delta t/\tau - (1 - e^{-\Delta t/\tau})} \quad (4.8)$$

Applying the ramp function deconvolution to a simulated signal in Figure 4.8, it can be seen that using typical detector response time constants the ramp function rings strongly compared to the step response deconvolution in Figure 4.6. The deconvolution becomes unstable because the time constant of the process is comparable to the time constant of the detector. This causes the signal to appear as a series of step changes instead of a smoothly varying function. Therefore, the deconvolution over-estimates the concentration for the next time step. Application of the ramp response to the same time series signal shown for the step response

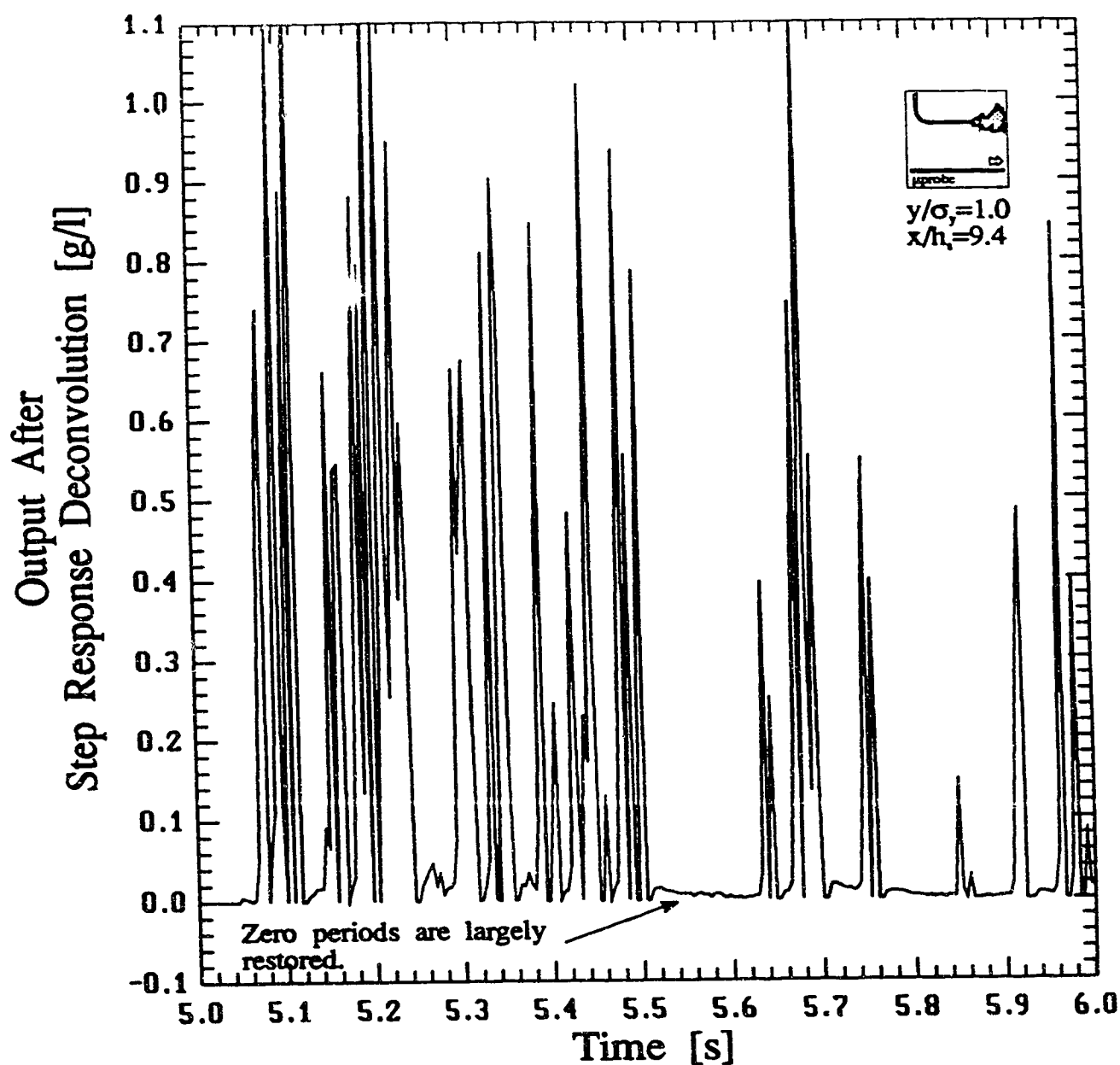


Figure 4.7: Step response deconvolution of a measured concentration signal showing an adequate reconstruction of the supposed true concentration signal. Data is for the jet/plume source using the glass-micro probes.

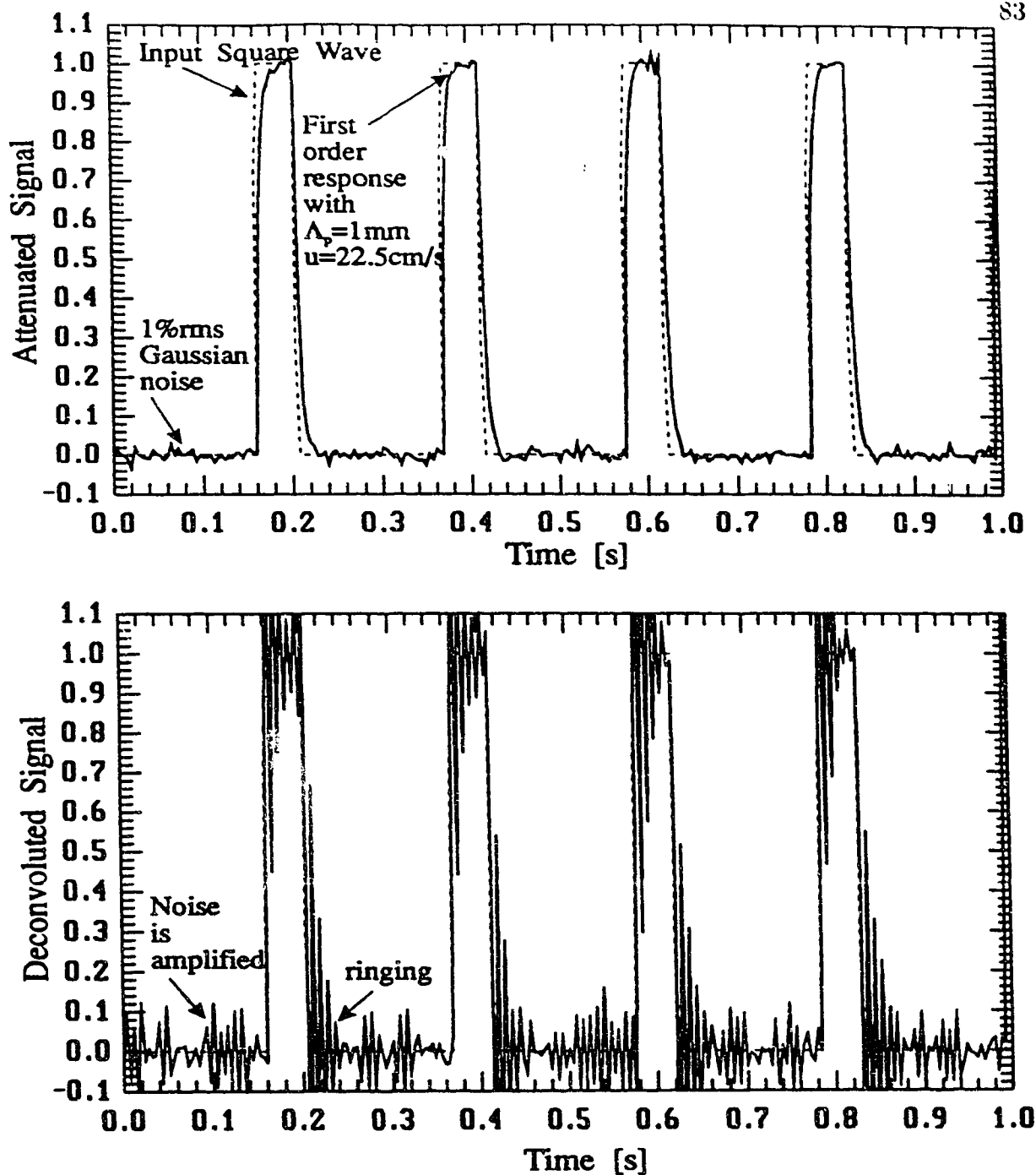


Figure 4.8: Simulated time series of a first order response probe ramp deconvolution illustrating the ability to reconstruct the original time series. Noise was added to the first order response to simulate a real signal. Note the large amount of ringing due to the comparative time constants of the process and the probe.

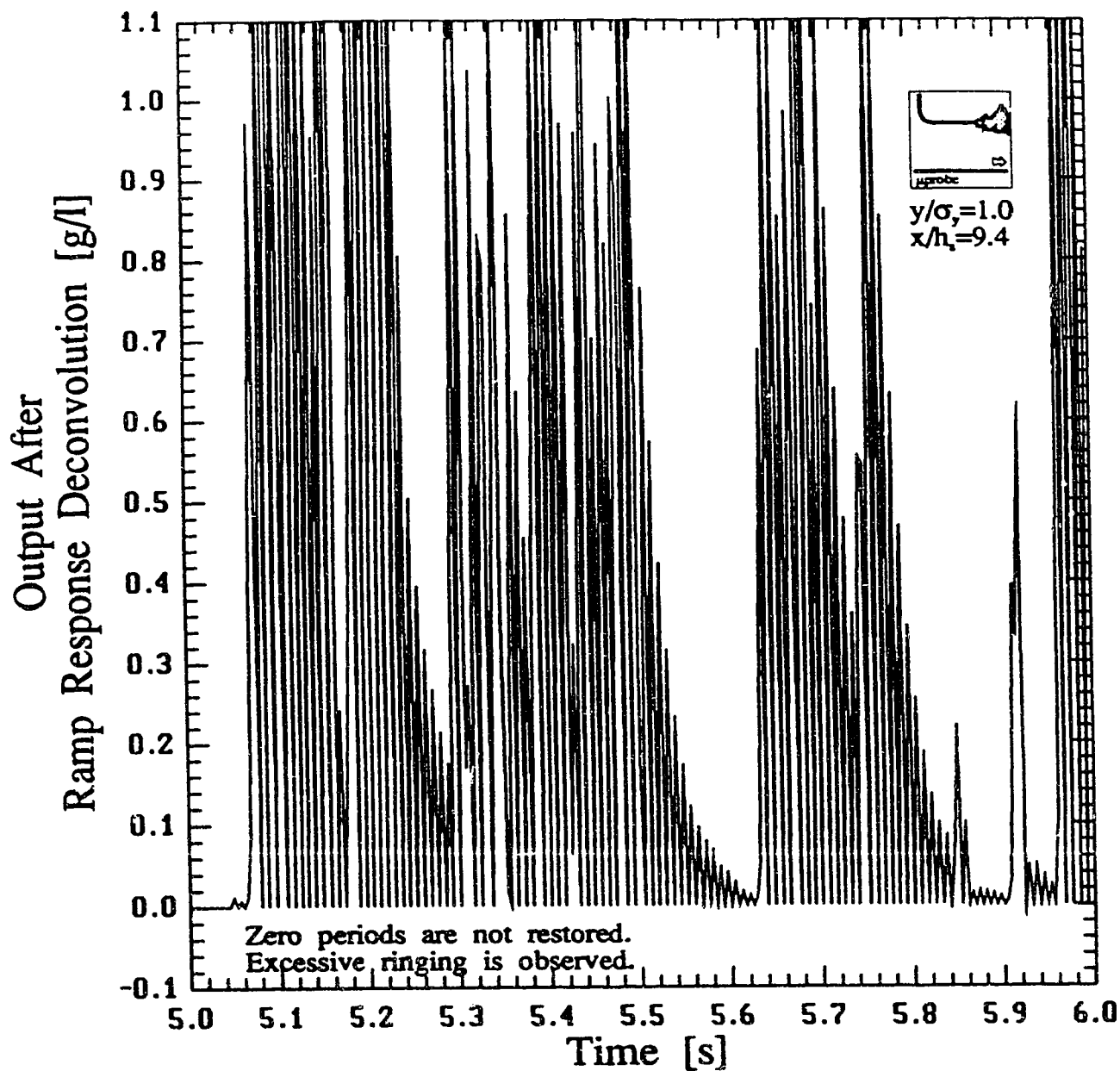


Figure 4.9: Ramp response deconvolution of a measured concentration signal showing a very noisy reconstruction of the supposed true concentration signal. Data is for the jet/plume source using the glass-micro probes.

deconvolution in Figure 4.9 demonstrates that the estimated signal is almost entirely hidden in high frequency noise.

If the ringing in the ramp response is entirely high frequency noise then it can be removed using a low-pass digital filter. In Figure 4.10 the power spectrum of the ramp deconvoluted signal is shown. Three important things are evident. Firstly, the ringing of the ramp deconvolution creates a large increase of high frequency noise. Secondly, digital filtering removes this high frequency noise effectively. Unfortunately, the last effect of the deconvolution is a large broadband increase in the spectra. The spectrum of the step response deconvolution in Figure 4.10, displays a much smaller increase in the high frequency noise which is adequately removed by digital filtering. The step response deconvolution does not generate the broad band noise.

The overall effect of the deconvolutions and digital filters on the time series signal is shown in Figure 4.11 and Figure 4.12. Clearly the ramp response does not produce the desired corrections. Intuitively, this is not expected since the ramp response more closely represents the actual physics of a real process. However, if the ratio of time constants of process to probe was large, then it can be shown that ramp response would model the process adequately.

In Figure 4.11 the step response corrects both the loss in the high peak concentration attenuations and the intermittent periods where the concentrations drop to zero. The restoration of the peak concentrations is important when the probability distributions are being considered because the response attenuation will truncate the distribution.

Another important difference between the two signals in Figure 4.11 is evident for the low concentration values. When the concentration signal falls from a high concentration to a low concentration the probe response smears out the drop in concentration so that the zero period is often missed. The deconvolution corrects this and reveals the actual zero period or best estimate of the true concentration value. The fraction of time that the plume concentration signal is present is dependent on being able to see the low concentration values. This is very important because the conditional concentration results depend on the fraction of time that the plume is present.

4.3 Spectral Response

The response of the probe to a dynamic signal has been shown to closely follow a first order system. This means that the amplitude response to a given frequency

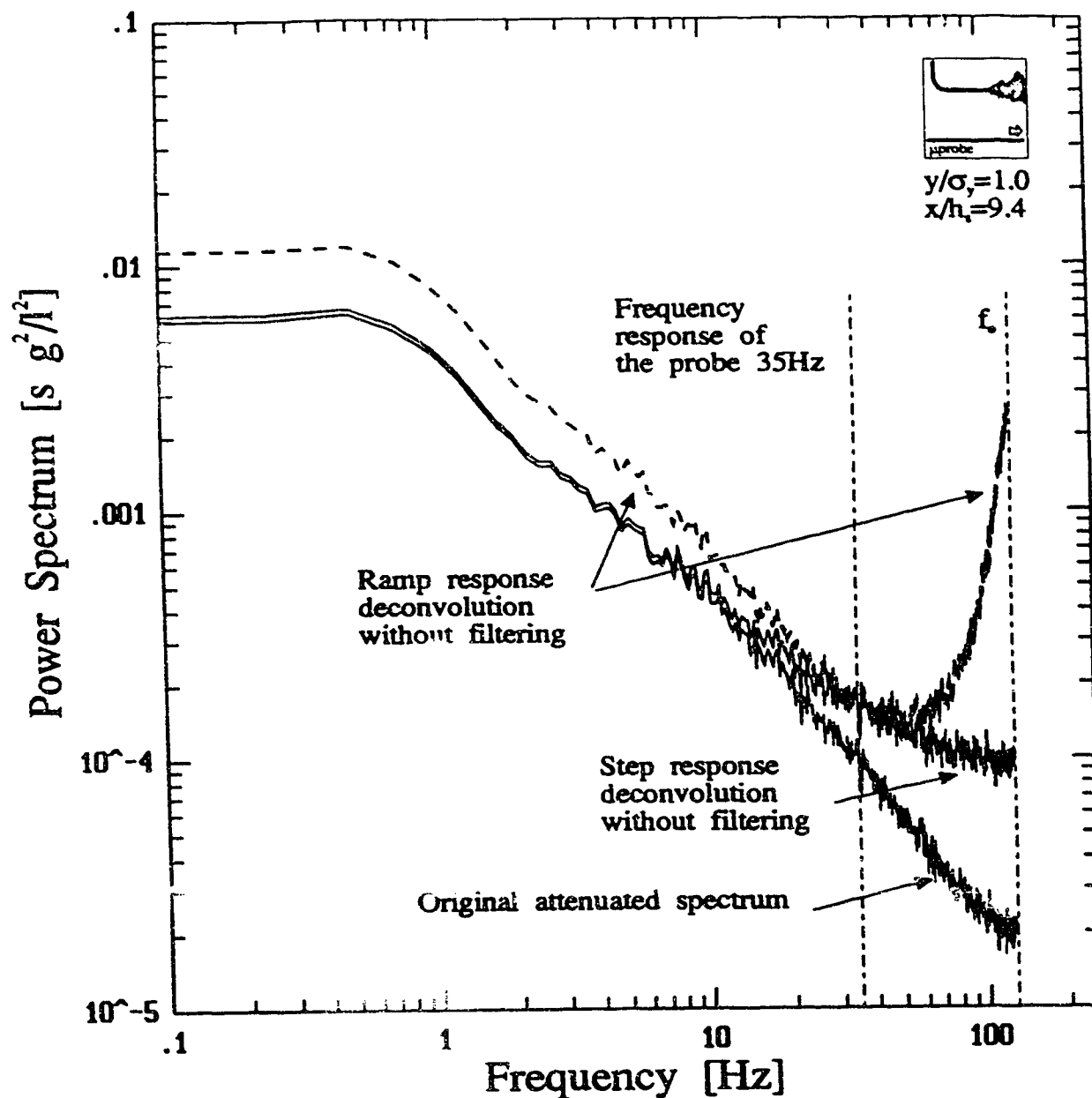


Figure 4.10: Spectra of the step response deconvolution and ramp response deconvolution. Data is for the jet/plume source using the glass-micro probes.

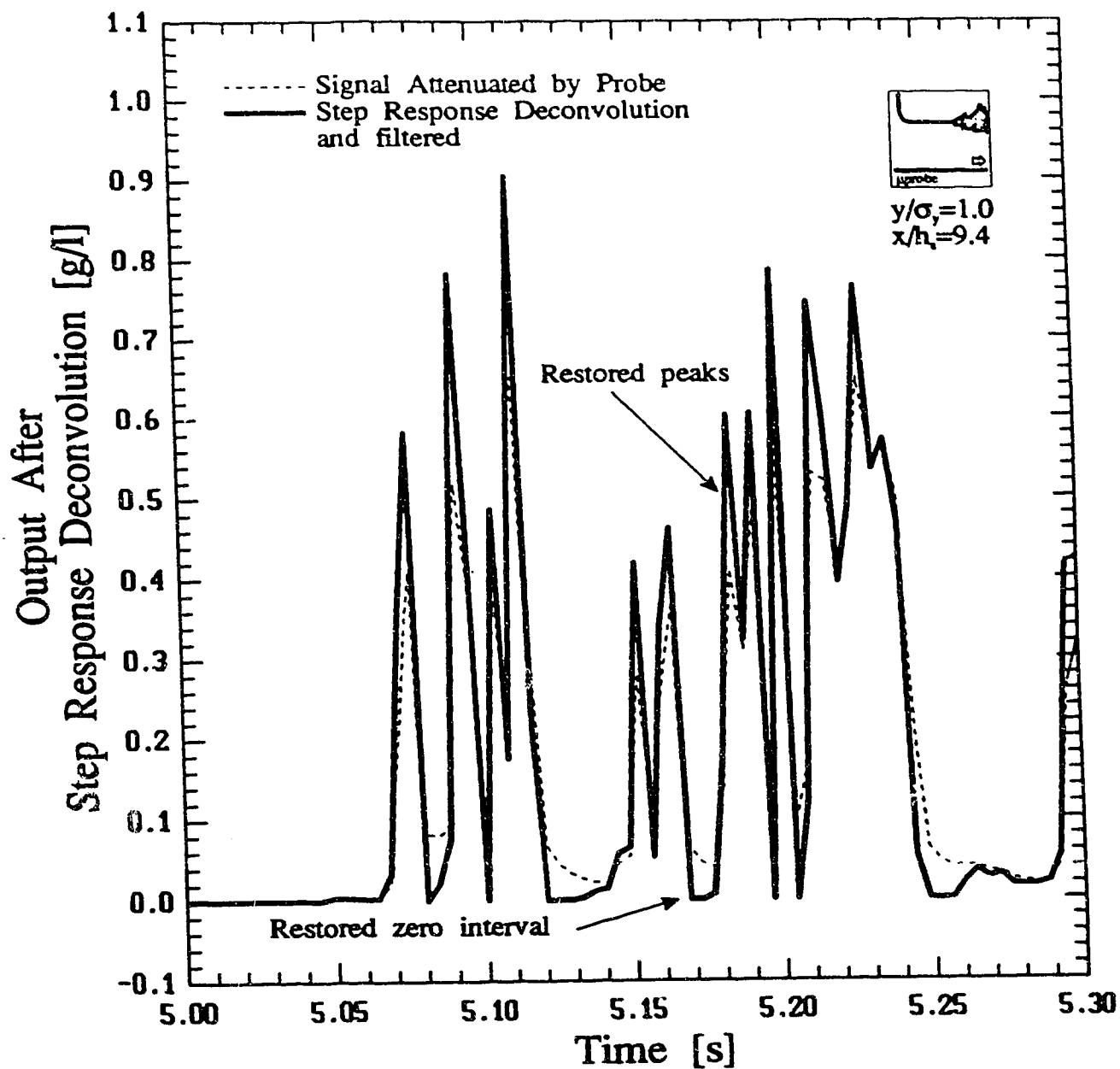


Figure 4.11: A typical concentration time series signal for the jet/plume source using the glass micro-probe with step response deconvolution and digital filtering.

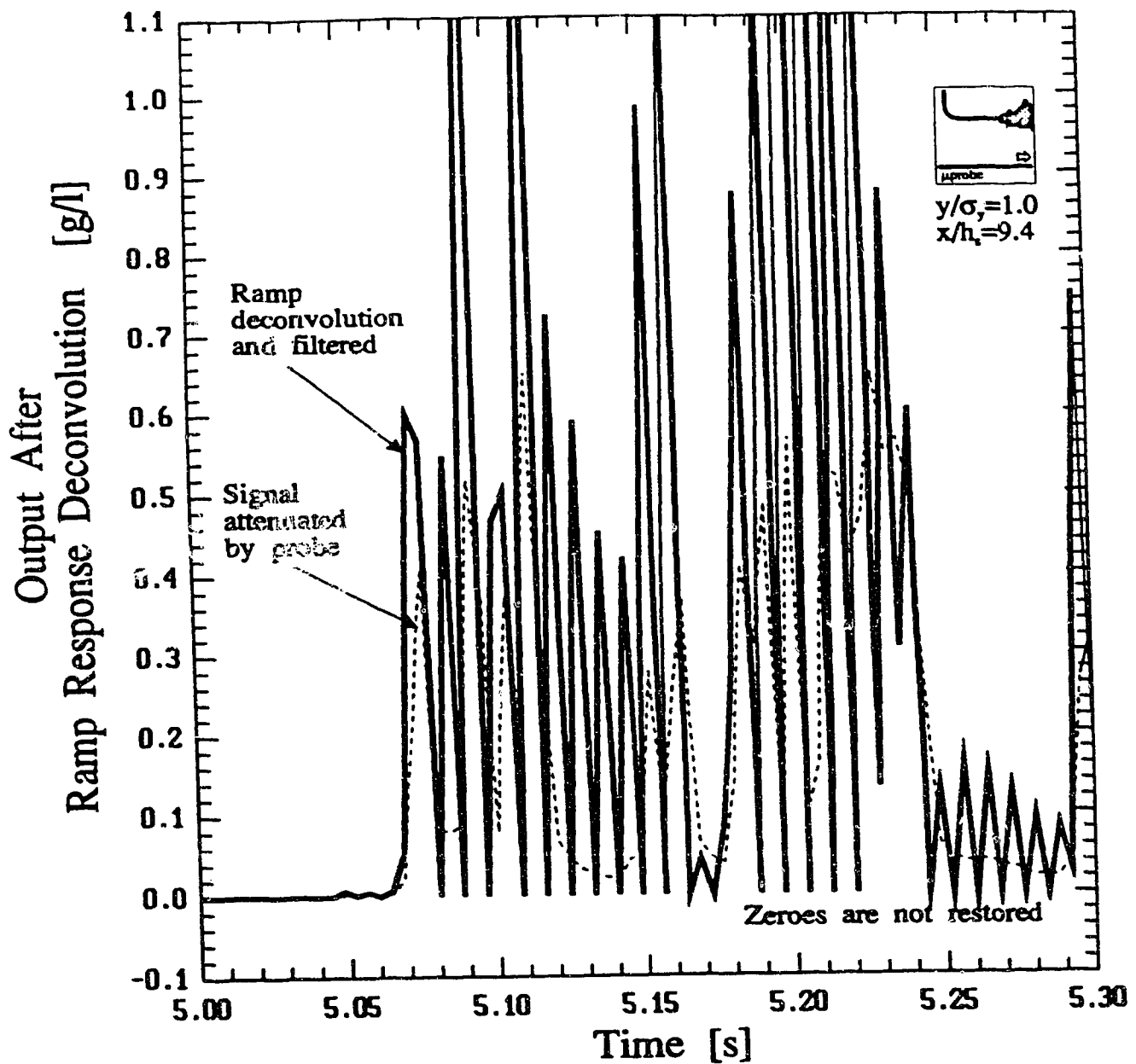


Figure 4.12: A typical concentration time series signal for the jet/plume source using the glass micro-probe with ramp response deconvolution and digital filtering.

Table 4.1: Typical Probe Time Responses with a 1.0 mm Flushing Length

z/H	f Hz
	28.2
	35.8
0.5	38.8
1.0	44.4

may be determined. Any signal fluctuation with a frequency higher than the cut-off frequency is filtered. Energy in the fluctuations above the cut-off frequency is attenuated at a rate of -3 dB per octave. The power spectra of a typical concentration signal for a probe are shown in Figure 4.13. There is noticeable attenuation of the signal after about 35 Hz, (for $\Lambda_p=1.0$ mm and $\bar{u}=22.5$ cm/s). When the signal is restored by correcting for the probe response, discretion must be used in analyzing the frequencies higher than the shoulder frequency. For the range of velocities found in the water channel, typical time responses are listed in Table 4.1.

At frequencies higher than the shoulder frequency, the signal may be restored. For a real signal, determining how much of the signal higher than the roll-off frequency still contains meaningful information is difficult. The computer A/D resolution and gain setting, noise levels, probe time response, and systematic error are among the factors which determine how much of the signal is actually present. The spectrum of a corrected probe response signal, Figure 4.13b, shows that above about 100 Hz an increasing trend in signal energy is observed. This is high frequency information and may be considered noise. This information must be removed to avoid drawing incorrect conclusions about the probability of signal fluctuations or concentration time scales which would be considerably affected.

The digital filter used to correct the probe time response was selected arbitrarily as a first order filter with the same behaviour as the detector. Using this filter type, the output signal would appear to have been taken by a detector with a better time response. The digital filter is set to a cut-off frequency higher than the original cut-off frequency of the detector. The spectral response function, $H^2(k)$, for the first order filter is,

$$H^2(k) = \frac{1}{1 + \Lambda_p^2 k^2} \quad (4.9)$$

where k is the spectral wave number and Λ_p is the detector length scale. The effective

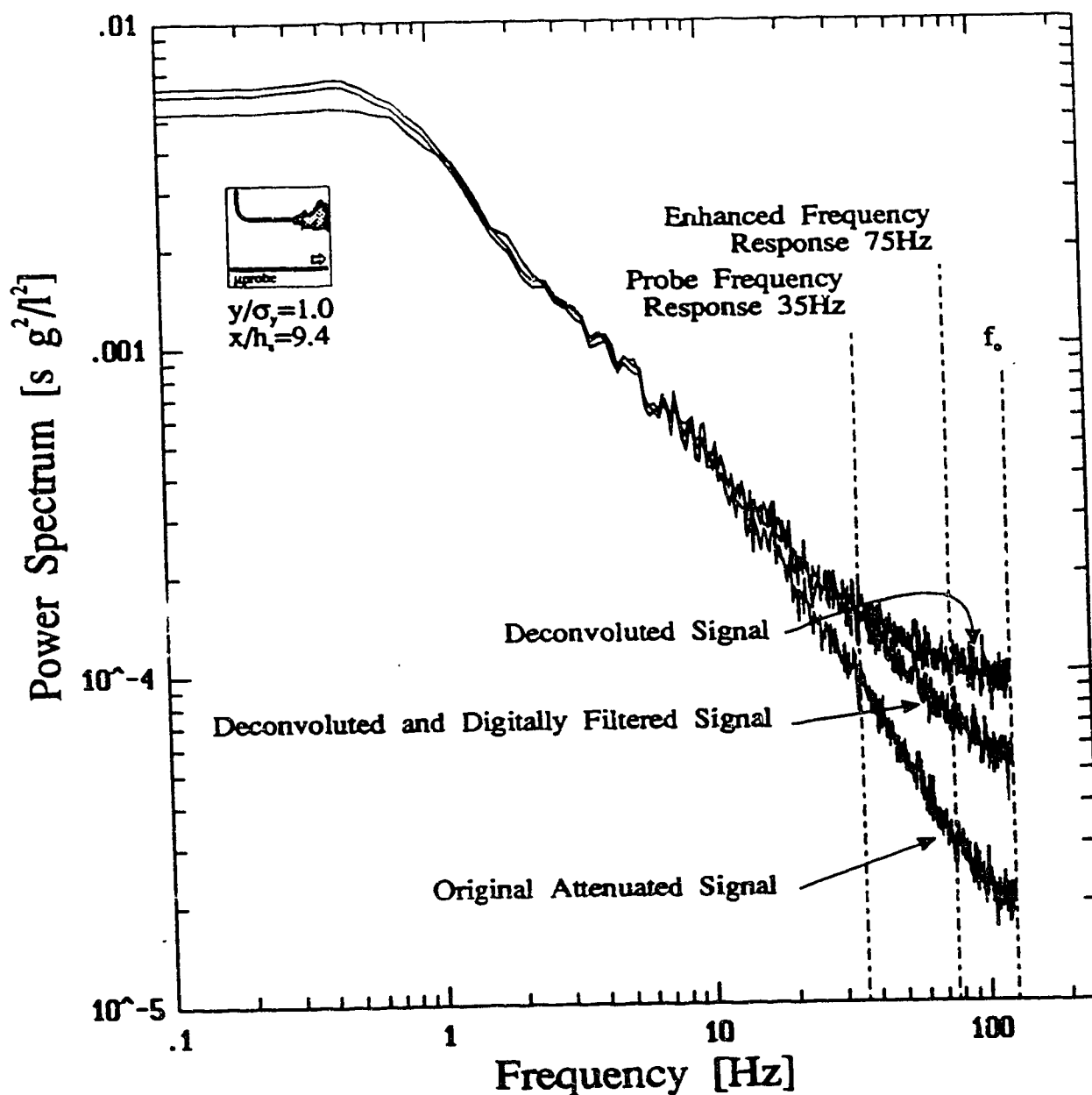


Figure 4.13: Example of the effect of: a) Energy spectrum, uncorrected for probe response. b) Energy spectrum corrected for probe response showing in the increased noise in high frequency ranges. c) Energy spectrum corrected and digitally filtered energy spectra. Data is for the jet/plume source using the glass micro-probe.

spectrum for a time series with filtering is given by,

$$E_{c,\text{eff}}(k) = H^2(k) E_c(k) \quad (4.10)$$

It was decided, based on examining the spectra that the probe response could be increased three fold for the stable new-probe data, and only two fold for the micro-probe data. Therefore, for the detector with an original response time of 35 Hz, the deconvoluted and digitally filtered signal has a response time of 105 Hz. The spectrum of the corrected and filtered signal is shown in Figure 4.13c. The spectrum is now clearly linear down to the 105 Hz cut-off frequency of the digital filter. This is an important achievement which allows much more information to be extracted from the time series signal from any instrument with an insufficient time response.

4.4 Conclusion

The improvements made in the conductivity detector over Bara's (1985) design are a 50% reduced time response and a reduced measuring volume. The aerodynamic design and inexpensive construction are other appealing features. The signal stability is still a problem however, for the micro-probe. The probe calibration has a tendency to drift, which increases quickly with age of the probe and time since calibration. Although it is believed that the drift has been reduced from the previous design, there is room for considerable improvement by maximizing the detection surface area, while minimizing the probe tip size.

In addition to the probe's increased time response, a procedure has been described to correct the time series signal for the response of the probe. This has increased the apparent frequency response of the probe by another factor of two to three.

Chapter 5

Concentration Probability Distributions

In this chapter, measurements of the concentration signal will be used to determine what probability distribution may be used to represent the dispersion of a tracer in a boundary layer.

5.1 Probability Models

Bilger (1980) and Pope (1985) present concise reviews of the expected probability distributions near the source of chemical reaction applications, mixing layers, jets, and reactor chambers. Taylor, Jakeman and Simpson (1986) and Jakeman, Simpson, and Taylor, (1986,1988) review a broad selection of probability models for use in dispersion modelling in the atmosphere and methods of fitting the models to atmospheric data sets. The large number of models may be reduced by rejecting those that have no physical process basis or are applied purely as empirical fits; the Students t-test, Logistic, and forms of the bi-Gaussian distributions. This leaves the Normal, log-Normal, Gamma, Beta, Weibull, and the Exponential distributions as possible models. These models have an advantage in that they are relatively simple to fit, have a physical process basis and are popular models for comparison to others in the literature.

The 'g&h' probability distribution suggested by Yee (1990) and Hoaglin and Peters (1979) is empirical but is a very flexible distribution, in that it is able to fit the probability distribution function under a wide range of conditions. Unfortunately, however, it is very complex to fit and does not lend itself well to engineering applications.

Pope (1980) has found the *most-likely* probability distribution, $f_n(\zeta)$, based on the first n measured concentration moments, is given by,

$$f_n(\zeta) = \exp \left(\sum_{i=0}^n A_i \zeta^i \right) \quad (5.1)$$

where ζ is the deviation from the mean. The $(n + 1)$ coefficients, A_i , are determined from the first n concentration moments and from the fact that $f_n(\zeta)$ should integrate to unity. This model has the important characteristic of being able to adequately incorporate the higher order moments in the model. The most-likely distribution has the ability to represent a bimodal distribution, (which is often found when the distance from the source is small), based on the first three concentration moments. Unfortunately, however, it is difficult to fit and is complex to use in engineering applications.

The Beta distribution provides a good model for concentration mixing processes because of the ease of fitting its parameters and because it is bounded between $0 \leq \zeta \leq 1$. The diffusing scalar, c , is normalized such that, $\zeta = c/c_{max}$. This works well for mixing processes, but for dispersion models c_{max} must be chosen as the maximum observed concentration at the receptor location or the source concentration. The maximum concentration at the receptor is generally not known. The source concentration is known, but, because the dilutions are quite large, the PDF is highly skewed and the Beta function provides a very poor fit from results in the water channel. Therefore, for dispersion work, the Beta model does not work well as a general PDF model.

The central limit theorem accounts for the occurrence of approximately Normal distributions in practice, since random phenomena are often additive combinations of several contributory variables. Close to the tracer source, a Normal distribution has been found (Dopazo, 1975, Sreenivasan, 1981, among many others). As one moves away from the source, the dilution becomes significant and near zero concentrations are observed. At this point, the Normal model becomes inappropriate because it predicts negative concentrations. However, if the negative values are clipped, and the remaining area renormalized to unity, a clipped-Normal distribution results and provides a good estimation of the distribution. Further still from the source, where intermittency effects become a significant influence, the present study will show the probability distribution evolves to something different than the Normal distribution.

Many probability distribution models have been proposed for the region far from the source;

- the Exponential or negative Exponential, (Barry, 1977),

- the clipped-Normal, (Lockwood and Naguib, 1975, Lewellen and Sykes, 1986, Sawford, 1987)
- the Gamma, (Marani, Lavagnini, Buttazzoni, 1986, Lienhard and Meyer, 1967, Bencala and Seinfeld, 1976),
- the Weibull (Marani, Lavagnini, Buttazzoni, 1986),
- the log-Normal, (Csanady, 1973, Wilson and Simms, 1985, Holland and Fitz-Simmons, 1982),
- the Beta, (Richardson, Howard, and Smith, 1953).

When Normal variables combine as random products, the log-Normal distribution is produced, Bury (1986). The log-Normal model has been justified for plumes when a receptor is continually being impacted by the plume, Csanady (1973). Barry (1977) predicts that the Exponential distribution is more appropriate for situations when a receptor is intermittently impacted by a plume and the resulting concentration is the sum of uncorrelated events. When variables (Normal) add as the sum of squares, then the Chi-squared, or Gamma, distribution is produced, Brooks and Carruthers (1953). Marani, Lavagnini, Buttazzoni (1982) applies the generalized (4 parameter) Gamma distribution to air pollution studies based on its physical basis in the study of propagation of noninteracting water particles subject to a conservation law, Lienhard (1967).

From the above descriptions it might be expected that no single probability distribution could be expected to fit the concentration dispersion process. However, several of the common distributions have shapes that evolve with their parameters. The Gamma distribution has a limiting form which is Gaussian or Exponential, depending on the values of its parameters. The Beta distribution has the ability to vary the sign of its skewness. The log-Normal distribution has a limiting form which is Gaussian or positively skewed. It is hoped, therefore, that a single distribution might be able to represent the evolution of the concentration fluctuation probability distribution with down-wind and cross-wind distance.

In the following sections the main features of the probability models to be investigated are presented. The probability models are presented in a form such that the parameters of the two parameter distributions may be predicted using the first three total concentration moments, (\bar{c} , \bar{c}^2 , and \bar{c}^3). Alternatively, the parameters could be determined using the first two conditional moments and the intermittency, (\bar{c}_p , \bar{c}_p^2 , and γ). The clipped-Normal distribution is a two parameter distribution, but has the intermittency inherently incorporated in its definition. Therefore, the

parameters of the clipped-Normal distribution can be determined using only the first two total moments. The Exponential distribution is a one parameter distribution and requires only the conditional mean concentration, or the first two total moments of concentration.

5.1.1 Conditional Probability Model

The general form of the probability density function, abbreviated PDF, that will be used in this study of concentration fluctuations is,

$$f(c) = \gamma f_p(c) + (1 - \gamma)\delta(c) \quad (5.2)$$

where:

- $f(c)$ is the probability density of the concentration signal including both zero periods and periods when the plume is present.
- $f_p(c)$ is the probability density of the conditional concentration signal, defined as $f_p(c|c > 0)$, the probability density of c given that $c > 0$.
- γ is the intermittency factor defined as the fraction (probability) that the measured signal is non-zero.
- $\delta(c)$ is the dirac delta function having an area of unity at a concentration of zero and has a magnitude of zero elsewhere.

The cumulative distribution function, (CDF), $F(c^*)$, is the probability that the concentration will be observed to be less than a specified value c^* , and is given by:

$$F(c^*) = \int_0^{c^*} f(c) dc. \quad (5.3)$$

Substituting (5.2) into (5.3),

$$F(c^*) = (1 - \gamma) + \gamma \int_0^{c^*} f_p(c) dc. \quad (5.4)$$

$$= (1 - \gamma) + \gamma F_p(c^*) \quad (5.5)$$

where:

$F(c)$ is the cumulative probability distribution of the concentration signal including zero periods and periods when the plume is present.

$F_p(c)$ is the cumulative probability distribution of the conditional concentration signal, defined as $F_p(c|c > 0)$, the cumulative probability distribution of c given that $c > 0$.

The fraction of time during which the concentration value exceeds the threshold value is the exceedance function, F' , referred to as the complementary cumulative distribution function, (CCDF):

$$\begin{aligned} F'(c^*) &= \int_{c^*}^{\infty} f(c) dc \\ &= 1 - \int_0^{c^*} f(c) dc \\ &= 1 - F(c^*) \end{aligned} \tag{5.6}$$

$$\begin{aligned} &= \gamma(1 - F_p(c^*)) \\ &= \gamma F'_p(c^*) \end{aligned} \tag{5.7}$$

where:

$F'(c)$ is the complementary cumulative probability distribution of the concentration signal including zero periods and periods when the plume is present.

$F'_p(c)$ is the complementary cumulative probability distribution of the conditional concentration signal, defined as $F'_p(c|c > 0)$, the complementary cumulative probability distribution of c given that $c > 0$.

The zero-based moments for the total (or unconditional) concentration are,

$$\overline{c^n} = \int_0^{\infty} c^n f(c) dc \tag{5.8}$$

However, when working with the PDF models of the concentration fluctuations, which are based on the conditional (non-zero concentrations only) values, the conditional moments may be determined from,

$$\overline{c_p^n} \equiv \mu'_n = \int_0^{\infty} c^n f_p(c) dc, \quad (0 < c) \tag{5.9}$$

where μ'_n is the n^{th} moment of the distribution about the zero origin. μ_n is defined to be the n^{th} moment of the fluctuations about the conditional mean value,

$$\overline{c_p'^n} \equiv \mu_n = \int_0^\infty (c - \overline{c_p})^n f_p(c) dc, \quad (0 < c) \quad (5.10)$$

The confusing notation of μ_n and μ'_n is a standard in the probability literature.

From (5.2) and (5.8), the conditional and total zero-based moments are related by,

$$\overline{c^n} = \gamma \overline{c_p^n} \quad (5.11)$$

5.1.2 Normal Distribution

The Normal distribution cannot be used as a concentration probability distribution model because its negative range is not physically applicable. However, the model is presented here for a basis of comparison.

The general form of the Normal PDF is given by,

$$f_{p,N}(c; \mu, \sigma) = \frac{1}{\sqrt{2\pi}\sigma} \exp \left(- \left(\frac{c - \mu}{\sqrt{2}\sigma} \right)^2 \right) \quad (5.12)$$

With $-\infty < \mu, c < \infty$ and $0 < \sigma$. μ is a location parameter, generally the distribution mean value, and σ is a scaling parameter, generally the distribution standard deviation.

The cumulative distribution may be determined using (5.3) to be,

$$F_{p,N}(c^*; \mu, \sigma) = \begin{cases} 1/2 \operatorname{erfc}(-\zeta), & \zeta < 0 \\ 1/2 (1 + \operatorname{erf}(\zeta)), & \zeta > 0 \end{cases} \quad (5.13)$$

where $\zeta = (c^* - \mu) / \sigma$.

The first four total conditional moments are easily determined to be,

$$\left. \begin{aligned} \mu'_1 &= \mu \\ \mu'_2 &= \mu^2 + \sigma^2 \\ \mu'_3 &= \mu^3 + 3\mu\sigma^2 \\ \mu'_4 &= \mu^4 + 6\mu^2\sigma^2 + 3\sigma^4 \end{aligned} \right\} \quad (5.14)$$

The moment estimators for this distribution are therefore,

$$\mu = \mu'_1 \quad (5.15)$$

$$\sigma = \mu'_2 - \mu_1'^2 \quad (5.16)$$

5.1.3 Log-Normal Distribution

The log-Normal distribution is, Bury (1986),

$$f_{p, LN}(c, \mu, \sigma) = \frac{1}{c\sigma\sqrt{2\pi}} \exp\left(-\left(\frac{\ln(c) - \mu}{\sqrt{2}\sigma}\right)^2\right) \quad (5.17)$$

where $-\infty < \mu < \infty$ and $0 < c, \sigma$. μ is a scale parameter related to the log-Normal mean, σ is a shape parameter related to the standard deviation.

The CDF for the log-Normal distribution is,

$$F_{p, LN}(c^*; \mu, \sigma) = 0.5 \left(1 + \operatorname{erf}\left(\frac{\ln(c^*) - \mu}{\sqrt{2}\sigma}\right)\right) \quad (5.18)$$

The $\operatorname{erf}(x)$ function, or standard error function, must be evaluated numerically, Press et al.(1988), or Abramowitz and Stegun, (1964).

The conditional total moments for the log-Normal distribution may be determined using,

$$\overline{c_p^n} = \mu'_n = \exp\left(\mu n + \frac{n^2 \sigma^2}{2}\right) \quad (5.19)$$

where n is real valued. The first four conditional moments are,

$$\left. \begin{aligned} \overline{c_p} &= \exp\left(\mu + \frac{\sigma^2}{2}\right) \\ \overline{c_p^2} &= \exp\left(2\mu + 4\frac{\sigma^2}{2}\right) = \overline{c_p}^2 \exp(\sigma^2) \\ \overline{c_p^3} &= \exp\left(3\mu + 9\frac{\sigma^2}{2}\right) = \overline{c_p}^3 \exp(3\sigma^2) \\ \overline{c_p^4} &= \exp\left(4\mu + 16\frac{\sigma^2}{2}\right) = \overline{c_p}^4 \exp(6\sigma^2) \end{aligned} \right\} \quad (5.20)$$

The central moments are given by,

$$\left. \begin{aligned} i_p^2 &= \exp(\sigma^2) - 1 \\ \overline{c_p^3} &= \overline{c_p}^3 (i_p^6 + 3i_p^4) \\ \overline{c_p^4} &= \overline{c_p}^4 (i_p^{12} + 6i_p^{10} + 15i_p^8 + 16i_p^6 + 3i_p^4) \end{aligned} \right\} \quad (5.21)$$

The moment estimators may be determined by solving (5.20)

$$\sigma = \sqrt{\ln(1 + i_p^2)} \quad (5.22)$$

$$\mu = \ln \left(\frac{\bar{c}_p}{\sqrt{1 + i_p^2}} \right) \quad (5.23)$$

A more convenient form of these estimators is available using the total moments. Solving (5.20) using (5.11), and the first three moments, after some algebra,

$$\sigma = \sqrt{\ln \left(\frac{\bar{c}^3 \bar{c}}{\bar{c}^2} \right)} \quad (5.24)$$

$$\mu = \ln \left(\frac{\bar{c}^4}{\sqrt{\bar{c}^3 \bar{c}^5}} \right) \quad (5.25)$$

$$\gamma = \frac{\bar{c}^3 \bar{c}^3}{\bar{c}^2} \quad (5.26)$$

The conditional mean, \bar{c}_p , and conditional intensity, i_p^2 , which are often used in engineering models, can be expressed in terms of the total moments as,

$$\bar{c}_p = \frac{\bar{c}^3}{\bar{c}^3 \bar{c}^2} \quad (5.27)$$

$$i_p^2 = \frac{\bar{c}^3 \bar{c}}{\bar{c}^2} - 1 \quad (5.28)$$

5.1.4 Clipped-Normal Distribution

The clipped-Normal distribution is created from the Normal distribution by truncating the distribution for c to the range $0 < c < \infty$, as illustrated in Figure 5.1. The remaining area under the clipped-Normal probability density curve is used to renormalize the PDF so that its area is again unity. The area under the curve which contained the negative values is equivalent to the zero intermittency. Therefore, in the total PDF formulation of (5.2), this area is represented by $(1 - \gamma)$ times a dirac delta function at zero concentration. The clipped-Normal distribution is therefore given by,

$$f_{p,CN}(c; \mu_o, \sigma_o) = \frac{1}{\sqrt{2\pi\sigma_o\gamma}} \exp \left(- \left(\frac{c - \mu_o}{\sqrt{2\sigma_o}} \right)^2 \right) \quad (5.29)$$

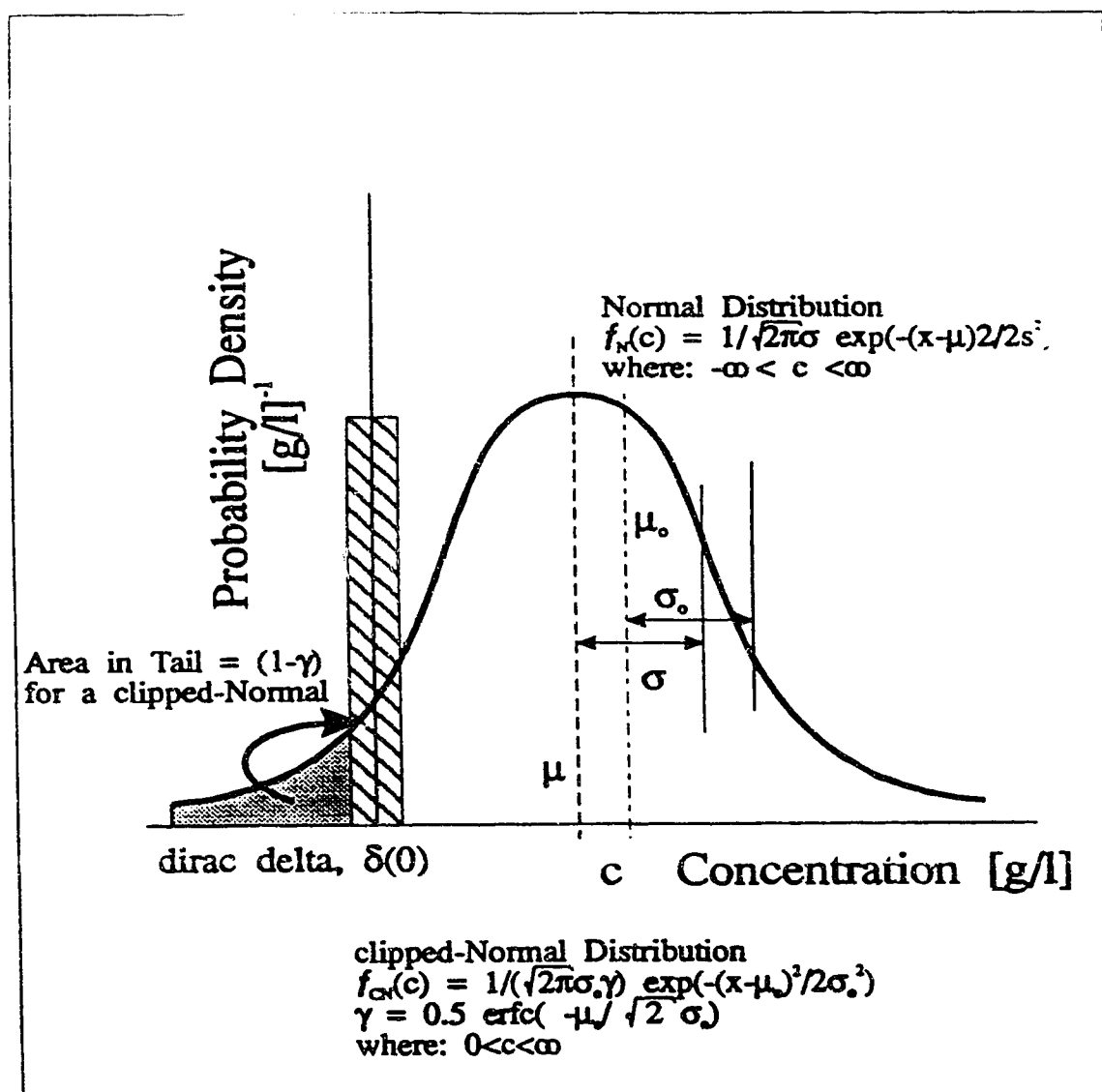


Figure 5.1: The clipped-Normal probability distribution is created from the Normal distribution by truncation of negative values and renormalization of the positive values so that the area under the curve is unity.

with $-\infty < \mu_o < \infty$ and $0 < c, \sigma_o$, where μ_o is a location parameter, and σ_o is a scaling parameter. The clipped-Normal CDF is therefore,

$$F_{p,CN}(c^*; \mu_o, \sigma_o) = \frac{\operatorname{erf}\left(\frac{c^* - \mu_o}{\sqrt{2}\sigma_o}\right)}{\operatorname{erfc}\left(\frac{-\mu_o}{\sqrt{2}\sigma_o}\right)} \quad (5.30)$$

The intermittency is,

$$\gamma = \frac{1}{2} \operatorname{erfc}\left(\frac{-\mu_o}{\sqrt{2}\sigma_o}\right) \quad (5.31)$$

The moments are determined using (5.8),

$$\overline{c^n} = \int_0^\infty c^n f_{CN}(c) dc \quad (5.32)$$

Then substituting (5.2),

$$\overline{c^n} = \int_0^\infty c^n \gamma f_{p,CN}(c) dc \quad (5.33)$$

By substitution of (5.29), the first four total moments are,

$$\left. \begin{aligned} \overline{c} &= \frac{\sigma_o}{\sqrt{2\pi}} \exp\left(-\frac{\mu_o^2}{2\sigma_o^2}\right) + \mu_o \gamma \\ \overline{c^2} &= \sigma_o^2 \gamma + \mu_o \overline{c} \\ \overline{c^3} &= 2\sigma_o^2 \overline{c} + \mu_o \overline{c^2} \\ \overline{c^4} &= \overline{c} (\sigma_o^2 \mu_o - 3\mu_o^3) + \gamma (5\mu_o^2 \sigma_o^2 + 4\mu_o^4 + 3\sigma_o^4) \end{aligned} \right\} \quad (5.34)$$

Substituting for γ , the first two conditional moments are easily determined,

$$\left. \begin{aligned} \overline{c_p} &= \frac{\sigma_o}{\gamma \sqrt{2\pi}} \exp\left(-\frac{\mu_o^2}{2\sigma_o^2} + \mu_o\right) \\ \overline{c_p^2} &= \sigma_o^2 + \mu_o \overline{c_p} \\ \text{or} \\ i_p^2 &= \frac{\sigma_o^2}{\overline{c_p}^2} + \frac{\mu_o}{\overline{c_p}} - 1 \end{aligned} \right\} \quad (5.35)$$

The higher order central moments for the clipped-Normal distribution are algebraically complicated and are given by Sawford (1987).

The moment estimators for this distribution must be determined by solving the first two moment equations, (5.35), by iteration. Using Newton's method (5.35) may be written as,

$$\mathcal{F}_1(\mu, \sigma) = \frac{\sigma}{\gamma\sqrt{2\pi}} \exp\left(-\frac{\mu^2}{2\sigma^2}\right) + \mu - \bar{c}_p \quad (5.36)$$

$$\mathcal{F}_2(\mu, \sigma) = \sigma^2 + \mu\bar{c}_p - \bar{c}_p^2 \quad (5.37)$$

where the functions \mathcal{F}_1 and \mathcal{F}_2 are to be minimized. If a Taylor series expansion of (5.37) is made, noting that the estimates of μ_o and σ_o are μ' and σ' ,

$$\mathcal{F}_1(\mu, \sigma) = \mathcal{F}_1(\mu', \sigma') + (\mu - \mu') \frac{\partial \mathcal{F}_1}{\partial \mu} + (\sigma - \sigma') \frac{\partial \mathcal{F}_1}{\partial \sigma} + \dots \quad (5.38)$$

$$\mathcal{F}_2(\mu, \sigma) = \mathcal{F}_2(\mu', \sigma') + (\mu - \mu') \frac{\partial \mathcal{F}_2}{\partial \mu} + (\sigma - \sigma') \frac{\partial \mathcal{F}_2}{\partial \sigma} + \dots \quad (5.39)$$

Near the solution of $\mu' \rightarrow \mu$ and $\sigma' \rightarrow \sigma$ the functions $\mathcal{F}_1 \approx 0$ and $\mathcal{F}_2 \approx 0$. Therefore (5.39) may be written in matrix form as,

$$\begin{Bmatrix} \mathcal{F}_1(\mu', \sigma') \\ \mathcal{F}_2(\mu', \sigma') \end{Bmatrix} = \begin{bmatrix} \frac{\partial \mathcal{F}_1}{\partial \mu} & \frac{\partial \mathcal{F}_1}{\partial \sigma} \\ \frac{\partial \mathcal{F}_2}{\partial \mu} & \frac{\partial \mathcal{F}_2}{\partial \sigma} \end{bmatrix} \begin{Bmatrix} \Delta\mu \\ \Delta\sigma \end{Bmatrix} \quad (5.40)$$

The derivatives in the Jacobian matrix in (5.40) may be determined by numerical integration. (5.40) was solved by iteration with dynamic relaxation which was optimized by trial and error. The solution was typically found in less than 20 iterations but increased above 100 in cases when the intermittency approached zero.

A characteristic of the clipped-Normal distribution is shown in Figure 5.2. When the intermittency is large, ($\gamma \rightarrow 1$), the conditional intensity is given as usual by $i_p^2 = \sigma_{cp}^2 / \bar{c}_p^2$. However, i_p^2 is always less than unity. When the intermittency is small, ($\gamma \rightarrow 0$), the tail of the clipped-Normal distribution is a type-I extreme value distribution, Bury (1986), and in the limit approaches an Exponential distribution. An Exponential distribution is a one parameter distribution with the characteristic that, $i_p^2 = \sigma_{cp}^2 / \bar{c}_p^2 \equiv 1.0$. However, often on the centre-line, and in the fringes of the plume, the conditional intensity is observed to be greater than unity. The failure to represent the $i_p > 1$ observations is the major deficiency of the clipped-Normal distribution. For this reason it is not an adequate overall model because it cannot represent the data in the fringes when $i_p > 1$. Therefore, the clipped-Normal distribution cannot be the correct representation of the dispersion process.

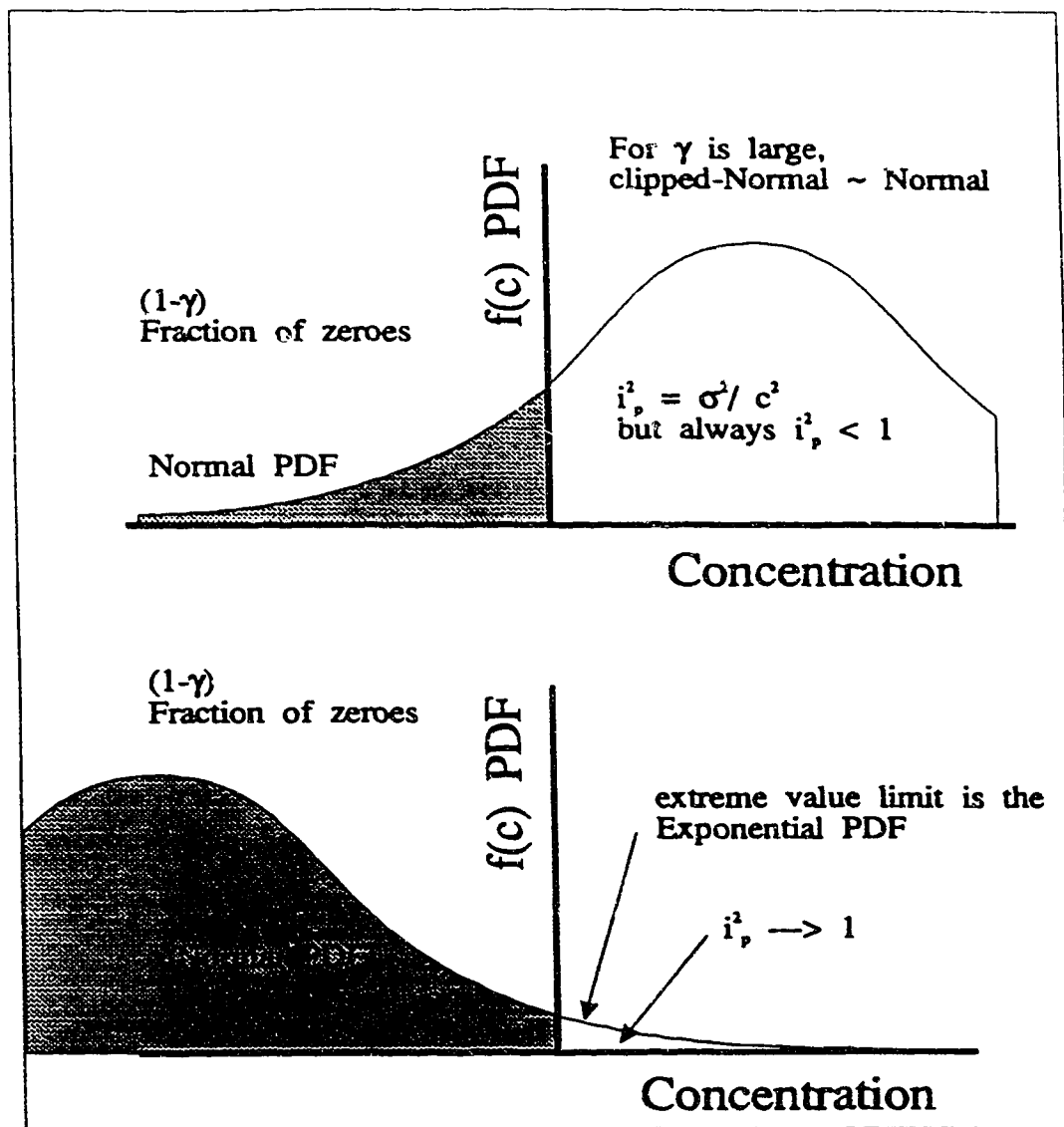


Figure 5.2: The transformation of the clipped-Normal distribution to the one parameter Exponential distribution when the intermittency varies from near unity to near zero.

5.1.5 Gamma Distribution

The general form of the Gamma PDF is given by, Bury (1986),

$$f_{p,G}(c; \sigma, \lambda) = \frac{1}{\sigma \Gamma(\lambda)} \left(\frac{c}{\sigma}\right)^{\lambda-1} \exp\left(-\frac{c}{\sigma}\right) \quad (5.41)$$

where $c, \lambda, \sigma > 0$, and σ is a scaling parameter and λ is a shape parameter. It can be seen from (5.41) that the scaling parameter, σ , determines the relative magnitudes with respect to c . The function $\Gamma(\lambda)$ is called the Gamma function. It is a real valued factorial function with the following property,

$$\Gamma(\lambda) = (\lambda - 1)\Gamma(\lambda - 1) \quad (5.42)$$

Numerical routines for determining the Gamma function were taken from Press et al., (1988).

The CDF for the Gamma function may be shown to be,

$$F_{p,G}(c; \sigma, \lambda) = \frac{\Gamma(\lambda, \frac{c}{\sigma})}{\Gamma(\lambda)} \quad (5.43)$$

where the function $\Gamma(\lambda, \frac{c}{\sigma})$ is a part of the incomplete Gamma function given by,

$$P(\lambda, x) \equiv \frac{\Gamma(\lambda, x)}{\Gamma(\lambda)} \equiv \int_0^x y^{\lambda-1} e^{-y} dy \quad (5.44)$$

A numerical routine for $P(\lambda, x)$ was taken from Press et al. (1988).

The moments of the Gamma distribution are determined by using (5.9) and may be shown to be,

$$\overline{c_p^n} = \sigma^n \frac{\Gamma(n + \lambda)}{\Gamma(\lambda)} \quad (5.45)$$

where n may be real valued. The first four moments are,

$$\left. \begin{aligned} \overline{c_p} &= \sigma \lambda \\ \overline{c_p^2} &= \sigma^2 (1 + \lambda) \lambda \\ \overline{c_p^3} &= \sigma^3 (2 + \lambda) (1 + \lambda) \lambda \\ \overline{c_p^4} &= \sigma^4 (3 + \lambda) (2 + \lambda) (1 + \lambda) \lambda \end{aligned} \right\} \quad (5.46)$$

and the central moments are

$$\left. \begin{aligned} \overline{c_p'^2} &= \sigma^2 \lambda \\ \overline{c_p'^3} &= 2\sigma^3 \lambda \\ \overline{c_p'^4} &= 3\sigma^4 \lambda (2 + \lambda) \end{aligned} \right\} \quad (5.47)$$

The moment estimators are determined using the first two conditional moments, by solving (5.46) using the first two moments,

$$\sigma = i_p^2 \overline{c_p} \quad (5.48)$$

$$\lambda = 1/i_p^2 \quad (5.49)$$

where i_p is the fluctuation intensity of the conditional concentration.

The moment estimators may also be expressed in terms of the total concentration moments using the first three moments in (5.46) and (5.2). After some algebra,

$$\sigma = \left(\frac{\overline{c^3}}{\overline{c^2}} \right) - \left(\frac{\overline{c^2}}{\overline{c}} \right) \quad (5.50)$$

$$\lambda = \frac{2\overline{c^2}^2 - \overline{c}\overline{c^3}}{\overline{c}\overline{c^3} - \overline{c^2}^2} \quad (5.51)$$

$$\gamma = \frac{\overline{c^2}\overline{c^2}}{2\overline{c^2}^2 - \overline{c}\overline{c^3}} \quad (5.52)$$

5.1.6 Exponential Distribution

When $\lambda = 1$ in the Gamma distribution, the resulting distribution is Exponential. Bury (1986), gives the general form for the one parameter Exponential PDF as,

$$f_{p,E}(c; \mu) = \frac{1}{\mu} \exp\left(-\frac{c}{\mu}\right) \quad (5.53)$$

The CDF for the Exponential distribution may be shown to be,

$$F_{p,E}(c^*; \mu) = 1 - \exp\left(-\frac{c^*}{\mu}\right) \quad (5.54)$$

The first four conditional moments are easily determined to be,

$$\left. \begin{aligned} \overline{c_p} &= \mu \\ \overline{c_p^2} &= 2\mu^2 \\ \overline{c_p^3} &= 6\mu^3 \\ \overline{c_p^4} &= 24\mu^4 \end{aligned} \right\} \quad (5.55)$$

The central conditional moments are,

$$\left. \begin{aligned} \overline{c_p'^2} &= \mu^2 \\ \overline{c_p'^3} &= 2\mu^3 \\ \overline{c_p'^4} &= 9\mu^4 \end{aligned} \right\} \quad (5.56)$$

The moment estimators for the Exponential distribution are simply $\mu = \overline{c_p}$.

$$\mu = \overline{c_p} \quad (5.57)$$

$$\gamma = 2 \left(\frac{\overline{c_p^2}}{\overline{c_p}^2} \right) \quad (5.58)$$

$$(5.59)$$

The conditional intensity is simply,

$$i_p^2 = 1 \quad (5.60)$$

5.1.7 Weibull Distribution

The standard form for the Weibull distribution is,

$$f_{p,W}(c; \sigma, \lambda) = \left(\frac{\lambda}{\sigma} \right) \left(\frac{c}{\sigma} \right)^{\lambda-1} \exp \left(- \left(\frac{c}{\sigma} \right)^\lambda \right), \quad 0 < c, \lambda, \sigma \quad (5.61)$$

where σ is a scale parameter and λ is a shape parameter. The CDF is given by,

$$F_{p,W}(c^*; \sigma, \lambda) = 1 - \exp \left(- \left(\frac{c^*}{\sigma} \right)^\lambda \right) \quad (5.62)$$

The first four moments of the distribution are given by,

$$\left. \begin{aligned} \overline{c_p} &= \sigma \Gamma \left(1 + \frac{1}{\lambda} \right) \\ \overline{c_p^2} &= \sigma^2 \Gamma \left(1 + \frac{2}{\lambda} \right) \\ \overline{c_p^3} &= \sigma^3 \Gamma \left(1 + \frac{3}{\lambda} \right) \\ \overline{c_p^4} &= \sigma^4 \Gamma \left(1 + \frac{4}{\lambda} \right) \end{aligned} \right\} \quad (5.63)$$

The equations for the central moments are algebraically complicated, refer to Bury (1986) p.408.

The moment estimators are not easily determined for the Weibull distribution. They must be determined by iterating a complicated function involving an algebraic combination of several gamma functions. Jakeman, Simpson, and Taylor (1986) give an approximation for the moment estimators discovered by Menon (1963), which is,

$$\lambda \approx \left((6/\pi^2) \overline{c_p^2} \right)^{0.5} \quad (5.64)$$

$$\sigma \approx \exp (\overline{c_p} + 0.5772/\lambda) \quad (5.65)$$

5.1.8 Beta Distribution

The standard form for the Beta model is given by,

$$f_{p,B}(\zeta; \lambda_1, \lambda_2) = \frac{\Gamma(\lambda_1 + \lambda_2)}{\Gamma(\lambda_1) \Gamma(\lambda_2)} \zeta^{\lambda_1-1} (1 - \zeta)^{\lambda_2-1} \quad (5.66)$$

where $0 < \zeta < 1$, $0 < \lambda_1, \lambda_2$, which are both shape parameters, and $\zeta = c/c_{max}$ is the normalized diffusing scalar.

The cumulative distribution is given by,

$$F_{p,B}(\zeta; \lambda_1, \lambda_2) = \frac{\Gamma(\lambda_1 + \lambda_2)}{\Gamma(\lambda_1) \Gamma(\lambda_2)} \int_0^\zeta \zeta^{\lambda_1-1} (1 - \zeta)^{\lambda_2-1} d\zeta \quad (5.67)$$

which is called the incomplete beta function. A numerical routine for this function is given by Press et al. (1988).

The Beta distribution works well for mixing processes, but for dispersion models c_{max} must be chosen arbitrarily. A good choice is the maximum observed concentration at the receptor location or the source concentration. The maximum concentration at the receptor is generally not a known parameter therefore is not a desirable selection for engineering predictions. The source concentration is generally known, but, because the dilutions are quite large, this normalization causes the Beta function to make an impossible fit.

5.2 Probability Distribution Truncation

An important step commonly overlooked in the PDF presentation of sampled data sets in the literature is the proper normalization of theoretical PDF curves when the entire random variable domain is not sampled. When long time-averages are not used to adequately sample all the statistics of a PDF, i.e. from 0 to ∞ , the theoretical PDF curve must be renormalized to account for this sample truncation. This is easily done by simply dividing the PDF function by the cumulative estimate at the highest observed statistic, or dividing the CDF by the cumulative estimate.

The theoretical PDF is given by,

$$\int_0^{\infty} f_{p,\infty}(c) dc = 1.0 \quad (5.68)$$

For a truncated range $c_{\min} < c < c_{\max}$ (where c_{\min} may be the threshold value or zero),

$$\int_0^{c_{\min}} f_{p,\infty}(c) dc + \int_{c_{\min}}^{c_{\max}} f_{p,\infty}(c) dc + \int_{c_{\max}}^{\infty} f_{p,\infty}(c) dc = 1.0 \quad (5.69)$$

Then rearranging,

$$\int_{c_{\min}}^{c_{\max}} f_{p,\infty}(c) dc = 1.0 - \int_0^{c_{\min}} f_{p,\infty}(c) dc - \int_{c_{\max}}^{\infty} f_{p,\infty}(c) dc \quad (5.70)$$

Since both integrals on the right hand side are positive real valued numbers less than unity,

$$\int_{c_{\min}}^{c_{\max}} f_{p,\infty}(c) dc = R; \quad R \leq 1 \quad (5.71)$$

The cumulative distribution is given by,

$$\Pr \{ \zeta < c \} = F_{p,\infty}(c) = \int_0^c f_{p,\infty}(c) dc \quad (5.72)$$

Therefore, for a truncated range of $c_{\min} < c < c_{\max}$,

$$\begin{aligned} \int_{c_{\min}}^{c_{\max}} f_{p,\infty}(c) dc &= \int_0^{\infty} f_{p,\infty}(c) dc - \int_0^{c_{\min}} f_{p,\infty}(c) dc - \int_{c_{\max}}^{\infty} f_{p,\infty}(c) dc \\ &= \int_0^{c_{\max}} f_{p,\infty}(c) dc - \int_0^{c_{\min}} f_{p,\infty}(c) dc \\ &= F_{p,\infty}(c_{\max}) - F_{p,\infty}(c_{\min}) \end{aligned} \quad (5.73)$$

This is a more convenient form since the cumulative distribution is known explicitly. Then,

$$R = F_{p,\infty}(c_{\max}) - F_{p,\infty}(c_{\min}) \quad (5.74)$$

The truncated PDF, $f_{p,t}(c)$, can be normalized so that the area will equal unity under the curve. This will ensure that the theoretical range equals the data range.

$$\frac{1}{R} \int_{c_{\min}}^{c_{\max}} f_{p,\infty}(c) dc = 1.0 \quad (5.75)$$

or

$$f_{p,t}(c) dc = \frac{1}{R} f_{p,\infty}(c) dc \quad (5.76)$$

The truncated CDF is given by,

$$F_{p,t}(c) = \frac{1}{R} (F_{p,\infty}(c) - F_{p,\infty}(c_{\min})) \quad (5.77)$$

and the truncated CCDF is given by,

$$F'_{p,t}(c) = \frac{1}{R} (F'_{p,\infty}(c) - F'_{p,\infty}(c_{\max})) \quad (5.78)$$

These corrections are applied, in the present study, using the observed values of c_{\max} and c_{\min} (the intermittency threshold).

In the present study the additive errors to $F_{p,t}(c)$ and $F'_{p,t}(c)$ are negligible when truncating for the possible data range of $0 < c < c_{\text{source}}$ instead of $0 < c < c_{\infty}$. This is because the plume tracer dilutes quickly such that $c < c_{\max} \ll c_{\text{source}}$ and the probability in the range $c_{\text{source}} < c < c_{\infty}$ is very small. However, the additive errors are not small when correcting the CCDF, $F'_{p,t}(c)$, for $c_{\max} < c < c_{\infty}$ because there is a significant fraction in the range $c_{\max} < c < c_{\text{source}}$ which can be seen in Figure 5.3. It is clear from the figure that the truncation correction will have an effect on which probability model might be selected.

If the theoretical PDF, is greater than the observed PDF data, for upper extreme values of concentration, it will be truncated appropriately using the method described. Because long time averages are used in the present study, the theoretical PDF in this case, is a *possible* representation of the data for extreme values, which may not have been sampled long enough. Conversely, if the theoretical PDF falls below the observed data in the upper extreme values, the PDF is an unlikely representation of the data, because observed data predicts a greater probability.

The domain of the PDF model is from 0 to ∞ , however the possible concentrations that may be observed can only range from 0 to c_{source} . The upper limit of c_{source} will be

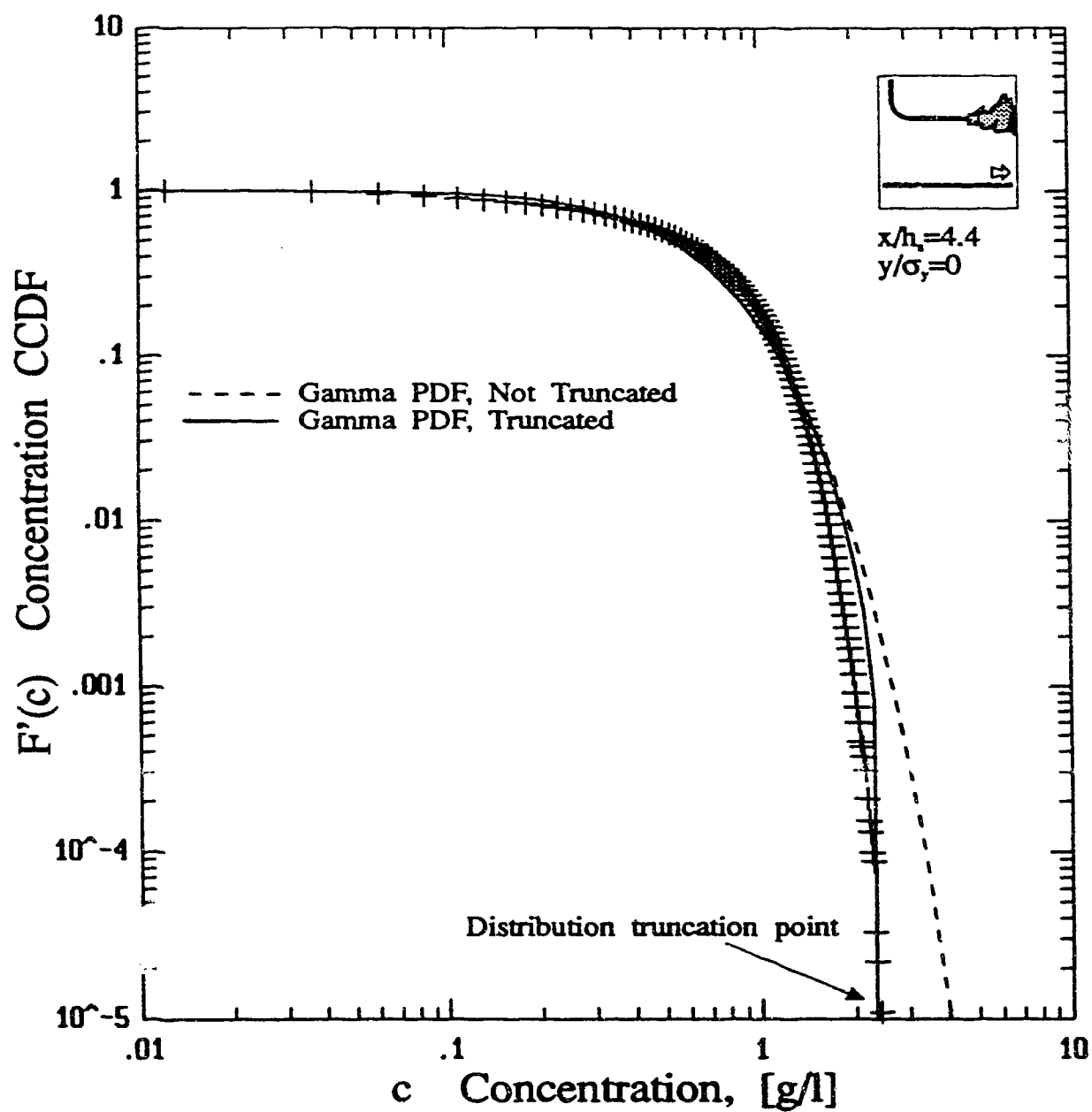


Figure 5.3: Effect of PDF truncation on the theoretical fit of a PDF model to a data set.

reduced significantly if molecular effects are considered. The theoretical PDF models should be truncated, if not to correct for the reduced range of the observed data set, then because of the possible range of the data being modelled. It is probably better to renormalize the truncated distribution to unity area rather than clipping the distribution and using a dirac delta function, as is done in the clipped-Normal distribution at zero concentration.

The Beta distribution model is a normalized model which naturally has a finite range from 0 to 1. From this standpoint the Beta model is a realistic model for the concentration PDF.

The truncation of the theoretical probability distributions requires that the parameters of the distributions be fit to the truncated distribution. For the present study, the long time averages sample much of the entire range of data. Therefore, the correction to the PDF is small, and is unlikely to change PDF model parameters significantly. The theoretical PDF distributions presented in this study have been fit to the truncated data. The PDF model parameters thus determined, are then truncated and displayed in the figures.

5.3 PDF Parameter Estimation

There are many different procedures for estimating the parameters of a PDF model. The two most popular are the maximum likelihood method and the moment estimator method. The maximum likelihood principle determines a PDF's parameters such that the PDF's likelihood function is maximized. The maximum likelihood estimation minimizes the difference between the observed probability distribution and the modelled distribution. Press et al. (1988) have a good description of the background to this theory. It may be compared to the least squares procedure, which is a special case of the maximum likelihood estimation using a Normal distribution. This procedure generally requires numerical solutions for finding the estimators. However, for most of the popular PDF models, maximum likelihood parameters can be expressed explicitly in terms of statistics which are easily determined from a data set. The moment estimator procedure is straight forward, solving the parameters for the PDF using the moment equations. This procedure however, often generates biased results, (Jakeman, Simpson, and Taylor 1986), or inefficient estimators, (Bury 1986).

Jakeman, Simpson, and Taylor (1986) investigate several of the popular PDF models and specifically examine the biasedness of the maximum likelihood method and the moment estimator method for each PDF model. Jakeman, Simpson, and

Table 5.1: Maximum Likelihood Estimates of Statistical Parameters

Distribution	Expression
log-Normal	$\mu = \frac{1}{N} \sum_{i=1}^N \ln(c_i)$ $\sigma^2 = \frac{1}{N} \sum_{i=1}^N (\ln(c_i) - \mu)^2$
Exponential	$\mu = \bar{c} = \frac{1}{N} \sum_{i=1}^N c_i$
Gamma	Numerical solution for λ of $\ln \lambda - \frac{d \ln \Gamma(\lambda)}{d\lambda} = \ln \bar{c} - \frac{1}{N} \sum_{i=1}^N \ln c_i$ then $\sigma = \lambda / \bar{c}$
Weibull	Numerical solution for λ of $\frac{N}{\lambda} - \frac{N \sum c_i^\lambda \ln c_i}{\sum c_i^\lambda} + \sum \ln c_i = 0$ then $\sigma = (\frac{1}{N} \sum c_i^\lambda)^{1/\lambda}$

Taylor (1986) and Bury (1986) give the maximum likelihood estimates of statistical parameters in Table 5.1.

In Figure 5.4, a selected data set is plotted and fit using the maximum likelihood method and the moment estimator method. The figures shows that different conclusions may be drawn from the fit results depending on the parameter fit method. One method does not provide a consistently better fit.

It may be concluded that although, in general, the maximum likelihood estimator method is more efficient at determining the parameters, Bury (1986) and Jakeman, Simpson, and Taylor (1986), the resulting fits may be no more or less better fitting by eye than the moment estimator method. In particular, the gamma function has purportedly poor efficiency when using the moment estimator method, however it provides no worse fit to the data.

In addition, models exist for the higher order moments of the concentration across a plume. If the maximum likelihood estimators are to be used for engineering predictive and hazard assessment purposes, a model for the specific PDF parameters must be developed. This would seem unlikely given the current state of knowledge about the dispersion process.

5.4 Concentration Probability Distributions

Given a probability distribution and a number of expected, or theoretical distributions to compare, a method must be found which will determine the best

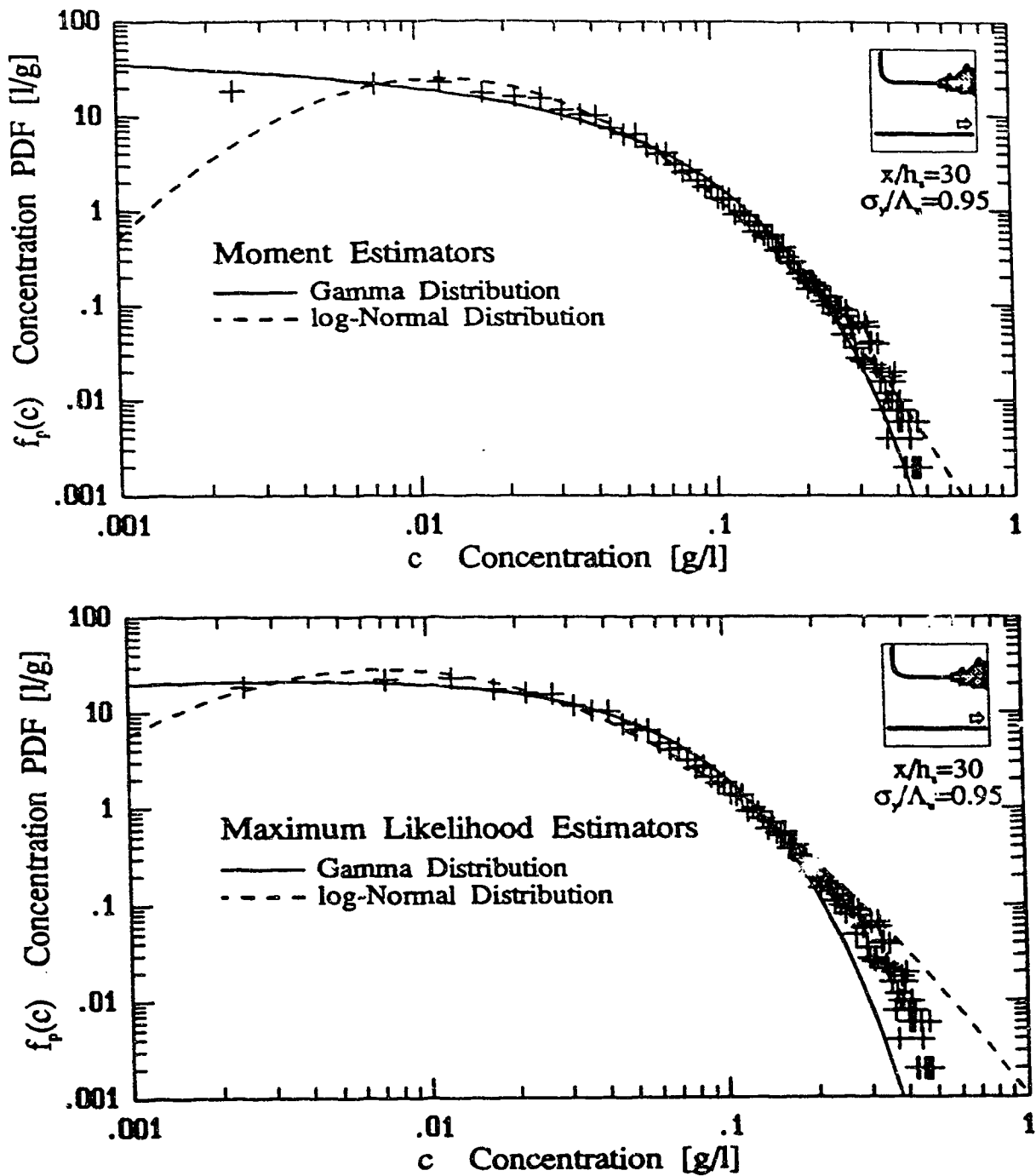


Figure 5.4: Comparison of PDF fit by the maximum likelihood procedure (a) and the moment estimator procedure (b), showing that different conclusions may be drawn about which PDF model better fits the data.

fit to the observed distribution. Therefore the question that must be answered is, given two distributions, are the two data sets drawn from the same distribution function or from different distribution functions? Statistically it is not possible to prove that the distributions are from the same distribution function. However, it is possible to disprove, to a certain level of significance, the null hypothesis that the two distributions are drawn from the same population distribution function, Press et al.(1988). The most common test is the chi-squared test, χ^2 , which compares the fractional squared difference between the distributions,

$$\chi^2 = \sum_{i=1}^N \frac{(\text{Pr}_{oi} - \text{Pr}_{ei})^2 \cdot n}{\text{Pr}_{ei}} \quad (5.79)$$

where:

Pr_{oi}	observed proportion of data falling in the i^{th} bin
Pr_{ei}	expected proportion of data falling in the i^{th} bin
n	total number of observations
N	total number of bins

Two other goodness of fit tests, Holland and Fitz-Simmons (1982), are the absolute deviation, AD,

$$\text{AD} = \sum_{i=1}^N \left| \text{Pr}_{oi} - \text{Pr}_{ei} \right| \cdot n \quad (5.80)$$

and the weighted absolute deviation, WAD,

$$\text{WAD} = \sum_{i=1}^N \left| \text{Pr}_{oi} - \text{Pr}_{ei} \right| \cdot n \cdot \text{Pr}_{ei} \quad (5.81)$$

The AD places less emphasis on large deviations between the expected and observed distributions than does the χ^2 statistic. The WAD statistic emphasizes the fit in the central area of the distribution. The log-maximum likelihood statistic is also used but in the fits produced here, the parameters were estimated using the moment estimator method. Therefore the log-maximum likelihood statistics are not necessarily minimum variance, unbiased estimates. When fitting the distribution parameters using maximum likelihood estimators, it would be consistent to test the goodness of fit using the log-maximum likelihood statistic.

An alternative to these procedures is a visual comparison, the so called 'chi-by-eye' method, Press et al.(1988), where the fit statistics are ignored and the best fit by eye is selected. Because it is possible to select by eye the function which best represents the physics, the 'chi-by-eye' method is favoured.

Table 5.2: Comparison of Goodness of Fit Results for Various Methods for a Single Selected Probability Distribution

Goodness of Fit Test ^a	log-Normal	Gamma	clipped-Normal
Absolute Deviation	77.5	58.0*	74.2
Weighted Absolute deviation	850.8	439.7	221.3*
χ^2 Statistic	77.5	58.2*	74.2
χ^2 Probability	0.9545	0.9997*	0.9753
Log Likelihood Statistic	255.5*	-81.7	-27.1

^athe symbol * indicates the best-fit distribution

A comparison of methods is shown in Table 5.2 for a typical probability distribution, which is also shown in Figure 5.5. The '*' indicates the best ranking of the selected probability distributions. Relative magnitudes between the distributions indicate the best fit. The different tests do not agree and the best fit by representation of the data, the log-Normal function, is confirmed only by the log likelihood goodness of fit test results. In this example, the CDF and CCDF may be used to show that the Gamma function is also a good representational fit to data, and that the goodness of fit tests, by majority, predict the correct function. However, in most cases, the results of the goodness of fit tests cannot be taken for granted without inspection. The chi-by-eye method therefore becomes more reliable, but a little less scientific.

Figure 5.6 is another example comparing the goodness of fit test results. For this source and location in the flow, the clipped-Normal distribution best represents the data, and this selection is confirmed only by the weighted absolute deviation statistic.

In Figure 5.5 and Figure 5.6, and others like them, the Normal, Exponential, Beta and Weibull distributions do not represent a PDF shape, or character, that is not represented by the clipped-Normal, Gamma and log-Normal distributions. All the distributions were fit to the data but, to simplify the presentation of the observed distributions in this study, only the above three are shown on the figures in the remainder of this study.

5.4.1 Plume Centre-line Probability Distributions

Probability distributions observed on the centre-line of a developing plume are presented in Figure 5.7 to Figure 5.10. The PDFs are presented in two forms: non-normalized, and normalized with respect to the local conditional mean concentration, \bar{c}_p . The non-normalized figures give an indication of how much the probability

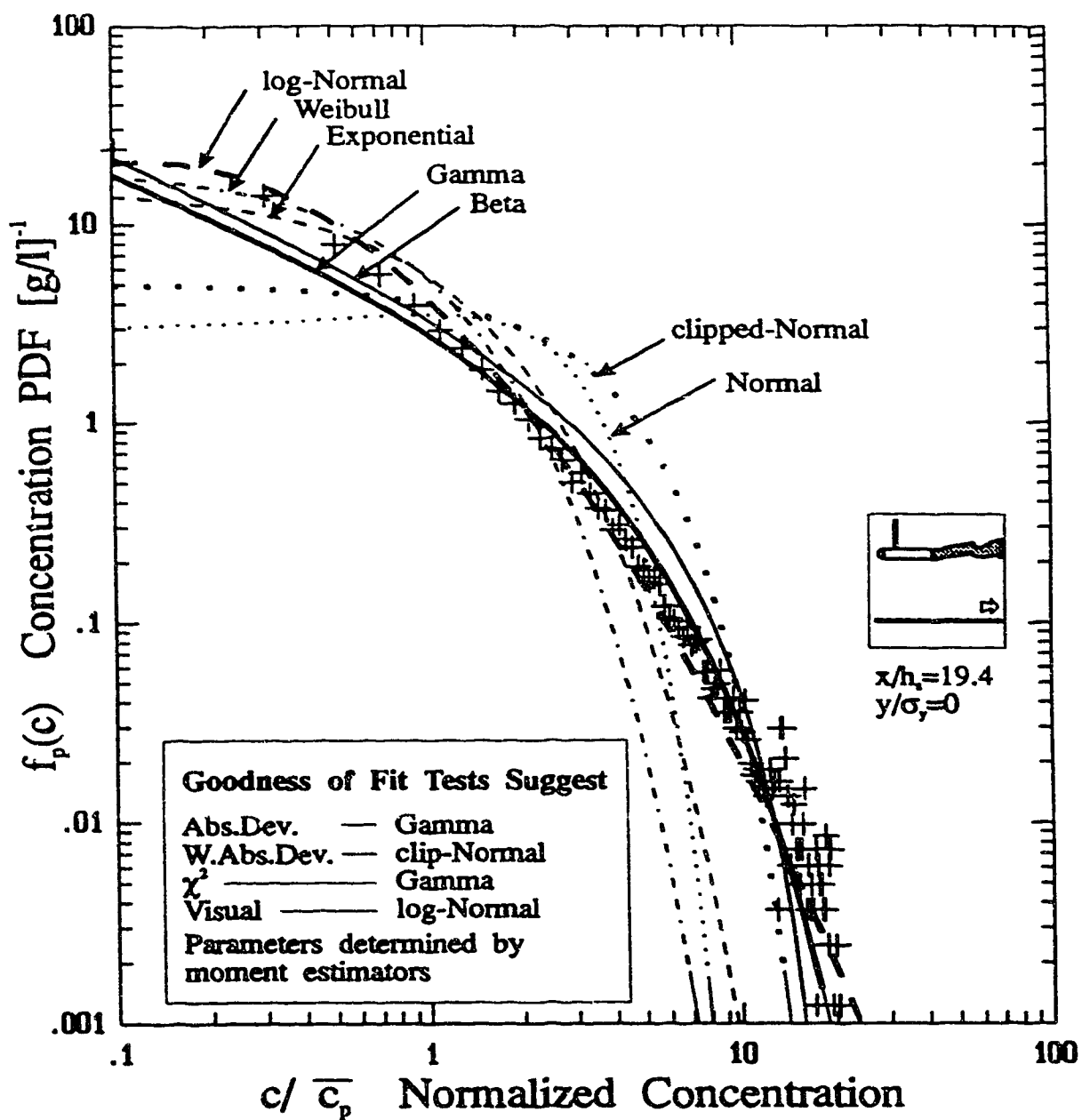


Figure 5.5: Example of goodness of fit test results on a typical observed probability distribution, far down-wind of the source.

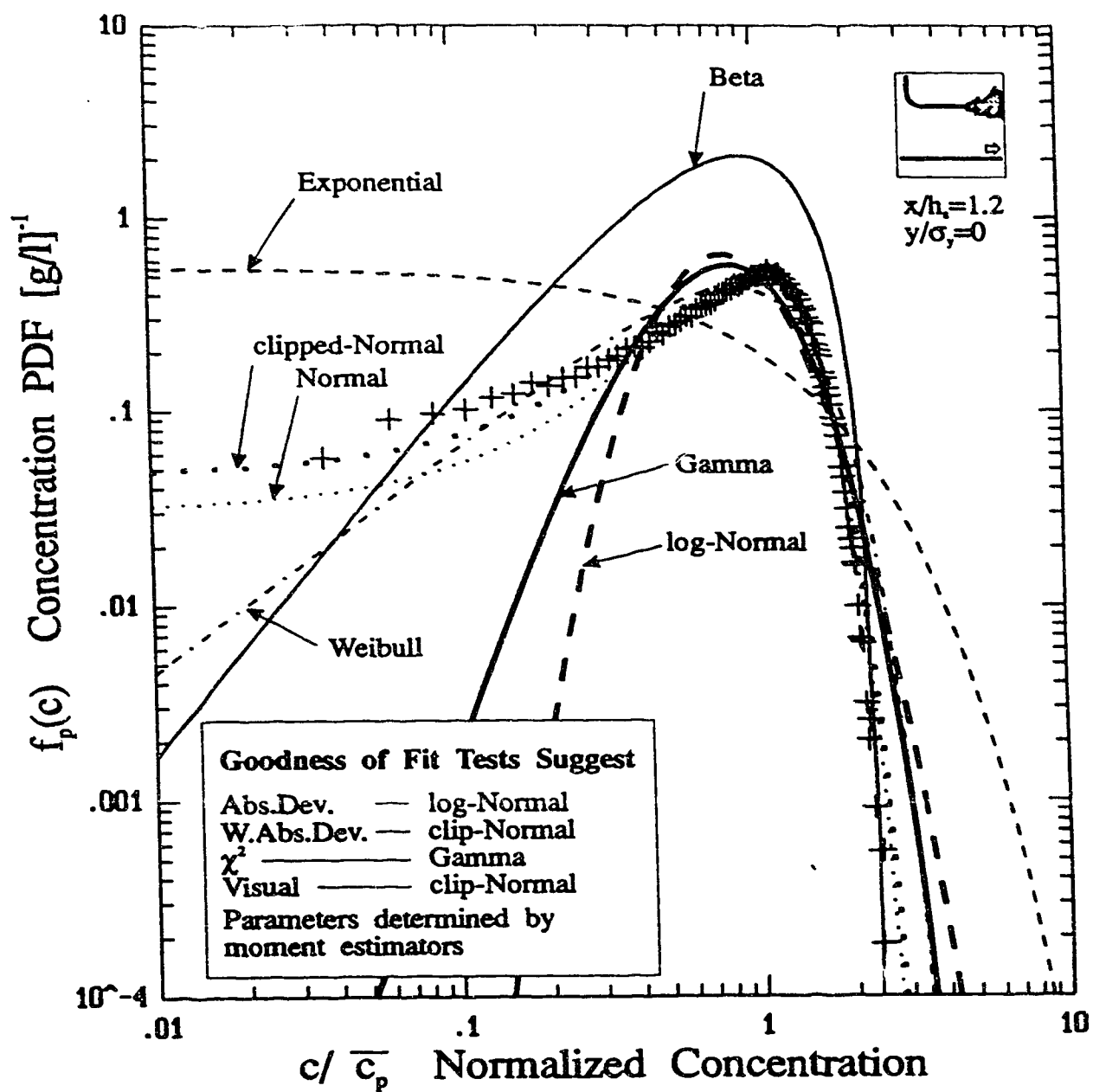


Figure 5.6: Example of goodness of fit test results on a typical observed probability distribution, near the source.

distribution is changing and a relative indication of the dilution that occurs for each source configuration. The normalized figures give an indication of the distribution of the concentration fluctuations relative to the conditional mean value. The fluctuation magnitude relative to the conditional mean is the important variable because it removes the effects of intermittency. What can be seen in Figure 5.7 to Figure 5.10 is that there is no single probability distribution shape that recurs for successive down-wind locations along the centre-line of the plume and that there exists some similarity of the PDFs for different source types.

These figures do not provide quantitative information about distribution fits. In Figure 5.11 to Figure 5.17 the moment estimator method is used to determine the parameters of the distributions shown. The theoretical distributions are renormalized according to the method described in section 5.2.

Close to the source, the probability distribution is not well described by any of the PDF distributions. The clipped-Normal distribution, however, represents the best alternative. For successive down-wind locations, the plume slowly evolves into a Gamma distribution (Figure 5.15), and then into a log-Normal distribution, (Figure 5.16). The transition from the clipped-Normal to a Gamma distribution is expected, Deardorff and Willis (1988). However, Deardorff and Willis speculate, that once a PDF has evolved into a Gamma distribution, further random mixing will simply generate another Gamma distribution. Based on the cross-wind homogeneous flow studied here, their conclusion does not appear correct. Further, the distributions vary across the width of the plume as well, (figures not shown). Therefore, the PDF on the centre-line of the plume is not necessarily the probability distribution in the fringes of the plume, especially near the source.

A more descriptive representation of the PDF fit results is presented in Figure 5.18 for each of the seven down-wind locations. PDF fits were also determined at cross-wind locations of $0.5\sigma_y$, $1.0\sigma_y$, $2.0\sigma_y$ and $3.0\sigma_y$. These fit results were used to create the general area maps for Figure 5.18. Is the evolution from clipped-Normal to Gamma to log-Normal result discovered here an artifact of the jet/plume source? To answer this, the results of the fits of the other sources must be considered. In Figure 5.19 to Figure 5.21, the results of the other sources are presented in the same manner as Figure 5.18.

An important observation from the figures is that the same evolution occurs for each of the sources, and that the transition points between types of distributions occur at *roughly* the same plume size, σ_y/Λ_u , locations. This means that knowing the plume size, and the distance off the plume centre-line, the probability distribution may be estimated. For the sources studied, the best fit distributions are determined by,

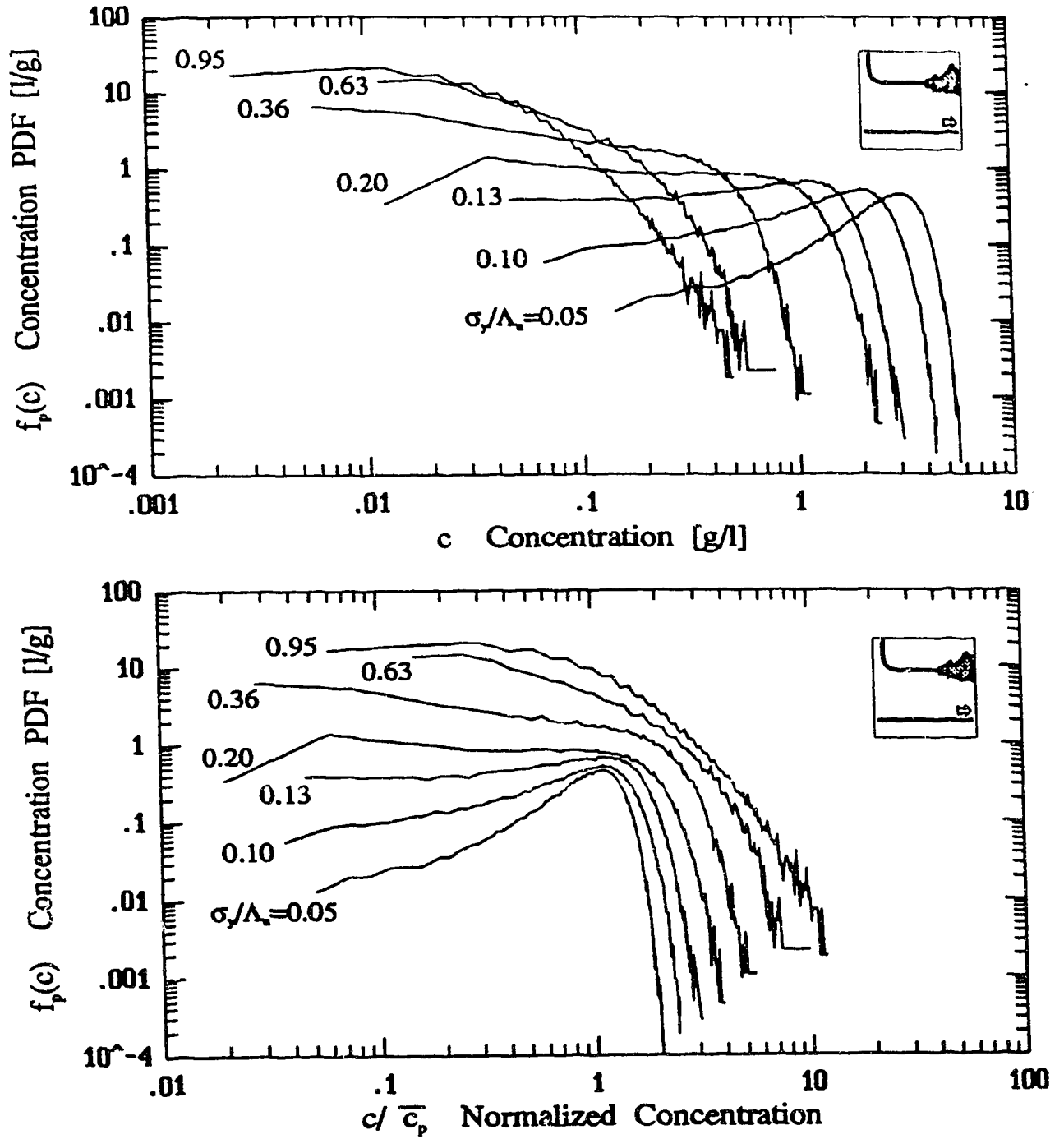


Figure 5.7: Evolution of the PDF on the centre-line of the jet/plume source. Data not normalized (top) and normalized by the conditional mean value (bottom).

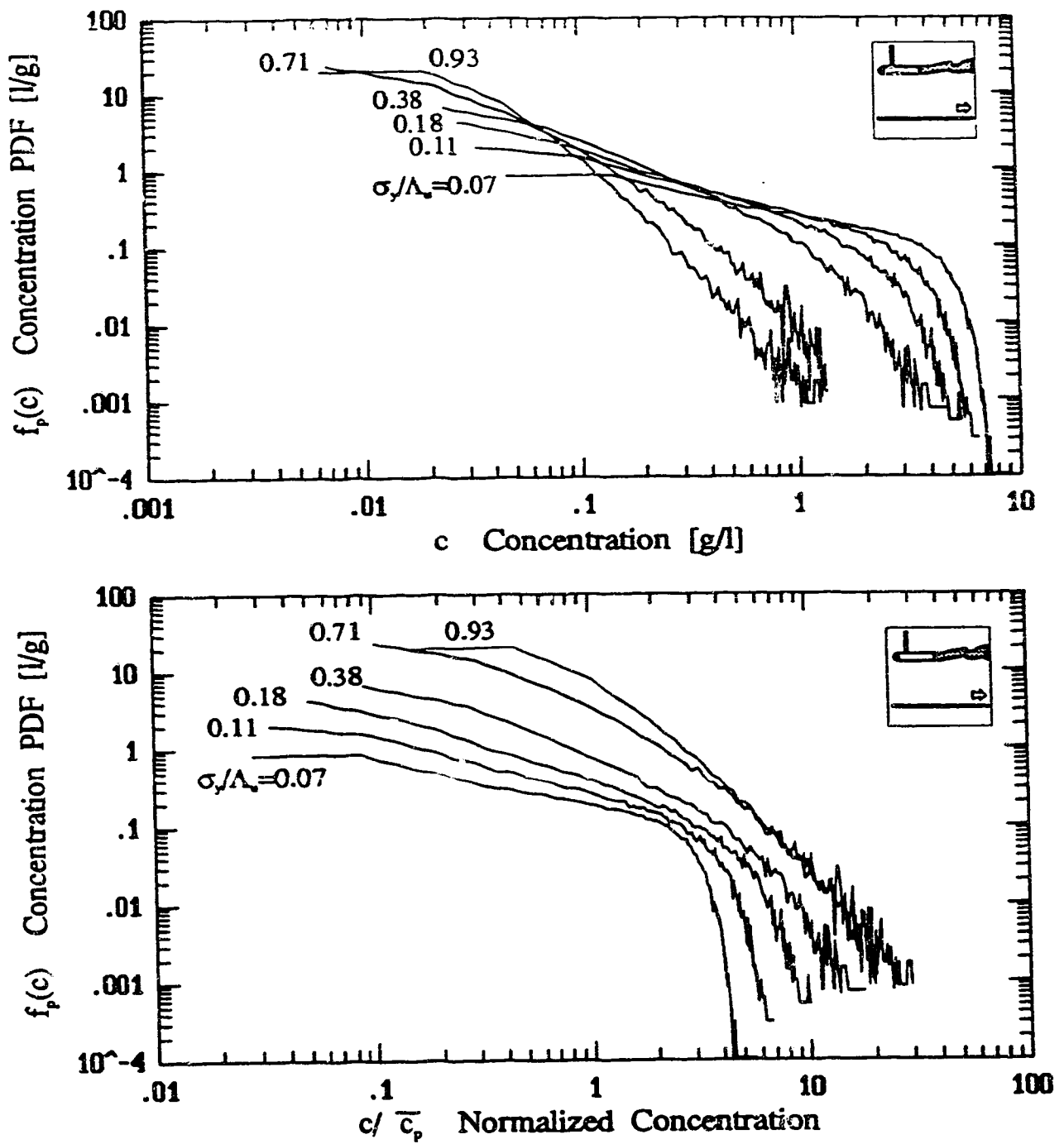


Figure 5.8: Evolution of the PDF on the centre-line of the iso-kinetic source. Data not normalized (top) and normalized by the conditional mean value (bottom).

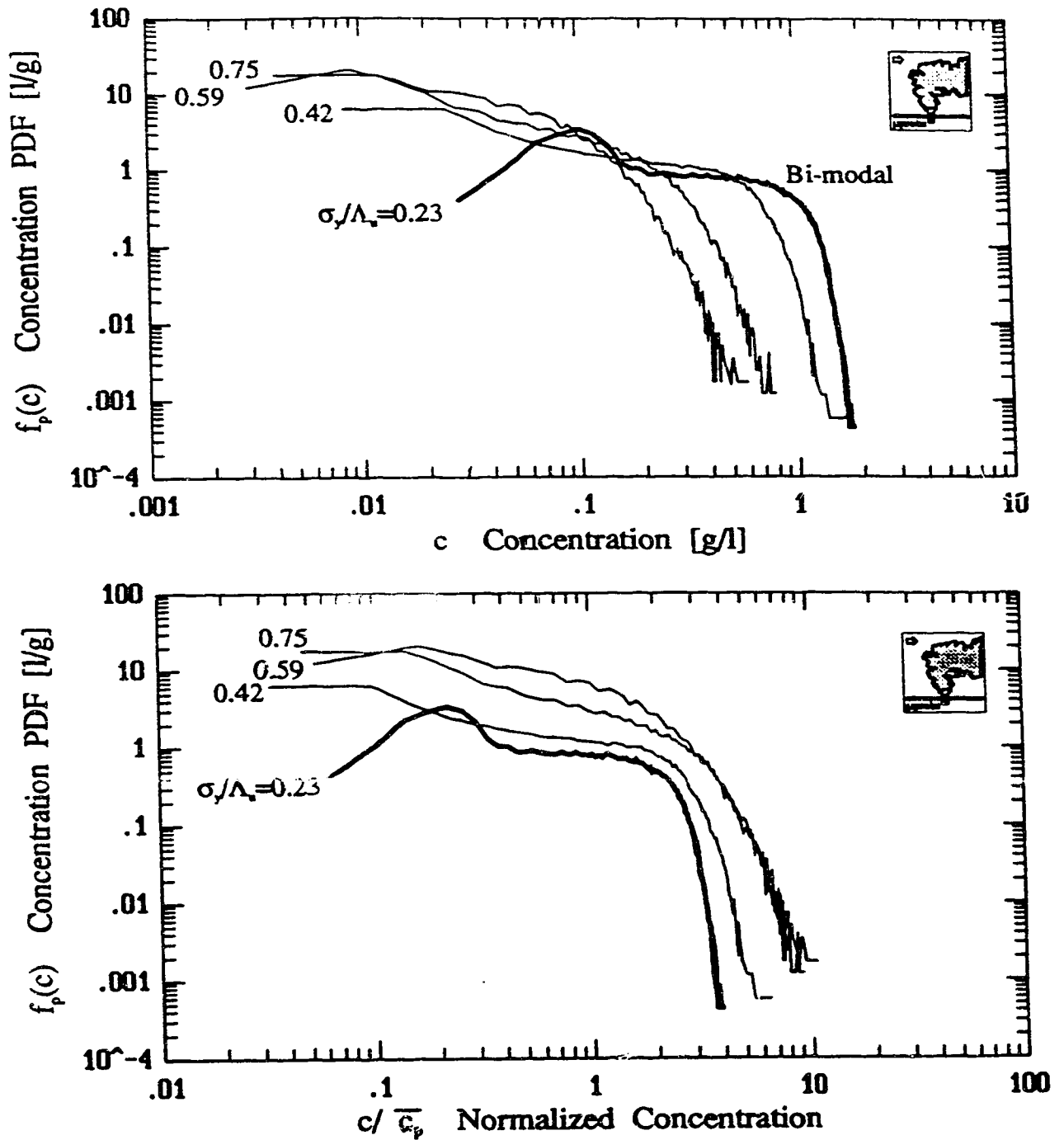


Figure 5.9: Evolution of the PDF on the centre-line of the vertical ground level source. Data not normalized (top) and normalized by the conditional mean value (bottom).

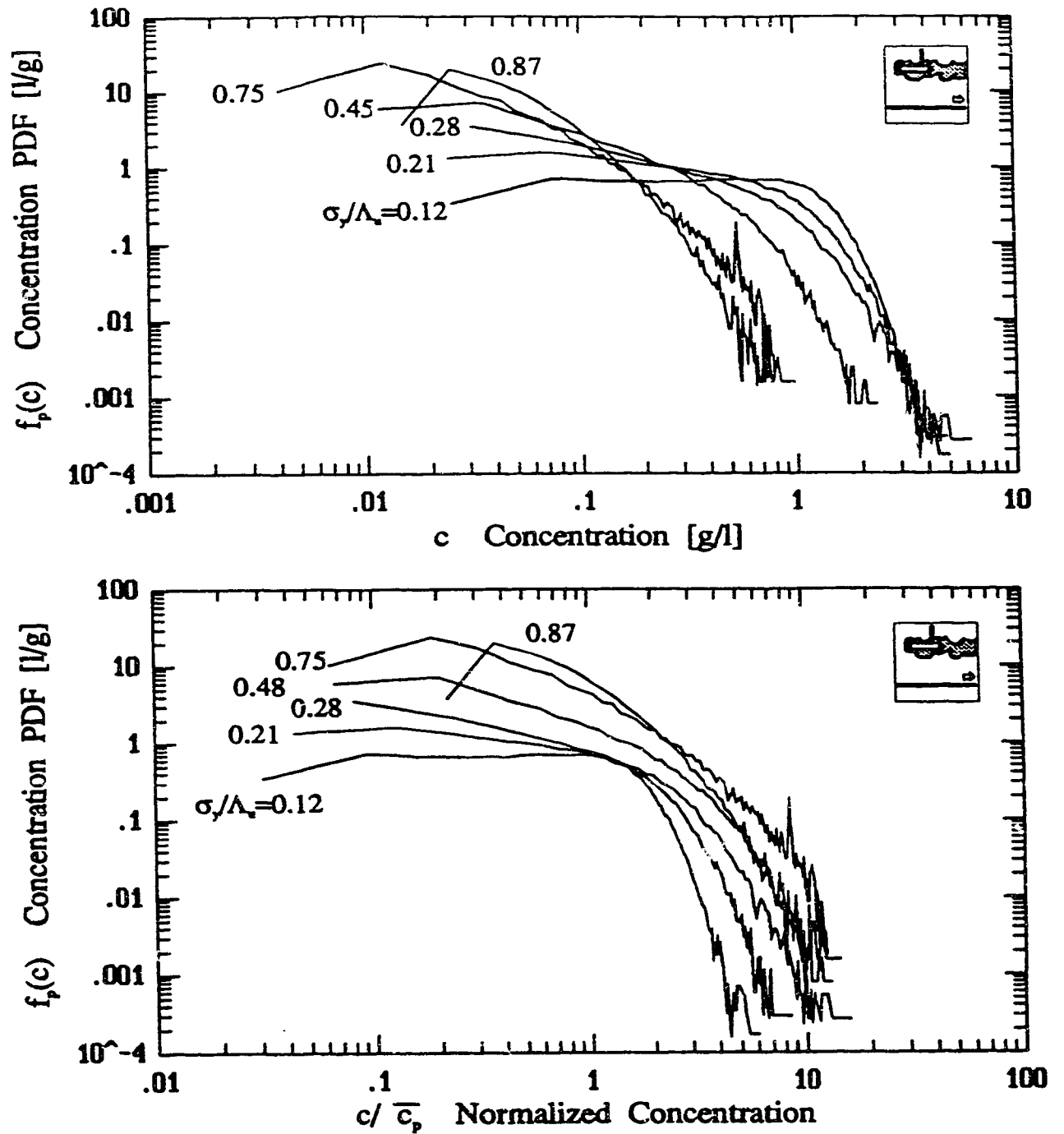


Figure 5.10: Evolution of the PDF on the centre-line of the up-stream facing iso-kinetic source. Data not normalized (top) and normalized by the conditional mean value (bottom).

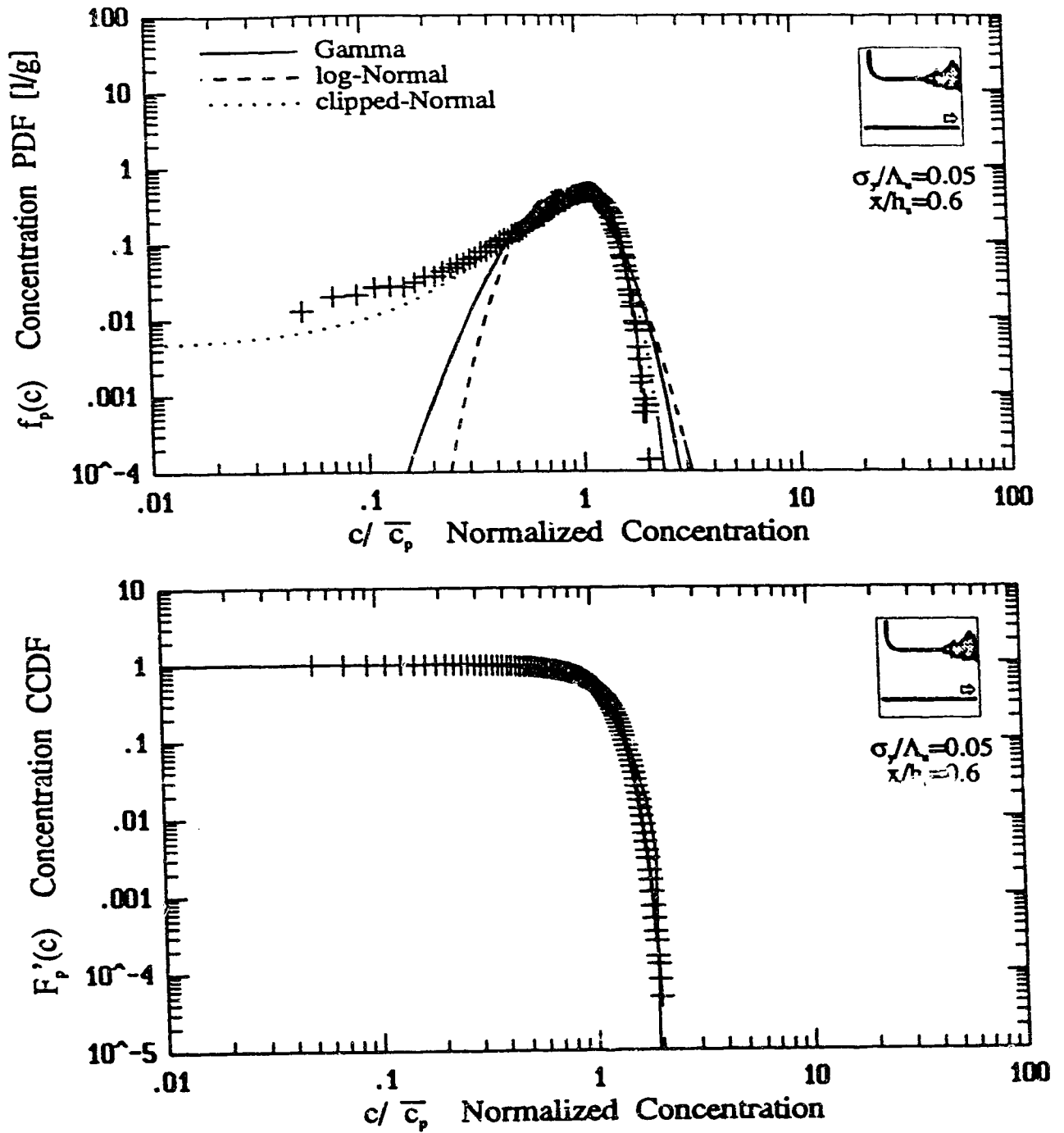


Figure 5.11: Truncated centre-line PDF (top) and truncated CCDF (bottom) of the jet/plume source at a location of $\sigma_y/\Lambda = 0.05$.

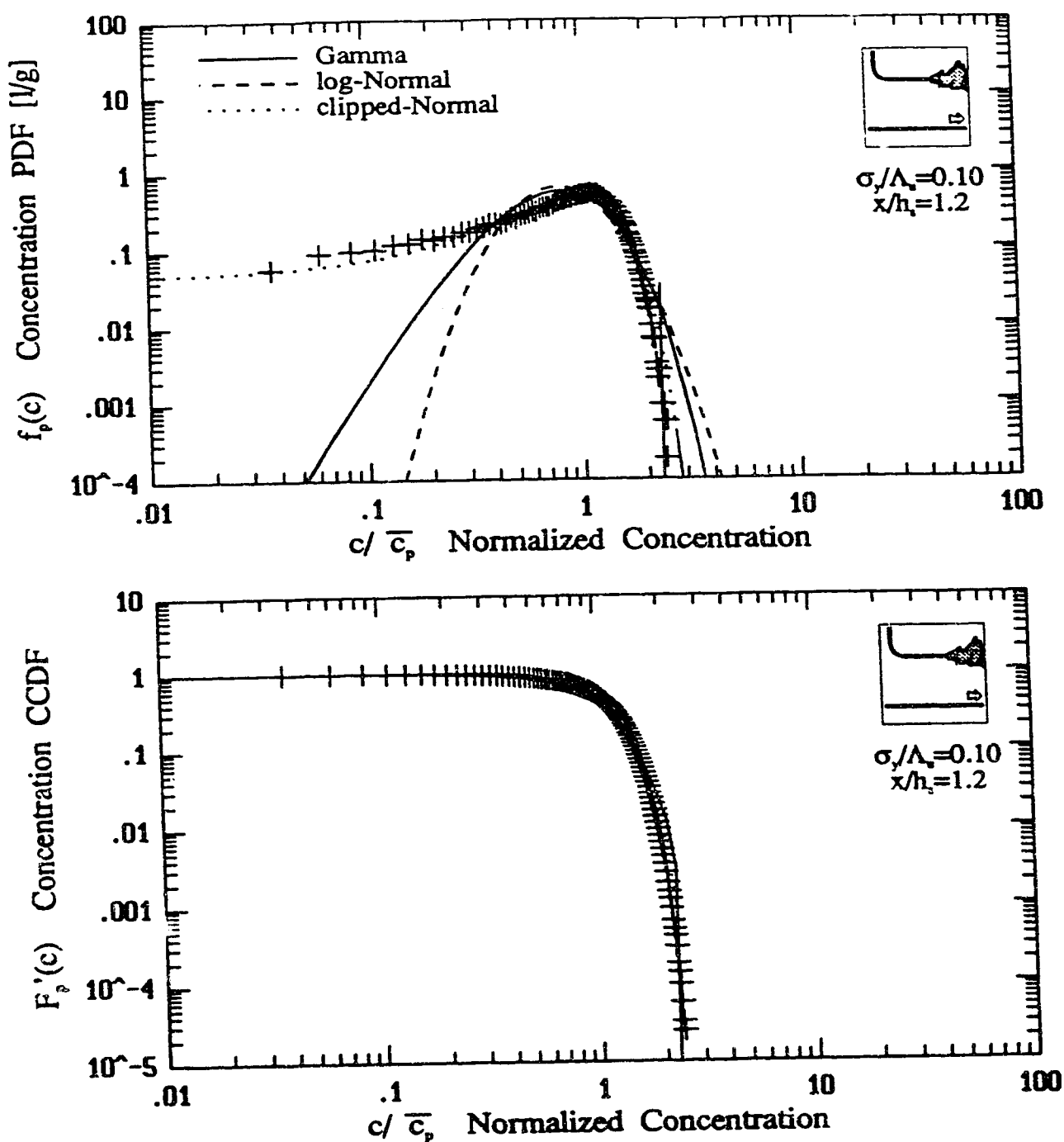


Figure 5.12: Truncated centre-line PDF (top) and truncated CCDF (bottom) of the jet/plume source at a location of $\sigma_y/\Lambda = 0.10$.

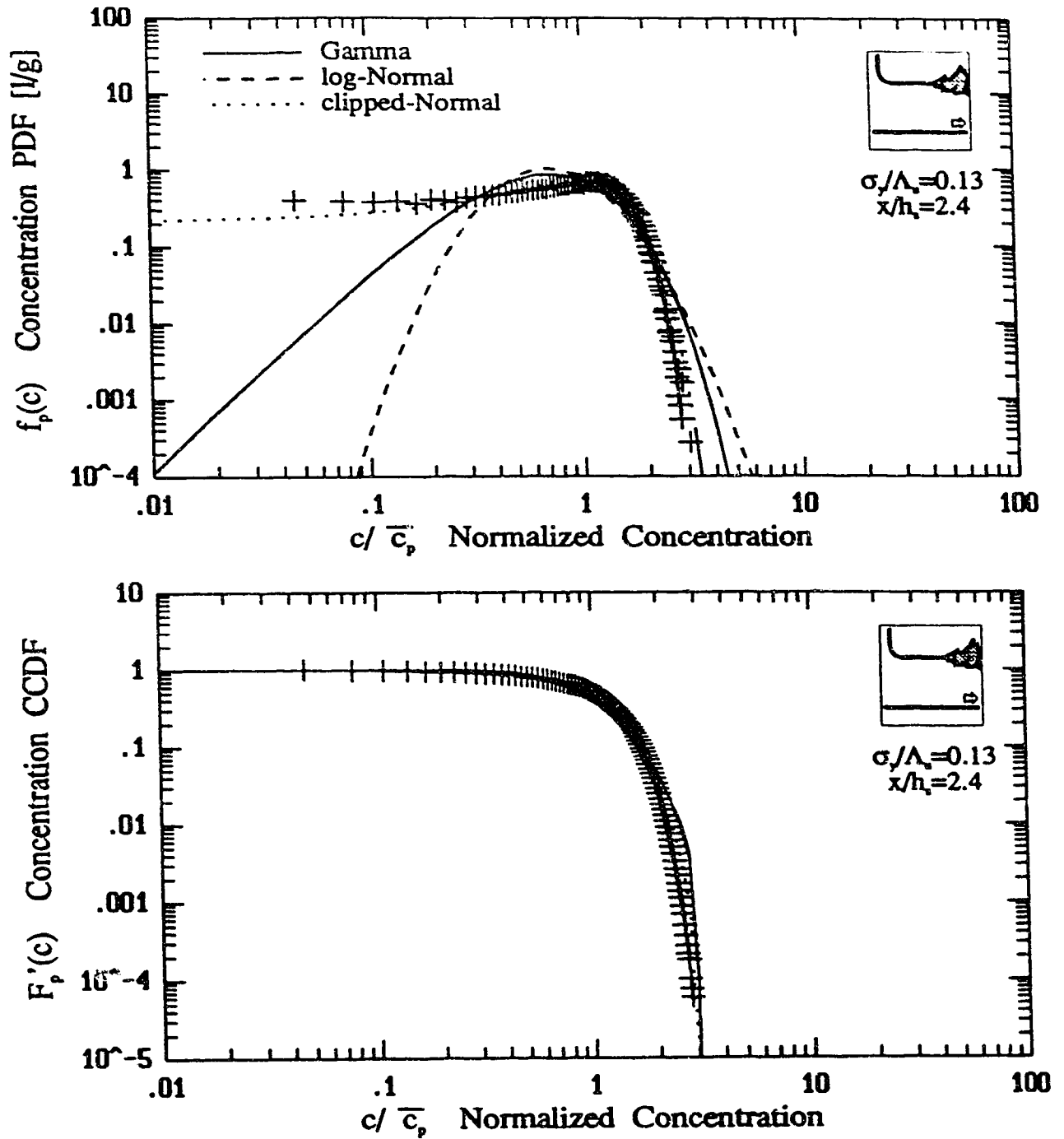


Figure 5.13: Truncated centre-line PDF (top) and truncated CCDF (bottom) of the jet/plume source at a location of $\sigma_v/\Lambda = 0.13$.

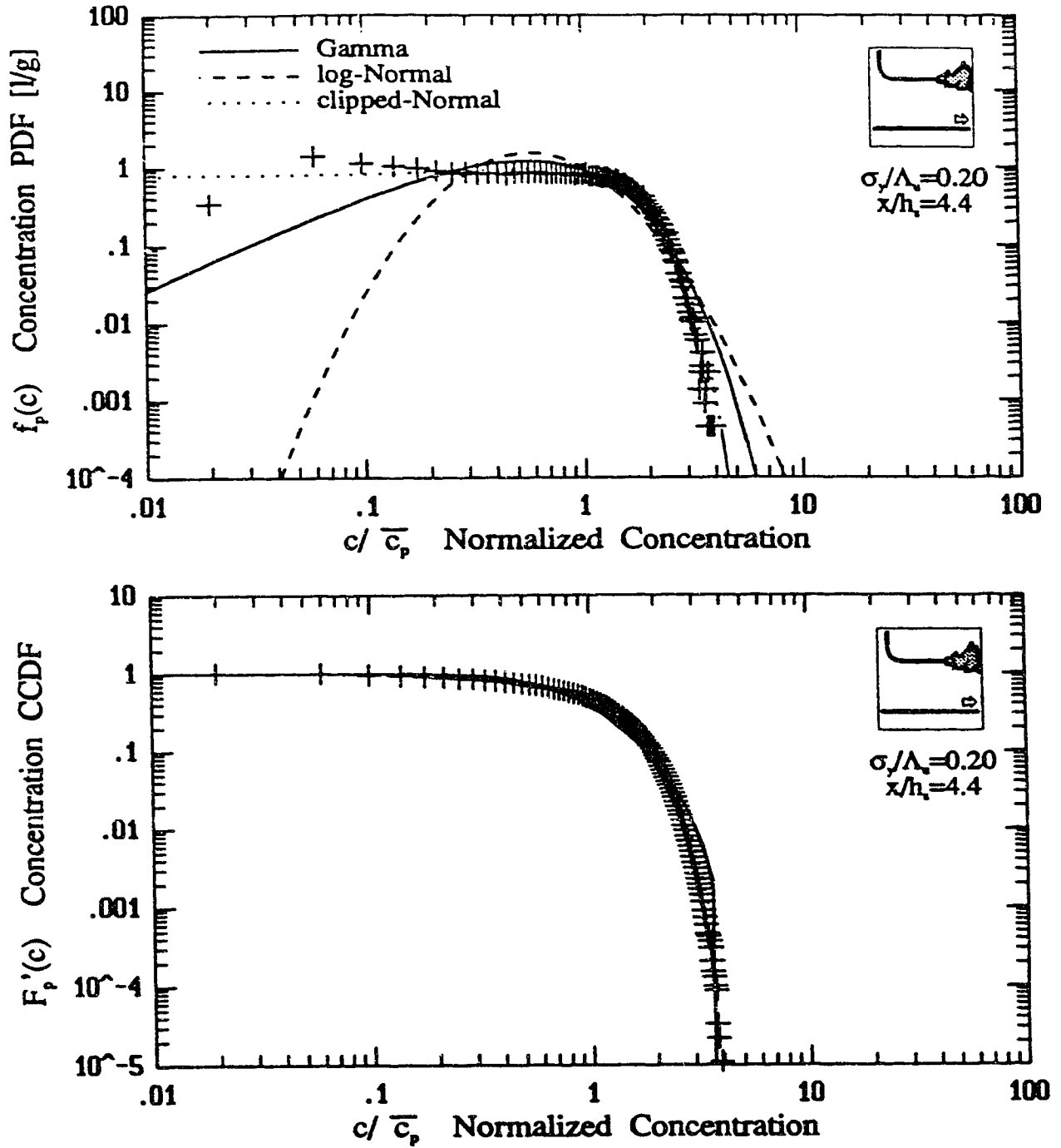


Figure 5.14: Truncated centre-line PDF (top) and truncated CCDF (bottom) of the jet/plume source at a location of $\sigma_v/\Lambda = 0.20$.

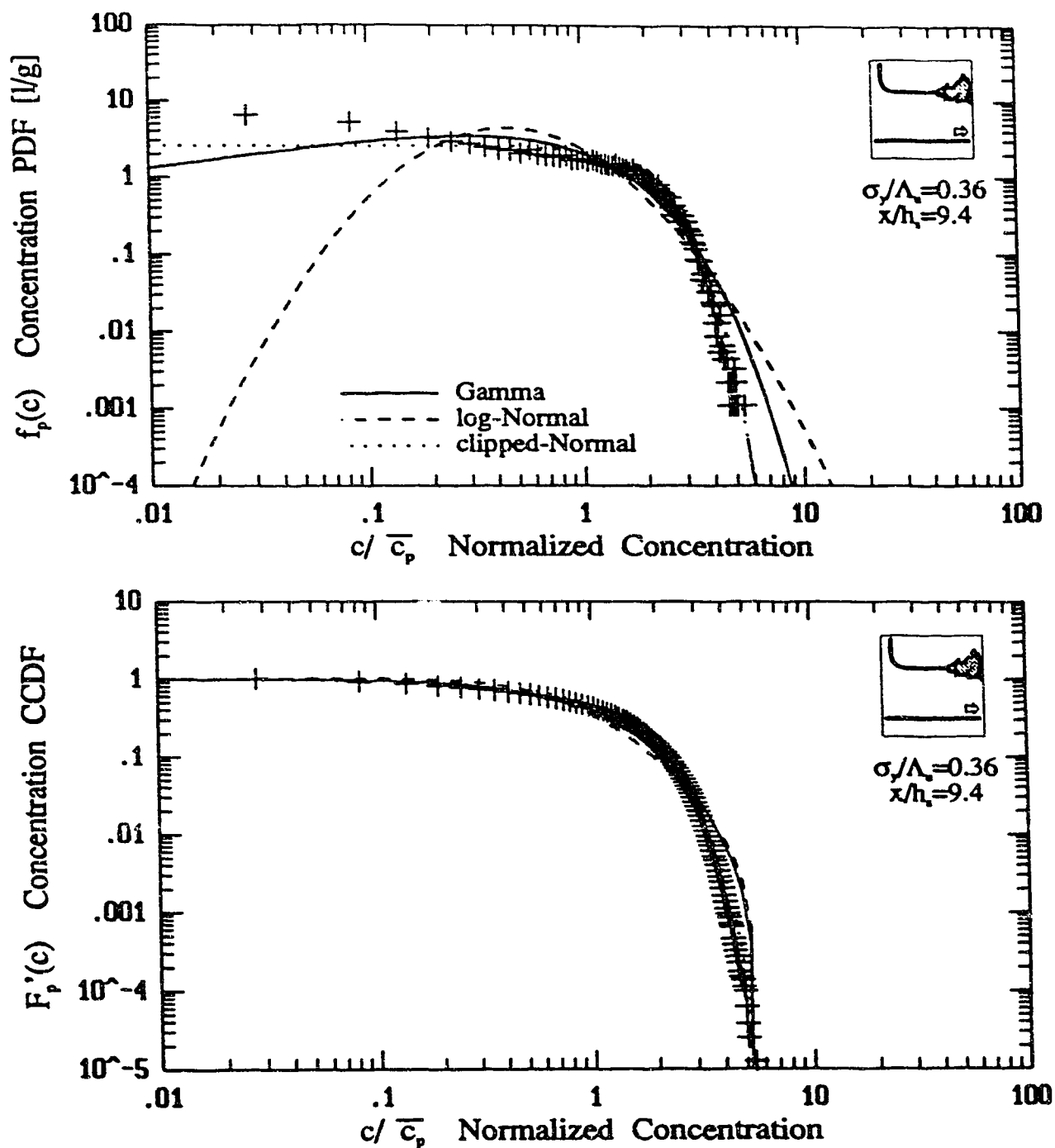


Figure 5.15: Truncated centre-line PDF (top) and truncated CCDF (bottom) of the jet/plume source at a location of $\sigma_y/\Lambda = 0.36$.

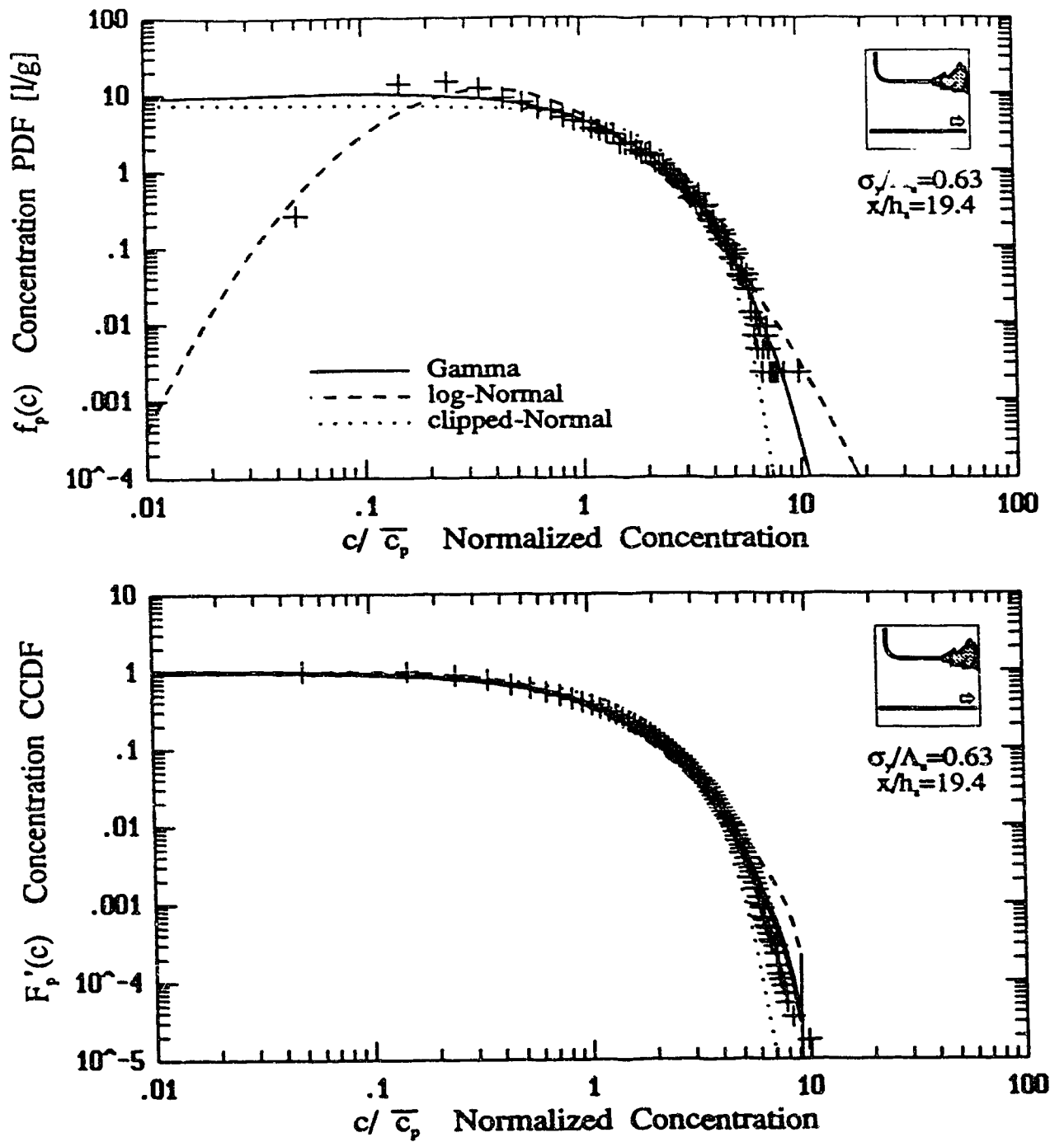


Figure 5.16: Truncated centre-line PDF (top) and truncated CCDF (bottom) of the jet/plume source at a location of $\sigma_y/\Lambda = 0.63$.

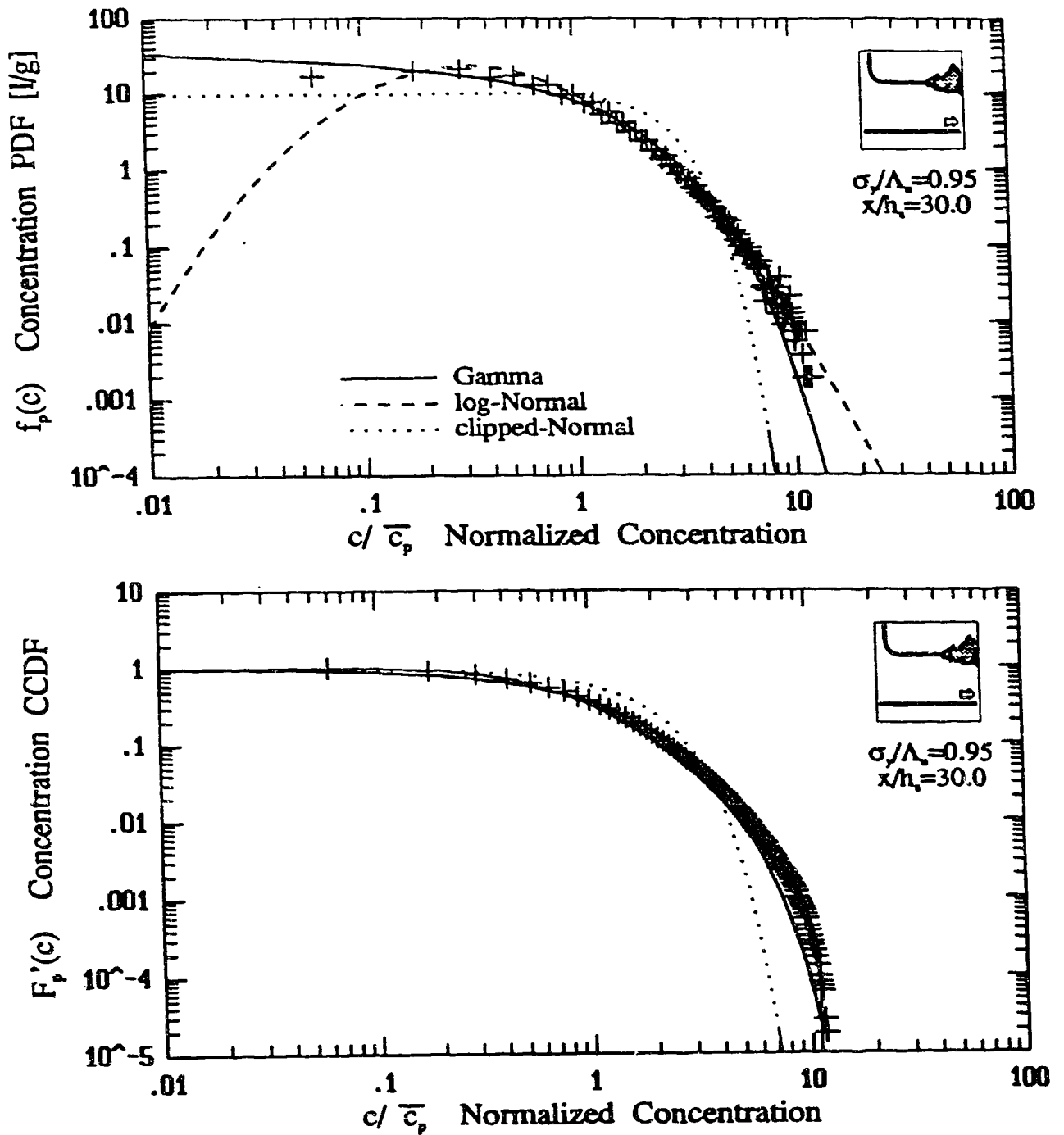


Figure 5.17: Truncated centre-line PDF (top) and truncated CCDF (bottom) of the jet/plume source at a location of $\sigma_v/\Lambda = 0.95$.

Jet/Plume Source (source 2)

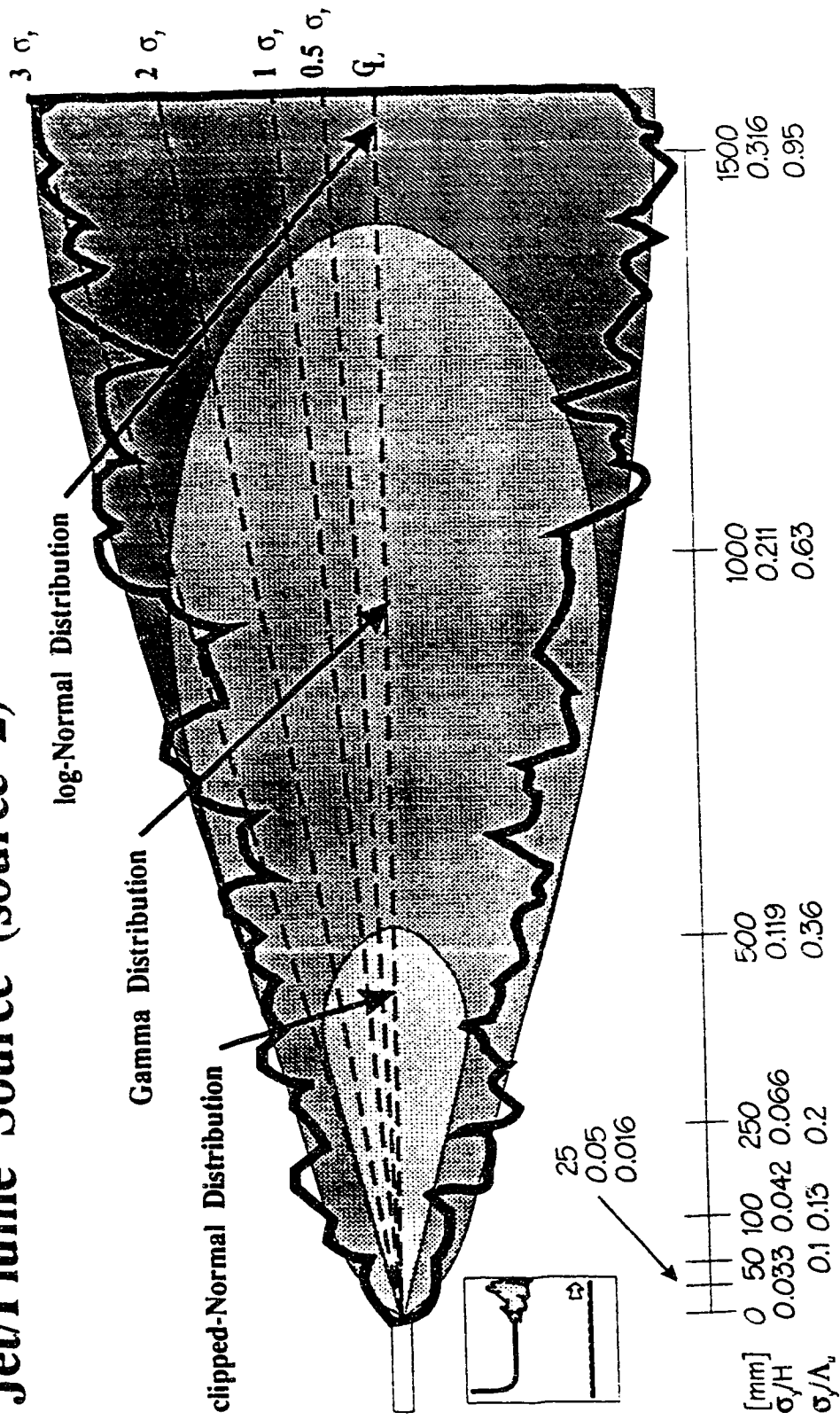


Figure 5.18: PDF fit results for the jet/plume source in the water channel boundary layer.

Iso-Kinetic Source -- Down Wind Facing (source 4)

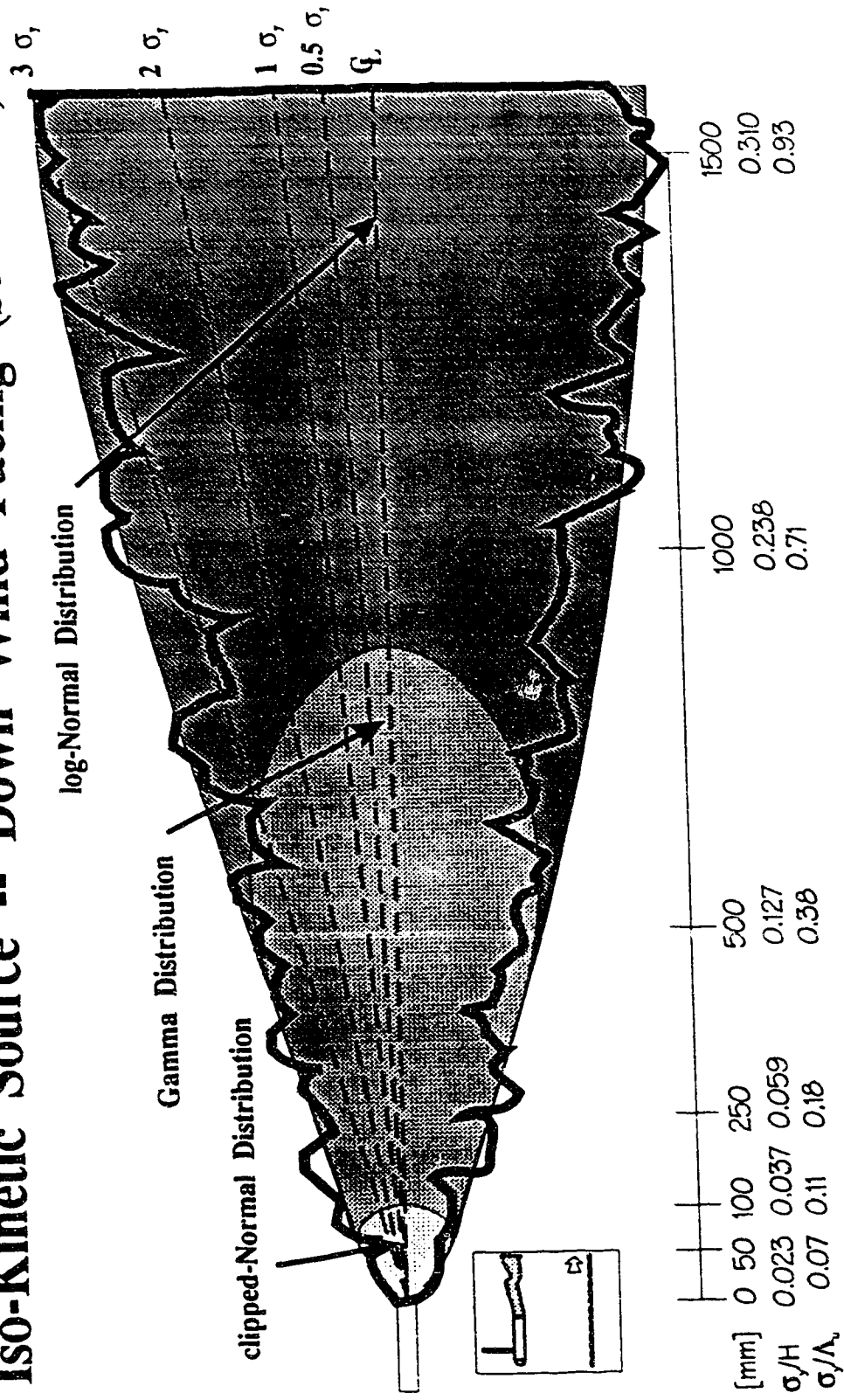


Figure 5.19: PDF fit results for the iso-kinetic source in the water channel boundary layer.

Vertical Jet Source (source 1)

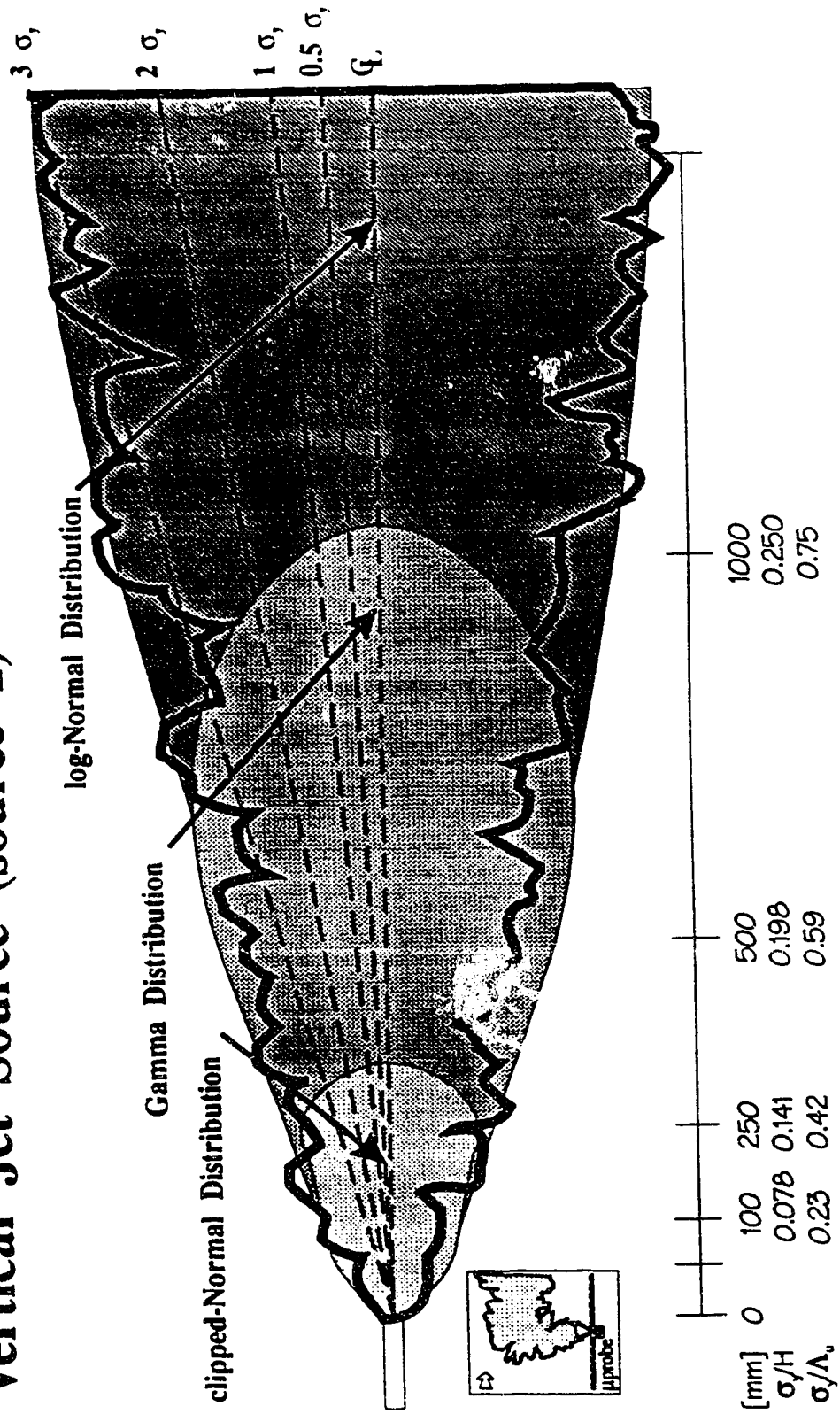


Figure 5.20: PDF fit results for the vertical jet source in the water channel boundary layer.

Iso-Kinetic Source -- Up Wind Facing (source 5)

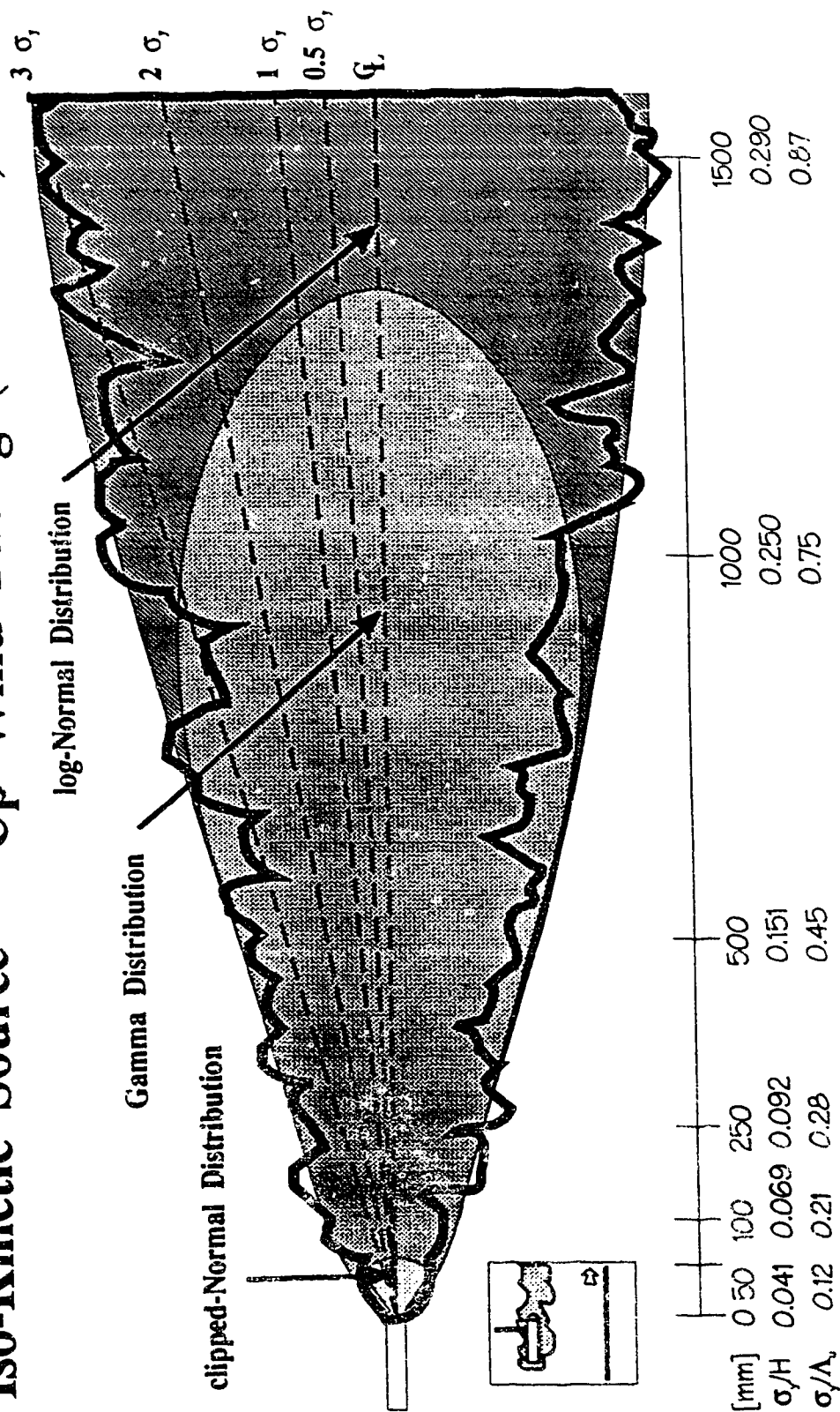


Figure 5.21: PDF fit results for the up-stream facing iso-kinetic source in the water channel boundary layer.

1. For small plume sizes. (approximately $\sigma_y/\Lambda_u < 0.2$). the conditional concentration PDF is near clipped-Normal distributed.
2. For large plume sizes. (approximately $\sigma_y/\Lambda_u > 0.7$), the conditional concentration PDF is near log-Normal distributed.
3. For mid-range plume sizes. ($0.2 < \sigma_y/\Lambda_u < 0.7$), the conditional concentration PDF is near Gamma distributed.

5.4.2 Overview

The analysis in this section has shown that there is no single simple probability distribution which can be used to describe dispersion of a tracer in a boundary layer. A wide variety of distributions is required to fit the centre-line PDFs for the source configurations examined. The analysis has found that for a given source configuration there is not a single probability distribution which may be used at all locations. It appears that the distribution evolves along the plume centre-line and across the plume from centre-line to plume fringes.

For the iso-kinetic source, near the source, the PDF is bimodal. This would suggest that some of the tracer is diffused very quickly, indicating vortex roll action or breaking waves such as near the edge of a shear layer.

Although only three probability distributions have been used here to describe the plume evolution, several other distributions were used to check for better fits in those regions where the three did not match closely. The Exponential, Weibull, 4 parameter Gamma, etc, did not yield better fits. The three PDF models, the clipped-Normal, Gamma, and log-Normal, were found to have sufficient character to represent the data.

5.5 Probability Distributions of Concentration Derivatives

The procedure for determining the derivative of the concentration was discussed in section B.2. It was shown that the higher order derivatives caused ringing to occur in the derivative signal, (refer to Figure B.4), but not in the lower order derivatives, (refer to Figure B.3). Further to the discussion in section B.2, the probability distributions of the derivatives for these two orders of derivative are shown in Figure 5.22 and Figure 5.23. The more accurate amplitude prediction using the 20th order FIR derivative approximation is reflected in the figure through its increased spread over

the 4th order result. Note also that the ringing of the 20th order causes a significant error in the near zero derivatives.

In Figure 5.22 and Figure 5.23 a Gaussian distribution is fit to both derivative approximations. It is clear that the 20th order derivative is non-Gaussian, and the 4th order derivative is also non-Gaussian. Antonia, Phan-Thien and Chambers (1980) have found that derivative of temperature fluctuations in an atmospheric flow are also non-Gaussian. Prasad and Sreenivasan (1990) measured passive scalar dissipation in a turbulent jet using laser-induced fluorescence, and have found that the probability distribution of the concentration gradients $\frac{\partial c}{\partial x}$, $\frac{\partial c}{\partial y}$, and $\frac{\partial c}{\partial z}$ are symmetric but non-Gaussian. The temporal derivatives may be inferred from these results using the Taylor approximation as in Antonia, Phan-Thien and Chambers (1980). Prasad and Sreenivasan (1990) also observed the characteristic peaks near zero and that the tails are exponential. The distributions are observed to be leptokurtic with a flatness factor of about 10 for the jets studied and nearly 100 for the wakes. These non-Gaussian characteristics were also observed by Kuo and Corrsin (1971) who studied dispersion in grid-generated nearly isotropic turbulence on the axis of a round jet and determined the temporal derivatives by analogue circuitry. Balachandar and Sirovich (1991) have recently made measurements of probability distribution functions of temperature fluctuations in Rayleigh-Benard convective cells. The temperature fluctuations are near Gaussian, but the derivatives and higher order derivatives are Exponential.

In Figure 5.23, an Exponential distribution is fit to the derivative of the concentration signal. The Exponential model is clearly the better model for the derivative for this location in the plume and jet/plume source conditions. The evolution of the derivative PDF for the jet/plume source is shown in Figure 5.24 and Figure 5.25. The distribution is observed to be very near Gaussian close to the source, and evolves to an Exponential beginning at approximately $x/h_s = 4.4$ or a plume size of $\sigma_y/\Lambda_u > 1.3$. At the furthest down-wind location, Figure 5.25 shows that the PDF is hyper-Exponential. This distribution is well represented by a Gamma distribution, (not shown). The Gamma distribution is not a good model for the derivative PDF because when the Gamma parameter $\lambda > 1$, the Gamma model predicts a zero PDF for zero derivatives. This not observed in the figures.

The evolution of the iso-kinetic source derivative PDF is shown in Figure 5.26 and Figure 5.27. The iso-kinetic source derivative PDF is not as well represented by the Gaussian distribution near the source or for plume sizes $\sigma_y/\Lambda_u < 1.3$. The Exponential distribution is a good representation of PDFs throughout the down-wind evolution although there are clear deviations near the source and far down-wind. Similar results are observed for the vertical jet source in Figure 5.30. The up-wind

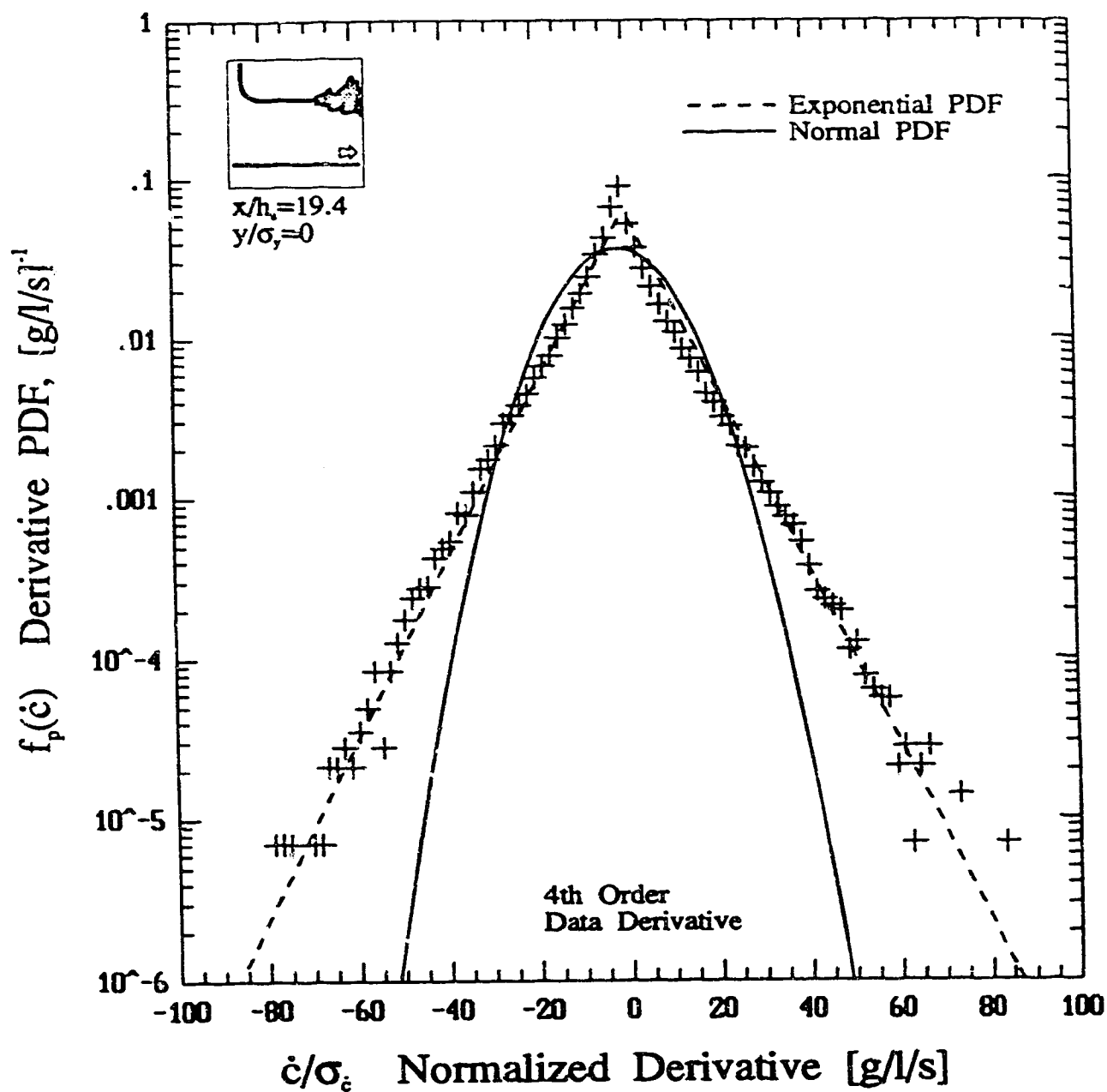


Figure 5.22: PDF of the derivative of concentration fluctuations using a 4th order windowed FIR derivative.

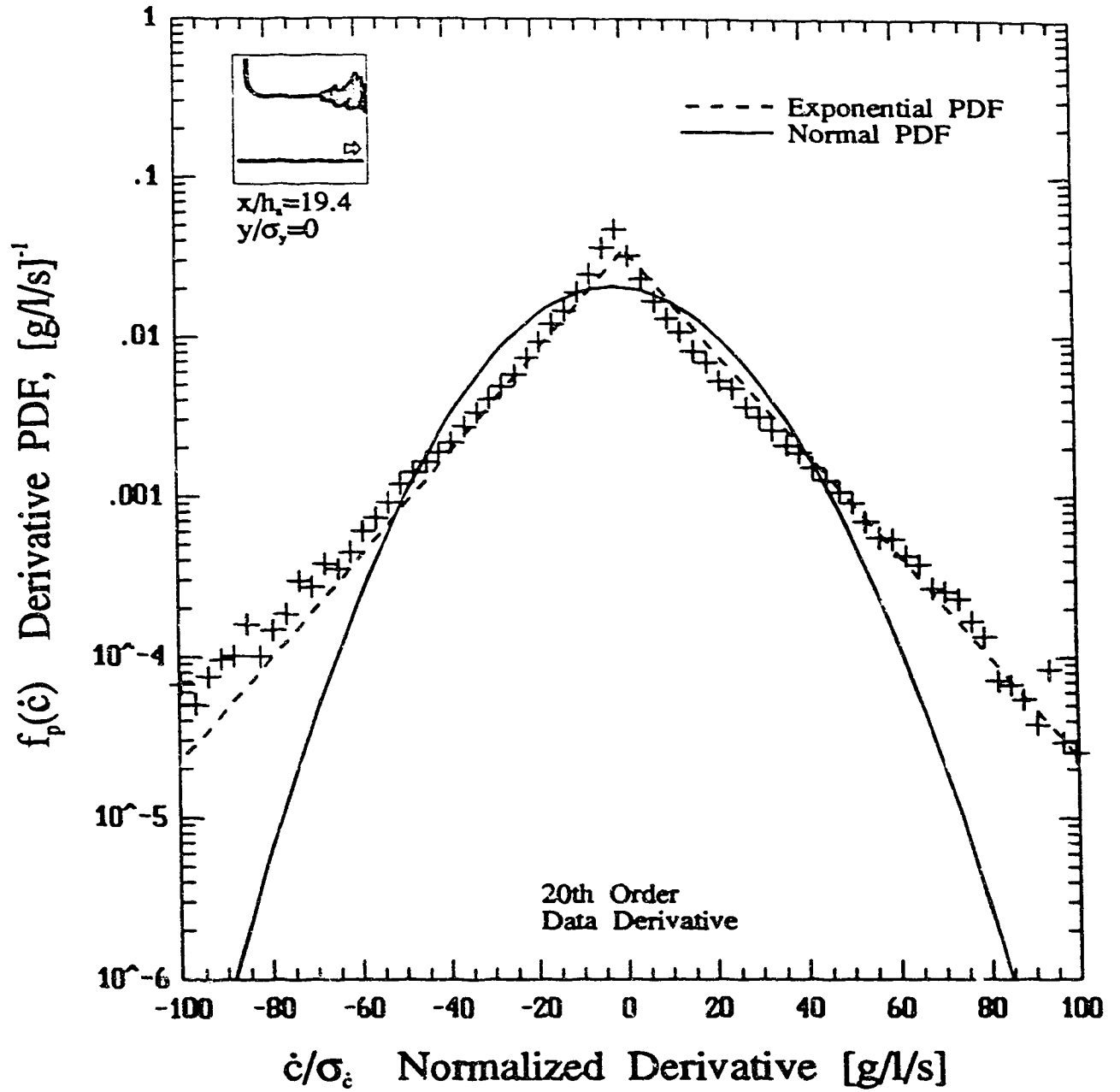


Figure 5.23: PDF of the derivative of concentration fluctuations using a 20th order windowed FIR derivative.

facing iso-kinetic source, shown in Figure 5.28 and Figure 5.29, is very well represented by the Exponential distribution near the source and not the Gaussian.

The cross-wind evolution of the derivative PDF for the jet/plume source is shown in Figure 5.31, near the source, and Figure 5.32, far from the source. The sparse data in the fringes of the plume in Figure 5.31 and Figure 5.32 are a result of the low intermittency in that region. The variation of the PDF distributions across the plume indicate that the PDF is clearly non-Gaussian, and evolves to a non-Exponential distribution.

Three general conclusions may be made concerning the derivative PDF, for the source types studied.

1. For small plume sizes, (approximately $\sigma_y/\Lambda_u < 0.15$), the derivative PDF is near Gaussian.
2. For large plume sizes, (approximately $\sigma_y/\Lambda_u > 0.7$), the derivative PDF is hyper-Exponential.
3. For mid-range plume sizes, ($0.15 < \sigma_y/\Lambda_u < 0.7$), the derivative PDF is well represented by the Exponential distribution.

If a single PDF must be chosen, the Exponential distribution is a better overall representation of the derivative PDF than the Gaussian distribution. The variation in the derivative PDFs in the present study confirm the observations and disagreements in the literature concerning the derivative distribution. The differences appear to be a function of source type and location in the plume. These transition points are roughly the same as the transition points observed in the evolution of the concentration PDF. Therefore, important observations concerning the dynamics of the concentration dilution process are as follows:

1. Where the concentration dilution process produces a clipped-Normal PDF distribution, the concentration time derivative PDF is near Gaussian.
2. Where the concentration dilution process produces a log-Normal PDF distribution, the concentration time derivative PDF is hyper-Exponential and may be Gamma distributed.
3. Where the concentration dilution process produces a Gamma PDF distribution, the concentration time derivative PDF is near Exponential.

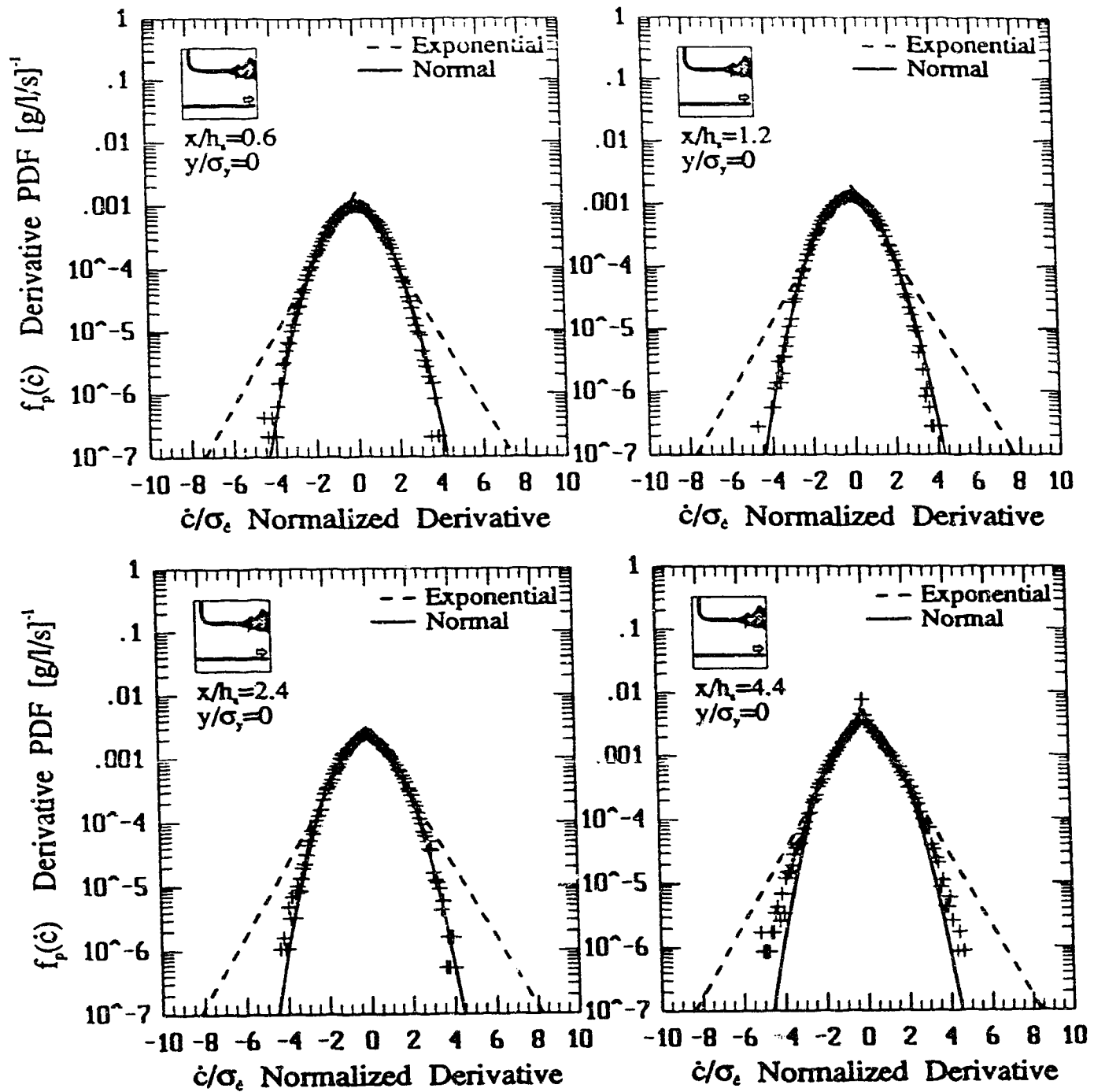


Figure 5.24: Down-wind evolution of the PDF of the derivative of concentration fluctuations using a 20th order FIR derivative for the jet/plume source.

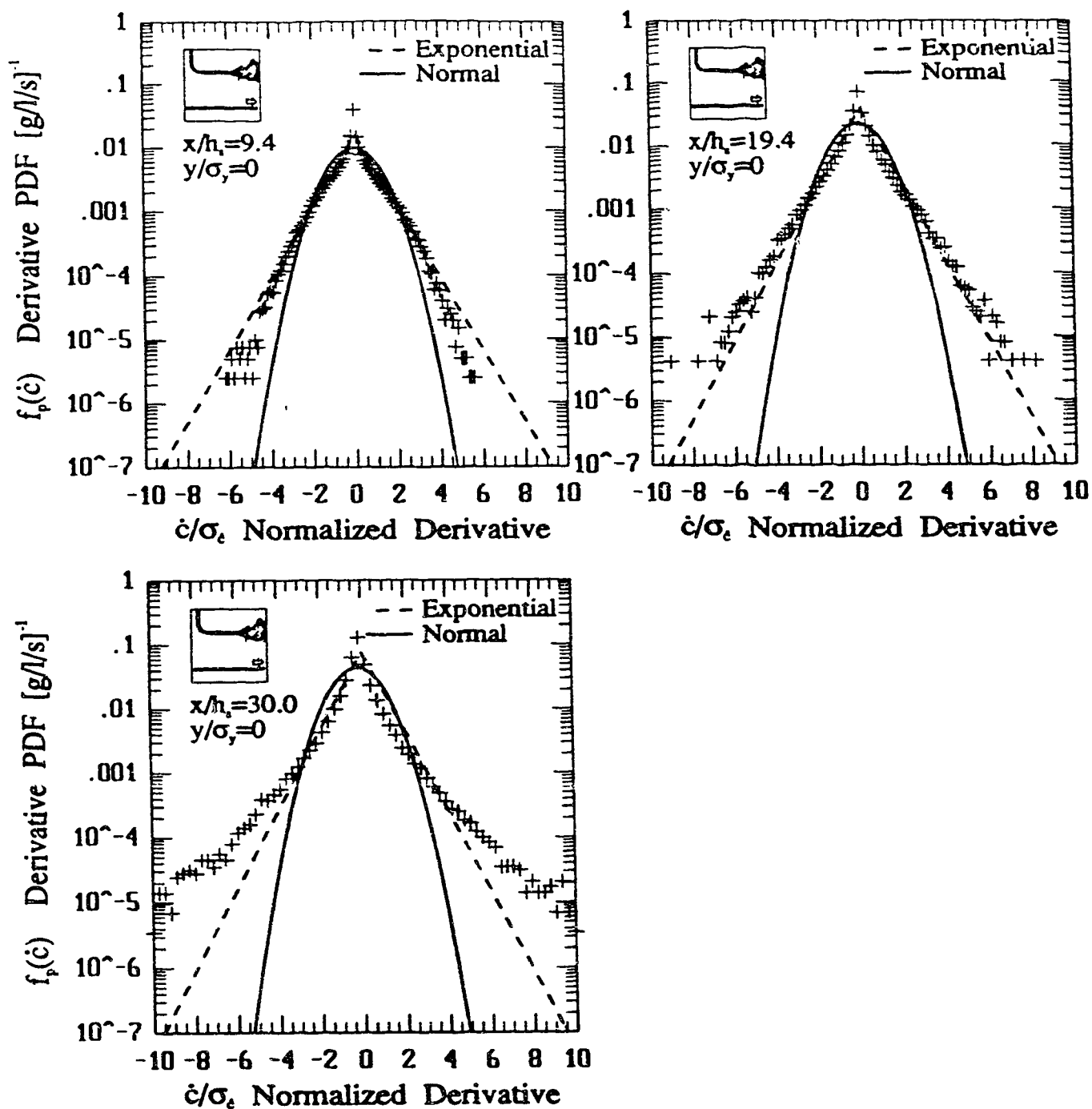


Figure 5.25: Down-wind evolution of the PDF of the derivative of concentration fluctuations using a 20th order FIR derivative for the jet/plume source.

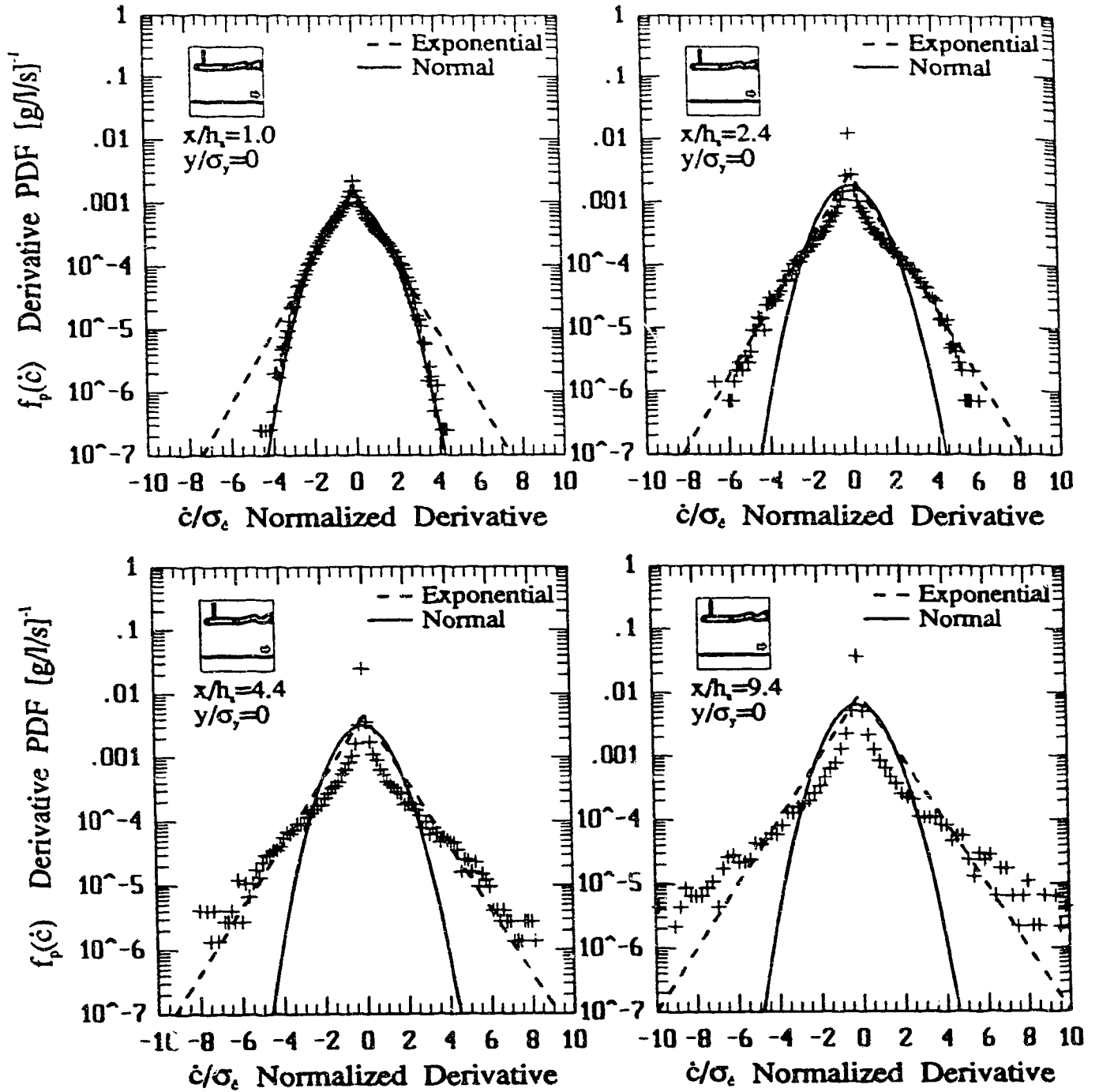


Figure 5.26: Down-wind evolution of the PDF of the derivative of concentration fluctuations using a 20th order FIR derivative for the iso-kinetic source.

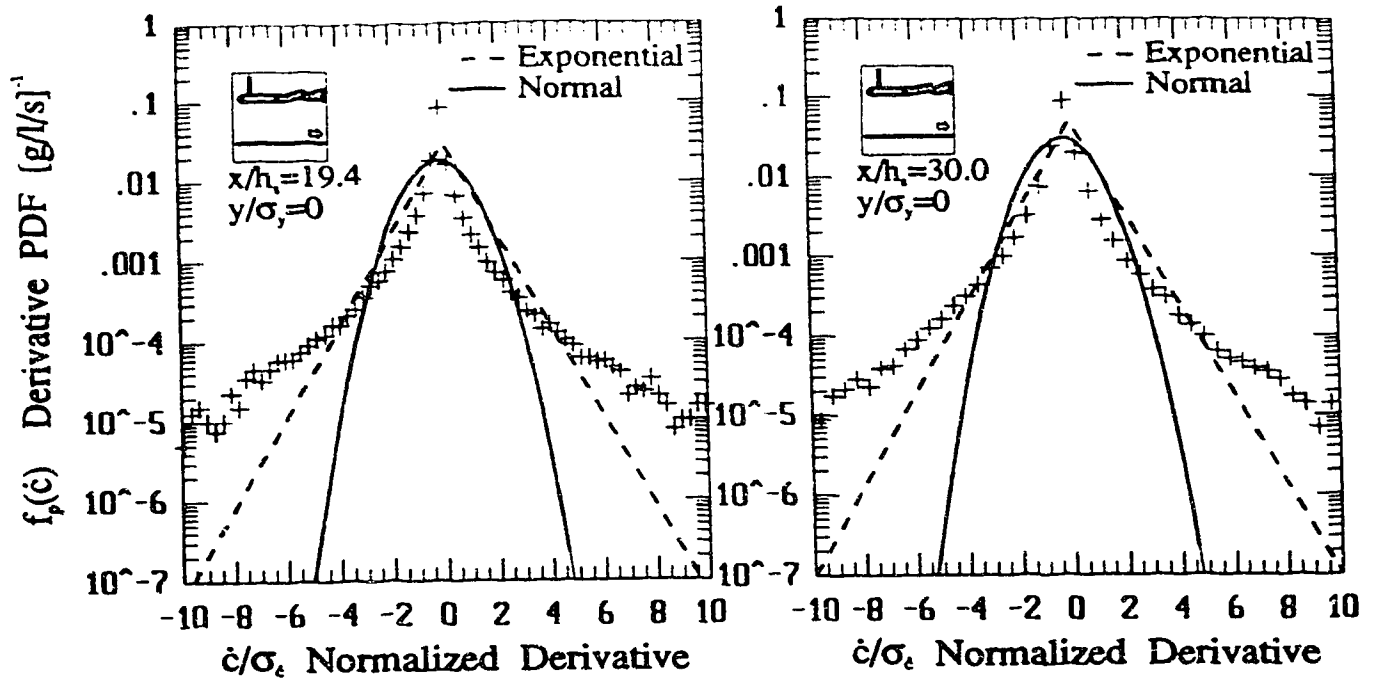


Figure 5.27: Down-wind evolution of the PDF of the derivative of concentration fluctuations using a 20th order FIR derivative for the iso-kinetic source.

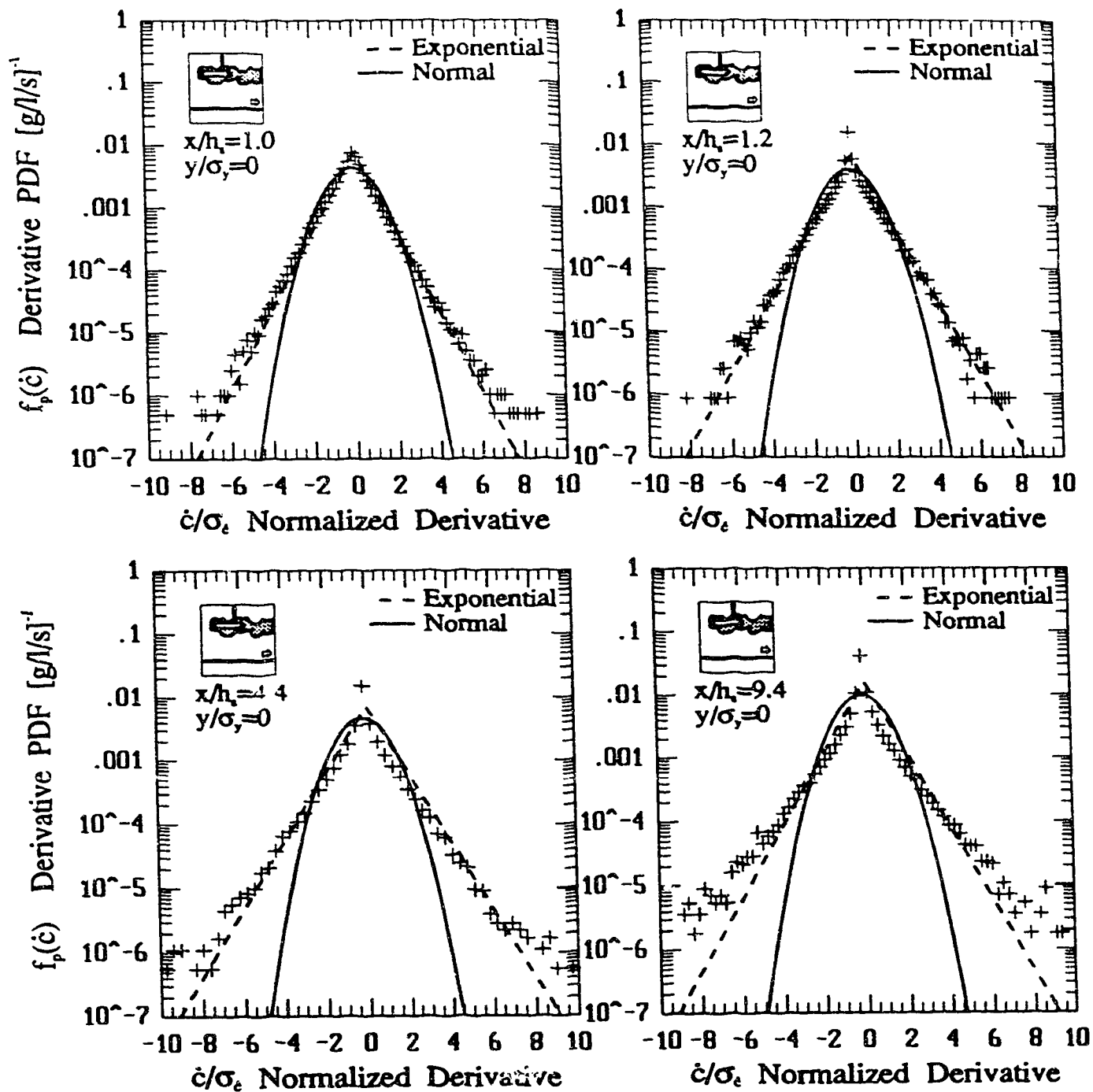


Figure 5.28: Down-wind evolution of the PDF of the derivative of concentration fluctuations using a 20th order FIR derivative for the up-wind facing iso-kinetic source.

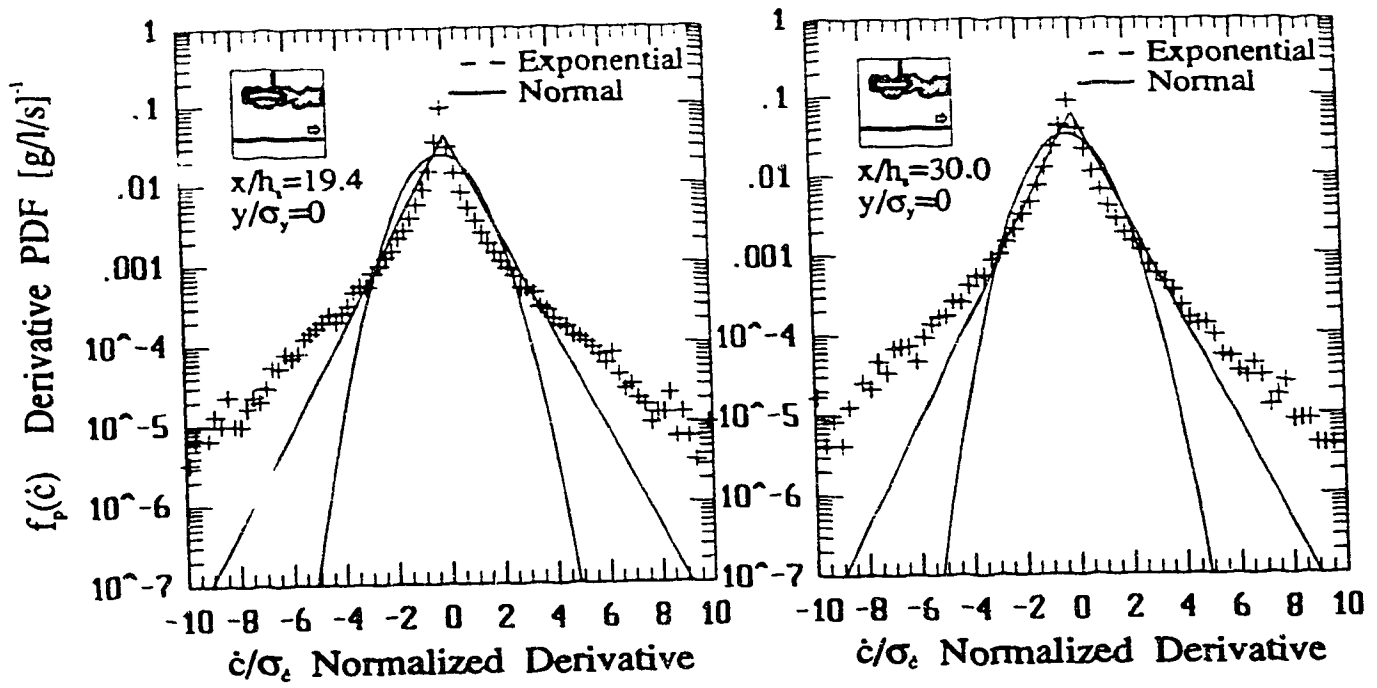


Figure 5.29: Down-wind evolution of the PDF of the derivative of concentration fluctuations using a 20th order FIR derivative for the up-wind facing iso-kinetic source.

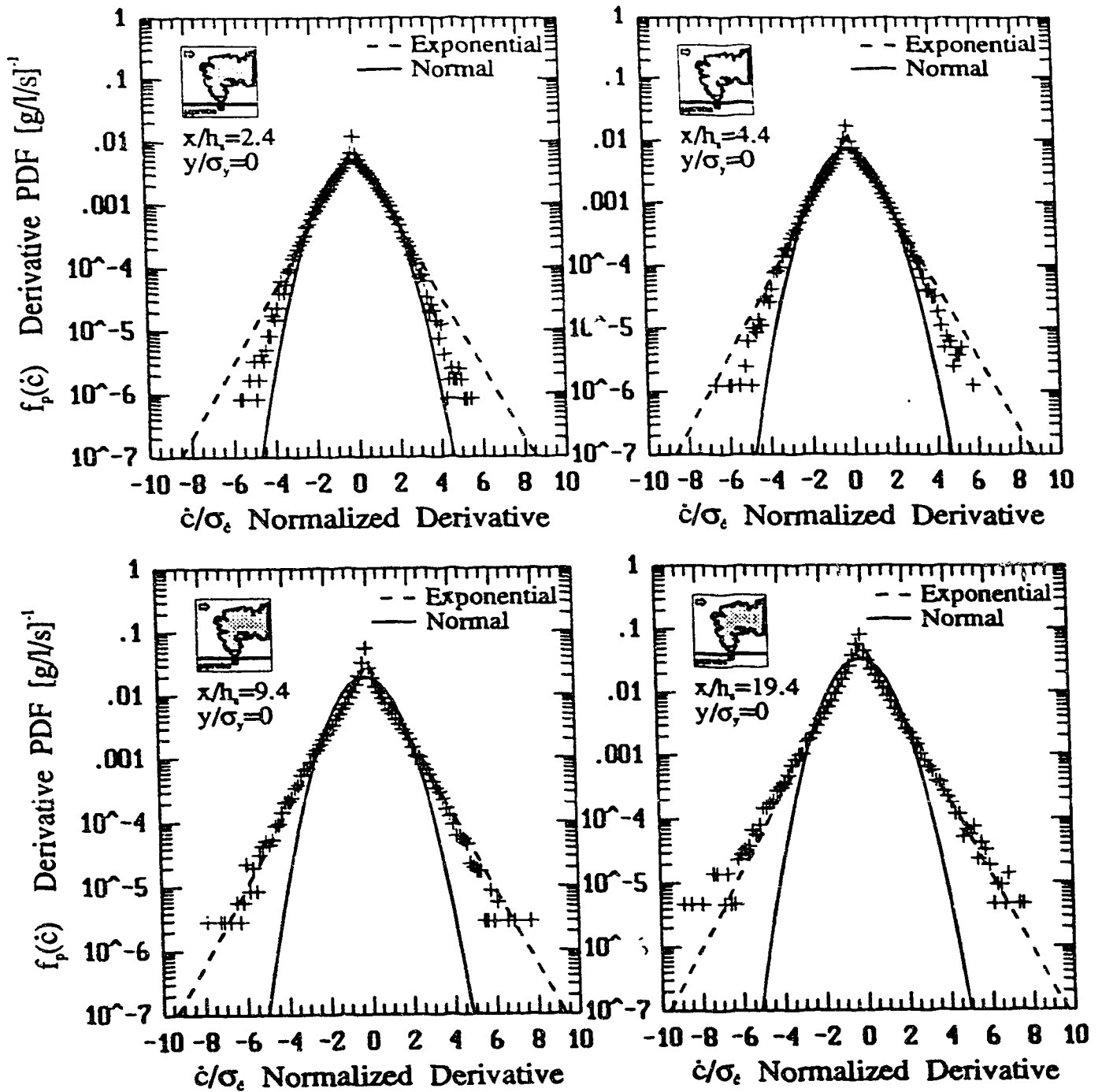


Figure 5.30: Down-wind evolution of the PDF of the derivative of concentration fluctuations using a 20th order FIR derivative for the vertical jet source.

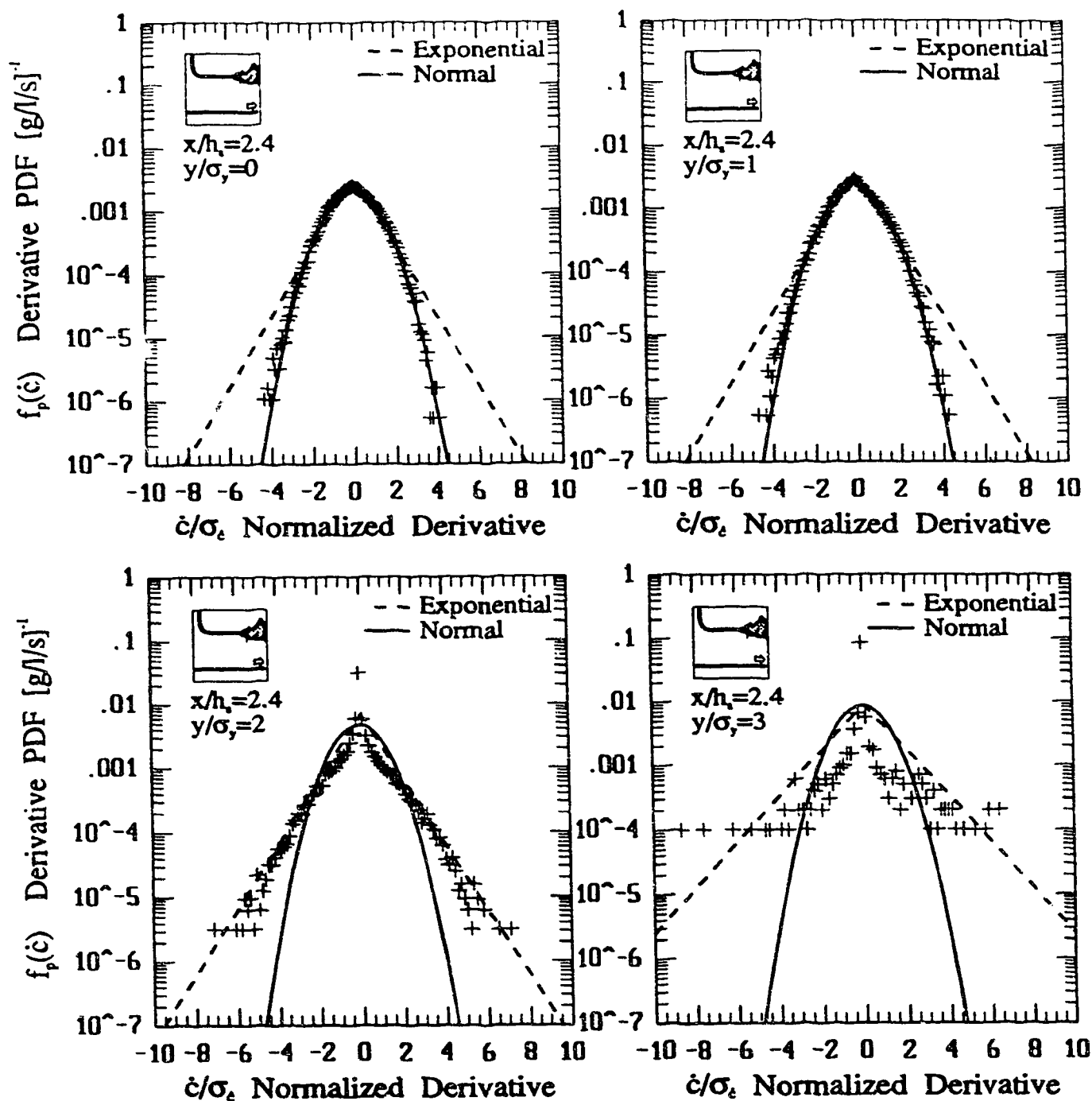


Figure 5.31: Cross-wind evolution of the PDF of the derivative of concentration fluctuations using a 20th order FIR derivative close to the jet/plume source.

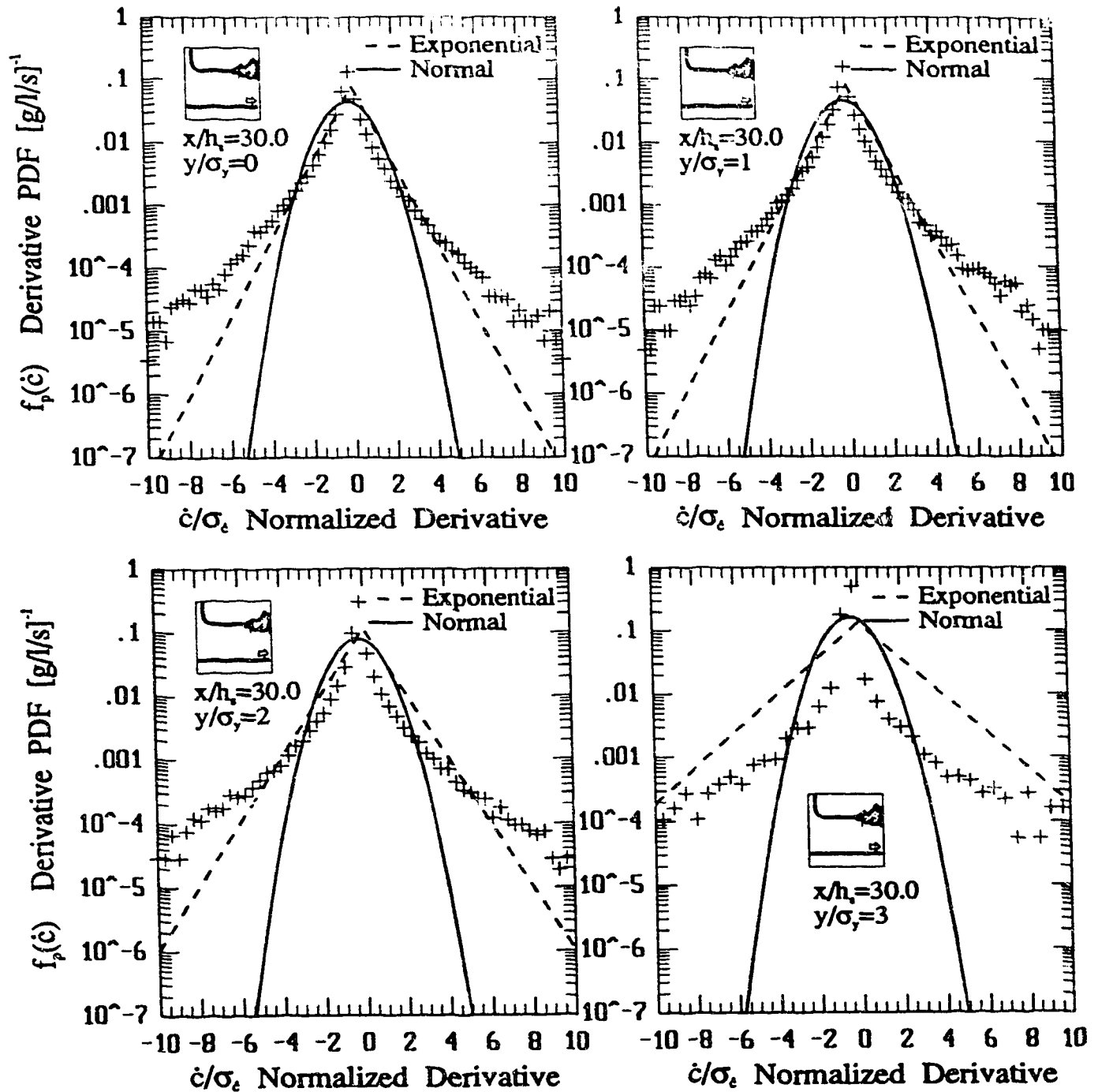


Figure 5.32: Cross-wind evolution of the PDF of the derivative of concentration fluctuations using a 20th order FIR derivative far down-wind of the jet/plume source.

It is known that a purely Gaussian process will produce a Gaussian derivative, (Dutton and Panofsky (1984) p.318 for example), therefore the association (1) above may be explained. Stochastic arguments for why the other pairs of distributions are observed have not been pursued.

An Exponential model indicates that the derivatives are uncorrelated, and have an increased probability of *rare* (large derivative) events. This is very different than the Gaussian model which indicates that a particular derivative is the result of the sum of random events. Therefore, the Exponential model provides not just a better representation of the distribution of the derivatives but also better insight to the possible process by which a high derivative is produced.

Is the observed Exponential distribution a result of the time series processing on an actual Gaussian distribution? Due to the large amounts of signal processing on the time series signal this is a valid question. The signal processing increases the expected lower derivatives therefore making the distribution shape look more exponential. If in Figure 5.23 the low derivatives are ignored, the high derivatives do not correspond to the expected parabola of a Gaussian distribution. Because the time series signal is digitally filtered, high frequency noise is removed. This would suggest that an originally Gaussian distribution, would appear to be more strongly rolled off, and the number of high derivatives would not be present in Figure 5.23. However, the figure shows that the reverse is true. Finally, Figure 5.23 shows that the 20th order numerical derivative approximation and the 4th order approximation both predict the same probability distribution. Therefore the 20th order approximation is not the cause of the observed distribution. Antonia, Phan-Thien and Chambers (1980) determined temperature and velocity derivatives numerically and found the distributions were Exponential. It may be concluded that it is unlikely that a Gaussian distribution would be distorted into an Exponential distribution by the signal processing of the time series. The effect of assuming that the distributions are Gaussian despite their being clearly non-Gaussian, is examined in Chapter 7.

There is evidence that the scalar gradient $|\nabla c|^2$, or dissipation, behaves like a log-Normal random variable (Lagrangian), (recently Gao and O'Brien, 1991, Antonia and Sreenivasan, 1977, Sreenivasan, Antonia, and Danh, 1977 and originally Oboukhov, 1962). The Gamma distribution is also a candidate for the dissipation distribution, Andrews and Shivamoggi, (1990). What these studies indicate is that perhaps the path to study is not to study the gradient of the scalar fluctuation field, but the behaviour of the variation in the dissipation. Based on the current literature, information about one from the other is not readily available or discernible. For the purposes of this study, only the scalar fluctuation gradient will be considered.

5.6 Intermittency Prediction

One of the important statistics that is required from a plume model is the prediction of the intermittency. Using the probability models based on the total moments of concentration, the intermittency may be determined for the two parameter PDFs using the first three total moments of concentration. The clipped-Normal distribution being the only exception which predicts the intermittency based on the first two total moments.

Using the log-Normal, Gamma and the clipped-Normal distributions the intermittency may be determined given the experimental concentration moment data points by substituting observed higher order moments and intermittency models for each PDF. (equations (5.26), (5.31) and (5.52)). In Figure 5.33 to Figure 5.35 the intermittency of the jet/plume source is presented at each of the down-wind locations, (except the closest location, where the data was too sparse for presentation). For those locations where the log-Normal, Gamma or clipped-Normal is expected to fit best on the centre-line, the appropriate PDF provides the best estimate. In Figure 5.33, the clipped-Normal provides an excellent prediction of the intermittency. However, all the figures show the typical trend observed in Figure 5.33, that is, the predicted intermittencies using the Gamma and the log-Normal are always 10 to 25% too low. One possibility is that the experimentally determined intermittency in the profile is too high. This might suggest that the intermittency threshold is selected too low, so that noise is detected as concentration signal. However, considering the analysis in section B.7, it seems unlikely that an improper threshold level for the data analysis is the cause of the discrepancy. (The threshold must be raised almost an order of magnitude to produce intermittencies that begin to agree with the theory.)

At the far down-wind locations, the Gamma distribution fails for some of the sources tested. The Gamma model is very sensitive to errors in \bar{c} , \bar{c}^2 and \bar{c}^3 , see (5.52). As a result of the complex interaction of the higher order total moments in (5.52), the intermittency is calculated incorrectly. This is caused by small errors in higher order moments which are not consistent with the expected inter-relationship determined by the Gamma distribution model. The Gamma model is therefore numerically sensitive to measured higher order moments at the far down-wind locations.

The centre-line evolution of the intermittency is shown in Figure 5.36 and Figure 5.37 for each of the sources. The characteristic low intermittency predictions are seen in each of the figures and may range from 10% to approximately 50% too low. The best fit intermittency is determined by the best fit PDF at each of the down-wind locations. The Gamma distribution prediction in the figures terminates prematurely as a result the errors described above.

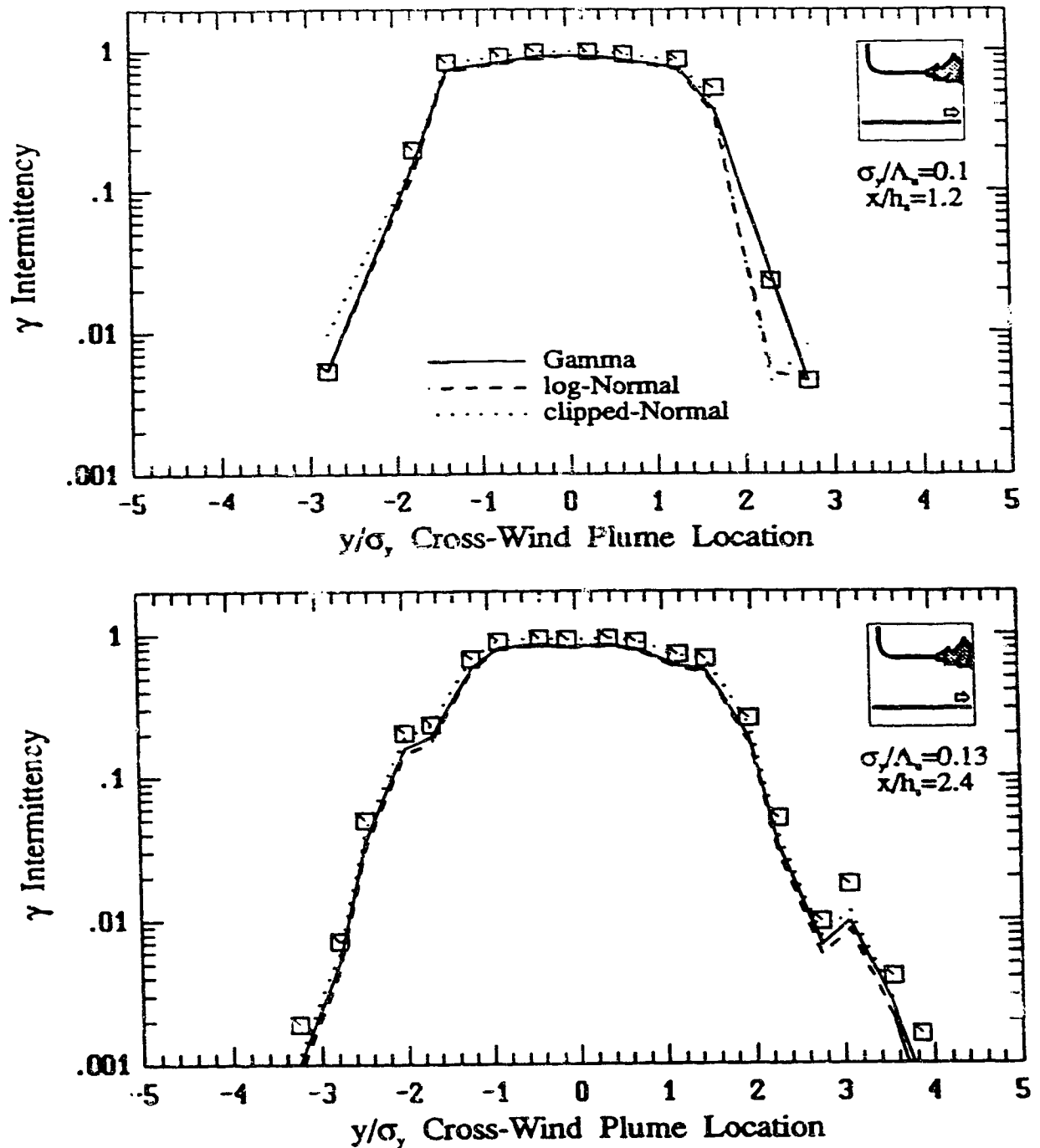


Figure 5.33: Profile of the predicted intermittency using the Gamma, log-Normal and clipped-Normal probability distributions and experimental higher order moments, for the jet/plume source at locations $x/h_s = 1.2$ and $x/h_s = 2.4$.

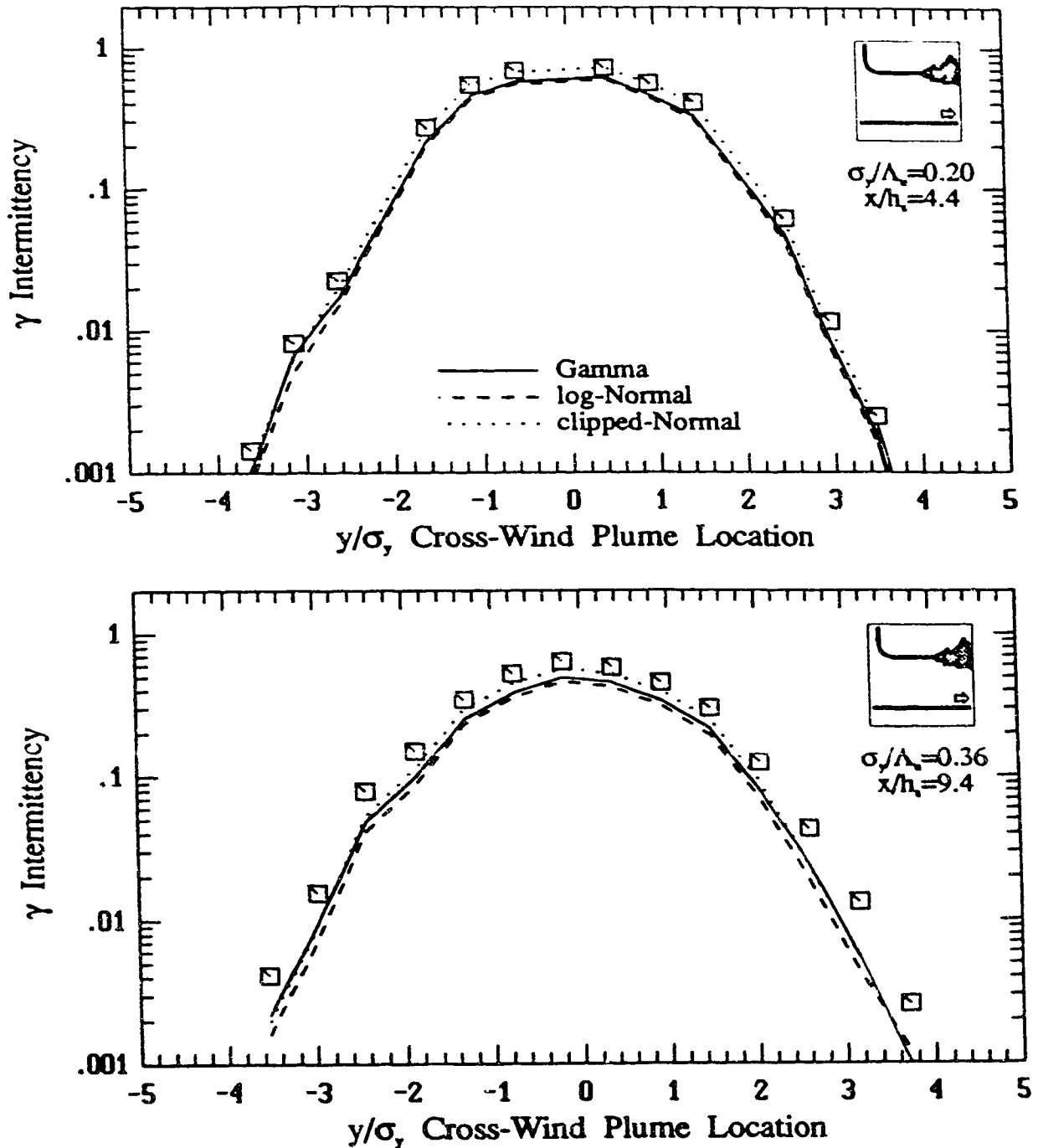


Figure 5.34: A typical profile of the predicted intermittency using the Gamma, log-Normal and clipped-Normal probability distributions and experimental higher order moments, for the jet/plume source at locations $x/h_s = 4.4$ and $x/h_s = 9.4$.

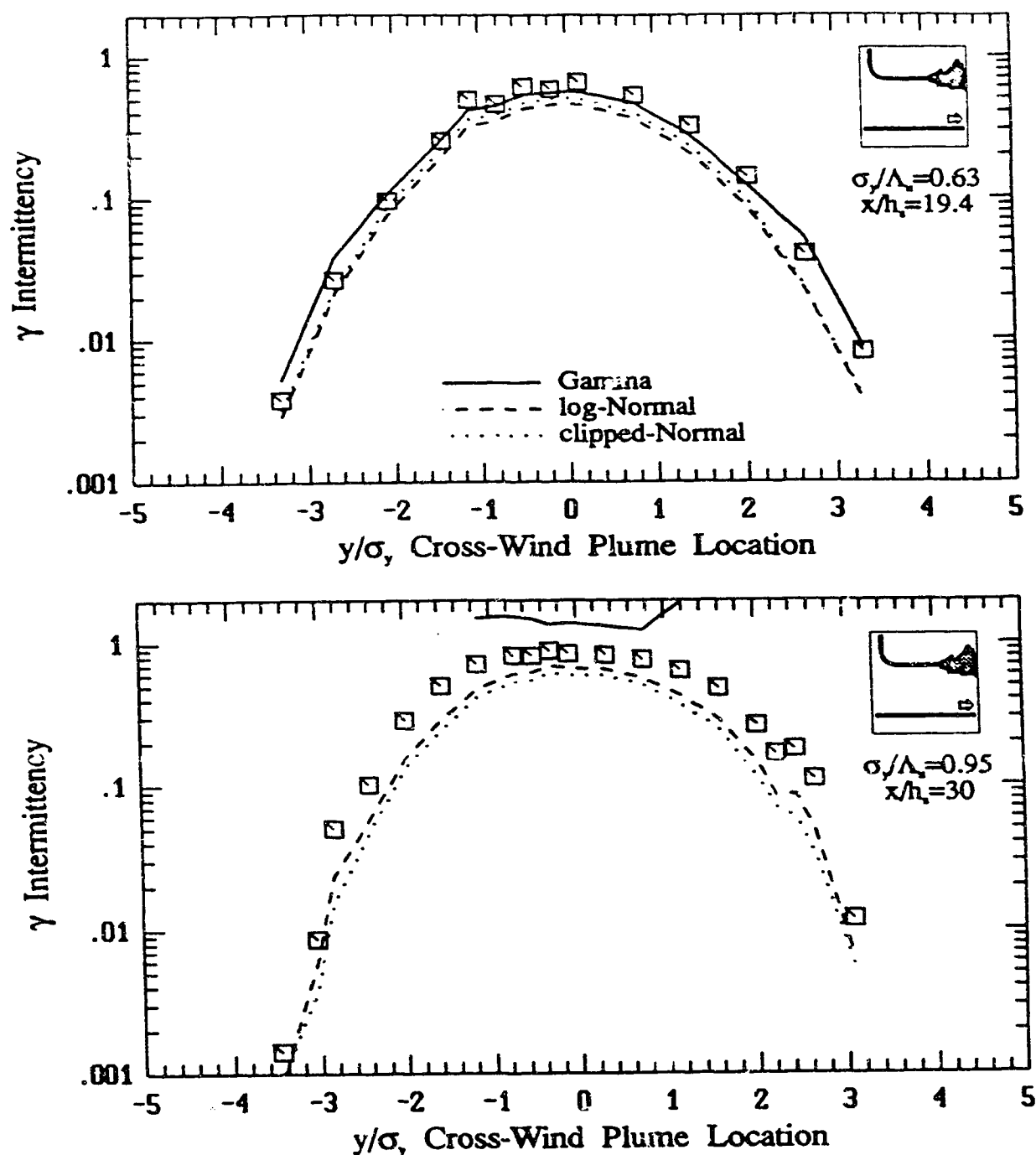


Figure 5.35: A typical profile of the predicted intermittency using the Gamma, log-Normal and clipped-Normal probability distributions and experimental higher order moments, for the jet/plume source at locations $x/h_s = 19.4$ and $x/h_s = 30.0$.

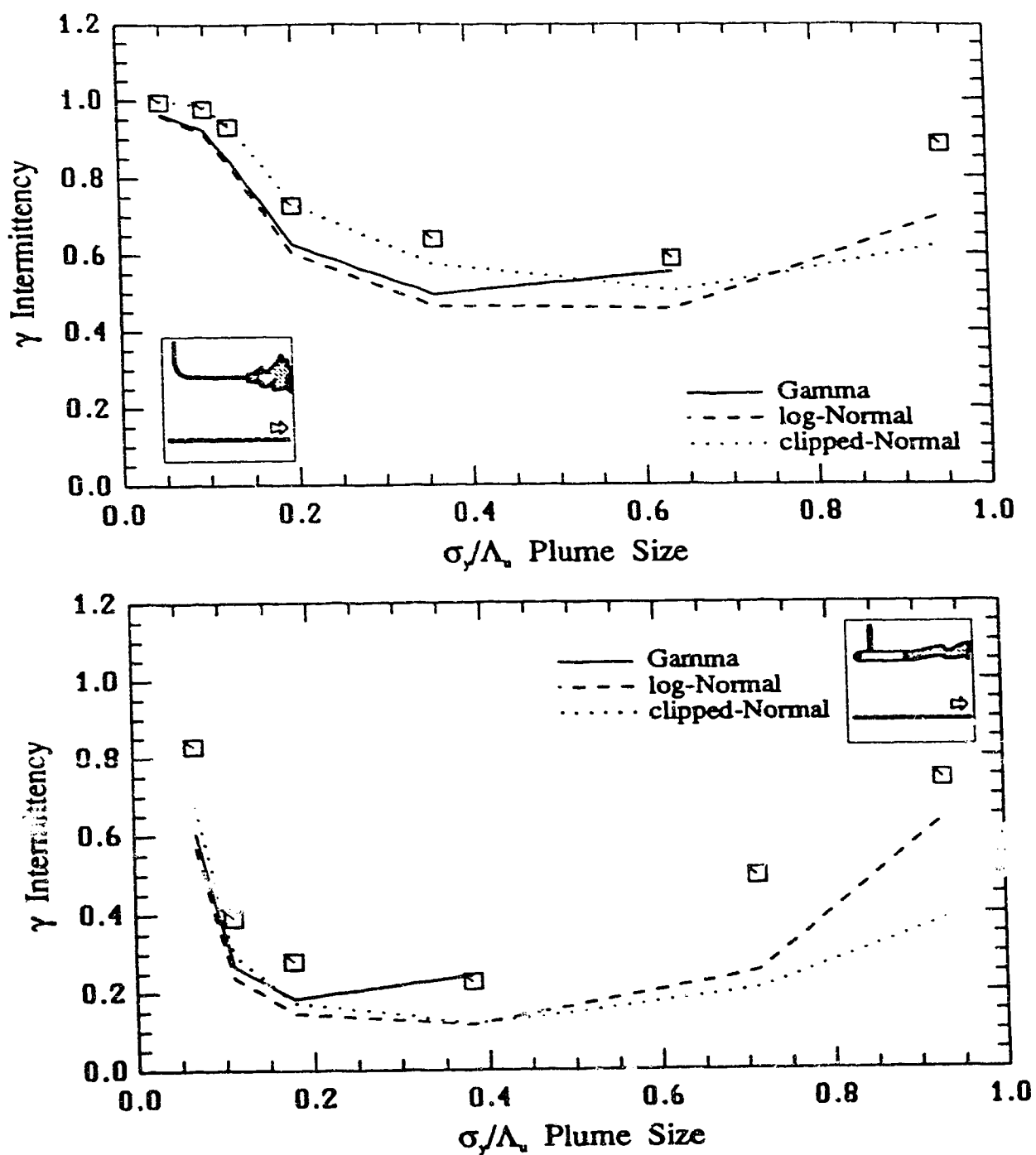


Figure 5.36: The centre-line evolution of the predicted intermittency using the PDF models for the jet/plume source and the iso-kinetic source.

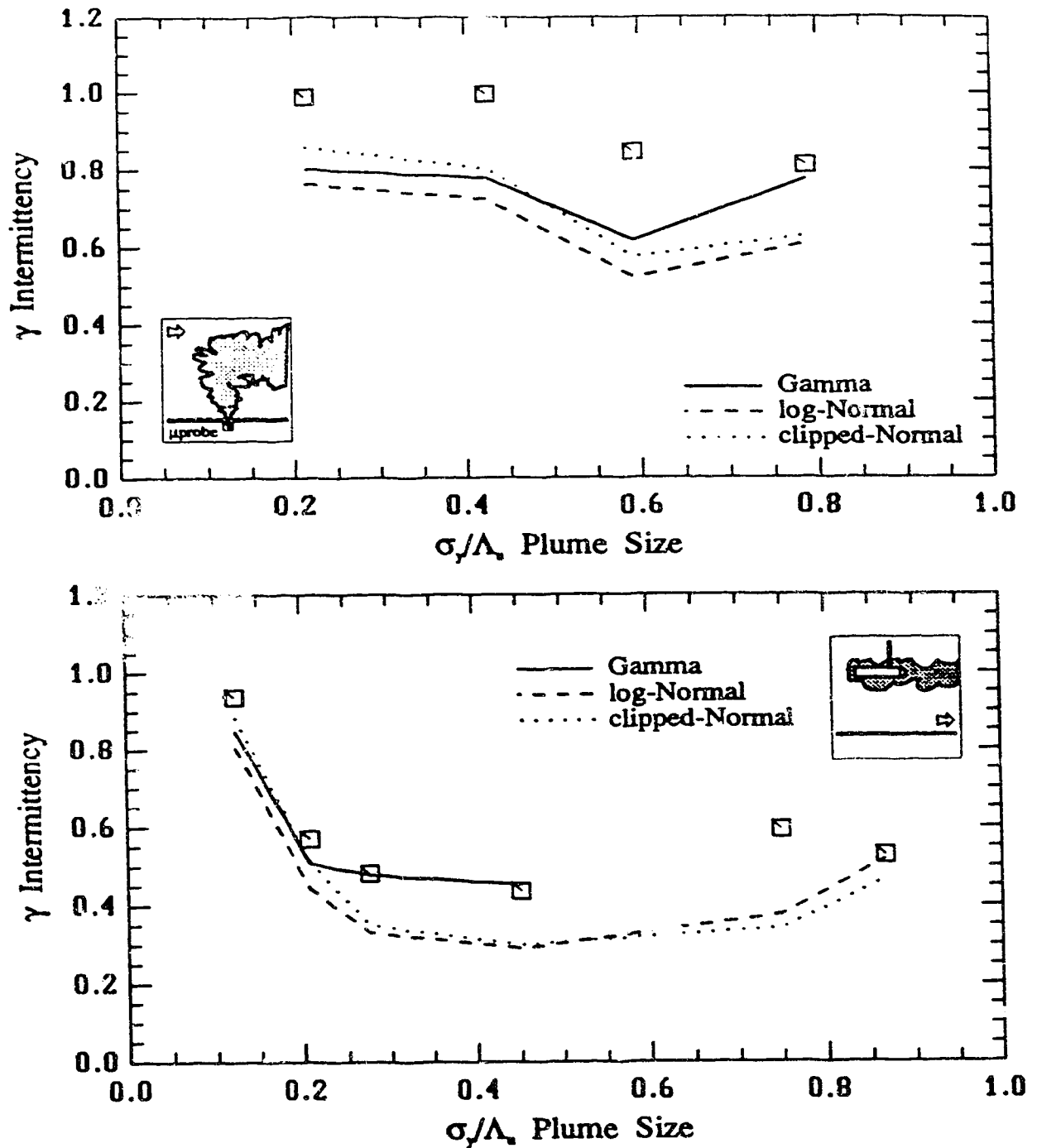


Figure 5.37: The centre-line evolution of the predicted intermittency using the PDF models for the vertical jet source and the up-stream facing iso-kinetic source.

5.7 Conclusions

The analysis in this chapter has shown that a single, simple probability distribution cannot be used to describe, at all locations and from all sources, the concentration field of a tracer in a boundary layer. It appears that the PDFs evolve when traversing a plume along its centre-line, and when traversing across the plume from centre-line to plume fringes. The data also appear to show that the points of distribution transition are approximately related to the plume size, σ_y/Λ_u . This means that a general dispersion model may be developed using this evolution which takes into account the different probability distributions a dispersing plume may have.

Several problems in determining goodness of fits to the measured distributions were discovered. The maximum likelihood estimators and the moment estimators were examined and found to predict quite different results as well. Truncation of the PDF due to histogram resolution and to experiment sample time was observed to have a significant effect on the goodness of fit.

The intermittency is generally predicted to be too low by all the PDF models. This may be because, the Gamma distribution is numerically sensitive to measured higher order moments at the far down-wind locations.

The derivative PDF was observed to evolve with down-wind location. The evolution of the derivative PDF appears to scale approximately with the plume size, σ_y/Λ_u , as does the evolution of the concentration PDF. If one PDF must be chosen, the Exponential distribution is a better representation of the derivative PDF than the Normal distribution.

Chapter 6

Concentration Fluctuation Statistics

The purpose of this chapter is to present the observed higher order moments of concentration in the water channel, and a model for the distribution of these moments as a function of cross-wind location.

The Von Kármán interpolating spectrum formula is generalized for a general spectrum with an arbitrary high-frequency slope (i.e. a spectrum of power n) and is applied to scalar fluctuations. The generalized Von Kármán spectrum is used as a model for the concentration derivative variance, σ_c^2 .

The concentration moments are used to predict the parameters of a probability distribution model and the intermittency of fluctuations based on the best fit PDF models investigated in Chapter 5. A sensitivity analysis is performed to show which of the best fit PDF models is the best model.

6.1 Description of a Similarity Theory

In this section the conservation equation for a tracer mass is examined to find the governing equations for the higher order moments of concentration. An Eulerian model is developed, using Reynolds decomposition of the random variables into the mean and fluctuating components. Specifically, $u = \bar{u} + u'$ and $c = \bar{c} + c'$, etc..., where \bar{u} and \bar{c} are the time-averaged components of u and c . Introduction of these variables leads to a closure problem, which is unavoidable in turbulence theory. A simple closure model is presented.

The investigation of the concentration fluctuation moments, in general, has followed the popular statistical procedure to investigate the central moments as opposed to zero-based moments. This is primarily because most observed statistical

fluctuations are mean based fluctuations, such as variations of temperature and wind speed. However, in the study of intermittent concentration fluctuations, the fluctuations are naturally based on the zero concentration value, and *not* the mean value. Gaussian models for the conservation of mass have been written in terms of the mean concentration, Csanady (1973), Netterville (1979), Hanna (1984), Lewellen and Sykes (1986). Following typical analysis methods, the higher order central moments have been studied and a Gaussian form for the $\overline{c'^2}$ has often been adopted. Variations of the $\overline{c'^2}$ Gaussian model have been proposed to account for the presence of observed off-centre-line peaks, Bara and Wilson (1985), or lack thereof.

Hanna (1984) and Sykes (1986) review the history and development of the study of concentration fluctuations. Sykes develops a conservation equation for the total second moment, $\overline{c^2}$.

In the near-field, close to a small source, Gifford's (1959) meandering plume model is appropriate for describing concentration fluctuations. Sawford and Stapountzis (1985) show that all $\overline{c^n}$ moments have Gaussian profiles when fluctuations are generated by the meandering of a plume whose \bar{c} is Gaussian. In the following sections, an eddy diffusivity model for $\overline{c^n}$ will be developed to show that a Gaussian profile for $\overline{c^n}$ is plausible in the far field, where an eddy diffusivity approximation is reasonable. The budget equations are developed without Reynolds decomposition into central moment equations. This will eliminate the production terms found in central moment budget equations and will produce governing equations for which an approximate solution for the cross-wind profiles of $\overline{c^n}$ is Gaussian.

6.1.1 Budget Equations for \bar{c} and $\overline{c'^2}$

The transport of a scalar, c , in a flow field is governed by the conservation of mass equation,

$$\frac{\partial c}{\partial t} = -\frac{\partial F_i}{\partial x_i} + Q \quad (6.1)$$

where Q is the rate of production of c and F_i is the flux density of c ,

$$F_i = u_i c - \mathcal{D} \frac{\partial c}{\partial x_i} \quad (6.2)$$

\mathcal{D} is the molecular diffusivity of c and is assumed to be a constant. Substituting (6.1) into (6.2), assuming $Q = 0$ and a non-divergent flow,

$$\frac{\partial c}{\partial t} + u_i \frac{\partial c}{\partial x_i} = \mathcal{D} \frac{\partial^2 c}{\partial x_i^2} \quad (6.3)$$

By averaging on (6.3), the mean conservation equation is, (Hinrichsen, 1975),

$$\frac{\partial \bar{c}}{\partial t} + \underbrace{\bar{u}_i \frac{\partial \bar{c}}{\partial x_i}}_{\text{advection of } \bar{c} \text{ by mean flow}} = \frac{\partial}{\partial x_i} \underbrace{\left(\mathcal{D} \frac{\partial \bar{c}}{\partial x_i} - \overline{u'_i c'} \right)}_{\text{flux of } \bar{c} \text{ by diffusion and turbulent convection}} \quad (6.4)$$

The budget equation for the variance of c is (Csanady, 1973),

$$\frac{\partial \overline{c'^2}}{\partial t} = - \frac{\partial}{\partial x_i} \underbrace{\left(\overline{u'_i c'^2} + \overline{u'_i c'^2} - \mathcal{D} \frac{\partial \overline{c'^2}}{\partial x_i} \right)}_{\text{flux of } \overline{c'^2}} - \underbrace{2 \overline{u'_i c'} \frac{\partial \bar{c}}{\partial x_i}}_{\text{production of } \overline{c'^2}} - \underbrace{2 \mathcal{D} \overline{\left| \frac{\partial c'}{\partial x_i} \right|^2}}_{\text{dissipation of } \overline{c'^2}} \quad (6.5)$$

6.1.2 Budget Equation for $\overline{c^2}$

The budget equation for $\overline{c^2}$ may be generated by multiplying (6.3) by $2c$,

$$2c \frac{\partial c}{\partial t} + 2cu_i \frac{\partial c}{\partial x_i} = 2c \mathcal{D} \frac{\partial^2 c}{\partial x_i^2} \quad (6.6)$$

Using the expansion,

$$2c \frac{\partial^2 c}{\partial x_i^2} = \frac{\partial^2 c^2}{\partial x_i^2} - 2 \left| \frac{\partial c}{\partial x_i} \right|^2 \quad (6.7)$$

then (6.6) becomes,

$$\frac{\partial c^2}{\partial t} + u_i \frac{\partial c^2}{\partial x_i} = \mathcal{D} \frac{\partial^2 c^2}{\partial x_i^2} - 2 \mathcal{D} \left| \frac{\partial c}{\partial x_i} \right|^2 \quad (6.8)$$

Reynolds decomposition of u_i and temporal averaging leads to,

$$\frac{\partial \overline{c^2}}{\partial t} + \underbrace{\bar{u}_i \frac{\partial \overline{c^2}}{\partial x_i}}_{\text{advection of } \overline{c^2} \text{ by mean flow}} = \frac{\partial}{\partial x_i} \underbrace{\left(\mathcal{D} \frac{\partial \overline{c^2}}{\partial x_i} - \overline{u'_i c^2} \right)}_{\text{flux of } \overline{c^2} \text{ by diffusion and turbulent convection}} - \underbrace{2 \mathcal{D} \overline{\left| \frac{\partial c}{\partial x_i} \right|^2}}_{\text{dissipation of } \overline{c^2}} \quad (6.9)$$

6.1.3 Budget Equation for $\overline{c^3}$

The budget equation for $\overline{c^3}$ may be generated by multiplying (6.3) by $3c^2$,

$$3c^2 \frac{\partial c}{\partial t} + 3c^2 u_i \frac{\partial c}{\partial x_i} = 3c^2 \mathcal{D} \frac{\partial^2 c}{\partial x_i^2} \quad (6.10)$$

Using the expansion,

$$3c^2 \frac{\partial^2 c}{\partial x_i^2} = \frac{\partial^2 c^3}{\partial x_i^2} - 3 \frac{\partial c}{\partial x_i} \cdot \frac{\partial c^2}{\partial x_i} \quad (6.11)$$

then (6.10) becomes,

$$\frac{\partial c^3}{\partial t} + u_i \frac{\partial c^3}{\partial x_i} = \mathcal{D} \frac{\partial^2 c^3}{\partial x_i^2} - 3 \mathcal{D} \frac{\partial c}{\partial x_i} \cdot \frac{\partial c^2}{\partial x_i} \quad (6.12)$$

Reynolds decomposition of u_i and temporal averaging leads to,

$$\frac{\partial \bar{c}^3}{\partial t} + \underbrace{\bar{u}_i \frac{\partial \bar{c}^3}{\partial x_i}}_{\text{advection of } \bar{c}^3 \text{ by mean flow}} = \frac{\partial}{\partial x_i} \underbrace{\left(\mathcal{D} \frac{\partial \bar{c}^3}{\partial x_i} - \overline{u'_i c^3} \right)}_{\text{flux of } \bar{c}^3 \text{ by diffusion and turbulent convection}} - \underbrace{3 \mathcal{D} \overline{\frac{\partial c}{\partial x_i} \cdot \frac{\partial c^2}{\partial x_i}}}_{\text{dissipation of } \bar{c}^3} \quad (6.13)$$

6.1.4 Budget Equation for \bar{c}^4

The budget equation for \bar{c}^4 may be generated by multiplying (6.3) by $4c^3$,

$$4c^3 \frac{\partial c}{\partial t} + 4c^3 u_i \frac{\partial c}{\partial x_i} = 4c^3 \mathcal{D} \frac{\partial^2 c}{\partial x_i^2} \quad (6.14)$$

Using the expansion,

$$4c^3 \frac{\partial^2 c}{\partial x_i^2} = \frac{\partial^2 c^4}{\partial x_i^2} - 4 \frac{\partial c}{\partial x_i} \cdot \frac{\partial c^3}{\partial x_i} \quad (6.15)$$

then (6.14) becomes,

$$\frac{\partial c^4}{\partial t} + u_i \frac{\partial c^4}{\partial x_i} = \mathcal{D} \frac{\partial^2 c^4}{\partial x_i^2} - 4 \mathcal{D} \frac{\partial c}{\partial x_i} \cdot \frac{\partial c^3}{\partial x_i} \quad (6.16)$$

Reynolds decomposition of u_i and temporal averaging leads to,

$$\frac{\partial \bar{c}^4}{\partial t} + \underbrace{\bar{u}_i \frac{\partial \bar{c}^4}{\partial x_i}}_{\text{advection of } \bar{c}^4 \text{ by mean flow}} = \frac{\partial}{\partial x_i} \underbrace{\left(\mathcal{D} \frac{\partial \bar{c}^4}{\partial x_i} - \overline{u'_i c^4} \right)}_{\text{flux of } \bar{c}^4 \text{ by diffusion and turbulent convection}} - \underbrace{4 \mathcal{D} \overline{\frac{\partial c}{\partial x_i} \cdot \frac{\partial c^3}{\partial x_i}}}_{\text{dissipation of } \bar{c}^4} \quad (6.17)$$

6.1.5 Closure Model

The conservation equations (6.4), (6.9), (6.13) and (6.17) may be simplified by considering diffusion in the far-field. In the far-field, an eddy diffusivity model is a reasonable assumption for the mean concentration gradient. This assumption allows the correlation $\overline{u'_i c'}$ to be modelled by a turbulence-transport or eddy-transport coefficient, K , by Boussinesq, (Hinze, 1975, p.30),

$$-\overline{u'_i c'} = K \frac{\partial \bar{c}}{\partial x_i} \quad (6.18)$$

Hinze points out that because $\overline{u'_i c'}$ and $\frac{\partial \bar{c}}{\partial x_i}$ are both vector quantities, the eddy diffusivity coefficients must either be a scalar or a second order tensor. Since it is unlikely that K is purely a scalar, the second order tensor is assumed. Therefore (6.18) may be expressed as,

$$-\overline{u'_i c'} = K_{ij} \frac{\partial \bar{c}}{\partial x_j} \quad (6.19)$$

For closure of the higher order mean concentration budget equations, the following will be assumed,

$$-\overline{u'_i c'^n} = K_{ij,n} \frac{\partial \bar{c}^n}{\partial x_j} \quad (6.20)$$

Therefore the general form for the mean higher order budget equation may be expressed as,

$$\frac{\partial \bar{c}^n}{\partial t} + \underbrace{\overline{u_i} \frac{\partial \bar{c}^n}{\partial x_i}}_{\text{advection of } \bar{c}^n \text{ by mean flow}} = \frac{\partial}{\partial x_i} \underbrace{\left(D \frac{\partial \bar{c}^n}{\partial x_i} + K_{ij,n} \frac{\partial \bar{c}^n}{\partial x_j} \right)}_{\text{flux divergence of } \bar{c}^n} - \underbrace{\epsilon_n}_{\text{dissipation of } \bar{c}^n} \quad (6.21)$$

6.1.6 Gaussian Solution for Higher Order Moments

Since there are no production terms in (6.21), and the functional form of the higher order moment budget equations is the same, it is probable that the higher order moment equations all have the same functional form.

In addition to the closure model in section 6.1.5, the following assumptions may also be made,

1. The flow is assumed steady, then $\frac{\partial \bar{c}^n}{\partial t} \rightarrow 0$.

2. The mean flow field is assumed to be either uniform over a significant period, or, to change slowly enough spatially and temporally that the plume centre-line may be defined. In essence, the flow field is assumed to be a horizontally homogeneous flow with a dominant flow in one direction,

$$\bar{u}_i = (\bar{u}, 0, 0) \quad (6.22)$$

3. The turbulent flux in the x direction is small, hence its divergence, $\frac{\partial(\bar{u}'c'_n)}{\partial x}$, is negligible.
4. The eddy diffusivities, $K_{ij,n}$, are much larger than the molecular diffusivity, $K_{ij,n} \gg \mathcal{D}$, and so the molecular transport terms may be neglected. The $K_{ij,n}$ and \mathcal{D} terms in (6.21) are additive, therefore a single diffusivity could be defined as,

$$K_{ij,n} = K_{ij,n} + \mathcal{D}$$

where \mathcal{D} forms a small additive offset. In the remaining discussions \mathcal{D} will be neglected.

5. The cross-component terms, ($i \neq j$), of $K_{ij,n}$ are assumed negligible so that,

$$K_{ii,n} \rightarrow K_{yy,n}, \quad K_{zz,n}$$

These terms are also assumed to be functions of x only.

6. The dissipation term is modelled in a way similar to Csanady (1973), but for higher order total moments as,

$$\epsilon_n = \frac{\overline{c^n}}{t_{d,n}} \quad (6.23)$$

where $t_{d,n}$ is a decay time scale for the $\overline{c^n}$ fluctuations, and is a linear function of travel time x/\bar{u} , (see Appendix H).

$$t_{d,n} = \frac{2}{\bar{u}\alpha}(x - x_o) \quad (6.24)$$

The dissipation is assumed to be a function of down-wind distance, x , only. Including (6.23) in the budget equation (6.21), causes the centre-line values of $\overline{c^n}$ to decay more quickly, (by a factor of $\exp(-x/t_{d,n}U)$). Since x/U is travel time, t_t , and Netterville (1979) has found that $t_d \propto t_t$, then t_t/t_d is expected to be a weak function of x or approximately constant. The exponential term is, therefore approximately a constant value. Hence, the decay time reduces the centre-line concentrations at each location by a constant fraction.

Substituting these assumptions into (6.21) produces a set of parabolic governing equations for \bar{c}^n .

$$\bar{u} \frac{\partial \bar{c}^n}{\partial x} = K_{yy,n} \frac{\partial^2 \bar{c}^n}{\partial y^2} + K_{zz,n} \frac{\partial^2 \bar{c}^n}{\partial z^2} \quad (6.25)$$

A solution of (6.25) is the Gaussian distribution, see Appendix H.

$$\bar{c}^n(x, y, z) = \bar{c}_o^n(x) \exp\left(-\frac{y^2}{2\sigma_{y,n}^2}\right) \exp\left(-\frac{z^2}{2\sigma_{z,n}^2}\right) \quad (6.26)$$

with

$$\bar{c}_o^n(x) = C_s^n \exp\left(-\frac{x}{t_{d,n}\bar{u}}\right)$$

where C_s^n is the centre-line value of the n^{th} moment in a non-dissipating environment in which $t_{d,n} \gg x/\bar{u}$. $\sigma_{y,n}^2 = 2K_{yy,n}x/\bar{u}$ and $\sigma_{z,n}^2 = 2K_{zz,n}x/\bar{u}$ are the standard deviations of the spread of the \bar{c}^n plume in the y and z directions.

In Figure 6.1 a typical mean concentration profile is presented in semi-log format. It can be seen that the Gaussian distribution is a good representation of the first moment out to 4 standard deviations. The observed 2nd through 4th higher order zero-based total moments of concentration are also presented in the figure. The concentration moments are normalized by their respective fitted centre-line maximum value and their fitted standard deviations, which are different for each moment. The Gaussian distribution for the higher order moments is seen to be an excellent representation of the data over a range of at least four orders of magnitude.

The higher order moments for the jet/plume source are shown in Figure 6.2 and Figure 6.3. Figure 6.4 and Figure 6.5 show the higher order moments for the iso-kinetic source, Figure 6.6 and Figure 6.7, for the up-wind facing iso-kinetic source, and Figure 6.8, the vertical/jet source. The Gaussian fit is a good representation of the data at each of the down-wind locations tested. Near the source, the plume spread is difficult to determine, because of data variability (see Appendix B.5), and some of the profiles are not as well represented by the Gaussian profile. However, overall the figures show that the Gaussian distribution is a good representation of the concentration higher order moments.

It should be noted that the $K_{yy,n}$'s in (6.25) are not equal, i.e. it is not generally true that $K_{yy,1} = K_{yy,2}$. This implies that it is not generally true that $\sigma_{y,1} = \sigma_{y,2}$. This is consistent with the meandering plume models which will be presented in section 6.2.2, that will demonstrate that $\sigma_{y,1} \neq \sigma_{y,2} \neq \sigma_{y,3}$ etc.. Csanady (1973), Netterville (1979) and others have assumed that the $K_{yy,1} = K_{yy,2}$ are equal and tried to model the fluctuating concentration variable \bar{c}'^2 .

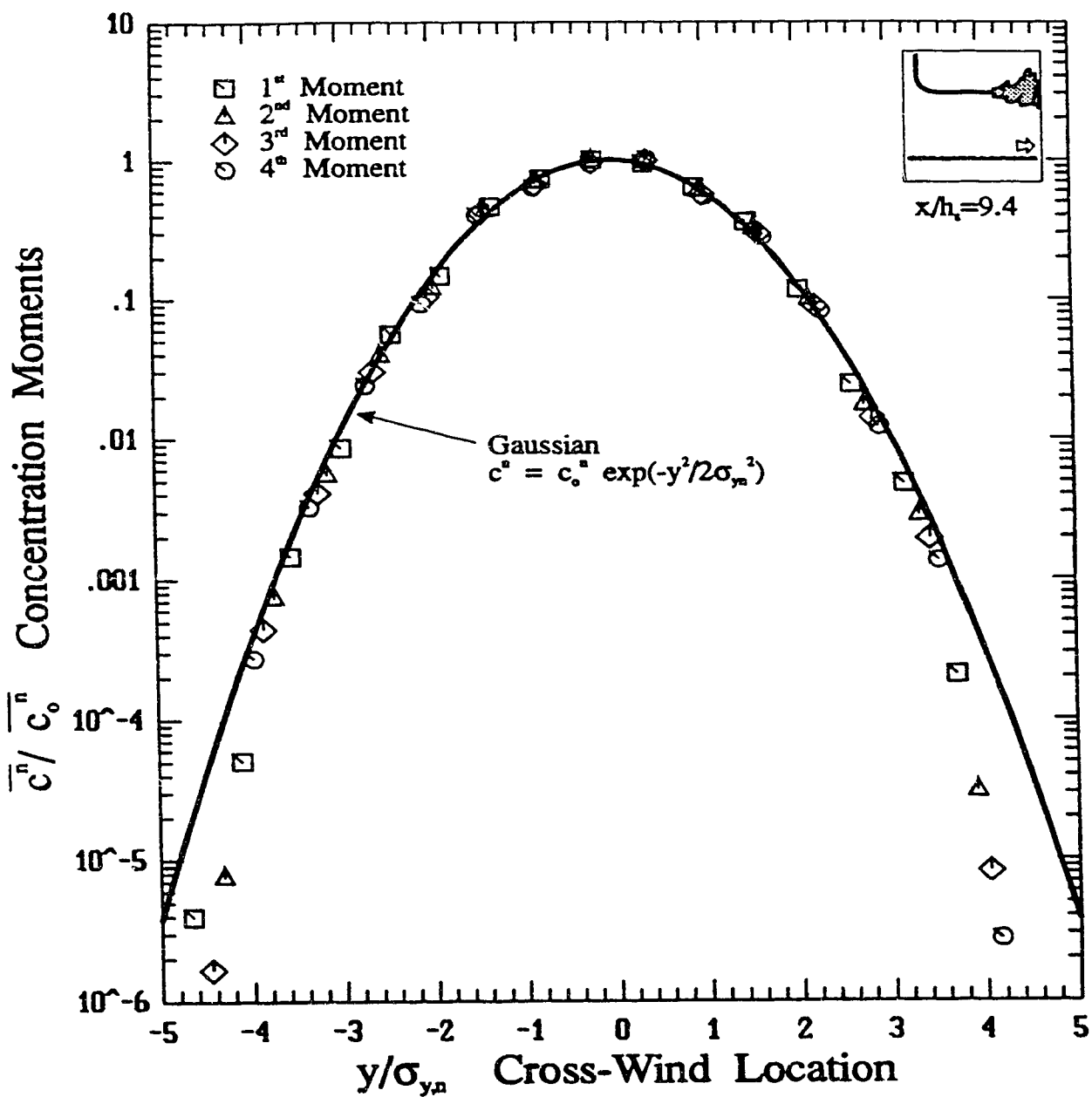


Figure 6.1: Gaussian fit to a typical set of the first four higher order moments for the jet/plume source. Each moment is normalized by its fit maximum centre-line value and its fit standard deviation.

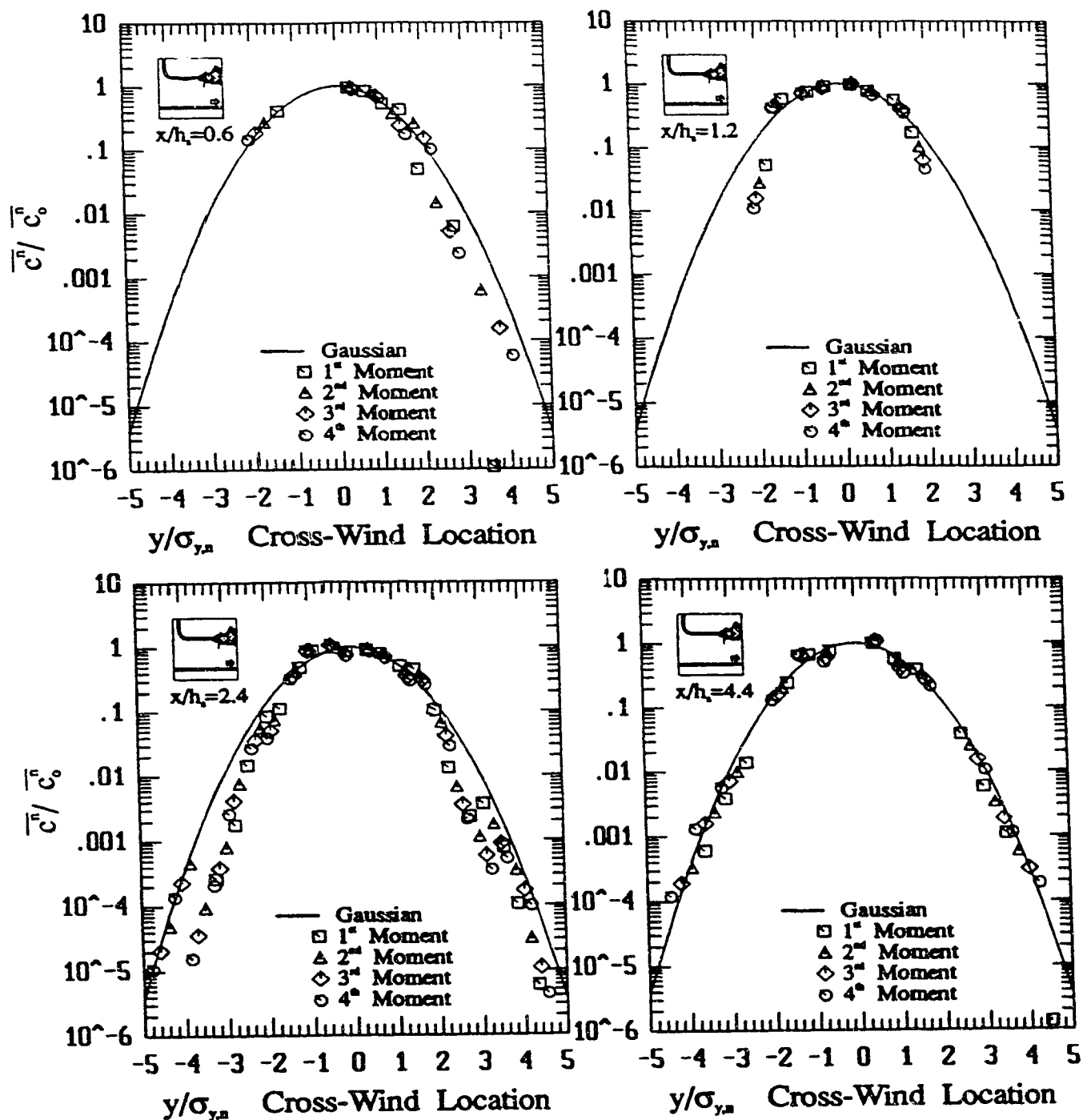


Figure 6.2: Normalized higher order moments with a Gaussian fit for the jet/plume source. Each moment is normalized by its fit maximum centre-line value and its fit standard deviation.

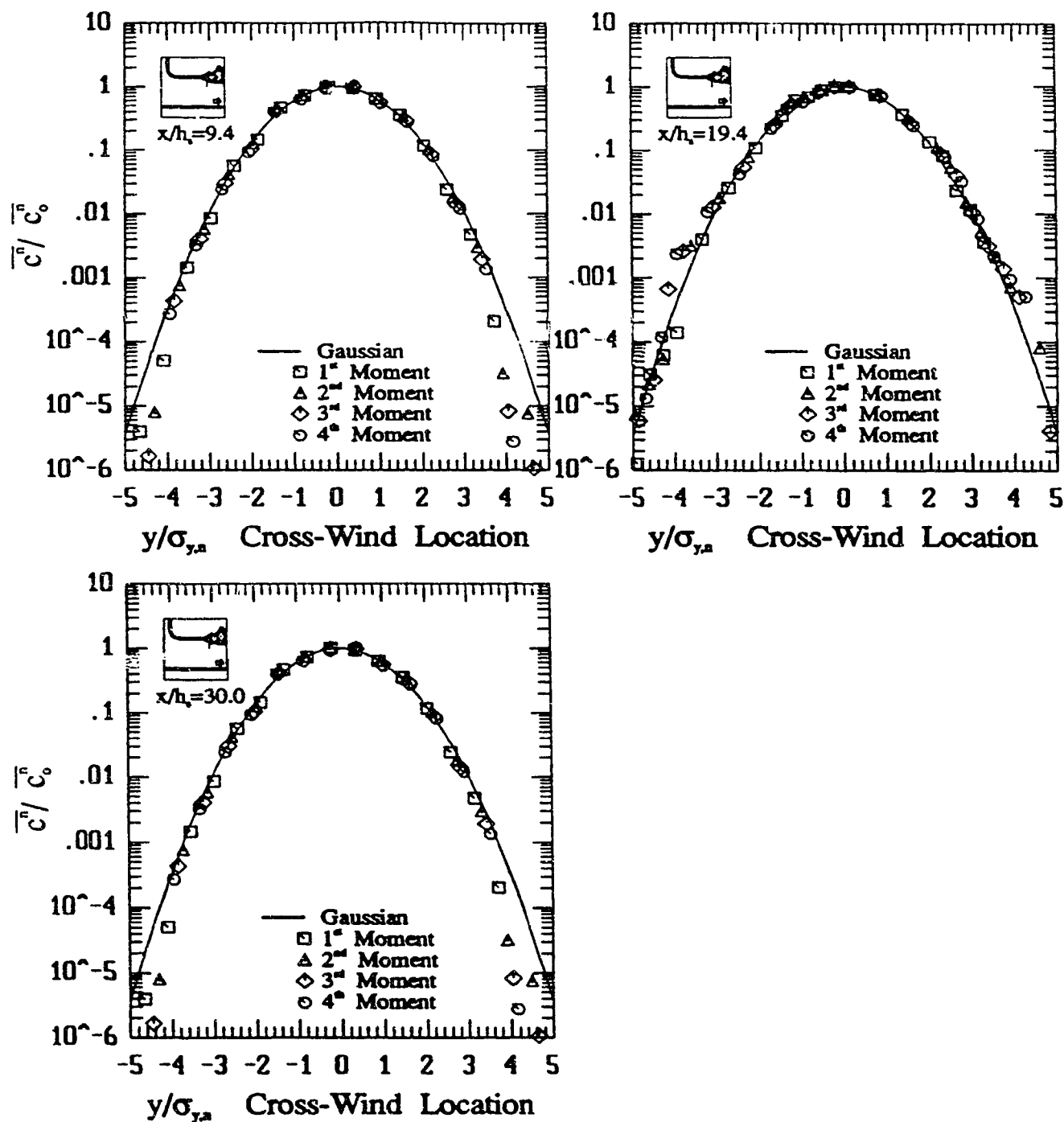


Figure 6.3: Normalized higher order moments with a Gaussian fit for the jet/plume source. Each moment is normalized by its fit maximum centre-line value and its fit standard deviation.

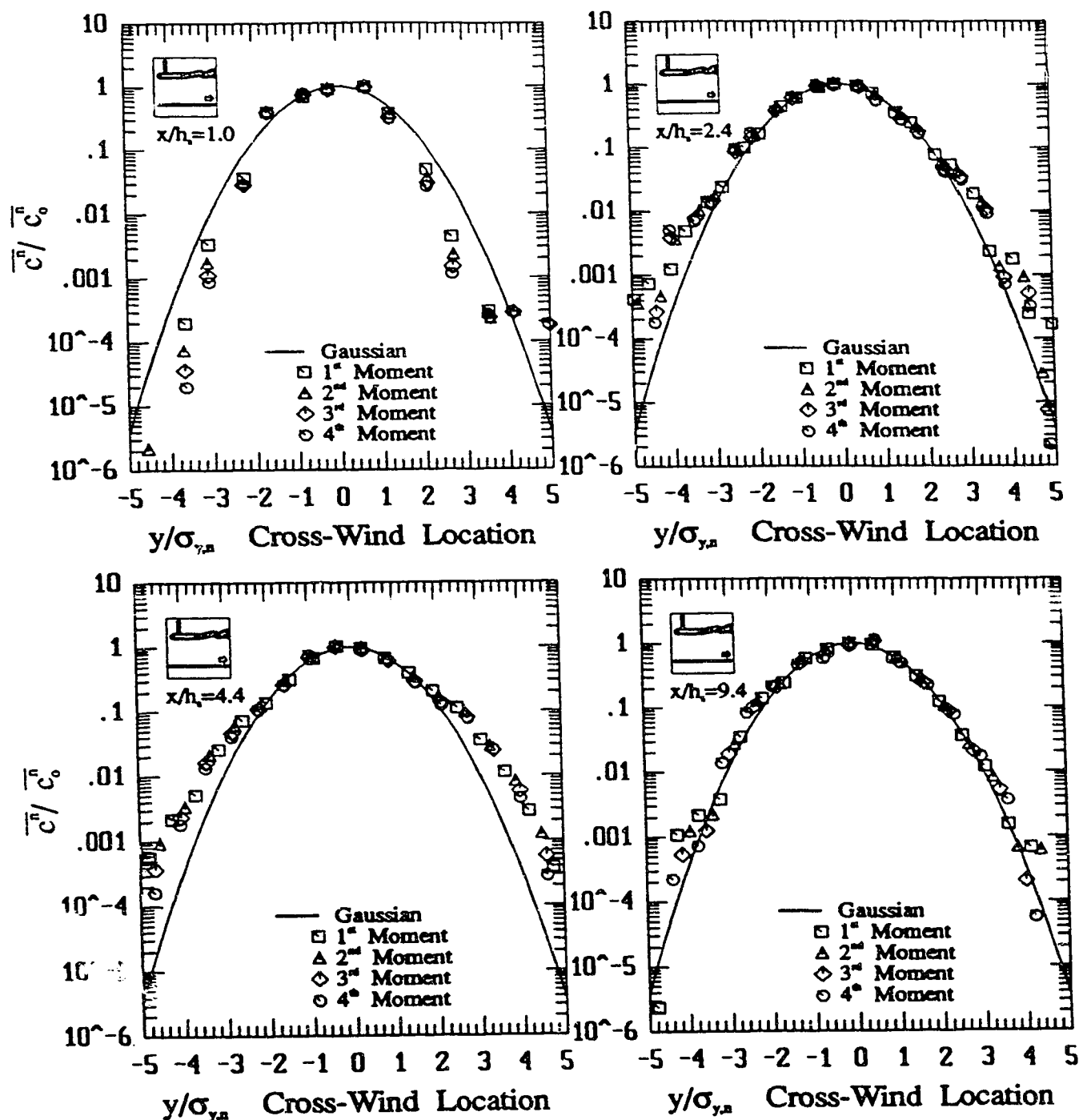


Figure 6.4: Normalized higher order moments with a Gaussian fit for the isokinetic source. Each moment is normalized by its fit maximum centre-line value and its fit standard deviation.

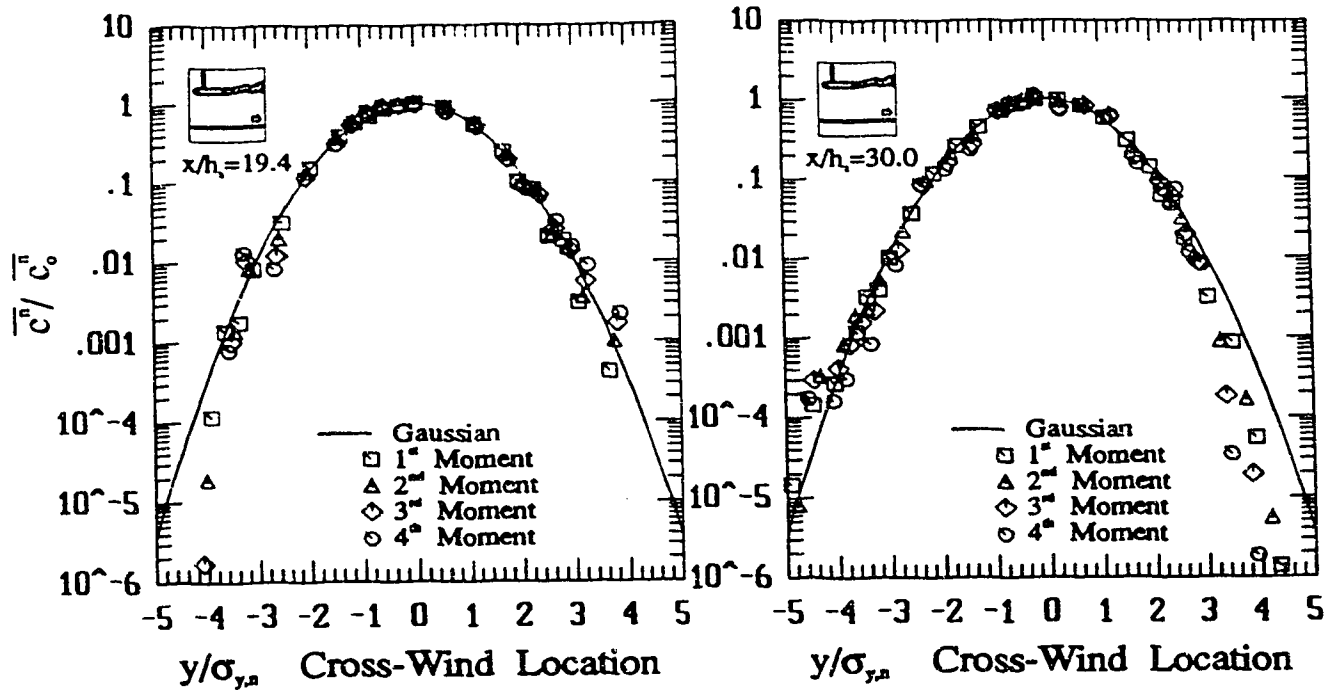


Figure 6.5: Normalized higher order moments with a Gaussian fit for the isokinetic source. Each moment is normalized by its fit maximum centre-line value and its fit standard deviation.

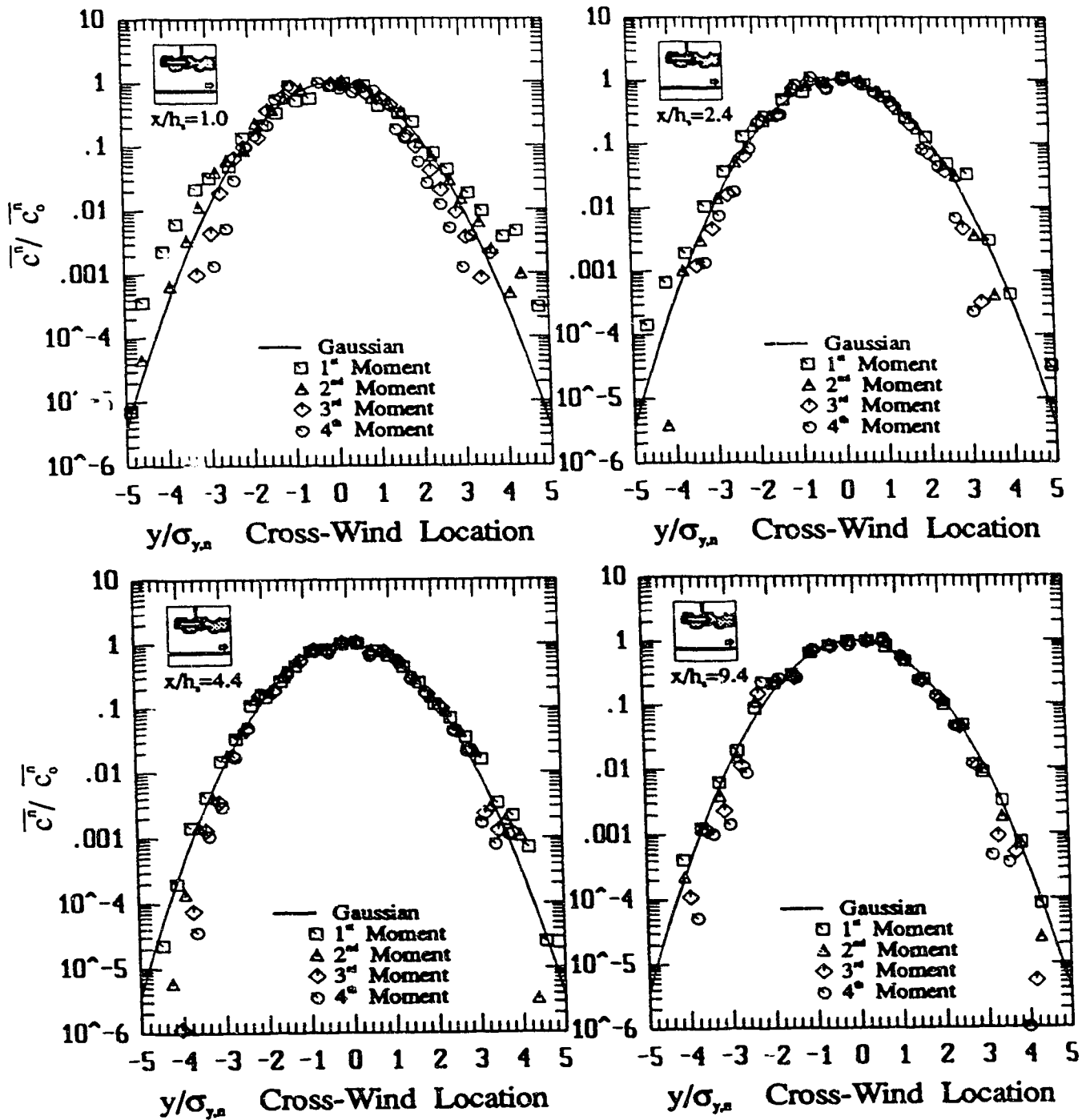


Figure 6.6: Normalized higher order moments with a Gaussian fit for the up-wind facing iso-kinetic source. Each moment is normalized by its fit maximum centre-line value and its fit standard deviation.

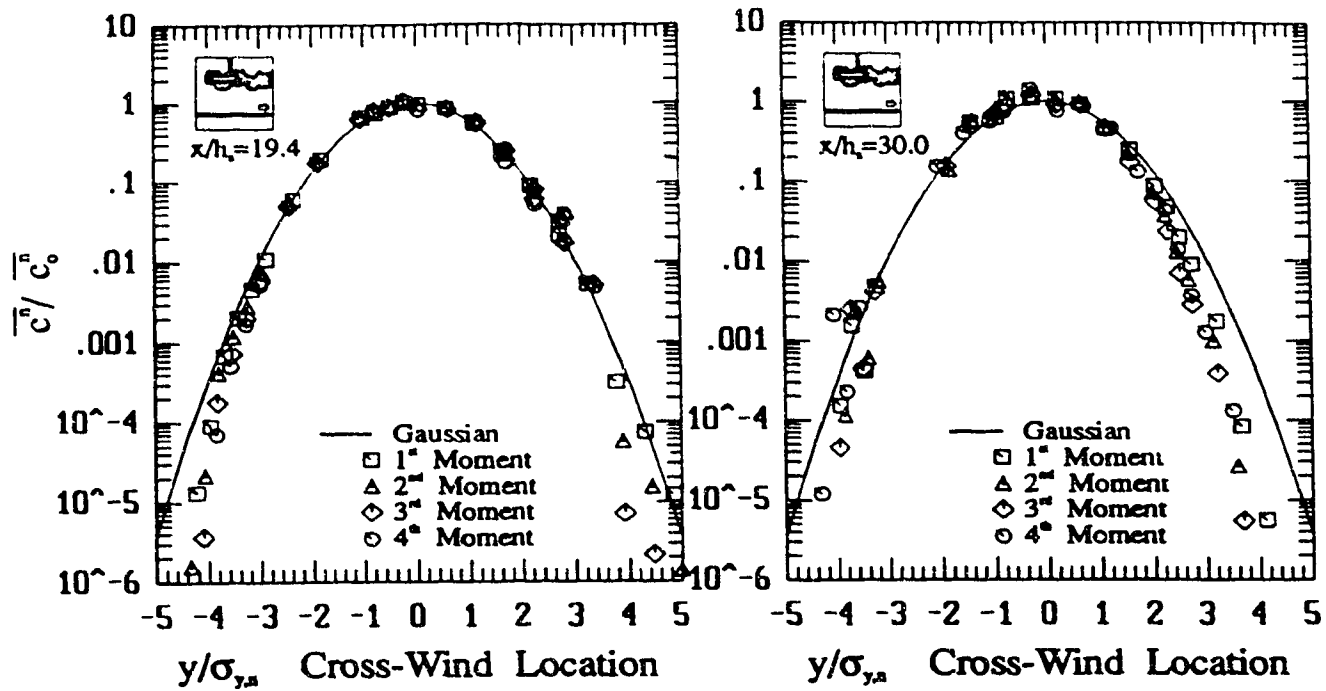


Figure 6.7: Normalized higher order moments with a Gaussian fit for the up-wind facing iso-kinetic source. Each moment is normalized by its fit maximum centre-line value and its fit standard deviation.

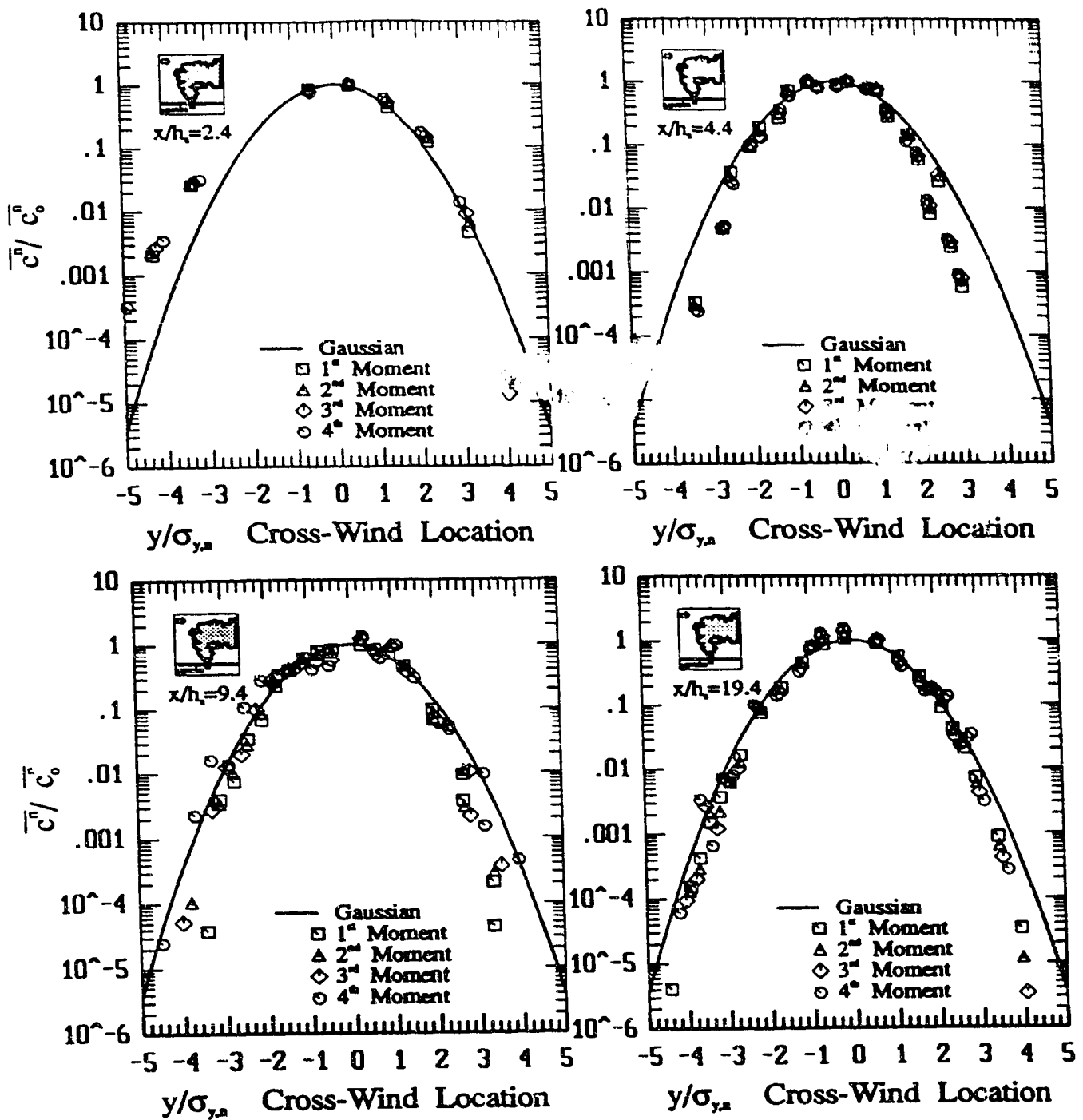


Figure 6.8: Normalized higher order moments with a Gaussian fit for the vertical jet source. Each moment is normalized by its fit maximum centre-line value and its fit standard deviation.

6.2 Plume Moment Standard Deviations

The concentration profile cross-wind plume standard deviations were calculated in four ways, discussed in Appendix B.4. In practice, it was found that the statistical method and the Gaussian fit method provide nearly the same results. (within at most 2-5% difference). The 10% method and the area/ C_{\max} method were avoided because of the problems noted in Appendix B.4. The Gaussian fit procedure was selected for use in this study over the simplicity of the statistical method because it also produced estimates for the plume centre-line value and the maximum concentration in the profile, as outlined in Appendix B.5.

The spread of the plume, σ_y , in (6.26), is well represented by a power law function of x relationship for the jet/plume source. Figure 6.9 and Figure 6.10 show the distributions of the cross-wind spreads with down-wind distance, and power law predictions for σ_y . The presence of sidewall boundaries in experimental plumes reduces the amount of meandering and as a result the plume spreads observed in the water channel indicate very stable conditions. Even the sources with perceived large amounts of meandering compared to the jet/plume source, such as the ground level source and the up-stream pointed source, also behave as if the release was in a strongly stable environment with little meandering.

Cross-wind spreads in near neutral conditions in full scale plumes in the atmosphere vary as $\sigma_y \propto x^{0.8}$, (Pasquill and Smith (1983), p.194 or 338). The power law relationships for the experimental sources are,

Jet/Plume Source

$$\sigma_y = 0.135 x^{0.73} \text{ mm} \quad (6.27)$$

Iso-Kinetic Source

$$\sigma_y = 0.097 x^{0.80} \text{ mm} \quad (6.28)$$

Vertical Ground level Source

$$\sigma_y = 0.372 x^{0.60} \text{ mm} \quad (6.29)$$

Up-stream Facing Jet Source

$$\sigma_y = 0.319 x^{0.59} \text{ mm} \quad (6.30)$$

An alternative functional form for the plume spread was given by Draxler (1976), and was investigated further by Gifford (1987). Draxler assumed the following simple

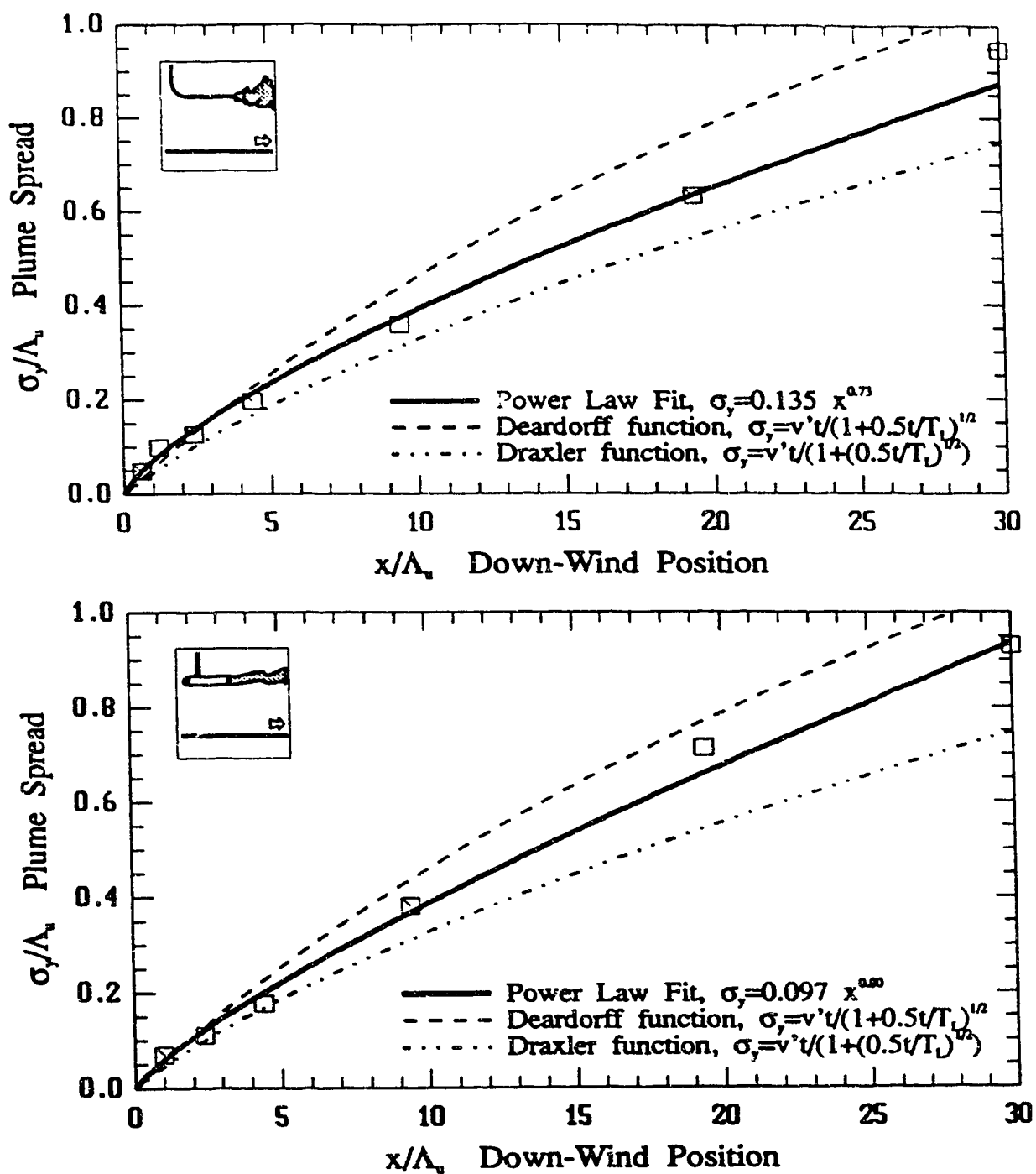


Figure 6.9: Jet/Plume source (top) and Iso-Kinetic source (bottom) plume spread evolution with down-wind distance.

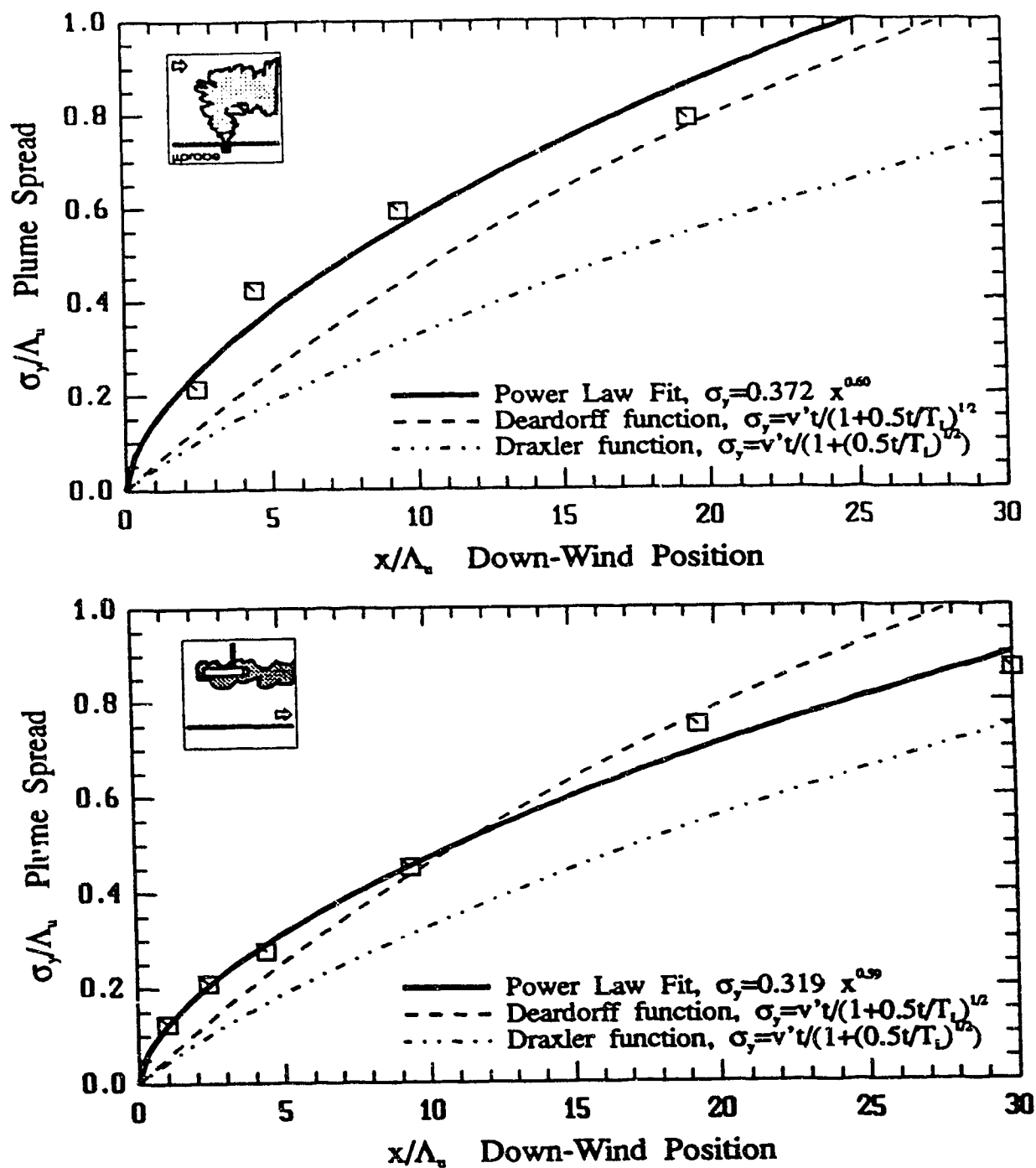


Figure 6.10: Vertical ejecting ground level source (top) and up-stream facing iso-kinetic source (bottom) plume spread evolution with down-wind distance.

curve,

$$\sigma_y = \frac{v' t}{1 + 0.9a(t/T_{L,v})^{1/2}} \quad (6.31)$$

where:

- v' is the standard deviation of the lateral component of the turbulent wind at the source
- $T_{L,v}$ is the Lagrangian time scale
- a is a fitted constant
- t is the travel time, $t \approx x/U$

Deardorff and Willis (1975) have suggested a similar functional form for the plume spread,

$$\sigma_y = \frac{v' t}{(1 + 0.5(t/T_{L,v}))^{1/2}} \quad (6.32)$$

The Lagrangian time scale may be estimated using the relation, (Hanna, Briggs and Hosker, 1982, p.10),

$$T_{L,v} \approx \frac{0.5}{v'/U} T_{E,v} \approx \frac{0.5\Lambda_v}{v'} \quad (6.33)$$

Substituting, this into (6.32),

$$\sigma_y = \frac{\left(\frac{v'}{U}\right) x}{\left(1 + \left(\frac{v'}{U}\right) \frac{x}{\Lambda_v}\right)^{1/2}} \quad (6.34)$$

From Panofsky and Dutton (1984) p.160, the turbulence quantities are estimated as $v'/u_* \approx 1.92$ and $u'/u_* \approx 2.39$, (see section 3.3.4). Then:

$$\frac{v'}{U} = \frac{1.92}{2.39} \left(\frac{u'}{U}\right) \approx 0.8 \left(\frac{u'}{U}\right) \quad (6.35)$$

In addition if $\Lambda_v \approx \Lambda_u$, then the Deardorff and Willis plume spread is approximately,

$$\sigma_y \approx \frac{0.8 \left(\frac{u'}{U}\right) x}{\left(1 + 0.8 \left(\frac{u'}{U}\right) \frac{x}{\Lambda_u}\right)^{1/2}} \quad (6.36)$$

Assuming, for simplicity that $a = 1/0.9$, and applying the same substitutions to (6.31), the Draxler plume spread is approximately,

$$\sigma_y \approx \frac{0.8 \left(\frac{u'}{U} \right) x}{1 + \left(0.8 \left(\frac{u'}{U} \right) \frac{x}{\Lambda_u} \right)^{1/2}} \quad (6.37)$$

Equations (6.36) and (6.37) are shown in Figure 6.9 and Figure 6.10, using the turbulence intensity at the source height, $u'/U \approx 0.09$, (see Figure 3.3), and $\Lambda \approx 50\text{mm}$. These functions show good agreement with the observed plume spreads. The Deardorff and Willis (1975) function over-estimates the plume spread by 5-10% and the Draxler (1976) function under-estimates the plume spread by about 5-10% for the jet/plume source and iso-kinetic source. The vertical jet source and the up-wind facing iso-kinetic source plume spreads are under-estimated by these two predictions by up to about 50%.

For general application, the plume spread function should incorporate a virtual origin of the form $x' = x + x_o$ or $\sigma_y' = \sigma_y + \sigma_o$. Both representations are easily added to the power law expressions or to (6.36) and (6.37). However, given the variability and the low resolution of the plume spread data, a virtual origin could not be accurately estimated.

6.2.1 Profile Normalization

In section B.5, a parametric study was performed using the Gaussian fit procedure on a statistically generated profile. The profile was generated by randomly selecting sixteen y/σ_y location across a standard Gaussian profile using a uniform random distribution, in the range $-5 < y/\sigma_y < 5$. One hundred simulations were performed to acquire a statistical representation. The estimated centre of the profile was determined to be within 0.3% of the expected value, compared to a 3% error using the statistical mass centroid. The spread and maximum values were within 2.5% and 4% respectively of the estimated value. Noise was added to individual points by adding Gaussian distributed absolute errors, and alternatively Gaussian distributed fractional errors. The errors were added selectively to both the y/σ_y location values and the concentration values. This simulated the possibility of a displacement error of the concentration detector and for actual noise or errors in the recorded data.

For large absolute errors in the concentration magnitude, 10% of maximum profile value, the profile centre was estimated within 10%. The profile spread was estimated

high by 25% of expected but had a statistical deviation of nearly 100%. The profile maximum value was estimated low by 8% of expected, with a statistical deviation of 25%. When fractional errors were introduced, more weight was given to points in the fringes of the profile. The fits for large fractional errors, 10% of the local concentration value, are slightly smaller than that for the large absolute errors, except for the maximum centre-line value. This point was consistently estimated low (at worst 50% too low, with a statistical deviation of 50%). Similar results were found when the actual error was a small fractional error and the assumed error in the numerical fitting procedure was a large fractional error, or vice versa.

The conclusion here, is that the Gaussian fit method provides a robust fit to the data profile. For data sets that are sparse and with large data variability, as simulated above, the plumes spreads determined by the Gaussian fit will be over-estimated and the maximum centre-line value will be under-estimated.

6.2.2 Plume Standard Deviations of Higher Order Moments

The budget equations do not predict what the plume standard deviations, $\sigma_{y,n}$, are, or the relationship of the plume standard deviations to each other. But they do predict that they are unequal and that they are less than the first moment spread. A similarity theory proposed by Wilson and combined with the experimental study by Zelt, produced a model for the relationship between the standard deviations of the higher order moments, Wilson and Zelt (1988). Although the basis of the profile similarity model is a two dimensional meandering plume in isotropic turbulence, it is able to accurately model the dispersion of a plume in a boundary layer.

The profile similarity theory for dispersion in homogeneous turbulence is based on two assumptions:

1. The cross-wind profiles of all $\overline{c^n}$ moments are Gaussian, each with a different standard deviation, $\sigma_{y,n}$.
2. The standard deviation, $\sigma_{y,n}$, for the n^{th} moment is the same as that of a meandering non-turbulent plume that exhibits the same centre-line fluctuation intensity, i_o , as the turbulent plume.

The second assumption allows Gifford's (1959) non-turbulent meandering plume model to form the basis for determining the higher order moment standard deviations, $\sigma_{y,n}$, in terms of the mean concentration (first moment) spread, σ_y .

Gifford (1959), uses a meandering plume model in two dimensions and in isotropic turbulence, with $\sigma_y = \sigma_z$, to show that,

$$\frac{\overline{c_o^2}}{\overline{c_o}^2} = \frac{(\sigma_{yi}^2 + \sigma_{ym}^2)^2}{\sigma_{yi}^2 (\sigma_{yi}^2 + 2\sigma_{ym}^2)} \quad (6.38)$$

where:

- σ_{yi} is the instantaneous spread of a plume which is a function of the distance from the source or travel time.
- σ_{ym} is the spread of the plume due to the large scale turbulence of the environment on the plume.

Normalization of the terms in (6.38), produces,

$$\frac{\overline{c_o^2}}{\overline{c_o}^2} = 1 + i_o^2 = \frac{(1 + M^2)^2}{1 + 2M^2} \quad (6.39)$$

where $M = \sigma_{ym}/\sigma_{yi}$. Sawford and Stapountzis (1986), show that for a two dimensional isotropic meandering plume, with $\sigma_y = \sigma_z$, the n^{th} moment is predicted as,

$$\sigma_{y,n}^2 = \frac{\sigma_{yi}^2 + n\sigma_{ym}^2}{n} \quad (6.40)$$

where:

- n is the higher order moment of interest,
- $\sigma_{y,n}$ is the plume standard deviation for the profile of n^{th} moment of concentration.
- $\sigma_{y,1}$ is σ_y the plume spread for the mean concentration \bar{c} .

Normalizing (6.40) by the first order prediction $\sigma_y^2 = \sigma_{ym}^2 + \sigma_{yi}^2$, produces,

$$\frac{\sigma_{y,n}^2}{\sigma_y^2} = \frac{1 + nM^2}{n(1 + M^2)} \quad (6.41)$$

The expression (6.41) predicts the standard deviation of the higher order moment profile given knowledge of σ_y and i_o^2 . M may be determined solving (6.39) by iteration for a specified i_o^2 .

The relationship (6.41) predicts that $\sigma_{y,n} < \sigma_{y,1}$. The water channel experiments show that (6.41) models the observed standard deviations, but for some observed profiles the fitted plume standard deviations are poor representations of the data, so

that (6.41) does not compare well to the fit plume standard deviations. However, the use of (6.41) to predict higher order plume standard deviations, and concentration higher order moments, produces good agreement with observed profiles, which will be presented later. Therefore, the poor representation of (6.41) to the data, is a result of a poor fit of the higher order plume standard deviations to the data profiles.

In Figure 6.11 and Figure 6.12, (6.41) is compared to the plume standard deviations of the higher order moments observed for the sources in the water channel. The higher order standard deviations were determined experimentally using the same procedure as when determining σ_y . It is worth noting, however, that with increasing order, the effects of data uncertainty on the fit tend to increase. With data uncertainty effects and poor data profile resolution, the higher order moments are often difficult to fit. These effects are clearly visible in the figures.

In general, the jet/plume source, Figure 6.11(top), and the iso-kinetic source, Figure 6.11(bottom), both agree well with the predicted trends of the standard deviations. Near the source the data profiles are sparse and variable, and the resulting fits are poor. Elsewhere in the evolution of the plume, the trend indicated by (6.41) is observed but not closely matched. Recall that in section 6.2.1, sparse, large variability or ill-defined data sets result in the fit centre-line maximum values being too low, and the spreads too high, by magnitudes of 5% to 25%. The deviation from the predicted behaviour is explained by these deviation errors.

The vertical ground level source, Figure 6.12(top), and the up-wind facing source, Figure 6.12(bottom), do not follow the trends indicated by (6.41). The reasons for this are not clear. The vertical jet source data is sparse which may cause the near source data to differ from that predicted. Although, the up-wind facing iso-kinetic source is not sparsely represented, the plume standard deviations do not represent the data well, according to a Gaussian profile, (see Figure 6.6).

An important restriction on the range of applicability of the eddy-diffusion model is discussed by Taylor (1921). The eddy-diffusion model is applicable only in the long time regime of $t \gg T_L$ (T_L being the Lagrangian time scale) where $\sigma_{y,n}$ exceeds the characteristic eddy size. The eddy-diffusion model developed here uses a Gaussian profile in both the far field and the near field, using a meandering plume model to predict the profile standard deviations. The meandering plume model, however, is more appropriate at short times, $t \ll T_L$. Sawford and Stapountzis (1986) have found that a Gaussian profile is expected for a two-dimensional meandering plume as well (see (6.43)). Therefore, the Gaussian profile predicted, in both the far field and the near field, by the model presented here seems valid.

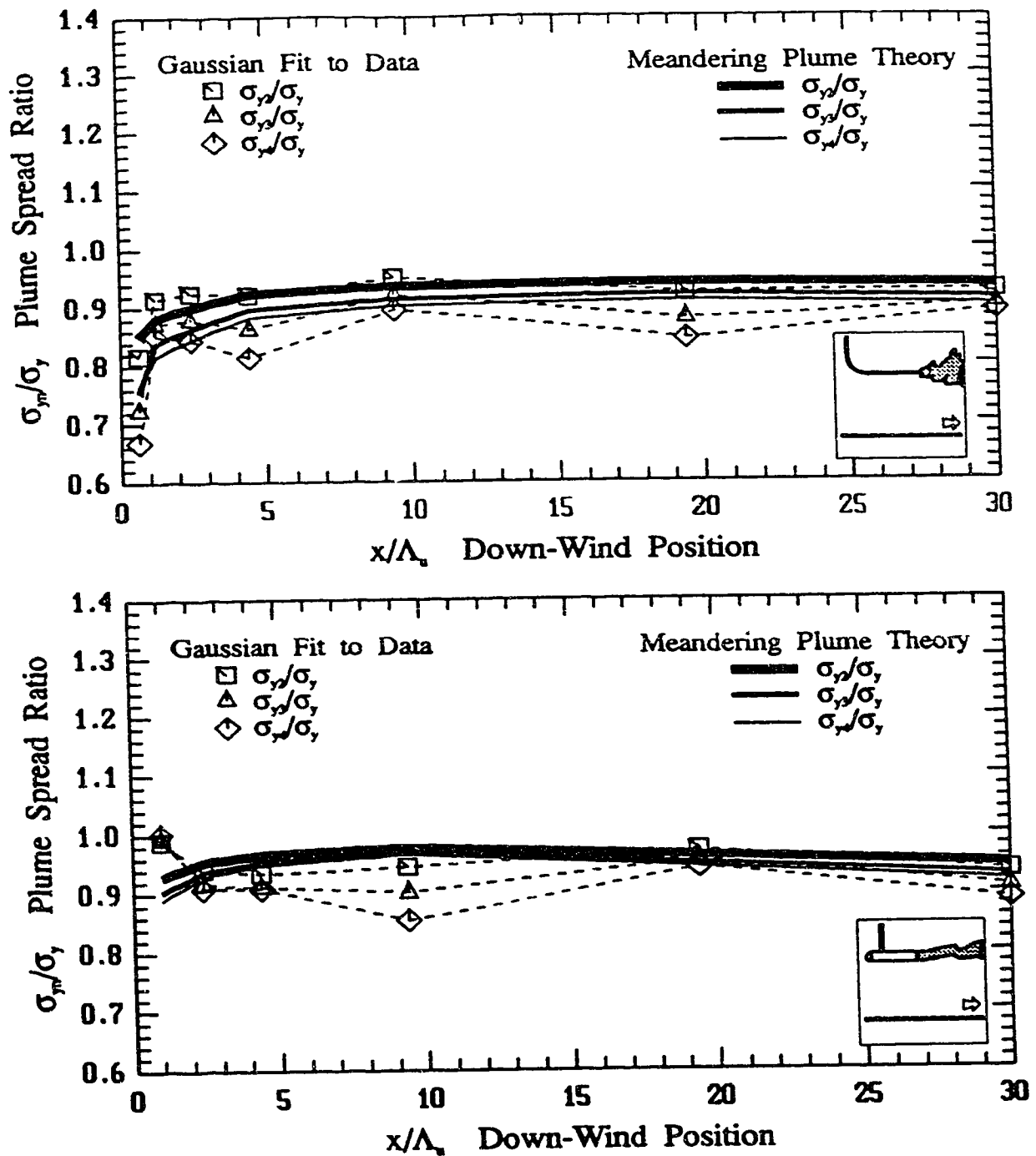


Figure 6.11: Jet/Plume source (top) and Iso-Kinetic source (bottom) higher order plume standard deviations ratio of $\sigma_{y,n}/\sigma_{y,1}$ evolution with down-wind distance. Solid lines are (6.68).

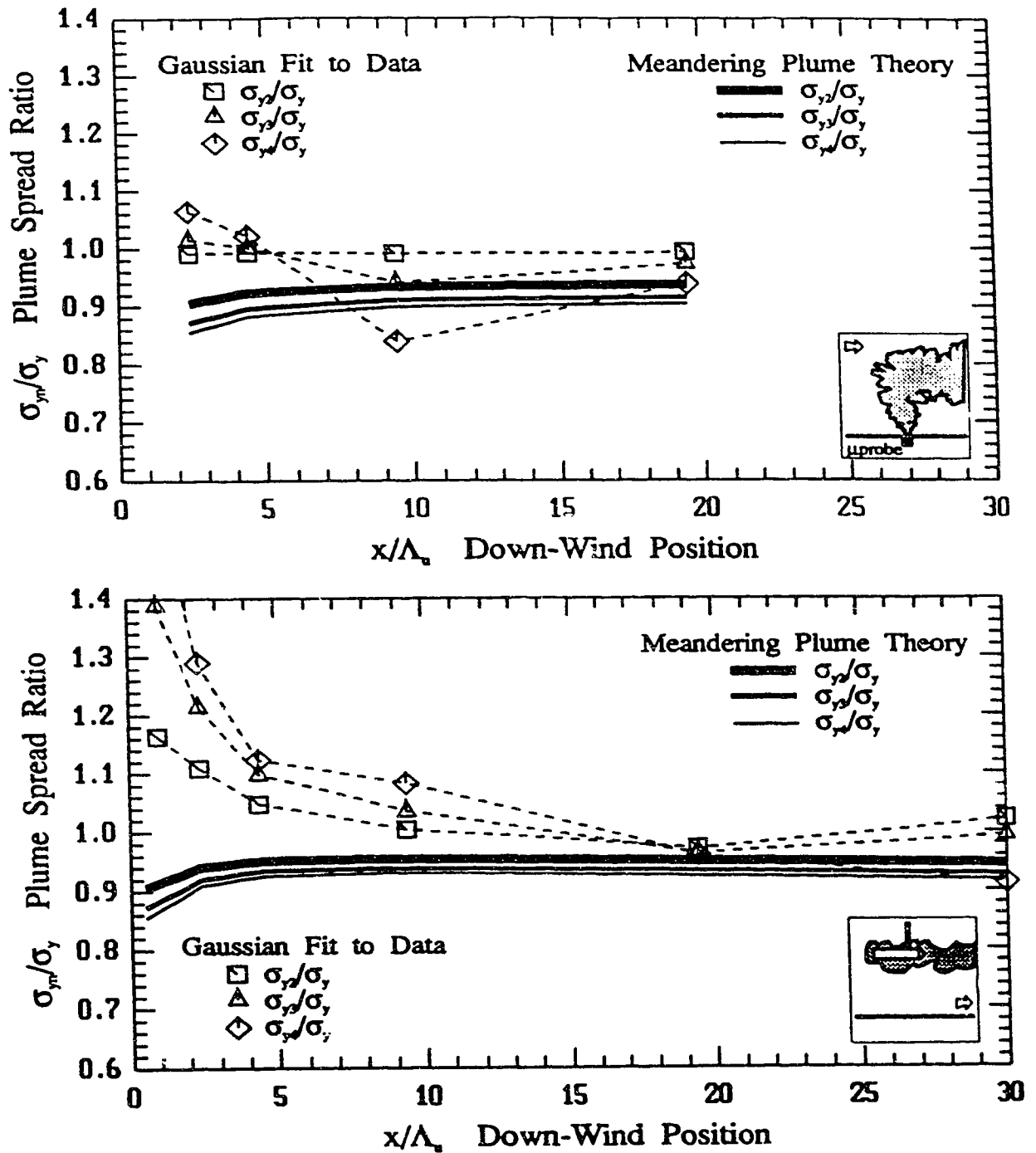


Figure 6.12: Vertical jet source (top) and up-stream facing horizontal source (bottom) higher order plume standard deviations ratio of $\sigma_{v,n}/\sigma_{v,1}$ evolution with down-wind distance. Solid lines are (6.68).

6.3 Intermittency Threshold

Of the three procedures described in section B.7 for determining signal presence or absence, the procedure based on a noise relative threshold yielded the best results. It, however, has some difficulties. The primary difficulty is selecting the appropriate number of σ_{noise} 's so that the data may be properly filtered to eliminate the effects of noise. The intermittency threshold was initially selected as $3\sigma_{\text{noise}}$'s which will include 99.87% of the noise according to the normal distribution curve. However, as the signal analysis improved and digital filtering was optimized, the contribution of the background noise level to the problem of determining the intermittency was reduced. The relative importance of the the probes short term drift and signal hysteresis then became significant. Therefore, it was necessary to increase the number of background noise standard deviations to include these fluctuations in the zero periods.

In Figure 6.13, the intermittency of the data in the far *far* fringes of the plume, where the concentration is known to be zero, shows how significant the threshold level is in determining the intermittency. The meaning of the threshold level, however, as a direct indication of the noise levels is lost. It was found that a threshold level equivalent to $8\sigma_{\text{noise}}$ was required to generate the proper intermittency levels.

6.4 Similarity Theory Application to Cross-Wind Profiles

The similarity theory is expected to represent the higher order concentration moments it was derived to explain. However, the real test of the theory is in its ability to accurately describe the other plume statistics of interest, such as the variance or intensity of concentration fluctuations, and the conditional counterparts.

The variance of the concentration fluctuations is shown in Figure 6.14(top) for the same set of data as in Figure 6.1. The variance is normalized by the centre-line first moment squared, \bar{c}_0^2 , and the solid line is the predicted variance by the similarity theory. Excellent agreement is observed for at least three plume sigmas and three orders of magnitude. In the Figure 6.14(bottom) a data set close to the up-stream facing iso-kinetic source was selected. The data here is also well described by the similarity theory which predicts the off-axis peaks in the variance profile which are observed in the data. The intensity of concentration fluctuations in Figure 6.16 shows close agreement with the predictions of the similarity theory.

To predict the conditional moments, a probability model must be selected to predict the intermittency. Using the relationships described in Chapter 5, the

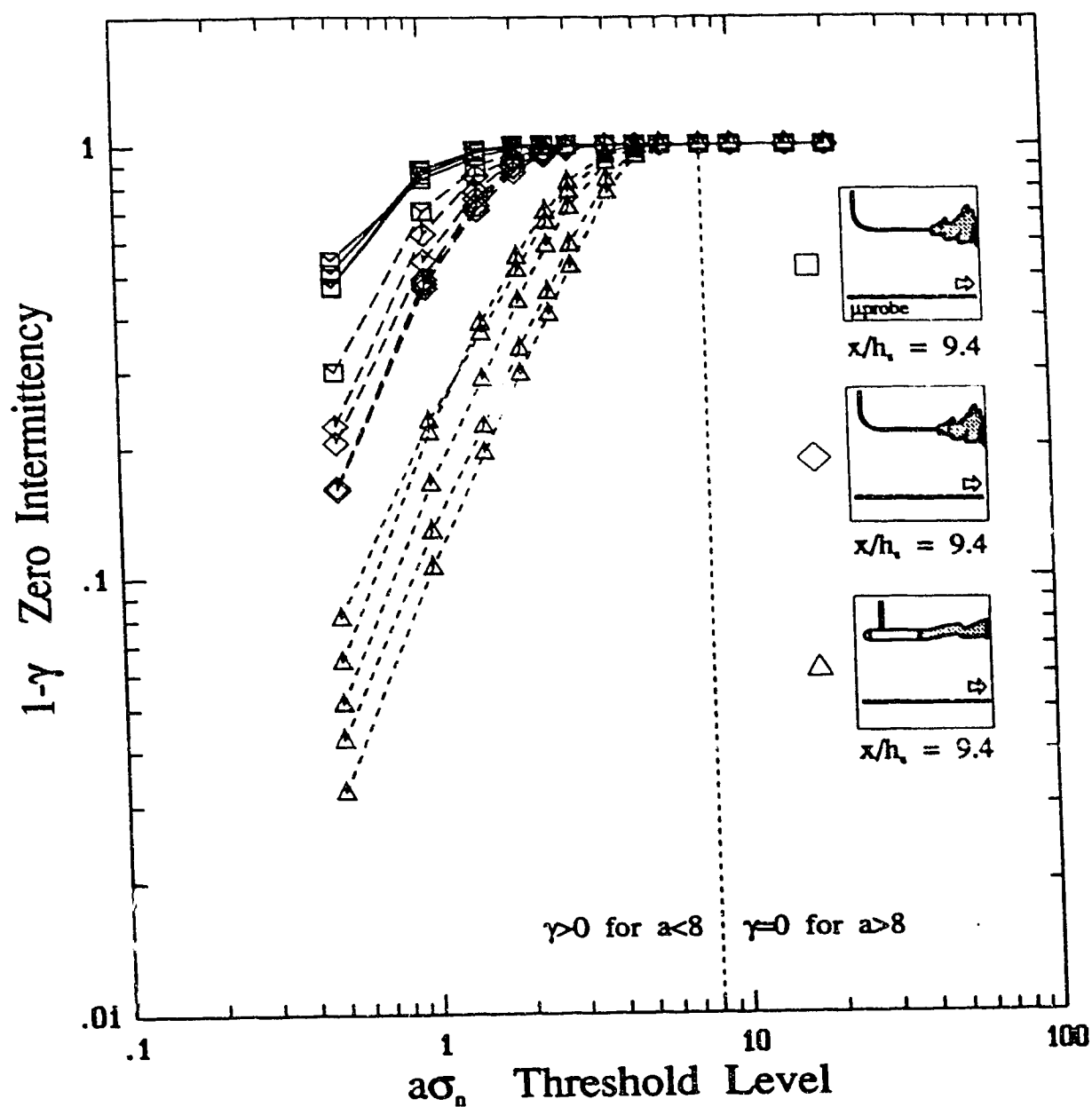


Figure 6.13: The effect of threshold level on the observed intermittency in the far fringes of the plume showing that a threshold level equivalent to $8 \sigma_{noise}$ is required.

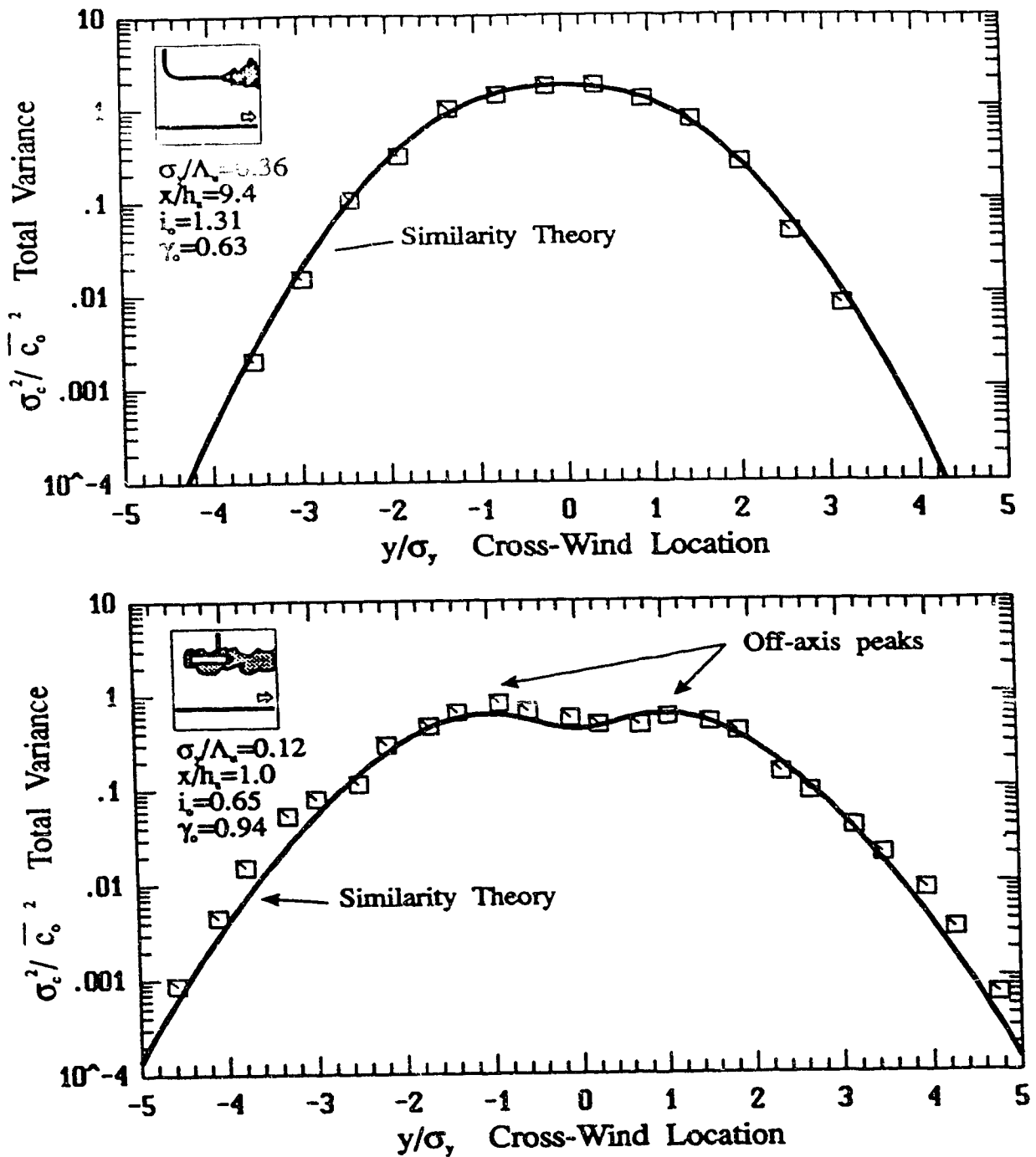


Figure 6.14: The variance of the concentration fluctuations for the data for the jet/plume source in Figure 6.1, (top), and for data near the upstream facing iso-kinetic source (bottom).

conditional concentration moments may be determined using the first three total concentration moments.

In Figure 6.15, the conditional first moment, \bar{c}_p , is shown for the same data presented in Figure 6.1. The figure does not show overwhelming agreement but the predicted physics are quite good. The data for this profile is well fit by the Gaussian distribution, and therefore the centre-line maximum values of \bar{c}_0 and \bar{c}_0^2 are within 2% of the observed values. Therefore, the difference between the theory and the data is a result of the inadequacy of the probability models to predict the intermittency, (see section 5.6). The scatter of the points in the far fringes, ($|\sigma_y| > 3$), is a result of insufficient time averaging. Because the intermittency is very low in these regions, a 500 second time average is insufficient to form a good statistical average. The points in the fringes may also be truncated by the data analysis digital filtering and the threshold levels.

The conditional intensity, i_p , is shown in Figure 6.16. The conditional intensity is not well predicted by the theory for this set of data, for some of the same reason described above. The clipped-Normal distribution is shown as a poor representation, because it cannot predict i_p values greater than one, see section 5.1.4. On the centre-line, the clipped-Normal was the better fitting probability distribution and here provides the best representation of i_p , being only 15% too low. In the fringes the Gamma distribution is the better probability distribution and this is also represented in the i_p prediction, but is a factor of two too low. This same trend is observed in the conditional first moment diagram in Figure 6.15, and is a typical observation for all the conditional moment profiles predicted in this way.

The Gamma PDF model has a singularity point that may be reached in the fringes of the plume, which is a complex function of the conditional intensity. The singularity occurs when, (see Appendix G),

$$y = \sqrt{\frac{-2 \ln \left(\frac{2\bar{c}_0^2}{\bar{c}_0^3 \bar{c}_0} \right)}{\left(\frac{1}{\sigma_y^2} + \frac{1}{\sigma_{y,3}^2} - \frac{2}{\sigma_{y,2}^2} \right)}} \quad (6.42)$$

This singularity affects the intermittency, and therefore all the conditional values, or statistics that are determined by the intermittency. Also when it is wrongly assumed that, $\sigma_y^2 = \sigma_{y,3}^2 = \sigma_{y,2}^2$, then i_p is a constant.

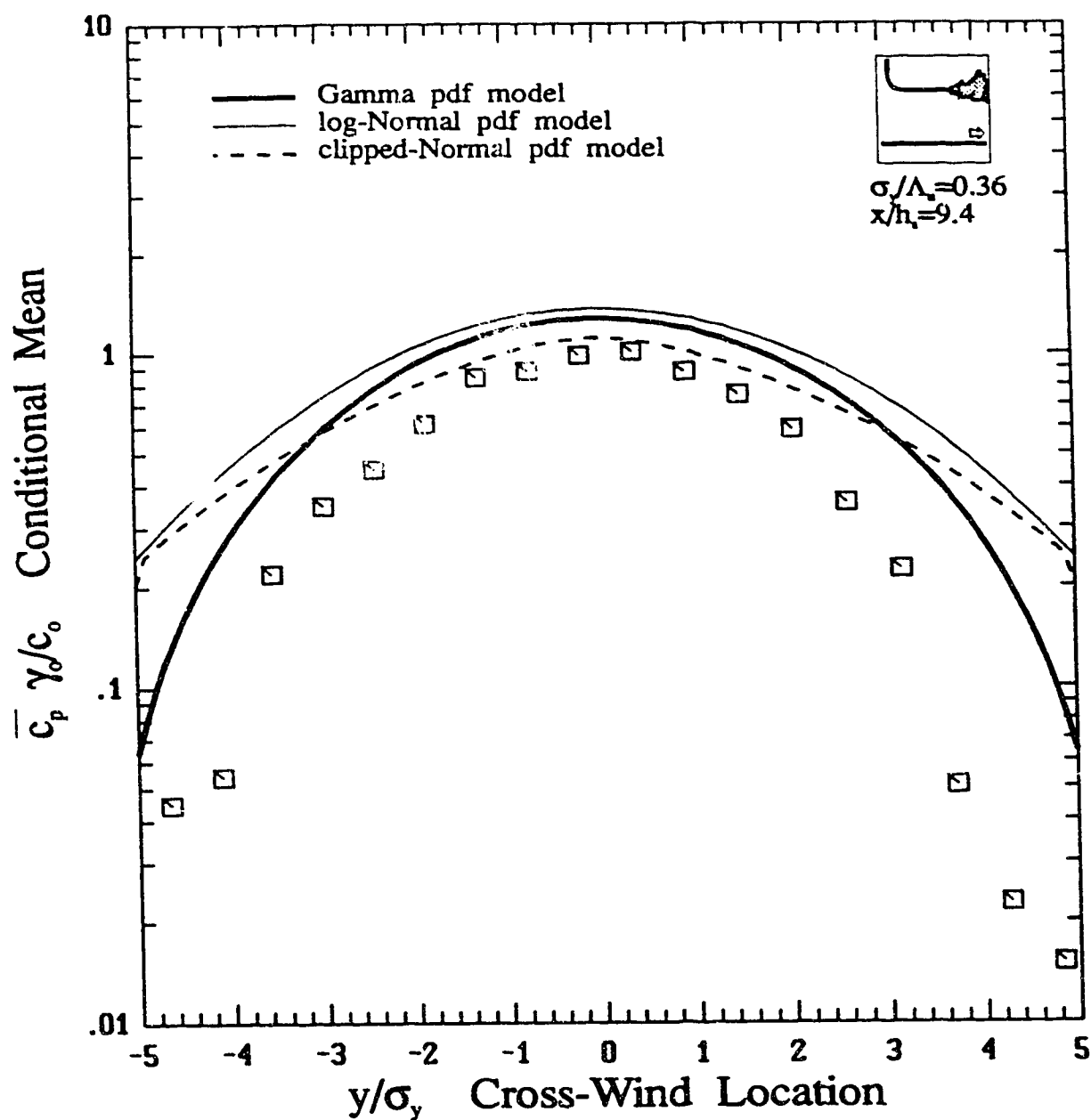


Figure 6.15: The conditional mean concentration for the jet/plume source data in Figure 6.1. Similarity and probability models used to determine the theory lines.

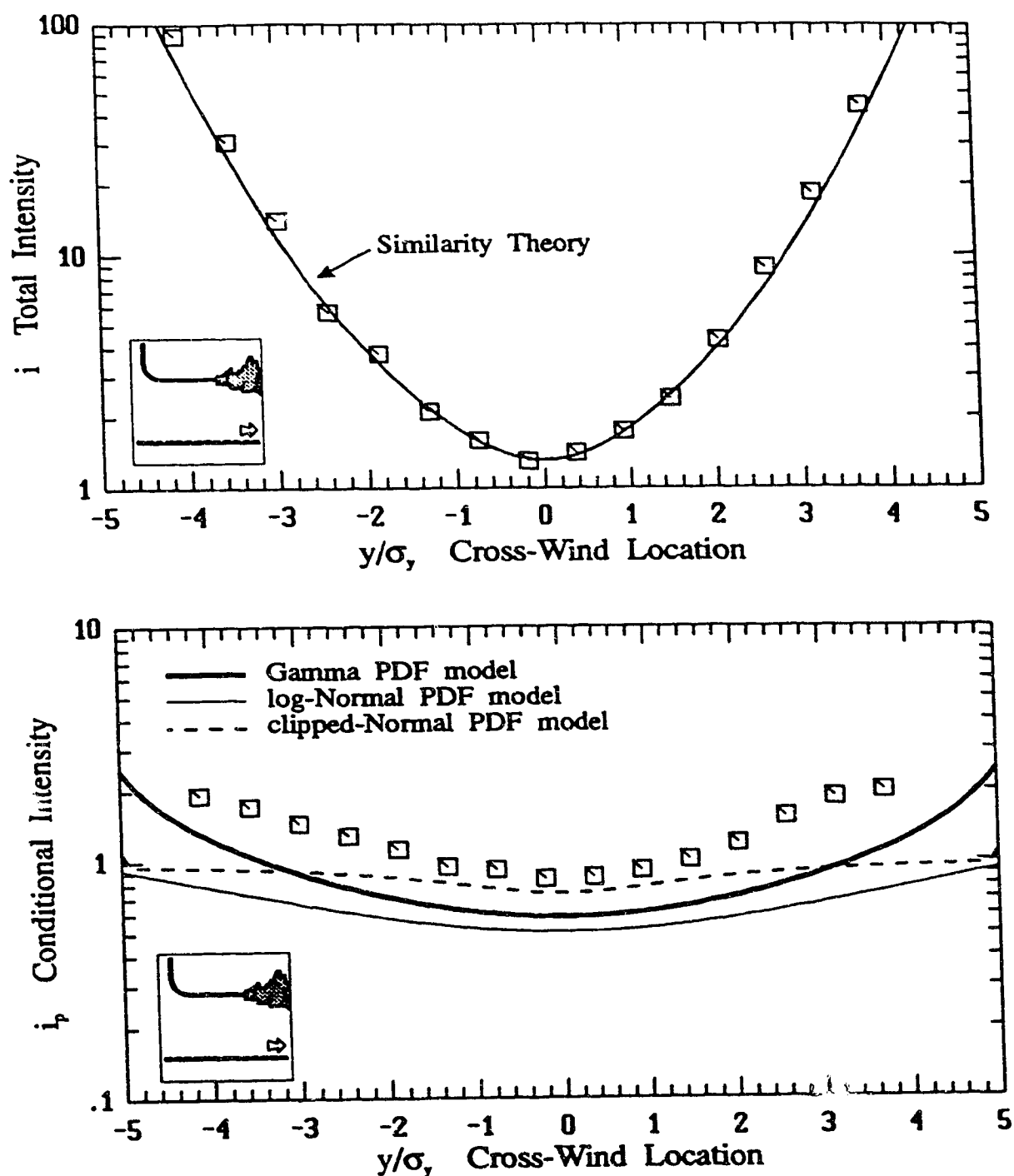


Figure 6.16: The intensity of concentration fluctuations for the data for the jet/plume source in Figure 6.1, (top), and the conditional intensity for the same set of data, (bottom).

6.5 Centre-line Evolution of the Concentration Total Moments

The Gaussian similarity theory predicted by (6.26) does not predict the centre-line normalization values, $\overline{c_o^n}$, which will not be modelled in this study. Since these are such an important aspect of a complete dispersion model, the behaviour of the higher order centre-line moment values need to be, at least, examined to show that there is hope for a model for their evolution.

In Figure 6.17 and Figure 6.18 the centre-line values for the higher order moments are presented for each of the source configurations considered. The striking feature in the figures is that the higher order moments seem to obey a simple power-law description as does the first moment, (a power-law is linear on log-log paper). The problem, however, is to be able to predict their magnitudes accurately. It was shown in section 5.6 that the Gamma distribution is very sensitive to these types of errors.

A possible model for the centre-line normalization values is to use a meandering plume model developed for higher order moments. Sawford and Stapountzis (1986) have shown that for two-dimensional meandering,

$$\overline{c^n} = \frac{\overline{c_o^n} \sigma_i^2}{\sigma_i^2 + n \sigma_m^2} \exp \left[-\frac{nr^2}{2(\sigma_i^2 + n \sigma_m^2)} \right] \quad (6.43)$$

where r is the distance from the plume centre-line. Therefore, on the centre-line, $r = 0$,

$$\overline{c_o^n} = \frac{\overline{c_o^n} \sigma_i^2}{\sigma_i^2 + n \sigma_m^2} \quad (6.44)$$

As $x \rightarrow 0$ then it is also expected that $\sigma_m \rightarrow 0$, therefore $\overline{c_o^n}(0)^n = \overline{c_o^n}(0)$. This, however, is not conclusively supported by water channel observations. In addition, use of (6.44) is not possible without a model for $\sigma_m(x)$ which is currently estimated using the centre-line values of the first two moments.

Further modelling of the mean concentration moments on the centre-line of the plume was beyond the scope of this study.

6.6 Concentration Spectra

In this section a general spectral equation which may be applied in the inertial subrange and in the convective-diffusive range is sought. The “-5/3” and the Markov

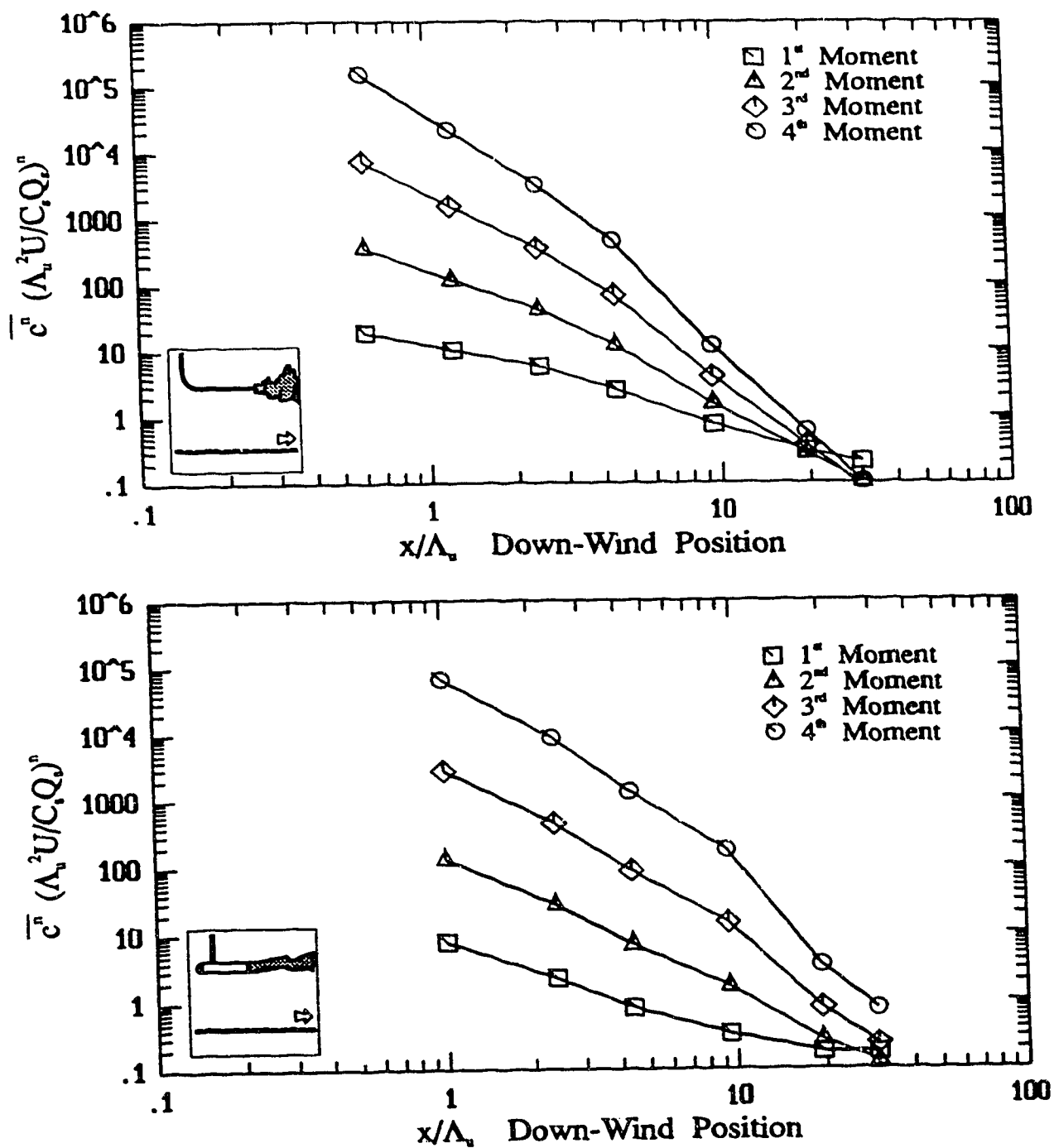


Figure 6.17: The centre-line evolution of the higher order total moments for the jet/plume source (top) and the iso-kinetic source (bottom).

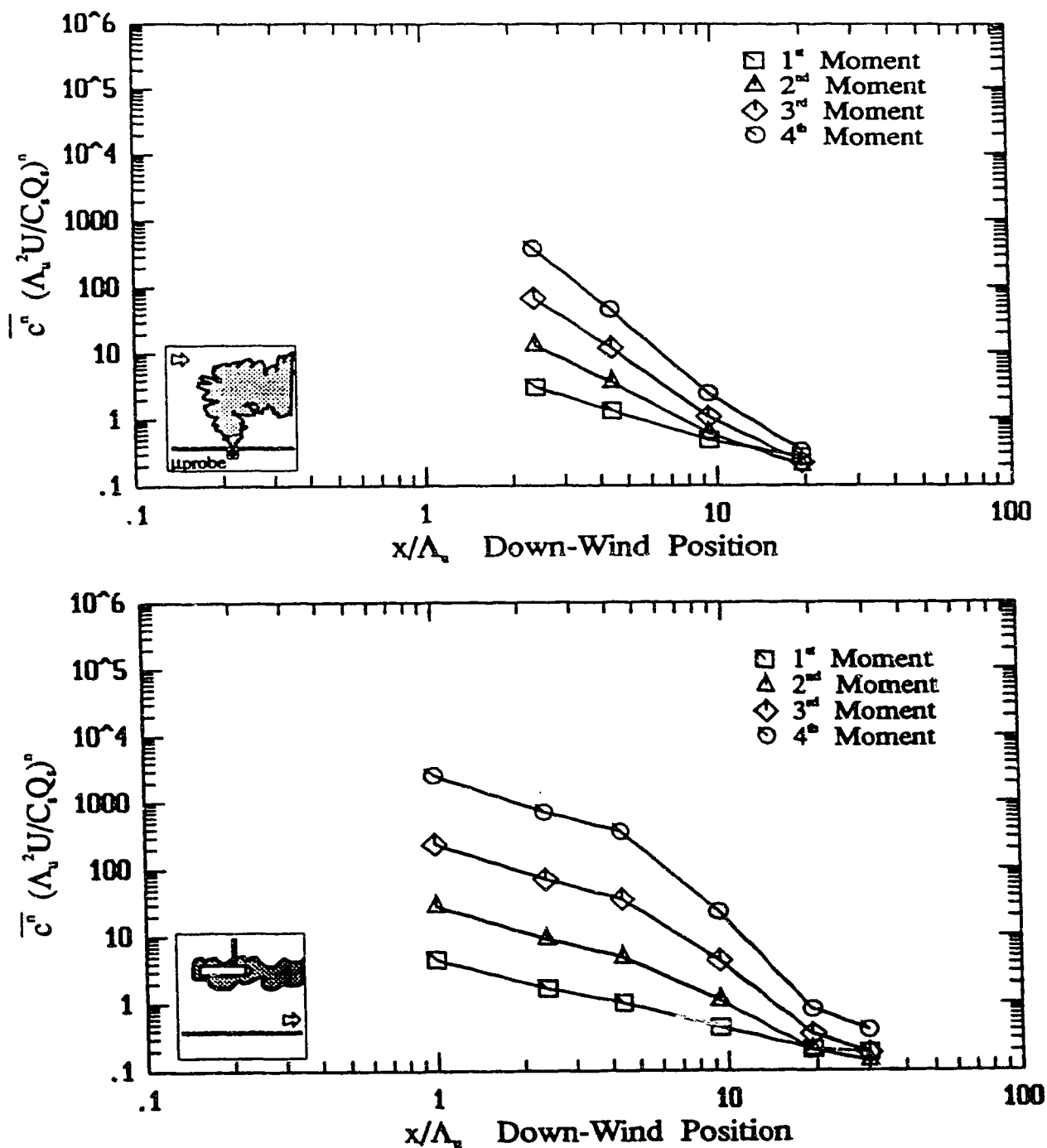


Figure 6.18: The centre-line evolution of the higher order total moments for the vertical jet source (top) and the up-stream facing iso-kinetic source (bottom).

"-6/3" spectral representations are applicable only in the inertial subrange. To meet this need, the Von Kármán spectrum is generalized and applied to other ranges.

Von Kármán introduced an interpolation formula, Hinze (1975) p.227, to cover the range of the spectrum between the energy containing eddies, (i.e. essentially from the wave number, $k = 0$), to the inertial subrange with the "-n" power law. (namely -5/3). This interpolation formula depends on the form of the dynamic equation for the energy spectrum. The Batchelor-Proudman theory, which is applicable to homogeneous isotropic turbulence, states the limit of the three-dimensional spectrum as,

$$\lim_{k \rightarrow 0} E(k, t) = I(t) k^4 \quad (6.45)$$

where $I(t)$ is the Loitsianskii's integral,

$$I(t) = \frac{u'^2}{3\pi} \int_0^\infty r^4 f(r, t) dt \quad (6.46)$$

Alternatively, Saffman (1962) considered the possibility,

$$\lim_{k \rightarrow 0} E(k, t) = I_1(t) k^2 \quad (6.47)$$

where $I_1(t)$,

$$I_1(t) = \frac{2u'^2}{\pi} \int_0^\infty r^2 f(r, t) dt \quad (6.48)$$

For the form stated by (6.45), the Von Kármán formula is:

$$E(k, t) = E(k_e, t) \frac{(k/k_e)^4}{(1 + (k/k_e)^2)^{17/6}} \quad (6.49)$$

which produces a -5/3 spectra as k/k_e gets large, Hinze (1975) p.245. Alternatively, following the Saffman proposal, the equivalent Von Kármán formula reads,

$$E(k, t) = E(k_e, t) \frac{(k/k_e)^2}{(1 + (k/k_e)^2)^{11/6}} \quad (6.50)$$

which also produces a -5/3 spectrum at large k/k_e . Hinze uses this form of the Von Kármán formula to produce a scalar spectral form which covers the same ranges, Hinze p.299. The Saffman formula may be easier to work with because the powers are lower, however the dynamic equations are derived based on $I(t)$ and are appropriate for grid-like turbulence.

It is easier to work with the one-dimensional form of (6.45), which Hinze (1975) p.247, shows to be,

$$E_1(k, t) = E(k_e, t) 2^{17/6} \frac{18}{55} (1 + (k/k_e)^2)^{-5/6} \quad (6.51)$$

The principal interest in this study is the one dimensional spectrum, and the general form proposed is,

$$E_1(k, t) = E(k_e, t) \frac{A}{(1 + (k/k_e)^2)^n} \quad (6.52)$$

where:

A is a constant.

$E(k_e, t)$ is the three dimensional spectrum evaluated at k_e .

k_e is the wave number of the energy containing eddies.

$E(k_e, t)$ will be determined using the autocorrelation function, $f(x)$, knowing that,

$$f(x) = \frac{1}{u'^2} \int_0^\infty E_1(k_1, t) \cos(kx) dk \quad (6.53)$$

evaluating the integral,

$$f(x) = \begin{cases} x \rightarrow \infty, & f(x) \rightarrow 0 \\ x \rightarrow 0, & f(x) \rightarrow 1 \end{cases} \quad (6.54)$$

Using (6.52), the three dimensional spectrum is determined by, Hinze (1975) p.208,

$$E(k_1, t) = 1/2 k_1^2 \frac{\partial^2 E_1(k_1, t)}{\partial k_1^2} - 1/2 k_1 \frac{\partial E_1(k_1, t)}{\partial k_1} \quad (6.55)$$

substituting (6.52) produces,

$$E(k_1, t) = 2n(n+1)AE(k_e, t) \frac{k_1^4/k_e^4}{(1 + k_1^2/k_e^2)^{n+2}} \quad (6.56)$$

For a $-5/3$ spectrum, $n = -5/6$, and (6.56) yields (6.49).

The unknown, $E(k_e, t)$, in (6.52) is determined using (6.53). By integration,

$$f(x) = \frac{E(k_e, t) A k_e}{u'^2} K_{n-1/2}(k_e x) (k_e x)^{n-1/2} \frac{\Gamma(1/2)}{\Gamma(n) 2^{n-1/2}} \quad (6.57)$$

where $K_\mu(x)$ is a *modified Bessel function* of order μ , and $\Gamma(x)$ is the Gamma function. Using (6.54), at $x=0$, $f(0)=1.0$, (6.53) becomes,

$$\overline{u'^2} = E(k_e, t) A k_e \int_0^\infty \frac{1}{(1 + k_1^2/k_e^2)^n} d(k_1/k_e) \quad (6.58)$$

which produces,

$$E(k_e, t) A = \frac{2\overline{u'^2} \Gamma(n)}{k_e \Gamma(n-1/2)} \quad (6.59)$$

Noticing that $\Gamma(1/2) = \sqrt{\pi}$, and substituting these into (6.52),

$$E_1(k_1, t) = \frac{2\Gamma(n) \overline{u'^2}}{\sqrt{\pi} \Gamma(n-1/2) k_e} \frac{1}{(1 + k_1^2/k_e^2)^n} ; n > 1/2 \quad (6.60)$$

Therefore, the correlation function $f(x)$ is given by,

$$f(x) = \frac{1}{2^{n-3/2} \Gamma(n-1/2)} (k_e x)^{n-1/2} K_{n-1/2}(k_e x) \quad (6.61)$$

and the three dimensional spectrum is,

$$E(k, t) = \frac{\frac{4n(n+1)\overline{u'^2}}{k_e} \frac{\Gamma(n)}{\sqrt{\pi} \Gamma(n-1/2)} (k^4/k_e^4)}{(1 + k^2/k_e^2)^{n+2}} \quad (6.62)$$

6.6.1 Relating k_e to Λ_f

As the wave number approaches zero, the spectrum may be used to determine the integral length scale, Λ_f , Hinze (1975) p.209,

$$\Lambda_f(t) = \frac{\pi}{2\overline{u'^2}} E_1(0, t) \quad (6.63)$$

Therefore, substituting (6.60) produces,

$$\frac{1}{k_e} = \ell_e = \frac{\Gamma(n-1/2)}{\sqrt{\pi} \Gamma(n)} \Lambda_f \quad (6.64)$$

Equation (6.64) has several interesting properties. Using $n = 1$, i.e. (6.52) represents a Markov spectrum, then, (6.64) predicts that,

$$\ell_e = \frac{\Gamma(1/2)}{\sqrt{\pi} \Gamma(1)} \Lambda_f = \Lambda_f \quad (6.65)$$

However, for $n = 5/6$, (6.52) represents an inertial subrange spectrum with $E_1 \propto k_1^{-5/3}$, then (6.64) predicts,

$$\ell_e = \frac{\Gamma(2/6)}{\sqrt{\pi}\Gamma(5/6)}\Lambda_f \simeq 1.33\Lambda_f \quad (6.66)$$

As $n \rightarrow 1/2$, i.e. (6.52) approaches a viscous convective range, $\ell_e \not\propto \Lambda_f$. In the viscous convective range it is physically realistic to expect that ℓ_e not be related to Λ_f .

Substituting (6.64) into (6.60) produces the final generalized Von Kármán spectrum function,

$$E_1(k_1, t) = \frac{2/\pi \overline{u'^2} \Lambda_f}{\left(1 + \left(\frac{\Gamma(n-1/2)}{\sqrt{\pi}\Gamma(n)}\right)^2 \Lambda_f^2 k_1^2\right)^n} ; n > 1/2 \quad (6.67)$$

Which produces the expected Markov spectrum when $n = 1$.

6.6.2 Von Kármán General Spectrum for Scalar Fluctuations

A form of the spectrum of scalar fluctuations similar to (6.52) may be assumed, however Hinze (1975) p.299, notes that as $k \rightarrow 0$, $E_{c1}(k_1, t)$ is proportional to k^2 not k^4 as is $E_1(k, t)$. Therefore, when determining $E_c(k, t)$ the following must be used, Hinze (1975) p.285,

$$E_c(k_1, t) = -k \frac{\partial E_{c1}(k_1, t)}{\partial k_1} \quad (6.68)$$

For the scalar spectrum the present study proposes that,

$$E_{c1}(k_1, t) = E_c(k_o, t) \frac{A}{(1 + (k/k_o)^2)^n} \quad (6.69)$$

where:

- A is a constant.
- $E_c(k_o, t)$ is the three dimensional spectrum evaluated at k_o .
- k_o is the wave number of the energy containing eddies.

Substituting (6.69) into (6.68) yields,

$$E_c(k_1, t) = \frac{2n E_c(k_o, t) A k_1^2 / k_o^2}{(1 + k_1^2 / k_o^2)^n} \quad (6.70)$$

$E_c(k_o, t)$ may be determined similarly to $E(k_e, t)$ and by similarity to (6.59), (6.69) becomes,

$$E_c(k_o, t) \Lambda_c = \frac{2\overline{c'^2} \Gamma(n)}{k_o \Gamma(1/2) \Gamma(n-1/2)} \quad (6.71)$$

Therefore, the general Von Kármán spectrum for scalar fluctuations is,

$$E_{c1}(k_1, t) = \frac{2\Gamma(n) \overline{c'^2}}{\sqrt{\pi} \Gamma(n-1/2) k_o} \frac{1}{(1 + k_1^2/k_o^2)^n} ; n > 1/2 \quad (6.72)$$

The correlation function $f(x)$ is given by,

$$f_c(x) = \frac{1}{2^{n-3/2} \Gamma(n-1/2)} (k_o x)^{n-1/2} K_{n-1/2}(k_o x) \quad (6.73)$$

and the three dimensional spectrum is,

$$E_c(k, t) = \frac{\frac{4n(n+1)\overline{c'^2}}{k_o} \frac{\Gamma(n)}{\sqrt{\pi} \Gamma(n-1/2)} (k^2/k_o^2)}{(1 + k^2/k_e^2)^{n+2}} \quad (6.74)$$

6.6.3 Relating k_o to Λ_c

As the wave number approaches zero, the spectrum may be used to determine the integral length scale for the concentration fluctuations, Λ_c ,

$$\Lambda_c(t) = \frac{\pi}{2\overline{c'^2}} E_{c1}(0, t) \quad (6.75)$$

Substituting (6.72) produces,

$$\frac{1}{k_o} = \ell_o = \frac{\Gamma(n-1/2)}{\sqrt{\pi} \Gamma(n)} \Lambda_c \quad (6.76)$$

Substituting (6.76) into (6.72) produces the final generalized Von Kármán scalar spectrum function,

$$E_{c1}(k_1, t) = \frac{2/\pi \overline{c'^2} \Lambda_c}{\left(1 + \left(\frac{\Gamma(n-1/2)}{\sqrt{\pi} \Gamma(n)}\right)^2 \Lambda_c^2 k_1^2\right)^n} ; n > 1/2 \quad (6.77)$$

Which produces the Markov spectrum when $n = 1$, and the inertial subrange spectrum when $n = 5/6$.

The frequency domain version of E_{c1} is determined by using,

$$E_{c1}(n) = \frac{2\pi}{\bar{u}} E_{c1}(k) \quad (6.78)$$

from Hinze (1975) p.203, and recalling that the wave number is $k = (2\pi/\bar{u})n$, then (6.77) written in the frequency domain is ,

$$E_{c1}(n, t) = \frac{4\bar{c}'^2 \Lambda_c / \bar{u}}{\left(1 + \left(\frac{\Gamma(n - 1/2)}{\Gamma(n)}\right)^2 4\Lambda_c^2 n^2\right)^n} ; n > 1/2 \quad (6.79)$$

6.6.4 Viscous Convective Range

The scalar spectrum given by (6.77) is not applicable in the viscous convective range, (also called the Batchelor range), where $E_c(k) \propto k^{-1}$ which requires $n = 1/2$. For this case, the integral in (6.58) may be re-evaluated by integrating (6.69) to some arbitrary limit, $\beta = k_m/k_o \gg 1$, rather than to infinity.

$$\bar{c}'^2 = E_{c1}(k_o, t) A k_o \int_0^\beta \frac{1}{(1 + k^2/k_o^2)^{1/2}} d(k/k_o) \quad (6.80)$$

$$= E_{c1}(k_o, t) A k_o \ln \left(\sqrt{1 + \beta^2} + \beta \right) \quad (6.81)$$

where $\beta = k_m/k_o$. Then rearranging,

$$E_{c1}(k_o, t) A = \frac{\bar{c}'^2}{\ln \left(\sqrt{1 + \beta^2} + \beta \right)} \quad (6.82)$$

where $\beta = k_m/k_o \gg 1$. The general form for the Von Kármán spectrum for scalar fluctuations in the Batchelor range is, from (6.52),

$$E_{c1}(k_1, t) = \frac{\left(\frac{\bar{c}'^2}{k_o \ln \left(\sqrt{1 + \beta^2} + \beta \right)} \right)}{\sqrt{1 + k^2/k_o^2}} ; n = 1/2 \quad (6.83)$$

This form of the spectral equation is not useful as it stands because β is not yet defined. In the next section β is related to the Λ_c , therefore making closure.

6.6.5 Relating k_o to Λ_c in Batchelor Range

Relating k_o to Λ_c is done as performed in (6.75). Substituting (6.83) produces,

$$k_o = \frac{\pi/2}{\Lambda_c \ln \left(\sqrt{1 + \beta^2} + \beta \right)} \quad (6.84)$$

Substituting, k_o into (6.83), produces,

$$E_{c1}(k_1, t) = \frac{\frac{2}{\pi} \overline{c'^2} \Lambda_c}{\left(1 + \left(\frac{2}{\pi} \ln \left(\sqrt{1 + \beta^2} + \beta \right) \right)^2 \Lambda_c^2 k_1^2 \right)^{1/2}} ; \beta = k_m/k_o \gg 1, n = 1/2 \quad (6.85)$$

The constant β may be determined by specifying some upper limit of the spectrum. For example, consider a fixed cutoff at k_m , then

$$\beta = \frac{k}{k_o} = \frac{k_m}{k_o}$$

therefore, using (6.84)

$$\beta = k_m \frac{2}{\pi} \Lambda_c \ln \left(\sqrt{1 + \beta^2} + \beta \right) \quad (6.86)$$

This equation converges rapidly for a specified k_m and Λ_c . For experimental applications k_m may selected as the sampling cutoff frequency,

$$k_m = \frac{2\pi}{\bar{u}} f_o = \frac{2\pi}{\bar{u}} \frac{f_s}{2}$$

where f_s is the data sampling frequency in Hertz, and f_o is the cutoff frequency (or folding frequency).

6.6.6 Observed Concentration Spectra

Before presenting the concentration spectra observed in the water channel it is appropriate to consider what might be expected. As shown in Figure 6.19, the expected spectrum changes its slope at a frequency of $f_\eta/50$, as predicted by Hinze (1975) p.298,

$$\frac{k_*}{k_d} = \left(\frac{3}{5} \frac{A_\gamma}{C} \right)^{3/2} \approx 0.02$$

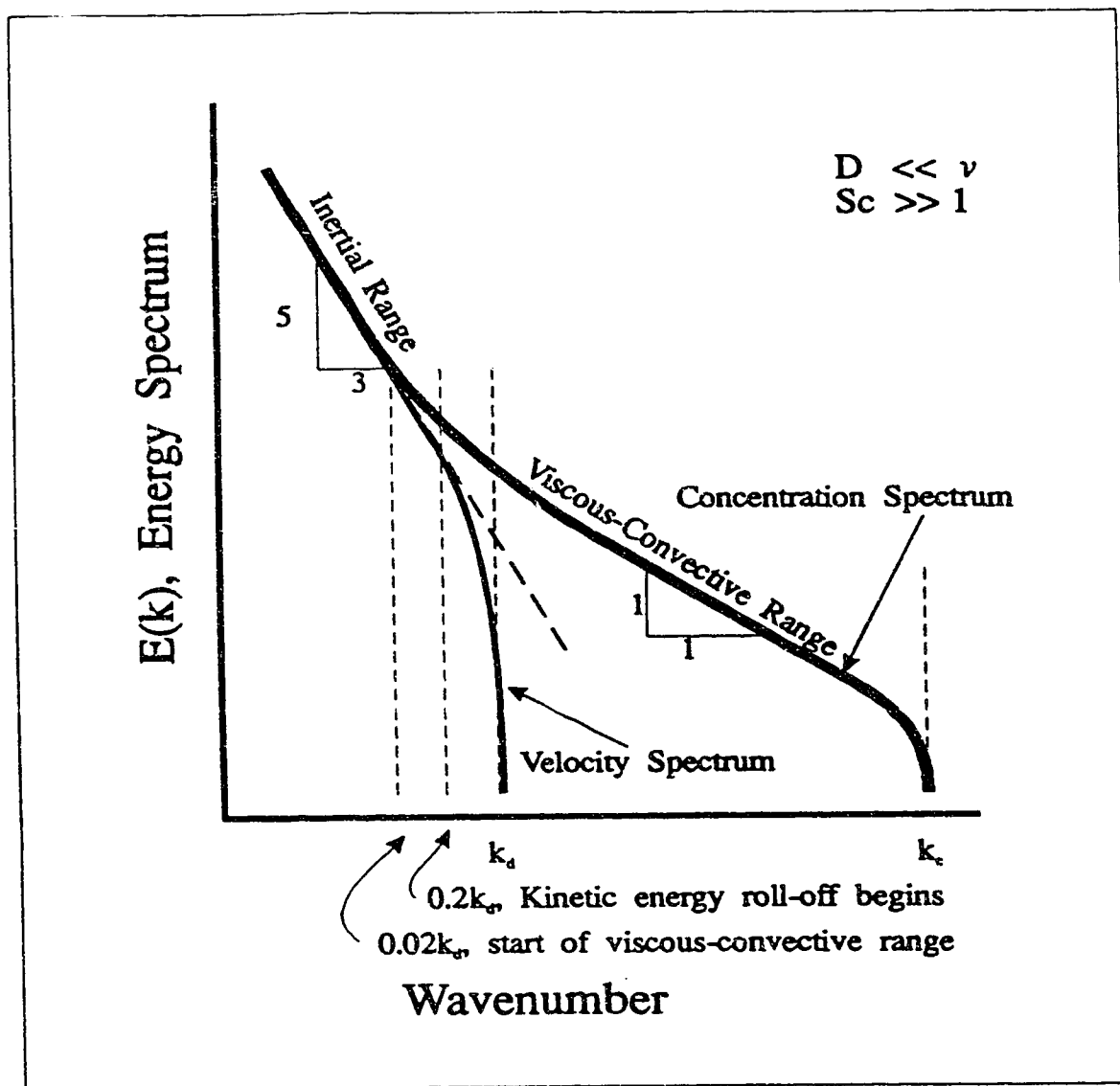


Figure 6.19: Influence of the concentration molecular diffusivity on the concentration fluctuation spectrum for large wave numbers.

where:

- k_* is the wave number cut-off between the inertial subrange and the viscous convective range.
- k_d is the wave number of the diffusive limit
- A_γ is a spectral constant, $A_\gamma = 0.48$, Hinze (1975) p.299.
- C is a constant, $C = 3.9$, Hinze (1975) p.298.

In terms of the Kolmogorov scales the spectrum changes at,

$$\frac{\eta}{\eta_{c*}} = 0.02 \quad (6.87)$$

Therefore, an estimate for η must be determined. For non-isotropic turbulence define,

$$u_s^2 = \frac{\overline{u'^2} + \overline{v'^2} + \overline{w'^2}}{3} \quad (6.88)$$

where $v' \propto 0.8u'$ and $w' \propto 0.6u'$, so

$$u_s = \left(\frac{1 + 0.64 + 0.36}{3} \right)^{\frac{1}{2}} u' = 0.82u' \quad (6.89)$$

Using (3.48), assuming an inertial subrange exists in the water channel, then

$$\epsilon \approx 0.8 \left(\frac{u_s^3}{\ell_e} \right) \approx 0.8 \left(\frac{(0.82u')^3}{1.33\Lambda_f} \right) \approx 1.02 \text{ cm}^2/\text{s}^3 \quad (6.90)$$

where:

- ϵ is the dissipation energy.
- ℓ_e scale of the energy containing eddies, (6.64).
- u_s is a characteristic velocity fluctuation scale
- $u' \approx 2.5 \text{ cm/s}$
- $\Lambda_f \approx 5 \text{ cm}$

The Kolmogorov scale may be determined using

$$\eta = \left(\frac{\nu^3}{\epsilon} \right)^{1/4} \approx \left(\frac{0.01^3}{1.02} \right)^{1/4} \approx 0.0315 \text{ cm}$$

The dissipation energy for the scalar fluctuations may be estimated by,

$$\epsilon_c \approx 12\mathcal{D} \frac{\overline{c'^2}}{\lambda_g^2} \approx 12\mathcal{D} \frac{i_c^2 \bar{c}^2}{0.5\bar{u}^2 \tau_c^2} \approx 3.375 \text{ g/l (cm/s)}^2 \quad (6.91)$$

where:

ϵ_c	is the scalar dissipation energy.
λ_g	dissipation scale of the scalar fluctuations.
τ_c	dissipation time scale of the scalar fluctuations.
\bar{c}	$\approx 1 \text{ g/l}$
i_c	≈ 1.2
\bar{u}	$\approx 25 \text{ cm/s}$
τ_c	$\approx 0.0128 \text{ s}$

The scalar Kolmogorov scale may be determined using

$$\eta_c = \left(\frac{\mathcal{D}^2 \nu}{\epsilon} \right)^{1/4} \approx \left(\frac{(1.5 \times 10^{-5})^2 0.01}{1.02} \right)^{1/4} \approx 0.00122 \text{ cm}$$

In the diffusive limit, the velocity spectrum falls off much faster than the saline concentration spectrum,

$$\frac{\eta}{\eta_c} = 25$$

The saline concentration spectrum falls off at approximately the following frequency,

$$f_d = \frac{\bar{u}}{2\pi\eta_c} \approx \frac{25}{2\pi 0.00122} \approx 3300 \text{ Hz}$$

Using (6.87), the frequency at which the Batchelor range begins is approximately,

$$f_{c*} = \frac{\bar{u}}{2\pi(50\eta)} \approx 3 \text{ Hz}$$

The effective range of the data collection system for the concentration detectors used in this experiment is $0.002 < f < 250 \text{ Hz}$. Therefore, based on the above analysis, it is expected that most of the data collected in the water channel will be in the Batchelor range, where $E_{c1}(k_1) \propto k^{-1}$.

A typical spectrum of the concentration fluctuations in the water channel is shown in Figure 6.20. What does the slope of the spectrum mean in terms of being able to model the atmosphere? Sreenivasan (1991) discusses the difference in structure of turbulence between the Batchelor range and the inertial range. He has found that the fractal dimension is different between the ranges. This would suggest that the turbulence structure is different.

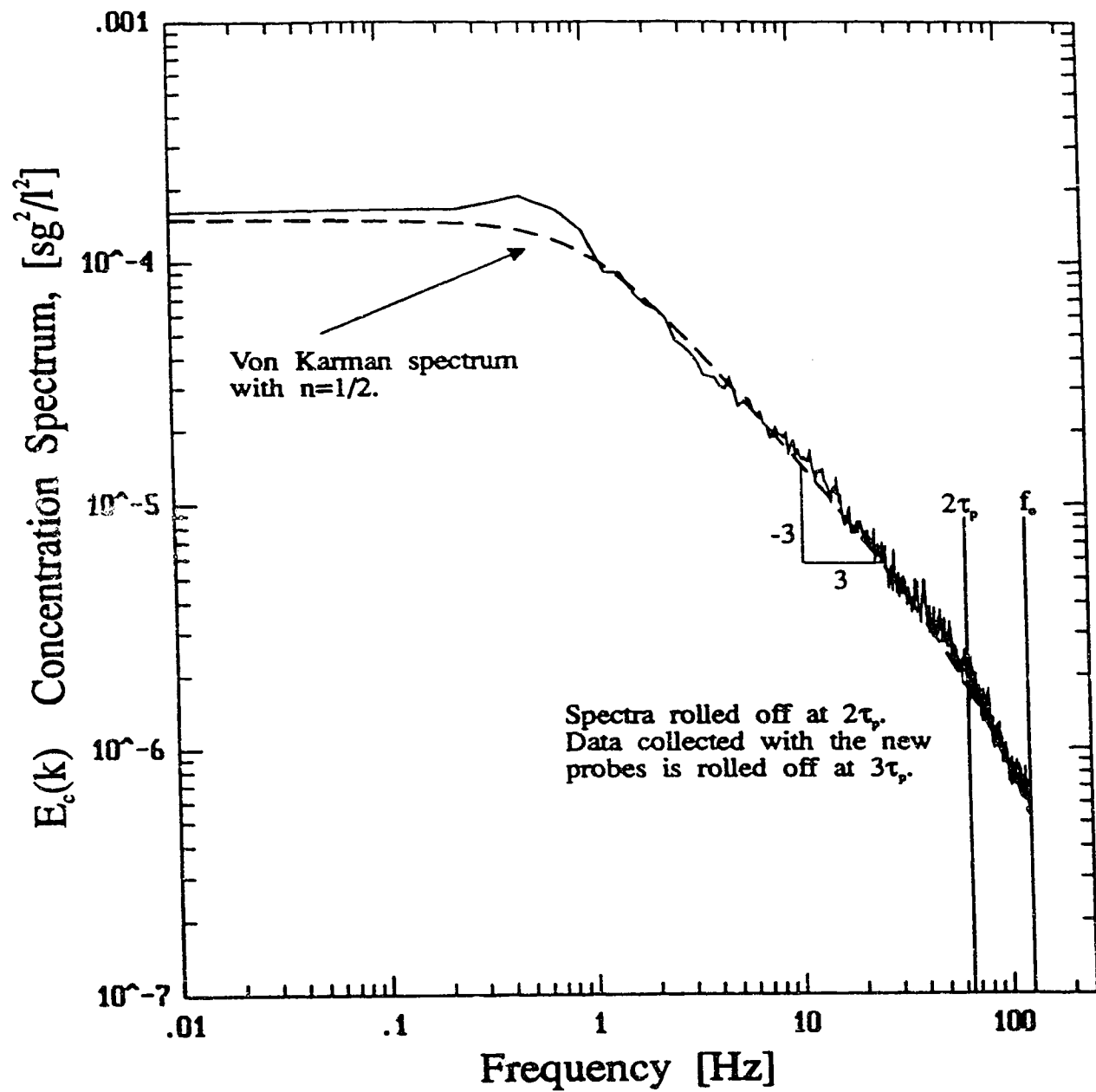


Figure 6.20: Spectrum of the concentration fluctuations in the water channel.
 Slope for large k is k^{-1} .

6.6.7 Concentration Integral Time Scales

The concentration integral time scales have been calculated using the procedure discussed in section 3.2.1. The calculation of the time scales across the plume profile is difficult because of intermittency in the fringes. Considerable scatter is observed in the fringes, even when 500 second time averages are used, (500 s is equivalent to $2000T_u$ or $10,000T_c$).

Figure 6.21 shows a typical concentration integral time scale profile. The profile shows that the integral scales are approximately constant across the plume profile for at least three plume spreads. Beyond that range, the calculations show that the integral scales drop to zero. However, it can be argued that the concentration scales should appear large, because of the long time periods between concentration bursts. The limiting values of the scales has been fully investigated. Although it is doubtful from examination of the data that the true behaviour of the integral scales is constant across the plume, this estimate provides a reasonable model, although somewhat crude.

The evolution of the integral scales is presented in Figure 6.22. For the jet/plume source, the integral time scales are observed to increase in the region near the source. This may be explained by the evolution of the strong jet into a plume. Beyond $\sigma_y/\Lambda_u \approx 3$, the integral scales are approximately constant. The other source types studied, which are observed visually to behave like plumes rather than jets, have integral time scales which are nearly constant with x . The vertical jet source has integral time scales which are characteristically larger than those of the jet/plume source. They are of the same magnitude as the integral time scales that the jet/plume source evolves to. The iso-kinetic sources have characteristically very small scales which are almost constant. Observation of the plumes by dye flow visualization showed that the iso-kinetic sources are stringy, laminar flow plumes. The low integral scales may be influenced by this stringy behaviour. The jet/plume and the vertical jet sources are turbulent and small scale mixing is much more evident. The integral scales for these source are therefore more likely to be related to the scales of the velocity turbulence. These principles are observed in general in Figure 6.22.

6.6.8 Lagrangian-Eulerian Time Scale Ratio

A model for the relationship between the concentration integral time scales and the Eulerian velocity integral time scales is presented in Sykes (1984). He estimates

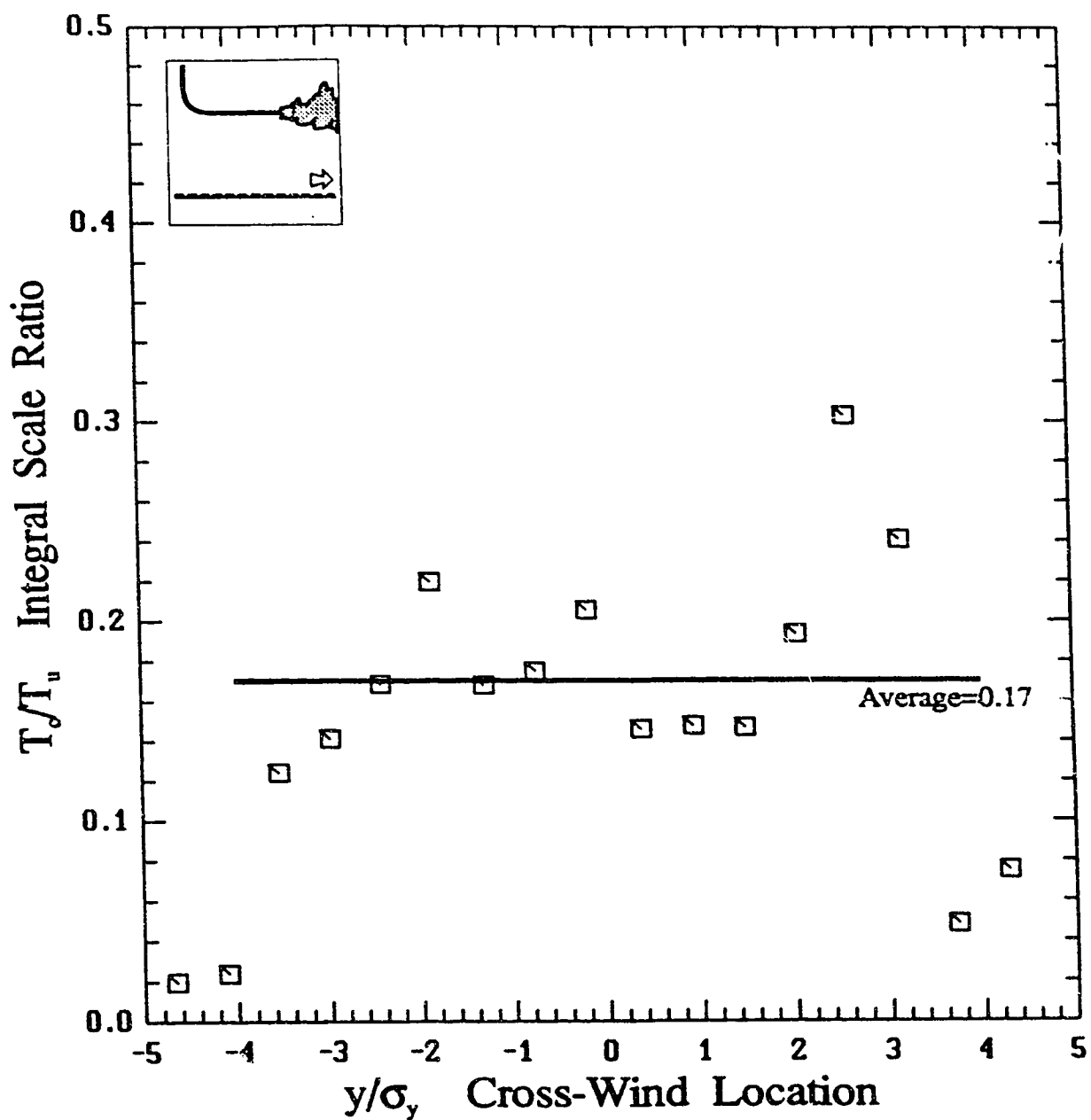


Figure 6.21: The concentration integral time scales across the jet/plume source at the same location as Figure 6.1.

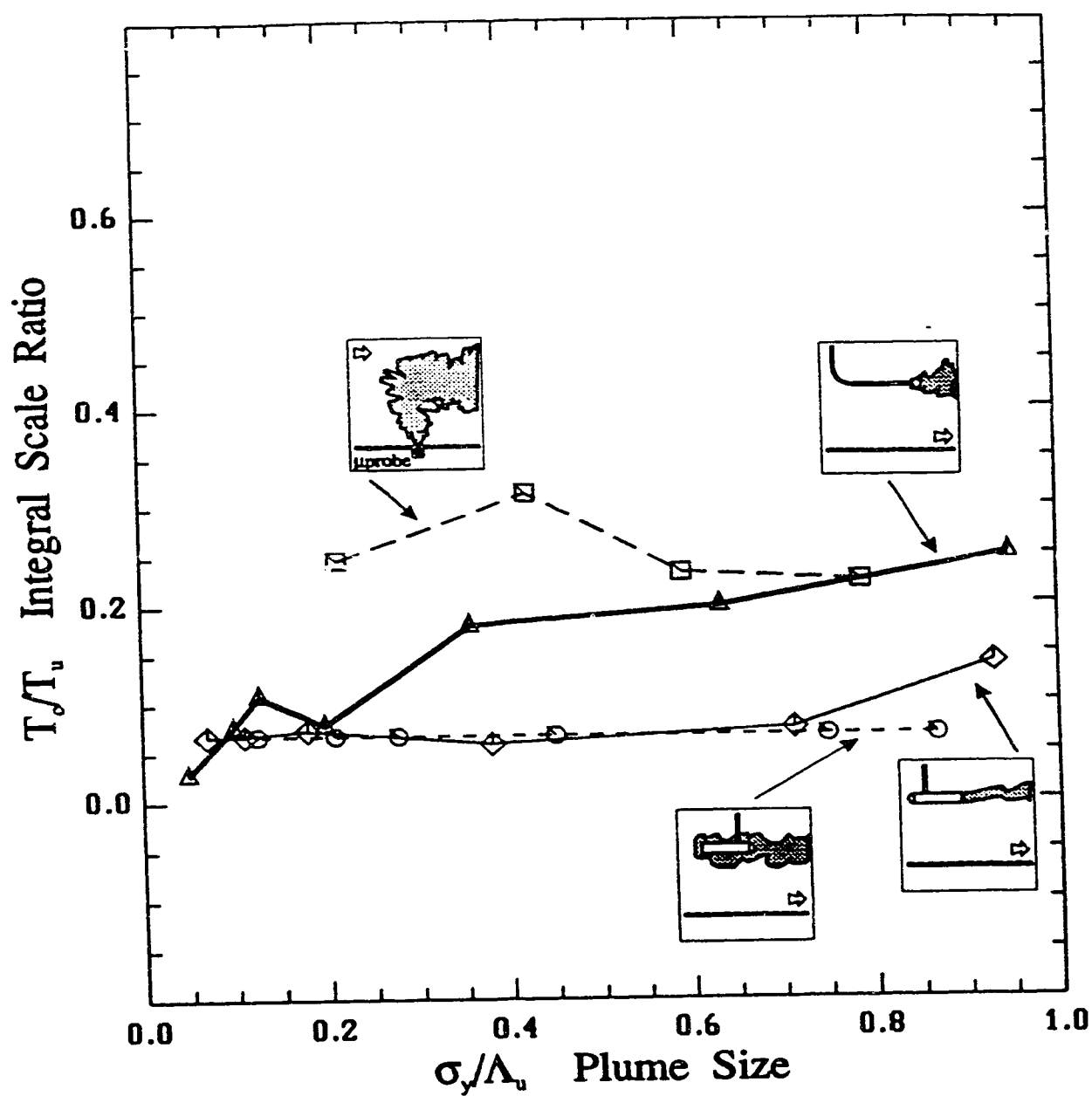


Figure 6.22: The evolution of the concentration integral time scale ratio, for all the sources, with down-wind distance.

the ratio of the integral time scales to be,

$$\frac{T_c}{T_E} = \frac{\langle c \rangle_o^2}{2\langle c'^2 \rangle_o} \ln \left[1 + 2 \frac{\langle c'^2 \rangle_o}{\langle c \rangle_o^2} \right] \quad (6.92)$$

where:

- $\langle c \rangle_o$ is the ensemble mean concentration
- $\langle c'^2 \rangle_o$ is the ensemble mean square fluctuations

The subscript "o" indicates a centre-line value, however Sykes uses this expression for off-axis locations as well. He finds that T_c is not constant across the plume and that (6.92) fits the data better in the off-axis locations.

Assuming that the ensemble averages are equal to the time averages, then,

$$\frac{T_c}{T_E} = \frac{1}{2i^2} \ln (1 + 2i^2) \quad (6.93)$$

where $i = \sqrt{\overline{c'^2}/\bar{c}^2}$. Figure 6.23 shows the ratio of the observed integral time scale ratio to that predicted by (6.93). Far from the source, the integral time scale ratio is observed to level off to a constant value, although it does not form the ratio predicted by Sykes. In the cross-wind direction the Sykes model does not appear constant at all, except for in the narrow range of $|y/\sigma_y| < 1$. It does not appear that this model would provide a better estimate than the assumption that the cross-wind scales are constant.

6.7 Concentration Microscales

The concentration microscale may be determined by,

$$\begin{aligned} \frac{1}{\tau_c^2} &= \frac{\int_0^\infty k^2 E_1(k) dk}{\int_0^\infty E_1(k) dk} \\ &= \frac{\overline{\dot{c}'^2}}{2\overline{c'^2}} \\ &= \frac{\sigma_{\dot{c}}^2}{2\sigma_c^2} \end{aligned} \quad \begin{array}{l} (6.94) \\ (6.95) \end{array}$$

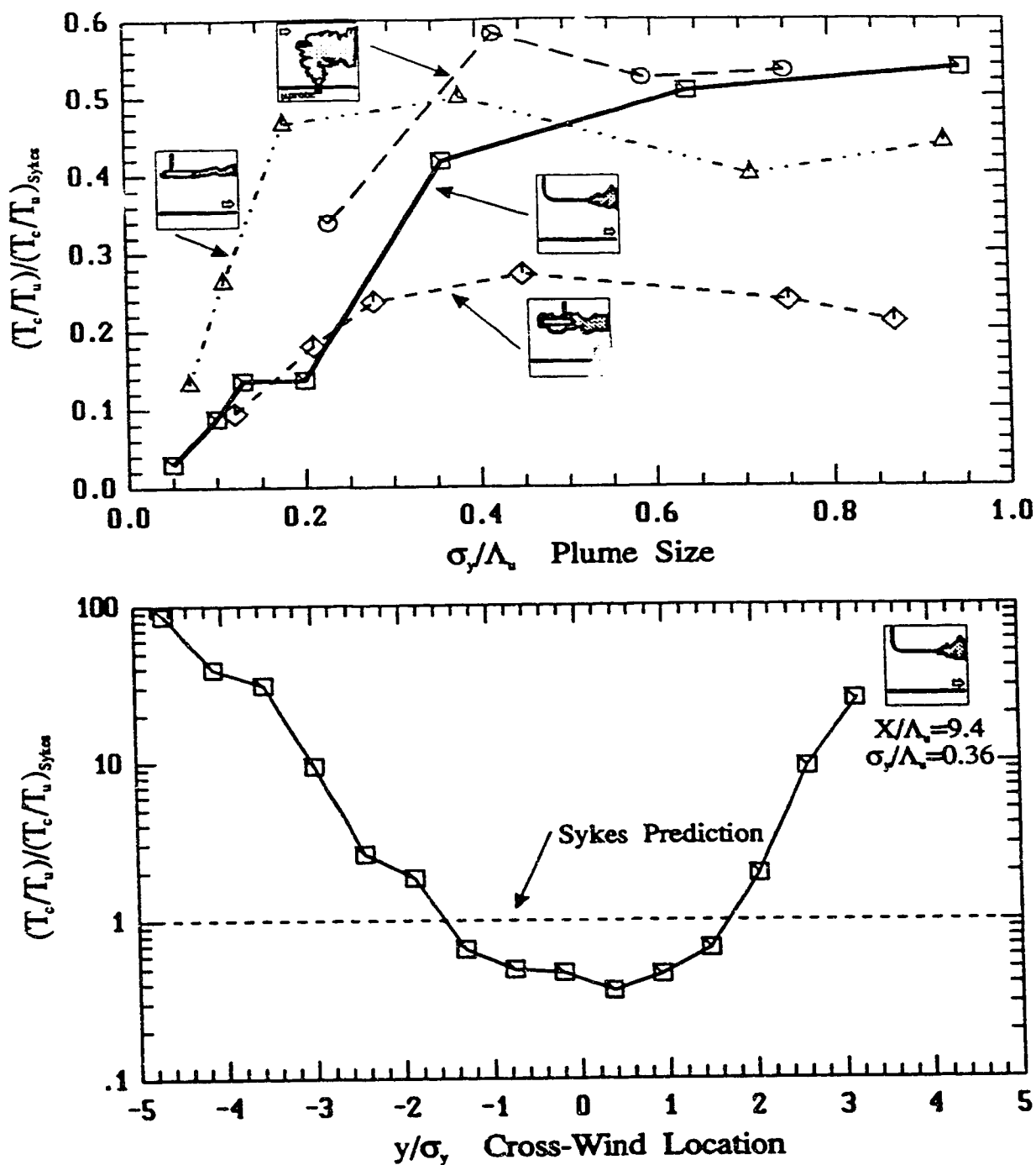


Figure 6.23: Comparison of the prediction of the ratio of the concentration integral time scale to Eulerian time scale by Sykes (1984).

Here the microscale, τ_c (time) or λ_c (length), is defined by the total concentration statistics. But for an intermittent plume, the microscale should be a function of the small scale concentration fluctuations, which should be independent of the intermittency.

To convert (6.95) to a conditional microscale, the intermittency factor definitions are required,

$$\gamma = \frac{\bar{c}}{\bar{c}_p} = \frac{\overline{c^2}}{\overline{c_p^2}} \quad (6.96)$$

Which may also be expressed as, Wilson, Robins and Fackrell (1985),

$$\gamma = \frac{1 + i_p^2}{1 + i^2} \quad (6.97)$$

or by rearranging,

$$i_c^2 = \frac{1}{\gamma} (1 + i_p^2) - 1 \quad (6.98)$$

Therefore the concentration variance may be expressed as,

$$\sigma_c^2 = \left\{ \frac{1}{\gamma} (1 + i_p^2) - 1 \right\} \bar{c}^2 \quad (6.99)$$

The conditional derivative variance is considered in the same way but is simplified because $\bar{c} = 0$. Therefore, the conditional derivative variance may be determined from,

$$\gamma = \frac{\overline{c^2}}{\overline{c_p^2}} = \frac{\sigma_c^2}{\sigma_{c_p}^2} \quad (6.100)$$

and,

$$\sigma_c^2 = \gamma \sigma_{c_p}^2 \quad (6.101)$$

Substituting (6.99) and (6.101) into (6.95),

$$\tau_c^2 = \frac{2 \left(\frac{1}{\gamma} (1 + i_p^2) - 1 \right) \bar{c}^2}{\gamma \sigma_{c_p}^2} \quad (6.102)$$

and rearranging, (using (6.96)),

$$\tau_c^2 = \frac{2\sigma_{c_p}^2}{\sigma_{c_p}^2} + \frac{2(1 - \gamma)}{i_p^2} \frac{\sigma_{c_p}^2}{\sigma_{c_p}^2} \quad (6.103)$$

It is convenient to define a conditional microscale, similar to the total concentration microscale in (6.95), which will be defined as,

$$\tau_{cp}^2 = \frac{2\sigma_{cp}^2}{\sigma_{cp}^2} \quad (6.104)$$

Substituting the conditional microscale in (6.103),

$$\tau_c^2 = \tau_{cp}^2 \left(1 + \frac{(1-\gamma)}{i_p^2} \right) \quad (6.105)$$

Since the term $(1-\gamma)/i_p^2$ is always positive, the total microscale will always be larger than the conditional microscale. Also, since $i_p^2 \approx 1$, (6.105) predicts that τ_c^2 will be between 1 and 2 times larger than τ_{cp}^2 .

The concentration micro-length scale and the conditional concentration micro-length scale, respectively, are defined as, ($U=22.5$ cm/s),

$$\lambda_c = U\tau_c \quad (6.106)$$

$$\lambda_{cp} = U\tau_{cp} \quad (6.107)$$

The variation of λ_c with down-wind distance (determined using (6.106) and (6.95)) is shown in Figure 6.24. The microscale is observed to be almost constant, $\lambda_c/\lambda_u \approx 0.13$ with plume size for $\sigma_y/\Lambda_u > 0.2$. The variation of λ_{cp} with down-wind distance (determined using (6.107) and (6.105)) is shown in Figure 6.25. The conditional microscale is observed to be almost constant, $\lambda_{cp}/\lambda_u \approx 0.12$ with plume size for $\sigma_y/\Lambda_u > 0.2$. λ_u is estimated using spectra at the source height and location and (3.46) ($\lambda_u \approx 1.15$ cm), whereas λ_c is inferred directly from the time series data.

The centre-line values shown in the figures was arbitrarily selected as the closest data point to the centre-line of the plume. This point may or may not be the best representative of the centre-line value. Therefore, for example, the last point of the jet/plume source in Figure 6.25, (heavy solid line), may be high by approximately 10% of the value shown. Lowering this point by 10% would bring it in line with the other values.

The cross-wind variation of the microscales is shown in Figure 6.26(top) for two locations in the jet/plume source. The cross-wind variation in microscale is almost constant in value. The conditional microscale values tend to flatten the distributions out more. However, as observed in Figure 6.99(bottom), when the curve is already flat, the conditional correction in (6.105) tends to correct for the larger magnitude of the total concentration microscale and the further flattening of the curve, to account for the intermittency, is negligible amongst the data variability.

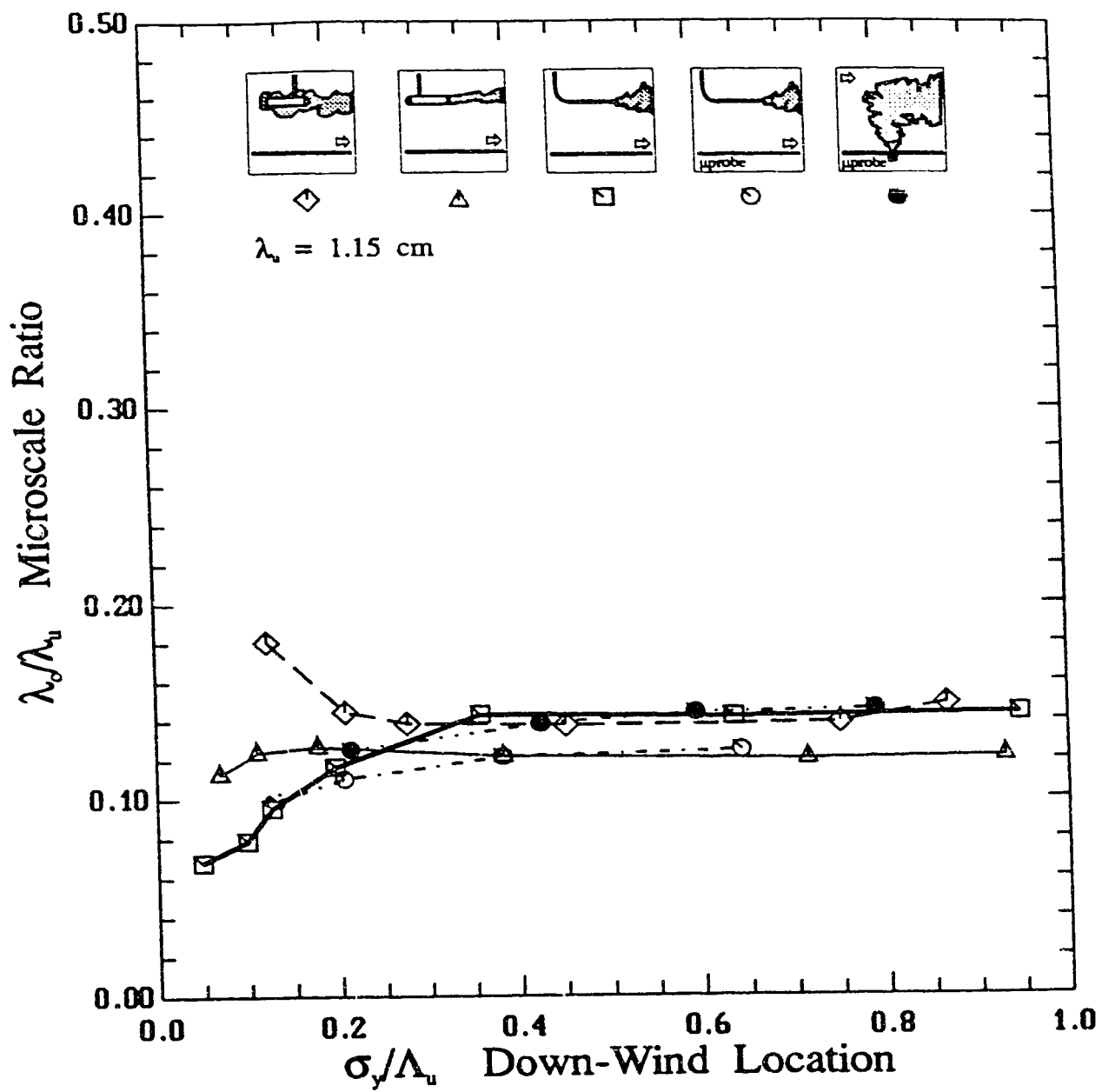


Figure 6.24: Microscale of concentration fluctuations on the plume centre-line for all the sources.

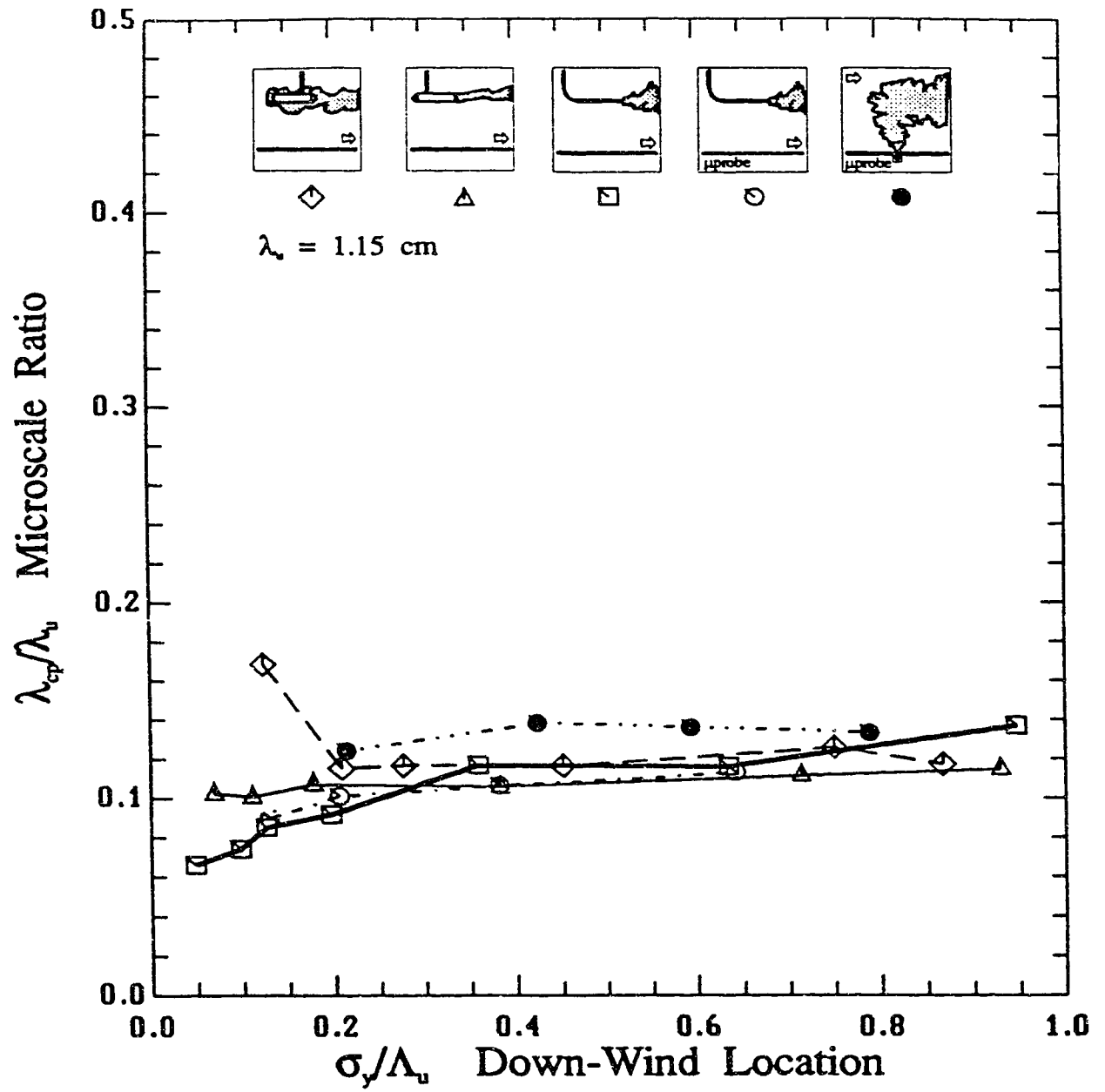


Figure 6.25: Conditional microscale of concentration fluctuations on the plume centre-line for all the sources.

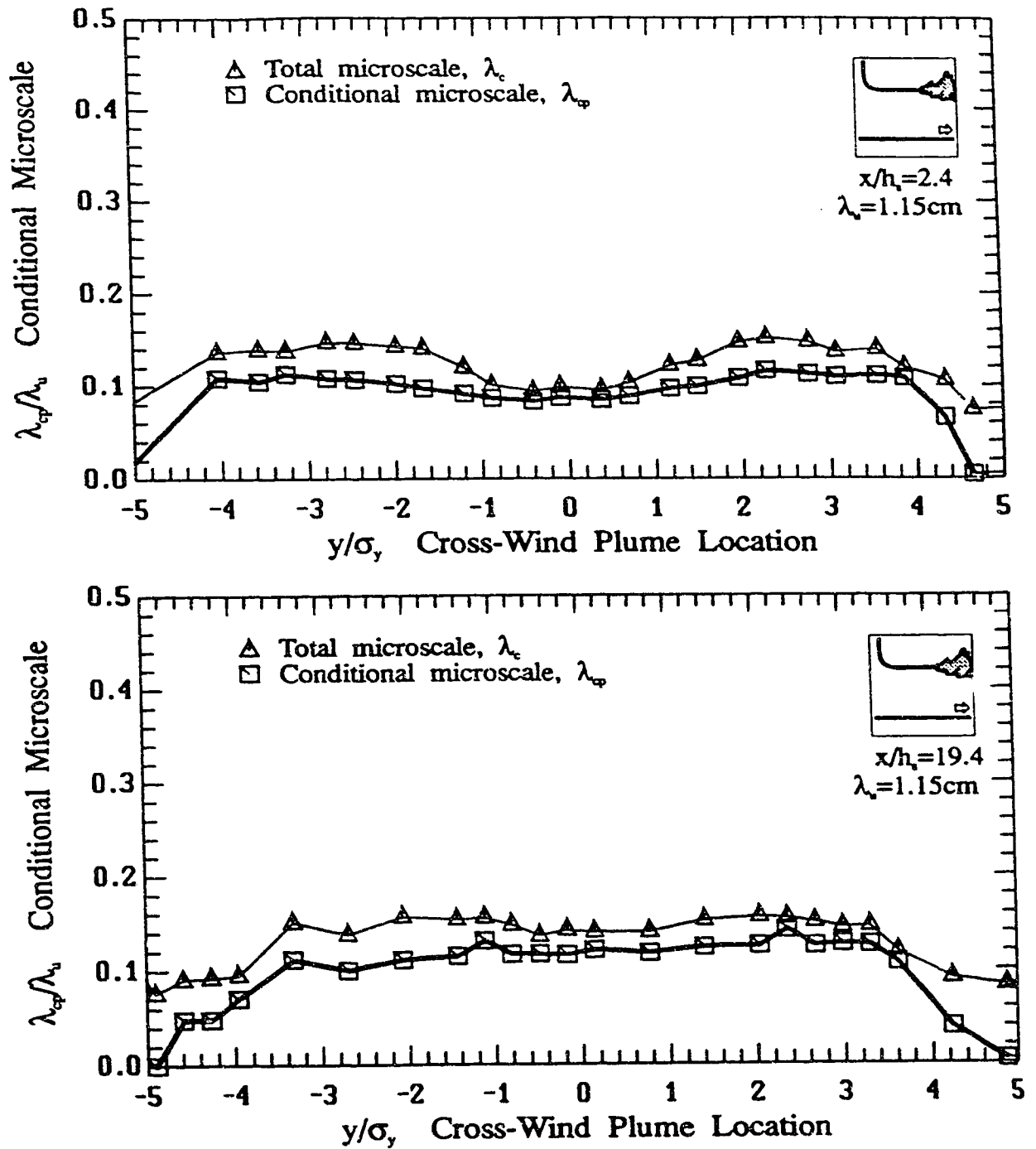


Figure 6.26: Cross-wind variation of conditional microscale of concentration fluctuations for the jet/plume source, ($\lambda_u \approx 1.15 \text{ cm}$)

6.8 Concentration Derivatives

In section 6.6 a general spectrum was developed from the Von Kármán spectrum. In this section, the derivative of the concentration time series is of interest, and specifically the variance of the derivative.

The derivative variance may be determined from the concentration spectrum through,

$$\sigma_c^2 = \bar{u}^2 \int_0^\infty k_1^2 E_{c1}(k_1) H^2(k_1) dk_1 \quad (6.108)$$

where $H^2(k_1)$ is the filtering effect of a receptor, (or detector), on the one dimensional spectrum, $E_{c1}(k_1)$, as discussed in section 4.3. Equations (6.77) and (6.85) may be substituted here for their specific ranges for n . When $H^2(k_1) = 1.0$, i.e. the receptor responds without filtering, the integral cannot be determined for values of $n \leq 3/2$. For $n > 3/2$, the integral exists but the spectrum does not represent spectra in practice. Since most applications have a receptor with some filtering, i.e. $H^2(k_1) = (1 + \Lambda_p^2 k_1^2)^{-1}$, it is useful to consider σ_c^2 including its effects on the spectrum. A solution is available for $n = 1$ only, using (6.77),

$$\sigma_c^2 = \frac{\bar{u}^2 \sigma_c^2 \left(\frac{\Lambda_p}{\Lambda_c} - 1 \right)}{\Lambda_c^2 \left(\frac{\Lambda_p^2}{\Lambda_c^2} - 1 \right)} \quad (6.109)$$

Equation (6.109) represents the derivative variance for a Markov spectrum, k_1^{-2} , with receptor filtering.

For values other than $n = 1$, a numerical integration is necessary. For $n = \frac{1}{2}$, (6.108) may be evaluated to some limit $k_m \rightarrow \text{large}$, and rather than for $k_m = \infty$. For $H^2(k_1) = 1.0$ and $n = \frac{1}{2}$, using (6.85),

$$\sigma_c^2 = \frac{\bar{u}^2 \sigma_c^2}{\pi \alpha^3 \Lambda_c^2} \left(x_m \sqrt{1 + x_m^2} + \ln \left| x_m + \sqrt{1 + x_m^2} \right| \right) \quad (6.110)$$

where $x_m = \alpha \Lambda_c k_m$ and k_m may be arbitrarily determined from the folding frequency of the data collection system. For $H^2(k_1) = (1 + \Lambda_p^2 k_1^2)^{-1}$ and $n = \frac{1}{2}$, using (6.85),

$$\sigma_c^2 = \frac{2 \bar{u}^2 \sigma_c^2}{\pi \alpha \Lambda_p^2} \left(\ln \left| x_m + \sqrt{1 + x_m^2} \right| + \frac{q}{2} \ln \left| \frac{v_m + q}{v_m - q} \right| \right) \quad (6.111)$$

where

$$k_m = \frac{2\pi}{\bar{u}} f_o$$

$$\begin{aligned}
x_m &= \alpha \Lambda_c k_m \\
\alpha &= \frac{2}{\pi} \ln \left| \beta + \sqrt{1 + \beta^2} \right| \\
q^2 &= (\alpha \Lambda_c / \Lambda_p)^2 / ((\alpha \Lambda_c / \Lambda_p)^2 - 1) \\
v_m &= \frac{x_m}{\sqrt{1 + x_m^2}}
\end{aligned}$$

The effects of numerical derivative approximation on the derivative variance are discussed in Appendix B.2.2. It was found that *very* large errors were observed because of the derivative measurements. However, a numerical integration appears to be required to take these effects into account.

Equations (6.109), (6.110) and (6.111) are three general models that may be used to determine the derivative variance using only the concentration variance and the concentration length scale. The ability of these spectra to accurately model the data is shown in Figure 6.27. It can be seen that the agreement between the data and the spectrum is exceptional. The theoretical spectrum shown in Figure 6.27, (using (B.45)), takes into account the effects of filtering because of the probe response and of the numerical derivative approximation. Note, that in Figure 6.27, the only input parameters are the concentration variance, concentration integral length scale, the probe length scale, and the derivative filter order. The figure is not normalized or fit in any way. Also shown in Figure 6.27 is the derivative spectrum that would be produced if the derivative did not filter the data. The difference between the two spectra is equivalent to a 11.8% error in the derivative variance. The derivative variance determined from the derivative of the time series, is easily corrected for the 11.8% error after the calculations.

In Figure 6.28, the derivative variance calculated using (6.111) is compared to the derivative calculated numerically from the data time series for randomly selected data sets. The spectral derivative estimation assumes that the concentration integral scale is constant across the plume and that the probe length scale is $\Lambda_p = 0.033\text{cm}$ which corresponds to the enhanced frequency response of the probe. The figure shows that the predicted values of the derivative are within $\pm 20\%$ of the numerically calculated derivatives, which is quite good considering approximations and experimental uncertainty. Individual data sets predict σ_ϵ well, so the statistical accuracy of the of the calculated σ_ϵ is better than the $\pm 20\%$ shaded region on the figure.

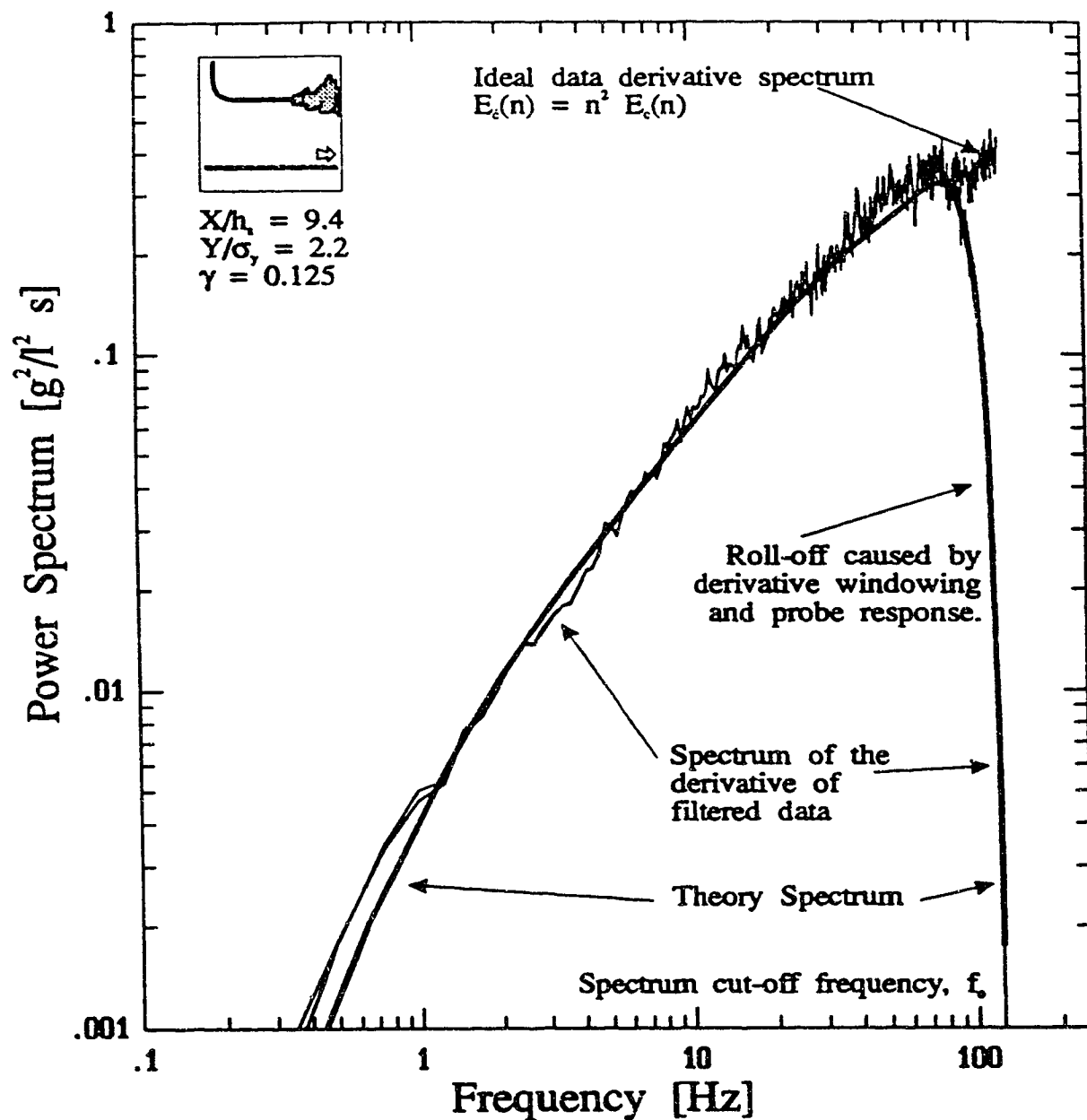


Figure 6.27: Power spectrum of the derivative of concentration fluctuations showing the exceptional agreement between the data, and the theoretical spectrum. The theory takes into account probe filtering and the filtering effects of the derivative procedure.

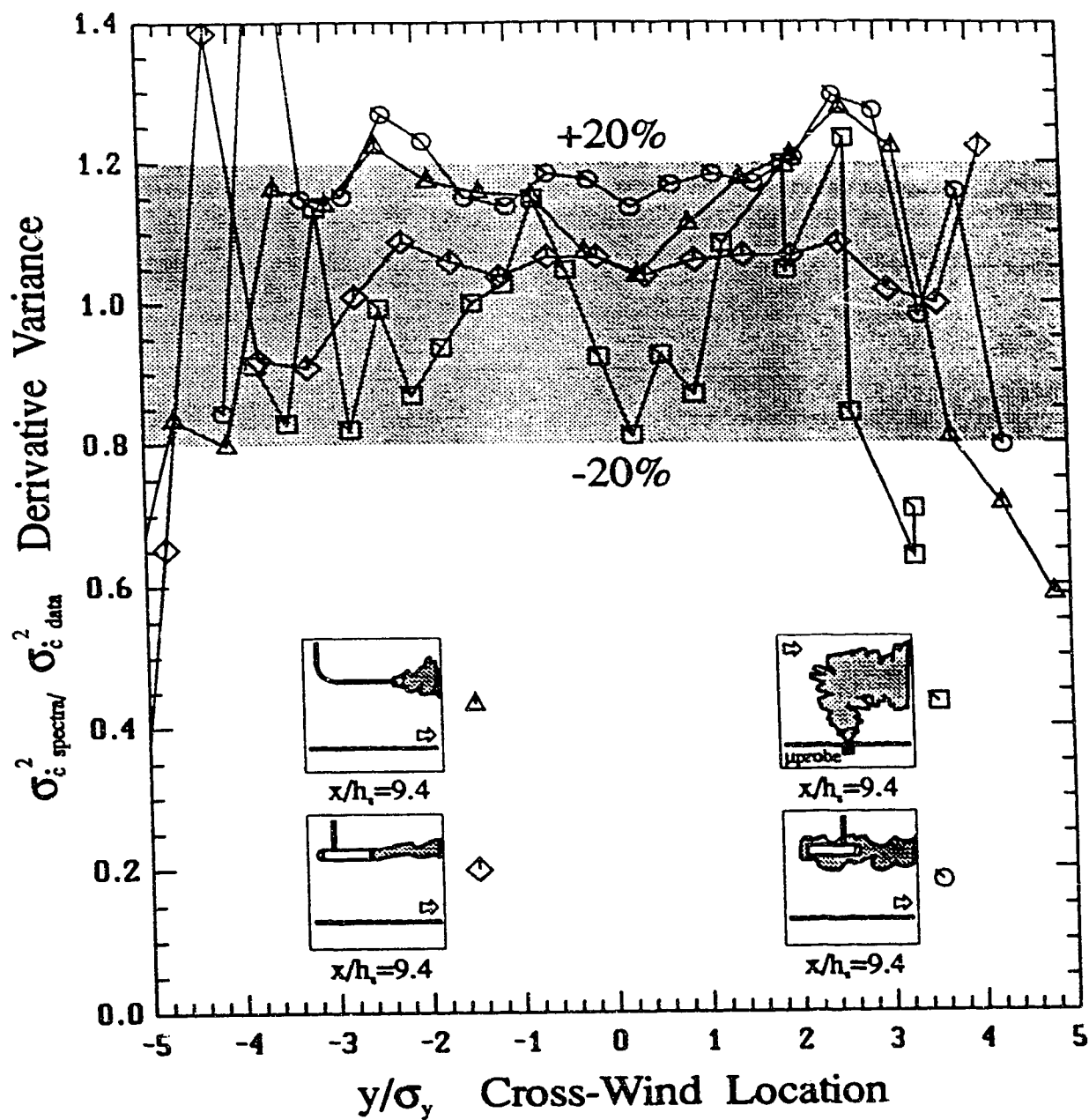


Figure 6.28: Comparison of the derivatives predicted by spectral techniques compared to the derivative determined numerically from the data.

6.9 Effect of Probe Response Time on Observed Variance

When the effects of the response time of an instrument are not corrected in the time series signal, as discussed in section 4.2, the high frequency fluctuations are attenuated. This causes the measured variance to be reduced and the integral time scales to be increased. The effects of the attenuation on the variance and the time scales may be determined by integrating the attenuated spectrum,

$$\overline{c'^2}_{\text{eff}} = \int_0^\infty E_{c1}(k_1) H^2(k_1) dk_1 \quad (6.112)$$

where $H^2(k_1)$ is the filtering effect of the receptor on the one dimensional spectrum, $E_{c1}(k_1)$. For a first order exponential detector response,

$$H^2(k_1) = \frac{1}{1 + \Lambda_p^2 k_1^2}$$

Wilson and Simms (1985), and Zelt, Wilson and Bara (1985), calculate $\overline{c'^2}_{\text{eff}}$ for a Markov spectrum

$$\overline{c'^2}_{\text{eff}} = \frac{\overline{c'^2}}{\left(\frac{1 + \Lambda_p^2}{\Lambda_c} \right)} \quad (6.113)$$

The effect of the detector response on the length scale is determined by assuming that $E_{c1}(0) \equiv E_{c,\text{eff}}(0)$ so that,

$$E_{c1}(0) = \frac{4\Lambda_c \overline{c'^2}}{\bar{u}} = \frac{4\Lambda_{c,\text{eff}} \overline{c'^2}_{\text{eff}}}{\bar{u}} \quad (6.114)$$

For the Markov spectrum, Wilson and Simms (1985), and Zelt, Wilson and Bara (1985),

$$\Lambda_c = \Lambda_{c,\text{eff}} - \Lambda_p \quad (6.115)$$

where:

- Λ_c is the integral length scale of turbulence fluctuations
- $\Lambda_{c,\text{eff}}$ is the integral length scale of turbulence fluctuations for the truncated spectrum
- $\overline{c'^2}$ is the variance of concentration fluctuations
- Λ_p is the flushing length of the probe.

For typical water channel values of $T_{c,\text{eff}} = 0.04\text{s}$ and $\tau_p = 0.004$ (6.113) predicts a correction of approximately 10% to the variance.

For the general Von Kármán spectrum, (6.77), the integration of (6.112) appears to require a numerical integration. For a Batchelor range spectrum, (6.85), the integration is not difficult and produces,

$$\overline{c'^2}_{\text{eff}} = \frac{\overline{c'^2}}{\alpha\pi\sqrt{a^2-1}} \ln \left| \frac{v_m\sqrt{a^2-1}+1}{v_m\sqrt{a^2-1}-1} \right| \quad (6.116)$$

$$a = \frac{\Lambda_p}{\alpha\Lambda_c} \quad (6.117)$$

$$v_m = \frac{\Lambda_c\alpha k_m}{\sqrt{1+(\Lambda_c\alpha k_m)^2}} \quad (6.118)$$

$$\alpha = \frac{2}{\pi} \ln \left| \beta + \sqrt{1+\beta^2} \right| \quad (6.119)$$

where:

k_m is an upper limit integration value consistent with (6.80)

β is determined using (6.86)

The ratio $\overline{c'^2}_{\text{eff}}/\overline{c'^2}$ is plotted in Figure 6.29 using (6.113) and (6.116). Figure 6.29 shows that the Batchelor range spectrum is more affected by the detector response than the Markov spectrum. Therefore, making the time response correction in the Batchelor range is very important.

The correction to the integral length scales using the Batchelor range spectrum may be determined using (6.114). The correction does not simplify on substitution of (6.116).

6.10 Conclusions

This chapter has presented a similarity model for the cross-wind variation of the higher order moments of concentration. It was shown that based on the conservation equations for the first four higher order moments, a Gaussian distribution could be expected. The data sets collected in the water channel boundary layer have shown that this model is a good representation of the data for a wide variety of source configurations. The model is not, however, fully developed, and does not yet predict the evolution of key centre-line values required for general application of the model.

In conjunction with a probability distribution model, the similarity model accurately predicts the conditional statistics in the plume. Large errors, (factors of two to ten), may be observed when the wrong PDF model is used.

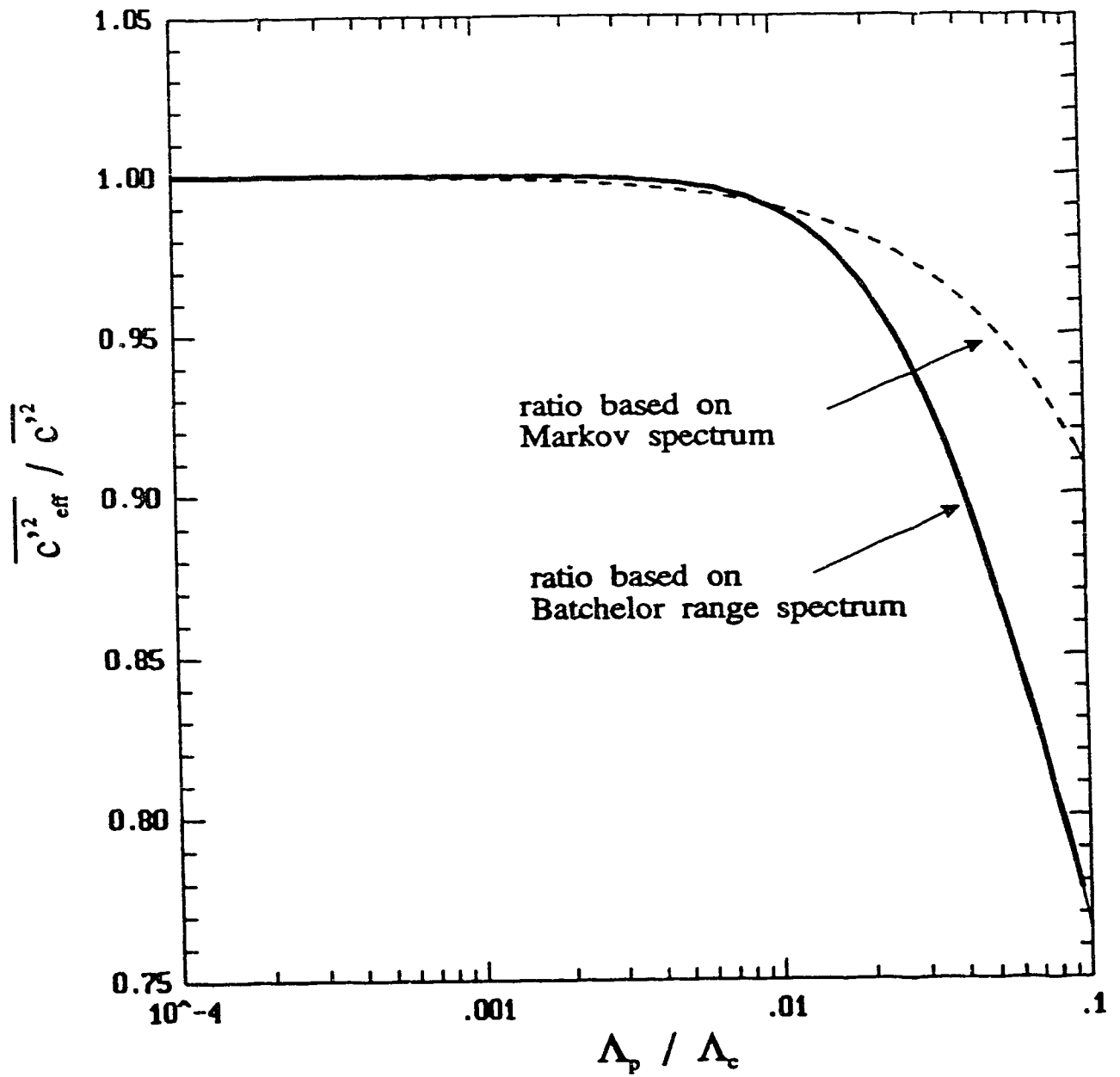


Figure 6.29: The effect of detector response on the concentration variance for a Markov spectrum and a Batchelor Range k^{-1} spectrum.

A model for the derivative variance was presented which was based on a generalization of the Von Kármán spectrum for scalar fluctuations. The derivative model uses only the concentration variance and the concentration integral length scale as inputs to the model. The model may be used to explain the receptor filter effects on the derivative variance, by including an estimate of the receptor time scale. The derivative variance is predicted within 20% of the values calculated numerically from the data set.

This chapter in combination with Chapter 5 forms the basis of a model which may be used to predict concentration fluctuations statistics for use in hazard assessment model calculations.

Chapter 7

Inter-Event time PDFs

The inter-event times and excursion times for concentration signals above a threshold have several important engineering applications. These include the ability to predict the average duration time of a concentration above a hazard threshold, which is important in hazard assessment and risk analysis. The time between excursions above a threshold are also important in hazard assessment as these times will dictate the possible evacuation scenarios in clean air. The distribution of the excursions above the intermittency threshold may be an indication of the actual eddy size. This distribution provides a different method for examining risk that is not given by the integral time scale size of the eddies provided by a spectral analysis of the time series.

In addition to the above, Rice (1944-45) made several important discoveries concerning the average duration of excursion times and the joint probability distribution of the concentration and its derivative. Rice's work, which was developed to analyze shot noise along telegraph wires, allows the concentration PDF to be used to draw conclusions about the temporal spacing of the eddies. Panofsky and Dutton (1984), and Kristensen, Weil, and Wyngaard (1988), have made use of the general conclusion of Rice's work, and applied it to concentration fluctuation excursion times. The analysis of Kristensen, Weil, and Wyngaard did not incorporate the intermittent nature of the concentration fluctuation process, as is included in this study. The Kristensen, Weil, and Wyngaard analysis is extended to investigate a variety of probability models for the concentration process and for the derivative of the concentration process.

7.1 Theory

Before diving into a slurry of probability distributions and applications from Rice's (1944-45) paper, it is appropriate to examine what might be expected. Statistics tells us that the number of excursions above a high concentration threshold for random, uncorrelated, statistically independent events, is likely to follow a Poisson counting process. The waiting time to the first excursion is therefore Exponentially distributed. The Exponential model has the important characteristic of being *memoryless*, in other words the waiting time to the next event is also Exponentially distributed, and therefore the Exponential model gives rise to the *inter-arrival time* between Poisson events. The actual distribution of the waiting times is given by the Erlang distribution, which is a specific case of the Gamma distribution with a positive, integer λ parameter. The Erlang distribution is related to the Poisson distribution by, (Bury, 1986, p.325).

$$\Pr \left(\begin{array}{l} \text{number of events observed} \\ \text{in time } x \text{ is less than or equal} \\ \text{to } \lambda - 1 \end{array} \right) = \Pr \left(\begin{array}{l} \text{waiting time for } \lambda \text{ events is} \\ \text{greater than or equal to } x \end{array} \right)$$

This is intuitively obvious and shows that the Erlang distribution is an equivalent representation of the Poisson process. We therefore expect, that in the water channel observations of the inter-arrival times should be Exponentially distributed. If the inter-arrival times are Exponentially distributed and equal the probability of the number of events in the time period, it follows that, for sufficiently high thresholds, the excursion time above the threshold must also be Exponentially distributed.

An alternative way of looking at the process is to consider the physical dilution process. One model that is proposed is that eddies of similar size combine and cause a halving of the concentration. This is a multiplicative process and would lead to the concentration distribution having a log-Normal distribution. In a similar but independent argument, it may be argued that the action of vortex stretching or rolling of sheets of tracer material and clean water would lead to a halving of the initial size of the eddy. This too is a multiplicative process which would lead us to expect a log-Normal distribution of the sizes of the eddies. The size of the eddy could be measured by assuming Taylor's frozen turbulence assumption and measuring the distribution of concentration excursions above the intermittency threshold. Therefore the duration of excursions above zero threshold would be expected to be log-Normally distributed, independent of the threshold level.

The Exponential distribution and the log-Normal distribution form two limiting possibilities for the duration of times above a threshold. Here, these will be tested with the water channel data.

7.1.1 Threshold Crossing Probabilities

To estimate the probability of exceeding a concentration value, c^* , during an exposure of length T , we require the probability per unit time of exceeding the threshold for the first time, (*the first passage problem*), Cox and Miller (1965). The nomenclature for threshold crossing is illustrated in Figure 7.1. Current time variables are expressed using lower case t , (with subscripts), and average time variables are expressed using upper case T , (with subscripts).

The probability of exceeding the threshold in a unit time Δt is simply the rate of exceeding c^* multiplied by Δt . The waiting time for a concentration value to exceed a threshold value c^* , is defined as t_R , (t is the current time). Assume the concentration is less than c^* for all time t before c^* . The PDF of first passage times is given by $g(t)$ and the associated CDF is denoted by $G(t)$. The two are related by,

$$g(t) = \frac{dG(t)}{dt}. \quad (7.1)$$

The reliability, or complimentary cumulative distribution function, CCDF, $G'(t)$, is related to $G(t)$ by,

$$G'(t) = 1 - G(t). \quad (7.2)$$

The CDF is the basic statistical model of the first passage time, t_R . The hazard rate, $h(t)$, is defined in terms of the number of passage times below the threshold. Bury (1986) p.487,

$$h(t) = \frac{g(t)}{1 - G(t)} = \frac{\frac{dG(t)}{dt}}{1 - G(t)}. \quad (7.3)$$

The hazard rate is interpreted as the instantaneous rate, (probability per unit time), of exceeding the threshold level given that it has not exceeded it yet in the time t . The hazard rate may be determined once $G(t)$ has been specified. In terms of the threshold level crossing in concentration fluctuations, the hazard rate is interpreted as the instantaneous rate of crossings at the time, t .

An additional statistical characterization of the first passage time is the mean time to exceed the threshold, (or *mean time to failure*), MTTF, which is defined as the expected first passage time, Bury (1986),

$$MTTF = E\{t\} = \int_0^\infty t g(t) dt. \quad (7.4)$$

Integrating the hazard function, (7.3), yields,

$$\int_0^t h(t) dt = \int_0^t \frac{dG(t)}{1 - G(t)} = -\ln(1 - G(t)) \Big|_0^t \quad (7.5)$$

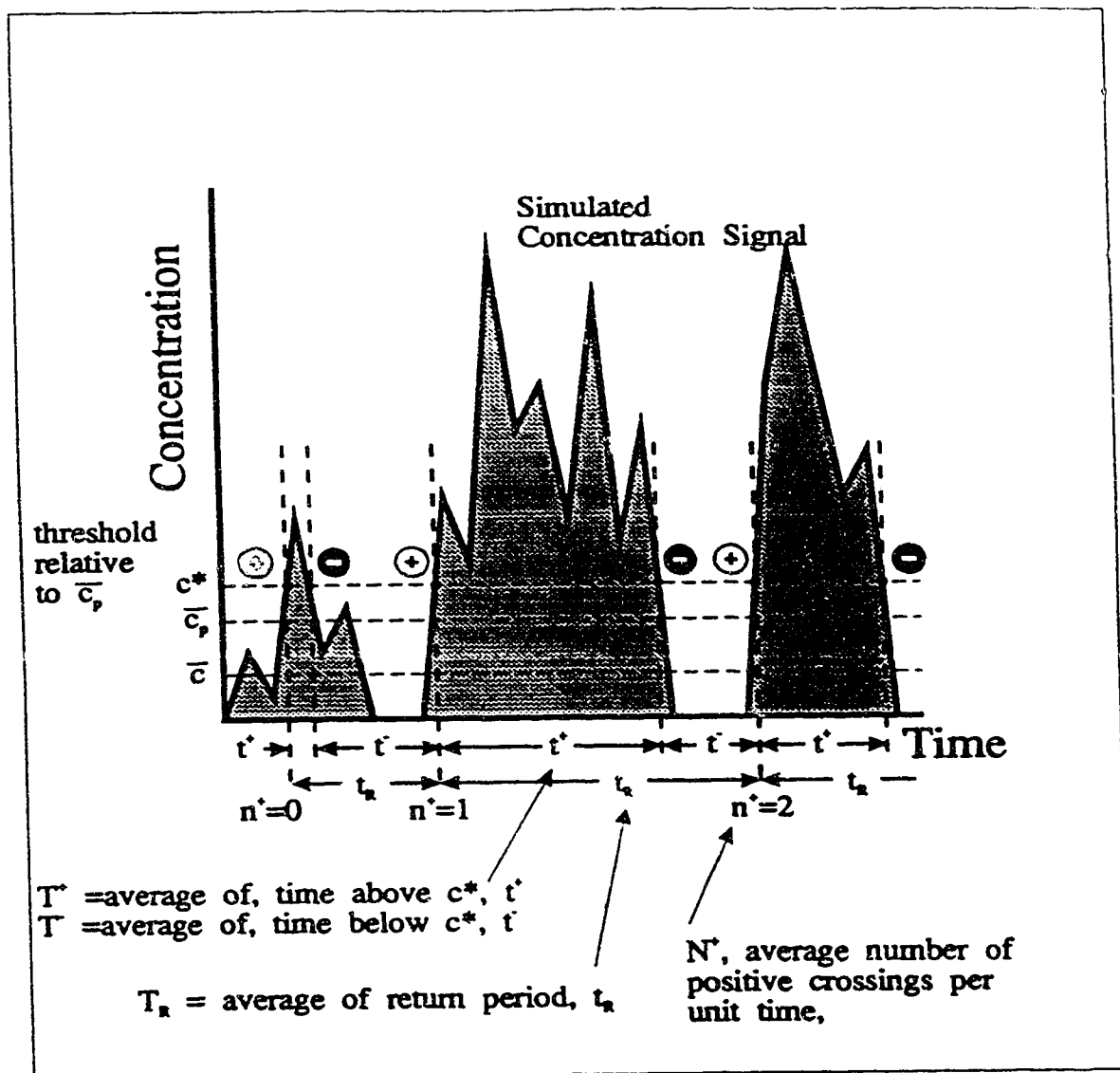


Figure 7.1: Illustration of the threshold crossing problem with the nomenclature used to describe it.

But since $G'(t = 0) = 0$ then,

$$\int_0^t h(t) dt = -\ln(G'(t)). \quad (7.6)$$

Rearranging this equation and substituting for the $G'(t)$, Roberts (1986), Bury (1986), the average return time, (mean time between c^* threshold crossings), for an exposure time of T_e , is,

$$\frac{T_R(t)}{T_e} = \exp \left(- \int_0^t h(t) dt \right). \quad (7.7)$$

Wilson and Simms (1985) evaluate the hazard rate, $h(t)$, the probability per unit time of exceeding the threshold c^* for the first time. The hazard rate $h(t)$ and the CCDF of concentration $F'(c)$ are identical probabilities. This conclusion requires two fundamental assumptions:

1. The hazard rate, $h(t)$, (the probability of exceeding a c^* threshold), for a unit time of exposure is equal to the probability of exceeding the threshold for an instant. That is, $h_{c^*}(t) = F'(c^*)/\Delta t$.
2. The probability that the j^{th} short exposure exceeds the threshold is independent of the probabilities of exceeding the threshold in any previous interval.

The first assumption implies that the probability of exceeding c^* during the short time interval Δt remains constant over the time interval. The second assumption implies that successive exposures are statistically independent. Therefore, successive exposures must be separated by a length of time to remove the correlation, i.e. the Eulerian time scale. The threshold level, c^* , must be selected in such a way that this is true. Wilson and Simms (1985) suggest that as a rough estimate, c^* must be larger than the mean concentration \bar{c} during an interval.

Examining (7.7) we see that the integrand may be substituted for the CCDF of concentration. For short exposure times, and if the $h(t)$ may be considered constant over the exposure time, T_e , then the integral may be evaluated to be,

$$T_R(t) = T_e \exp(-h(t)T_e). \quad (7.8)$$

This implies that the waiting time for a high exposure of concentration is exponentially distributed in this case, (Bury, 1986, p.489, and Roberts, 1986).

7.1.2 Joint PDF Approach

The probability, $F(t | c_o, \dot{c}_o)$, that the first passage will not occur in the interval T_R , given the initial concentration, c_o , and the initial concentration derivative, \dot{c}_o , is,

$$F(t | c_o, \dot{c}_o) = \int \int_R f(c, \dot{c}; t | c_o, \dot{c}_o) dc d\dot{c} \quad (7.9)$$

The process governing the joint probability distribution, $f(c, \dot{c}; t | c_o, \dot{c}_o)$, is the Fokker-Planck-Kolmogorov equation,

$$\frac{\partial f}{\partial t} = -g(c_o, \dot{c}_o) \frac{\partial f}{\partial \dot{c}_o} + \dot{c}_o \frac{\partial f}{\partial c_o} + \frac{I}{2} \frac{\partial^2 f}{\partial \dot{c}_o^2} \quad (7.10)$$

where $g(c_o, \dot{c}_o)$ is a general, non-hereditary function, and I is a noise source strength term, Roberts (1986). Closed form solutions for f in (7.10) have not been discovered.

Following Rice (1935), Panofsky and Dutton, (1984) p.320, and Roberts, (1986), the present study avoids the second assumption (used by Wilson and Simms, 1985) by considering the joint PDF of concentration and its derivative, $f(c, \dot{c})$. This joint PDF is the fraction of time interval, t , the concentration value is c and \dot{c} . Consider the joint process, $f(c, \dot{c})$, assuming that $f(c, \dot{c})$ is a vector, two dimensional continuous Markov process, or in other words a vector diffusion process. For this process, the unconditional transition density function $f(c, \dot{c}; t | c_o, \dot{c}_o)$ is a complete probabilistic description. $f(c, \dot{c}; t | c_o, \dot{c}_o)$ is the probability that $c \leq c(t) \leq c + dc$ and $\dot{c} \leq \dot{c}(t) \leq \dot{c} + d\dot{c}$ at time t , given that $c = c_o$ and $\dot{c} = \dot{c}_o$ at time $t = 0$. We can also define $f(c, \dot{c}; t | c_o, \dot{c}_o)$ to be the conditional transition density, denoting $f(c^*, \dot{c}^*; t | c_o, \dot{c}_o)dc d\dot{c}$ as the probability that $c \leq c(t) \leq c + dc$ and $\dot{c} \leq \dot{c}(t) \leq \dot{c} + d\dot{c}$ at time t without having exceeded c^* and \dot{c}^* .

Let $N^+(c^*)$ denote the average number of upward crossings per unit time through the concentration level $c = c^*$, \dot{c} the temporal derivative of c , and $f(c^*, \dot{c})$ the joint probability distribution function of c and \dot{c} . For a stationary random process, the exceedance rate function is given by, Rice (1944-45),

$$N^+(c^*) = \int_0^\infty \dot{c} f(c^*, \dot{c}) d\dot{c} \quad (7.11)$$

The exact form of $f(c^*, \dot{c})$ is not yet known, nor is the form for the distribution of the number of zero crossings per unit time, $f_{N^+}(c)$. Note that (7.11) does not require the assumption that the threshold level be large compared to the mean concentration value. It is an assumption that eddies must be separated by a period of time large compared to the integral time scale of turbulence.

To apply (7.11), the joint probability, $f(c^*, \dot{c})$, may be assumed to be independent to help simplify the analysis here and later. (Ylvisaker (1965) has shown that the same result may be achieved without the independence assumption, Sreenivasan, Prabhu and Narasimha (1983)). If $c(t)$ is a stationary time series, Kristensen, Weil, and Wyngaard (1988) show that the covariance is,

$$\langle c(t)\dot{c}(t) \rangle = \frac{1}{2} \frac{d}{dt} \langle c^2(t) \rangle = 0 \quad (7.12)$$

which proves that $c(t)$ and $\dot{c}(t)$ are not correlated. However, a zero correlation coefficient does not prove independence, although the reverse is true. Mark (1990), shows that whenever changes in the local variance of the turbulent component, $r(t)$, are negligible over time intervals equal to the microscale of $r(t)$, the correlation coefficient between $r(t)$ and its temporal derivative $\dot{r}(t)$ is negligible. (The random process $r(t)$ may be non-stationary.) Although independence cannot be proven, it seems a reasonable approximation and is assumed here. With independence,

$$f(c, \dot{c}) = f(c) f(\dot{c}) \quad (7.13)$$

and (7.11) may be expressed as

$$N^+(c^*) = f(c^*) \int_0^\infty \dot{c} f(\dot{c}) d\dot{c} \quad (7.14)$$

Average Interval Time

The average interval time, or return time, $T_R(c^*)$, between successive positive threshold crossings at level c^* is,

$$T_R(c^*) = \frac{1}{N^+(c^*)} \quad (7.15)$$

The average probability of crossing c^* in a lifetime, t , is given by, $\text{Pr}_t(c^*)$,

$$\text{Pr}_t(c^*) = N^+(c^*) t, \quad (N^+(c^*) t) \leq 1 \quad (7.16)$$

The average duration of excursions above c^* is $T^+(c^*)$, which may be determined from $\text{Pr}_t(c^*)$. Expressing it as the probability of exceeding c^* , it follows that,

$$N^+(c^*) T^+(c^*) = \text{Pr}_t(c^*) = \int_{c^*}^\infty f(c) dc \quad (7.17)$$

Rearranging, gives an expression for T^+ ,

$$T^+(c^*) = \frac{1}{N^+(c^*)} \int_{c^*}^{\infty} f(c) dc \quad (7.18)$$

which is equivalent to,

$$T^+(c^*) = \frac{1}{N^+(c^*)} \int_{c^*}^{\infty} \int_{-\infty}^{+\infty} f(c, \dot{c}) d\dot{c} dc \quad (7.19)$$

where:

- N^+ is the average number of positive threshold crossings per unit time
- T^+ is the average time duration a signal is above the threshold
- c^* is the concentration threshold level
- T_R is the average time interval between a threshold crossing and the next threshold crossing

Similarly, the average duration of excursions below c^* may be defined as $T^-(c^*)$. $T^-(c^*)$ is defined by the CDF of the concentration process, which is the cumulative probability that the threshold, c^* , has not been exceeded.

$$T^-(c^*) = \frac{1}{N^+(c^*)} \int_0^{c^*} f(c) dc \quad (7.20)$$

These expressions may be reduced once models for $f(c)$ and $f(\dot{c})$ are determined.

7.2 Threshold Crossing Intermittent Signals

The standard probability distributions do not model the intermittency concentration process, and therefore the zero periods must be incorporated into a refined probability model. The standard probability models are used to represent the conditional concentrations, (i.e. when the signal is observed), and expressions such as (5.2) are used to develop the complete probability model. Kristensen, Weil, and Wyngaard (1988) did not perform this important step in their analysis of the threshold crossing.

Similar to (5.2), the following model, (7.21), is assumed to exist also for the derivative of the concentration.

$$f(\dot{c}) = \gamma f_p(\dot{c}) + (1 - \gamma)\delta(c) \quad (7.21)$$

A consequence of (7.21) and the fact that the mean derivative value is zero, i.e. the derivative is a symmetric, centred distribution, is that,

$$\overline{\dot{c}^2} = \gamma \overline{\dot{c}_p^2} \quad (7.22)$$

Therefore, since $\bar{\dot{c}} = 0$,

$$\sigma_{\dot{c}} = \sqrt{\gamma} \sigma_{\dot{c}_p} \quad (7.23)$$

It would be wrong to substitute both (5.2) and (7.21), into the models for N^+ and T^+ , because the intermittency would be accounted for twice. Therefore the following model for the behavior of the joint probability density in an intermittent signal is proposed,

$$f(c, \dot{c}) = \gamma f_p(c, \dot{c}) + (1 - \gamma) \delta(c) \delta(\dot{c}) \quad (7.24)$$

where:

- $f_p(c, \dot{c})$ is the joint conditional distribution, $f(c, \dot{c} | c > 0)$.
- γ is the fraction of time the plume is present, i.e. when the concentration is non-zero.
- $\delta(c)$ is the dirac delta function at a concentration of zero.
- $\delta(\dot{c})$ is the dirac delta function at a zero concentration derivative.

Assuming independence for $f_p(c, \dot{c})$ for simplicity,

$$f_p(c, \dot{c}) = f_p(c) f_p(\dot{c}) \quad (7.25)$$

$f_p(c)$ is the conditional concentration probability distribution and $f_p(\dot{c})$ is the conditional derivative PDF of the concentration. Substituting (7.24) into (7.14),

$$N^+(c^*) = \int_0^\infty \dot{c} (\gamma f_p(c, \dot{c}) + (1 - \gamma) \delta(c) \delta(\dot{c})) d\dot{c} \quad (7.26)$$

This reduces to,

$$N^+(c^*) = \gamma f_p(c) \int_0^\infty \dot{c} f_p(\dot{c}) d\dot{c} \quad (7.27)$$

The integral in (7.27) represents the mean of the derivative distribution for positive derivatives.

The average excursion duration above a threshold, may be determined by substituting (7.24) into (7.19),

$$T^+(c^*) = \frac{1}{N^+(c^*)} \int_{c^*}^\infty (\gamma f_p(c) + (1 - \gamma) \delta(c)) dc \quad (7.28)$$

$$= \frac{\gamma}{N^+(c^*)} \int_{c^*}^{\infty} f_p(c) dc \quad (7.29)$$

$$= \frac{\gamma F'_p(c^*)}{N^+(c^*)} \quad (7.30)$$

where:

N^+	is the average number of threshold crossings per unit time
T^+	is the average time duration a signal is above the threshold
c^*	is the concentration threshold level
γ	is the intermittency or the fraction of time the concentration is non-zero.
$F'_p(c^*)$	is the conditional CCDF of concentration

It was found in section 5.5, that there are two possible distributions for the probability of $\dot{c}(t)$: the Normal and the Exponential distribution. The present study focusses on the above two distributions for $\dot{c}(t)$ and the log-Normal, Gamma and the clipped-Normal distributions for $c(t)$.

In Appendix E the exceedance equations are developed assuming the $\dot{c}(t)$ PDF is Gamma distributed. The Gamma distribution was observed in section 5.5 to represent the derivative PDF under the limitation that the Gamma parameter $\lambda < 1$. In Appendix E, the exceedance equations were found to depend on $|\overline{\dot{c}_p}|$, which was not determined by the data analysis. Therefore, the Gamma representation of the derivative PDF has not been pursued.

The notation used in the following sections for N^+ and T^+ include the names of the PDFs for the concentration and the derivative. The letter names are consistent with the distributions described in Chapter 5, and are,

- G** the Gamma distribution
- LN** the log-Normal distribution
- CN** the clipped-Normal distribution
- E** the Exponential distribution
- N** the Normal distribution

7.2.1 Normal PDF for the Concentration Derivative

In this section, the exceedance relationships are developed assuming the derivative $\dot{c}(t)$ has a Normal distribution.

$$f_{N,p}(\dot{c}) = \frac{1}{\sqrt{2\pi}\sigma_{\dot{c},p}} \exp\left(-\frac{(\dot{c} - \mu_{\dot{c},p})^2}{2\sigma_{\dot{c},p}^2}\right), \quad -\infty < \dot{c} < \infty \quad (7.31)$$

Here $\mu_{\dot{c},p} = 0$ is the zero mean value of the concentration derivative. This is observed to be true in data collected in the water channel. $\sigma_{\dot{c},p}$ is the standard deviation of the conditional derivative time series. Substituting (7.31) into (7.27) yields,

$$\begin{aligned} N^+_{N,N}(c^*) &= f_p(c^*) \frac{\gamma}{\sqrt{2\pi}\sigma_{\dot{c},p}} \int_0^\infty \dot{c} \exp\left(-\frac{\dot{c}^2}{2\sigma_{\dot{c},p}^2}\right) d\dot{c} \\ &= \frac{\gamma\sigma_{\dot{c},p}}{\sqrt{2\pi}} f_p(c^*) \end{aligned} \quad (7.32)$$

where $N^+_{N,N}(c^*)$ is the average number of exceedances per unit time for a derivative with a Normal distribution and an unspecified concentration PDF. Substituting, (7.32) into (7.30),

$$T^+_{N,N}(c^*) = \frac{\gamma}{\left(\frac{\gamma\sigma_{\dot{c},p}}{\sqrt{2\pi}}\right)} \frac{(1 - F_p(c^*))}{f_p(c^*)} \quad (7.33)$$

$$= \frac{\sqrt{2\pi}}{\sigma_{\dot{c},p}} \left(\frac{1 - F_p(c^*)}{f_p(c^*)} \right) \quad (7.34)$$

The expressions, (7.32) and (7.34), are suitable for application once the PDF for $f_p(c^*)$ is specified. Note that (7.34) is independent of the intermittency which is intuitively obvious, for an exceedance period.

Substituting for $f_p(c^*)$, the Normal (5.12), the log-Normal (5.17), the Gamma (5.41), and the clipped-Normal (5.29) distributions,

$$N^+_{N,N}(c^*) = \frac{\sigma_{\dot{c},p}\gamma}{2\pi\sigma} \exp\left(-\frac{(c^* - \mu)^2}{2\sigma^2}\right) \quad (7.35)$$

$$N^+_{LN,N}(c^*) = \frac{\sigma_{\dot{c},p}\gamma}{2\pi\sigma c^*} \exp\left(-\frac{(\ln(c^*) - \mu)^2}{2\sigma^2}\right) \quad (7.36)$$

$$N^+_{G,N}(c^*) = \frac{\sigma_{\dot{c},p}\gamma}{\sqrt{2\pi}\sigma\Gamma(\lambda)} \left(\frac{c^*}{\sigma}\right)^{\lambda-1} \exp\left(-\frac{c^*}{\sigma}\right) \quad (7.37)$$

$$N^+_{CN,N}(c^*) = \frac{\sigma_{\dot{c},p}}{2\pi\sigma_o} \exp\left(-\frac{(c^* - \mu_o)^2}{2\sigma_o^2}\right) \quad (7.38)$$

Note that the first expression, (7.35), represents a joint Normal probability distribution for $c(t)$ and $\dot{c}(t)$. This is not a feasible PDF for plume dilution, but is an important distribution for other processes, and will be discussed later. Also, note that σ , σ_c , λ , and μ_c are parameters of their respective PDFs and may be determined from the moments \bar{c} , \bar{c}^2 , \bar{c}^3 as discussed in section 5.1.

Cox and Miller (1965) p.295, show that for a joint Normal process the number of threshold crossings per unit time is proportional to the autocorrelation function, ρ ,

$$N^+ = \frac{\sqrt{-\frac{\partial^2 \rho}{\partial t^2}(0)}}{2\pi} \quad (7.39)$$

Therefore, for a process with $\rho \propto e^{-t/\tau}$, then $N^+ = \infty$. Which means that near zero, the processes will jitter back and forth infinitely often. In practice, the response time of a measurement instrument would smooth this out, and so this would not be observed. The zero limit for the Lagrangian correlation function, Csanady (1973) p.55 for example, has a finite $\frac{\partial^2 \rho(0)}{\partial t^2}$. For the Von Kármán spectrum the correlation function (6.73) could be used to determine an approximate joint Normal limit.

7.2.2 Exponential PDF for the Concentration Derivative

The exceedance relationships developed here assume $\dot{c}(t)$ has an Exponential distribution. The experiments in the present study show that this may be a better approximation for $\dot{c}(t)$ than the Normal PDF. The Exponential model for $f_p(\dot{c})$ is given by,

$$f_{E,p}(\dot{c}) = \frac{1}{2\mu} \exp\left(-\frac{|\dot{c}|}{\mu}\right), \quad -\infty < \dot{c} < \infty \quad (7.40)$$

where $\mu = \sigma_{\dot{c},p}/\sqrt{2}$, from the second moment of (7.40) with \dot{c} . Substituting (7.40) into (7.27),

$$\begin{aligned} N^+_{E(c^*)} &= f_p(c^*) \frac{\gamma}{\sqrt{2}\sigma_{\dot{c},p}} \int_0^\infty \dot{c} \exp\left(-\frac{\sqrt{2}|\dot{c}|}{\sigma_{\dot{c},p}}\right) d\dot{c} \\ &= \frac{\gamma\sigma_{\dot{c},p}}{2\sqrt{2}} f_p(c^*) \end{aligned} \quad (7.41)$$

Substituting, (7.41) into (7.30),

$$T^+_{E(c^*)} = \frac{\gamma}{\left(\frac{\gamma\sigma_{\dot{c},p}}{2\sqrt{2}}\right)} \frac{(1 - F_p(c^*))}{f_p(c^*)} \quad (7.42)$$

$$= \frac{2\sqrt{2}(1 - F_p(c^*))}{\sigma_{\dot{c},p} f_p(c^*)} \quad (7.43)$$

The expressions, (7.41) and (7.43), are suitable for application once the PDF for $f_p(c^*)$ is specified.

Substituting for $f_p(c^*)$, the log-Normal (5.17), the Gamma (5.41), and the clipped-Normal (5.29) distributions,

$$N^+_{LN,E}(c^*) = \frac{\sigma_{\dot{c},p}\gamma}{4\sqrt{\pi}\sigma c^*} \exp\left(-\frac{(\ln(c^*) - \mu)^2}{2\sigma^2}\right) \quad (7.44)$$

$$N^+_{G,E}(c^*) = \frac{\sigma_{\dot{c},p}\gamma}{2\sqrt{2}\sigma\Gamma(\lambda)} \left(\frac{c^*}{\sigma}\right)^{\lambda-1} \exp\left(-\frac{c^*}{\sigma}\right) \quad (7.45)$$

$$N^+_{CN,E}(c^*) = \frac{\sigma_{\dot{c},p}}{4\sqrt{\pi}\sigma_o} \exp\left(-\frac{(c^* - \mu_o)^2}{2\sigma_o^2}\right) \quad (7.46)$$

Since the expressions for $F(c)$ are complex, substitution for $F(c)$ in (7.43) and (7.34) does not provide any insight into the nature of the equations. However, a further reduction of (7.43) and (7.34), may be performed by substituting the hazard rate, (7.3). Therefore, (7.43) may be expressed as,

$$T^+_E(c^*) = \frac{2\sqrt{2}}{\sigma_{\dot{c},p} h_p(c^*)} \quad (7.47)$$

and for the Normal model (7.34),

$$T^+_N(c^*) = \frac{\sqrt{2\pi}}{\sigma_{\dot{c},p} h_p(c^*)} \quad (7.48)$$

The difference between the Exponential derivative PDF and the Normal derivative PDF is not large but it is significant. Taking the ratio yields,

$$\frac{T^+_N(c^*)}{T^+_E(c^*)} = \frac{\sqrt{2\pi}}{2\sqrt{2}} = 0.88 \quad (7.49)$$

Therefore, the return time to threshold crossings could be estimated as 12% too low by using the Normal derivative model instead of the observed Exponential model.

The dependence of N^+ and T^+ on the concentration intermittency may be observed by examining (7.41) and (7.43), or (7.32) and (7.34). That is,

$$N^+ \propto \gamma \sigma_{\dot{c},p} \quad \text{is directly proportional to intermittency}$$

$$T^+ \propto \frac{1}{\sigma_{\dot{c},p}} \quad \text{is not a function of intermittency}$$

However, when modelling N^+ and T^+ using the total concentration moments $\sigma_{\dot{c},p}$ must be estimated from $\sigma_{\dot{c}}$ using (7.23). In practice the model depends on intermittency in this way,

$$N^+ \propto \gamma \sigma_{\dot{c},p} \propto \gamma^{1/2}$$

$$T^+ \propto \frac{1}{\sigma_{\dot{c},p}} \propto \gamma^{1/2}$$

Therefore, the ability of the exceedance theory to make accurate predictions depends on the ability of the PDF model to accurately predict the intermittency.

The nature of the hazard rate function near zero concentration makes the prediction of the T^+ very difficult as $c^* \rightarrow 0$. Figure 7.2 demonstrates the behaviour of T^+ which is proportional to the inverse of the hazard rate function, for the three probability models for $f_p(c)$. The log-Normal distribution will always tend to infinity near zero, whereas the Gamma distribution may or may not, depending on the parameters of the distribution,

$$\begin{aligned} \lambda > 1 \quad (i_p^2 < 1) \quad &\text{then } f(c) \rightarrow 0 \text{ as } c \rightarrow 0 \\ \lambda = 1 \quad (i_p^2 = 1) \quad &\text{then } f(c) \rightarrow 1 \text{ as } c \rightarrow 0 \\ \lambda < 1 \quad (i_p^2 > 1) \quad &\text{then } f(c) \rightarrow \infty \text{ as } c \rightarrow 0 \end{aligned}$$

The Gamma distribution rises very slowly to infinity compared to the log-Normal distribution. The clipped-Normal distribution is non-zero at $c = 0$ so that $T^+(0)$ remains finite at zero concentration. It is expected then, that the Gamma or the clipped-Normal distribution, provide a better prediction for T^+ for threshold levels near zero.

In conclusion, what is wrong with most theoretical PDFs is that they tend to zero as $c \rightarrow 0$. This behaviour is inconsistent with observed PDFs which tend to a non-zero value as $c \rightarrow 0$. The clipped-Normal PDF is the only distribution with this behaviour. Because the probability models do not predict values at zero, and because the intermittency is implicitly incorporated in the derivation of N^+ and T^+ , the theory cannot be used to predict exceedance statistics for zero concentration, ($N^+(0)$ and $T^+(0)$).

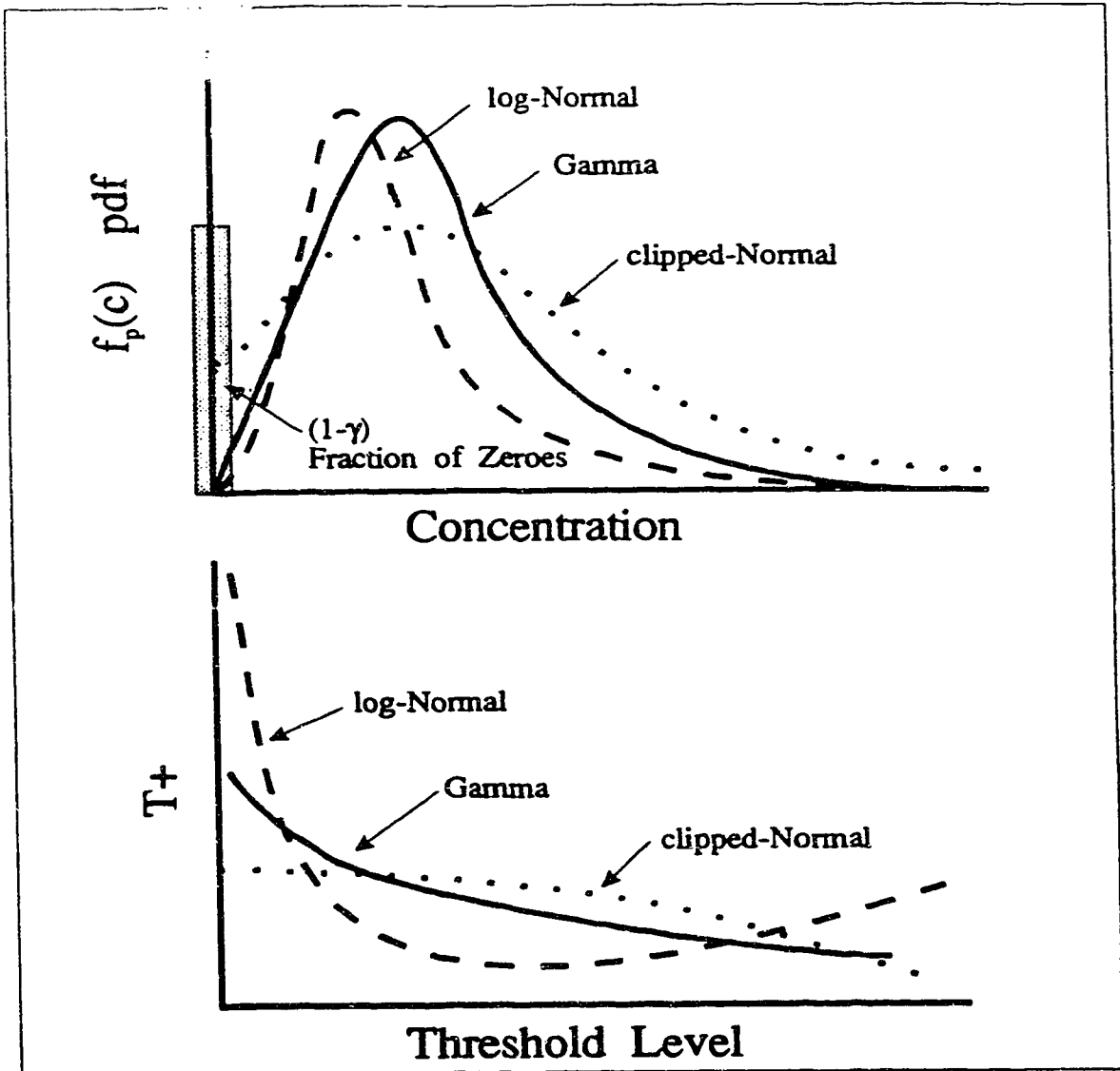


Figure 7.2: Schematic illustration of $T^+ \propto 1/f_p(c)$ near zero threshold level compared to the conditional mean.

7.3 Average Number of Exceedances

Application of the N^+ theory to the water channel data set may be done in several ways. Four ways that are to be presented here are:

Normal PDF Derivative Model (or Normal Model) The concentration derivative PDF may be modelled as a Normal distribution. The remaining methods use the Exponential distribution for the concentration time derivative PDF.

\bar{c}^n Model (or Total Model) Inputs to the model consist of \bar{c} , \bar{c}^2 , \bar{c}^3 and σ_c in conjunction with a selected PDF for the concentration. The intermittency is predicted by the concentration moments for the selected PDF model.

\bar{c}_p^n Model (or Conditional Model) Inputs to the model consist of the conditional moments, \bar{c}_p , \bar{c}_p^2 , the observed intermittency and σ_c in conjunction with a selected PDF for the concentration.

Similarity Model Inputs to the model are only the centre-line values of \bar{c}_o , \bar{c}_o^2 , \bar{c}_o^3 , Λ_{co} and σ_y . Then, using moment similarity theory, the generalized Von Kármán spectrum and a PDF model, the off-axis \bar{c}^n and $\sigma_c(y)$ values may be determined. (Λ_c is assumed to be constant across the plume).

A threshold level relative to the conditional mean concentration must also be selected. For the present study eight threshold levels have been arbitrarily selected: 0, 0.1, 0.2, 0.5, 1, 2, 5 and 10 times \bar{c}_p . Since $c^*/\bar{c}_p = 1.0$ is an important threshold level in terms of risk assessment and for other applications, it will be the main threshold level discussed.

The jet/plume source is analyzed in Figure 7.3 and Figure 7.4 for the prediction methods described above. The data are well described by the N^+ theory which has been modified for an intermittent plume. At the location selected, $\sigma_y/\Lambda_u = 3.6$, the concentration PDF is best described by the Gamma model. The figures for N^+ show that the Gamma model produces the best estimate of N^+ for this location.

The Normal model prediction is observed to over-predict N^+ compared to the total model (which uses the Exponential derivative PDF), as expected by the previous analysis. The conditional model, Figure 7.4 (top), performs slightly better than its total moment counter part in Figure 7.3 (top). This is because the conditional moment model does not have to predict the intermittency, therefore the PDF parameters provide a better fit to the observed PDF data.

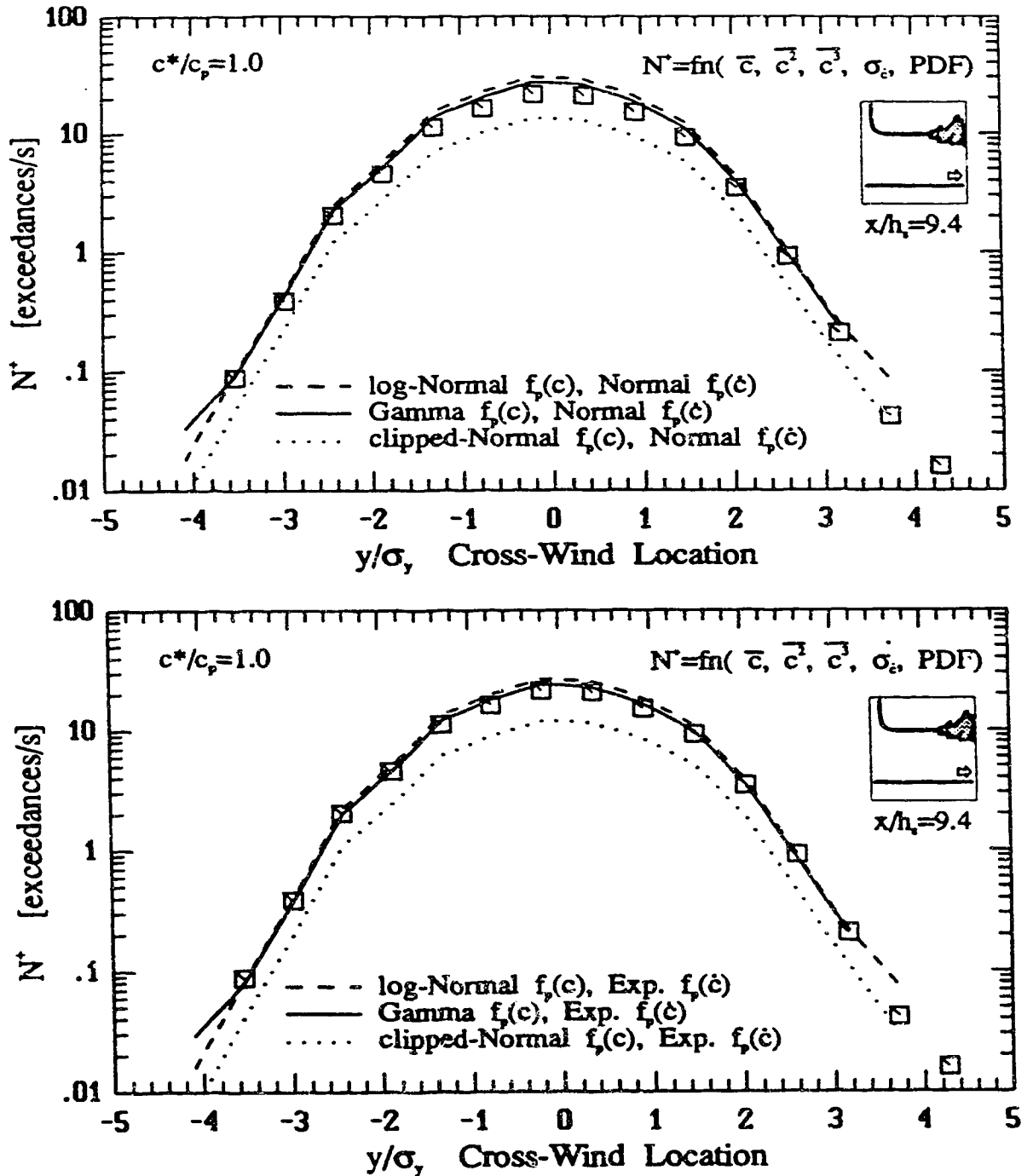


Figure 7.3: Cross-wind distribution of the number of exceedances per second for the jet/plume source at a threshold level of $c^*/\bar{c}_p = 1.0$. Normal PDF derivative (top) and total model (bottom).

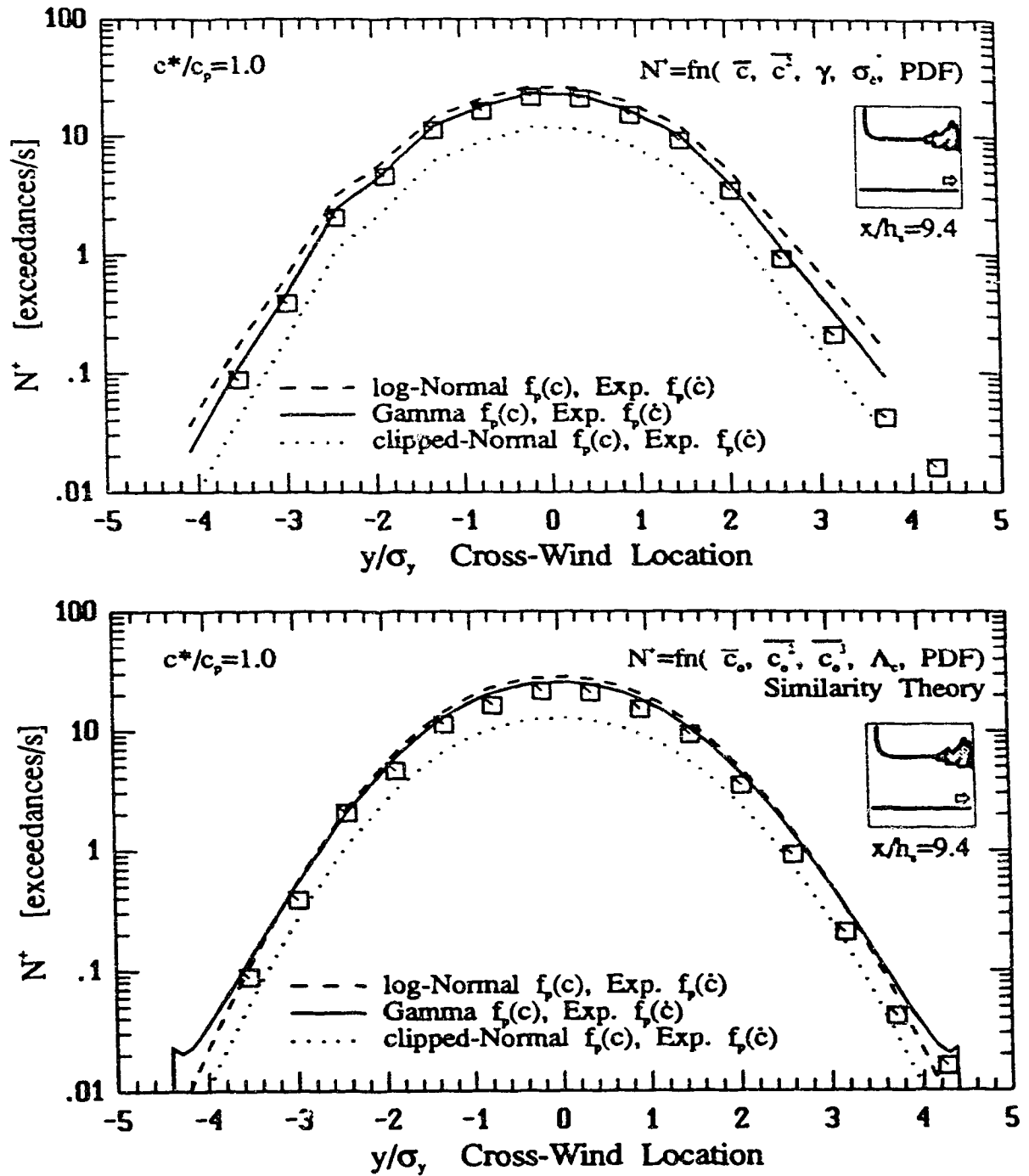


Figure 7.4: Cross-wind distribution of the number of exceedances per second for the jet/plume source at a threshold level of $c^*/\bar{c}_p = 1.0$. Conditional model (top) and similarity model (bottom).

The similarity theory in conjunction with the Von Kármán spectrum predicts the data very well. The Gamma distribution prediction is shown to have a singularity in the far fringes, as described in Appendix G, but is not a problem as it occurs in the far fringes.

The ability of the model to predict the exceedance rate well is further illustrated in Figure 7.5 and Figure 7.6. The figures compare the predicted exceedance rate for threshold levels of one fifth and one half \bar{c}_p , and for threshold levels of twice and five times \bar{c}_p , respectively. The model predictions based on the the observed concentration moments data and based on the similarity theory, which uses only the observed centre-line data points, agree very well with each other for all the threshold levels examined. Therefore, confidence in the use of the similarity theory further strengthened by this exceedance data.

The predictions for threshold levels $c^*/\bar{c}_p < 1$ show generally good agreement with the water channel data. The clipped-Normal distribution performs the better for very low threshold levels, even though the Gamma distribution describes the concentration process better, because the clipped-Normal distribution has a non-zero PDF at zero threshold. The log-Normal prediction does not represent the data well for low thresholds because it does not represent the near zero concentrations in the PDF well. The log-Normal distribution tends to under-predict the fraction of concentrations near $c = 0$.

The predictions for threshold levels $c^*/\bar{c}_p > 1$ are a good representation of the data trends, however may be different by an order of magnitude for the larger thresholds in the fringes. The agreement is good when it is understood that the estimates are for conditional values (i.e. the events occur only a small fraction of the time) and are very high conditional peaks.

For the $c^*/\bar{c}_p = 5$ threshold, at this location in the plume, the data set has off-axis peaks, or a saddle shape. This saddle shape is also predicted by the similarity theory, although the magnitudes of the peaks are in error. What does the saddle mean? For high threshold levels, eg. $c^*/\bar{c}_p = 5$, the lower conditional mean concentration off the plume centre-line falsely implies overall lower concentrations. However, the flapping nature of the plume distributes centre-line concentrations to the plume edge. Therefore, although the average concentration is low in the fringes, there are still a large number of high peaks compared to the number of peaks at the centre-line. The other sources exhibit similar trends, and the N^+ and similarity theory produce generally good fits to the data.

In summary, the Gamma and clipped-Normal pdf models predict exceedance rates within a factor of two for thresholds $c^*/\bar{c}_p \leq 1.0$. This is true even in the fringes of the plume where $\gamma < 0.01$, (see also Figure 5.34), and the peaks, c^*/\bar{c} , are 100 times

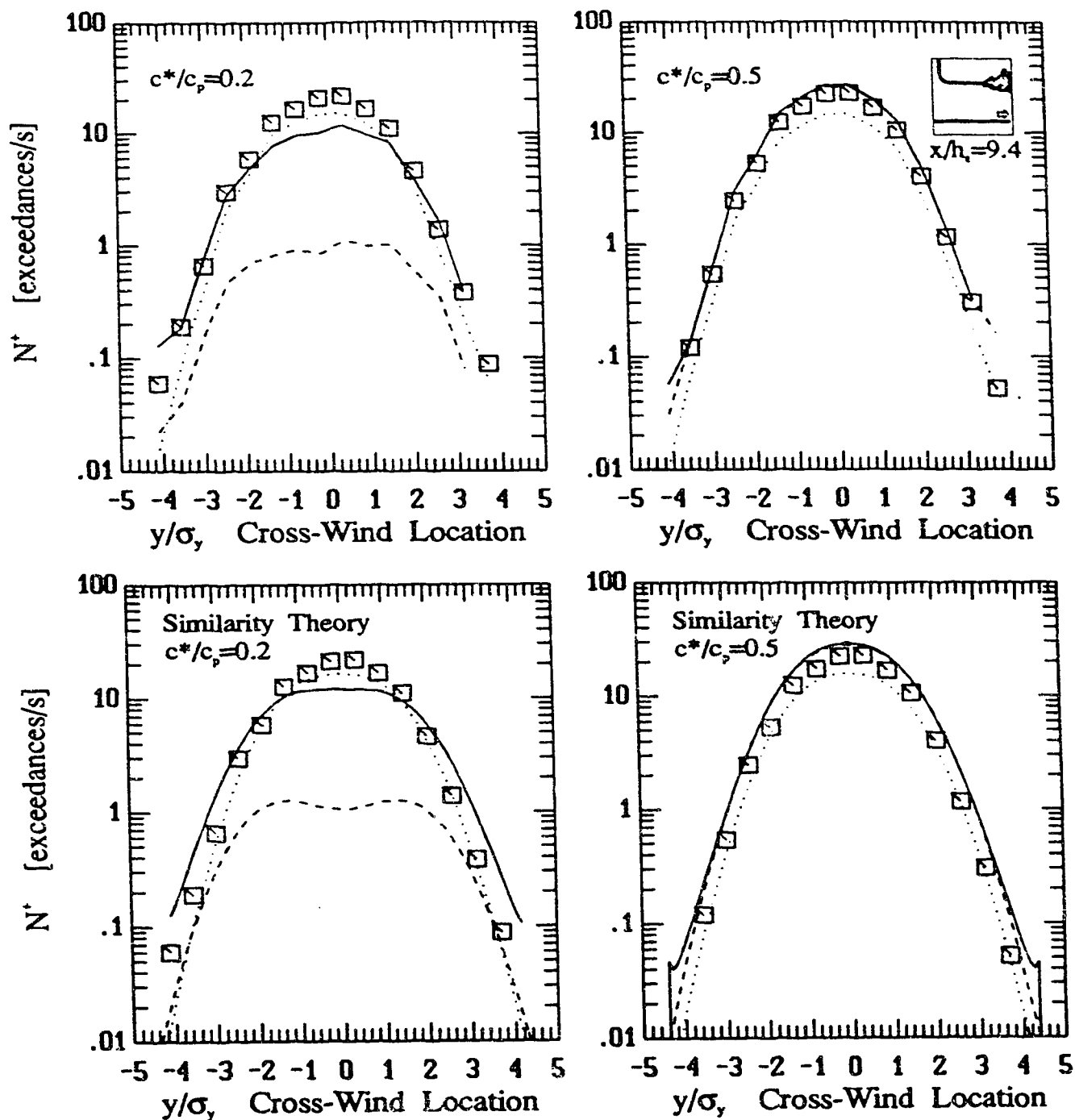


Figure 7.5: Cross-wind distribution of the number of exceedances per second for the jet/plume source at a threshold level of $c^*/\bar{c}_p = 0.2$ (left) and $c^*/\bar{c}_p = 0.5$ (right). Prediction using the total moments (top) and by the similarity theory (bottom). Symbols as per Figure 7.3

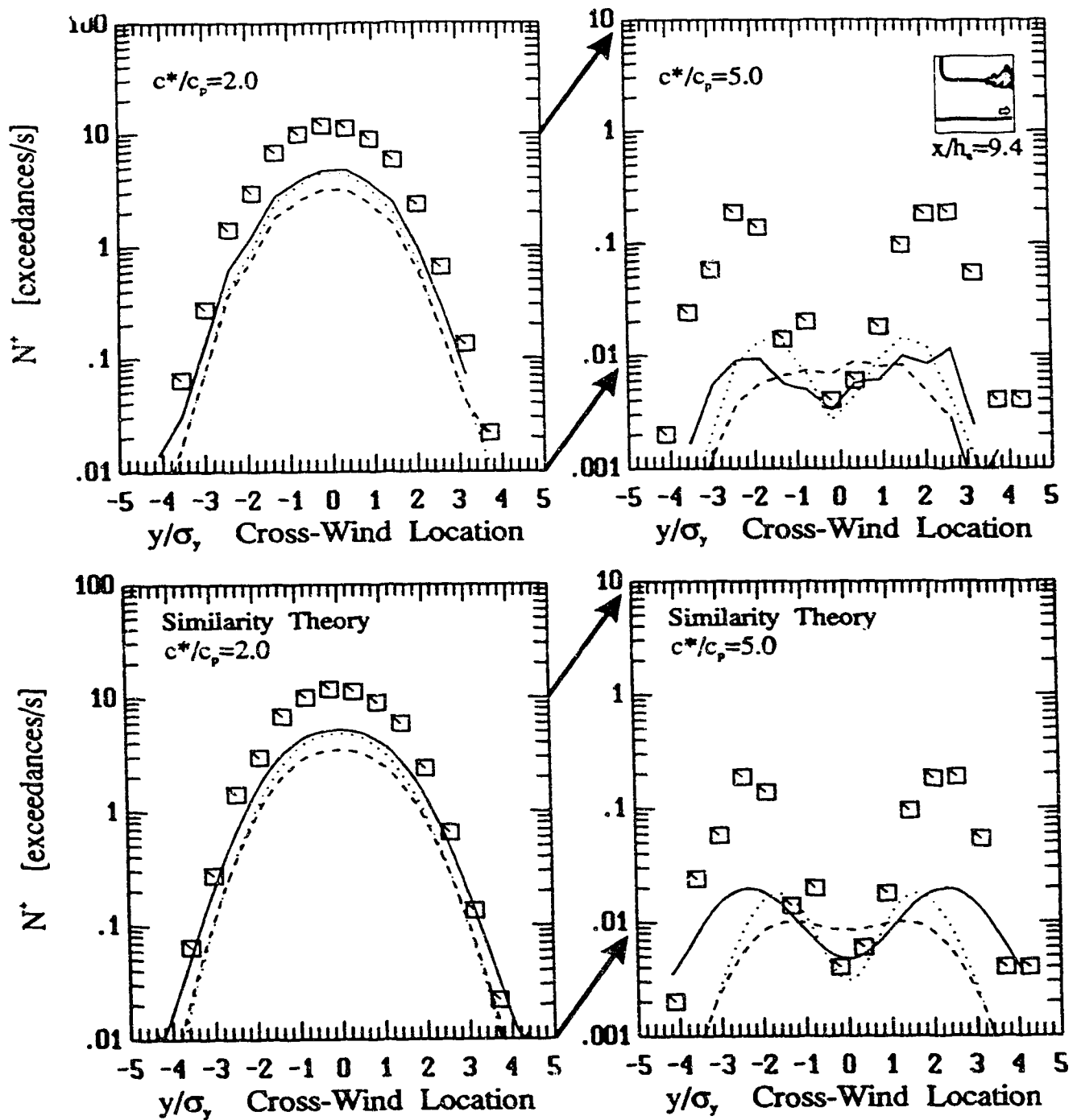


Figure 7.6: Cross-wind distribution of the number of exceedances per second for the jet/plume source at a threshold level of $c^*/\bar{c}_p = 2.0$ (left) and $c^*/\bar{c}_p = 5.0$ (right). Prediction using the total moments (top) and by the similarity theory (bottom). Symbols as per Figure 7.3

the total mean concentration. At high concentration threshold levels, $c^*/\bar{c}_p = 5.0$, all the pdf models consistently underpredict the crossing rate, N^+ , in the fringes of the plume by about a factor of 10. However, considering that this threshold represents concentration peaks that are 500 times the total mean concentration, in the fringes where $\gamma < 0.01$, the failure of the models is understandable.

The down-wind variation of N^+ is shown for sources in Figure 7.7 for $c^*/\bar{c}_p = 1$. The N^+ corrected data in the figure is corrected for the intermittency, and normalized by the concentration microscale. The intermittency correction predicts the number of exceedances per second that would have occurred if the intermittency was $\gamma = 1$. The data for all the sources are approximately linear for the range tested. There is a small decrease of $N^+ \lambda_c / \gamma \bar{u}$ with distance down-wind indicating that the peaks in concentration relative to the mean concentration are being slowly removed. The fact that all the sources behave similarly is encouraging in that a unifying simple model may be applied to a wide range of source conditions.

7.4 Average Duration of Excursions Above a Threshold

The data are presented in the same form as in section 7.3, and can be seen in Figure 7.8 and Figure 7.9. The predictions of the average duration of excursions above a threshold, T^+ , are generally poor, but they are representative of the physics of the data. The difficulty found with the predictions here is that the probability models must fit the hazard rate function. Therefore, the best fit T^+ is the one which best fits the hazard rate, $h(c)$, of the data, which is a combination of fitting both $f(c)$ and $F'(c)$ well. The differences between the predictions and the data may be explained by the inadequate simultaneous fit of the two distributions.

The Exponential derivative model is observed to predict the data marginally better than the Normal derivative model, Figure 7.8 (top). The conditional model, Figure 7.9 (top), also works slightly better than the total moment model, Figure 7.8 (bottom). This is not a result of a poor prediction of the intermittency, because T^+ is independent of γ . Rather, the conditional model generally has a better fit because the PDF parameter estimates are not trying to adjust for the intermittency, therefore causing the parameter fits to be poorer. Additionally, the total moment model is not independent of γ because σ_{cp} must be determined from σ_c using the estimated γ . Perhaps the better fit in this model could have been to assume that σ_{cp} was known from the data and to use the observed γ to predict it.

The similarity model is also not independent of γ since it must predict σ_{cp} in the same way as the total moment model, Figure 7.8 (bottom). The agreement for the

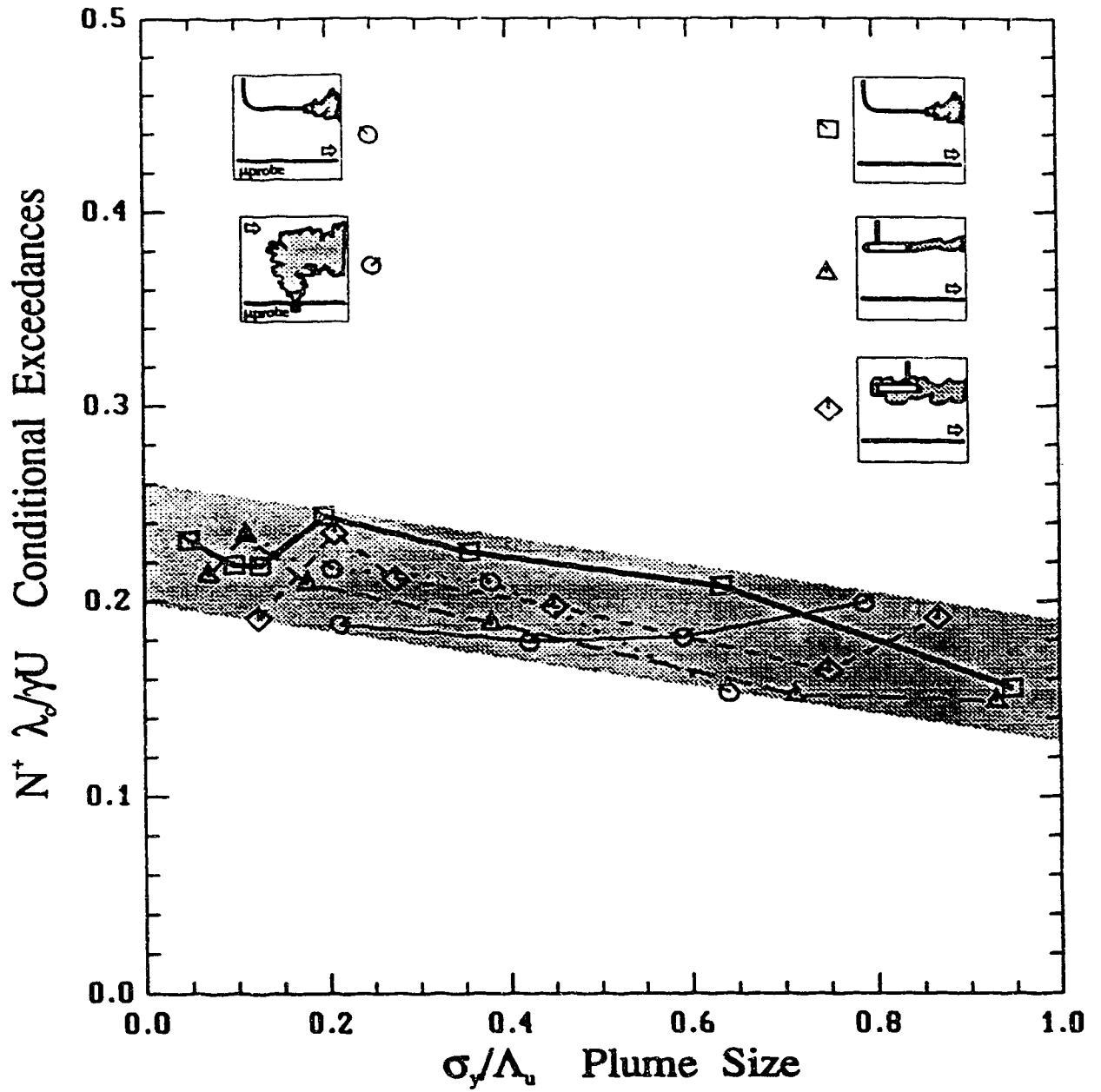


Figure 7.7: Down-wind distribution of the number of exceedances per second for a threshold level of $c^*/\bar{c}_p = 1$ and data for all sources. Prediction using the total moments.

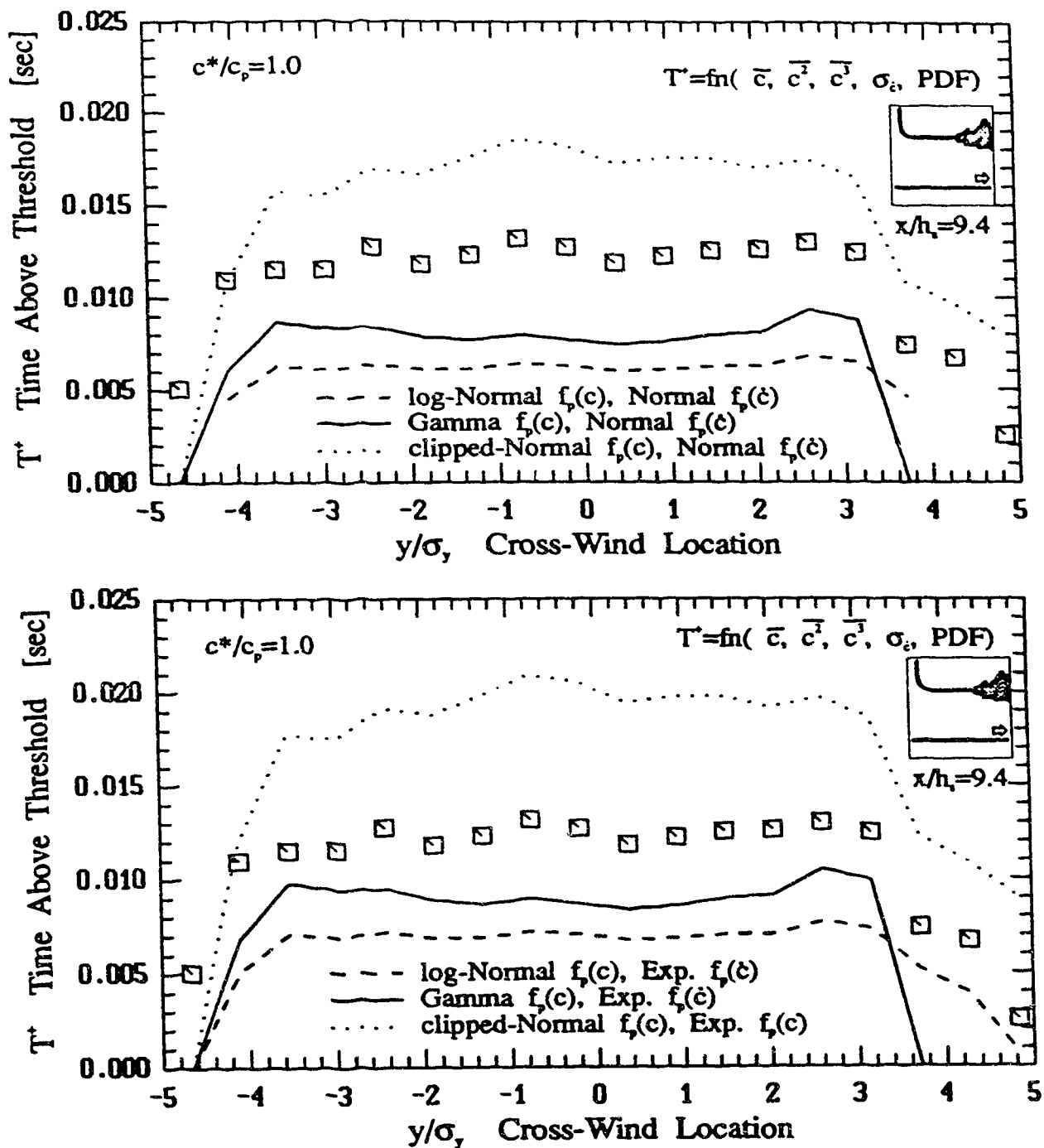


Figure 7.8: Cross-wind distribution of the average duration of exceedances for the jet/plume source at a threshold level of $c^*/\bar{c}_p = 1$. Normal PDF derivative (top) and total model (bottom).

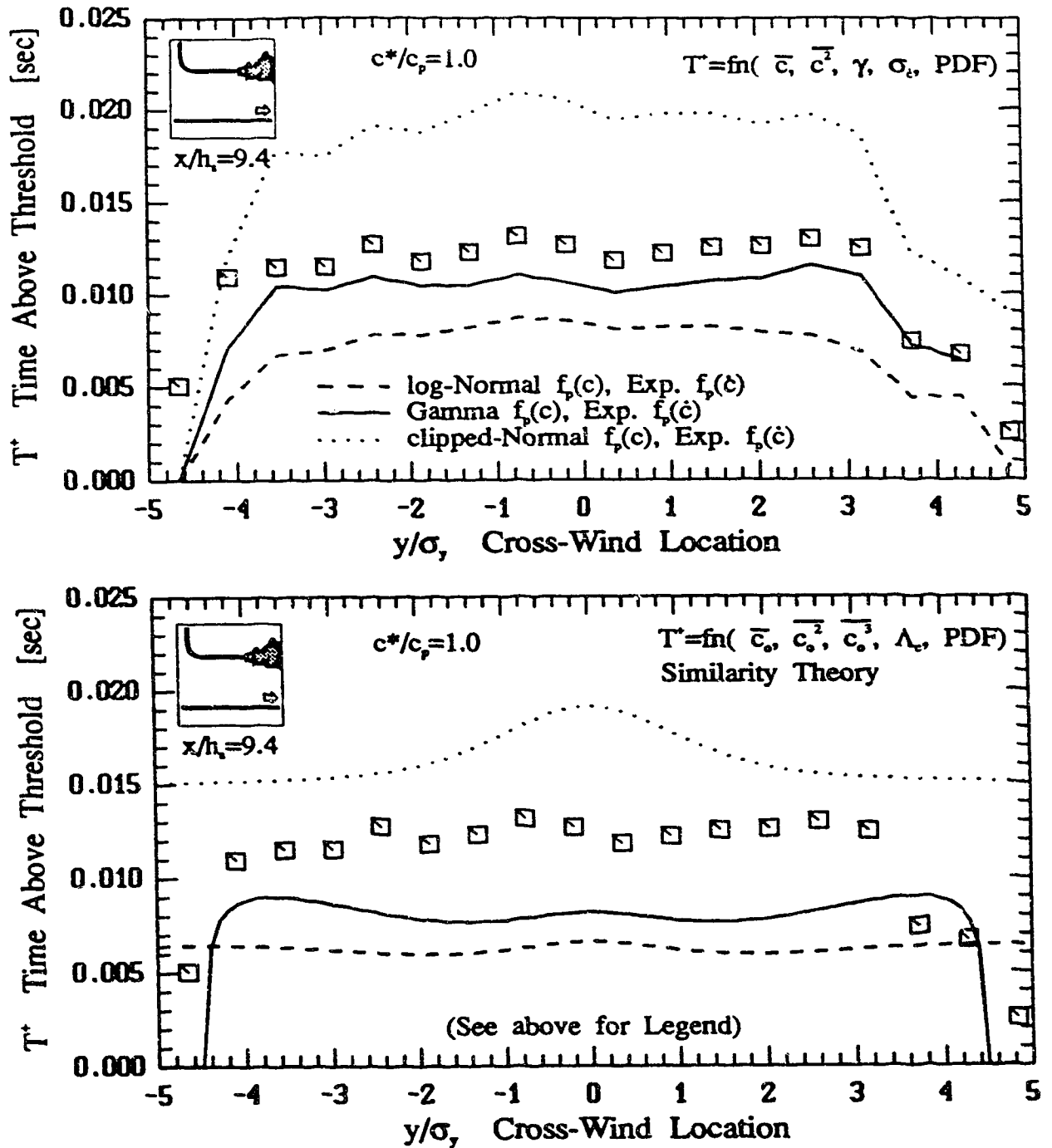


Figure 7.9: Cross-wind distribution of the average duration of exceedances for the jet/plume source at a threshold level of $c^*/\bar{c}_p = 1$. Conditional model (top) and similarity model (bottom).

similarity model is as good as the total moment model. The similarity theory for the Gamma distribution matches the behaviour of the data very well. The clipped-Normal does not match the data in the fringes of the plume because the data i_p^2 values increase above unity, and the clipped-Normal model cannot represent the data there properly.

The ability of the model to predict the exceedance time, T^+ , well is further illustrated in Figure 7.10 and Figure 7.11. The figures compare the predicted exceedance rate for threshold levels of one fifth and half \bar{c}_p , and for threshold levels of twice and five times \bar{c}_p , respectively. Again it is observed that the two model predictions agree very well with each other.

The predictions for T^+ for the $c^*/\bar{c}_p < 1$ threshold reveal a problem with the log-Normal distribution, Figure 7.10, and the Gamma distribution. Because the observed hazard rates are not well represented by these distributions for low thresholds, T^+ is not predicted well. When the fits of the PDFs of these two distributions near zero concentration are labelled poor, it is assumed that the 'true' PDF of the data has a zero intercept, which is observed in practice. However, this could be attributed to molecular diffusion, background noise, or probe response. The existence of a zero concentration intercept was one incentive behind the clipped-Normal distribution, and supports the use of the three parameter log-Normal and three parameter Gamma distributions, (or clipped-log-Normal and clipped-Gamma).

The predictions for T^+ for the $c^*/\bar{c}_p > 1$ threshold are sparse because of the low relative intermittency for the given threshold level. The shape of the $T^+(y)$ profile is predicted well, although the magnitude is over estimated five to ten times for large c^*/\bar{c}_p thresholds. Again, the agreement is good when it is understood that the estimates are for conditional values (i.e. the events occur only a small fraction of the time) and are very high conditional peaks.

The down-wind variation of T^+ is presented in Figure 7.12, Figure 7.13 and Figure 7.14 for threshold values of $c^*/\bar{c}_p = 0, 1, 5$. For small plume sizes the T^+ normalized by the concentration microscale rises, indicating that the T^+ is much larger than the microscale. The jet/plume source has a much greater energy, and therefore smaller λ_c , which is observed in the figures. At larger plume sizes the T^+ becomes comparable to the microscale and almost constant at a value of 4.

When $c^*/\bar{c}_p = 1$, in Figure 7.13, the normalized T^+ is comparable to $2\lambda_c$ for all sources and plume sizes. This is another surprising finding given the diversity of the source configurations. Notice that even the vertical jet data, taken with the micro-probes, behaves similarly.

The constant T^+ ratio is lost when $c^*/\bar{c}_p = 5$, Figure 7.14. The data show a general increasing trend with plume size. This indicates the preservation of exceedance times

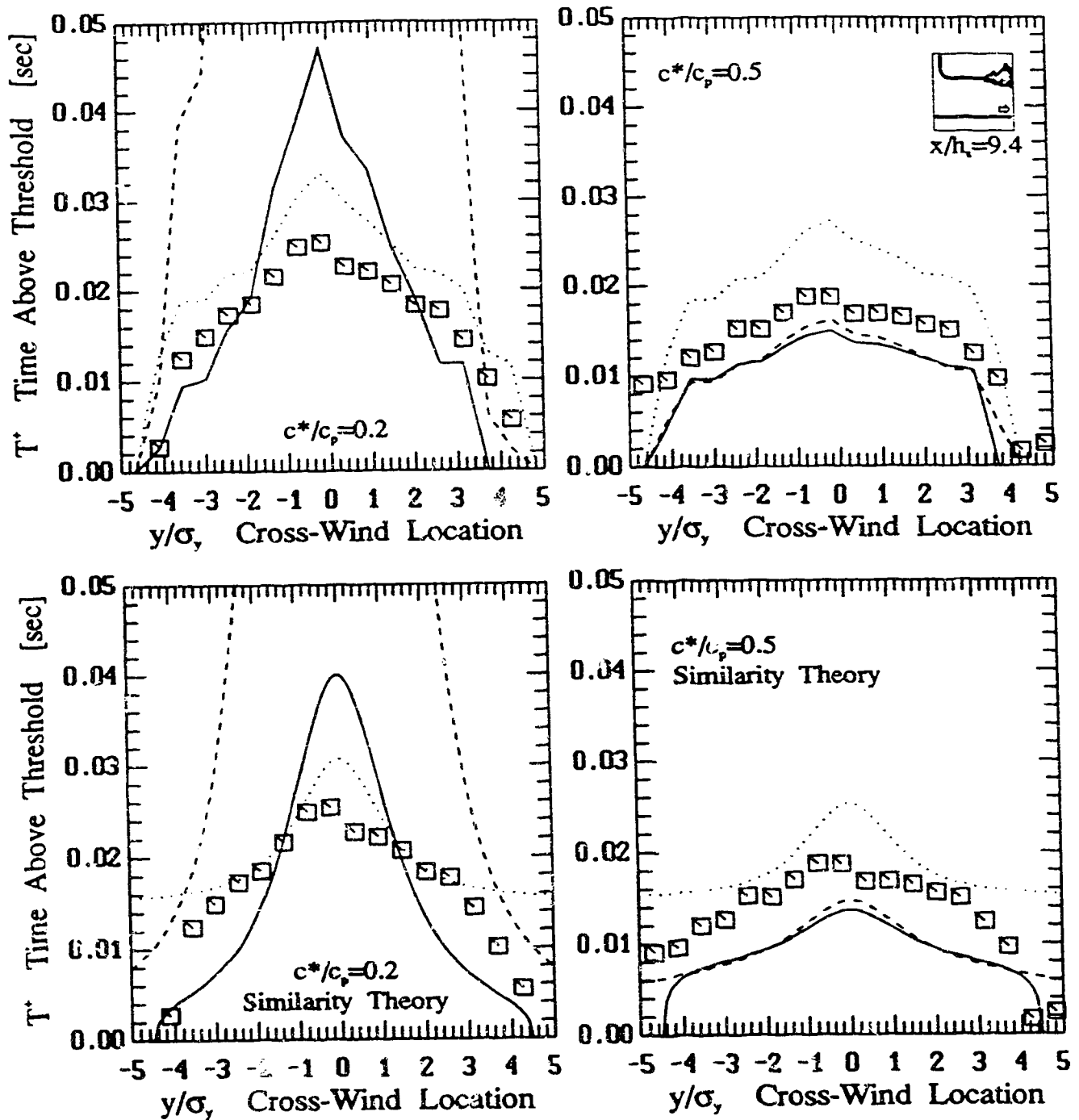


Figure 7.10: Cross-wind distribution of the average duration of exceedances for the jet/plume source at a threshold level of $c^*/\bar{c}_p = 0.2$ (left) and $c^*/\bar{c}_p = 0.5$ (right). Prediction using the total moments (top) and by the similarity theory (bottom). Symbols as per Figure 7.3

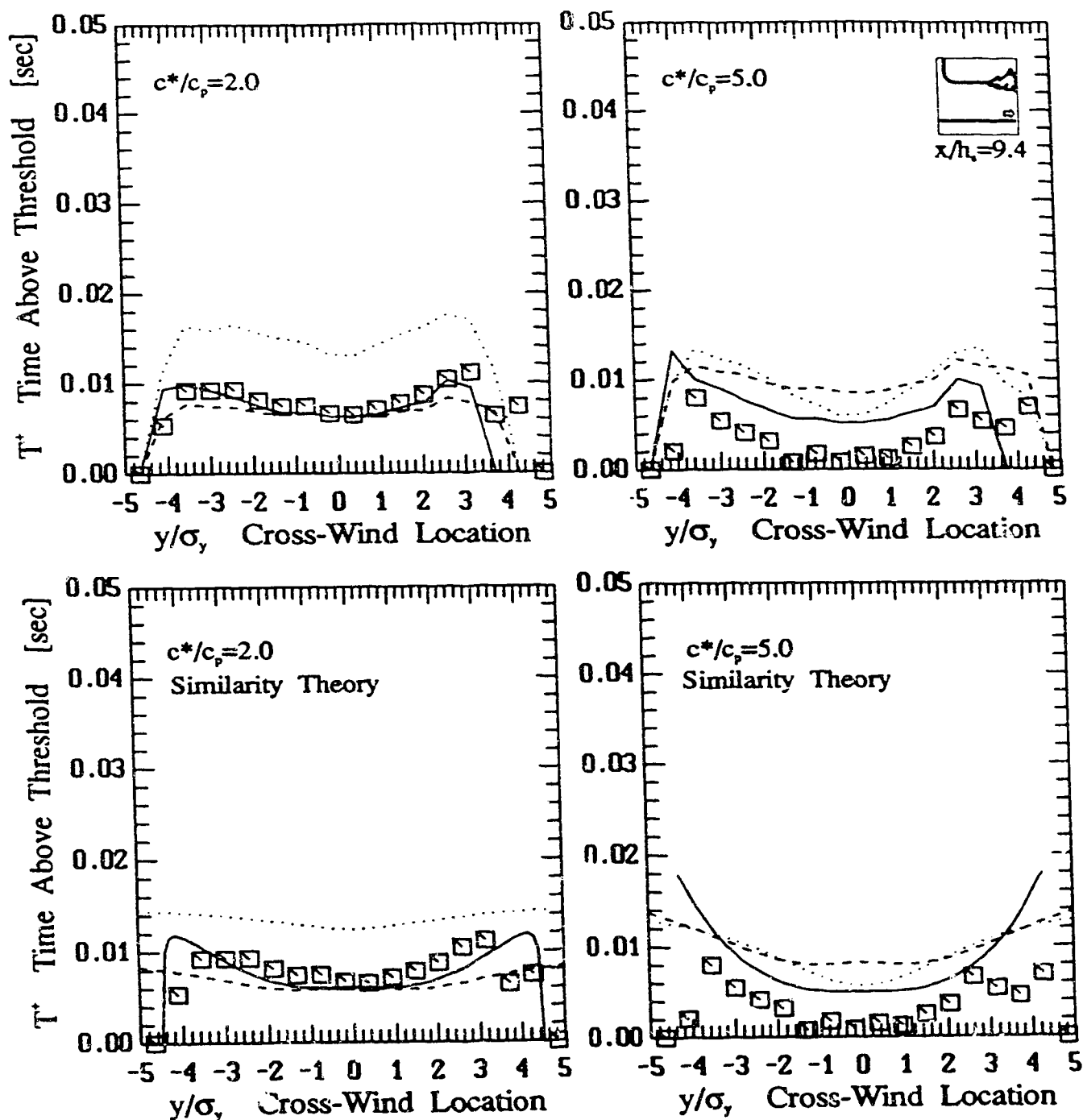


Figure 7.11: Cross-wind distribution of the average duration of exceedances for the jet/plume source at a threshold level of $c^*/\bar{c}_p = 2.0$ (left) and $c^*/\bar{c}_p = 5.0$ (right). Prediction using the total moments (top) and by the similarity theory (bottom). Symbols as per Figure 7.3

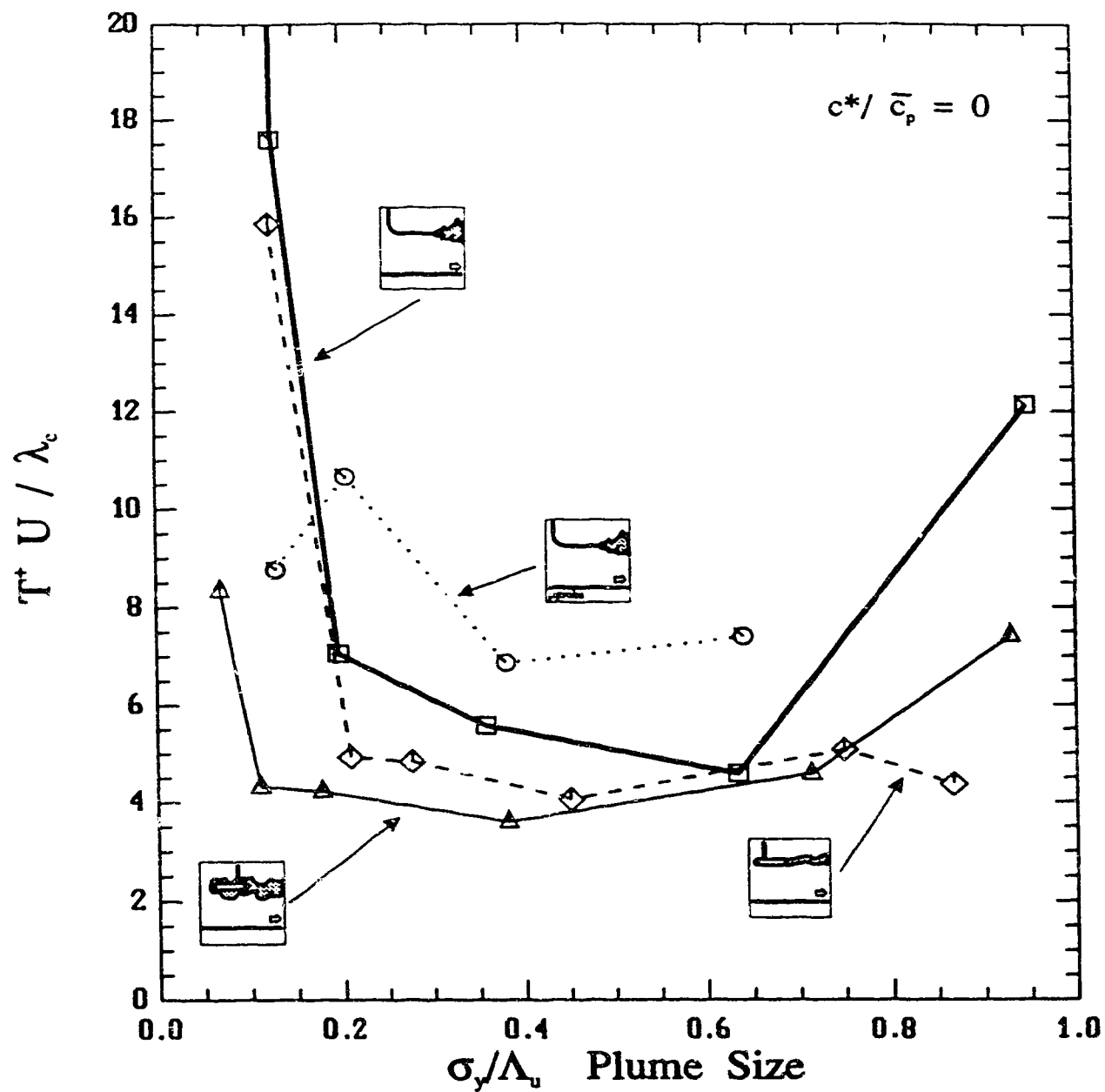


Figure 7.12: Down-wind distribution of the average duration of exceedances for a threshold level of $c^* / \bar{c}_p = 0$ and data for all sources. Prediction using total moments.

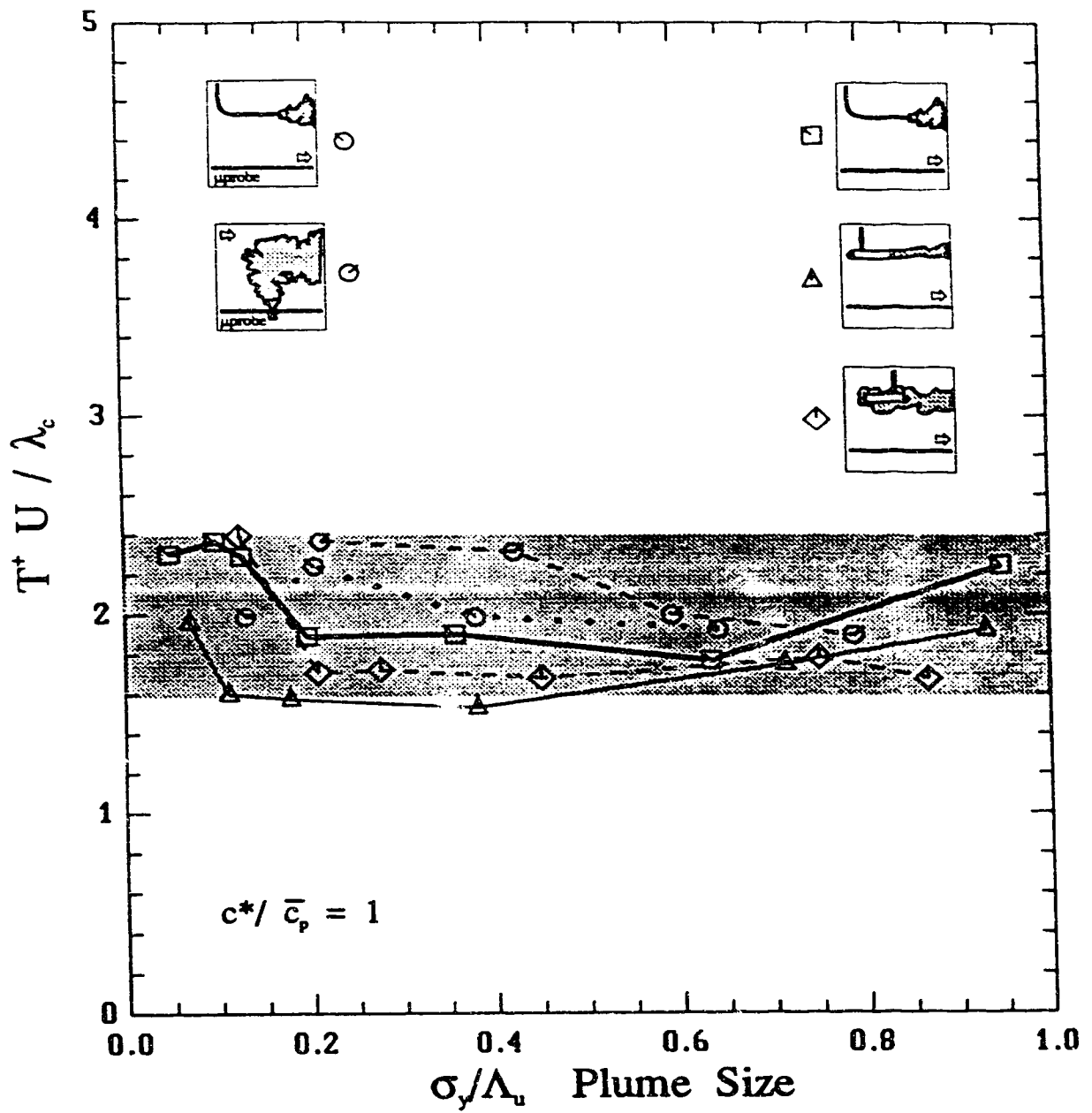


Figure 7.13: Down-wind distribution of the average duration of exceedances for a threshold level of $c^* / \bar{c}_p = 1$ and data for all sources. T^+ determined using total moments.

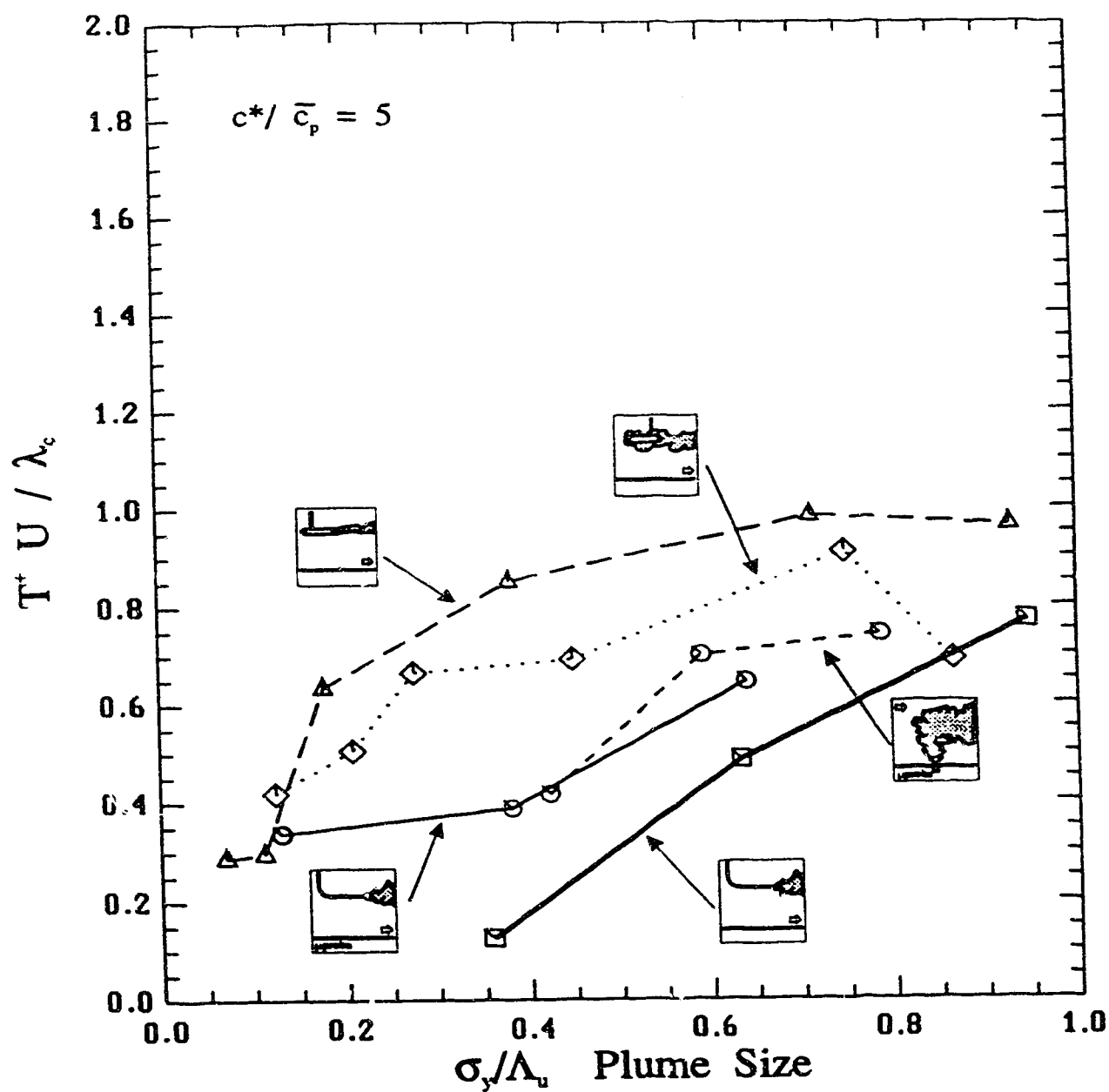


Figure 7.14: Down-wind distribution of the average duration of exceedances for a threshold level of $c^* / \bar{c}_p = 5$ and data for all sources. T^+ determined using total moments.

for peaks while the \bar{c}_p is decaying with distance down-wind. Since the number of exceedances was observed to decrease with distance down-wind, this result would suggest that eddies of concentration are diffusing thus creating longer exceedance times, (as expected). The preservation of peaks was observed in the water channel by dye flow visualization of the iso-kinetic source tracer.

7.5 Down-Wind Predictions of N^+ and T^+

The previous sections have presented the normalized evolution of N^+ and T^+ with plume size. Here, the data are presented in its non-normalized form with down-wind location, and predictions are made of N^+ and T^+ based on the observed centre-line values. The data are presented in order of increasing threshold level in Figure 7.15 to Figure 7.19 for the jet/plume source. The figures show that for low thresholds the clipped-Normal distribution predicts the water channel observations the best. For higher thresholds the Gamma distribution predicts N^+ and T^+ the best. Based on these figures, the Gamma model appears useful as a general model even though it is not the best fit PDF model for $f(c)$ in all the ranges.

7.6 Exceedance Time PDFs

Rice (1944-45) was unable to predict the functional form of the probability distribution of the exceedance times. For large threshold values, the time between threshold crossings, T_R , becomes large and the probability of occurrence of a threshold crossing becomes independent of the previous crossing probability, (Rice, 1944-45). This type of process is a Poisson process. Therefore for large thresholds an Exponential distribution is expected. In other words, for small threshold levels, a different probability distribution may be observed, but as T_R gets large, the distribution is expected to be Exponential. There is no simple theory which describes the expected probability distributions for small T_R , or small threshold values, (Sreenivasan, Prabhu and Narasimha, 1983).

Sreenivasan, Prabhu and Narasimha (1983) have found that in a boundary layer, for velocity zero crossings, two Exponential distributions approximate the data well. One Exponential is fit to low T_R and another for large T_R . They quote Badri, Narayanan, Rajagopalan and Narasimha (1977) finding that a log-Normal distribution fits the data throughout the boundary layer, for large and small T_R , to good approximation. However, less well for large T_R .

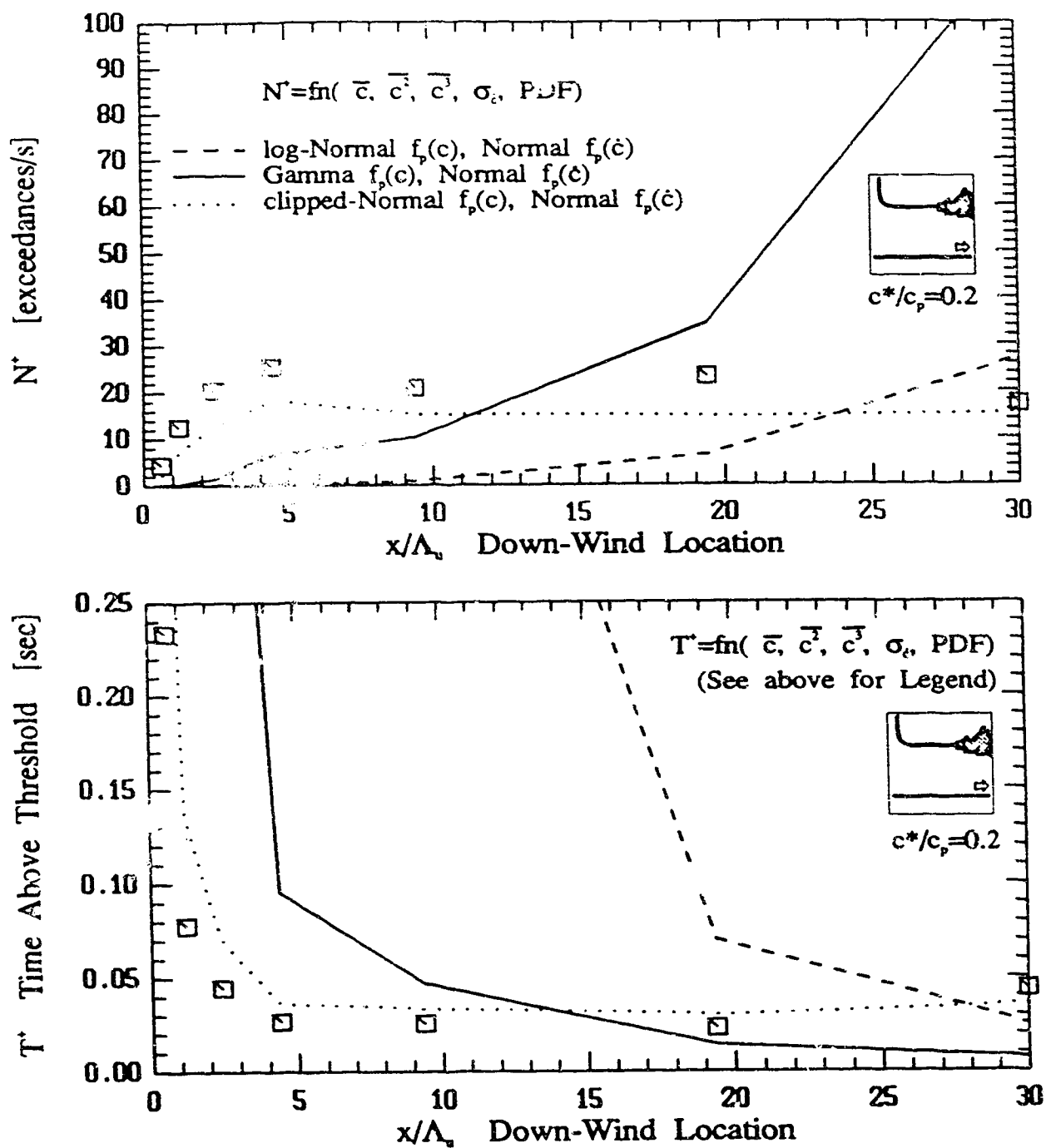


Figure 7.15: Down-wind distribution of N^+ and T^+ for the jet/plume source at a threshold level of $c^*/\bar{c}_p = 0.1$. N^+ and T^+ determined using total moments.

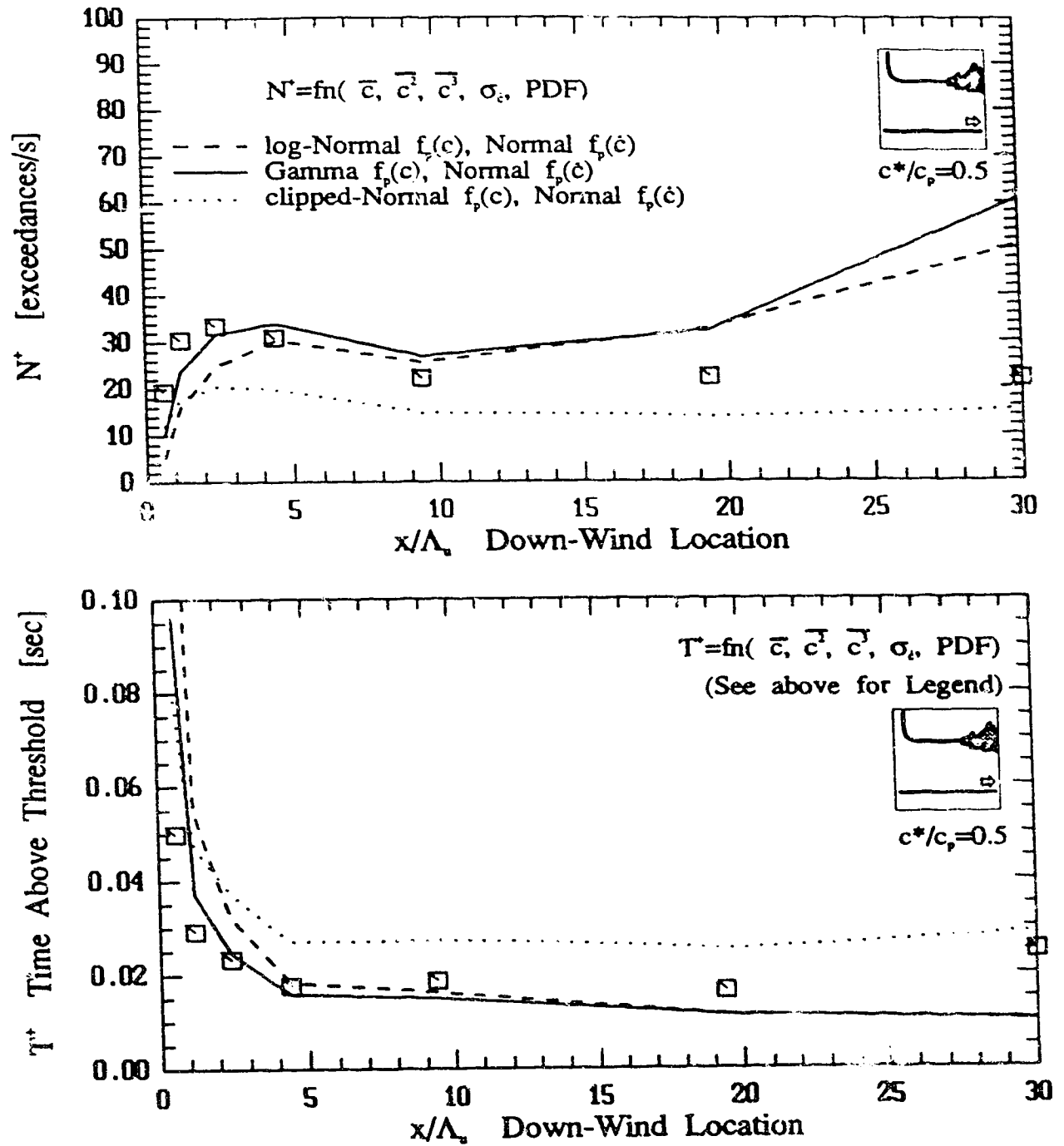


Figure 7.16: Down-wind distribution of N^+ and T^+ for the jet/plume source at a threshold level of $c^*/\bar{c}_p = 0.2$. N^+ and T^+ determined using total moments.

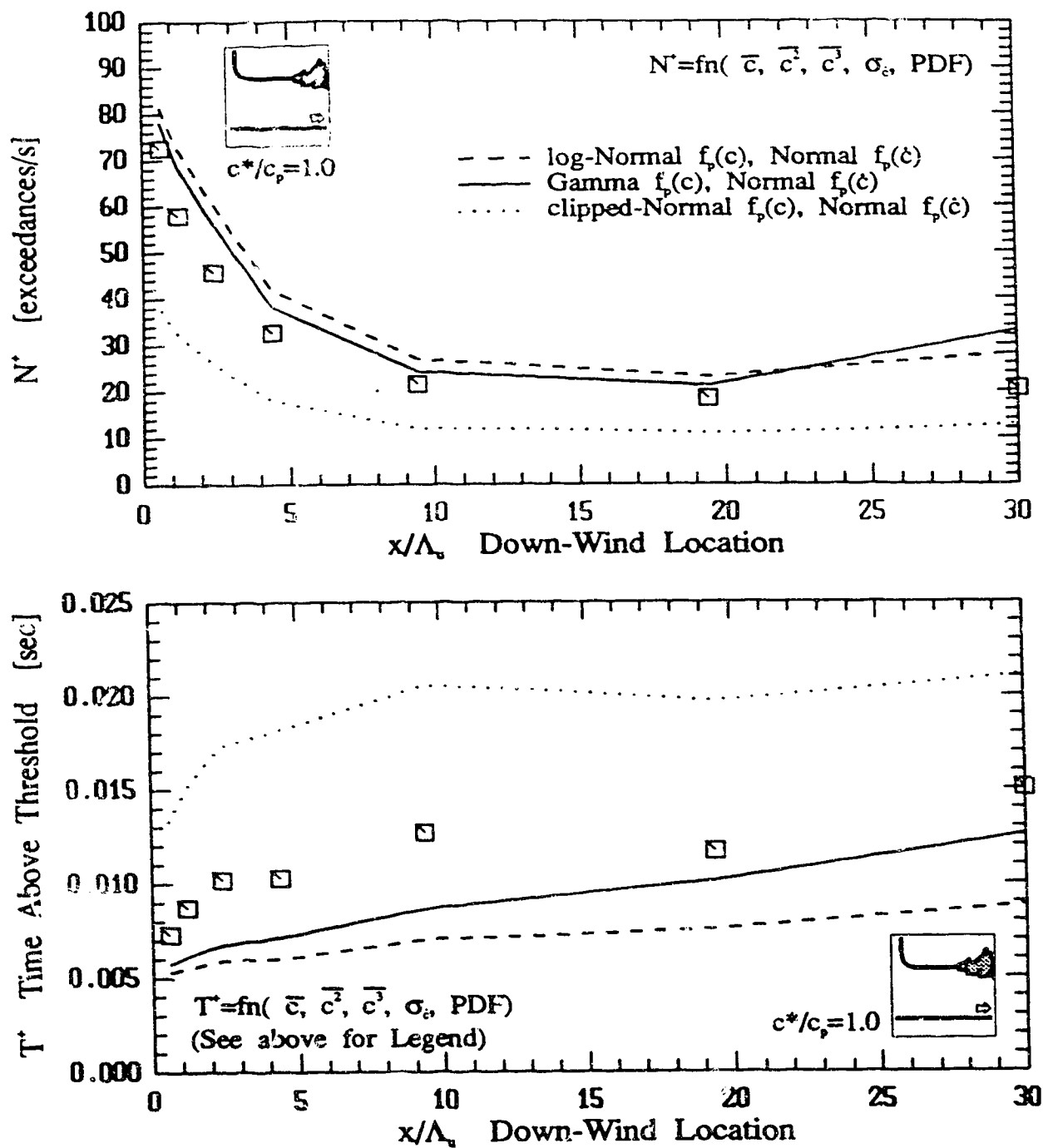


Figure 7.17: Down-wind distribution of N^+ and T^+ for the jet/plume source at a threshold level of $c^*/\bar{c}_p = 1$. N^+ and T^+ determined using total moments.

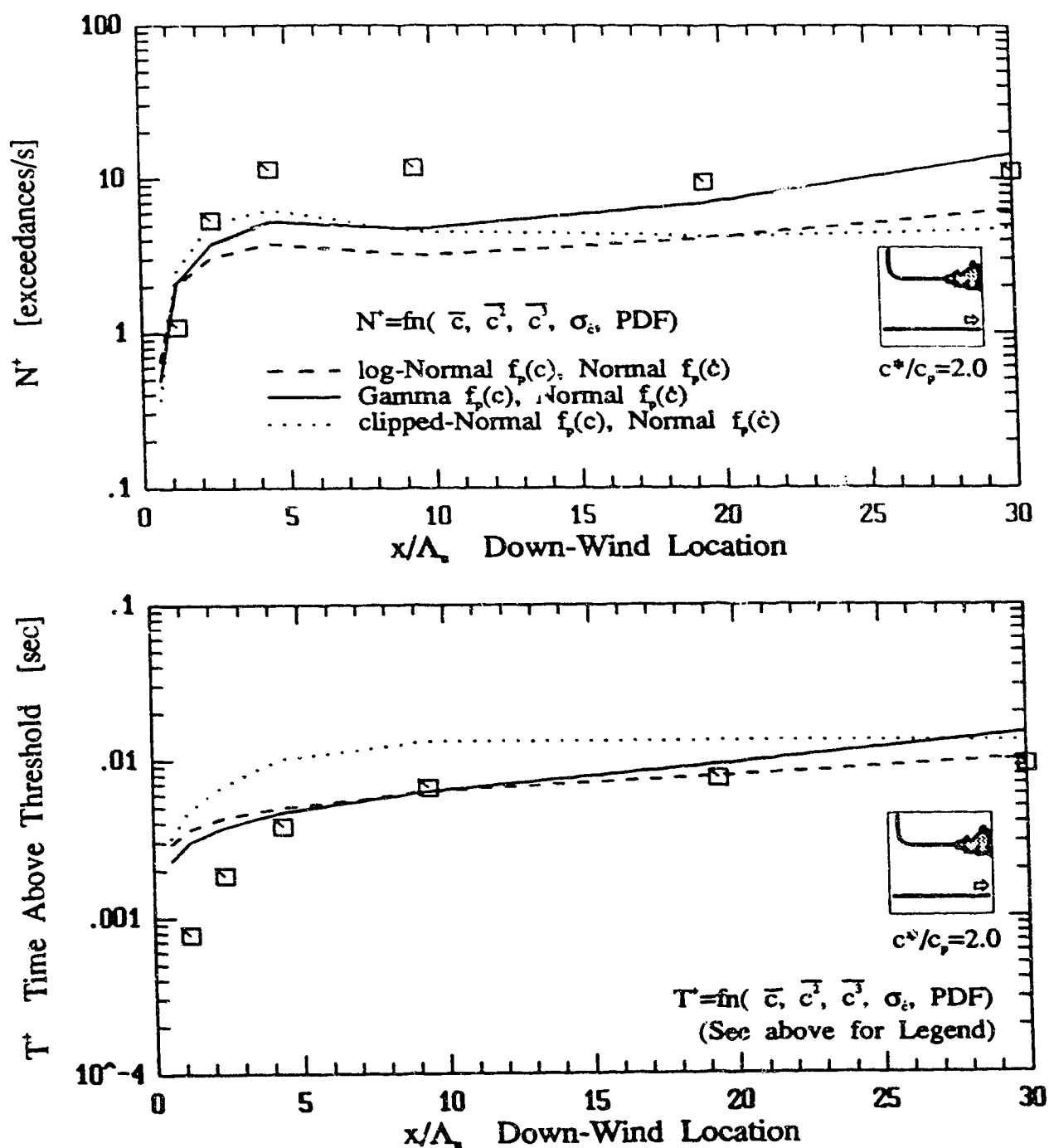


Figure 7.18: Down-wind distribution of N^+ and T^+ for the jet/plume source at a threshold level of $c^*/\bar{c}_p = 2$. N^+ and T^+ determined using total moments.

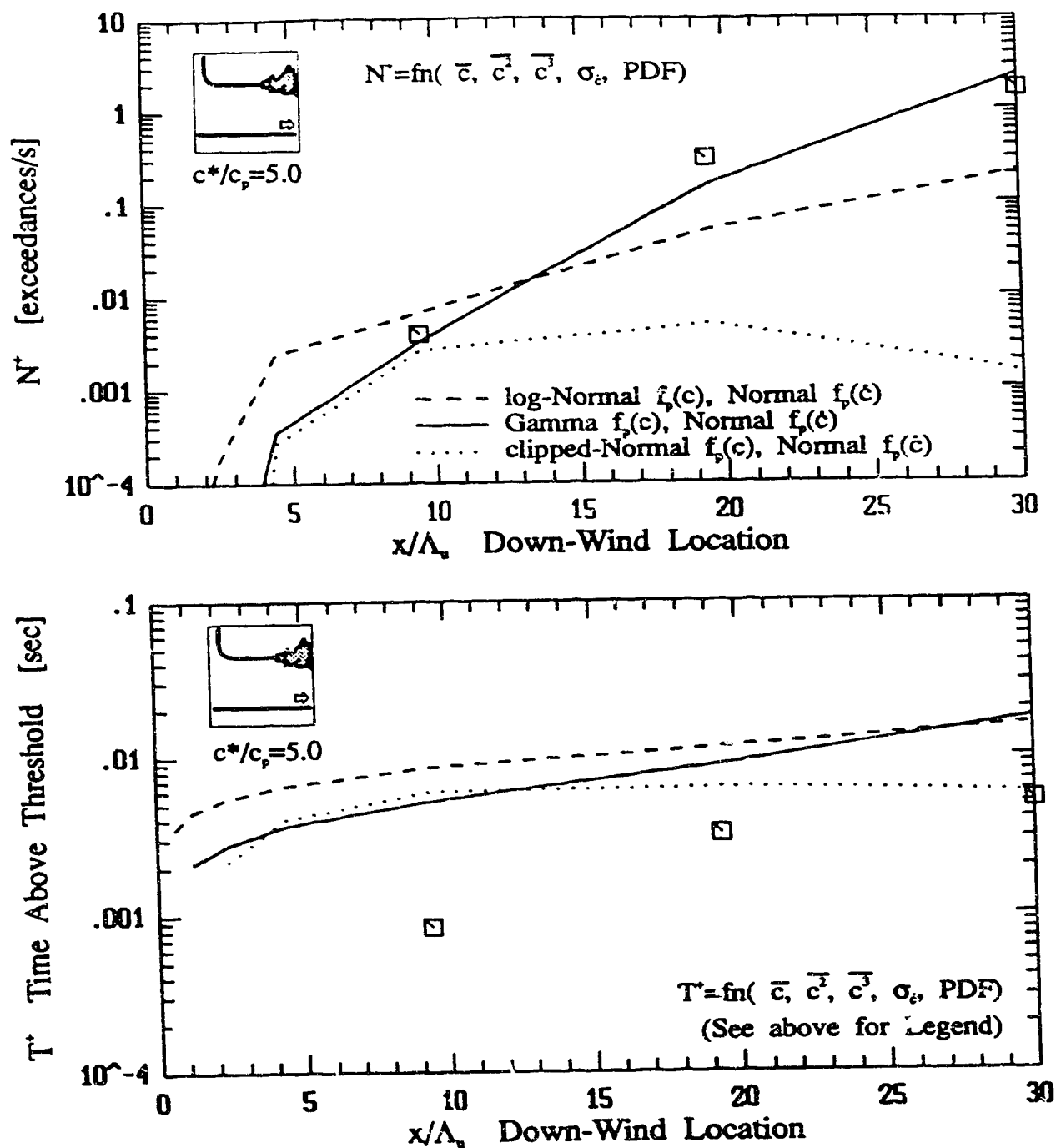


Figure 7.19: Down-wind distribution of N^+ and T^+ for the jet/plume source at a threshold level of $c^*/\bar{c}_p = 5$. $nplus$ and T^+ determined using total moments.

A more interesting distribution to consider is the exceedance time, which, since it is a fraction of the return time, should be distributed in the same way. This is true if the distribution is log-Normal or Exponential, and may be true if it is Gamma¹. Since this distribution is more interesting, in terms of hazard assessment, only the exceedance time distributions will be presented. However, the return time distributions, T_R , were found to be similar.

The exceedance times observations in the water channel, Figure 7.20 to Figure 7.22 for $c^*/\bar{c}_p = 0, 0.2, 1, 2, 5$, and 10, indicate that a log-Normal distribution best represents the distribution of T^+ , or T_R , up to $c^*/\bar{c}_p \leq 2$ and an Exponential or a Gamma distribution best represent the data above $c^*/\bar{c}_p > 2$. These distributions are observed for all the sources independent of distance from the source, or distance from the centre-line of the plume.

Wilson and Simms (1985) suggest that in order for the distribution of exceedance times to be considered Exponential, a threshold above the mean concentration is required. The data found here for all sources considered, suggest that the threshold be at least $2\bar{c}_p$, which may be considerably larger than \bar{c} .

The log-Normal distribution is a good representation of the distribution of the excursion times and return times for threshold levels less than about two times the conditional mean concentration. Above twice the conditional mean concentration the Exponential distribution best represents the observed probability distributions, as suggested by Rice (1944-45) or by rare event theories.

7.7 Threshold Crossing Scale

An interesting statistic that is important in flammability studies and chemical reactivity studies is the zero-crossing frequency, $N^+(c^*/\bar{c}_p = 0) = N^+_o$, (see (7.35)). For a joint Normal process, (where both c and \dot{c} are Normally distributed),

$$N^+_o = \frac{\sigma_c}{2\pi\sigma_{\dot{c}}} \quad (7.50)$$

Define two scales, using the notation of Sreenivasan, Prabhu and Narasimha (1983),

$$\Lambda = (2\pi N^+_o)^{-1} \quad (7.51)$$

$$\lambda = \sigma_c/\sigma_{\dot{c}} \quad (7.52)$$

¹The additive property of two Gamma distributions requires that the parameter, σ , be the same, for the distribution above the threshold and below the threshold, for example.

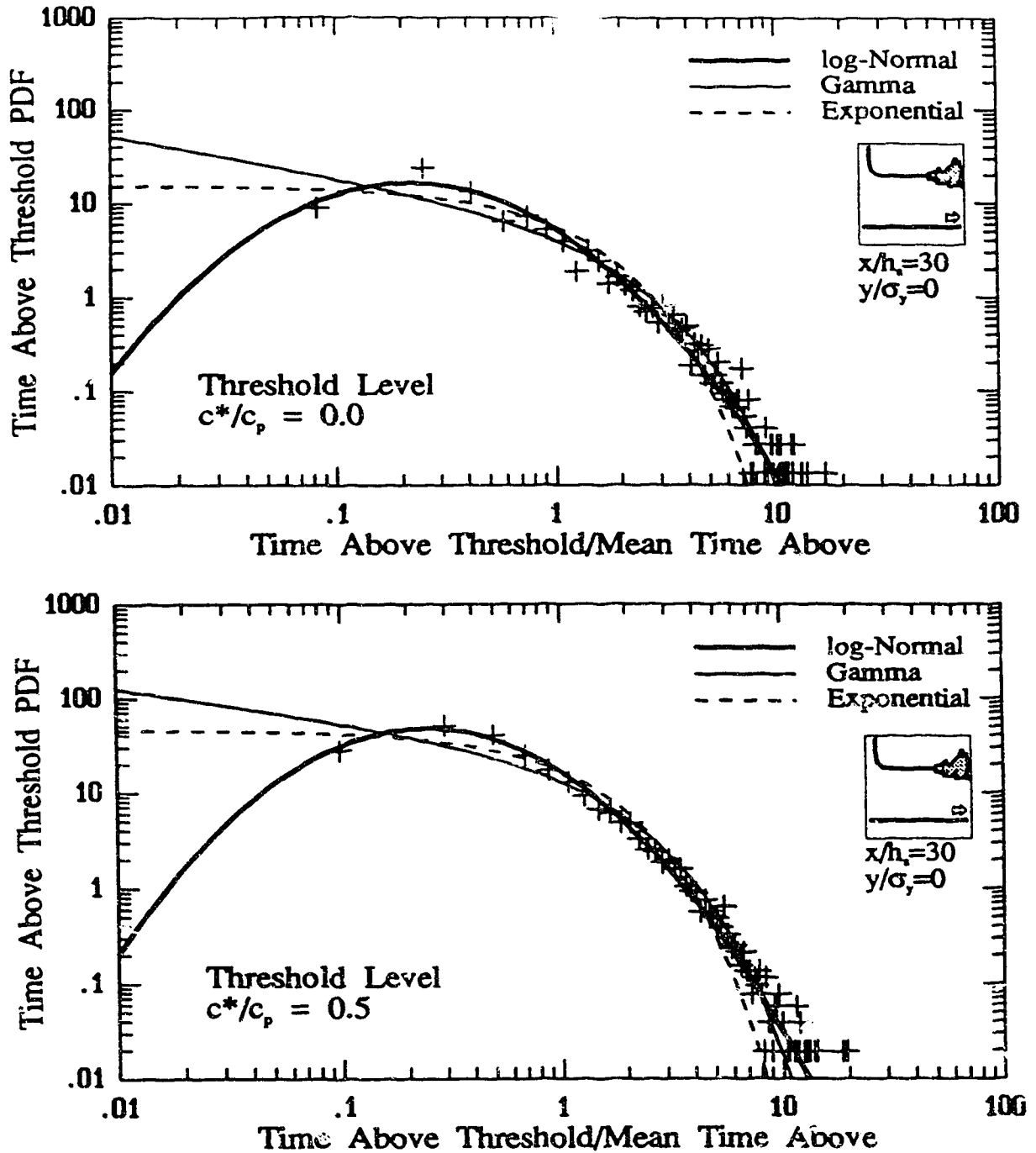


Figure 7.20: The distribution of the exceedance times, T^+ , above a threshold for the jet/plume source with a threshold of $c^*/\bar{c}_p = 0$ (top) and $c^*/\bar{c}_p = 0.2$ (bottom).

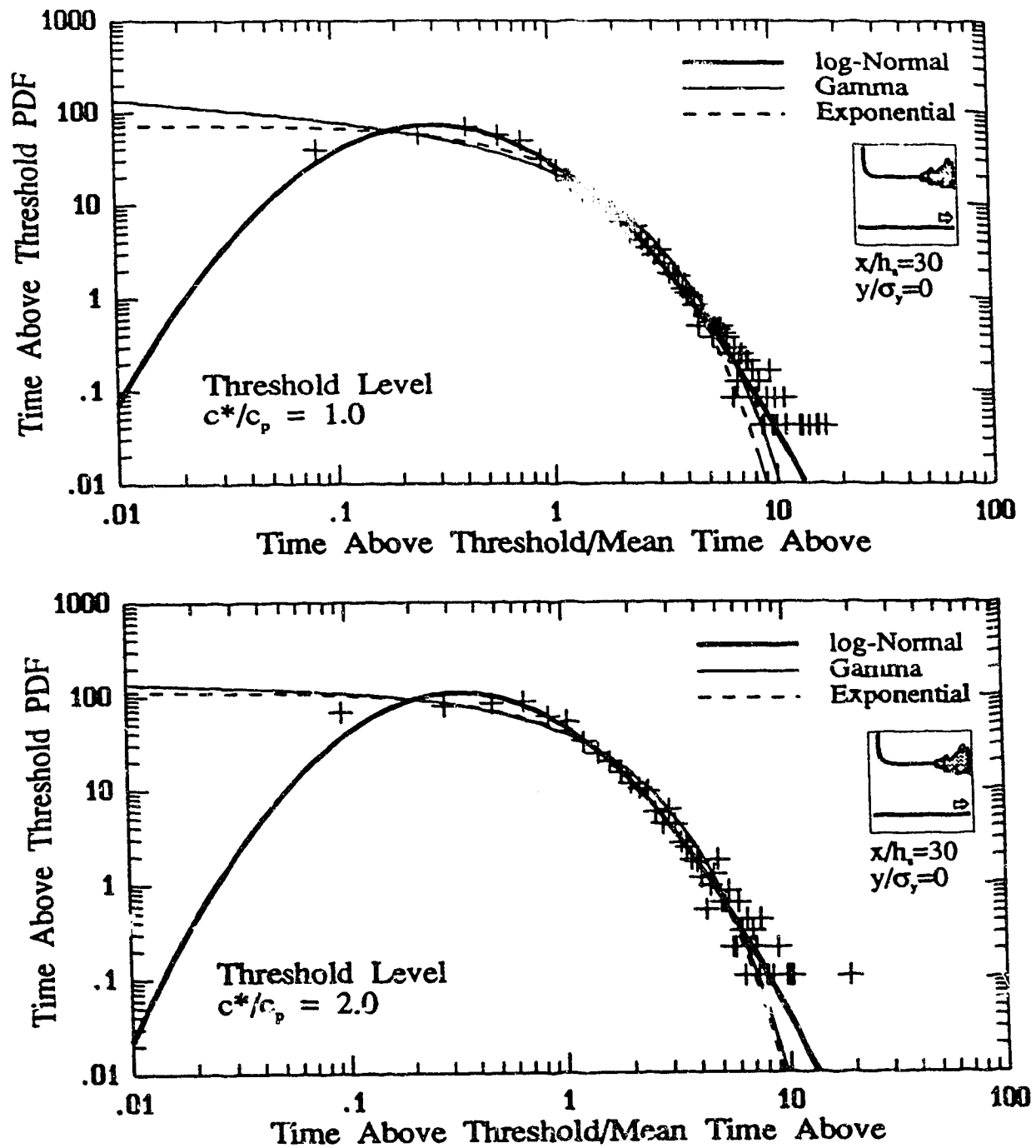


Figure 7.21: The distribution of the exceedance times, T^+ , above a threshold for the jet/plume source with a threshold of $c^*/\bar{c}_p = 1$ (top) and $c^*/\bar{c}_p = 2$ (bottom).

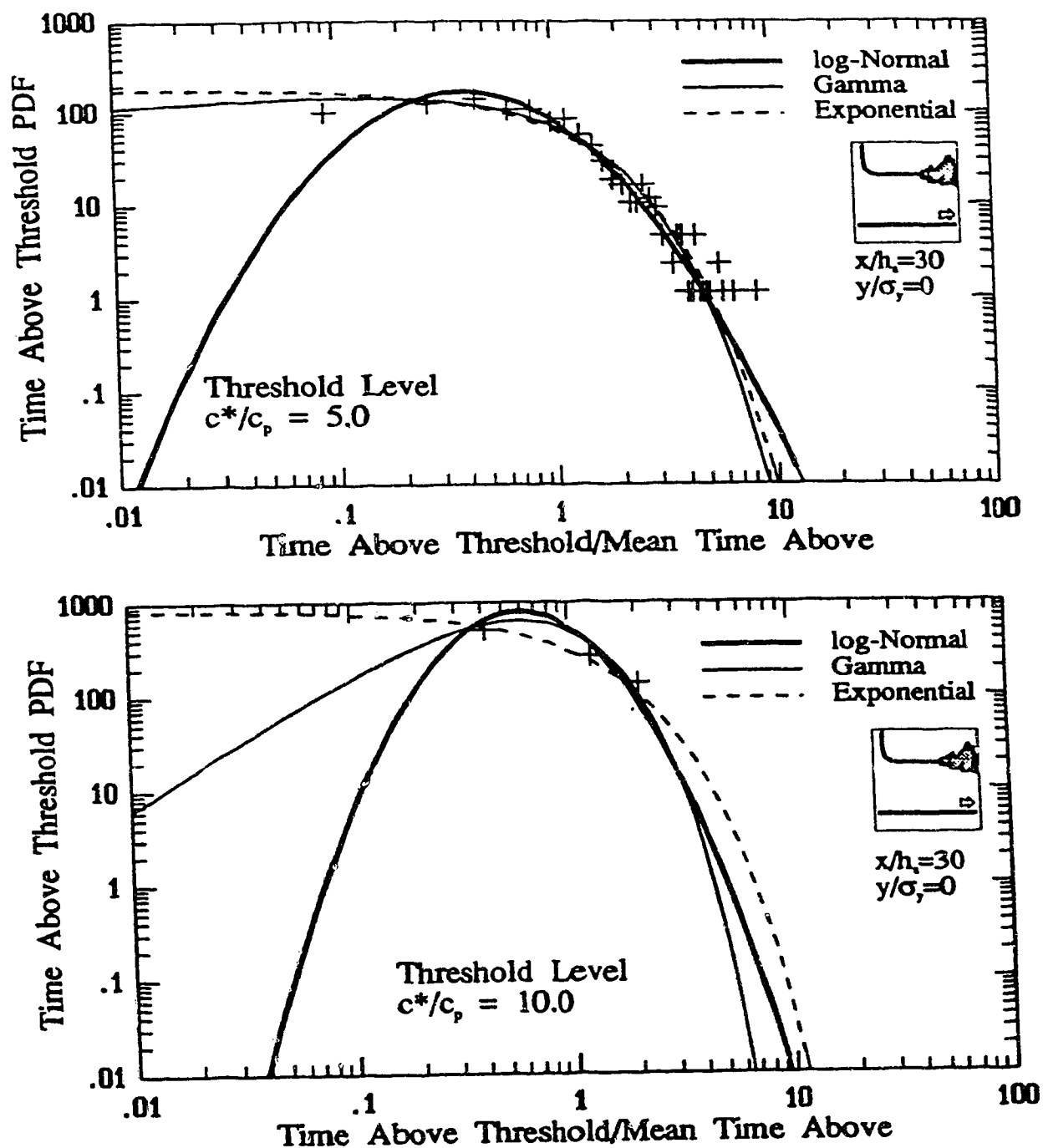


Figure 7.22: The distribution of the exceedance times, T^+ , above a threshold for the jet/plume source with a threshold of $c^*/\bar{c}_p = 5$ (top) and $c^*/\bar{c}_p = 10$ (bottom).

where:

- Λ is a zero-crossing, 'Liepmann', microscale
- λ is proportional to the 'Taylor' microscale, λ_c

The zero-crossing theory by Rice (1944-45) may be restated by asserting that $\Lambda = \lambda$ for joint Normal processes of c and \dot{c} . Since the observed process is not a Normal process, the relation is not expected to hold exactly, however, Sreenivasan, Prabhu and Narasimha (1983) review several findings that show to good approximation that $\Lambda \approx \lambda$.

The purpose of this section, finally, is to show whether in the study of concentration fluctuations, the relation $\Lambda \approx \lambda$ is a good approximation, especially if the derivative of concentration is desired from it. In velocity or reactivity experiments, the zero threshold is designed such that it is equivalent to this study's conditional concentration mean value. Therefore, the threshold level of $c^*/\bar{c}_p = 1.0$ will be used to test whether $\Lambda \approx \lambda$.

In Figure 7.23 (top) the cross-wind distribution of the crossing scale ratio for the conditional mean threshold is shown. For the data within $\sigma_y < 3$, $\Lambda/\lambda \approx 1.3$ across the plume, which is not $\Lambda = \lambda$. The discussion in section 7.2.2, which describes that the derivative is Exponential not Normal, accounts for 12% of the deviation from unity. The remaining difference is explainable by the concentration fluctuation process being Gamma, log-Normal or clipped-Normal and not Normal. For an approximation of the value of λ or of Λ , the joint Normal assumption is shown in Figure 7.23 to be within about 30%.

The data for large plume sizes, Figure 7.23 (top), tends to deviate more from the simple theory that $\Lambda/\lambda = 1$. For the jet/plume source the crossing scale ratio increases to 1.4, then to 1.6. For other sources the ratio may be greater than 2. Sreenivasan, Prabhu and Narasimha (1983) review others who have found similarly large values, but no details were given for a more direct comparison. The concentration probability distribution in this region of the plume size is log-Normal. Therefore, the data collected in the water channel indicates that when the concentration process is log-Normal, the crossing scale ratio is a poor indication of the Taylor microscales.

The other tracer sources studied show a similar behaviour. In Figure 7.23 (bottom), the same plume size was selected for different sources, and the crossing scales are remarkably similar. Also marked on the figure are the approximate intermittencies for each of the sources which vary greatly, $\gamma = 0.25$ to $\gamma = 1$. These data suggest that approximation of the joint Normal assumption for the crossing

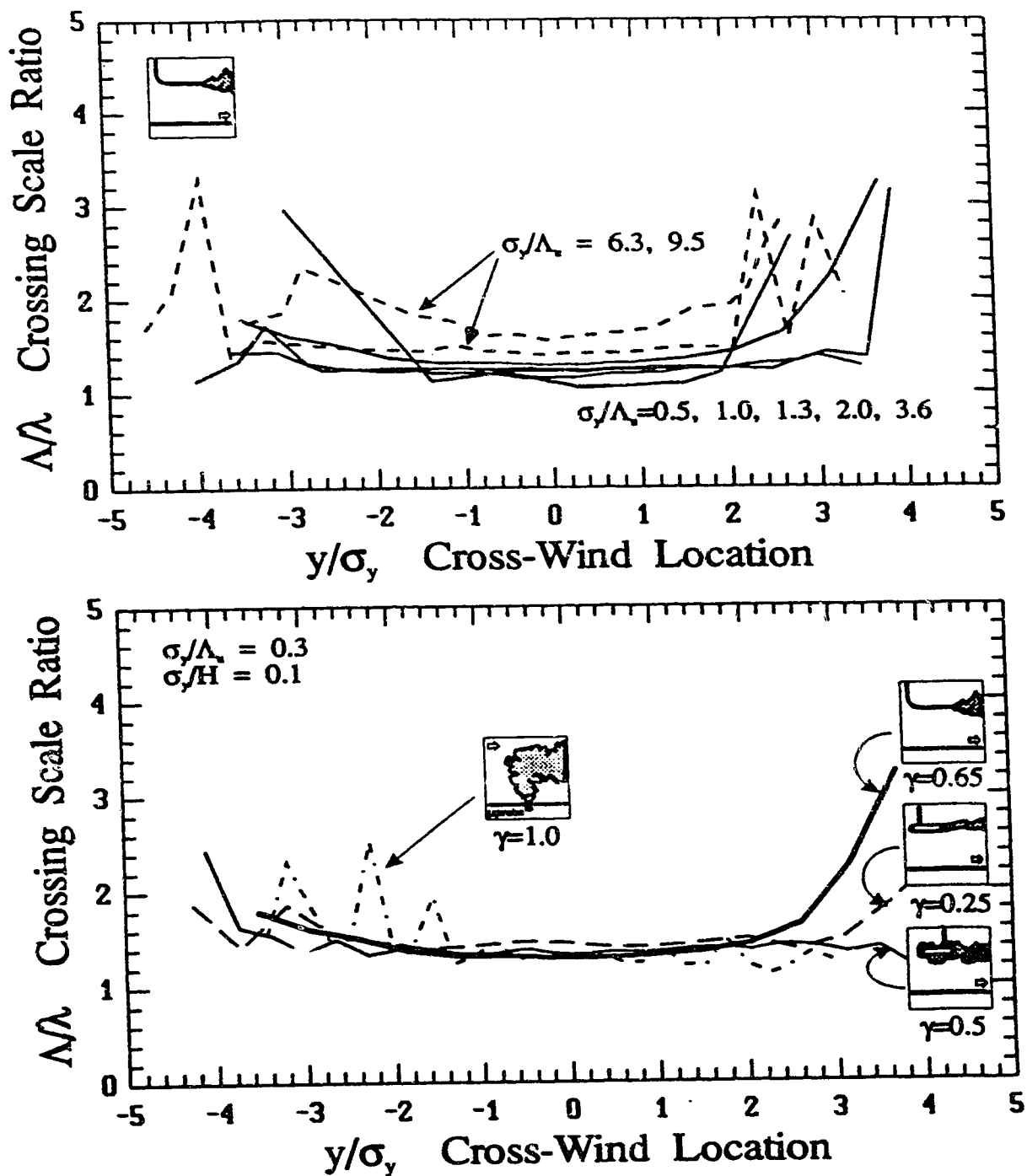


Figure 7.23: The cross-wind variation of the crossing scale ratio for the jet/plume source (top) and cross-wind profiles at the same plume size locations for all sources (bottom).

scale ratio works well, regardless of source configuration, but for plume sizes of about $\sigma_y/\Lambda_u < 5$.

For the purposes of extracting the derivative variance from the crossing scale ratio, (from the Taylor microscale), the joint Normal assumption is not warranted. The results may be within 25% for small source sizes, but can vary to a factor of two. Also, considerable effort must be made to get the number of threshold crossings. For an equal amount of effort, the derivative may be determined directly from the data by higher order derivative techniques which are considerably more accurate, (section B.2). Alternatively, knowing the spectrum, the derivative variance may be determined with equal or better accuracy knowing only the concentration variance and the concentration integral length scale, (section 6.8).

7.8 Conclusions

The threshold crossing model proposed by Kristensen, Weil, and Wyngaard (1988) has been extended to an intermittent plume. The theory has been applied using an Exponential derivative PDF, which has been used to predict threshold crossing estimates. The Normal derivative model is in error 12% when the actual distribution is Exponential. The Exponential derivative model has been combined with the similarity model and the Von Kármán generalized spectrum to produce a model which accurately describes the water channel data.

The Gamma PDF was found to be a good overall predictor of the the number of c^* threshold exceedances per second, N^+ , and the time duration of excursions above a threshold. For thresholds near zero, the rate of exceedances was found to be best represented by a clipped-Normal distribution.

The normalized rate of exceedances and the normalized excursion times for the conditional mean threshold level were both found to be a simple function of the plume size for all the sources studied.

The log-Normal distribution is a good representation of the distribution of the excursion times, T^+ , and the return times for threshold levels less than about two times the conditional mean concentration. Above twice the conditional mean concentration the Exponential distribution best represents the observed probability distributions, as suggested by Rice (1944-45) or by rare event theories.

Chapter 8

Conclusions

At the time of this study, dispersion modelling was undergoing a change in its focus from the investigation of the mean concentration and variance to a statistical probability description. The current literature is inconsistent in its reports of best fit distributions for the sources studied, and no consistent comparison of the probability distributions down-wind of different sources has been reported. This study has investigated the dispersion of a tracer in a boundary layer to determine if a single best fit probability distribution exists. The study used four tracer sources and found that three probability distributions may be used to represent the data. All of the sources studied exhibited similar development of the probability distribution of concentration, from a near clipped-Normal distribution, to Gamma and then to log-Normal. The evolution of the distribution changes scaled approximately with the plume size.

The predictions of the higher order moments of concentration in a dispersing plume are not modelled in the literature past the second order. The second central moment is usually modelled but requires closure modelling of the production terms in the governing equations. The present study has developed budget equations for the first four total moments of concentration which do not require production term closure models. The higher order equations have been shown to reduce to a Gaussian solution with different plume spreads for each moment. A simple similarity model was presented which predicts the plume spreads for the higher order moments based on a one-dimensional meandering plume theory by Gifford (1959) and Sawford and Stapountzis (1986). This simple similarity theory predicts the cross-wind concentration statistics based on observed centre-line values of $\overline{c_0^n}$ and plume spread, σ_y .

The probability density of the concentration derivative is usually approximated by a Normal distribution, Kristensen, Weil and Wyngaard (1988). Prasad and

Sreenivasan (1990), observed that it can have other than Normal distributions. This study has observed that derivative distributions evolve with down-wind position and cross-wind position. Near the source, the Normal distribution is the best representation of the derivative, however the Exponential distribution is a good overall representation of the derivative observations for all down-wind locations.

A spectral representation of the data is frequently required in dispersion modelling. Because the saline dispersion experiments were in the viscous-convective range of the spectrum, and no practical spectral model existed for this range, a spectral model was developed by generalizing the Von Kármán spectrum for a k^{-1} spectrum. This spectral model was found to be a good representation of the observed concentration spectrum and its time derivative. The variance of the time derivative for the concentration time series was determined from the derivative spectrum with the use of an upper frequency cutoff. The variance determined by derivative spectrum closely matched the observed variance determined directly from the concentration time series.

Risk and hazard analyses of toxic plume releases, and flammability and chemical reactivity analyses, are dependent on exceedance statistics, which predict how often and for how long a concentration threshold will be exceeded. Kristensen, Weil and Wyngaard (1988) have applied Rice's (1944-45) exceedance statistics theory to a dispersing plume. The present study has extended this work by developing the exceedance theory for an intermittent plume and by modelling the concentration derivative variance with an upper frequency cutoff. The present study develops the exceedance theory for an intermittent plume using the log-Normal, Gamma and clipped-Normal concentration distributions and using the Normal, Exponential and Gamma concentration time derivative distributions.

8.1 Theoretical/Analytical/Computational

The following summarizes the theoretical, analytical and computational advances made during this study:

1. A fast response conductivity probe was developed and methods were devised to correct for its noise, calibration drift, non-linear calibration and response time.
2. Two data acquisition programs have been written for automatic computer control of the laser doppler anemometer system; one for the tracker signal processor and one for the counter signal processor.
3. A concentration data acquisition system for conductivity probe calibration drop tests, which collected and analyzed the data interactively, was developed.

4. A concentration data acquisition system to collect data from a rake of eight conductivity detectors was written for interactive data collection.
5. Computer data analysis procedures were developed for
 - velocity bias corrections
 - velocity shear stress measurements
 - adaptive filter of the velocity records
 - digital filtering
 - derivative measurements
 - moment analysis
 - probability density analysis
 - probe response correction
 - transient probe calibration routines
 - threshold analysis
 - threshold crossing probabilities
 - smoothed variance technique for the length scales calculations
 - spectral power density
6. The Von Kármán spectrum was generalized for a spectrum of k^n instead of $k^{-5/3}$. This spectrum was applied to the velocity and concentration data. It was also applied to the concentration derivative data.
7. The known time response of the probe was used to deconvolute the concentration time series, which restores much of the original spectrum. The correction procedure can be used for any first order response instrument.
8. Probability distributions have been corrected for the observed data ranges by truncating the fitted theoretical distribution. The normalization of the distributions removes the high concentration tails of the distributions, which extend to infinity.
9. A similarity model for the concentration higher order moments was developed based on the conservation equation.
10. The inter-event time statistics based on Rice's (1944-45) work and applied by Panofsky and Dutton (1984), and Kristensen, Weil and Wyngaard (1988), were extended to include;

- intermittent concentration signals
- Exponential probability distributions for the derivative
- three common PDF models for the concentration fluctuation distributions.

8.2 Observed and Predicted Concentration Fluctuation Statistics

Summarized here are the conclusions derived from the observed and predicted concentration fluctuation statistics:

1. The water channel shear flow provides a good approximation of the atmospheric boundary layer at 3300:1 scale.
2. No single PDF fully describes the concentration dispersion process, but three PDF models work well for specific ranges for all sources tested.
3. No single PDF fully describes the concentration time derivative, but three PDF models work well for specific ranges for all sources tested.
4. The saline tracer concentration PDF results indicate that the evolution of PDF processes may be the same function of plume size for a wide range of source types studied. The clipped-Normal concentration PDF has a near Normal derivative PDF. The Gamma concentration PDF has a near Exponential derivative PDF. The log-Normal concentration PDF has a hyper-Exponential derivative PDF, which may be Gamma.
5. The intermittency can be predicted using the best fit PDF but was under-predicted by the three probability models studied.
6. The cross-wind distribution of the higher order moments of concentration is well described by the simple Gaussian similarity model. A simple relationship between the spreads of the higher order moments was developed and was found to describe the $\sigma_{y,n}$ well.
7. The generalized Von Kármán spectrum matches the observed concentration data very well in the viscous-convective range and may be used to determine $\overline{c'^2}$ using an estimate of $\overline{c'^2}$ and Λ_c .

8. The inter-event times are approximately log-Normal distributed for thresholds less than twice the conditional mean concentration, $< 2\bar{c}_p$. For thresholds greater than twice the conditional mean concentration, $> 2\bar{c}_p$, the Exponential distribution works well as expected.
9. The Gamma distribution is the better general PDF model for predicting the plume concentration fluctuation statistics, compared to the log-Normal or the clipped-Normal distributions.

8.3 Theoretical Developments

New theoretical developments presented in this thesis are summarized below:

1. The concentration spectrum follows a generalized Von Kármán spectrum of power, $n = \frac{1}{2}$, such that $E_c \propto k^{-1}$. The concentration derivative variance may be determined from the spectra and accounts for the effects of the receptor response.
2. The concentration dispersion process may be modelled by a combination of the clipped-Normal, Gamma, and log-Normal distributions.
3. The concentration moments may be modelled using a Gaussian profile family, based on the conservation equations and ignoring dissipation. The profile standard deviations are successively smaller for each higher order moment.
4. A two-dimensional meandering plume model is used to determine the relationship between the higher order moments, based on Gifford (1959), Sawford and Stapountzis (1986) and Wilson and Zelt (1988).
5. Rice's (1944-45) exceedance statistics model has been extended following Panofsky and Dutton (1984) and Kristensen, Weil and Wyngaard (1988), to account for the presence of intermittency and a derivative PDF which is Exponential. Expressions are also presented for other than Gamma concentration PDFs.

8.4 Unresolved Issues

Unresolved issues and specific issues that merit further study are summarized below:

1. The observations of the concentration PDF and the concentration derivative PDF have produced intriguing results concerning the underlying concentration dilution process. A more detailed data set should be collected to better quantify the evolution of the PDFs with down-wind distance.
2. A similarity model for the cross-wind variation of the higher order concentration moments, $\overline{c^n}$, was developed. However, the model requires the prediction of the development of the centre-line values, $\overline{c_0^n}$, with down-wind location. This study has used observed values of $\overline{c_0^n}$ on the centre-line of the plume.
3. A model for the development of the concentration integral time scale with down-wind position and cross-wind position has not been developed. This study has used observed values on the centre-line of the plume and has assumed that the length scales are constant across the plume.
4. The spectrum for saline dispersion in the water channel has been found to be in the viscous-convective range, k^{-1} , whereas atmospheric spectra are observed to be in the inertial sub-range, $k^{-5/3}$. Sreenivasan (1991) has found that the fractal dimensions for these two ranges are different. The applicability of the models to atmospheric flows and implications of these findings on observed behaviour of the intermittency, N^+ , T^+ , and similarity theory have not been investigated.
5. In the analysis of the concentration microscale, a conditional microscale was defined. A microscale by definition may be determined from the energy spectrum by,

$$\frac{1}{\tau_{cp}^2} = \frac{2\pi^2}{\sigma_{cp}^2} \int_0^\infty n^2 E_{cp}(n) dn \quad (8.1)$$

Where $E_{cp}(n)$ would be the conditional spectrum. The conditional spectrum might be measurable by considering the time series analysis of discontinuous processes. The development of a conditional spectrum for intermittent plumes has not been investigated here.

References

- Abramowitz,M., Stegun,I., (1964), **Handbook of Mathematical Functions**. Applied Mathematics Seies, vol. 55, (Washington Bureau of Standards).
- Adrian,R.J., (1983), **Laser Velocimetry, Fluid Mechanics Measurements**, Chapter Five, Hemisphere Pub. Corp., Washington, pp.155-244.
- Andrews,L.C., Shivamoggi,B.K., (1990), The gamma distribution as model for temperature dissipation in intermittent turbulence, *The Physics of Fluids A*, **2(1)**, pp.105-110.
- Antonia,R.A., Phan-Thien,N., Chambers,A.J., (1980). Taylor's hypothesis and the probability density functions of temporal velocity and temperature derivatives in turbulent flow, *Journal of Fluid Mechanics*, **100(1)**, pp.193-208.
- Antonia,R.A., Sreenivasan,K.R., (1977), Log-Normality of temperature dissipation in a turbulent boundary-layer, *The Physics of Fluids*, **20(11)**, pp.1800-1804.
- Badri Narayanan,M.A., Rajagopalan,S., Narasimha,R., (1977), *Journal of Fluid Mechanics*, **80**, p.237.
- Balachandar,S., Sirovich,L., (1991), Probability distribution functions in turbulent convection, *Physics of Fluids A*, **3(5)**, pp.919-927.
- Baldwin,L.V., Mickelsen,W.R., 1962, *Proceedings of the American Society of Civil Engineering*, **88** EM2, 37.

- Bara, B., and Netterville, D.D.J., (1985), Determination of Plume Sigmas and Turbulence Integral Length Scales from Acoustic Doppler Measurements of Plume-Level Wind Fluctuations. Presented at the PNWIS/APAC Annual General Meeting, Calgary, Canada.
- Barry, P.J., (1977), Chapter 7: Stochastic Properties of Atmospheric Diffusivity, **Sulphur and its Inorganic Derivatives in the Canadian Environment**, NRC Pub #15015, pp.313-358.
- Bencala, K.E., Seinfeld, J.H., (1976), On frequency Distributions of air Pollutant Concentrations, *Atmospheric Environment*, No.10, pp.941-950.
- Bilger, R.W., (1980), Chap 3: Turbulent Flows with Non-premixed Reactants, **Turbulent Reacting Flows**, Ed. Libby, P.A., and Williams, F.A., Springer-Verlag, New York, pp.65-113.
- Brooks, C.E.P., Carruthers, N., (1953), **Handbook of Statistical Methods in Meteorology**, Her Majesty's Stationary Office, London.
- Buchhave, P., George, W.K.Jr., (1978), Bias Correction in Turbulence Measurements by the Laser Doppler Anemometer, **Laser Velocimetry and Particle Sizing**, ed. H.Doyle Thomson, Warren H.Stevenson, Hemisphere Pub. Corp., Washington. pp.110-119.
- Bury, K.V., (1986), **Statistical Models in Applied Science**, R.E.Krieger Pub.Co., Malabar, Florida.
- Chua, S.K., Cleaver, J.W., Millward, A., (1986), The measurement of Salt Concentration in a Plume using a Conductivity Probe, *J. of Hydraulic Research*, V.25, N.3, pp.171-178.
- Counihan, J., (1975), Review Paper, Adiabatic atmospheric boundary layers: A review and analysis of data from the period 1880-1972, *Atmospheric Environment*, 9, pp.871-905.
- Cox, D.R., Miller, H.D., (1965), **The Theory of Stochastic Processes**, Chappman and Hall, London.

- Csanady, G.T., (1973), **Turbulent Diffusion in the Environment**, D. Reidel Publishing Company, Dordrecht.
- Deardorff, J.W., Willis, G.E., (1975), A parameterization of diffusion into the mixed layer, *Journal of Applied Meteorology*, **14**, pp.1451-1458.
- Deardorff, J.W., Willis, G.E., (1988), CHAP 8: Concentration Fluctuations within a Laboratory Convectively Mixed Layer, **Lectures on Air Pollution Modeling**, Ed. Venkatram, A., and Wyngaard, J.C., American Meteorological Society, Boston, pp.356-384.
- Dinar, N. Kaplan, H., Kleiman, M., (1988), Characterization of concentration fluctuations of a surface plume in a neutral boundary layer, *Boundary-Layer Meteorology*, **45**, pp.157-175.
- Dopazo, C., (1975), Probability density function for a turbulent axisymmetric jet. Centre-line evolution, *the Physics of Fluids*, **18(4)**, pp.397-404.
- Dowben, R.M., and Rose, J.E., (1953), A Metal-Filled Microelectrode, *Science*, **118**, pp.22-24.
- Draxler, R.R., (1976), Determination of Atmospheric Diffusion Parameters, *Atmospheric Environment*, **10**, pp.99-105.
- Dutton, J.A., (1970), Effects of Turbulence on Aeronautical Systems, *Progress in Aerospace Sciences*, **11**, Ed. D. Kuchemann, Pergamon Press, Oxford, pp.67-109.
- Durst, F., Melling, A., Whitelaw, J.H., (1976), **The Principles and Practice of laser-doppler anemometry**, London Academic Press.
- Dyer, A.J., and Bradley, E.F., (1982), An alternative analysis of flux-gradient relationships at the 1976 ITCE. *Boundary Layer Meteorol.*, **22**, pp.1-19.
- Feller, W., (1950), **An introduction to Probability Theory and its Applications**, Volume 1, Third Edition, John Wiley and Sons, New York.

- Fletcher, R., Powell, M.J.D., (1963), Determination of atmospheric diffusion parameters, *Atmospheric Environment*, **10**, pp.99-105.
- Gao, F., O'Brien, E.E., (1991), Joint probability density function of a scalar and its gradient in isotropic turbulence, *Physics of Fluids A*, **3**(6), pp.1625-1632.
- Gaster, M., Roberts, J.B., (1977), The spectral analysis of randomly sampled records by a direct transform, *Proc. Roy. Soc. Lond. A.*, **354**, pp.27-58.
- Gerald, C.F., (1978), **Applied Numerical Analysis**, Addison-Wesley Pub. Co., Reading, Mass.
- Gesteland, R.C., Howland, B., Lettvin, J.Y., and Pitts, W.H., (1959), Comments on Microelectrodes, *Proceedings of the IRE*, **47**, pp.1856-1862.
- Gibson, C.H., Schwartz, W.H., (1977), Detection of Conductivity Fluctuations in a Turbulent Flow Field, *Journal of Fluid Mechanics*, **16**, pp.357-364.
- Gifford, F.G., (1959), Statistical properties of a fluctuating plume dispersion model, *Advances in Geophysics*, **6**, pp.117-137.
- Gifford, F.G., (1982), Horizontal Diffusion in the Atmosphere: A Lagrangian-Dynamical Theory, *Atmos. Env.*, **16**, no.3, pp.505-512.
- Gifford, F.G., (1987), The Time-Scale of Atmospheric Diffusion Considered in Relation to the Universal Diffusion Function, f_1 , *Atmospheric Environment*, **21**(6), pp.1315-1320.
- Grass, A.J., (1971), Structural features of turbulent flow over smooth and rough boundaries, *Journal of Fluid Mechanics*, **50 part 2**, pp.233-255.
- Hay, J.S., Pasquill, F., (1959), *Advances in Geophysics*, vol. **6**, p.345.
- Hanna, S.R., (1984), Concentration Fluctuations in a Smoke Plume, *Atmospheric Environment*, **18**(6), pp.1091-1106.
- Hanna, S.R., Briggs, G.A., and Hosker, R.P., (1982), **Handbook of Atmospheric Diffusion**, Technical Information Center, U.S. Dept. of Energy.

- Head, M.J., (1983), *The Use of Miniature Four-Electrode Conductivity Probes for High Resolution Measurement of Turbulent Density or Temperature*, Ph.D. Thesis. University of California, University Microfilms International #8312227.
- Hewitt, G.F., (1960) Tables of the resistivity of Aqueous Sodium Solutions. *Atomic Energy Research Establishment*, Great Britain, Rept. R3497, Chem. Abstracts Citation #55:6123d.
- Hinze, J.O., (1975), *Turbulence*, 2nd Ed., McGraw Hill.
- Hoaglin, D.C., Peters, S.C., (1979), Software for Exploring Distribution Shape, in J.F. Gentleman (Ed.) *Proceedings of Computer Science and Statistics: Twelfth Annual Symposium on the Interface*, University of Waterloo, Ontario, pp.418-423.
- Hogstrom, (1985), *J. of Atmos. Sci.*, **42**.
- Holland, D.M., Fitz-Simons, R., (1982), Fitting Statistical Distributions to Air Quality Data by the Maximum Likelihood Method, *Atmospheric Environment*, **16**(5), pp.1071-1076.
- Howroyd, G.C., Slawson, P.R., (1977), The mesoscale diffusion of plumes from the Plant Bowen Power Generating Facility and large industrial source at Sudbury, Ont. Envirodyne Ltd. Report.
- Jakeman, A.J., Simpson, R.W., Taylor, J.A., (1986), Modeling Distributions of Air Pollutant concentrations - II. Estimation of One and Two Parameter Statistical Distributions, *Atmospheric Environment*, **22**(1), pp.163-174.
- Jakeman, A.J., Simpson, R.W., Taylor, J.A., (1988), Modeling Distributions of Air Pollutant concentrations - III. The Hybrid Deterministic-Statistical Distribution Approach, *Atmospheric Environment*, **22**(1), pp.163-174.
- Jackson, P.S., (1981), On the displacement height in the logarithmic velocity profile, *J. Fluid Mechanics*, **111**, pp.15-25.

- Johnson,D.A., Modarress.D., Owen,F.K., (1984), An Experimental Verification of Laser-Velocimeter Sampling Bias and its Correction, *J. Fluid Mechanics*, **106**, pp.5-12.
- Kaimal,J.C., Clifford,S.F., Lataitis,R.J., (1989), Effect of finite sampling on atmospheric spectra, *Boundary-Layer Meteorology*, **47**, pp.337-347.
- Kline,S.J., McClintock,F.A., (1953). Describing uncertainties in single sample experiments, *Mech.Eng.*, Jan., pp.3-8.
- Klinov,F.Ya., Poltavskii,V.V., (1963), The Measurement of the Wind Velocity in the Bottom 300-meter Atmospheric Layer on an upper-air Meteorological Mast, *Investigation of the Bottom 300-Meter Layer of the Atmosphere*, N.L. Byzova, Editor, Izdatel'stvo Akademii Nauk SSSR, Moskova, pp.57-63.
- Kristensen,L., Weil,J.C., Wyngaard,J.C., (1988), Recurrence of High Concentration Values in a Diffusing, Fluctuating Scalar Field, *Boundary-Layer Meteorology*, **47**, pp.263-276.
- Kuo,A.Y., Corrsin,S., (1971), Experiments on internal intermittency and fine-structure distribution functions in fully turbulent fluid, *Journal of Fluid Mechanics*, **50**(2), pp.285-319.
- Lewellen,W.S., Sykes,R.I., (1986), Analysis of Concentration Fluctuations from Lidar Observations of Atmospheric Plumes, *American Meteorological Society*, **25**, pp.1145-1154.
- Lienhard,J.H., Meyer,P.L., (1967), A Physical Basis for the Generalized Gamma Distribution, *Quarterly of Applied Mathematics*, **25**, pp.330-334.
- Lockwood,F.C., Naguib,A.S., (1975), The Prediction of the Fluctuations in the Properties of Free, Round-Jet, Turbulent, Diffusion Flames, *Combustion and Flame*, **24**, pp.109-124.
- Marani,A., Lavagnini,I., Buttazzoni,C., (1986), Statistical Study of Air Pollutant Concentrations via Generalized Gamma Distribution, *Journal of Air Pollution Control Ass.*, **36**, pp.1250-1254.

- Mark, W.D., (1989), Probability Density and Exceedance Rate Functions of Locally Gaussian Turbulence, *J. Sound Vib.*, **135**, pp.143-160.
- McDougall, T.J., (1980), Bias Correction for individual realization LDA measurements, *J. Phys. E. Sci. Instrum.*, **13**, pp.53-60.
- McCormick, W., Slawson, P.R., Tang, J.S., (1979), Diffusion field trials at Whiteshell Nuclear Research Establishment, Waterloo Research Institute, University of Waterloo, Progress Report #1.
- McLaughlin, D.K., Tiederman, W.G., (1973), Biasing Correction for Individual Realization of Laser Anemometer Measurements in Turbulent Flows, *Physics of Fluids*, **16**, No.12, pp.2082-2088.
- Menon, M.V., (1963), Estimation of the shape and scale parameters in the Weibull distribution, *Technometrics*, **5**, pp.175-182.
- Nakagawa, H., Nezu, I., Ueda, H., (1975), Turbulence of Open Channel Flow Over Smooth and Rough Beds, *Proc. of JSCE*, **241**, pp.155-168.
- Netterville, D.D.J., (1979), Concentration Fluctuations in Plumes, *Environmental Research Monograph 1979-4*, A Public Service of Syncrude Canada Ltd., 288pp.
- Nezu, I., Rodi, W., (1986), Open-Channel Flow Measurements with a Laser Doppler Anemometer, *Journal of Hydraulic Engineering*, **112**, No.5, pp.335-355.
- Norsworthy, K.H., (1978), Fourier Transform and Spectrum Analysis of Sparsely Sampled Signals, *Laser Velocimetry and Particle Sizing*, ed. H.D Thompson, W.H.Stevenson, Hemisphere Publishing Co., Washington, pp.314-327.
- Oboukhov, A.M., (1962), Some specific features of atmospheric turbulence, *Journal of Fluid Mechanics*, **13**, pp.77-81.
- Panofsky, H.A., Dutton, J.A., (1984), Atmospheric Turbulence – Models and Methods for Engineering Applications, John Wiley and Sons, Toronto.

- Pasquill,F., (1961), The statistics of turbulence in the lower part of the atmosphere.
Paper 4, *Symp. on Atmos. Turb. and its Relation to Aircraft*, R.A.E.,
Farnborough.
- Pasquill,F., Smith,F.B., (1983), Atmospheric Diffusion, 3rd Ed., Ellis Horwood
Lim., pp.20-29.
- Peled,A., Liu,B., (1976), Digital signal Processing, Theory, Design, and
Implementation, John Wiley and Sons, New York.
- Plate,E.J., (1971), **Aerodynamic Characteristics of Atmospheric Boundary
Layers**, U.S. Atomic Energy Commission, Office of Information
Services.
- Plumes2 User's Guide, (1988), Alberta Environment- Environmental Protection
Services.
- Pope,S.B., (1980), Probability Distributions of Scalars in Turbulent Shear Flow,
Turbulent Shear Flows 2, pp.7-16.
- Pope,S.B., (1985), PDF Methods for Turbulent Reactive Flows, *Prog. Energy
Combust. Sci.*, 11, pp.119-192.
- Powers,D.L., (1972), **Boundary Value Problems**, 2nd Ed., Academic Press, New
York.
- Prasad,R.R., Sreenivasan,K.R., (1990), Quantitative three-dimensional imaging and
the structure of passive scalar fields in fully turbulent flows, *Journal
of Fluid Mechanics*, 216, pp.1-34.
- Press,W.H, Flannery,B.P., Teukolsky,S.A., Vetterling,W.T., (1988), **Numerical
Recipes in C**, Cambridge University Press.
- Priestley,M.B., (1981), **Spectral Analysis and Time Series, Volume 1:
Univariate Series, Volume 2: Multivariate Series, Prediction
and Control**, Ed. Z.W.Birnbaum and E. Lukacs, Academic Press,
Inc., Harcourt Brace Jovanovich, Publishers, London.

- Reid, J.D., (1979), Markov Chain Simulations of Vertical Dispersion in the Neutral Surface Layer for Surface and Elevated Releases, *Boundary-Layer Meteorology*, **16**, pp.3-22.
- Rice, S.O., (1944), Mathematical Analysis of Random Noise, Volume I, *Bell System Technical Journal*, **23**, pp.282-332.
- Rice, S.O., (1945), Mathematical Analysis of Random Noise, Volume II, *Bell System Technical Journal*, **24**, pp.46-156.
- Richardson, J.M., Howard, H.C., Smith, R.W., (1953), *Fourth Symposium (International) on Combustion*, Williams and Wilkins, pp.814-817.
- Roberts, J.B., (1986), First-passage probabilities for randomly excited systems: Diffusion methods, *Probabilistic Engineering Mechanics*, **1(2)**, pp.66-81.
- Ross, S.M., (1983), **Stochastic Processes**, John Wiley and Sons, New York.
- Sakiyama, S.K., (1981), Plume dispersion Modelling at the Whiteshell Nuclear Research Establishment, B.A.Sc., University of Waterloo.
- Sackinger, P.A., Reible, D.D., Shair, F.H., (1982), Uncertainties Associated with the ESTimation of Mass Balances and Parameters from Atmospheric Tracer Studies, JAPCA.
- Saffman, P.G., (1962), An Approximate Calculation of the Lagrangian Auto-correlation Coefficient for Stationary Homogeneous Turbulence, *Appl. Sci. Res., Sec. A*, **11**, pp.245-255.
- Sawford, B.L., (1984), The basis for, and some limitations of, the Langevin equation in atmospheric relative dispersion modelling, *Atmospheric Environment*, **18(11)**, pp.2405-2411.
- Sawford, B.L., (1987), Conditional Concentration Statistics for Surface Plumes in the Atmosphere, *Boundary-Layer Meteorology*, **38**, pp.209-223.

- Sawford, B.L., Stapountzis, H., (1986), Concentration Fluctuations According to Fluctuating Plume Models in One and Two Dimensions, *Boundary-Layer Meteorology*, **37**, pp.89-105.
- Simiu, E., (1973), Logarithmic Profiles and Design Wind Speeds, *Journal of the Engineering Mechanics Division*, Proc. ASCE., **99**, No. EM5, pp.1073-1083.
- Sreenivasan, K.R., (1981), Evolution of the Centre-line probability density function of temperature in a plane turbulent wake, *Physics of Fluids*, **24(7)**, pp. 1232-1234.
- Sreenivasan, K.R., (1991), Fractals and Multifractals in Fluid Turbulence, *Annu. Rev. Fluid Mech.*, **23**, pp.539-600.
- Sreenivasan, K.R., Antonia, R.A., Danh, H.Q., (1977), Temperature dissipation fluctuations in a turbulent boundary layer, *The Physics of Fluids*, **20(8)**, pp.1238-1249.
- Sreenivasan, K.R., Prabhu, A., Narasimha, R., (1983), Zero-crossings in turbulent signals, *Journal of Fluid Mechanics*, **137**, pp.251-272.
- Stanely, W.D., Dougherty, G.R., Dougherty, R., (1984), Digital Signal Processing, 2nd Ed., Prentice-Hall Co., Preston.
- Steffler, P.M., Rajaratnam, N. and Peterson, A.W., (1983), LDA Measurements of Mean Velocity and Turbulence Distribution in a Smooth Rectangular Open Channel, *Water Resources Engineering*, Report 83-4, Dept. of Civil Eng., Univ. of ALberta, Canada.
- Swakowski, E.W., (1979), Calculus with Analytical Geometry, 2nd Ed., Prindle, Weber and Schmidt.
- Sykes, R.I., (1984), The Variance in Time-Averaged Samples from an Intermittent Plume, *Atmospheric Environment*, **18(1)**, pp.121-123.
- Sykes, R.I., (1986), Chap 7: Concentration Fluctuations in Dispersing Plumes, *Lectures on Air Pollution Modelling*, Ed. A Venkatram and J.C.Wyngaard, American Meteorological Society, Boston, pp.324-356.

- Taylor, J.A., Jakeman, A.J., Simpson, R.W., (1986), Modeling Distributions of Air Pollutant concentrations - I. Identification of statistical models, *Atmospheric Environment*, **20**, pp.1781-1789.
- Tennekes, H., Lumley, J.L., (1972), A First Course in Turbulence, MIT Press.
- Tennekes, H., (1973), The Logarithmic Wind Profile, *J. Atmos. Sci.*, **30**, pp.234-238.
- Thom, A.S., (1971), Momentum absorption by vegetation, *Quart. J. Roy. Met. Soc.*, **97**, pp.414-428.
- Townsend, A.A., (1976), *The Structure of Turbulent Shear Flow*, 2nd Ed., Cambridge University Press, Cambridge.
- Tropea, C., (1983), A note Concerning the use of a One-component LDA to Measure Shear Stress Terms, *Experiments in Fluids*, **1**, pp.209-210.
- TSI Model 1980B Counter Type Signal Processor Instruction Manual (1984), TSI inc.
- Uberoi, M.S., Corrsin, S., (1953), *Natl. Advisory Committee. Aeronaut. Tech. Repts. No. 1142*.
- van Dop, H., Nieuwstadt, F.T.M. and Hunt, J.C.R., (1985), Random walk models for particle displacements in inhomogeneous unsteady turbulent flows, *Physics of Fluids*, **28(6)**, pp.1639-1653.
- Wang, L.P., Stock, D.E., Lamb, B.K., (1988), On the Relationship between Lagrangian and Eulerian scales for Kraichnan's Gaussian Random Velocity field, *Proceedings of the Eighth Symposium on Turbulence and Diffusion, April 25-29, American Meteorological Society*, pp.92-95.
- Wells, M.R., (1982), The Effects of Crossing Trajectories on the Diffusion of Particles in a Turbulent Fluid, *Ph.D. Thesis*, Washington State University.
- Wilson, D.J., Robins, A.G., Fackrell, J.E., (1985), Intermittency and conditionally-averaged concentration fluctuation statistics in plumes, *Atmospheric Environment*, **19**, No.7, pp.1053-1064.

- Wilson,D.J., Simms,B.W., (1985), Exposure time effects on concentration fluctuations in plumes, Departmental Report No.47, prepared for Pollution Control Division, Alberta Environment, Edmonton.
- Wilson,D.J., Zelt,B.W., (1988), Measured Probability Distributions and Moments of Concentration Fluctuations in a Laboratory Plume, Proceedings of EURASAP Meeting of Modelling Concentration Fluctuations in the Atmosphere, (unpublished abstracts), Brunel University, London, April, 1988.
- Yee,E., (1990), The shape of the probability density function of short-term concentration fluctuations of plumes in the atmospheric boundary layer, *Boundary-Layer Meteorology*, **51**, pp.269-298.
- Ylvisaker,N.D., (1965), *Ann. Math. Stat.*, **36**, p.1034.
- Zelt,B.W., Wilson,D.J., Barr,B., (1987), Correcting Turbulent Concentration Measurements for Detector Spatial Resolution, *Proceedings of the 11th Canadian Congress of Applied Mechanics*.

Appendix A

Velocity Analysis Procedures

In this section the analysis procedures for velocity measurements which are characteristic of the LDA analysis only are discussed.

The treatment of the velocity data originating from the LDA is unique for three reasons: the data is available at random rather than regular time intervals; there is a characteristic bias of the averaged velocity towards a measurement of the higher velocities; and there is a tendency of the LDA to record measurements from particles moving perpendicular to the fringe orientation, thereby not recording the true velocity vector of interest. Each of these characteristics of the LDA generated data is handled in turn in the sections to follow.

The procedure used for determining the integral scales of turbulence is described in the Appendix B.

A.1 Position Change Due to Change in Index of Refraction

The LDA system measures the velocity in the flowing water channel using laser beams which pass through optics on the outside (air side) of the water channel. As the laser beams pass from air, through the flume glass side walls and into the water, the laser beams are bent twice. The change in position of the laser beam crossing point must be accounted for to determine the actual measurement volume location. The crossing point location correction was performed by the data acquisition system and the true location of the crossing point was saved in the data files.

The laser crossing point was positioned, or zeroed, at the inside glass wall surface. This eliminated the need to know the exact thickness of the glass plate because it becomes an initial offset in the calculations.

The adjustment to the apparent beam position can be seen in Figure A.1. The true beam position, L_3 , in the water channel is given by,

$$L_3 = b \cot \phi_3 \quad (\text{A.1})$$

$$b = L_2 \tan \phi_1 \quad (\text{A.2})$$

Where ϕ_1 is the half angle of the beams in air and ϕ_3 is the half angle of the beams in water. Therefore in terms of the location L_2 ,

$$L_3 = L_2 \frac{\tan \phi_1}{\tan \phi_3} \quad (\text{A.3})$$

The location L_2 is determined by,

$$a = (d + L_1) \tan \phi_1 \quad (\text{A.4})$$

$$b = L_2 \tan \phi_1 \quad (\text{A.5})$$

$$b = a - d \tan \phi_2 \quad (\text{A.6})$$

Then, from (A.5) and (A.6),

$$a = L_2 \tan \phi_1 + d \tan \phi_2 \quad (\text{A.7})$$

and substituting this into (A.4),

$$L_2 = L_1 + d \left(1 - \frac{\tan \phi_2}{\tan \phi_1} \right) \quad (\text{A.8})$$

The law of sines may be used to relate the half angles to the respective indices of refraction,

$$\frac{\sin a_2}{\sin a_1} = \frac{m_1}{m_2} \quad (\text{A.9})$$

Then,

$$\frac{\tan \phi_2}{\tan \phi_1} = \left(\frac{\sin \phi_2}{\sin \phi_1} \right) \frac{\cos \phi_1}{\cos \phi_2} = \left(\frac{m_1}{m_2} \right) \frac{\cos \phi_1}{\cos \phi_2} \quad (\text{A.10})$$

$$= \left(\frac{m_1}{m_2} \right) \frac{\cos \phi_1}{\sqrt{1 - \sin^2 \phi_2}} \quad (\text{A.11})$$

$$= \frac{\cos \phi_1}{\sqrt{\left(\frac{m_2}{m_1} \right)^2 - \sin^2 \phi_1}} \quad (\text{A.12})$$

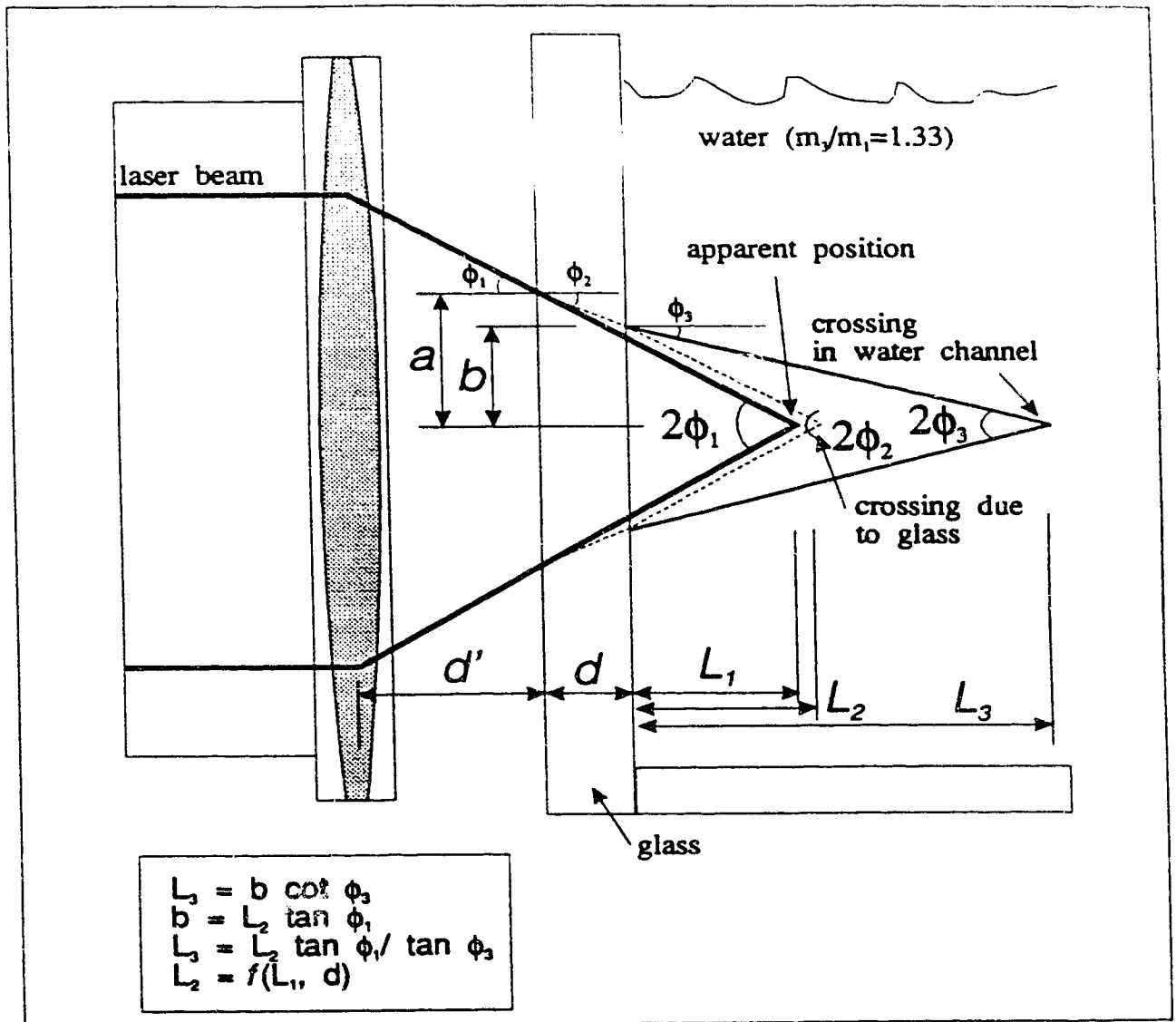


Figure A.1: Correcting the apparent LDA crossing point for refraction angles into the water channel.

Therefore,

$$L_2 = L_1 + d \left(1 - \frac{\cos \phi_1}{\sqrt{\left(\frac{m_2}{m_1}\right)^2 - \sin^2 \phi_1}} \right) \quad (\text{A.13})$$

Similarly,

$$\frac{\tan \phi_1}{\tan \phi_3} = \frac{\sqrt{\left(\frac{m_3}{m_1}\right)^2 - \sin^2 \phi_1}}{\cos \phi_1} \quad (\text{A.14})$$

Substituting this result and L_2 into (A.3) yields,

$$L_3 = \left(L_1 + d \left(1 - \frac{\cos \phi_1}{\sqrt{\left(\frac{m_2}{m_1}\right)^2 - \sin^2 \phi_1}} \right) \right) \frac{\sqrt{\left(\frac{m_3}{m_1}\right)^2 - \sin^2 \phi_1}}{\cos \phi_1} \quad (\text{A.15})$$

Where m_1 is usually taken as unity and m_3 for water is given as 1.33 in the literature and was verified experimentally. The true location of the crossing point, relative to the wet side of the water channel glass side wall is,

$$L_3 = L_1 \frac{1}{\cos \phi_1} \sqrt{\left(\frac{m_3}{m_1}\right)^2 - \sin^2 \phi_1} \quad (\text{A.16})$$

This correction was applied to the position location in the data acquisition system before being saved to mass storage. The data sets do not, therefore, require adjustment for measurement volume location.

The laser crossing point was traversed using stepping motors in the vertical and cross-stream directions. The crossing point could be moved manually over a length of approximately a meter in the water channel stream-wise direction, using a measuring scale for reference, with an accuracy within a millimetre. The stepping motors produced 200 steps per revolution and were mounted on threaded rods have 5 threads per inch. The vertical thread was geared with a ratio of 125/36; producing a resolution of 0.007 mm. The horizontal thread was geared 1/1; producing a resolution of 0.025 mm.

A.2 Spectral Estimation Techniques

The problem of determining the spectral representation of the LDA signal is hampered by the random time steps of the data. The LDA signals are discrete measurements of a Poisson process. There is a considerable amount of information in published literature on the processing of random time series and making use of the Poisson statistics. Gaster and Roberts (1977) have shown that spectral analysis of the signal is free from aliasing. However, Norsworthy (1978) points out that the analysis must be done to preserve the random nature of the data and preserve the anti-aliasing characteristics of Poisson distributed data.

Gaster and Roberts (1977) suggest that the characteristic frequency of the LDA time series is the inverse of the average time between samples in the data record. However, analysis of the time series by using the FFT algorithm, essentially makes the time series periodic with the above determined sampling rate. Therefore, aliasing is again a problem. Norsworthy (1978) suggests a method by which the the highest frequency of interest is selected and time intervals of $\Delta t = f_{max}/2$ determines a new equivalent sampling rate. The time series is then divided into Δt intervals. Observations within each interval are averaged, and if no observations occur in a time interval a zero fluctuation (or mean value) is substituted for the average. A fast and stable result is produced but has induced spectral folding around a frequency of $1/2\Delta t$ and has poor signal-to-noise characteristics. Recall that the Nyquist theorem predicts that periodic sampling leads to spectral folding about a frequency equal to one half the sampling rate.

For the purposes of this study, the Gaster and Roberts (1977) procedure was used at the expense of a low folding frequency. Since the spectra were used primarily to determine integral scales of turbulence using the lowest frequencies, and to validate results of another procedure, the low folding frequency did not present a problem. The effects of low folding frequency can be seen in the increased noise near the folding frequency in Figure 3.25. Since the spectral energy which is folded back is four orders of magnitude less than the low frequency energies it is unlikely that the low frequency energies are affected. The observed slope of -5/3 or -6/3 is also not significantly affected by the low folding frequency.

A.3 Velocity Bias Correction Techniques

The LDA instrument produced a velocity data point when a particle passes through its measuring volume. The LDA can process only one particle at a time.

Because fast moving particles pass through the measuring volume in less time than slow moving particles, leaving the measuring volume free for another measurement of a fast moving particle, more velocity readings are processed for fast moving particles than for slow moving particles. The result of an arithmetic average of the velocities is therefore biased towards the fast moving particles, McLaughlin and Tiederman (1973), McDougall (1980), Johnson, Modarress, and Owen, (1984), Steffler, Rajaratnam, and Peterson (1983), TSI Model 1980B Counter Type Signal Processor Instruction Manual (1984).

Consider a velocity signal that alternates between velocities V and $2V$ in a step change fashion, see Figure A.2. The small ticks indicate possible velocity measurements of the LDA counter and indicate twice the probability of receiving a fast velocity, $2V$, as a slow velocity, V , due to the residence time of the particle in the LDA measuring volume. The larger ticks indicate a velocity observation output by the LDA counter that has been verified and reflects a fixed measurement validation of only one in six.

The problem is to determine the true average velocity, \bar{u} , using the appropriate weighting function ω .

$$\bar{u} = \sum_{i=1}^N \omega_i u_i / \sum_{i=1}^N \omega_i \quad (\text{A.17})$$

The true average velocity of the velocity signal in this case is $\bar{u} = 1.5V$. If the data points, large ticks, are averaged as a time-average, i.e. as a sample and hold analogue output of the LDA counter, the coarse sample rate gives the incorrect velocity average of $1.67V$. If the sample rate is increased, i.e. following the smaller tick marks, then the correct solution is approached for finer and finer time intervals.

The average of individual data points, as would be done by digitally averaging the LDA output shown in Figure A.2(b), produces the incorrect average of $1.67V$. The weighting function in this case is $\omega = 1.0$. Even if the sample rate is increased, the result is always incorrect because the number of $2V$ data points is always twice the number of V data points.

In Figure A.2(c), the velocity data points are weighted with the reciprocal of the velocity magnitude at that point, (Durst, Melling and Whitelaw (1976), Johnson, Modarress, and Owen, 1984, and others, but first by McLaughlin and Tiederman, 1973). For a spherical sensing volume, this weighting factor is given by,

$$\omega_i = 1/(u_i^2 + v_i^2 + w_i^2)^{1/2}. \quad (\text{A.18})$$

where u_i , v_i and w_i are the instantaneous velocities in the three principal directions. If the sensing volume may be considered to be cylindrical, then the correct weighting

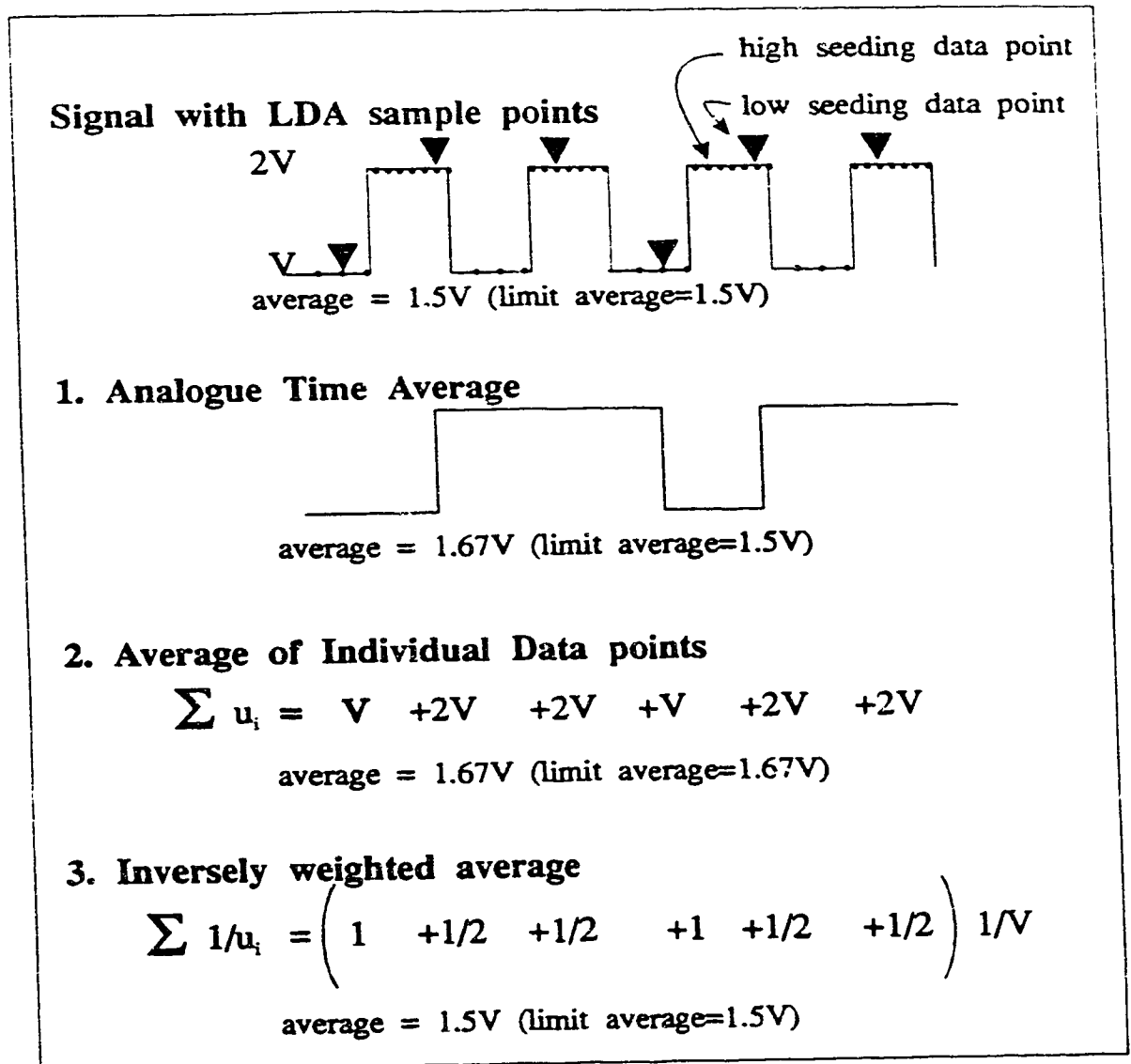


Figure A.2: Schematic illustrating the velocity bias in laser Doppler measurements.

factor is given by,

$$\omega_i = 1 / \left[(u_i^2 + w_i^2)^{1/2} + \frac{\pi d}{4 l} v_i \right], \quad (\text{A.19})$$

where d and l are the diameter and length of the cylinder, respectively. When the cylinder is long compared with its diameter, a two-dimensional weighting factor may be used and is given by,

$$\omega_i = 1 / (u_i^2 + w_i^2)^{1/2}. \quad (\text{A.20})$$

For the data taken for this work the sensing volume may be approximated by a cylinder with dimension ratio $d/l \approx 1/15$.

Further, since the turbulence level in the water channel is sufficiently low, less than .20, and the flow is primarily in the stream-wise direction,

$$\omega_i = 1 / ((U + u'_i)^2 + v'^2_i + w'^2_i)^{1/2}. \quad (\text{A.21})$$

Where U is free stream velocity, and u'_i , v'_i and w'_i are the velocity fluctuations in the three principal directions. In a boundary layer, $v' \approx 0.5u'$ and $w' \approx 0.7u'$ near the rough surface. Therefore the weighting function is approximately,

$$\omega_i = 1 / ((U + u'_i)^2 + .25u'^2_i + .5u'^2_i)^{1/2}. \quad (\text{A.22})$$

The u' component is typically less than $0.4 U$, so using $u' = 0.4U$,

$$\omega_i = 1 / (1.96 U^2 + .04 U^2 + .08 U^2)^{1/2}. \quad (\text{A.23})$$

The first term, representing the along-stream component, is the dominant term, so the bias correction may therefore be easily approximated by a one dimensional weighting factor.

$$\omega_i = 1 / u_i \quad (\text{A.24})$$

Although the flow is three-dimensional, this one dimensional weighting factor may be used to reduce the sampling bias. Johnson, Modarress, and Owen, (1984) show that the results for the one-dimensional model are virtually identical to two-dimensional model. The effect of the sampling bias for this correction is primarily to shift the probability density function toward lower velocities, with the measured variances remaining nearly unchanged.

For the *one dimensional flow* the averaging may be reduced to,

$$U = \frac{\sum_{i=1}^N u_i \left(\frac{1}{u_i} \right)}{\sum_{i=1}^N \left(\frac{1}{u_i} \right)} = N \left(\sum_{i=1}^N \left(\frac{1}{u_i} \right) \right)^{-1} \quad (\text{A.25})$$

The correct average is obtained independent of sampling rate using (A.25). This assumes that no data points are missed because of processing computation time, which would cause a different bias. When the flow is not one dimensional, weighting with the reciprocal velocity is incorrect since it would be weighting with only one component of the velocity. In the water channel the along-stream direction of the flow is nearly one dimensional. However, when measuring the velocities other than the along-stream direction, such as at $\pm 45^\circ$, this averaging process would not be correct.

Alternatively, instead of the weighting in (A.24), the signal may be weighted according to the duration of the signal burst, (residence time of the particle in the measurement volume), Adrian (1983), Buchhave and George (1978), and T.S.I Manual (1984). The residence time is provided by the LDA counter processor. There are several disadvantages to this correction, however. They include: i) the measurement of the signal duration is inaccurate and ii) the signal duration will vary with the particle size and the location of the particle and its path through the sensing volume. Therefore, additional biases may occur.

The bias correction used in this study is the the reciprocal velocity weighting, using the one dimensional approximation. Johnson, Modarress, and Owen, (1984), note that only at extreme levels of turbulence, at the approximate turbulence intensity of 20%, do sampling-bias effects become important. And even at this fluctuation level the bias error is less than 5% using the one dimensional weighting, (A.25). The sampling bias at lower levels of turbulence intensity are generally less than the overall experimental error. Near the rough surface in the water channel boundary layer, the turbulence intensities exceed the suggested 20% criterion, so the bias correction given by (A.25) provides the best estimate of the velocity statistics in that region of the flow. The velocity statistics in this region of the flow are important for determining the flow's u_* and z_o , as discussed in section 3.3.1.

A.4 Fringe Bias Correction Techniques

Fringe bias is a bias in the velocity measurements towards particles whose vectors are perpendicular to the LDA fringe orientation. These particles will generate the maximum number of scatter pulses in the photo optics of the LDA electronics, therefore being more likely to qualify for a valid signal. Since particles travelling perpendicular to the fringe orientation are *preferred*, a bias is created in the averaged velocity taken from these data points. The true composition of the along-stream velocity, however, is made up of a velocity vectors in all directions, refer to Figure A.3. The larger number of the fringe biased particles, in line with the flow when measuring

the along-stream component of velocity, would bias the velocity towards the along-stream velocity.

There are several procedures to account for the fringe bias, Durst, Melling and Whitelaw, (1976). The method used in the present study was to avoid the fringe bias by frequency shifting the laser light, known as Bragg frequency shifting. The Bragg frequency shift slightly alters the frequency of one of the laser light beams used to create the fringe pattern in the fluid media. The slightly different frequency of one of the laser beams creates a moving fringe pattern. By controlling the Bragg frequency, a predetermined fringe pattern velocity may be generated, which produces a fixed offset in the observed flow speed with a vector perpendicular to the fringe direction. The amount of required frequency shifting is not precisely specified, but a good rule of thumb to minimize fringe bias errors is to use a frequency corresponding to the mean flow speed, for moderately fluctuating flows, Durst, Melling and Whitelaw, (1976). The effect of Bragg frequency shifting, is to allow all particles to reflect more fringe patterns, (i.e. produce more scatter pulses), therefore allowing all particles the chance to generate a valid velocity observation.

A.5 Detecting and Eliminating Stray Velocity Processing Errors

The LDA counter signal processor was equipped with data filters at both high and low frequencies. These filters, combined with the internal comparison of particle volume occupancy times, eliminate most of the noise pulses received by the counter processor. However, occasionally the counter processor logic allowed an unrealistic velocity reading to appear. These readings are very difficult to detect because the number of fringes and occupancy times create a valid velocity but its value is unrealistic in comparison to the other velocity points in the data sample. Typically, the stray points have very long residence times in the measuring volume, i.e. very low equivalent velocity values. When these stray points are averaged into a weighted sum their effect on the resulting average may be significant. This is especially true with the inverse weighted velocity average which is inherently particularly sensitive to lower velocities.

The stray points may be visualized by plotting the rather peculiar combination of number of fringe crossings to measurement volume residence time, see Figure A.4. Both these values are output by the LDA counter processor. There is a recognizable linear trend in Figure A.4 and therefore the stray points may be removed.

The above averaging problem was solved by determining the mean and standard

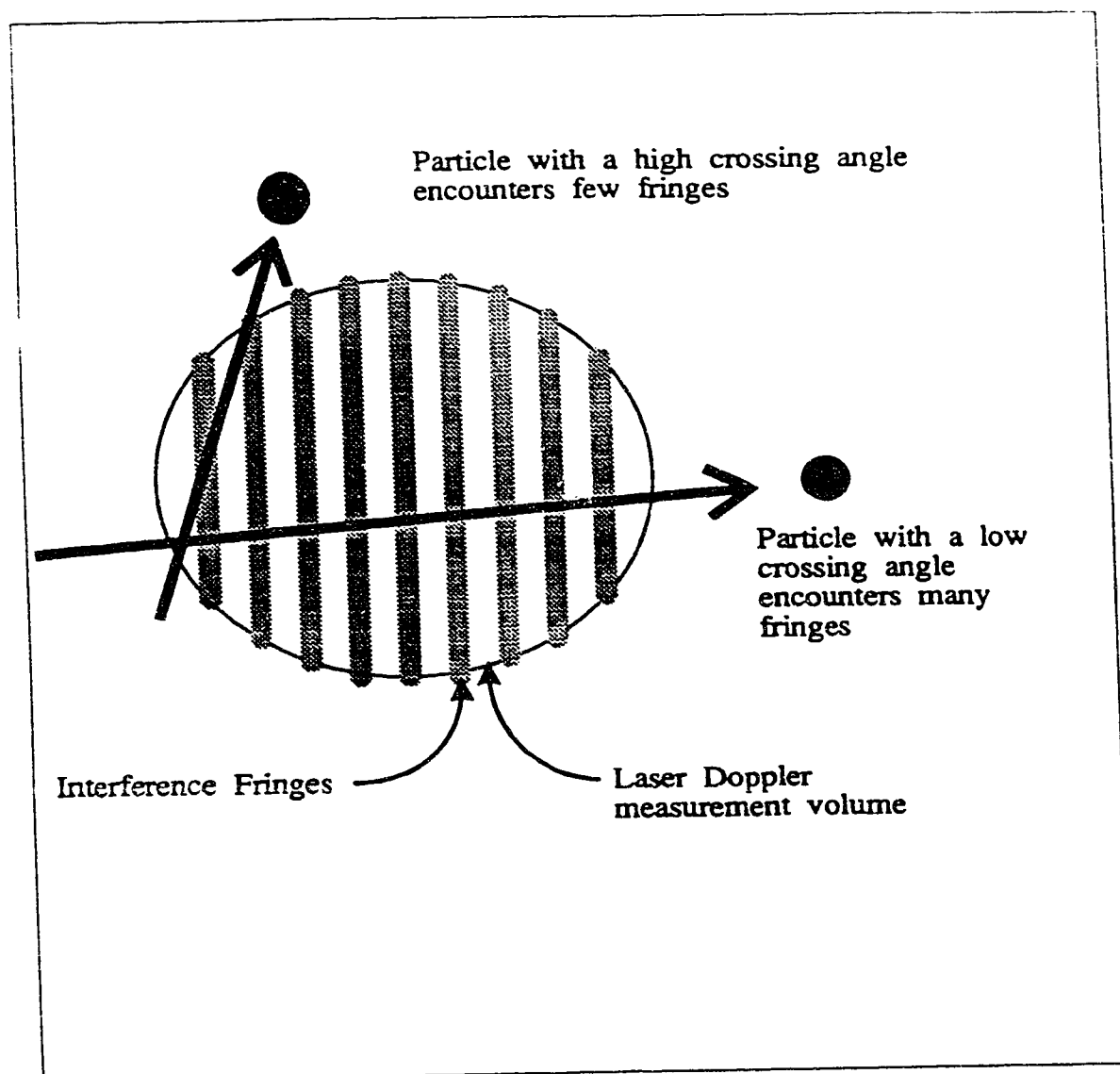


Figure A.3: Schematic showing how fringe bias error occur.

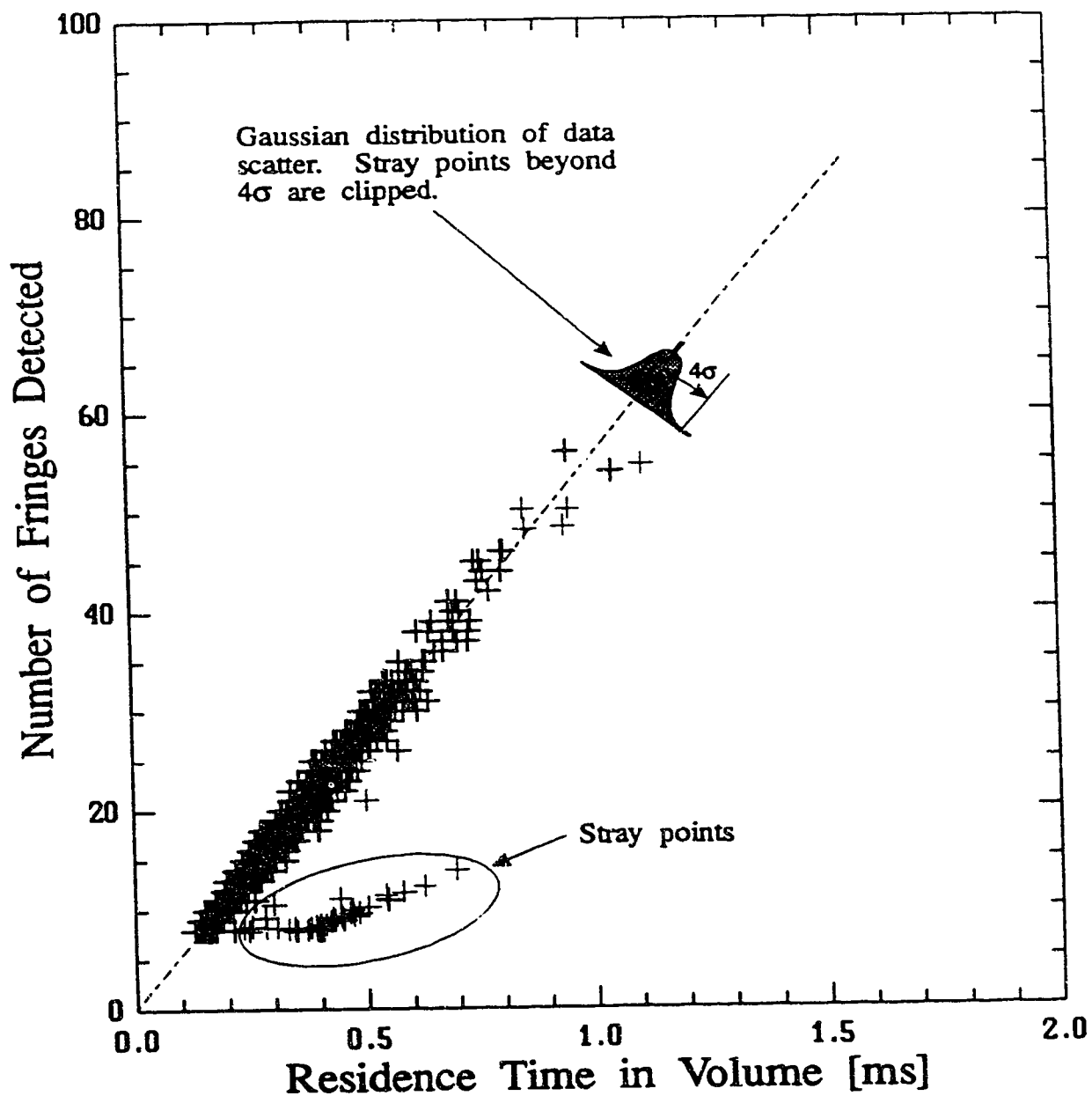


Figure A.4: Example of stray points recorded by the LDA counter processor. Data collected at $x=1000$ mm from the source at the source height.

deviation of the first 128 data points ¹ in the data set then rejecting points greater than four standard deviations from the mean. The mean and standard deviation was updated as each new point was included in the average. The four standard deviation threshold rejects less than 0.01% of the data sample. For a typical sample size of 100,000 points, less than ten points would be statistically rejected from a "perfect" data set with no abnormally stray points described above. This rejection rate is considered small. Normally, one might simply discard the data point as "bad". However, using this self-correcting, or adaptive filtering procedure, the data points may be retained with no loss in accuracy.

A.6 Velocity Shear Stress Measurements

Velocity turbulent shear stress measurements may be made by determining the covariance of $\overline{u'w'}$, where u' is the fluctuation component of velocity in the along-stream direction of flow and w' is the vertical component of velocity fluctuations. This requires simultaneous measurement of velocity in both directions, which cannot be done with the single component laser Doppler system used in the study.

Tropea (1983) provides a procedure for the measurement of shear stress terms, using a single component laser system. When the laser beams are rotated at some angle, Θ , with respect to the along-stream direction of flow, the measured velocity component is a function of U and W given by,

$$U_{\Theta} = (U + u') \cos \Theta + (W + w') \sin \Theta \quad (\text{A.26})$$

When measurements are taken at angles of $\Theta_0 = 0^\circ$, Θ_1 , and $\Theta_2 = -\Theta_1$, it is easy to show that (A.26) may be used to produce the following cross-component velocity terms,

$$U = U_{\Theta=0^\circ} \quad (\text{A.27})$$

$$\overline{u'^2} = \overline{u'^2}_{\Theta=0^\circ} \quad (\text{A.28})$$

$$W = \frac{U_{+\Theta} - U_{-\Theta}}{2 \sin^2 \Theta} \quad (\text{A.29})$$

$$\overline{w'^2} = \frac{u'^2_{+\Theta} + u'^2_{-\Theta} - 2u'^2_{\Theta=0^\circ} \cos^2 \Theta}{2 \sin^2 \Theta} \quad (\text{A.30})$$

¹The data was collected using a data acquisition system designed by the author on an LSI/11-23 computer. The data from the TSI Inc. counter processor digital output is written to the computer's hard disk. The LSI/11-23 computer is a low level computing device and has a simple format for storing information on the hard disk in 512 byte blocks. This is equivalent to 256 integers or 128 velocity readings from the LDA counter. 128 therefore forms a convenient block of data.

$$\overline{u'w'} = \frac{u'^2_{+\Theta} - u'^2_{-\Theta}}{4 \cos \Theta \sin \Theta} \quad (\text{A.31})$$

Tropea shows that by making an error estimate of the terms in (A.30) and (A.31), as done by Kline and McClintock (1953), the optimal angle selection for Θ_1 and Θ_2 is $+63^\circ$ and -63° . The optimal angle for (A.30) is of course 90° and the optimal angle for (A.31) is $\pm 45^\circ$. In the present study, the particle seeding density was quite low, so the angles $\pm 45^\circ$ were selected to produce increased sample rates while forfeiting the less than 1% change in estimated error. There are also errors present in the beam alignments. These are not accounted for in the error estimate by Tropea, and were not accounted for in the present study.

To make use of this procedure, velocity measurements were taken at the three angle rotations for each desired location in the flow. The averaged moments $\overline{U_\Theta}$ and $\overline{u'^2_\Theta}$ were used to determine the shear stress $\overline{u'w'}$. Note that this procedure requires three measurements at the same location in flow, therefore the flow must be very steady, as also suggested by Tropea. The water channel flow was very steady and 500 second time-averages (2000 Eulerian time scales) were used to ensure reliable averages.

Velocity bias corrections for the $\pm 45^\circ$ rotated measurements were made using the inverse velocity correction. Although the treatment of the rotated data should reflect its two-dimensional nature, consistency in the analysis was considered to be more important, and it was analyzed the same as the horizontal along-wind component. Differences in the computed results using different bias correction schemes reflected that this procedure did not introduce significant errors.

A.7 Turbulence Time Scale of Vertical Velocity Component

Measurement of the velocity time scales in the vertical direction, using the single component laser doppler system, is difficult because an insufficient sample rate when the beams are rotated vertically. Additionally, when the beams are rotated vertically, the measurement volume cannot be positioned close to the bottom wall of the water channel due to interference of the laser beams with the bottom wall. Therefore, the measurements made at the $\Theta = \pm 45^\circ$ must be used to estimate the vertical time scales.

One way of doing this is to estimate the variance and the smoothed variance in the vertical direction using the three directions $\Theta = 0^\circ$ and $\pm 45^\circ$, and the methods described in section A.6, equation (A.30). Then the vertical time scale may be

calculated using the method described in section 3.2.1. This procedure does not work well, because the smoothed variance in the vertical direction cannot be estimated with enough accuracy.

An alternative procedure to determine the time scale in the vertical direction is by an empirical method. The time scale in the vertical direction was estimated from the calculated time scales in the three directions measured, T_{Θ} , $T_{-\Theta}$ and $T_{+\Theta}$, each of which were determined using the method described in section 3.2.1. The vertical time scale was estimated by assuming that the time scale would vary smoothly and monotonically from $\Theta = 0$ to $\Theta = 90^\circ$. In addition, it was assumed that at $\Theta = 0$ and at $\Theta = 90^\circ$, the time scale would vary so as not to form a cusp, i.e. the time scale would be symmetric for small changes of $\pm\Theta$ about $\Theta = 0$ or 90° . These assumptions suggest an ellipse as a simple model for the variation of the time scales with Θ . Figure A.5 schematically illustrates these assumptions. The vertical scale using the ellipse method is given by the empirical assumption,

$$\frac{T_u^2}{a^2} + \frac{T_w^2}{b^2} = 1 \quad (\text{A.32})$$

where,

$$a = T_{\Theta=0}$$

$$b = \sqrt{\frac{\sin^2 T_{\Theta}^2}{1 - \frac{\cos^2 T_{\Theta}^2}{T_{\Theta=0}^2}}}$$

and T_{Θ} may be estimated by averaging the two data samples at $\pm 45^\circ$.

$$T_{\Theta} = \frac{1}{2} (T_{\Theta=+45^\circ} + T_{\Theta=-45^\circ})$$

In the absence of a two component or a three component laser doppler system, this procedure provides an estimate of the vertical component integral time scales.

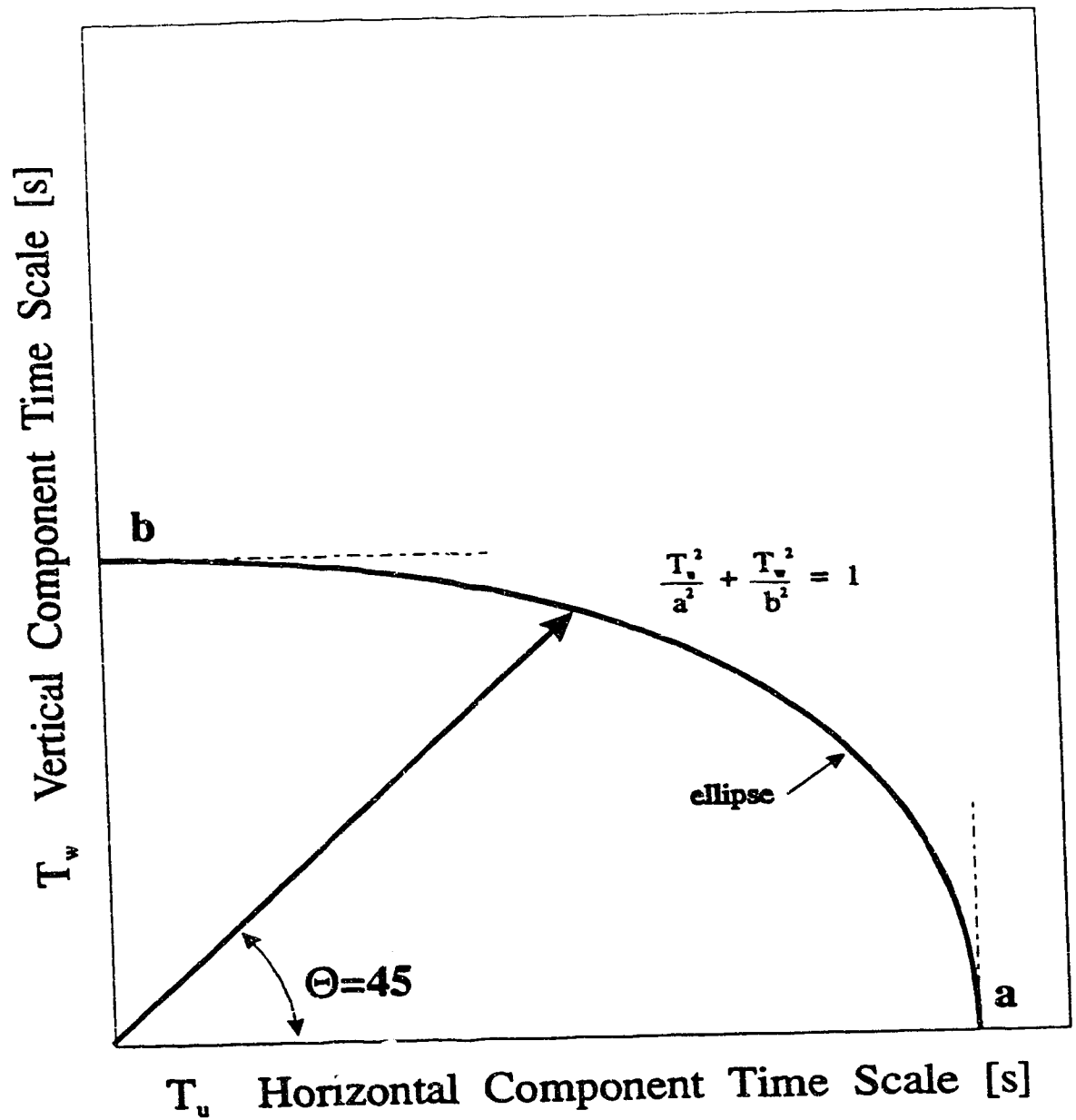


Figure A.5: Estimation of the variation of the time scales of velocity fluctuations when rotating the laser optics through 90 degrees using an ellipse.

Appendix B

Concentration Analysis Procedures

In this section the analysis procedures which are characteristic of the conductivity measurement system are discussed. The treatment of the concentration data is somewhat simpler than the LDA data because of its uniform temporal spacing.

One characteristic of the concentration data is its abundance. The data was collected using an array of eight detectors at a sample rate of 250 Hz for 500 s resulting in a 125,000 samples collected for each of the eight probes. Computational efficiency in the data analysis is essential for these large data sets.

The design development and the computational procedures for the calibration of the conductivity probe to measure the concentration of the plume in the water channel are discussed in Chapter 4.

B.1 Digital Filtering

In Chapter 4 the conductivity probe output signal is calibrated and de-convoluted for the effects of probe response time. The deconvolution procedure amplifies noise in the probe signal which appear primarily at the higher frequencies. The noise can have a detrimental effect on the measurement of intermittency, threshold crossing times, the probability distributions of concentration and on the measurement of the derivative of the concentration signal. It is, therefore, of interest to remove the noise. One way of doing this is to digitally filter the calibrated, de-convoluted concentration signal. This section briefly describes the theory behind designing a digital filter for the above use.

There are two principal digital filter models based on the series length used to represent an input impulse to a response system. The first is the pulse-transfer

function which is more commonly known as the infinite impulse response (IIR) model. An IIR filter is one in which the impulse response, $h(n)$, has an infinite number of samples. IIR filters are generally recursive realizations, which means that the present value of the output depends both on the input values, and previous values of the output. The second filter model is a finite impulse response (FIR) model. A FIR filter is one in which the impulse response $h(n)$ is limited to a finite number of samples. FIR filters are generally non-recursive (or direct convolution) realizations, which means that the present value of the output depends only on the present and past values of the input. A higher order FIR filter is normally required to obtain the same sharpness of amplitude response control as an IIR filter. An FIR filter, therefore, requires more computation time. Also, an IIR filter provides a better approximation of the desired response than does the FIR filter model. For these reasons, an IIR filter was used in filtering the concentration data sets.

The IIR filter design and implementation is easily programmed, and has been included in the signal analysis package by the author. An example of an FIR filter is discussed in section B.2 in reference to the creation of a derivative transfer function.

The procedure for determining the filter coefficients was taken largely from Stanely, Dougherty, and Dougherty (1984), Peled and Liu (1976) and Priestley (1981). The general procedure is to determine a discrete transfer function $H(z)$, (where z is complex), such that the output response, $Y(z)$, derived from the input response, $X(z)$, has the desired frequency response.

$$\frac{Y(z)}{X(z)} = H(z) = \frac{a_0 + a_1 z^{-1} + a_2 z^{-2} + \dots + a_k z^{-k}}{1 + b_1 z^{-1} + b_2 z^{-2} + \dots + b_k z^{-k}} \quad (\text{B.1})$$

There are several different ways of determining the coefficients in (B.1), which also depend on the response characteristics of the desired filter. Two common families of filters are the Butterworth and the Chebychev filters. They differ in the number of, and height of the ripple in passband and stopband, and the length of the transition band.

For example, a Butterworth filter of second order has the desired frequency response for an analysis problem and may be realized for computational use as follows. The sampling frequency, $f_s = 250\text{Hz}$, sets the folding frequency or Nyquist frequency, f_o , which is the frequency at which the spectral energy folds back onto itself, ($f_o = f_s/2$). The shoulder frequency, $f_r = 50\text{Hz}$, often defined by the point where the frequency response is attenuated by 3 dB, is decided in conjunction with the attenuation frequency, f_a , which is the frequency terminating the fall of the frequency response from the shoulder to the start of the stop band frequencies. For a Butterworth filter of a given order, the f_a may be determined and used to select a

proper f_r to remove the frequency range of interest. The amplitude response of the Butterworth filter is given by,

$$A^2(f) = \frac{1}{1 + (f/f_o)^{2k}} = \frac{1}{1 + (\omega/\omega_o)^{2k}} \quad (\text{B.2})$$

where k is the filter order, ($k = 2$ for a second order filter), and ω is the radian frequency equivalent to f . Assume a normalized frequency for simplicity, such that $\omega_o = 1$. Set $\omega^2 = -s^2$ to determine the steady state continuous transfer function $G(s)$,

$$G(s)G(-s) = \frac{1}{1 - s^4} \quad (\text{B.3})$$

Therefore, $G(s)$ may be determined to be,

$$G(s) = \frac{1}{1 + \sqrt{2}s + s^2} \quad (\text{B.4})$$

This rational polynomial may be transformed first to the desired frequency by variable substitution, p ,

$$p = \frac{s}{2\pi f_o} \quad (\text{B.5})$$

and then by substitution again to get the desired filter response,

low pass	$p = s$
band pass	$p = \frac{s^2 + \omega_{\text{centre}}^2}{s}$
band rejection	$p = \frac{\omega_{\text{centre}}^2 s}{s^2 + \omega_{\text{centre}}^2}$
high pass	$p = \frac{\lambda_r \omega_r}{s}$

Where λ_r is a particular low pass prototype reference radian frequency which can be used to normalize the equations rather than substituting for ω_r . Usually λ_r is taken to be the folding frequency, so that $\lambda_r = 1.0$. For a low pass filter, the following is obtained,

$$G(p) = \frac{1}{1 + 1.4142 \frac{p}{\lambda_r} + \frac{p^2}{\lambda_r^2}} \quad (\text{B.6})$$

The resulting polynomial is transformed into the z domain, using,

$$p = \lambda_r C \left[\frac{1 - z^{-1}}{1 + z^{-1}} \right] \quad (\text{B.7})$$

where $C = \cot(\frac{\pi f_c}{2f_o})$, which also transforms back to the desired shoulder frequency. This results in the following discrete transfer function,

$$H(z) = \frac{0.2066(1 + 2z^{-1} + z^{-2})}{1 - 0.3695z^{-1} + 0.6887z^{-2}} \quad (\text{B.8})$$

This equation may be realized by taking the inverse Z-transform, yielding the following difference equation,

$$y(t) - 0.3695y(t-1) + 0.6887y(t-2) = 0.2066x(t) + 0.4132x(t-1) + 0.2066x(t-2) \quad (\text{B.9})$$

or the current output of the process, $y(t)$, may be determined using: the current input point, $x(t)$, a sequence of input data points, $x(t-n)$, and the previous output points, $y(t-n)$:

$$y(t) = 0.2066x(t) + 0.4132x(t-1) + 0.2066x(t-2) + 0.3695y(t-1) - 0.6887y(t-2) \quad (\text{B.10})$$

Combining filters of different orders or cutoff frequencies may be done in *cascade* form using,

$$G(p) = G_1(p)G_2(p)G_3(p) \dots G_m(p) \quad (\text{B.11})$$

or in *parallel* form using

$$G(p) = G_1(p) + G_2(p) + G_3(p) + \dots + G_n(p) \quad (\text{B.12})$$

B.2 Derivative measurement

The calculation of the derivative of a sampled data set is complicated by several factors. First, the frequency range of the data set determines what sampling frequency is to be used to collect the data set. However, the spectra of the concentration data is continuous and therefore a *desired* frequency range must be selected which encompasses all the important frequencies. Secondly, the derivative is sensitive to high frequencies, and are dominated by the small-scale structure of the scalar field (Gao and O'Brien 1991), even when they contain significantly less energy than dominant low frequencies. Thirdly, the time scale of the process fluctuations in comparison to the sampling frequency must be low. This is due to Gibb's phenomenon which will be discussed later. Finally, noise in the sampled data set, whether it originated from the detector or electronically, causes the results of the derivative to become erratic.

All the above considerations must be considered when selecting a filter function to be applied to a data set to determine the derivative. The following sections describe two different procedures for deriving derivative transfer functions, and their applications to the data set.

B.2.1 Newton-Gregory Approximating Function

The Newton-Gregory forward interpolation approximating function was used to derive a differentiating formula to determine the first derivative from the regularly space concentration data set, Gerald (1978). The interpolating formula is given by,

$$\phi_n(x_s) = y_0 + \binom{s}{1} \Delta y_0 + \binom{s}{2} \Delta^2 y_0 + \binom{s}{3} \Delta^3 y_0 + \dots + \binom{s}{n} \Delta^n y_0 \quad (\text{B.13})$$

where, $\phi_n(x_s)$ is the interpolated value (of order n) for equispaced points of spacing h and interpolation order n , and

$$s = \frac{x - x_0}{h}$$

$$\binom{s}{n} = \frac{s(s-1)(s-2)\dots(s-n+1)}{n!}$$

The variables y_0 are the data points (constants) and $\Delta^n y_0$ may be determined from a difference table. The first derivative formula is determined by differentiating, (B.13),

$$\phi'_n(x_s) = \frac{\partial y_0}{\partial x} + \frac{\partial \left\{ \binom{s}{1} \Delta y_0 \right\}}{\partial x} + \frac{\partial \left\{ \binom{s}{2} \Delta^2 y_0 \right\}}{\partial x} + \dots \quad (\text{B.14})$$

Simplifying,

$$\begin{aligned} \phi'_n(x_s) &= \Delta y_0 \frac{\partial \{s\}}{\partial x} + \frac{\Delta^2 y_0}{2!} \frac{\partial \{s(s-1)\}}{\partial x} + \frac{\Delta^3 y_0}{3!} \frac{\partial \{s(s-1)(s-2)\}}{\partial x} + \dots \\ &= \frac{\Delta y_0}{h} + \frac{\Delta^2 y_0}{2!h} (2s-1) + \frac{\Delta^3 y_0}{3!h} (3s^2 - 4s + 2) + \dots \end{aligned} \quad (\text{B.15})$$

The simplest, and fastest approximation in terms of computation speed, is a first order approximation. Only the first term of (B.15) is used. This requires data points x_0 and x_1 for a forward difference approximation or x_0 and x_{-1} for a backward difference approximation. In this case, the first order approximation of the first derivative, forward difference formulation, is given by,

$$\phi'_1(x_0) = \frac{1}{h} (y_1 - y_0) \quad (\text{B.16})$$

or the backward difference formulation,

$$\phi'_1(x_0) = \frac{1}{h} (y_0 - y_{-1}) \quad (\text{B.17})$$

The first order, first derivative is plotted in Figure B.1, for the backward difference formulation. It is seen in the figure that there is a strong positive skew given to the data. This skew is unacceptable in the analysis of the joint probability of concentration and its first derivative. The skew in the first order, first derivative adversely biases the results, and this approach was abandoned.

It is therefore required that a central difference approximation be used. This limits us to the second or fourth order difference equations. For the second order interpolating polynomial, if we let $s = 1$ for a central fit, and it is easy to show that,

$$\phi'_{2(-1)} = \frac{1}{h} \left(\frac{y_2 - y_0}{2} \right) + \text{error} \quad (\text{B.18})$$

The error term is approximately given by the first term dropped from the interpolating equation, (B.15), and is approximately given by,

$$\text{error} \sim \frac{h^2}{6} y_s''' \quad (\text{B.19})$$

and is therefore of $\mathcal{O}(h^2)$. The error for a small enough time step therefore is small, unless the data set's third derivative $y_s''' \rightarrow \infty$. The second order, first derivative is plotted in Figure B.2 and shows no skew of the data as was observed in the first order, first derivative. It can be concluded that a central difference equation, or in other words, approximating functions of even order, should be used on a data set. In the next section the frequency response of the derivative is considered.

B.2.2 FIR Filter Approximating Function

Finite impulse response (FIR) filters are characterized by the impulse function, $h(n)$, being limited to a finite number of samples defined over a range, $n_1 \leq n \leq n_2$, where both n_1 and n_2 are finite. FIR filters are generally non-recursive, and therefore requiring only previous input values to determine the current output value.

An FIR filter impulse response may be expressed as,

$$\begin{aligned} h(n) &= a_n \quad 0 \leq n \leq k \\ &= 0 \quad \text{elsewhere} \end{aligned} \quad (\text{B.20})$$

or equivalently

$$h(n) = \sum_{i=0}^M a_i \delta(n - i) \quad (\text{B.21})$$

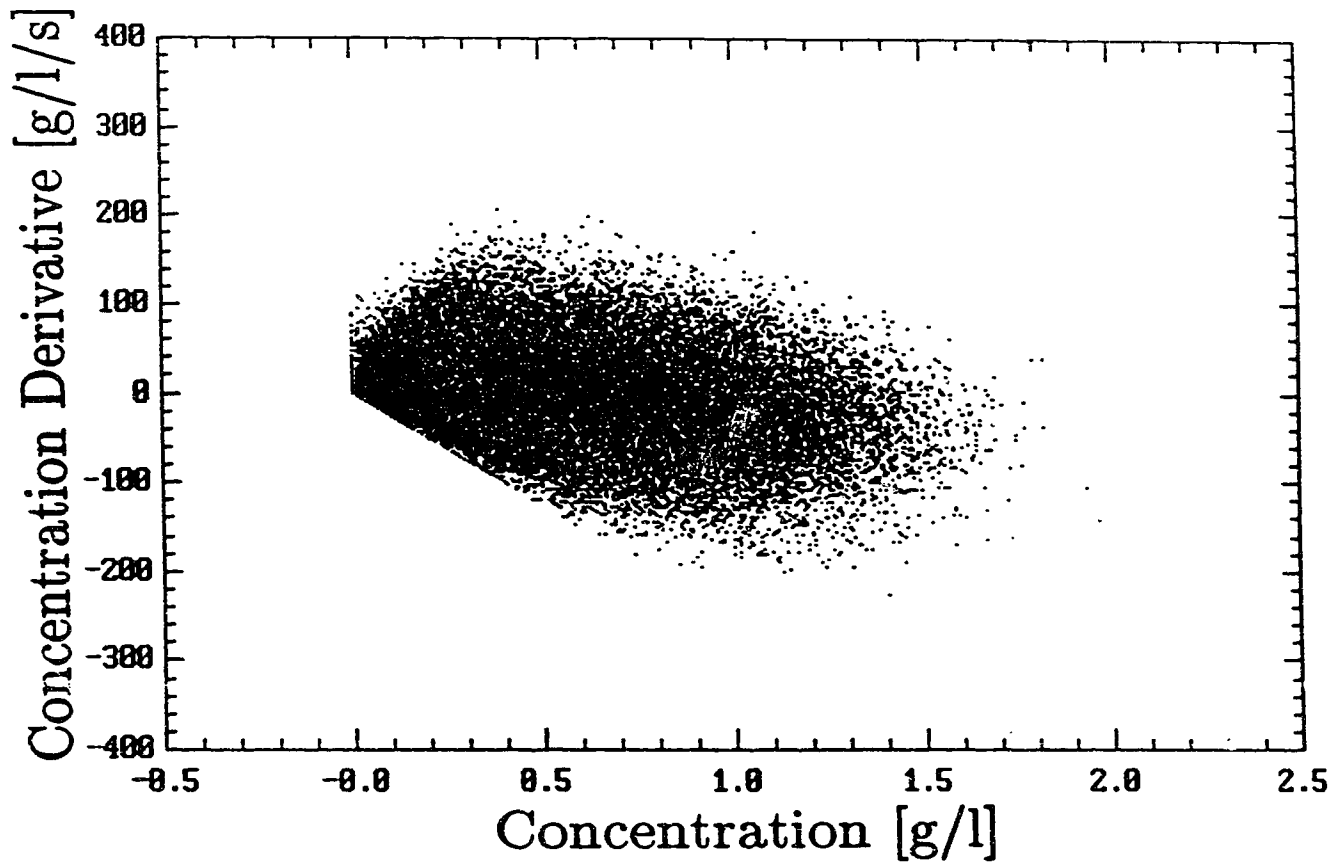


Figure B.1: Positive skew error caused by the first order, backward difference approximation of the first derivative for the concentration data set. Data is jet/plume source at $x/h_s = 4.4$, $y/\sigma_y = 0$ at the source height.

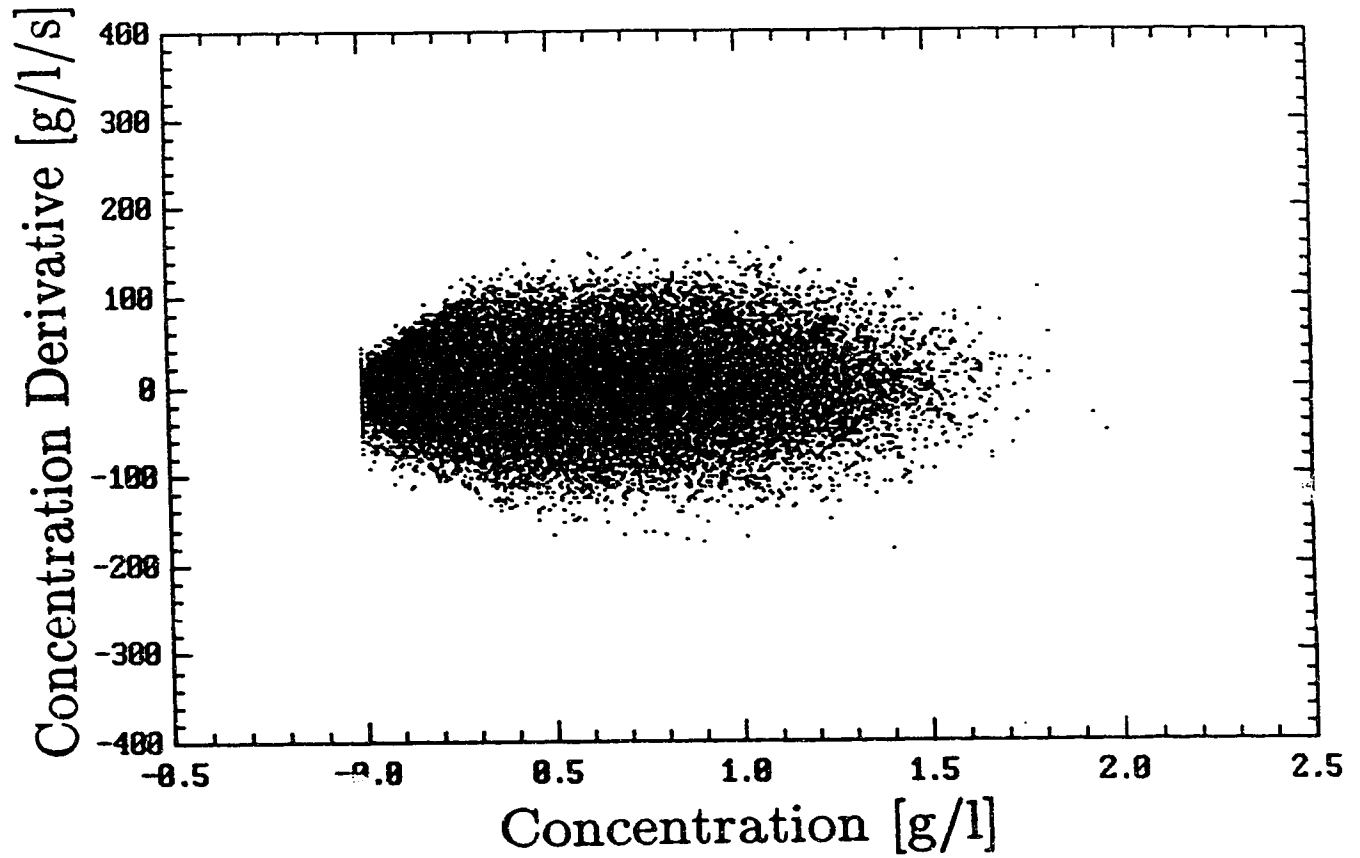


Figure B.2: Negligible skew error for second order, central difference approximation of the first derivative for the concentration data set. Data is jet/plume source at $x/h_s = 4.4$, $y/\sigma_y = 0$ at the source height.

The discrete transfer function for the above two equations is given by,

$$H(z) = \sum_{m=0}^M a_m z^{-m} = a_0 + a_1 z^{-1} + a_2 z^{-2} + \dots + a_M z^{-M} \quad (\text{B.22})$$

Where M represents the order of the filter. Since there are no coefficients missing in (B.22), there are $M + 1$ coefficients in the realized difference equation, $h(1) = a_1, h(2) = a_2, \dots$. The difference equation relating the input to output is expressed as,

$$y(n) = \sum_{i=0}^M a_i x(n-i) = \sum_{i=0}^M h(i) x(n-i) \quad (\text{B.23})$$

This is a non-recursive equation and hence the output $y(t)$ is a direct convolution of the input $x(t)$.

Two formulations for the FIR filters may be used, an odd (or sine) representation, or an even (or cosine) representation. The form that is selected depends on the desired result. The coefficients for a sine series (odd) representation, d_m , are given by the Fourier analysis,

$$d_m = \frac{2}{f_s} \int_0^{f_s/2} A_d(f) \sin(2\pi m T f) df \quad (\text{B.24})$$

where:

f_s is the sampling frequency
 T is the time period between samples, $T = 1/f_s$.
 m is the coefficient index

$A_d(f)$ is the desired amplitude response of the filter.

These functions are usually reflected so that $d_{-m} = -d_m$, and for a sine series $d_0 = 0$. The reflection therefore doubles the filter order to $2M$. The resulting reflected transfer function is,

$$H_{\text{sine}}(z) = \sum_{i=0}^{2M} a_i z^{-i} \quad (\text{B.25})$$

where $a_i = d_{M-i}$.

Because the FIR filters characteristically cut off the spectrum at a frequency, Gibb's phenomenon occurs. Gibb's phenomenon states that abrupt termination of the frequency spectrum may result in poor convergence of the resulting series, particularly in the vicinity of a discontinuity. Poor convergence usually shows itself in the form of "ringing" before and after the discontinuity. Terminating the series after a finite

number of terms may be thought of as multiplying the infinite length impulse response by a finite width window function. For example, a simple series termination is a rectangular window. By changing the shape of the window the convergence problems may be somewhat resolved. The abrupt termination of the rectangular window is the source of most of the problem which results in the ringing. Because the windowing functions are a direct convolution, window coefficients may be applied directly to the FIR coefficients,

$$d'_m = w_m d_m \quad (\text{B.26})$$

where w_m are the coefficients of the window function, and d'_m are the windowed sine coefficients.

Defining, $\tau = 1/(f_s/2)$, some popular windowing functions are given by, .

Rectangular Window

$$\begin{aligned} w(t) &= 1 \quad \text{for } |t| \leq \tau/2 \\ &= 0 \quad \text{elsewhere} \end{aligned} \quad (\text{B.27})$$

Triangular Window

$$\begin{aligned} w(t) &= 1 - \frac{2|t|}{\tau} \quad \text{for } |t| \leq \tau/2 \\ &= 0 \quad \text{elsewhere} \end{aligned} \quad (\text{B.28})$$

Hanning Window

$$\begin{aligned} w(t) &= 0.5 \left(1 + \cos \left(\frac{2\pi t}{\tau} \right) \right) \quad \text{for } |t| \leq \tau/2 \\ &= 0 \quad \text{elsewhere} \end{aligned} \quad (\text{B.29})$$

As an example, consider the derivation of an ideal differentiator. The desired response in one period is,

$$A_d(f) = \omega = 2\pi f \quad \text{for } -\frac{f_s}{2} < f < \frac{f_s}{2} \quad (\text{B.30})$$

where for the concentration data $f_s = 250\text{Hz}$. The coefficients are determined using a sine series because $A_d(f)$ is odd. Using (B.24),

$$d_m = \frac{2}{f_s} \int_0^f A_d(f) \sin(2\pi m T f) df$$

Table B.1: Coefficients for a Fourth Order FIR filter Differentiator

Coefficients	Sine Series	Window	Final
a_0, a_4	-0.5	0.0	0.0
a_1, a_3	1.0	0.5	0.5
a_2	0.0	0.0	0.0

$$\begin{aligned}
&= \frac{2}{f_s} \int_0^f 2\pi f \sin(2\pi m T f) df \\
&= \frac{T}{\pi} \left[\frac{2\pi f \cos 2\pi m T f}{mT} - \frac{\sin 2\pi m T f}{(mT)^2} \right] \quad (B.31)
\end{aligned}$$

$$= -\frac{\cos m\pi}{mT} \quad \text{for } f = f_s/2 \quad (B.32)$$

Expression (B.31) may be used to take the derivatives of noisy signals by setting $f < f_s/2$. This would create a wideband differentiator in cascade with a low pass filter. For the discussion to follow, the signal is assumed to be noise free.

Using the Hanning window, where $t = nT$ and $\tau = 2MT$, then (B.29) becomes

$$w(m) = 0.5(1 + \cos \frac{m\pi}{M}) \quad (B.33)$$

For a fourth order, filter the coefficients are shown in Table B.1. These same coefficients are a special case since they would also be produced by the triangle window. Also, since the first and last coefficients are zero the resulting order of the approximation is only 2. Note that these coefficients are the same as the Newton-Gregory approximating coefficients for a second order derivative. This is not true for higher order approximations.

The final response function for the FIR differentiator is,

$$H(z) = 0 z^0 - .5 z^{-1} + 0 z^{-2} + .5 z^{-3} - 0 z^{-4} \quad (B.34)$$

which results in a difference equation of

$$y_m = 0 x_m - .5x_{m-1} + 0x_{m-2} + .5x_{m-3} + 0x_{m-4} \quad (B.35)$$

One of the benefits of the FIR derivative formulation, is the ease of finding the amplitude response of the filter. Since the energy spectrum, $E(w)$, is just the amplitude squared,

$$E(f) = A^2(f) \quad (B.36)$$

Where $A(f)$ is determined from the inverse Z-transform of (B.25),

$$A(f) = \sum_{-M}^{+M} d_m \sin(2\pi m f / f_s) \quad (\text{B.37})$$

The area under the energy spectrum for the ideal differentiator is related to the variance by,

$$\sigma_{\dot{x}}^2 = 4\pi^2 \int_0^{\infty} E_{\dot{x}}(f) df \quad (\text{B.38})$$

which, truncated for the sampled data to $f_o = f_s/2$, where f_s is the sample rate,

$$\sigma_{\dot{x}}^2 = 4\pi^2 \int_0^{f_o} E_{\dot{x}}(f) df \quad (\text{B.39})$$

For the ideal derivative of a flat spectrum, the variance is,

$$\sigma_{\dot{x},d}^2 = \frac{1}{3}(f_o)(2\pi f_o)^2 = \frac{1}{6}\pi^2 f_s^3 \quad (\text{B.40})$$

Using the spectrum of the concentration data set, the analysis may be repeated to determine the error in the experimental derivative variance. The desired or true variance is given by,

$$\sigma_{\dot{c},true}^2 = 4\pi^2 \int_0^{f_o} f^2 E_c(f) df \quad (\text{B.41})$$

and the observed derivative based on the approximation is given by,

$$\sigma_{\dot{c},obs}^2 = 4\pi^2 \int_0^{f_o} A^2(f) E_c(f) df \quad (\text{B.42})$$

where:

- $A^2(f)$ is the amplitude response squared and may be determined based on the selected window used in the FIR differentiator.
- $E_c(f)$ is the energy spectrum that represents the concentration data.
- f_o is $f_s/2$, f_s is the sample rate.

Therefore, the ratio of the two gives the correction factor that can be used to multiply the observed $\sigma_{\dot{c},obs}^2$ to determine the correct $\sigma_{\dot{c}}^2$.

$$\frac{\sigma_{\dot{c},true}^2}{\sigma_{\dot{c},obs}^2} = \frac{4\pi^2 \int_0^{f_o} f^2 E_c(f) df}{4\pi^2 \int_0^{f_o} A^2(f) E_c(f) df} \quad (\text{B.43})$$

Table B.2: Ratio of the Derivative Approximation for the Hanning and Triangle Window for White Noise spectrum, $\sigma_{\dot{c},true}^2/\sigma_{\dot{c},obs}^2$.

Order	Hanning	Triangle
4	6.423	6.423
6	2.778	3.400
8	2.024	2.541
10	1.710	2.140
20	1.269	1.516
40	1.114	1.272
100	1.014	1.081

The area under the energy spectra may be determined by numerical integration. Table B.2 compares the triangle window and Hanning window approximations to the ideal derivative for an energy spectrum $E(f) = 1.0$ over the data range, $0 < f < f_o$. Particular attention should be given to the fourth order triangle window approximation which gives a variance which is 640% too low! The variance truncation error does not become acceptable until a 20th order approximation is used.

Using the general energy spectrum below, which describes the concentration data well, Table B.3 was created to show the accuracy of the approximations for different windowing schemes. This spectrum takes into account the filtering of a receptor with a response length scale of Λ_p .

$$E_c(k_1, t) = A^2(k_1) E_c(k_1, t) \quad (\text{B.44})$$

$$E_c(k_1, t) = \frac{2}{\pi} \frac{\bar{u}^2 \sigma_c^2 \Lambda_c}{(1 + \alpha^2 \Lambda_c^2 k_1^2)^{1/2}} \frac{1}{(1 + \Lambda_p^2 k_1^2)} \quad (\text{B.45})$$

$$\alpha = \frac{2}{\pi} \ln \left(\sqrt{1 + \beta^2} + \beta \right) \quad (\text{B.46})$$

$$\beta = \frac{2f_s \Lambda_c}{\bar{u}} \ln \left(\sqrt{1 + \beta^2} + \beta \right)$$

Refer to section 6.6 for more details on this spectral function. An approximate value of $\Lambda_c = 1.0\text{cm}$ was used in the tabulation. The results vary in the second and third decimal place for changes in Λ_c by factors of 2. The results do not depend on the variance, σ_c , since it is only a scaling parameter. The receptor length scale was selected to equal the enhanced concentration probe length scale of 0.033 cm. The spectrum for the concentration does not contain as much energy at the higher

Table B.3: Ratio of the Derivative Approximation for the Hanning and Triangle Window for a k^{-1} spectrum, $\sigma_{\dot{c},true}^2/\sigma_{\dot{c},obs}^2$, for 125 Hz cutoff and $\Lambda_c=1$ cm.

Order	Hanning	Triangle
4	3.146	3.146
6	1.695	2.312
8	1.423	1.846
10	1.299	1.560
20	1.118	1.309
40	1.050	1.162
100	1.006	1.054

frequencies which contain a significant amount of the derivative variance. Therefore, the lower order approximations for the real spectrum provide a more accurate *looking* prediction.

The significantly increased accuracy in the estimated derivative variance as shown in Table B.3 is deceiving when the time series of the derivative is examined. Figure B.3 shows an example of the concentration signal time series and its derivative using a fourth order Hanning window. The derivative appears to follow the data well. It is positive when the signal rises in concentration and negative when the signal decreases in concentration. And note that when the concentration is zero, the derivative has a zero value, as expected. In Figure B.4, a 20th order Hanning window derivative approximation is used, and it can be seen that Gibb's phenomenon is active at all the apparent discontinuities. Gibb's phenomenon appears as ringing before and after the sharp peaks, and rise and falls from zero concentrations. Note also that during the concentration zero periods, there is a measured derivative due to the ringing, which is incorrect. However, the magnitude of the derivative is more accurate and may be several times that measured by the 4th order derivative shown in Figure B.3. Note that, the redistribution of the energy, from the high frequencies not present in the derivative approximation to the cutoff frequency, predicts the correct variance because the process is linear. The ringing, although ugly and unwanted, represents real, but misplaced, variance in the time series signal.

In Figure B.5, the Hanning window is used to show the amplitude response of the FIR differentiator for various filter function orders using (B.45). The area under the curves represents the derivative variance. It is easy to see in Figure B.5, the error in the variance for filter functions with low order.

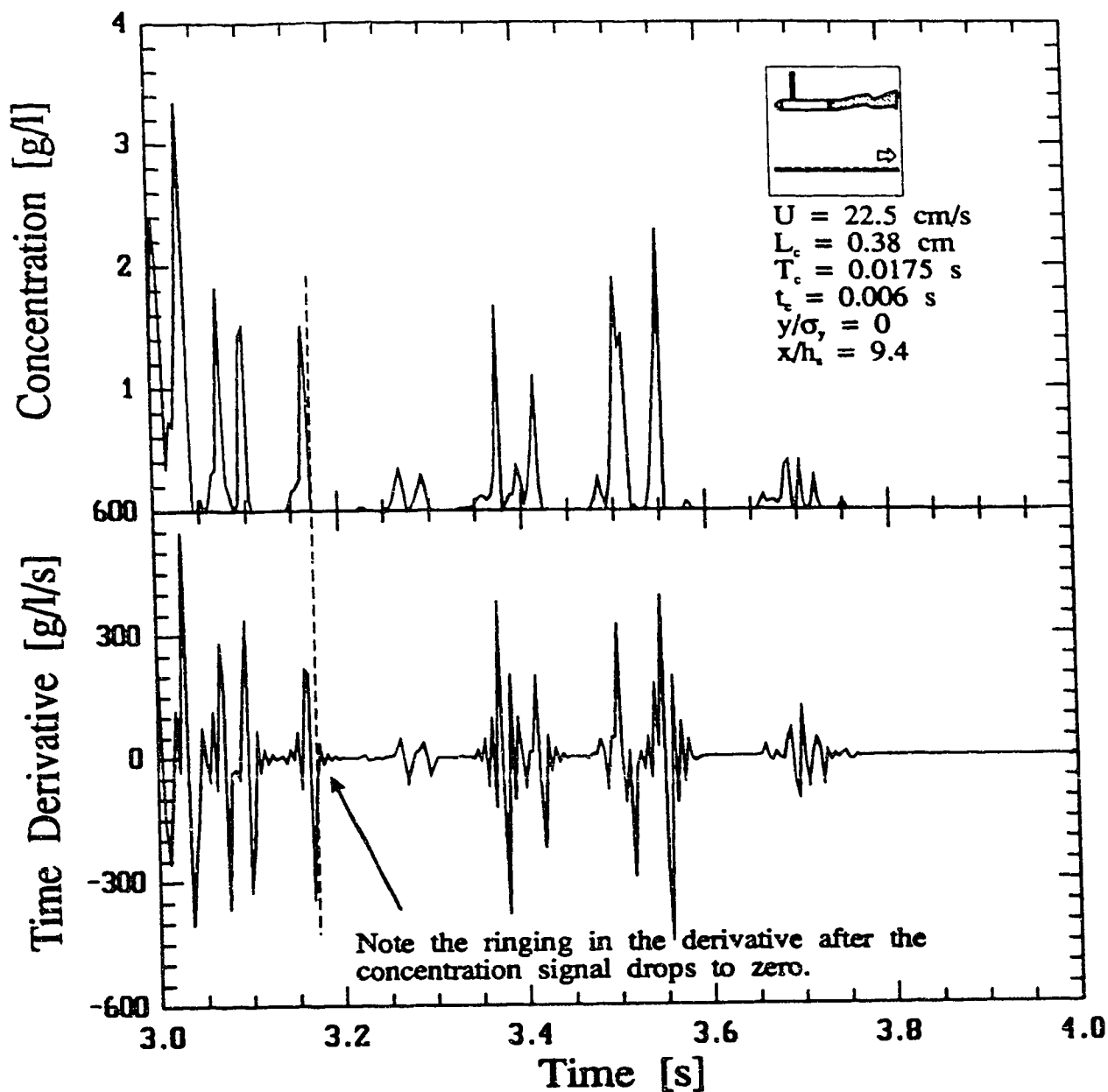


Figure B.3: 4th order Hanning window derivative approximation time series, showing the accurate derivative behaviour, but inaccurate magnitudes.

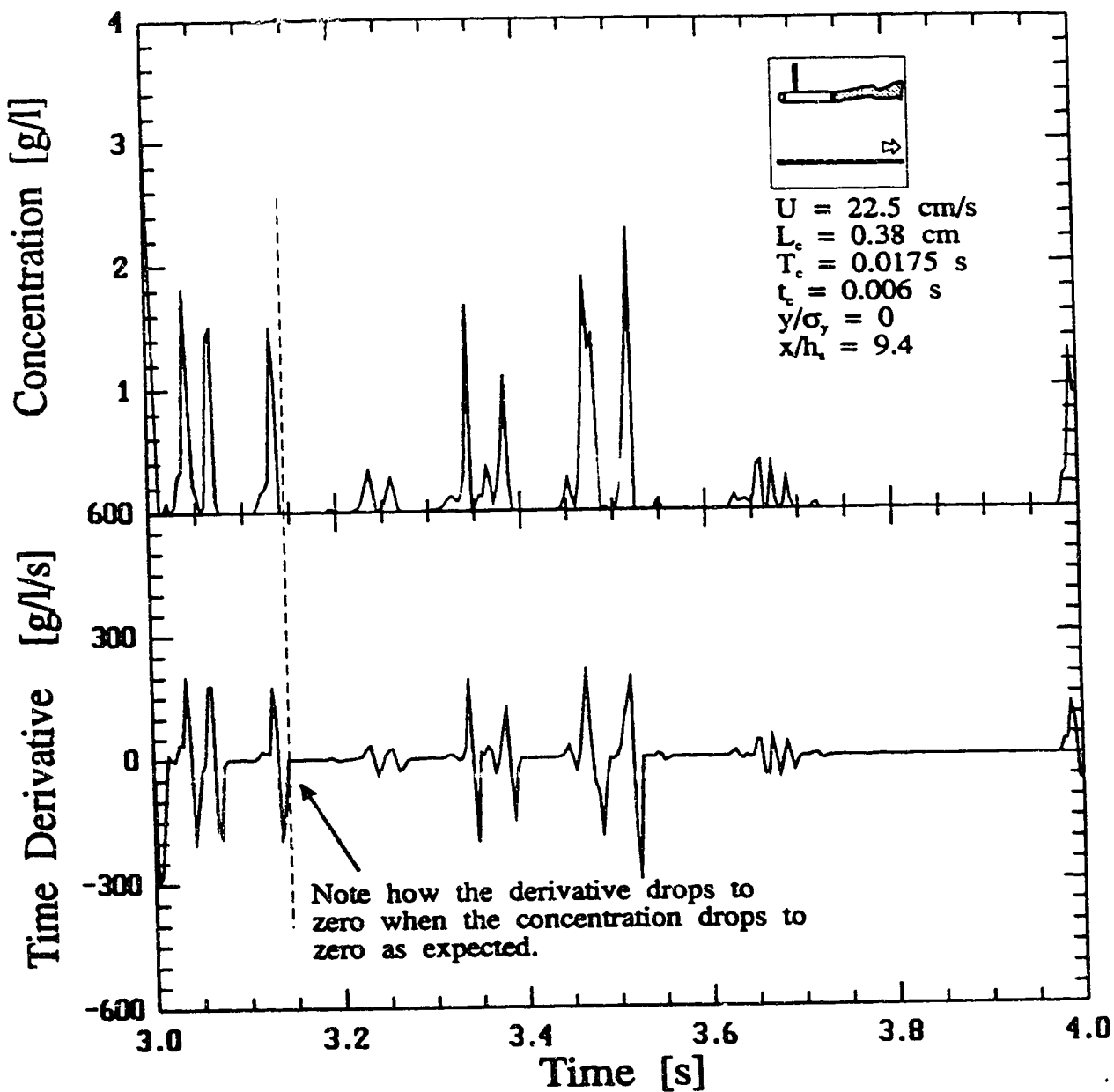


Figure B.4: 20th order Hanning window derivative approximation time series, showing the ringing due to Gibb's phenomenon.

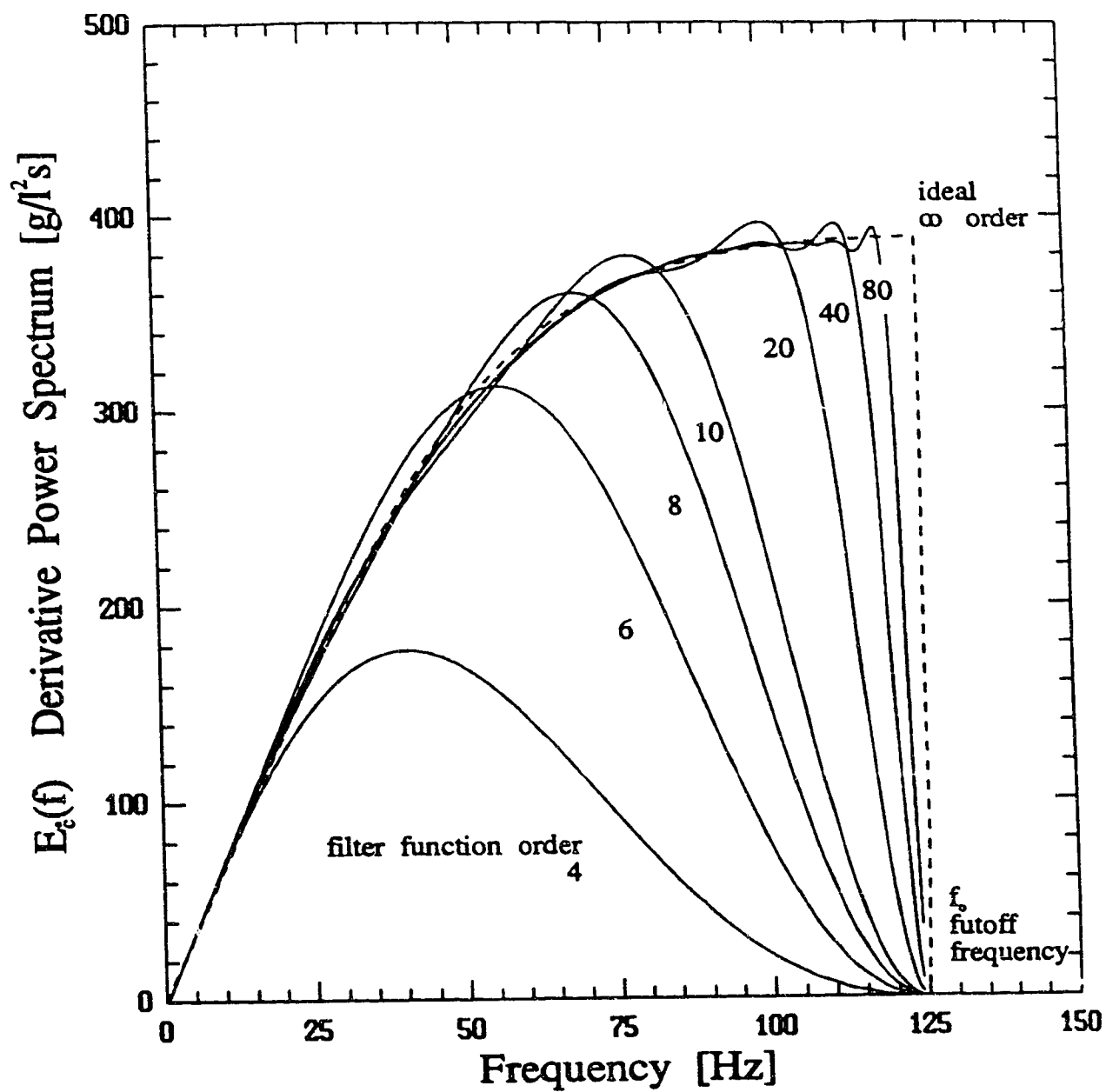


Figure B.5: Amplitude response of the ideal FIR differentiator using a Hanning window for increasing order of the derivative approximation.

These two sources of error cause a dilemma. If a 4th order derivative is used, a more accurate time series results, which is important when the probability distribution is required for the derivative, however, the magnitude of the derivative is grossly in error. In contrast, a 20th order derivative does not provide an accurate time series of the derivative, but does give an accurate magnitude. It was decided that the error reduction in the variance for the 20th order derivative was more important than the cleaner time series of the 4th order. The 20th order derivative is only 12% too low, which, considering all the other errors, can be neglected or corrected after the time series analysis at a later time. For higher order functions than 20, the computation time becomes considerable for the large data sets considered in this study.

B.3 Moment Analysis

The statistical moments may be determined from any sampled data set for the variable x and are described by,

$$\overline{x^n} = \sum_{i=1}^N \omega_i x_i^n / \sum_{i=1}^N \omega_i \quad (\text{B.47})$$

where ω_i is a weighting function for the i^{th} data point. Since the data samples are quite large there is no need to account for the bias incurred by using x as an estimate of $\overline{x^n}$. In the analysis of concentration time series, the weighting function is simply, $\omega = 1.0$.

If the Taylor averaging method is used for a turbulence variable x_i , then

$$x_i = \overline{x} + x'_i$$

The integer moments may then be determined by Taylor averaging the turbulence variable x_i as in,

$$\overline{x^n} = \overline{(x_i)^n} = \overline{(\overline{x} + x'_i)^n}$$

which, for the first four moments, results in

$$\left. \begin{aligned} \overline{x^1} &= \overline{x^1} \\ \overline{x^2} &= \overline{x'^2} + \overline{x}^2 \\ \overline{x^3} &= \overline{x'^3} + 3\overline{x'^2} \overline{x} + \overline{x}^3 \\ \overline{x^4} &= \overline{x'^4} + 6\overline{x'^2} \overline{x}^2 + 4\overline{x'^3} \overline{x} + \overline{x}^4 \end{aligned} \right\} \quad (\text{B.48})$$

These equations may be rearranged in terms of the central moments as,

$$\left. \begin{aligned} \overline{x'^1} &= 0 \\ \overline{x'^2} &= \overline{x^2} - \bar{x}^2 \\ \overline{x'^3} &= \overline{x^3} - 3\overline{x^2}\bar{x} + 2\bar{x}^3 \\ \overline{x'^4} &= \overline{x^4} + 6\overline{x^2}\bar{x}^2 - 4\overline{x^3}\bar{x} - 3\bar{x}^4 \end{aligned} \right\} \quad (\text{B.49})$$

Non-integer moments may be determined with the knowledge of the probability distribution function, $f(x)$, of the random process being studied and using,

$$\overline{x^r} = \int_{-\infty}^{+\infty} x^r f(x) dx \quad (\text{B.50})$$

or through the use of the PDF and the moment generating function for the pdf.

The specific moments of interest in analyzing the concentration data include, Bury p.150 (1986).

$$\left. \begin{aligned} \text{mean} &= \bar{x} \\ \text{variance} &= \sigma^2 = \overline{x^2} - \bar{x}^2 \\ \text{intensity} &= i^2 = \sigma^2 / \bar{x}^2 \\ \text{skewness} &= \gamma_1 = \overline{x'^3} / \sigma^3 \\ \text{kurtosis} &= \gamma_2 = \left(\overline{x'^4} / \sigma^4 \right) - 3 \end{aligned} \right\} \quad (\text{B.51})$$

The skewness is an indicator of the model's distribution about its mean value. The kurtosis is generally represented as above with the -3 for comparison to a Gaussian profile. Therefore, if the kurtosis is negative, then the the time series is said to be platykurtic and has a pdf characteristically flatter than a Gaussian profile. If the kurtosis is positive, then the the time series is said to be leptokurtic and has a pdf forming a characteristic cusp at the centre point. The intensity, skewness and kurtosis are important indicators in the analysis of concentration fluctuations because they form a description of the nature of the fluctuations relative to the mean concentration. Hence a positively skewed, leptokurtic distribution indicates that large concentrations are more widely distributed than small concentrations and that the concentration observations are characteristically not close to the mean value.

B.4 Determining Profile Cross-Wind Spreads

In the analysis of concentrations and concentration fluctuations the normalizing parameter for the size of a plume is the plume spread. The plume spread is not well defined in the literature but is often defined by the profile's second central moment of distance from the profile centroid. The plume spread defined this way is often given the symbol σ_y or σ_z for the cross-wind and vertical components respectively. *Top hat* superpositions define the plume spread as the point where the concentration falls to half the centre-line value. The profiles are often fit to a Gaussian profile and the plume spread given by the point where the concentration is half the centre-line value. This plume spread is often given the symbol δ_y or δ_z for the cross-wind and vertical components respectively. This form of the plume half-width is related to the plume spread by $\delta_y = \sqrt{2 \ln(2)} \sigma_y$.

There are four principal procedures for determining the plume spread,

Statistical Method. This method is the same as the second or moment method. The plume spread is determined by finding the second moment of the mass distributed about its centroid.

$$\sigma_y^2 = \frac{\int_{-\infty}^{+\infty} (y - \bar{y})^2 c(y) dy}{\int_{-\infty}^{+\infty} c(y) dy} \quad (\text{B.52})$$

or in "data space", (which is written for unequally spaced data),

$$\sigma_y^2 = \frac{\sum_{i=0}^{N-1} \left(\frac{1}{2}(y_{i+1} + y_i) - \bar{y} \right)^2 \frac{1}{2}(c_{i+1} + c_i)(y_{i+1} - y_i)}{\sum_{i=0}^{N-1} \frac{1}{2}(c_{i+1} + c_i)(y_{i+1} - y_i)} \quad (\text{B.53})$$

and \bar{y} , the profile centroid, is determined similarly,

$$\bar{y} = \frac{\sum_{i=0}^{N-1} \frac{1}{2}(y_{i+1} + y_i) \frac{1}{2}(c_{i+1} + c_i)(y_{i+1} - y_i)}{\sum_{i=0}^{N-1} \frac{1}{2}(c_{i+1} + c_i)(y_{i+1} - y_i)} \quad (\text{B.54})$$

An alternative formulation provides more information; following the notation from Sackinger, Reible, Shair (1982),

$$I_0 = \int_{-\infty}^{+\infty} c(y) dy \quad (\text{B.55})$$

$$I_1 = \int_{-\infty}^{+\infty} y c(y) dy \quad (\text{B.56})$$

$$I_n = \int_{-\infty}^{+\infty} y^n c(y) dy \quad (\text{B.57})$$

where $c(y)$ is the concentration at some cross-wind location y . The first few total moments are determined by,

$$\bar{y} = \left(\frac{I_1}{I_0} \right) \quad (\text{B.58})$$

$$\overline{y^2} = \left(\frac{I_2}{I_0} \right) \quad (\text{B.59})$$

$$\overline{y^n} = \left(\frac{I_n}{I_0} \right) \quad (\text{B.60})$$

Then, without assuming any shape of the concentration profile, the profile spread, σ_y , skewness, γ_{1y} , and kurtosis, γ_{2y} , are given by the moment equations in section (B.48).

Various integration schemes may be used depending on whether the data is regularly spaced or not. For regularly spaced data profiles the trapezoid rule or Simpson's rule for integration are generally adequate. The trapezoid rule will yield identical results to the simple data moment summations when the data points near both ends of the profiles approach zero. In practice, therefore, the three procedures yield identical results.

10% Method. The plume edge is defined as the point where the concentration reaches 10% of the maximum, of the 10% point on a Gaussian curve, Howroyd and Slawson (1977). This distance is related to the plume standard deviation, (using a Gaussian curve),

$$\sigma_y = \frac{\text{10\% plume width}}{4.292} \quad (\text{B.61})$$

Area/ C_{\max} Method. The area under the profile is equated to the area under the Gaussian profile. This method preserves the observed maximum concentration,

$$\sigma_y = \frac{\text{area}}{2.507 C_{\max}} \quad (\text{B.62})$$

Gaussian Fit. The concept here is to fit the Gaussian distribution and minimize the relative error. The Gaussian is,

$$c = C_{\max} \exp \left(-\frac{(y - \bar{y})^2}{2\sigma_y^2} \right) \quad (\text{B.63})$$

Fletcher and Powell (1963) present a minimization technique, using the least squares method, which may be used to fit the Gaussian. Press, et al. (1988)

provide a general non-linear method which uses a form the maximum-likelihood estimate to minimize χ^2 , the Levenberg-Marquardt method. Errors are assumed to be Gaussian, but need not be equally distributed. Individual error estimates may be used to provide better results.

Control of how the method fits the data may be influenced through the selection of the error estimate. The χ^2 merit function is,

$$\chi^2 = \sum_{i=1}^N \left(\frac{y_i - y(x_i, \alpha)}{\sigma_i} \right)^2 \quad (\text{B.64})$$

where:

y_i is the observed data point
 $y(x_i, \alpha)$ is the predicted value of the function at x_i using a list of function parameters α
 σ_i is the error estimate for the data point i .

If σ_i is constant, then each data point is weighted equally. However, large the data points with the greater magnitude, (i.e. ones near the centre of the Gaussian profile), will influence the fit more strongly than the smaller data points in terms of percentage error. If σ_i is variable but set by absolute magnitude, then the smaller the σ_i , the more strongly weighted that data point becomes.

Because non-linear fitting techniques, in general, are somewhat unpredictable in their ability to find solutions, a reasonably accurate guess often aids the speed and ability to find solutions. The centre and the spread determined by the statistical method were used for initial guesses into the routine. The Area/Statistical Spread Method, described in the next section, was used as an initial guess for C_{\max} .

Each of the methods described above has its unfavourable aspects,

Statistical Method. The statistical method can be in error when the entire plume width is not sampled. Sackinger, Reible and Shair (1982) discuss the errors for the case where the concentration profile is not fully represented by the data. For the data sets in the present study, the entire plume profile is well represented and extremity points are several orders of magnitude less than the centre-line value. The data sets covered at least $\pm 5\sigma_y$ on either side of the plume centroid.

An error also occurs if the plume profile was not taken perpendicular to the along-wind direction. McCormick, Slawson, and Tang (1979) have shown that

if the angle is less than 30° , the maximum error in the concentration distribution in the cross section is less than 15%.

Additionally, the spread of the plume is determined statistically, which is not necessarily the best Gaussian sigma, when the distribution is not closely Gaussian.

10% Method. Often the 10% point is not well described or is unknown. When it is not well described by the data, it too must be fit.

Area/ C_{\max} Method. This method is also sensitive to incompletely sampled plume profiles. A problem also arises determining the start of the plume, i.e. discerning the plume from the noise in the fringes. Sakiyama (1981) found that an error of 2-28% may result because of this in practice. A poor estimate may be made when the distance between points is large because a linear estimate of the concentration is used between points. However, the method is not sensitive to the profile shape. The value of C_{\max} must also be determined. Which, for sampled data sets is often ambiguous, and requires fitting, (this is discussed in the next section).

Gaussian Fit. This method eliminates the truncation error problem and the location of the endpoints. It is also flexible, using the Levenberg-Marquardt method, to incorporate individual errors in data points. The main problem with this method is that a Gaussian profile is implied in the fit. This will bias the plume spreads towards Gaussian if other profile shapes are being tested. Otherwise Sakiyama (1981) and Sackinger, Reible and Shair (1982) agree that this is the best procedure.

In practice, it was found that the statistical method and the Gaussian fit method provided nearly the same results, within at most 2-5%. The 10% method and the area/ C_{\max} method were avoided because of the problems noted in section B.4. The Gaussian fit procedure was selected for use in this study over the simplicity of the statistical method because it also produced estimates for the plume centre-line value and the maximum concentration in the profile, as outlined in section B.5.

B.5 Normalization of Profile Moments

In addition to the plume spread, the concentration moment profile centre-line value is an important characteristic value that is used in model development for the prediction of off-centre-line values and for normalization. Determining the profile

centre-line value is difficult because often there is no data point directly on the profile centre-line, and because there is scatter associated with each experimentally determined data set.

Three methods were investigated to determine the maximum or centre-line value, of a single profile,

Area/Statistical Spread Method. Similar to the area/ C_{\max} method, this procedure determines the maximum point of a Gaussian profile by matching the area under the observed profile to the area under a Gaussian profile with the same spread. This method requires that the spread of the profile be defined, which may be determined using the statistical method.

For sparse or noisy data sets, this method often produces unrealistic results, compared to the other methods tested, and therefore was not reliable for a general purpose procedure.

Quartic Function Fit. A general procedure to determine the point of interest is to fit a function to the data in such a way that the point may be interpolated. Selection of the function may be done so as not to bias the data normalization toward any particular function if the data is to be later fit to different functional forms. The concentration moment profiles are probably Gaussian, however, so as not to cause a bias, the profiles were fit to following polynomial in the "core" region of the plume,

$$f(y) = a_0 y^4 + a_1 y^2 + a_2, \quad |y| < 1.5\sigma_y \quad (\text{B.65})$$

This function is symmetric and is flexible enough to allow a good fit for most data profile shapes without having to presuppose a functional form. The "core" range selected, $|y| < 1.5\sigma_y$, is somewhat arbitrary but reflects the characteristic values within the plume half width region, and close to the centre-line value of interest.

This method also produced unrealistic results and proved to be unreliable for general use. The selection of an alternative function or an interpolation function was not attempted. Generally, interpolation is not what is desired, because a noisy profile requires some smoothing.

Gaussian. For suspected Gaussian profiles, the Gaussian fit procedure described in the last section, provides an estimate of the plume spread, C_{\max} , and the centre-line value. Therefore the method produces a consistent fit of all three parameters.

Fit by Eye. For profiles with no specific functional form, such as the intermittency profile or concentration micro-scale profile, the normalization value was determined by eyeball smoothing of the data set. When approximate values are required, the data point closest to the centre-line was selected.

A parametric study discussed in section 6.2.1 showed that the Gaussian fit method provides a robust fit to the data profile. For data sets that are sparse and noisy, the predicted spreads will be too high and the maximum centre-line value will be estimated too low.

B.6 Probability and Threshold Crossing Distributions

The data collected in the concentration analysis is real valued and therefore represents a continuous data set. Continuous data may be analyzed in the form of a cumulative probability distribution. This distribution may then be differentiated to obtain the probability density distribution. However, this procedure requires sorting a very large data set and differentiating data. The generated cumulative distribution data sets are the size of the original data sets, which causes computer storage logistic problems. The alternative is to bin the data into arbitrary ranges with the loss of some information.

The data set may be divided into bins distributed equally between the maximum possible value and the minimum possible value. In the analysis of the concentration time series, this would correspond to the source concentration and zero concentration. To allow for an adequate resolution of the histogram, many bins would be required because the data is frequently close to zero concentration. The higher concentration bins would be found to contain zeroes and are therefore wasted.

Alternatively the bins may be distributed equally between the maximum observed concentration and the minimum observed data point which, in the case of the concentration data collected in this study, is also the minimum possible concentration of zero. This procedure makes more efficient use of the bins without the added complexity of possibly using unequal spacing of bins, such as logarithmic or geometric spacing. The disadvantage of the procedure is that it requires the prior knowledge of the maximum observed data point. This requires an additional quick pass through the data set.

The time duration that a concentration is above a threshold value, and the time below a threshold, are determined by linearly interpolating between the end points of the samples and the threshold level, see Figure B.6. An efficient computer algorithm

determines all the threshold crossing times in one step, and records the threshold and the time to a temporary file. A second pass, determines the time since the last positive bound crossing, the time above a threshold level, and the time below a threshold level. The duration times are now real valued, therefore the distribution of these times may be determined in the same way as the concentration data.

Once the continuous data is binned, the probability mass distribution, pmd , may be determined by dividing each bin by the total number of binned observations such that for each bin the probability of an observation in that bin is $P(x_i < x < x_{i+1})$. The cumulative distribution is determined simply by summing bins to the current bin.

Plotting of the probability distributions in Chapter 5 is simplified by using the value of the arithmetic centre probability distribution bin. For example, when a log-Normal probability distribution is assumed, it is proper to use the geometric mean of the bin instead of the arithmetic mean. Since a large number of bins are used to describe the probability distribution, the bin size is small and the shift in the bin centre is not noticed. The only time that the bin centre may become an issue is when the low concentration bins are expanded in semi-logarithmic plots of the probability distributions. However, because a large number of candidate probability distributions are being examined, the change of bin centring was not attempted.

B.7 Concentration Intermittency Threshold Level

It is important to separate the periods where signal is present and where there is only a zero or background concentration level. The total summed time period of signal to the total summed time period of zeros forms the signal intermittency, which is discussed in section 5.1.1. The ability to discern the difference between a data point that is signal and one which is a zero is difficult using real data because of the presence of noise in the recorder time series signal. This means that points near zero may be considered zero, up to some critical level or zero threshold level. The threshold level may be a function of the concentration, the derivative, or other influence on the signal or noise behaviour.

Several schemes were tried to determine the appropriate intermittency threshold level. They include the following:

A fixed concentration intermittency threshold level. By examining many data sets, a fixed concentration threshold may be selected which will produce about the right intermittency overall. This method was used by Bara

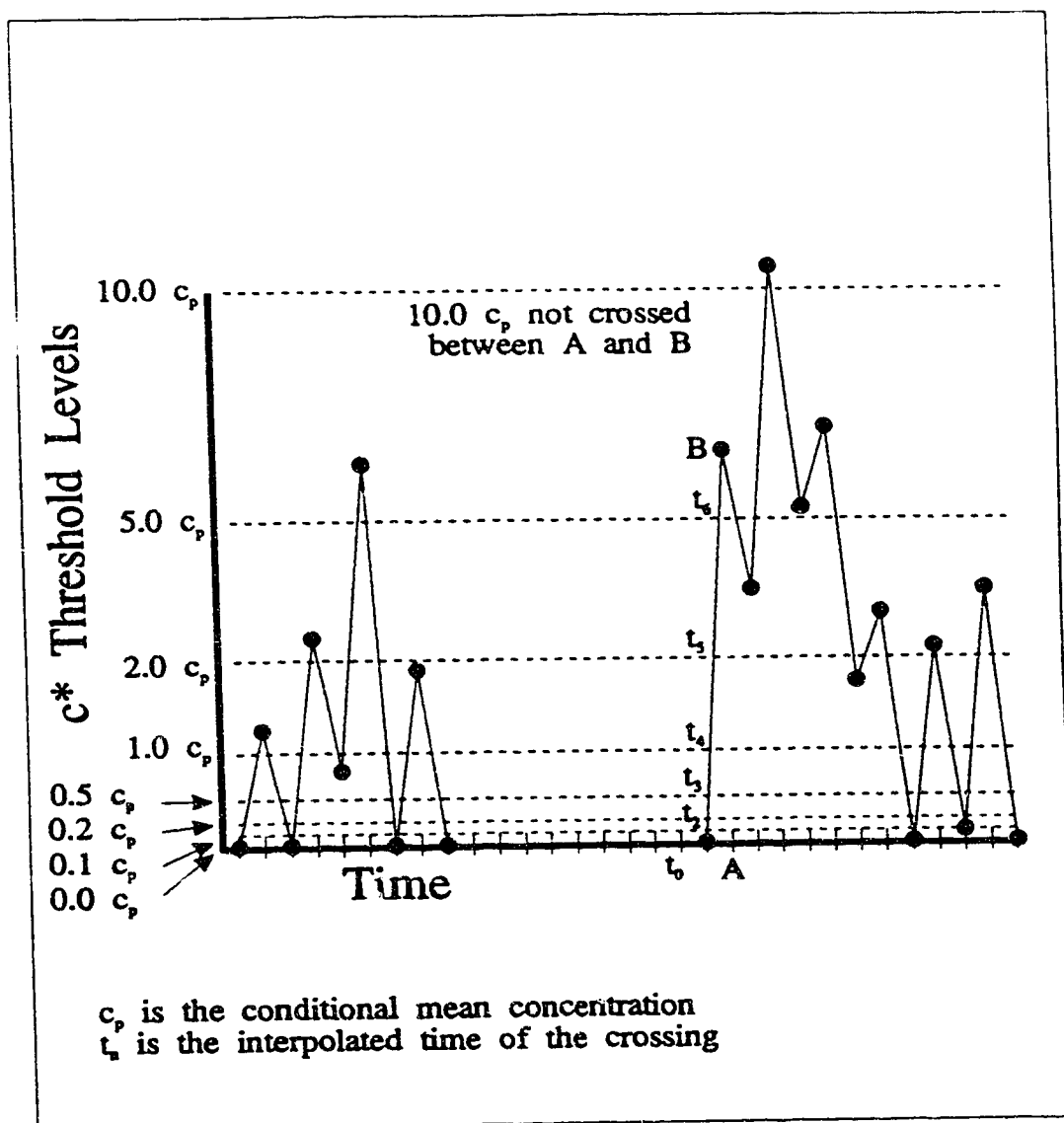


Figure B.6: Threshold times determined by linearly interpolation between data sample end points.

(1985) in his analysis of a concentration time series signal. However, the analysis methods used in this study are much more complex and reveal more aspects of the concentration fluctuations than did the study by Bara. In addition, Bara's work involved a ground level tracer release in which case Bara expected to find intermittency levels near 1.0. Therefore, close attention to this problem was not as necessary. The major problem with this procedure for the concentration time series in this study, is that it does not predict the intermittency well for individual data sets.

A derivative based intermittency threshold. During the period when the tracer signal is assumed present, a large derivative activity is usually present. This is especially true for the rising edge of the concentration signal and the start of the fall periods to zero. Therefore, a fixed derivative threshold level may be determined which reports when the tracer signal is present. Between the rise and fall, however, the derivative may or may not be near zero, which requires that in addition to the derivative threshold, a tracer concentration threshold must also be applied. Bara (1985) tried this, as did the author in this study. It, however, did not yield more accurate results than the fixed tracer concentration threshold procedure.

A noise relative intermittency threshold. The entire problem of trying to determine the threshold level is essentially a problem of the background noise levels present during the zero periods. The procedure for collecting the data sets incorporates a measurement of the background concentrations before and after each time series measurement. From these background signals, the variance of the signal may be determined which forms a measurement of the amount of noise present during the zero periods when the tracer is being released, see Figure B.7. The background noise signals were represented well by a Gaussian and therefore, a intermittency threshold level of some multiple of the background noise levels standard deviations may be used, a σ_{noise} .

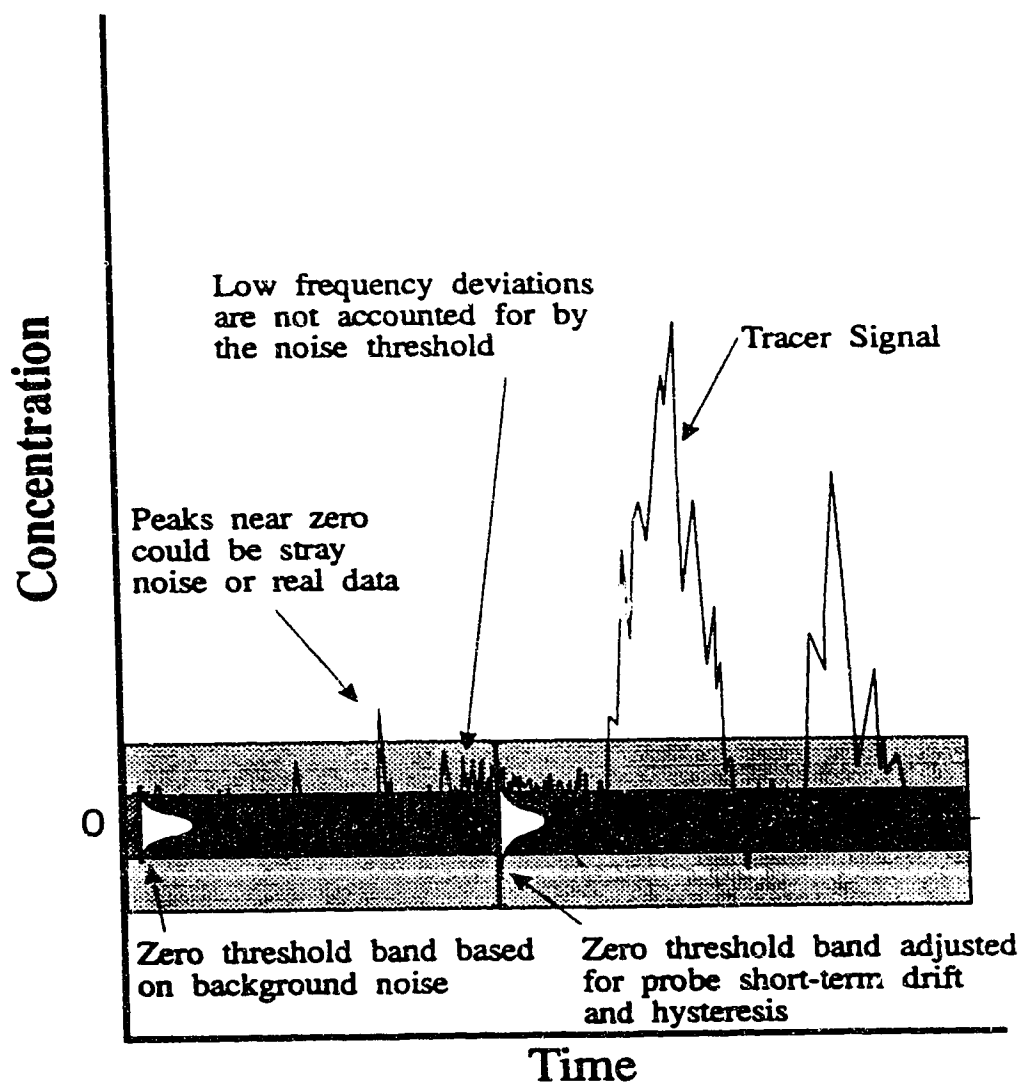


Figure B.7: Schematic representation of how the background noise level is used to form a tracer concentration threshold level.

Appendix C

One-Dimensional Energy Spectrum

Fluctuation time scales may be determined using Taylor's one-dimensional energy spectrum analysis. The Lagrangian velocity spectrum is defined in terms of the Fourier transform pair with the auto-correlation function,

$$F(f) = 4 \int_0^{\infty} R(\xi) \cos(2\pi f \xi) d\xi \quad (C.1)$$

$$R(\xi) = \int_0^{\infty} F(f) \cos(2\pi f \xi) df \quad (C.2)$$

with the Lagrangian spectrum being defined by,

$$\overline{u'^2} = \int_0^{\infty} E(f) df \quad (C.3)$$

where $E(f)$ is the spectral density of $\overline{u'^2}$ and $F(f) = E(f)/\overline{u'^2}$.

If a Markov spectrum is assumed then,

$$R(\xi) = \exp(-\xi/T) \quad (C.4)$$

where T is the time scale of the fluctuations. Substituting (C.2) into (C.4) and integrating by parts,

$$F(f) = 4 \int_0^{\infty} \exp(-\xi/T) \cos(2\pi f \xi) d\xi \quad (C.5)$$

$$\begin{aligned} &= 4 \exp(-\xi/T) \left(\frac{1}{2\pi f} \right) \sin(2\pi f \xi) \Big|_0^{\infty} \\ &\quad - 4 \int_0^{\infty} \frac{-1}{2\pi T f} \exp(-\xi/T) \sin(2\pi f \xi) d\xi \end{aligned} \quad (C.6)$$

Integrating by parts again leads to,

$$F(f) = \frac{\left[\left(\frac{4}{2\pi f} \right) \sin(2\pi f\xi) - \frac{-4}{4\pi^2 f^2 T} \cos(2\pi f\xi) \right] \exp(-\xi/T) \Big|_0^\infty}{1 + \frac{1}{(2\pi T f)^2}} \quad (\text{C.7})$$

$$= \frac{4T}{1 + (2\pi T f)^2} \quad (\text{C.8})$$

Therefore the time scale, T , may be determined from the energy spectra, $E(f)$, at the zero intercept by,

$$F(0) = 4T \quad (\text{C.9})$$

or

$$E(0) = 4T\sigma^2 \quad (\text{C.10})$$

Appendix D

Conductivity Detector Design

The primary problem in the measurement of saline conductivity is acquiring a stable output in a very short period of time. Today's market does not provide a fast response conductivity detector to meet the needs of research. This requires in-house construction of a detector to meet the requirements of the experiments. In this chapter the design, construction procedure and testing of a new concentration detector will be presented.

D.1 Recent Developments in Conductivity Probes

The new concentration detector was created based on the concepts of the detector designed by Bara (1985) while attempting to solve its inherent problems Bara's design incorporated a pair of 26 gauge platinum wires mounted in a pointed teflon tip, see Figure D.1. This probe was designed principally on the recent work of Gibson and Schwartz (1963). The new conductivity detector is based largely on the detectors designed by Gesteland (1959) and Dowben & Rose (1953), which are metal filled, glass probes used in pharmacology research. There are consistent problems with all of these detectors which were not eliminated in Bara's design and needed to be addressed in the new design. Three of the main points that needed addressing are listed below.

1. The probe has a large size. The size of the probe contributes to a large spatial resolution. Because the measurements are being conducted in a water channel simulation with a scale factor of 3000:1 the full scale size of the spatial resolution was inadequate. The small scales of turbulence could not be measured with this probe.

2. The probe has a two electrode sensing design. The design of the probe incorporates two wires; one of which is held at a constant voltage, and the other is a ground. This design allows electrical cross-talk between adjacent probes and to the water channel structure which is also grounded.
3. The calibration tends to drift quite quickly. The probe, once calibrated for a range of saline solutions, tends to lose its calibration in a matter of several minutes.

D.1.1 Design of the Micro-Probe

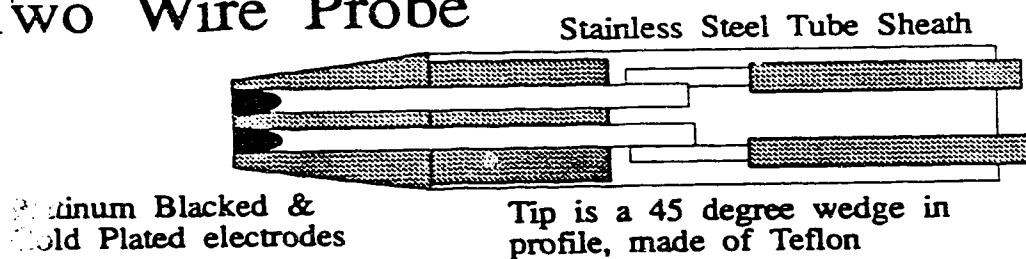
The micro-probe is constructed from 3 mm glass tubing which is heated and drawn down to a fine point, see Figure D.1. The inside diameter may be made anywhere in the range of several micrometers to several hundred micrometers. Durability and stability of the output signal, (to be discussed later) were governing considerations which lead to a probe diameter in the range of 100-200 μ . The hollow tube is filled with Wood's metal which is easily extruded through the fine tip using the a wire inserted through the trailing end of the 3 mm tubing. The probe tip is then ground to a 45° angle to provide an aerodynamic shape. Appendix D.4, contains a step by step review of the probe construction procedure.

The size of the new micro-probe is one tenth the diameter of one of Bara's electrode wires so it might be expected that a smaller sensing volume is produced. An approximation of the size of the sensing volume may be made for the micro-probe by letting the probe tip approximate a spherical electrode with the same diameter. The sensitivity of this sphere to the conductivity of the surrounding quiescent fluid falls off like the inverse of the distance. Therefore, 99% of what the probe will "see" is contained in a sphere with a diameter of about 10,000 μ m or 1 cm. Bara approximated the sensing volume about his two-wire probe to be 2 cm. Therefore the new probe design offers both a physical size reduction and a sensing volume reduction. An array of micro-probes may be used with a spacing of 1 cm with little electrical cross-talk.

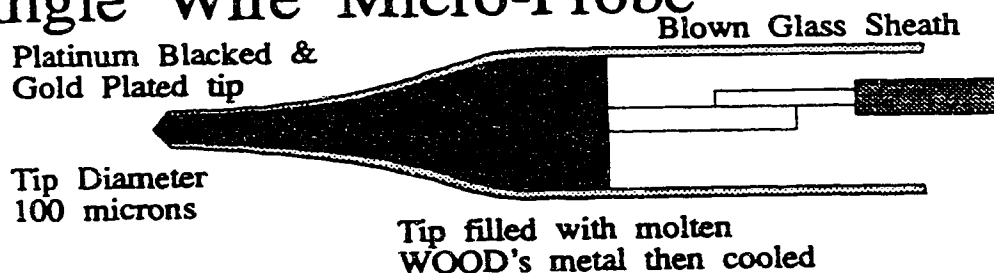
D.1.2 Design of the Aspirated Probe

One problem associated with Bara's probe and the micro-probe is stability of the output signal which is a function of the surface stability in a conductive solution. A large surface area greatly increases the stability however increasing the physical size. An aspirating tip developed by Mumford, University of Cambridge, (unpublished)

Two Wire Probe



Single Wire Micro-Probe



Single Wire Aspirated Probe

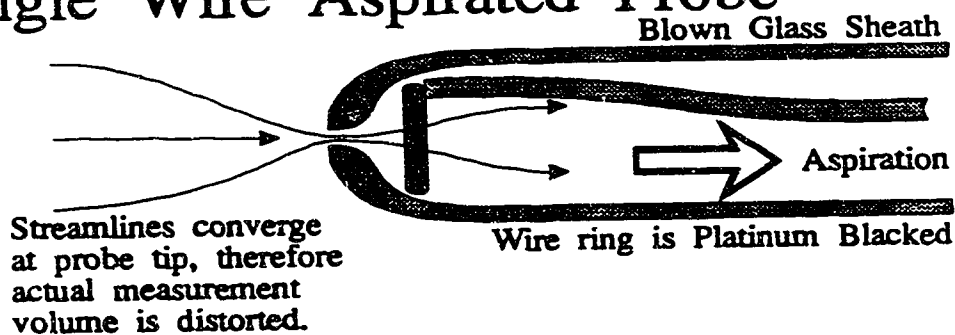


Figure D.1: Schematic of three conductivity probes; the two-wire probe developed by Bara (1985), the single electrode micro probe and the single electrode aspirated probe.

was conceived based on an aspiration probe. The idea being a large conductivity detecting surface could be used within an aspirating probe, that would detect the solution conductivity in the throat of probe. A probe was developed in this study following this concept which solved many of the problems of the Mumford probe.

A glass sheath was used to provide an electrically insulate probe, see Figure D.1. The glass probe tip was blown into a shape that provided an aerodynamic shape on the exterior and a free flowing yet blunt throat on the interior. A platinum blacked wire loop was used as the detecting surface. This large surface greatly increased the short term stability of the probe over the micro-probe however, the long term stability remained a problem.

The amount of aspiration required to make the probe work did not seem to be a problem. Aspiration varying between the equivalent environment outer flow speed to a strong suction did not greatly alter the measured conductivity.

The concept was finally abandoned in place of developments on other probe designs. Some of the difficulties associated with this probe design are:

1. Aspirating eight probe simultaneously was difficult.
2. Long term stability of the conductivity calibration was poor.
3. The probes tended to dirty quite quickly, since the electrical surface was contained internally, in a very small probe, and could not be cleaned.
4. Water born air bubbles and small debris in the water channel posed practical problems for the small throat of the aspirated probes.

D.1.3 Design of a New Stable Probe

The efforts to design a robust, stable conductivity probe have taken a research team approach. A new probe was designed based on the four electrode probe of Head (1983). The prototypes were first developed by the author and modified to form a working version. The research team created a polished version and further modified the electronics required to drive probe. The details of the probe are currently being published elsewhere.

The benefits of this probe are an equally fast response as the glass micro-probe plus a long term calibration stability. The drift of the calibration was reduced so that calibrations needed to be performed once per day rather than for each data sample. In

practice, it was convenient to calibrate the probes more often to simplify the logistics with the data analysis.

The sections to follow specifically refer to the glass micro-probe, but are applicable to the new stable probe as well.

D.2 Probe Stability

The exposed Wood's metal surface of the probe is electrically conductive, but not chemically stable. This is because the surface area of the probe is relatively small and will change with any build up of microscopic material.

To increase the stability of the probe, and its relatively long term stability, the probe tip is electroplated with platinum, using a 0.01 M chloroplatinic acid solution. This creates a very porous surface with a large surface area. The surface is so porous that the usual shiny metallic platinum surface is now jet black. The procedure is generally called platinum blacking for this reason. To enhance the adhesion of the platinum to the Wood's metal the probe tip is first electroplated with gold, using a gold cyanide solution.

D.2.1 Plating Procedure

A straightforward and repeatable procedure for plating the probe tip surface was designed following the extensive study on probe stability and design by Head (1983). The probe tip surface area was approximated and a capacitive charge/discharge arrangement was designed based on the probe tip surface area, see Figure D.2.

Each probe tip is consecutively electroplated beginning with a 16 coulombs charge in the gold cyanide solution, then three times with 16 coulombs of charge in the chloroplatinic acid solution, and once with 32 coulombs of charge in the chloroplatinic acid solution. Between each platinum blacking, the probe was allowed to sit at least one hour in the open air. Head suggested that the probes be aged in a saline solution while being electrically excited by the detector circuitry, however it was found that this did not affect the response of the probe. In general, the aging period was found to be crucial for the development of a stable probe response and allowing the probes to dry, was simple and provided good results. The completed probe is allowed to dry and harden in the open air.

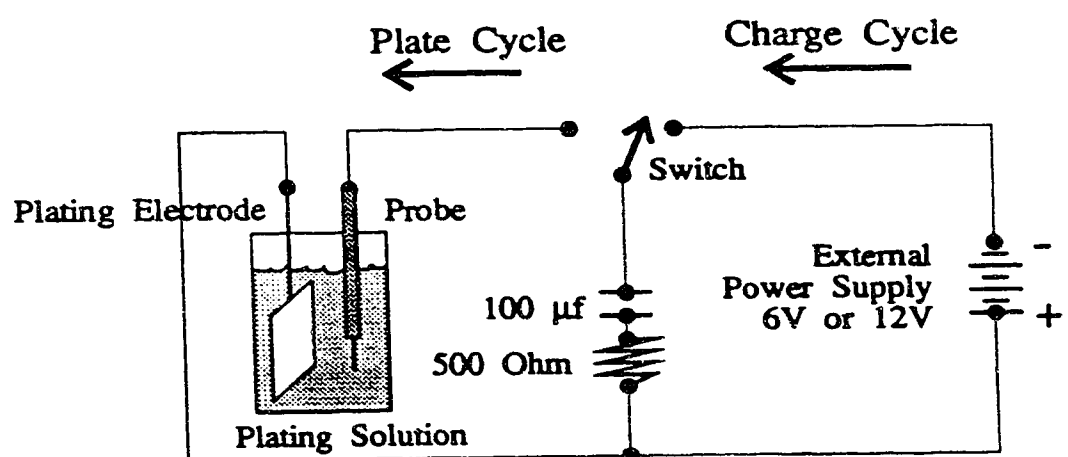


Figure D.2: Micro-probe electroplating circuit design.

D.3 Calibration

The output of the conductivity probe is known to be proportional in some way to the conductivity of the solution in which it is immersed. However, the calibration of the output from output voltage to conductivity is very complex and must be examined in several different ways. The static calibration, or long-term steady state calibration, is the calibration which relates the output voltage to conductivity or concentration. The static calibration is a non-linear function with an approximately linear range for low concentrations. The behaviour of the ungrounded concentration detectors causes an additional non-linearity to be observed. If the probe is subjected to a changing concentration then a dynamic calibration must be performed to determine the transient response of the probe to the change. A final complication on the calibration of the conductivity probes is the effect of temperature. These four topics are discussed in the following sections.

D.3.1 Static Calibration

The static calibration of the micro-probes was investigated by Bara (1985). It was concluded that the conductivity detector was linear to approximately 3% up to a concentration of 2 g/l. Repeating the calibration procedure it was found that this range could be extended easily up to 10 g/l.

Errors due to the assumption of a linear relationship between voltage and concentration, were considered to be far less significant than those errors caused by probe calibration drift. This drift was monitored throughout the experiment and used to correct the probe signal gain transient. It was determined that the mean absolute drift in calibration was determined to be,

1. 0.123 volts at maximum gain setting resulting in a 3% error in the upper span calibration point.
2. 0.042 volts at minimum gain setting resulting in a 42% error in the lower span calibration point.

Although a much larger drift is observed with the higher gain settings, the percentage errors that are caused in the lower gain settings contribute a greater effect to the overall error. These errors should be cause for concern for the development of a new generation conductivity probe.

The change in calibration and drift of the calibration is due to the change in resistance of the probe tip, R_t . Since the conductivity is a measure of resistance, R_c , which is read in series with the probe tip resistance to produce the signal, $R_s = R_c + R_t$, any changes in the probe tip resistance appear as a calibration drift. The change in R_t may be caused by many occurrences such as, a suspended particulate landing on the probe tip, a small air bubble caught in the porous platinum blacking material or the observed crystalline growth which tends to appear on older probes.

D.3.2 Describe Non-Linear Calibration System

The conductivity measured by the detector is affected in a non-linear way by the near field ion resistance and the far field ion resistance. The results in this section were developed by through a group effort. The analytical correction formula was developed by D.J.Wilson.

The effective resistance as seen by the probe in a conducting solution is represented in Figure D.3 and is written as

$$R_{probe} = R_{tip} + R_{path} \quad (D.1)$$

The output voltage is directly proportional to conductance; $C = 1/R$, so we may write the probe output conductance as,

$$\frac{1}{C_{probe}} = \frac{1}{C_{tip}} + \frac{1}{C_{path}} \quad (D.2)$$

From this equation the C_{tip} conductance is the quantity of interest.

Multiplying both sides of (D.2) by $C_{tip}C_{probe}$,

$$C_{tip} = C_{probe} + C_{tip} \frac{C_{probe}}{C_{path}} \quad (D.3)$$

Which may be rearranged to,

$$C_{tip} = \frac{C_{probe}}{1 - \frac{C_{probe}}{C_{path}}} \quad (D.4)$$

If the probe is immersed in a homogeneous background solution in the absence of any local saline variations, the probe tip conductance would be the background value, given by,

$$C_{tip,b} = \frac{C_{probe,b}}{1 - \frac{C_{probe,b}}{C_{path}}} \quad (D.5)$$

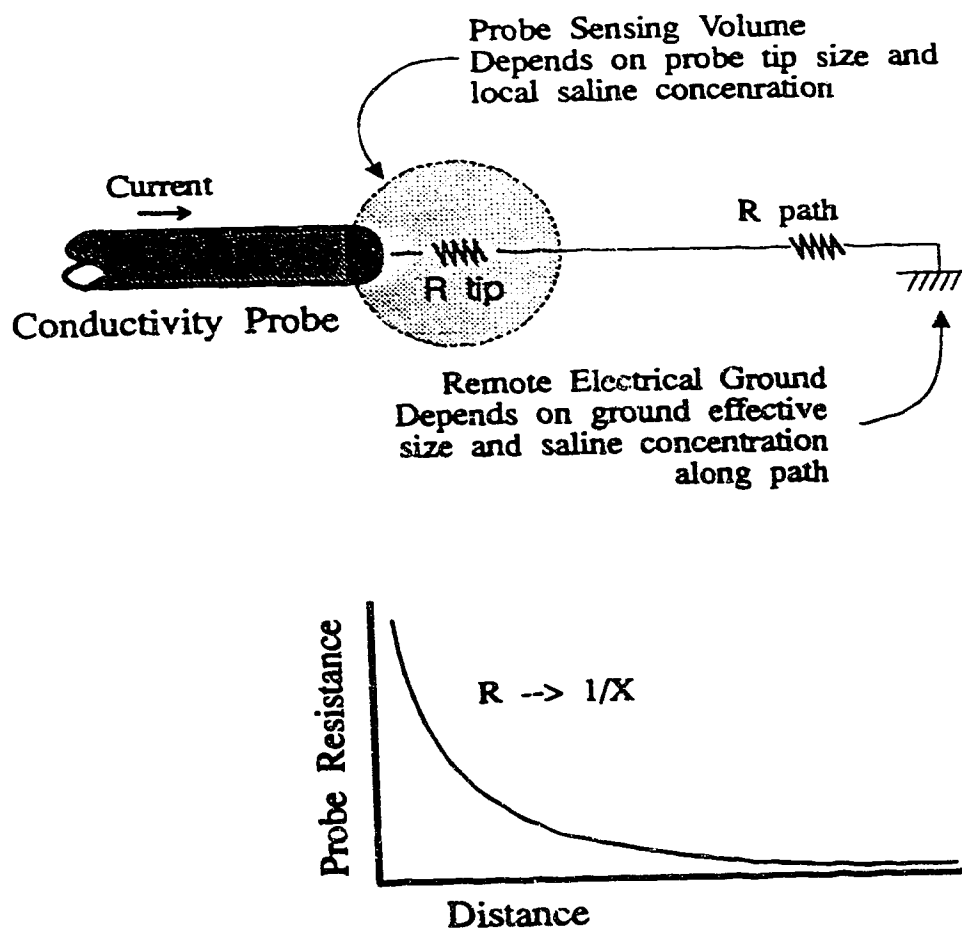


Figure D.3: Effective resistance of a probe in a conducting solution.

It is assumed that the path conductance will remain the same in the background solution and in the presence of local saline fluctuations. If (D.2) is rearranged, solving for the path conductance, so that (D.5) may be expressed as,

$$C_{path} = \frac{C_{probe,b}}{1 - \frac{C_{probe,b}}{C_{tip,b}}} \quad (D.6)$$

For a homogeneous saline fluid it might be assumed that the ratio of probe conductance to tip conductance be a fixed constant — dependent on perhaps the background concentration level, probe tip geometry, remote ground distance and effective size. Then from (D.2) define Y as,

$$Y = \frac{C_{probe,b}}{C_{path}} = 1 - \frac{C_{probe,b}}{C_{tip,b}} \quad (D.7)$$

Then dividing (D.4) by C_{probe} yields,

$$\frac{C_{tip}}{C_{probe,b}} = \frac{\left(\frac{C_{probe}}{C_{probe,b}} \right)}{1 - \frac{\left(\frac{C_{probe}}{C_{probe,b}} \right)}{\left(\frac{C_{path}}{C_{probe,b}} \right)}} \quad (D.8)$$

and substituting for Y .

$$\frac{C_{tip}}{C_{probe,b}} = \frac{\frac{C_{probe}}{C_{probe,b}}}{1 - Y \frac{C_{probe}}{C_{probe,b}}} \quad (D.9)$$

or just

$$C_{tip} = \frac{C_{probe}}{1 - Y \frac{C_{probe}}{C_{probe,b}}} \quad (D.10)$$

For concentrations less than about 5 g/l NaCl the non-linearity is less than 5%. Therefore, for low concentration saline solutions, the conductance may be assumed approximately linearly proportional to the concentration. The concentration, χ , in g/l units,

$$C = A (E - E_z) \quad (D.11)$$

$$\chi = S^{-1} (E - E_z) \quad (D.12)$$

where A and S are constants and E_z is a voltage at the theoretical zero concentration, (S is a span and A is a gain). Substituting this expression into (D.10) yields,

$$\chi = S^{-1} (E_{tip} - E_z) = S^{-1} \frac{E_{probe} - E_z}{1 - Y \frac{E_{probe} - E_z}{E_{probe,b} - E_z}} \quad (D.13)$$

When a probe is immersed in a background solution (D.13) reduces to

$$\chi_b = S^{-1} (E_{tip} - E_z) = S^{-1} \frac{E_{probe} - E_z}{1 - Y} \quad (D.14)$$

When this is done in the calibration bath, and the output $E_{probe} - E_z$ is calibrated to units of g/l, and not $E_{tip} - E_z$. Therefore, in the water channel, the correct calibration must take the factor of $1 - Y$ into account. Therefore, the final non-linear calibration equation is given by,

$$\chi = \frac{1 - Y}{S} (E_{tip} - E_z) = \frac{1 - Y}{S} \frac{E_{probe} - E_z}{1 - Y \frac{E_{probe} - E_z}{E_{probe,b} - E_z}} \quad (D.15)$$

The E_z voltage may be estimated from the calibration baths by linear extrapolation to zero. It is assumed that the E_z value is the same in the water channel and in the calibration baths. The factor Y was determined experimentally to be $Y = 0.025$.

D.3.3 Temperature Sensitivity Correction

The conductivity of a solution is a function of, among other things, temperature. Therefore, as a data sample in the water is being collected and the water is slowly heated by the recirculating pumps, the change in temperature must be accounted for in the calibration. There may also be a problem if the calibration bath solutions are not the same temperature as the water channel water. In this case temperature compensation is between the bath temperature and the flume water temperature.

Temperature compensation is the ability to interpret the conductivity measurements of one solution at a temperature T to a solution at temperature T_{ref} . Head (1983) states that the compensation is a function of T and T_{ref} and only weakly on the actual conductivity. Head quoted the results of Hewitt (1960) made his own experimental measurements. Temperature sensitivity measurements were

Table D.1: Effects of temperature on conductivity measurements

ΔT	$\frac{c(T)}{c(T_{\text{ref}})}$	% Error
-10.0	0.781846	-21.52
-5.0	0.888927	-11.11
-1.0	0.977468	-2.25
1.0	1.02269	2.27
5.0	1.115	11.50
10.0	1.23378	23.38

also performed by the author for the present study which confirmed the corrections presented here.

The basic form of the temperature correction for a concentration as quoted by Hewitt (1960) is given by, (T is in $^{\circ}\text{C}$)

$$\frac{c(T)}{c(T_{\text{ref}})} = 1 + b(T - T_{\text{ref}}) \quad (\text{D.16})$$

$$b = \sum_{n=0}^4 a_n T^n \quad (\text{D.17})$$

Where Hewitt (1960) uses a reference temperature of 18°C and the coefficients a_n are,

$$\begin{aligned} a_0 &= 2.1179818 \times 10^{-2} \\ a_1 &= 7.8601061 \times 10^{-5} \\ a_2 &= 1.543826 \times 10^{-7} \\ a_3 &= -6.2634979 \times 10^{-9} \\ a_4 &= 2.2794885 \times 10^{-11} \end{aligned}$$

Head has repeated this calibration and arrived a similar set of results which are within 1% of Hewitt's calibration curve.

The extent of the effect of temperature compensation may be seen in Table D.1 and Figure D.4 which shows that a considerable error may be generated when temperature differences are observed.

Both Hewitt and Head suggest that there is a slight dependence of the calibration with concentration. This is typically an error showing -0.0004% by weight NaCl at

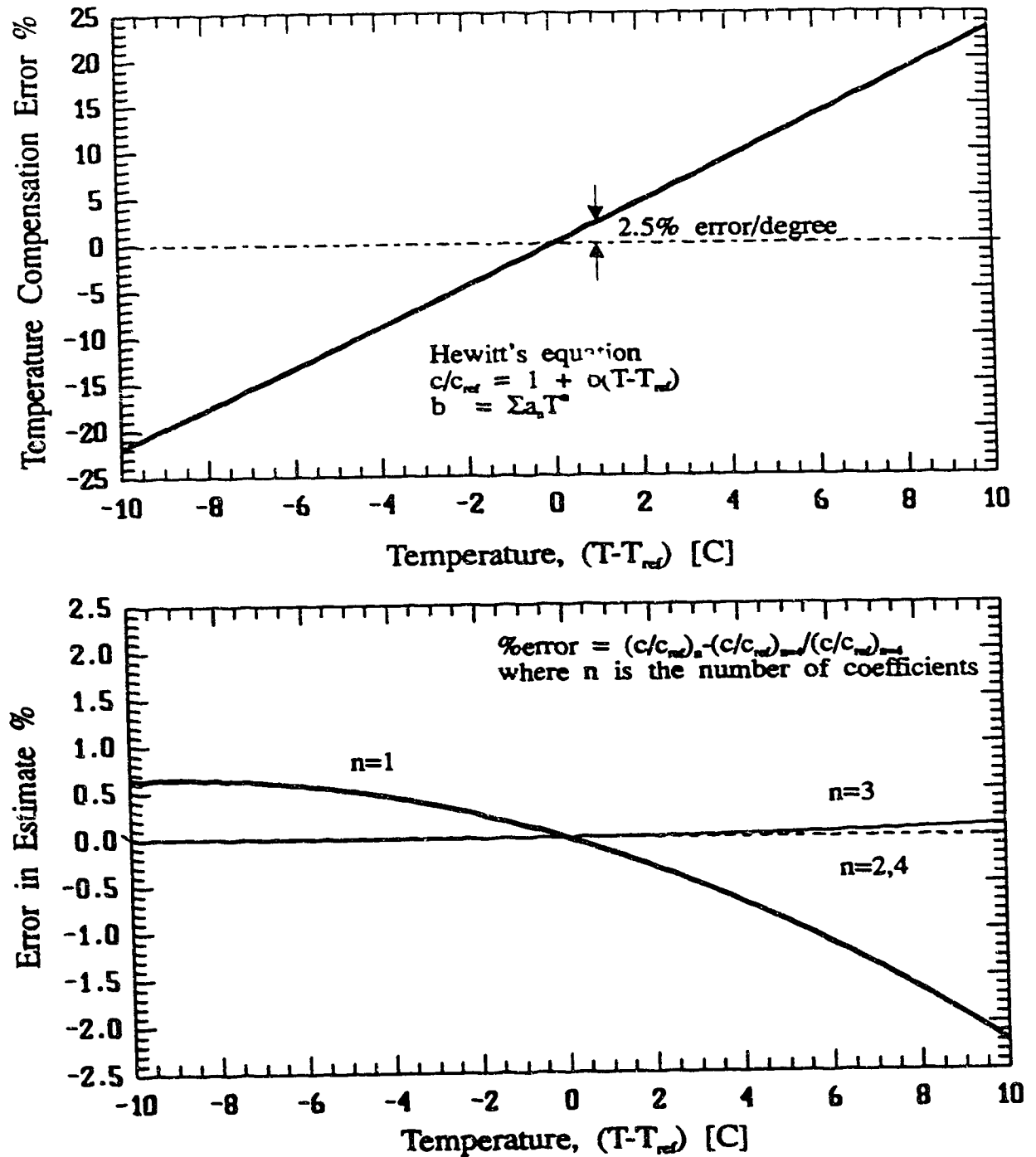


Figure D.4: Effect of temperature on the measured conductivity relative to a reference temperature using equation (D.16) (top). Relative fractional error of temperature compensation using a reduced number of coefficients with respect to the complete Hewitt equation (D.16). (bottom)

50°C for 5.0% by weight NaCl, therefore much less than a percentage of the solution strength, and is not an important correction.

Chua, Cleaver and Millward (1986) suggests that the temperature compensation follows the following form,

$$\frac{c(T)}{c(T_{\text{ref}})} = 0.035 \left(\frac{T - T_{\text{ref}}}{c(T_{\text{ref}})} \right) + 1 \quad (\text{D.18})$$

This form of the correction shows a significant variation of the correction with salt concentration. Both Head and Hewitt however say that only small variation may be expected. The results of Head and Hewitt were for low salinity values, typically $c \leq 5\%$ by weight, whereas Chua investigates much higher concentrations of, $c \geq 40\%$ by weight. Although the source concentration in this thesis work is 50 g/l, or approximately 25% NaCl, the measured concentrations are much less than 5%. For this reason, the Hewitt equation will be used for temperature compensation in the present study.

For computational speed, the number of coefficients of the Hewitt equation required for an accurate correction was determined. The percentage compensation predicted by Hewitt's equation is shown in Figure D.4. It can be seen that including only the first coefficient provides an acceptable level of error and is computationally much faster than using all of the coefficients. Therefore, Hewitt's calibration equation may be simplified to,

$$\frac{c(T)}{c(T_{\text{ref}})} = 1 + 0.02118 (T - T_{\text{ref}}) \quad (\text{D.19})$$

To minimize the problem of temperature compensation, the calibration solutions were kept at the same temperature as the water channel. This can be done in the water channel with relative ease by using a water bath. However, since an exact match of the temperatures is not always possible, the temperature compensation equation was used. The concentration at the temperature of the reference baths is given by,

$$c(T_{\text{ref}}) = \frac{1 + 0.02118 (T - T_{\text{ref}})}{c(T)} \quad (\text{D.20})$$

D.4 Construction Procedure of the Micro-Probe

The design of the micro-probe was fashioned after an electrode used by pharmacologists to detect electrical signals in nerves and cells. The size of the micro-electrode did not suite the requirements of concentration signal recording in the water channel, but the physical design concept was useful with modifications.

The conductivity micro-probe is constructed from 3 mm O.D. glass tubing, see Figure D.1, which is necked down under heat from a hand held torch. The glass tubing is spun slowly with an electric motor while being heated so that the heat is applied evenly, around the tube circumference at the center of a 350 mm length of tubing. By its own weight, the glass tubing necks down to a fine thread. After the glass begins to neck, the heat is removed so that the glass will harden. With a steady hand and good timing a probe shape and neck length is achieved consistently. The glass thread connecting the glass tube may be severed easily, which completes the glass blowing of two probes.

The probe tip is then ground down by drawing the probe at a 45° angle across 100 μ m grinding emery paper, while rotating the probe with the fingers. An inside probe diameter of approximately 100 μ is desirable although $\pm 50\%$ is allowable. The diameter of the probe may easily be measured using a machinists microscope with back lighting.

Using slender tygon tubing of approximately 1.5 mm diameter, and a No.4 syringe, molten Wood's metal is drawn into the tubing. Soon after being drawn into the tubing the Wood's metal hardens. While still pliable, the Tygon tubing is straightened and allowed several minutes to cool. When completely cool and hard, the Tygon tubing is peeled away from the Wood's metal by drawing a sharp razor blade down the length of the tube. Wood's metal slugs are then cut into 5 to 7.5 mm lengths.

A 16 gauge tinned copper wire roughly 50% longer than the glass micro-probe is used as an electrical connector. One end is folded back in 5 mm lengths twice. This will form a plunger and anchor for the Wood's metal tip.

To complete the probe construction, one of the slugs of Wood's metal is slipped down the probe core followed by the tinned copper plunger. While applying slight pressure on the plunger, the fine tipped end of the probe is held over a hot plate preheated to approximately 200 °C, and rotated for even heating. Only the first third of the Wood's metal slug is exposed to the heat at this point in time. When the Wood's metal begins to melt, it is extruded slowly out the end of the probe. The rest of the Wood's metal is then heated and allowed to anchor the tinned copper plunger into the Wood's metal. Again, timing is important. When the entire Wood's metal slug begins to melt the probe is removed from the heat source and allowed to cool several seconds. Constant pressure must be applied on the molten Wood's metal all the time to avoid air gaps which would break electrical contact to the probe tip. A small spherical ball of the hardened Wood's metal, usually present upon completion, is easily removed with gentle finger tip pressure or a tap on the side of the probe.

The probe tip is ground again to apply a 45° conical geometry on the glass and Wood's metal exceeding the glass length. This procedure leaves the probe with a nice

aerodynamical shape important to the flushing characteristics required later. Care must be taken to not bend the glass tip while drawing it over the emery paper so that the Wood's metal core, nor the toughened glass tube, do not fracture. The final inner probe diameter is recorded and should lie in the range of 100 to 200 μm .

The probe is then electroplated with gold and then platinum as described in Chapter 4.

Appendix E

Gamma PDF for Derivative

- In this section, the exceedance relationships are developed assuming $\dot{c}(t)$ has a Gamma distribution. The Gamma model for $f_p(\dot{c})$ is given by,

$$f_{G,p}(\dot{c}) = \frac{1}{2\sigma\Gamma(\lambda)} \left(\frac{\dot{c}}{\sigma}\right)^{\lambda-1} \exp\left(-\frac{\dot{c}}{\sigma}\right), \quad -\infty < \dot{c} < \infty, 0 < \lambda, \sigma \quad (\text{E.1})$$

Using the first two moments of (E.1), the distribution parameters are,

$$\sigma = \frac{\overline{\dot{c}_p'^2} - \overline{|\dot{c}_p|}^2}{\overline{|\dot{c}_p|}} \quad (\text{E.2})$$

$$\lambda = \frac{\overline{|\dot{c}_p|}^2}{\overline{\dot{c}_p'^2} - \overline{|\dot{c}_p|}^2} \quad (\text{E.3})$$

where,

$\overline{\dot{c}_p'^2}$ is the variance of the derivative, $(\text{g/l/s})^2$.

$\overline{|\dot{c}_p|}$ is the average of the absolute value of the derivative, g/l/s .

The number of exceedances per second, N^+ , is determined by substituting (E.1) into (7.27),

$$\begin{aligned} N^+_{X,G(c^*)} &= f_p(c^*) \frac{\gamma}{2\Gamma(\lambda)} \int_0^\infty \frac{\dot{c}}{\sigma} \left(\frac{\dot{c}}{\sigma}\right)^{\lambda-1} \exp\left(-\frac{\dot{c}}{\sigma}\right) d\dot{c} \\ &= \gamma f_p(c^*) \sigma \lambda \\ &= \gamma f_p(c^*) \overline{|\dot{c}_p|} \end{aligned} \quad (\text{E.4})$$

Substituting, (E.4) into (7.30), the average duration time above c^* , T^+ , is,

$$T^+_{X,G}(c^*) = \frac{\gamma}{\gamma |\dot{c}_p|} \frac{(1 - F_p(c^*))}{f_p(c^*)} \quad (\text{E.5})$$

$$= \frac{1}{|\dot{c}_p|} \frac{(1 - F_p(c^*))}{f_p(c^*)} \quad (\text{E.6})$$

The difference between the Gamma distribution models, (E.4) and (E.6), and the Normal model, (7.32) and (7.34), and Exponential model, (7.41) and (7.43), is the use of the $|\dot{c}_p|$ instead of $\overline{\dot{c}_p^2}$. The variable, $|\dot{c}_p|$, was not calculated from the experimental data sets.

Appendix F

Data Set Statistics

Normalization values used in the thesis include.

H = 150 mm boundary layer height
 h_s = 50 mm source height
 Λ_u = 50 mm Eulerian integral length scale

Table F.1: Vertical Jet Source— Micro-Probe Data

Data Set	Location mm	σ_y mm	x/h_s	σ_y/H	σ_y/Λ_u	γ_o	i_o ms	T_{co}
CAA00701	120	11.72	2.4	0.078	0.23	0.869	0.910	39.1
CAA00600	220	21.18	4.4	0.141	0.42	0.888	0.882	27.5
CAA00500	470	29.65	9.4	0.198	0.59	0.713	1.314	31.3
CAA00400	970	37.42	19.4	0.250	0.75	0.726	1.450	50.6

Table F.2: Jet/Plume Source

Data Set	Location mm	σ_y mm	x/h_s	σ_y/H	σ_y/Λ_u	γ_o	i_o	T_{co} ms
CAA05600	30	2.44	0.6	0.016	0.05	0.994	0.329	6.5
CAA05501	60	4.90	1.2	0.033	0.10	0.977	0.452	19.3
CAA05401	120	6.33	2.4	0.042	0.13	0.931	0.603	25.8
CAA02316	220	9.85	4.4	0.066	0.20	0.728	0.990	21.0
CAA04238	470	17.91	9.4	0.119	0.36	0.640	1.297	45.6
CAA02205	970	31.71	19.4	0.211	0.63	0.588	1.455	48.1
CAA04305	1500	47.40	30.0	0.316	0.95	0.833	1.191	69.3

Table F.3: Iso-Kinetic Source

Data Set	Location mm	σ_y mm	x/h_s	σ_y/H	σ_y/Λ_u	γ_o	i_o	T_{co} ms
CAA05800	50	3.48	1.0	0.023	0.07	0.828	1.093	19.8
CAA05701	120	5.55	2.4	0.037	0.11	0.390	2.141	13.3
CAA04702	220	8.89	4.4	0.059	0.18	0.280	2.989	17.0
CAA04631	470	19.11	9.4	0.127	0.38	0.227	3.704	13.9
CAA04500	970	35.67	19.4	0.238	0.71	0.494	2.671	19.0
CAA04400	1500	46.50	30.0	0.310	0.93	0.741	1.792	39.0

Table F.4: Iso-Kinetic Facing Up Stream Source

Data Set	Location mm	σ_y mm	x/h_s	σ_y/H	σ_y/Λ_u	γ_o	i_o	T_{co} ms
CAA06600	50	6.21	1.0	0.041	0.12	0.937	0.718	35.0
CAA06500	120	10.43	2.4	0.069	0.21	0.570	1.438	20.4
CAA05200	220	13.85	4.4	0.092	0.28	0.482	1.918	19.9
CAA06000	470	22.57	9.4	0.151	0.45	0.437	2.126	29.0
CAA05100	970	37.48	19.4	0.250	0.75	0.593	1.945	29.7
CAA06700	1500	43.50	30.0	0.290	0.87	0.527	1.543	64.4

Appendix G

Gamma PDF Singularity

Cross-wind profiles of the intermittency determined by the similarity theory and the Gamma PDF exhibit a singularity in the fringes on the profile. The location of the singularity is determined by considering the intermittency predicted by the Gamma PDF. From section 5.1.5,

$$\gamma = \frac{\overline{c^2} \overline{c^2}}{2\overline{c^2}^2 - \overline{c} \overline{c^3}} \quad (\text{G.1})$$

Which is equivalent to, by inversion,

$$\frac{1}{\gamma} = 2\frac{\overline{c^2}}{\overline{c}^2} - \frac{\overline{c^3}}{\overline{c}^3} \frac{\overline{c}^2}{\overline{c^2}} \quad (\text{G.2})$$

Since, (from Wilson, Robins, Fackrell, (1985)),

$$\gamma = \frac{1 + i_p^2}{1 + i^2} \quad (\text{G.3})$$

and that,

$$(1 + i^2) = \frac{\overline{c^2}}{\overline{c}^2} \quad (\text{G.4})$$

then, substituting these into (G.2),

$$\frac{1 + i^2}{1 + i_p^2} = 2(1 + i^2) - \frac{\overline{c^3}}{\overline{c}^3} \frac{1}{(1 + i^2)} \quad (\text{G.5})$$

or

$$\frac{1}{1 + i_p^2} = 2 - \frac{\overline{c^3}}{\overline{c}^3} \frac{1}{(1 + i^2)^2} \quad (\text{G.6})$$

Rearranging,

$$2 - \frac{1}{(1 + i_p^2)} = \frac{\bar{c}_3}{\bar{c}_3^2} \frac{1}{(1 + i^2)^2} \quad (\text{G.7})$$

$$\frac{2(1 + i_p^2) - 1}{(1 + i_p^2)} = \frac{\bar{c}_2}{\bar{c}_3^2} \frac{1}{(1 + i^2)^2} \quad (\text{G.8})$$

$$\left(\frac{1 + 2i_p^2}{1 + i_p^2} \right) = \frac{\bar{c}_3}{\bar{c}_3^2} \frac{1}{(1 + i^2)^2} \quad (\text{G.9})$$

The similarity model predicts that,

$$\bar{c} = \bar{c}_o \exp \left(-\frac{y^2}{2\sigma_y^2} \right) \quad (\text{G.10})$$

$$\bar{c}^2 = \bar{c}_o^2 \exp \left(-\frac{y^2}{2\sigma_{y,2}^2} \right) \quad (\text{G.11})$$

$$\bar{c}^3 = \bar{c}_o^3 \exp \left(-\frac{y^2}{2\sigma_{y,3}^2} \right) \quad (\text{G.12})$$

then

$$\frac{\bar{c}_3}{\bar{c}_o^3} = \frac{\bar{c}_o^3}{\bar{c}_o^3} \exp \left(-\frac{y^2}{2} \left(\frac{1}{\sigma_{y,3}^2} - \frac{3}{\sigma_y^2} \right) \right) \quad (\text{G.13})$$

Similarly,

$$\frac{\bar{c}_2}{\bar{c}_o^2} = \frac{\bar{c}_o^2}{\bar{c}_o^2} \exp \left(-\frac{y^2}{2} \left(\frac{1}{\sigma_{y,2}^2} - \frac{2}{\sigma_y^2} \right) \right) \quad (\text{G.14})$$

and

$$\frac{1}{(1 + i^2)^2} = \frac{\bar{c}_o^{-4}}{\bar{c}_o^2} \exp \left(\frac{y^2}{2} \left(\frac{2}{\sigma_{y,2}^2} - \frac{4}{\sigma_y^2} \right) \right) \quad (\text{G.15})$$

Substituting (G.13) and (G.15) into (G.9),

$$\left(\frac{1 + 2i_p^2}{1 + i_p^2} \right) = \frac{\bar{c}_o^3 \bar{c}_o^{-4}}{\bar{c}_o^3 \bar{c}_o^2} \exp \left(-\frac{y^2}{2} \left(\frac{1}{\sigma_{y,3}^2} - \frac{3}{\sigma_y^2} \right) + \frac{y^2}{2} \left(\frac{2}{\sigma_{y,2}^2} - \frac{4}{\sigma_y^2} \right) \right) \quad (\text{G.16})$$

$$= \frac{\bar{c}_o^3 \bar{c}_o^{-4}}{\bar{c}_o^2} \exp \left(-\frac{y^2}{2} \left(\frac{1}{\sigma_y^2} + \frac{1}{\sigma_{y,3}^2} - \frac{2}{\sigma_{y,2}^2} \right) \right) \quad (\text{G.17})$$

$$= \mathcal{F}(y) \quad (\text{G.18})$$

Rearranging, using $\mathcal{F}(y)$,

$$1 + 2i_p^2 = (1 + i_p^2)\mathcal{F}(y) \quad (\text{G.19})$$

$$1 + 2i_p^2 = \mathcal{F}(y) + i_p^2\mathcal{F}(y) \quad (\text{G.20})$$

$$i_p^2(2 - \mathcal{F}(y)) = \mathcal{F}(y) - 1 \quad (\text{G.21})$$

Which may be expressed as,

$$i_p^2 = \frac{\mathcal{F}(y) - 1}{2 - \mathcal{F}(y)} \quad (\text{G.22})$$

Therefore, (G.22) predicts that a singularity in the Gamma PDF model will occur when $\mathcal{F}(y) = 2$.

The location this occurs at is determined by solving $\mathcal{F}(y) = 2.0$,

$$\mathcal{F}(y) = 2 = \frac{\overline{c_o^3 c_o}}{\overline{c_o^2}^2} \exp \left(-\frac{y^2}{2} \left(\frac{1}{\sigma_v^2} + \frac{1}{\sigma_{v,3}^2} - \frac{2}{\sigma_{v,2}^2} \right) \right) \quad (\text{G.23})$$

then

$$\ln \left(\frac{2\overline{c_o^2}^2}{\overline{c_o^3 c_o}} \right) = -\frac{y^2}{2} \left(\frac{1}{\sigma_v^2} + \frac{1}{\sigma_{v,3}^2} - \frac{2}{\sigma_{v,2}^2} \right) \quad (\text{G.24})$$

Solving for y ,

$$y = \sqrt{\frac{-2 \ln \left(\frac{2\overline{c_o^2}^2}{\overline{c_o^3 c_o}} \right)}{\left(\frac{1}{\sigma_v^2} + \frac{1}{\sigma_{v,3}^2} - \frac{2}{\sigma_{v,2}^2} \right)}} \quad (\text{G.25})$$

An interesting result that may be determined from (G.22) is that if $\sigma_v = \sigma_{v,2} = \sigma_{v,3}$ then $i_p = \text{constant}$.

Appendix H

Higher Order Moment Gaussian Solutions

In this appendix, a Gaussian solution for the diffusion equation is sought,

$$\frac{\partial \bar{c}^n}{\partial t} + \bar{u}_i \frac{\partial \bar{c}^n}{\partial x_i} = \frac{\partial}{\partial x_i} \left(\mathcal{D} \frac{\partial \bar{c}^n}{\partial x_i} - \overline{u'_i c^n} \right) - \varepsilon_n \quad (\text{H.1})$$

The following assumptions are used,

1. The flow is assumed steady, then $\frac{\partial \bar{c}^n}{\partial t} \rightarrow 0$.
2. The mean flow field is assumed to be either uniform over a significant period, or, to change slowly enough spatially and temporally that the plume centre-line may be defined. In essence, the flow field is assumed to be a horizontally homogeneous flow with a dominant flow in one direction,

$$\bar{u}_i = (\bar{u}, 0, 0) \quad (\text{H.2})$$

3. The turbulent flux in the x direction is small, hence its divergence, $\frac{\partial(\overline{u'_i c'^n})}{\partial x}$, is negligible.
4. The eddy diffusivities, $K_{ij,n}$, are much larger than the molecular diffusivity, $K_{ij,n} \gg \mathcal{D}$, and so the molecular transport terms may be neglected. The $K_{ij,n}$ and \mathcal{D} terms in (6.21) are additive, therefore a single diffusivity could be defined as,

$$K_{ij,n} = K_{ij,n} + \mathcal{D} \quad (\text{H.3})$$

where \mathcal{D} forms a small additive offset. In the remaining discussions \mathcal{D} will be neglected.

5. The cross-component terms, ($i \neq j$), of $K_{ij,n}$ are assumed negligible so that,

$$K_{ii,n} \rightarrow K_{yy,n}, \quad K_{zz,n}$$

These terms are also assumed to be functions of x only.

6. The dissipation term is modelled similar to Csanady (1973), but for higher order total moments as,

$$\epsilon_n = \frac{\overline{c^n}}{t_{d,n}} \quad (\text{H.4})$$

where $t_{d,n}$ is a decay time scale for the $\overline{c^n}$ fluctuations, and is assumed to be a function of down-wind distance, x , only.

Using these assumptions, (H.1) becomes,

$$\bar{u} \frac{\partial \overline{c^n}}{\partial x} = K_{yy,n} \frac{\partial^2 \overline{c^n}}{\partial x^2} - \frac{\overline{c^n}}{t_{d,n}} \quad (\text{H.5})$$

H.1 One Dimensional Solution

Consider the diffusion in y , or cross-wind direction only. The cross-component terms, ($i \neq j$), of $K_{ij,n}$ are assumed negligible so that $K_{ii,n} = K_{yy,n}$. Then (H.5) may be written as,

$$\bar{u} \frac{\partial \overline{c^n}}{\partial x} = K_{yy,n} \frac{\partial^2 \overline{c^n}}{\partial y^2} - \frac{\overline{c^n}}{t_{d,n}} \quad (\text{H.6})$$

With initial conditions that,

$$\begin{aligned} \overline{c^n}(0, y) &= f(y) \\ \overline{c^n}(x, y) &= \text{bounded as } y \rightarrow \pm\infty \end{aligned}$$

Assuming a separable solution, let $\overline{c^n} = T(x)Y(y)$. Substituting,

$$\bar{u}Y(y) \frac{\partial T}{\partial x} = K_{yy,n}T(x) \frac{\partial^2 Y}{\partial y^2} - \frac{T(x)Y(y)}{t_{d,n}} \quad (\text{H.7})$$

or, by rearranging,

$$\frac{\bar{u}}{K_{yy,n}T} \frac{dT}{dx} + \frac{1}{K_{yy,n}t_{d,n}} = \frac{d^2Y}{dy^2} \quad (\text{H.8})$$

The only way this can be true, is if both sides equal a constant, say λ . However, a positive constant can be shown to lead to an unbounded solution for large x . Therefore a negative constant must be used, such as,

$$\frac{\bar{u}}{K_{yy,n}T} \frac{dT}{dx} + \frac{1}{K_{yy,n}t_{d,n}} = \frac{d^2Y}{dy^2} = -\lambda^2 \quad (\text{H.9})$$

It is not hard to show that,

$$T(x) = \exp \left(- \left(\lambda^2 + \frac{1}{t_{d,n}K_{yy,n}} \right) \frac{K_{yy,n}}{\bar{u}} x \right) \quad (\text{H.10})$$

$$Y(y) = A \cos \lambda y + B \sin \lambda y \quad (\text{H.11})$$

where A and B are constants yet to be determined. Combining solutions $T(x)Y(y)$, in the form of an integral,

$$\bar{c}^n(x, y) = \int_0^\infty (A(\lambda) \cos \lambda y + B(\lambda) \sin \lambda y) \exp \left(- \left(\lambda^2 + \frac{1}{t_{d,n}K_{yy,n}} \right) \frac{K_{yy,n}}{\bar{u}} x \right) d\lambda \quad (\text{H.12})$$

The initial condition is satisfied by choosing,

$$\left. \begin{matrix} A(\lambda) \\ B(\lambda) \end{matrix} \right\} = \frac{1}{\pi} \int_{-\infty}^\infty f(y) \left\{ \begin{matrix} \cos \lambda y \\ \sin \lambda y \end{matrix} \right\} dy \quad (\text{H.13})$$

At $x = 0$, the initial condition has the form of a Fourier integral,

$$f(y) = \int_0^\infty (A(\lambda) \cos \lambda y + B(\lambda) \sin \lambda y) d\lambda \quad (\text{H.14})$$

Changing variables from y to ξ , then substituting (H.14) into (H.12),

$$\begin{aligned} \bar{c}^n(x, y) &= \frac{1}{\pi} \int_0^\infty \left(\int_{-\infty}^\infty f(\xi) \cos \lambda \xi d\xi \cos \lambda y \right. \\ &\quad \left. + \int_{-\infty}^\infty f(\xi) \sin \lambda \xi d\xi \sin \lambda y \right) \exp \left(- \left(\lambda^2 + \frac{1}{t_{d,n}K_{yy,n}} \right) \frac{K_{yy,n}}{\bar{u}} x \right) d\lambda \end{aligned}$$

Combining terms,

$$\begin{aligned} \bar{c}^n(x, y) &= \frac{1}{\pi} \int_0^\infty \int_{-\infty}^\infty f(\xi) (\cos \lambda \xi \cos \lambda y + \sin \lambda \xi \sin \lambda y) d\xi \\ &\quad \exp \left(- \left(\lambda^2 + \frac{1}{t_{d,n}K_{yy,n}} \right) \frac{K_{yy,n}}{\bar{u}} x \right) d\lambda \\ &= \frac{1}{\pi} \int_0^\infty \int_{-\infty}^\infty f(\xi) \cos \lambda (\xi - y) d\xi \exp \left(- \left(\lambda^2 + \frac{1}{t_{d,n}K_{yy,n}} \right) \frac{K_{yy,n}}{\bar{u}} x \right) d\lambda \end{aligned}$$

If the order of integration may be reversed, then,

$$\begin{aligned}\bar{c}^n(x, y) &= \frac{1}{\pi} \int_{-\infty}^{\infty} f(\xi) \int_0^{\infty} \cos \lambda(\xi - y) \exp \left(- \left(\lambda^2 + \frac{1}{t_{d,n} K_{yy,n}} \right) \frac{K_{yy,n}}{\bar{u}} x \right) d\lambda d\xi \\ &= \frac{\exp \left(-\frac{x}{t_{d,n} \bar{u}} \right)}{\pi} \int_{-\infty}^{\infty} f(\xi) \int_0^{\infty} \cos \lambda(\xi - y) \exp \left(-\frac{\lambda^2 K_{yy,n} x}{\bar{u}} \right) d\lambda d\xi\end{aligned}$$

The inner integral may be shown to be, (p.83 Powers (1972)),

$$\sqrt{\frac{\pi}{4 K_{yy,n} x / \bar{u}}} \exp \left(-\frac{(\xi - y)^2}{4 K_{yy,n} x / \bar{u}} \right)$$

Therefore, the concentration profile is given by,

$$\bar{c}^n(x, y) = \frac{\exp \left(-\frac{x}{t_{d,n} \bar{u}} \right)}{\sqrt{4\pi K_{yy,n} x / \bar{u}}} \int_{-\infty}^{\infty} f(\xi) \exp \left(-\frac{(\xi - y)^2}{4 K_{yy,n} x / \bar{u}} \right) d\xi \quad (\text{H.15})$$

For a point source, the initial condition $f(\xi) = C_s^n \delta(\xi)$ at $\xi = 0$, (δ is the dirac delta function). Therefore the integral in (H.15) produces,

$$\bar{c}^n(x, y) = \frac{C_s^n}{\sqrt{4\pi K_{yy,n} x / \bar{u}}} \exp \left(-\frac{x}{t_{d,n} \bar{u}} \right) \exp \left(-\frac{y^2}{4 K_{yy,n} x / \bar{u}} \right) \quad (\text{H.16})$$

Using, $2 K_{yy,n} x / \bar{u} = \sigma_{y,n}^2$, then (H.16) may be expressed as,

$$\bar{c}^n(x, y) = \frac{C_s^n}{\sqrt{2\pi} \sigma_{y,n}} \exp \left(-\frac{x}{t_{d,n} \bar{u}} \right) \exp \left(-\frac{y^2}{2\sigma_{y,n}^2} \right) \quad (\text{H.17})$$

Since x/\bar{u} is travel time, t_t , and Netterville (1979) has found that $t_d \propto t_t$, then t_t/t_d is expected to be a weak function of x or approximately constant. The exponential term is, therefore approximately a constant value. The effect of the decay time reduces the centre-line concentrations at each location by a constant fraction.

The cross-wind variation of \bar{c}^n in (H.16) is a Gaussian profile.

H.2 Axisymmetric Solution

The higher order moment budget equation may be expressed as,

$$\bar{u} \frac{\partial \bar{c}^n}{\partial x} = K_{r,n} \nabla^2 \bar{c}^n - \frac{\bar{c}^n}{t_{d,n}} \quad (\text{H.18})$$

Where ∇_1^2 is the Laplacian in the y and z directions. This assumes the diffusion in the x direction is small. Following Csanady (1973), if the solution is assumed axisymmetric, then the plume spread $\sigma_{r,n} = \sigma_{y,n} = \sigma_{z,n}$, and in nondimensional form, the cross-plume dimension is $\xi = r/\sigma_{r,n} = \sqrt{y^2 + z^2}/\sigma_{r,n}$. A self-similar profile is assumed, with the form,

$$\bar{c}^n = c_o^n f(\xi) \quad (\text{H.19})$$

Continuity requires that the source strength, q_s , be constant at any down-wind location,

$$\frac{q_s}{\bar{u}} = \int \int \bar{c} \, dA = \text{const. } c_o \sigma_r^2 \quad (\text{H.20})$$

therefore,

$$\frac{d}{dx} \left(\frac{q_s}{\bar{u}} \right) = 0 = \frac{d}{dx} (\text{const. } c_o \sigma_r^2) \quad (\text{H.21})$$

$$= 2c_o \sigma_r \frac{d\sigma_r}{dx} + \sigma_r^2 \frac{dc_o}{dx} \quad (\text{H.22})$$

or

$$\frac{dc_o}{dx} = -\frac{2c_o}{\sigma_r} \frac{d\sigma_r}{dx} \quad (\text{H.23})$$

Substitution of these into (H.18), using cylindrical coordinates,

$$\nabla_1^2 = \frac{d^2}{d\xi^2} + \frac{1}{\xi} \frac{d}{d\xi} \quad (\text{H.24})$$

$$\begin{aligned} \frac{\partial \bar{c}^n}{\partial x} &= f(\xi) n c_o^{n-1} \frac{dc_o}{dx} + c_o^n \frac{df}{d\xi} \frac{\partial \xi}{\partial x} \\ &= -\frac{2nc_o^n}{\sigma_r} \frac{d\sigma_r}{dx} f(\xi) - \frac{c_o^n}{\sigma_r} \frac{d\sigma_r}{dx} \xi \frac{df}{d\xi} \end{aligned} \quad (\text{H.25})$$

Then (H.18) becomes,

$$\frac{d^2 f}{d\xi^2} + \frac{1}{\xi} \frac{df}{d\xi} + \frac{\bar{u} \sigma_r}{K_{r,n}} \frac{d\sigma_r}{dx} \left(2nf + \xi \frac{df}{d\xi} \right) - \frac{\sigma_R^2}{K_{r,n} t_{d,n}} f = 0 \quad (\text{H.26})$$

In order for self similar forms to be produced, the two nondimensional terms must be independent of x . For homogeneous shear-free turbulence, assume that $K_{r,n}$ for all higher orders of magnitude follow, (based on $K_{r,1} = \frac{\bar{u}}{2} \frac{d\sigma_r^2}{dx}$, Csanady (1973) p.235),

$$K_{r,n} = \frac{\bar{u}}{2} \frac{d\sigma_{r,n}^2}{dx} \quad (\text{H.27})$$

Using $2K_{r,n}x/\bar{u} = \sigma_{r,n}^2$, the first nondimensional term is,

$$\frac{\bar{u}\sigma_r}{K_{r,n}} \frac{d\sigma_r}{dx} = \frac{K_{r,1}}{K_{r,n}} = \frac{\sigma_r^2}{\sigma_{r,n}^2} = \alpha_1 \quad (\text{H.28})$$

From section 6.2.2 the ratio $\sigma_{r,n}/\sigma_r \approx 0.9$, and it is observed that, except very near the source, $\sigma_{r,n}/\sigma_r \approx \text{constant}$.

Assume that,

$$\frac{\sigma_r^2}{K_{r,n}t_{d,n}} = \alpha \quad (\text{H.29})$$

then (H.26) becomes,

$$\frac{d^2f}{d\xi^2} + \left(\frac{1}{\xi} + \alpha_1\xi\right) \frac{df}{d\xi} + (2n - \alpha)f = 0 \quad (\text{H.30})$$

If a Gaussian solution is assumed for $f(\xi) = e^{-\xi^2/2}$, then

$$\frac{df}{d\xi} = -\xi e^{-\xi^2/2} \quad (\text{H.31})$$

$$\frac{d^2f}{d\xi^2} = \xi^2 e^{-\xi^2/2} - e^{-\xi^2/2} \quad (\text{H.32})$$

Substituting these into (H.30) produces an expression for α ,

$$\alpha = 2n\alpha_1 - 2 + (1 - \alpha_1)\xi^2 \quad (\text{H.33})$$

Csanady (1973) observes that for sufficiently large plume size,

$$\sigma_r^2 = 2 \frac{u'}{\bar{u}} x_o (x - x_o) \quad (\text{H.34})$$

then, his variance decay time scale varies like,

$$t_d = \frac{2}{\bar{u}\alpha_2} (x - x_o) \quad (\text{H.35})$$

Where α_2 is a constant, with a value of approximately 2 or 3. This linear variation of the decay time with down-wind location was observed by Netterville (1979) in his wind tunnel experiments. Following, the same arguments, the decay time scale for the c^n fluctuations has a similar form given by,

$$t_{d,n} = \frac{2}{\bar{u}\alpha} (x - x_o) \quad (\text{H.36})$$

where $\alpha = 2n\alpha_1 - 2 + (1 - \alpha_1)\xi^2$. Since α_1 has a typical value near 1, α is only a weak function of the cross-wind plume location, ξ . On the centre-line, $\xi = 0$, then the decay time scale has a linear growth with travel distance from the source.

H.3 Order of magnitude Analysis for ϵ_n

In this section, an order of magnitude analysis is performed to determine if the molecular dissipation term in the higher order moment budget equation can be neglected, compared to the eddy diffusivity term. The first analysis examines the terms in the second moment dissipation term. The second analysis uses a dissipation model to examine the scaling.

The budget equation for the n^{th} higher order moment of $\overline{c^n}$ is given by,

$$\frac{\partial \overline{c^n}}{\partial t} + \overline{u_i} \frac{\partial \overline{c^n}}{\partial x_i} = \frac{\partial}{\partial x_i} \left(K_{ij,n} \frac{\partial \overline{c^n}}{\partial x_j} \right) - \epsilon_n \quad (\text{H.37})$$

Recall that the cross-component terms, ($i \neq j$), of $K_{ij,n}$ are assumed negligible so that,

$$K_{ii,n} \rightarrow K_{yy,n}, \quad K_{zz,n}$$

If the dissipation term is to be neglected, then the eddy diffusivity term must be sufficiently large in comparison,

$$\frac{\partial}{\partial x_i} \left(K_{ij,n} \frac{\partial \overline{c^n}}{\partial x_j} \right) \gg \epsilon_n \quad (\text{H.38})$$

or for example,

$$K_{yy,n} \frac{\partial^2 \overline{c^n}}{\partial x_i^2} \gg \epsilon_n \quad (\text{H.39})$$

The mean concentration moment gradients scale with the size of the plume,

$$\frac{\partial \overline{c^n}}{\partial x_i} \approx \frac{\overline{c^n}}{\sigma_n} \quad (\text{H.40})$$

The eddy diffusivity term is a large scale parameter, and may be scaled as,

$$K_{yy,n} \approx u' \Lambda_u \quad (\text{H.41})$$

Where Λ_u is the Eulerian length scale of the velocity fluctuations and u' is the fluctuation velocity.

If the dissipation is modelled as,

$$\epsilon_n = \frac{\overline{c^n}}{t_d} \quad (\text{H.42})$$

Where t_d is scaled by as suggested by Sykes, Lewellen and Parker (1984) as,

$$\epsilon_n \approx \frac{B_1 u' \overline{c^n}}{\sigma_{i,n}} \quad (\text{H.43})$$

Where σ_i is the instantaneous plume width and B_1 is a constant with a value near 0.5. If the dissipation term was to be assumed negligible, then according to (H.39),

$$\left(u' \Lambda_u \right) \frac{\overline{c^n}}{\sigma_n} \gg \frac{B_1 u' \overline{c^n}}{\sigma_{i,n}} \quad (\text{H.44})$$

This may be simplified by rearrangement to,

$$\left(\frac{\sigma_{i,n}}{\sigma_n} \right) \left(\frac{\Lambda_u}{\sigma_n} \right) \gg B_1 \quad (\text{H.45})$$

Alternatively, if the dissipation is assumed to be an in-plume function of the turbulent flow only, then the conditional higher order moment should be used in (H.26), such as,

$$\epsilon_{n,p} = \frac{\overline{c_p^n}}{t_d} \quad (\text{H.46})$$

However, the total amount of dissipation in the budget equation is determined by multiplying by the fraction of time that the plume is present,

$$\epsilon_n = \gamma \epsilon_{n,p} = \gamma \frac{\overline{c_p^n}}{t_d} \quad (\text{H.47})$$

However, since,

$$\gamma = \frac{\overline{c_p^n}}{\overline{c^n}} \quad (\text{H.48})$$

Then

$$\epsilon_n = \frac{\overline{c^n}}{t_d} \quad (\text{H.49})$$

Which is equivalent to (H.42).

The condition set by (H.45) indicates that since,

$$\begin{aligned} B_1 &\approx 0.5 \approx \mathcal{O}(1) \\ \frac{\sigma_{i,n}}{\sigma_n} &\approx \mathcal{O}(1) \end{aligned}$$

Then (H.45) becomes,

$$\frac{\Lambda_u}{\sigma_n} \gg 1 \quad (\text{H.50})$$

In the water channel, near the source $\Lambda_u/\sigma_n \sim 20$ and far down-wind $\Lambda_u/\sigma_n \sim 1$. Therefore, this order of magnitude analysis shows that dissipation term can probably not be neglected in comparison to the eddy diffusivity diffusion term.

The model for dissipation, given by (H.42), is independent of the molecular diffusivity, \mathcal{D} . This may be adequate when \mathcal{D} is near unity (water vapour into air for example), however, in the water channel where \mathcal{D} is very small the dissipation given by,

$$\epsilon_n = \mathcal{D} \overline{\left| \frac{\partial c}{\partial x_i} \right|^2} \quad (\text{H.51})$$

may be negligible.

The order of magnitude analysis presented here does not conclusively support neglecting the molecular dissipation. The dissipation term should probably, therefore, be accounted for in the budget equation.